Studies of event shape observables with the OPAL detector at LEP

By

Matthew Thomas Ford

of

Trinity College

A dissertation submitted to the University of Cambridge
for the degree of Doctor of Philosophy

February 2004

Declaration

This dissertation is the result of my own work, and includes nothing which is the outcome of work done in collaboration except where specifically indicated in the text.

Matthew Ford

Studies of event shape observables
with the OPAL detector at LEP

Matthew T. Ford

Abstract

During the years 1989–2000, the LEP experiments at CERN studied electron-positron annihilation in the energy range $\sqrt{s} = 91$–209 GeV. Data from the four detectors have been used to test the Standard Model of particle physics, to measure its parameters, and to constrain the possibilities for new phenomena.

In quark-antiquark pair production at LEP, many features of the hadronic final state can be predicted by quantum chromodynamics (QCD). Using data collected by the OPAL experiment, we present the statistical distributions of fourteen "event shape observables," which describe the inclusive kinematic properties of events producing three or more jets. For six of these observables, we compare the measured distributions with those calculated in perturbative QCD. By optimising the agreement between theory and data, we measure the strong coupling α_S at a range of energy scales. We also test the predictions of three Monte Carlo event generators, for all fourteen observables.

Over the years since the LEP experiments began operating, many similar analyses have been published, and have contributed to the world average measurements of α_S. However, several improvements have now been made, both in the theoretical calculations and in the experimental analysis techniques. We therefore present a complete reanalysis of the OPAL data, over the full range of LEP collision energies. Particular attention is given to the estimation of uncertainties, including the large contribution due to uncalculated higher-order terms of the theory predictions.

In collaboration with the LEP QCD Working Group, we have combined the α_S measurements obtained from event shape observables by all four experiments. Detailed investigations were undertaken to ensure consistent implementation of the theoretical predictions and uncertainty estimates, and to take account of correlations between measurements. Our combined preliminary value for the strong coupling at the Z^0 mass scale, including contributions from measurements at higher energies, is

$$\alpha_S(M_Z) = 0.1201 \pm 0.0003 \text{ (stat.)} \pm 0.0048 \text{ (syst.)} \quad .$$

Our result is in good agreement with the current world average.

Acknowledgements

First and foremost I would like to thank my supervisor, David Ward, for his dedicated support and encouragement throughout my time working on OPAL, and for his thorough reading of this document. His advice has always been dependable, and much appreciated.

I also owe considerable gratitude to my collaborators in the OPAL and LEP QCD Working Groups. Within OPAL my work has profited from the experience of Stefan Kluth[1], who developed many of our current techniques and software tools during his PhD research with David Ward in the early 1990s. In the latter stages of my OPAL analysis work, correspondence with Mike Donkers[2] and Christoph Pahl[1] led to some invaluable discussion and cross-checking of our results. Throughout my time on OPAL, our quarterly plenary meetings have provided a friendly environment in which to present new results and ideas, and to receive constructive comments and questions; I would like to thank our Physics Coordinators and plenary organisers for making this possible.

My involvement with the LEP QCD Working Group has enabled me to participate in a unique and rewarding project, combining results from the four experiments. I would like to thank all members of the group for entrusting a major part of this work of this work to me. In particular, our group convener, Roger Jones[3], has been responsible for the efficient organisation and documentation of countless meetings and telephone conferences, which have maintained the focus and momentum of our work. I am also indebted to Hasko Stenzel[4], Daniel Wicke[5] and Gavin Salam[6] for many enthusiastic discussions, and for the work they have contributed to our LEP α_S measurements.

For financial support I am obliged to PPARC, who provided three years of generous funding: this included travel expenses, allowing me to attend many productive meetings at CERN. In addition, I would like to thank the Cavendish Laboratory in Cambridge for awarding me a J.J. Thomson studentship, which provided a full extra term of funding. I am also grateful to Christ's College for employing me as a

Contents

Introduction

Since the end of the nineteenth century, several revolutions have occurred in our understanding of fundamental physics. Firstly, we have progressed from a world in which the atom was considered indivisible, to a scenario where both the nucleus and the nucleon are composite objects. Secondly, the discoveries of relativity and quantum mechanics have redefined our interpretation of space, time, causality and observation. The formulation of relativistic quantum mechanics led to a remarkable explanation for the origin of 'spin', and for the Exclusion Principle, which plays a central rôle in atomic physics and chemistry; it also predicted the existence of an antiparticle for every particle in nature. By quantising the wavefunctions representing elementary particles, and by applying the principle of *local gauge invariance* motivated by classical electromagnetism, a model emerged to explain three of the four known forces of nature. The electromagnetic and weak interactions were unified to form a single electroweak field theory, in which the symmetry of the two forces is spontaneously broken; the strong interaction, which accounts for the internal binding of atomic nuclei, was described by a separate theory called quantum chromodynamics (QCD).

The existence of a 'hidden' quantum degree of freedom, which we now recognise as colour, was initially proposed in 1964 on the basis of baryon spectroscopy [1]: baryons were suspected to contain three identical 'quarks' of half-integral spin, but in order to antisymmetrise the baryon wavefunction, one would have to introduce a new quantum number. In 1972 a non-Abelian SU(3) gauge theory was developed to describe the dynamics of colour [2]; this theory, in which the strong interaction of quarks is mediated by eight gauge bosons called gluons, became known as QCD. As in any quantum field theory, the interaction vertices in QCD are subject to an infinite series of perturbative corrections: one is therefore forced to *renormalise* the theory, resulting in a coupling strength α_S which varies as a function of the

1

interaction energy. It was proven in 1973 that the strength of QCD interactions must decrease with increasing energy scales [3]; this is in contrast to quantum electrodymanics, in which the electromagnetic coupling α is largest in high-energy interactions. The phenomenology predicted in QCD was therefore very different from that of electromagnetism.

Experiments have established conclusively the need for exactly three quark colours [4]. The decay rate of the π^0 meson into two photons is predicted to scale quadratically with the number of colours N_c; measurements as early as 1963 [5] were sensitive to this effect. More recently, the LEP Collaborations have measured the partial width for hadronic decays of the Z^0 boson [6], which varies linearly with N_c. Compared with the electroweak theory, however, which has now been tested and verified to a high degree of precision,[1] the detailed dynamics of colour presents more difficulties. The established technique of perturbation theory is not applicable to low-energy processes in QCD, such as those responsible for the binding of hadrons. Furthermore, the complicated gauge structure and large coupling strength have limited the precision of most high-energy predictions to the level of a few percent. Nonetheless, experiments have made significant progress to affirm the place of QCD within the Standard Model. Since 1979, when the first gluon jets were observed in e^+e^- collisions at PETRA [7], the large samples of high-energy collision data at LEP and HERA have confirmed a wide variety of QCD predictions.

In experimental work, we cannot directly observe the quarks and gluons participating in hard interactions. The particles seen in our detectors are hadrons, produced by low-energy fragmentation processes which cannot be predicted in perturbation theory. One must therefore define physical observables, based on these final-state hadrons, to probe the 'perturbative' stage of the event. In this work, we will use data from the OPAL detector to study the distributions of fourteen *event shape observables*, which offer sensitivity to the QCD interactions in e^+e^- annihilation events. By fitting experimental data to the theoretical predictions, we will then measure the strong coupling constant α_S.

The analysis presented here represents a continuation of previous OPAL studies [8–11], which have measured eleven of the event shape observables at centre-of-mass collision energies in the range 91–189 GeV. Several improvements have been

---

[1]The Higgs mechanism is the only aspect of the electroweak theory *not* to have been confirmed so far. According to the Standard Model, this is responsible for symmetry-breaking between the weak and electromagnetic gauge fields.

introduced since the original results were published, however, both in the theoretical predictions and in our experimental methods. We have therefore performed a complete re-analysis of the OPAL data, in the energy range 91–207 GeV. These results will supersede the published measurements where applicable.[2]

As the LEP experiments have now ceased operating, we must consider how to extract global results from the complete dataset. By combining measurements of α_S obtained at different centre-of-mass energies, we can not only test the predicted energy-dependence of the strong interaction, but can also calculate a single result for α_S at a fixed energy scale. The uncertainties is this measurement can be further reduced by combining fits from different experiments, and from different event shape observables. Our final result will therefore be a LEP average value for α_S obtained from e^+e^- event shape measurements.

The dissertation is organised as follows:

Chapter 1 introduces the Standard Model of particle physics, with a particular emphasis on the theory of QCD. We define the event shape observables to be measured in our analysis, and describe the techniques used in perturbative QCD to predict their distributions. The theoretical uncertainties of our α_S measurements are then discussed, using a new approach developed in collaboration with the LEP QCD Working Group [12]. We also describe the Monte Carlo simulation models used to account for non-perturbative effects in our analysis. Finally we list a few of the other methods by which QCD can be studied experimentally.

Chapter 2 gives an historical and technical overview of the LEP collider, and of the OPAL detector.

Chapter 3 describes our measurements of event shape observables using multi-hadronic events at OPAL, and our fits to the theoretical predictions. We also list the areas in which our new analysis differs from the published measurements, and compare the old and new values of α_S where appropriate. We finally present a combined OPAL measurement of α_S, using the methods to be discussed in Chapter 4.

---

[2]It is possible that further small modifications will occur before final publication. The results given in this work should therefore be regarded as preliminary.

Chapter 4 explains the procedure for combining α_S values obtained at different energy scales, with different observables and different experiments. We first describe an investigation into the consistency of the analysis procedures used by the four LEP Collaborations. We then discuss the estimation of uncertainties and correlations in the α_S measurements, and the use of the covariance matrix to extract a weighted mean. We explain in general terms why the most naïve choice of correlations leads to an unreliable fit; a more suitable covariance matrix is then proposed and tested. Finally we present the combined α_S values from all LEP event shape measurements, and from various subsets.

Chapter 5 summarises our final conclusions, and the outlook for future extensions to the work.

Chapter 1

Theoretical background

We begin this chapter by presenting a brief overview of quantum chromodynamics (QCD), and its place within the Standard Model. In Section 1.4 we discuss the specific application of QCD to the study of hadron production in e^+e^- annihilation. We define in Section 1.5 a set of event shape observables, which will form the basis for our experimental work; Sections 1.6–1.8 will discuss the theoretical predictions for some of these observables, and their associated uncertainties. In Section 1.9, we introduce the models implemented in three Monte Carlo programs to simulate the non-perturbative aspects of QCD. Finally, Section 1.10 will give an overview of other techniques used to measure the coupling α_S and to test the validity of QCD.

1.1   The elements of the Standard Model

In our present understanding of particle physics, the elementary building-blocks of matter comprise twelve spin-$\frac{1}{2}$ fermions and their twelve antiparticles. The particles can be grouped into three families, each containing two quarks, one charged lepton and one neutrino, as shown in Table 1.1. In the absence of interactions, each fermion is represented by the quanta of a field ψ, satisfying the Dirac Equation

$$(i\gamma^\mu\partial_\mu - m)\,\psi \;=\; 0 \quad,\tag{1.1}$$

which corresponds to the Lagrangian density

$$\mathcal{L}_{\mathrm{D}} \;=\; \bar{\psi}\,(i\gamma^\mu\partial_\mu - m)\,\psi \quad.\tag{1.2}$$

Quarks		Leptons	
Down (d)	Up (u)	Electron (e^-)	Electron neutrino (ν_e)
$Q = +2/3$	$Q = -1/3$	$Q = -1$	$Q = 0$
$m = 5.0–8.5$ MeV	$m = 1.5–4.5$ MeV	$m = 0.511$ MeV	$m < 3$ eV (95% CL)
Strange (s)	Charm (c)	Muon (μ^-)	Muon neutrino (ν_μ)
$Q = +2/3$	$Q = -1/3$	$Q = -1$	$Q = 0$
$m = 80–155$ MeV	$m = 1.0–1.4$ GeV	$m = 106$ MeV	$m < 0.19$ MeV (90% CL)
Bottom (b)	Top (t)	Tau (τ^-)	Tau neutrino (ν_τ)
$Q = +2/3$	$Q = -1/3$	$Q = -1$	$Q = 0$
$m = 4.0–4.5$ GeV	$m = 174 \pm 5$ GeV	$m = 1.78$ GeV	$m < 18$ MeV (95% CL)

Table 1.1: The elementary fermions of the Standard Model. The charge Q for each particle is expressed in units of the proton charge. The masses m are taken from Ref. [13].

The spinor ψ has four components, which collectively correspond to the helicity states of the particle and antiparticle.

Interactions are explained in the Standard Model by imposing *local gauge symmetries* on the fields: an example will be described in the next section. These symmetries require the existence of four vector fields, whose quanta are the spin-1 gauge bosons listed in Table 1.2. Additional terms are introduced into the Dirac Lagrangian, leading to interactions between the fermions and gauge fields, and between the gauge fields themselves. The photon and the $W^\pm$ and Z^0 bosons are responsible for the electroweak interaction, and the gluon is the carrier of the strong interaction. Although a further gauge boson, the 'graviton' has been postulated, no complete theory of gravity currently exists within the Standard Model.

One additional particle, the scalar Higgs boson (H^0), is predicted to exist, but has not yet been observed conclusively. The Higgs field introduces a *spontaneously broken symmetry* into the Standard Model, thereby offering an explanation for the non-zero masses of the $W^\pm$ and Z^0 bosons. It also accounts for the mass terms in the Dirac Lagrangian, but does not predict the masses of the individual fermions.

Comprehensive discussions of the Standard Model can be found in many textbooks, such as Refs. [14,15]. A more detailed treatment of QCD is given in Ref. [4].

	Charge	Mass (GeV)	Direct couplings to other particles						
			Quarks	$e^\pm$, $\mu^\pm$, $\tau^\pm$	ν_e, ν_μ, ν_τ	γ	$W^\pm$	Z^0	g
Photon (γ)	0	0	•	•			• †	†	
$W^\pm$ bosons	±1	80.4	•	•	•	• †	†	• †	
Z^0 boson	0	91.2	•	•	•	†	• †		
Gluon (g)	0	0	•						• †

Table 1.2: The gauge bosons of the Standard Model, and a summary of their interactions. Couplings indicated with bullets (•) arise from trilinear terms in the Lagrangian, while those with daggers (†) are quartic; when expressed in Feynman diagram notation, these correspond respectively to 'three-point' and 'four-point' vertices. The direct interaction of the photon and Z^0 boson is possible only via the quartic $WWZ\gamma$ vertex.

1.2 The Lagrangian of QCD

In QCD the six quark flavours are represented by quantum fields $q = \{u, d, s, c, b, t\}$, which behave identically, apart from their differing masses, and do not directly interact with one another. The quark fields have an extra degree of freedom known as colour; each of the three components q_a ($a = 1, 2, 3$) is a Dirac spinor. Treating them as non-interacting fermion fields, the Dirac Lagrangian would therefore become

$$\mathcal{L} = \sum_a \bar{q}_a \left(i\gamma^\mu \partial_\mu - m \right) q_a \quad . \tag{1.3}$$

We now consider the effect of a unitary "phase transformation" applied to the three-component colour vector q

$$q_a \rightarrow q'_a = \sum_b \Omega_{ab} q_b \equiv \sum_b \exp\left[i \sum_A \alpha^A \lambda_{ab}^A \right] q_b \quad , \tag{1.4}$$

where the 3×3 Hermitian matrices λ^A ($A = 1, 2, \ldots 8$) are the generators of the Lie group SU(3), and α^A are eight arbitrary constants. The Lagrangian given in Equation (1.3) is invariant under this global transformation, due to the unitary property of the matrices; this is analogous to the invariance of the Dirac Lagrangian under the phase transformation $\psi \rightarrow \psi' = \psi e^{i\phi}$.

Our global colour transformation demonstrates the conservation of colour in a non-interacting theory, but does not introduce any physical dynamics. The theory of QCD is derived by requiring the invariance of the Lagrangian under *local* SU(3) colour transformations: instead of choosing the same unitary matrix,

$\Omega = \exp[i \sum_A \alpha^A \lambda^A]$, at all points in space and time, we allow the coefficients α^A to vary, giving

$$q_a \rightarrow q'_a = \sum_b \Omega_{ab}(x) q_b \equiv \sum_b \exp\left[i \sum_A \alpha^A(x) \lambda^A_{ab}\right] q_b \ . \tag{1.5}$$

Substituting this transformed quark field into Equation (1.3), we find that the Lagrangian is no longer invariant, because the space-time derivatives act on the coefficients $\alpha^A(x)$. To restore the invariance of the Lagrangian, we must first replace the partial derivative ∂_μ with a *covariant derivative*

$$(D_\mu)_{ab} = \partial_\mu \delta_{ab} + \frac{ig}{2} \sum_A \mathcal{A}^A_\mu \lambda^A_{ab} \ , \tag{1.6}$$

where we have introduced eight *gauge fields* $\mathcal{A}^A$, each with four space-time components μ; the free parameter g is a universal coupling constant. The Lagrangian now becomes

$$\mathcal{L} = \sum_{a,b} \bar{q}_a \left(i\gamma^\mu D_\mu - m\right)_{ab} q_b \tag{1.7}$$

$$\equiv \sum_a \bar{q}_a \left(i\gamma^\mu \partial_\mu - m\right) q_a + \frac{ig}{2} \sum_{a,b} \sum_A \bar{q}_a \left(\gamma^\mu \mathcal{A}^A_\mu\right) \lambda^A_{ab} q_b \ . \tag{1.8}$$

In the last line, we have decomposed $\mathcal{L}$ into two contributions: the first is the Dirac Lagrangian for three non-interacting components of a fermion field, and the second introduces interactions between the gauge fields and the quarks. The quanta of the eight fields $\mathcal{A}^A$ are called gluons, and are responsible for the observed strong interactions of quarks. To complete the process of establishing local gauge invariance, the transformation properties of the gluon fields must be chosen such that the covariant derivative $\sum_b (D_\mu)_{ab} q_b$ transforms in the same way as the quark field itself,

$$\sum_b (D'_\mu)_{ab} q'_b = \sum_{b,c} \Omega_{ab}(x) (D_\mu)_{bc} q_c \ . \tag{1.9}$$

This is achieved with the relationship

$$\sum_A \mathcal{A}'^A_\mu \lambda^A = \Omega(x) \left[\sum_A \mathcal{A}^A_\mu \lambda^A\right] \Omega^{-1}(x) + \frac{2i}{g} (\partial_\mu \Omega(x)) \Omega^{-1}(x) \ , \tag{1.10}$$

where we have suppressed the colour indices of the λ^A and $\Omega(x)$ matrices.[1]

---

[1] A simpler transformation law, of the form $\mathcal{A}'^A = \mathcal{A}^A + \delta \mathcal{A}^A$, exists when the gauge transformation $\Omega(x)$ differs only infinitesimally from from the identity matrix.

One further contribution must be inserted in the Lagrangian, to specify the equations of motion for the gluon fields. In quantum electrodynamics, the Lagrangian for the photon field A is given by

$$\mathcal{L}_{\text{photon}} = -\frac{1}{4} F_{\mu\nu} F^{\mu\nu} \quad , \tag{1.11}$$

where F is simply a quantised form of Maxwell's electromagnetic field strength tensor

$$F_{\mu\nu} = \partial_\mu A_\nu - \partial_\nu A_\mu \quad . \tag{1.12}$$

Applying the Euler-Lagrange Equations to $\mathcal{L}_{\text{photon}}$ gives the familiar Maxwell Equations, governing the internal dynamics of the field. An analogous term appears in the Lagrangian of QCD,

$$\mathcal{L}_{\text{gluon}} = -\frac{1}{4} \sum_A F^A_{\mu\nu} F^{\mu\nu}_A \quad , \tag{1.13}$$

but here the eight field strength tensors for the gluons are

$$F^A_{\mu\nu} = \partial_\mu \mathcal{A}^A_\nu - \partial_\nu \mathcal{A}^A_\mu - g \sum_{B,C} f^{ABC} \mathcal{A}^B_\mu \mathcal{A}^C_\nu \quad , \tag{1.14}$$

where the structure constants f^{ABC} are defined by the commutation relations of the SU(3) generators, $\left[\lambda^A, \lambda^B\right] = 2i f^{ABC} \lambda^C$. The last term of Equation (1.14), which is derived by imposing local SU(3) gauge symmetry on the octet of gluon fields, arises because the gauge transformations of QCD do not commute. When we expand out the product $F^A_{\mu\nu} F^{\mu\nu}_A$ in Equation (1.13), we find an array of terms containing products of two, three and four gluon fields. The three- and four-gluon terms in the Lagrangian give rise to the self-interaction of the gluon field, which has no analogue in QED.

Collecting all terms together, we arrive at the complete Lagrangian density of QCD: [2]

$$\mathcal{L}_{\text{QCD}} = \sum_a \bar{q}_a \left(i\gamma^\mu \partial_\mu - m\right) q_a + \frac{ig}{2} \sum_{a,b} \sum_A \bar{q}_a \left(\gamma^\mu \mathcal{A}^A_\mu\right) \lambda^A_{ab} q_b - \frac{1}{4} \sum_A F^A_{\mu\nu} F^{\mu\nu}_A \quad . \tag{1.15}$$

---

[2] When performing practical calculations, some further terms need to be inserted to fix the gauge. These are discussed in Ref. [4].

It is beyond the scope of this work to derive the Feynman rules associated with the QCD Lagrangian, or indeed to discuss the formal interpretation of Feynman diagrams; a list of the QCD Feynman rules can be found in Ref. [4]. However, a quick examination of the terms in the Lagrangian shows that the permitted vertices are as shown in Figure 1.1.
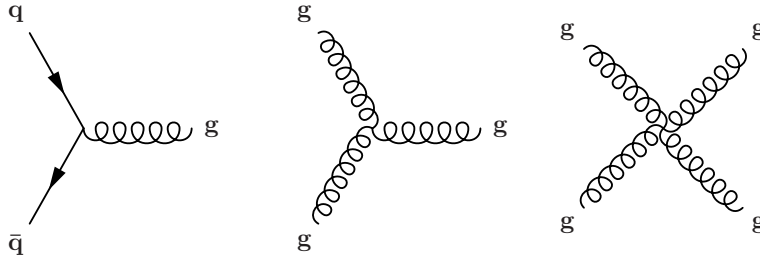
Figure 1.1: Feynman vertices in QCD

Up to this point, the coupling constant of QCD has been denoted g. From now on, however, we will use the related quantity $\alpha_{\mathrm{S}} = g^2/4\pi$.

The idea of local gauge invariance under non-Abelian transformations was first proposed by Yang and Mills in 1954 [16], and has subsequently provided the foundation for both the strong and electroweak field theories of the Standard Model; the simpler Abelian case gave us quantum electrodynamics.

1.3   Renormalisation and the running coupling

When using perturbation theory to calculate predictions for a physical observable in a quantum field theory, one must typically sum a series of Feynman diagrams corresponding to the appropriate initial and final states. In Figure 1.2, for example, diagram (b) is a higher-order contribution to the electromagnetic scattering process shown in diagram (a). Unfortunately, however, most Feynman diagrams with loops lead to divergent integrals; whereas diagram (b) should introduce a small correction to the cross section, it appears that it will instead cause a finite cross section to become infinite! This problem was first identified in QED, and was solved by the principle of renormalisation.

The apparent paradox of the infinite loop integrals can addressed in QED by a redefinition of the fine-structure constant, α_{em}. One must remember that no laboratory experiment can distinguish between the two processes shown in Figure 1.2,
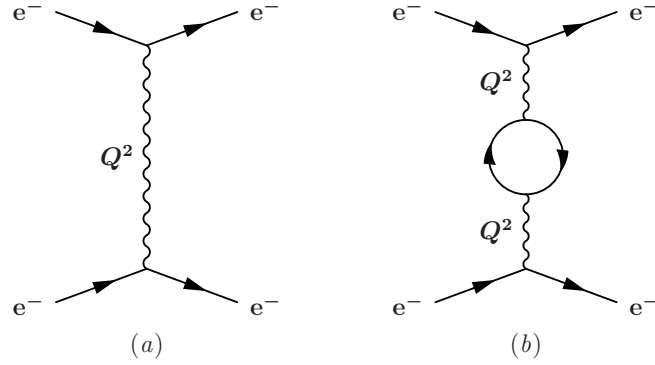
Figure 1.2: Leading QED contributions to the scattering of two electrons

and therefore any observations of electromagnetic scattering will already 'include' the higher-order contributions. Remarkably enough, it can be shown that the effect of these corrections is to modify the effective *coupling strength* of the photon (albeit by an infinite factor), without altering its detailed properties as a photon. Hence we should not try to build Feynman diagrams out of the original 'bare' photons, but instead use the 'ready-assembled' photons provided by nature, which include all of the loop diagrams such as Figure 1.2(b).

We cannot, however, ignore the loop integrals altogether. Even though the higher-order diagrams contain divergent integrals, they remarkably have a *finite* dependence on the squared four-momentum Q^2 of the exchanged photon. Consequently, if two experiments study photons of different Q^2, they will observe different effective coupling strengths: photons of higher virtuality interact more strongly.

An analogous situation arises in QCD: the two loop diagrams in Figure 1.3 contain divergent integrals, which can be absorbed into a redefinition of the gluon coupling strength α_S. There is a very significant difference between the QCD and QED cases, however. The sign of the Q^2-dependence for the gluon self-interaction loop in Figure 1.3(c) is opposite to that for the fermion loops in Figures 1.2(b) and 1.3(b). As a consequence of this extra diagram, which is not present in QED, the strong coupling α_S *decreases* at high virtualities. Conversely, α_S grows without limit as the virtuality of the gluon approaches zero. Therefore quarks will appear to be "asymptotically free" in very high energy interactions, while at low energy scales their interactions are so strong that free quarks are never observed. This low-energy behaviour of QCD prevents the reliable use of perturbation theory at
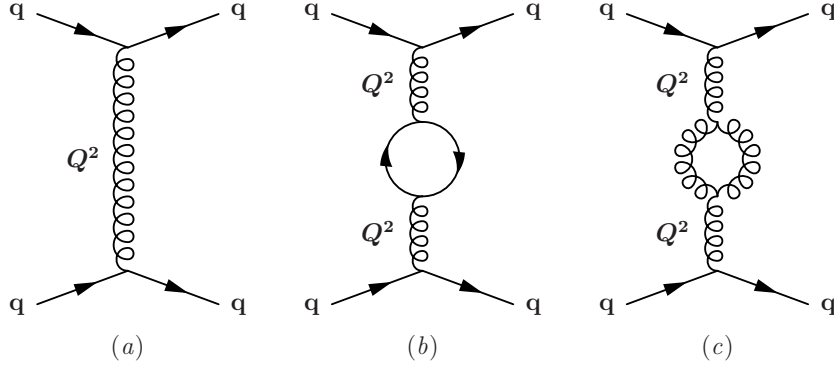
Figure 1.3: Leading QCD contributions to the scattering of two quarks

scales below a few GeV; in particular, the process of *hadronisation*, by which free quarks are converted into observable hadrons, is not well understood.

The scale-dependence of the "running coupling" $\alpha_S(Q)$ is given by the Renormalisation Group Equation (RGE):

$$Q\frac{\partial \alpha_S}{\partial Q} = 2\beta(\alpha_S) \quad , \tag{1.16}$$

where the β-function is of the form

$$\beta(\alpha_S) = -\frac{\beta_0}{4\pi}\alpha_S^2 - \frac{\beta_1}{8\pi^2}\alpha_S^3 - \frac{\beta_2}{128\pi^3}\alpha_S^4 + \mathcal{O}(\alpha_S^5) \quad . \tag{1.17}$$

The coefficients β_n are functions of the number of kinematically accessible quark flavours, and are listed in Ref. [13]. To first order, the solution of the RGE for N_f flavours[3] can be written as

$$\alpha_S(Q) = \alpha_S(Q_0)\left[1 - \frac{\alpha_S(Q_0)}{12\pi}(33 - 2N_f)\ln\left(\frac{Q^2}{Q_0^2}\right)\right]^{-1} \quad , \tag{1.18}$$

where $\alpha_S(Q)$ and $\alpha_S(Q_0)$ are the values of α_S at two different scales; for the purposes of our analysis, however, we will use numerical solutions of the RGE with coefficients up to β_2 included.

When calculating the effects of divergent loop diagrams in a physical process, one must choose an energy scale μ at which to 'renormalise' the diagrams. In QED, for example, we can calculate the Q^2-dependence of a divergent diagram by

---

[3]All of the QCD calculations applied in our analysis will use $N_f = 5$.

comparing it with $Q = 0$ case. For the strong interaction, however, the scale $Q = 0$ would be an inappropriate reference point. Instead we choose a scale $Q = \mu$, close to the characteristic energy scale of the physical process. This "renormalisation scale" is an unphysical parameter, and plays no part in the QCD Lagrangian; hence we should not expect physical observables to depend on it. However, as we shall see later in this chapter, the cancellation of μ from physical predictions will be incomplete unless the calculation itself is complete. Schematically, we can write the prediction for an observable R as

$$R(\alpha_{\mathrm{S}}) = R_{\mathrm{known}}(\alpha_{\mathrm{S}}, \mu) + R_{\mathrm{unknown}}(\alpha_{\mathrm{S}}, \mu) \tag{1.19}$$

where

$$\frac{\mathrm{d}R}{\mathrm{d}\mu} = 0 \;, \quad \text{but} \quad \frac{\mathrm{d}R_{\mathrm{known}}}{\mathrm{d}\mu} \neq 0 \tag{1.20}$$

The magnitude of the derivative $\mathrm{d}R_{\mathrm{known}}/\mathrm{d}\mu$ is often used to estimate the size of the unknown term, since it should approach zero as $R_{\mathrm{known}} \rightarrow R$.

1.4   QCD perturbation theory in $\mathbf{e^+e^- \rightarrow}$ hadrons

In e^+e^- annihilation, the simplest process yielding hadrons in the final state is shown in Figure 1.4. The quark and antiquark carry both colour and electric charge, however, so they may interact further before fragmenting into hadrons. Although both strong and electroweak processes are possible, we will concern ourselves only with the strong interactions,[4] which lead to further quark or gluon jets in the final state.

Provided the running coupling $\alpha_{\mathrm{S}}(Q)$ is suitably small, perturbation theory should allow us to calculate the matrix element and cross section for any configuration of partons. So far, however, the technicalities of handling loops in QCD diagrams have limited the precision of such predictions to second order in α_{S}.

---

[4]Electroweak processes in which further Z^0 or $W^\pm$ bosons are produced, or in which photons are radiated from the initial state, will be considered as a background in our experimental analysis.
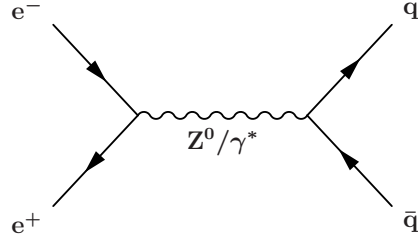
Figure 1.4: Simple quark pair production diagram in e^+e^- annihilation
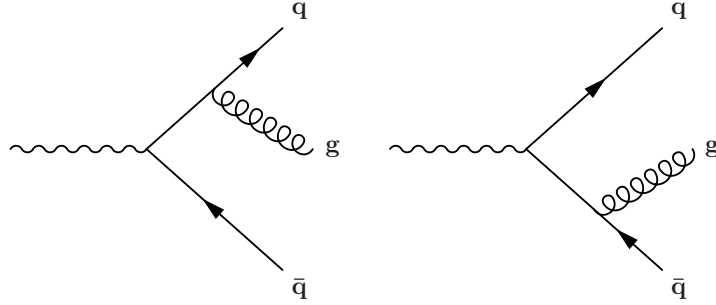
Figure 1.5: First order QCD matrix element contributions, $\mathcal{M}_i \propto \alpha_S^{1/2}$

1.4.1   Cross sections at $\mathcal{O}(\alpha_S^2)$

According to Fermi's Golden Rule, the transition rate from an initial state 'i' to a final state 'f' is given by

$$\Gamma \;=\; \frac{2\pi}{\hbar}\,\left|\mathcal{M}_{(i\to f)}\right|^2 \rho\left(p_1, p_2, \ldots p_N\right) \quad, \tag{1.21}$$

where $\mathcal{M}_{(i\to f)}$ is the matrix element connecting states 'i' and 'f' in the perturbed Hamiltonian,[5] and ρ is the density of possible momentum states in phase space for the final state 'f'.

In a quantum field theory such as QCD, the matrix element $\mathcal{M}_{(i\to f)}$ is a sum of transition amplitudes $\mathcal{M}_i$ represented by Feynman diagrams. The diagrams may be grouped conveniently by the number of strong interaction vertices, each of which contributes a factor $\alpha_S^{1/2}$ to the corresponding amplitude. In Figures 1.5, 1.6 and 1.7, we list the diagrams containing one, two and three strong vertices respectively (the initial e^+e^- state is not shown).

For any given final state, an infinite number of diagrams exist with differing numbers of loops. For example the process $e^+e^- \to q\bar{q}g$ has two tree-level diagrams

---

[5]In the annihilation of unpolarised particle beams, one actually takes the average squared matrix element $\left\langle \left|\mathcal{M}_{(i\to f)}\right|^2 \right\rangle$ for the possible initial states.

(a) $q\bar{q}$ diagram with one loop
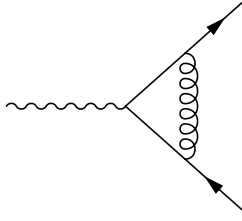
(b) $q\bar{q}q\bar{q}$ tree level diagrams
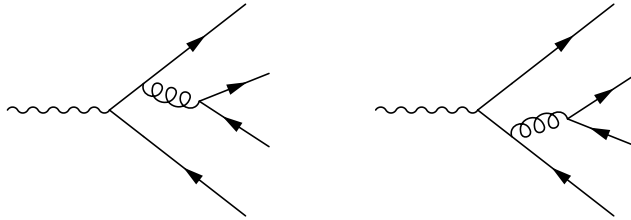
(c) $q\bar{q}gg$ tree level diagrams
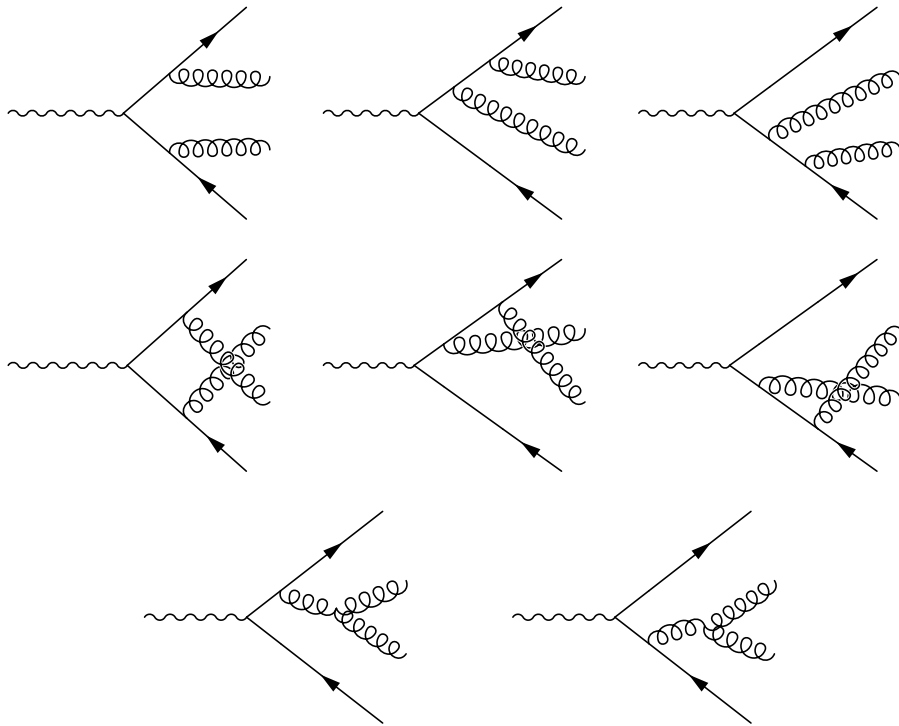
Figure 1.6: Second order QCD matrix element contributions, $\mathcal{M}_i \propto \alpha_{\mathrm{S}}$

(a) $q\bar{q}g$ diagrams with one loop
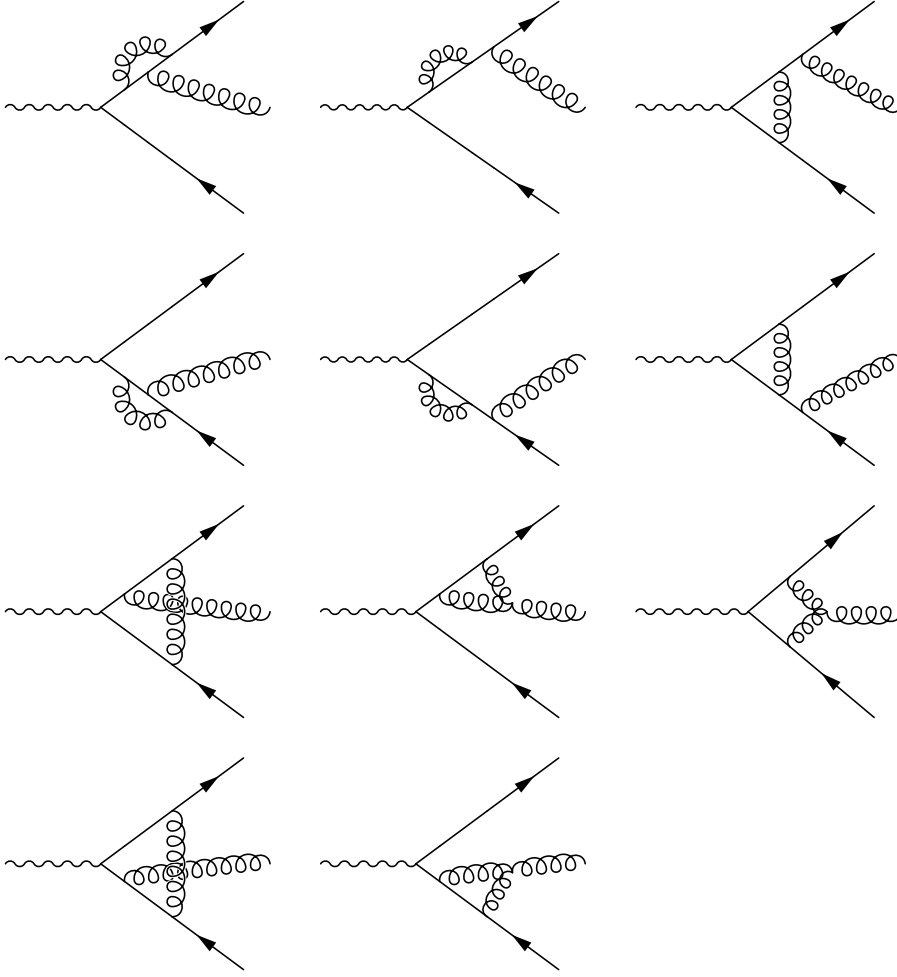
(b) $q\bar{q}q\bar{q}g$ and $q\bar{q}ggg$ tree level diagrams

+ many others …
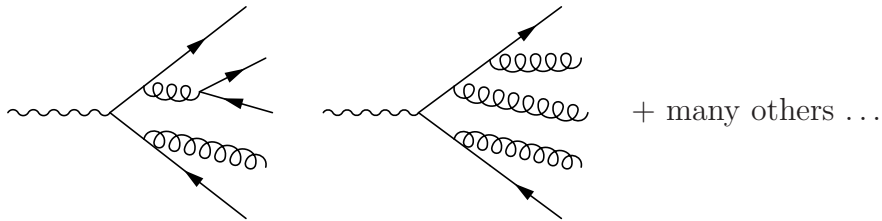
Figure 1.7: Third order QCD matrix element contributions, $\mathcal{M}_i \propto \alpha_{\mathrm{S}}^{3/2}$

with $\mathcal{M}_i \propto \alpha_{\mathrm{S}}^{1/2}$, shown in Figure 1.5, and eleven one-loop diagrams with $\mathcal{M}_i \propto \alpha_{\mathrm{S}}^{3/2}$, shown in Figure 1.7(a).[6] For a general N-jet final state, the total matrix element is given by

$$\mathcal{M}_{(\mathrm{i}\rightarrow\mathrm{f})} = \underbrace{\sum_i \mathcal{M}_i}_{\substack{(\text{tree}) \\ \propto \alpha_{\mathrm{S}}^{(N-2)/2}}} + \underbrace{\sum_i \mathcal{M}_i}_{\substack{(\text{1 loop}) \\ \propto \alpha_{\mathrm{S}}^{N/2}}} + \underbrace{\sum_i \mathcal{M}_i}_{\substack{(\text{2 loop}) \\ \propto \alpha_{\mathrm{S}}^{(N+2)/2}}} + \ldots \quad . \tag{1.22}$$

To calculate the transition rate, and hence the differential cross section $\mathrm{d}\sigma/\mathrm{d}\Omega$, we multiply this total matrix element by its complex conjugate $\mathcal{M}^*_{(\mathrm{i}\rightarrow\mathrm{f})}$:

$$\left|\mathcal{M}_{(\mathrm{i}\rightarrow\mathrm{f})}\right|^2 = \underbrace{\sum_i \sum_j \mathcal{M}^*_i \mathcal{M}_j}_{\substack{(\text{tree}) (\text{tree}) \\ \propto \alpha_{\mathrm{S}}^{N-2}}} + \underbrace{\sum_i \sum_j \mathcal{M}^*_i \mathcal{M}_j}_{\substack{(\text{tree}) (\text{1 loop}) \\ \propto \alpha_{\mathrm{S}}^{N-1}}}$$

$$+ \underbrace{\sum_i \sum_j \mathcal{M}^*_i \mathcal{M}_j}_{(\text{tree}) (\text{2 loop})} + \underbrace{\sum_i \sum_j \mathcal{M}^*_i \mathcal{M}_j}_{(\text{1 loop}) (\text{1 loop})} + \ldots \tag{1.23}$$
$$\underbrace{\phantom{\sum_i \sum_j \mathcal{M}^*_i \mathcal{M}_j + \sum_i \sum_j \mathcal{M}^*_i \mathcal{M}_j}}_{\propto \alpha_{\mathrm{S}}^{N}}$$

Thus for a full description of multihadronic final states at $\mathcal{O}(\alpha_{\mathrm{S}}^2)$, one must calculate all two-parton diagrams with up to two loops, all three-parton diagrams with up to one loop, and all four-parton diagrams at tree level.[7] Many of the higher-order diagrams contribute only through interference with those of lower order. The explicit evaluation of these matrix elements is discussed in Ref. [17].

1.5   Event shape observables

In order to make experimental tests of perturbative QCD, and to measure its free parameter α_{S}, one must first define some physical observables. These should be as sensitive as possible to the high-energy perturbative process, and as insensitive as possible to the subsequent non-perturbative effects of hadronisation and decays.

---

[6]We do not include diagrams containing loops on the external 'legs', as these are already taken into account by the renormalised particle masses.

[7]In the calculation of event shape distributions at $\mathcal{O}(\alpha_{\mathrm{S}}^2)$, however, we are not directly concerned with two-parton events; these appear only in the total hadronic cross section used to normalise the distributions.

Theorists have proposed many standard observables, called event shapes, each of which probes slightly different aspects of the final state. Event shapes are functions of the 3-momenta $\boldsymbol{p}_i$, and energies E_i of all particles i detected in the final state, and do not require identification of particle types.[8] It is therefore straightforward to make comparisons between data and theory, and between different experiments, without resorting to complicated and inefficient selection criteria. Many other tests of QCD require, for example, some discrimination between quark and gluon jets; in event shape measurements, we do not even need to assign the final-state particles to jets.

1.5.1   Thrust, thrust major, thrust minor and oblateness

Thrust, T is defined by

$$T = \max_{\hat{\boldsymbol{n}}} \left(\frac{\sum_i |\boldsymbol{p}_i \cdot \hat{\boldsymbol{n}}|}{\sum_i |\boldsymbol{p}_i|} \right) \ , \tag{1.24}$$

where the thrust axis $\hat{\boldsymbol{n}}_T$ is defined as the unit 3-vector $\hat{\boldsymbol{n}}$ which maximises the expression. For a perfectly 'pencil-like' two-jet event, the thrust axis lies parallel to the jets, so $|\boldsymbol{p}_i \cdot \hat{\boldsymbol{n}}_T| = |\boldsymbol{p}_i|$, yielding $T = 1$. In the case of a 'spherical' event, with an infinite number of particles distributed isotropically in the final state, the thrust becomes a ratio of solid angle integrals:

$$T = \frac{\int |\cos\theta| \, \mathrm{d}\Omega}{\int \mathrm{d}\Omega} = \frac{2\pi}{4\pi} = \frac{1}{2} \ . \tag{1.25}$$

It can be shown that all events satisfy $\frac{1}{2} < T < 1$. All the other event shapes considered here approach zero in the two-jet limit; for consistency, we will therefore define the observable $y = 1 - T$ which shares this property.

The concept of thrust was already in use before the advent of QCD. In 1964 [18], a "principal axis" equivalent to $\hat{\boldsymbol{n}}_T$ was proposed for the analysis of jets observed in hadron collisions, though the origin of the jets was hitherto unexplained. Later, in 1977 [19], it was recognised that this "maximum directed momentum" represented a calculable quantity in perturbative QCD.

---

[8]In principle, one needs to know the mass of the particle to determine its energy, given a precise measurement of the momentum. In our analysis, however, we will assume the masses of all particles to be that of the pion; any bias introduced by this assumption will be corrected by Monte Carlo simulations.
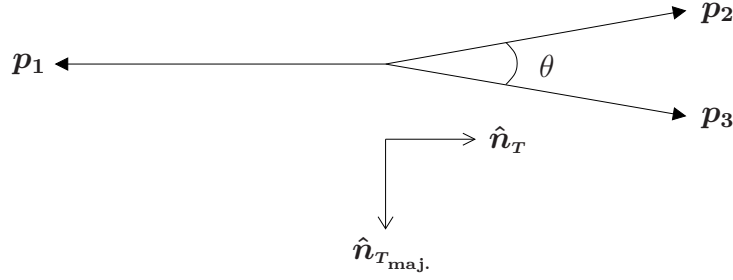
Figure 1.8: A three-jet event approaching the two-jet limit

Thrust major, $T_{\mathrm{maj.}}$ is defined in the same way as thrust, except that the axis $\hat{\boldsymbol{n}}$ is constrained to be orthogonal to the thrust axis:

$$T_{\mathrm{maj.}} = \max_{\hat{\boldsymbol{n}} \perp \hat{\boldsymbol{n}}_T} \left(\frac{\sum_i |\boldsymbol{p}_i \cdot \hat{\boldsymbol{n}}|}{\sum_i |\boldsymbol{p}_i|} \right) \quad . \tag{1.26}$$

The axis which maximises the quantity in parentheses is $\hat{\boldsymbol{n}}_{T_{\mathrm{maj.}}}$.

Thrust minor, $T_{\mathrm{min.}}$ is analogous to T and $T_{\mathrm{maj.}}$ except that $\hat{\boldsymbol{n}}$ is orthogonal to both $\hat{\boldsymbol{n}}_T$ and $\hat{\boldsymbol{n}}_{T_{\mathrm{maj.}}}$:

$$T_{\mathrm{min.}} = \frac{\sum_i |\boldsymbol{p}_i \cdot \hat{\boldsymbol{n}}_{T_{\mathrm{min.}}}|}{\sum_i |\boldsymbol{p}_i|} \quad , \quad \text{where} \quad \hat{\boldsymbol{n}}_{T_{\mathrm{min.}}} = \frac{\hat{\boldsymbol{n}}_T \times \hat{\boldsymbol{n}}_{T_{\mathrm{maj.}}}}{\left| \hat{\boldsymbol{n}}_T \times \hat{\boldsymbol{n}}_{T_{\mathrm{maj.}}} \right|} \tag{1.27}$$

Oblateness, O is simply the difference between thrust major and thrust minor:

$$O = T_{\mathrm{maj.}} - T_{\mathrm{min.}} \tag{1.28}$$

The thrust major and thrust minor are both zero for a perfect two-jet event, since all particle momenta are parallel to the thrust axis, and hence orthogonal to $\hat{\boldsymbol{n}}_{T_{\mathrm{maj.}}}$ and $\hat{\boldsymbol{n}}_{T_{\mathrm{min.}}}$. Furthermore, the thrust minor is zero for a three-jet event,[9] since momentum conservation dictates that all particles must lie in the plane orthogonal to $\hat{\boldsymbol{n}}_{T_{\mathrm{min.}}}$. For a spherical event, both $T_{\mathrm{maj.}}$ and $T_{\mathrm{min.}}$ approach a maximum value of 1/2. The oblateness is unusual, in that it vanishes for both two-jet events and spherical events.

---

[9]These statements are only valid for perfectly narrow jets, or partons. In reality, hadronisation and particle decays introduce some transverse momentum within the jet.
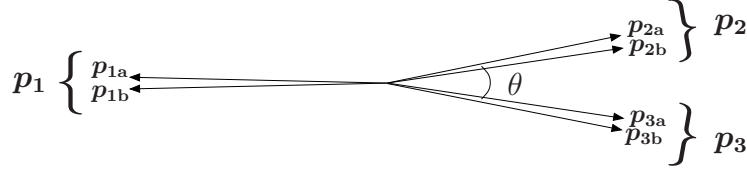
Figure 1.9: Collinear branching of partons within a three-jet event

When a three-jet event approaches the two-jet limit, as depicted in Figure 1.8, the four observables have differing sensitivities to the opening angle θ:

$$
\begin{aligned}
1 - T &\sim 1 - \cos\theta \sim \theta^2 \\
T_{\text{maj.}} &\sim \sin\theta \quad\;\; \sim \theta \\
T_{\text{min.}} &= 0 \\
O &= T_{\text{maj.}} \quad\;\; \sim \theta
\end{aligned}
$$

Hence we expect, for example, that the thrust major should be affected to a greater extent than the thrust by the effects of hadronisation and particle decays.

All four observables are linear with respect to the momenta $\boldsymbol{p}_i$. Hence if one particle splits into two, such that both final state particles continue on the same trajectory as shown in Figure 1.9, the observables do not change. In perturbative QCD, the matrix element for a process involving soft or collinear gluon emission becomes infinite in the limit of small momentum transfers. This leads to "infrared divergences" in quantities which are sensitive to such processes. We can therefore only calculate distributions for observables such as those considered above, which are "infrared safe".

1.5.2   Sphericity, aplanarity and the C- and D-parameters

The sphericity tensor $S^{\alpha\beta}$ is defined [20] as

$$
S^{\alpha\beta} = \frac{\sum_i p_i^\alpha p_i^\beta}{\sum_i |\boldsymbol{p}_i|^2} \quad , \tag{1.29}
$$

where $\alpha, \beta = 1, 2, 3$ correspond to the three spatial components. The three eigenvalues λ_i are ordered such that $\lambda_1 < \lambda_2 < \lambda_3$. Then the **sphericity**, $\boldsymbol{S}$ and **aplanarity**, $\boldsymbol{A}$ are defined by

$$
S = \frac{3}{2}\left(\lambda_1 + \lambda_2\right) \quad\text{and}\quad A = \frac{3}{2}\lambda_1 \quad . \tag{1.30}
$$

Sphericity is a 'three-jet' observable, approaching zero in the two-jet limit, while aplanarity is a 'four-jet' observable (like thrust minor), which vanishes in the three-jet planar limit. Since the sphericity tensor is quadratic in the momentum components $p_i^{\alpha,\beta}$, it is not infrared safe; the sphericity will differ between the events shown in Figures 1.8 and 1.9.[10] While the sphericity and aplanarity provide an interesting test of the Monte Carlo models for non-perturbative physics, they cannot be predicted reliably in perturbation theory.

As a generalisation of $S^{\alpha\beta}$, the power of the momentum dependence may be modified:

$$S^{(r)\alpha\beta} = \frac{\sum_i |\boldsymbol{p}_i|^{r-2}\, p_i^\alpha\, p_i^\beta}{\sum_i |\boldsymbol{p}_i|^r} \quad . \tag{1.31}$$

The sphericity tensor corresponds to the case $r = 2$. It can be argued [21] that higher values of r should give better experimental sensitivity to the parton structure of the event. This is because transverse momentum fluctuations during fragmentation have a proportionally smaller effect on particles with large momenta. However, to avoid infrared divergences in perturbation theory, we must choose the linearised form $r = 1$ [22]:

$$M^{\alpha\beta} = S^{(1)\alpha\beta} = \frac{\sum_i p_i^\alpha\, p_i^\beta/|\boldsymbol{p}_i|}{\sum_i |\boldsymbol{p}_i|} \quad . \tag{1.32}$$

Once again, this tensor is conveniently parameterised by its eigenvalues λ_1, λ_2 and λ_3. Since M is constructed with unit trace, the eigenvalues are bound by the constraint $\lambda_1 + \lambda_2 + \lambda_3 = 1$. We can thus form two independent combinations called the **C-** and **D-parameters** [17], which are symmetric in the three eigenvalues:

$$C = 3\,(\lambda_1\lambda_2 + \lambda_2\lambda_3 + \lambda_3\lambda_1) \quad \text{and} \quad D = 27\,\lambda_1\lambda_2\lambda_3 \tag{1.33}$$

The factors of 3 and 27 ensure that both parameters are in the range 0–1, reaching their maximum value for an isotropic event with $\lambda_1 = \lambda_2 = \lambda_3 = 1/3$. In the case of a planar event, one of the eigenvalues will be zero; the D-parameter is therefore a four-jet observable, while C is three-jet. It is worth noting that the C-parameter can be expressed explicitly in terms of the particle momenta $\boldsymbol{p}_i$, since it is related

---

[10]The aplanarity will also differ, in general, though it is zero for both of the planar events in Figures 1.8 and 1.9.

to the second Fox-Wolfram moment [23] by

$$C = 1 - H_2 \quad , \qquad \text{where} \quad H_2 = \sum_{i,j} \frac{|\boldsymbol{p}_i|\,|\boldsymbol{p}_j|}{E_{\text{vis.}}^2} \, P_2\left(\cos\theta_{ij}\right) \quad . \tag{1.34}$$

Here $E_{\text{vis.}}$ is the total visible energy of the event, θ_{ij} is the opening angle between particles i and j, and $P_2(x) \equiv \frac{1}{2}\left(3x^2 - 1\right)$ is the second Legendre polynomial.

1.5.3   The heavy and light jet masses

Unlike the observables discussed so far, the heavy and light jet masses do not involve a global sum over all particles in the event. Instead, we split the event into two 'hemispheres', divided by a plane orthogonal to the thrust axis $\hat{\boldsymbol{n}}_T$. Denoting the hemispheres by H_1 and H_2, the two corresponding jet masses $M_{1,2}$ are defined by the invariant masses in each half of the event:

$$M_{1,2}^2 = \left(\sum_{i \in H_{1,2}} E_i \right)^2 - \left| \sum_{i \in H_{1,2}} \boldsymbol{p}_i \right|^2 \quad . \tag{1.35}$$

The **heavy jet mass, $M_{\mathbf{H}}$**, and **light jet mass, $M_{\mathbf{L}}$** are the larger and smaller of these masses respectively. The dimensionless quantities $M_{\text{H}}/\sqrt{s}$ and $M_{\text{L}}/\sqrt{s}$ are infrared-safe event shape observables,[11] whose distributions have been predicted by perturbative QCD. Referring to Figure 1.8, we see that M_{L} vanishes in a three-particle system, since one of the hemispheres contains only a single particle.[12] Like all four-jet observables, however, it will acquire a small positive value due to hadronisation. The heavy jet mass M_{H} is three-jet observable, sensitive to the momentum transfer of single hard gluon emissions.

1.5.4   The wide, narrow and total jet broadenings

Again the event is divided into two hemispheres H_1 and H_2 by a plane orthogonal to the thrust axis. In each half of the event, we define the jet broadening [24]

$$B_{1,2} = \frac{\sum_{i \in H_{1,2}} |\boldsymbol{p}_i \times \hat{\boldsymbol{n}}_T|}{2 \sum_i |\boldsymbol{p}_i|} \quad . \tag{1.36}$$

---

[11]Often in the literature the factors $\frac{1}{\sqrt{s}}$ are included in the definitions of M_{H} and M_{L}.

[12]In reality the heavy and light jet masses are never zero, due to the finite masses of the individual particles. This effect becomes increasingly less significant in high energy collisions, however, and will be neglected in the theoretical predictions used for our analysis.

In terms of B_1 and B_2, the wide, narrow and total broadenings are given by:

$$\textbf{Wide jet broadening} \quad B_\mathrm{W} = \max{(B_1, B_2)}$$

$$\textbf{Narrow jet broadening} \quad B_\mathrm{N} = \min{(B_1, B_2)}$$

$$\textbf{Total jet broadening} \quad B_\mathrm{T} = B_\mathrm{W} + B_\mathrm{N} = B_1 + B_2 \qquad (1.37)$$

The total broadening B_T is similar to the thrust major, in that it measures momentum components orthogonal to the thrust axis of a three-jet event. In fact to $\mathcal{O}(\alpha_\mathrm{S})$ in perturbation theory, $B_\mathrm{T} = B_\mathrm{W} = \frac{1}{2}T_\mathrm{maj.} = \frac{1}{2}O$. The broadenings all vanish in the two-jet limit, while for a spherical event $B_\mathrm{T} = \pi/8$ and $B_\mathrm{W} = B_\mathrm{N} = \pi/16$. The theoretical maxima, which exceed the values for the spherical case, are unknown. The total and wide jet broadenings are three-jet observables, while B_N is four-jet.

1.5.5 The transition parameter, y_{23}, between two and three jets in the Durham algorithm

Various algorithms exist to determine the number of jets in an hadronic final state. Generally the aim is to group particles together such that we reconstruct the directions and momenta of the partons produced in the hard interaction. However, information about this partonic state is inevitably lost during hadronisation and decays. The jet-finding algorithms typically include at least one free "resolution parameter," and the number of reconstructed jets will depend on its chosen value.

In the Durham algorithm[13] [25], a "scaled transverse momentum" y_{ij} is defined for every pair of particles i, j in the final state:

$$y_{ij} = \frac{2 \min{\left(E_i^2, E_j^2\right)} \left(1 - \cos\theta_{ij}\right)}{E_\mathrm{vis.}^2} \quad , \qquad (1.38)$$

where $E_{i,j}$ are the energies of the particles, θ_{ij} is the angle between them, and $E_\mathrm{vis.}$ is the total visible energy in the event. The pair with the smallest y_{ij} is then replaced by a single 'pseudoparticle' with momentum $\boldsymbol{p}_{(ij)} = \boldsymbol{p}_i + \boldsymbol{p}_j$ and energy

---

[13]The Durham algorithm (also known as the $k_\perp$-algorithm) derives its name from the Durham Workshop on Jet Studies at LEP and HERA, December 1990, where it was first discussed.

$E_{(ij)} = E_1 + E_2$.[14] The process is repeated until all pairs of particles have $y_{ij} > y^{\text{cut}}$, for some fixed resolution parameter y^{cut}. The remaining pseudoparticles are then regarded as jets.

For small values of y^{cut} the algorithm will terminate at an early stage, yielding a large number of jets, whereas for values approaching unity the whole event will be combined into a single jet. As a measure of how 'N-jetlike' an event is, we define the transition parameter $y^{\text{cut}}_{N-1,N}$ as the highest the value of y^{cut} for which the event is resolved into N jets. We consider here the case $y^{\text{cut}}_{2,3}$, at which the number of resolved jets changes from two to three. For events which genuinely contain three or more jets, we expect $y^{\text{cut}}_{2,3}$ to be large, while for two-jet events at LEP collision energies $y^{\text{cut}}_{2,3} \lesssim 10^{-3}$. If an event is resolved into three identical jets 120° apart, $y^{\text{cut}}_{2,3}$ takes its maximum possible value of $1/3$.

Hereafter we will follow the convention of the literature[15] by denoting this observable y_{23}; this should not be confused with our earlier notation y_{ij}, which refers to an individual pair of particles or pseudoparticles within the event.

1.6   Perturbative predictions for the event shapes

In an experiment, one measures the value of each event shape observable for every event which has been selected as 'multihadronic'.[16] Being a quantum theory, QCD makes physical predictions for these event shapes in the form of frequentist probabilities. We therefore seek to measure the probability density function for each observable, and compare it directly with the best available prediction.

For a generic observable y, we can statistically estimate the form of the differential cross section $\mathrm{d}\sigma/\mathrm{d}y$. This tells us the expected density of events, per unit luminosity, at a given value of the event shape y. Dividing this by the total cross section for multihadron production, $\sigma_{\text{tot.}}$, gives the corresponding probability density

---

[14]The algorithm has been constructed such that the combined pseudoparticle has a 4-momentum equal to the sum of its constituent particles' 4-momenta. This choice is not unique. One could instead define the energy $E_{(ij)} = |\boldsymbol{p}_i + \boldsymbol{p}_j|$, such that the resulting jets are massless. Alternatively, the momentum could be scaled such that $|\boldsymbol{p}_{(ij)}| = E_i + E_j$. These three "recombination schemes" are known as the E-, P- and E0-schemes respectively; they have been studied experimentally [26] by OPAL using the JADE algorithm [27], which defines $y_{ij} = 2E_i E_j (1 - \cos\theta_{ij})$ in place of Equation (1.38). Here we will only consider the E-scheme, as described above. Often the Durham algorithm itself is confusingly referred to as the D-scheme, when in fact the same choice of recombination schemes exists in both the Durham and JADE algorithms.

[15]Some authors use the symbols D_2 or y_3 for this same observable.

[16]Our precise signal definition and selection criteria will be discussed in Chapter 3.

function. In theoretical work, authors more often refer to the *cumulative* probability function $R(y)$, defined by

$$R(y_0) = \frac{1}{\sigma_{\text{tot.}}} \int_0^{y_0} \frac{\mathrm{d}\sigma}{\mathrm{d}y} \, \mathrm{d}y \quad . \tag{1.39}$$

The probability density may then be written as the derivative of this function, $R'(y)$. The total multihadronic cross section $\sigma_{\text{tot.}}$ is largely determined by electroweak physics; however it differs slightly from the cross section for the 'bare' process $e^+e^- \rightarrow (Z^0/\gamma)^* \rightarrow q\bar{q}$, due to QCD corrections. These have been evaluated as follows: [28, 29]

$$\sigma_{\text{tot.}} = \sigma_0 \left[1 + \frac{\alpha_S}{\pi} + 1.411 \left(\frac{\alpha_S}{\pi} \right)^2 - 12.8 \left(\frac{\alpha_S}{\pi} \right)^3 + \ldots \right] \quad , \tag{1.40}$$

where σ_0 is the Born cross section for the bare electroweak process.

Before proceeding further, we will list the six event shapes whose perturbative predictions will be studied. For various reasons, the variables y used in theoretical expressions are not always identical to the event shape itself:

$$
\begin{aligned}
\text{Thrust:} \quad & y = 1 - T \\
\text{Heavy jet mass:} \quad & y = M_{\text{H}}^2/s \\
C\text{-parameter:} \quad & y = C/6 \\
\text{Total jet broadening:} \quad & y = B_{\text{T}} \\
\text{Wide jet broadening:} \quad & y = B_{\text{W}} \\
\text{Durham } y_{23}: \quad & y = y_{23}
\end{aligned}
\tag{1.41}
$$

1.6.1 $\mathcal{O}(\alpha_S^2)$ predictions

In Section 1.4, we discussed the calculation of cross sections for two-, three- and four-parton final states at $\mathcal{O}(\alpha_S^2)$ in perturbative QCD. As we saw in Equation (1.23), the squared matrix element $|\mathcal{M}|^2$ for any final state can be expressed as a power series in α_S:

$$|\mathcal{M}|^2 = \left[|\mathcal{M}|^2 \right]_0 + \alpha_S \left[|\mathcal{M}|^2 \right]_1 + \alpha_S^2 \left[|\mathcal{M}|^2 \right]_2 \quad . \tag{1.42}$$

A Monte Carlo program called EVENT2 [30] has been written, which generates parton-level 'events' using the probabilities associated with the squared matrix el-

ements $\left[|\mathcal{M}|^2\right]_i$ at each order. By generating large samples covering the whole of phase space, one can then infer the cumulative probability function for any event shape y:

$$R(y) \; = \; 1 \; + \; \mathcal{A}(y)\alpha_{\mathrm{S}} \; + \; \mathcal{B}(y)\alpha_{\mathrm{S}}^2 \quad . \tag{1.43}$$

In the limit of small α_{S}, the effects of QCD will be "switched off," and all events will be two-jet. We have assumed $y \to 0$ for such events, so that the cumulative distribution becomes a step function $R(y) = \Theta(y)$, and the corresponding probability density becomes a delta function $R'(y) = \delta(y)$. This is true of all the variables y listed in Equations (1.41).

In this work, we use numerical values of $\mathcal{A}(y)$ and $\mathcal{B}(y)$ that were generated for other recent OPAL analyses.

1.6.2   NLLA resummations

A perturbation expansion up to $\mathcal{O}(\alpha_{\mathrm{S}}^2)$ will only be useful if it converges rapidly. One would naïvely expect the convergence of $R(y)$ to be satisfactory at LEP energy scales, since $\alpha_{\mathrm{S}} \sim 0.1$. However, this will only be true if the coefficients $\mathcal{A}(y)$, $\mathcal{B}(y)$, $\mathcal{C}(y)$, … do not grow faster than α_{S}^{-n} $(n = 1, 2, 3, \ldots)$

As we have seen, there is a high probability of soft or collinear gluons being emitted in a quark or gluon jet. To avoid singularities in the distributions, we defined a set of infrared-safe observables, which are invariant under any perfectly collinear splitting. However, if gluons are emitted at a small non-zero angle, there will still be a corresponding small change in the observables y. Since the number of gluons may be quite large, as depicted in Figure 1.10, this effect will enhance the coefficients of high powers of α_{S} in the distribution $R(y)$. We therefore expect the convergence of the series to break down near the two-jet limit, when y is small. This divergence is manifested in large factors $(-\ln y)^n$, which appear in the coefficients $\mathcal{A}(y)$, $\mathcal{B}(y)$, $\mathcal{C}(y)$, … with various powers n.

Fortunately help is at hand, as an alternative formalism exists for dealing with multiple soft and collinear emissions. Rather than computing matrix elements for individual diagrams such as Figure 1.10, a system of differential equations is devised to describe the sequence of emissions from a parton as it evolves from the hard interaction down to lower mass scales. These DGLAP[17] equations [31] are based

---

[17]Dokshitzer-Gribov-Lipatov-Altarelli-Parisi
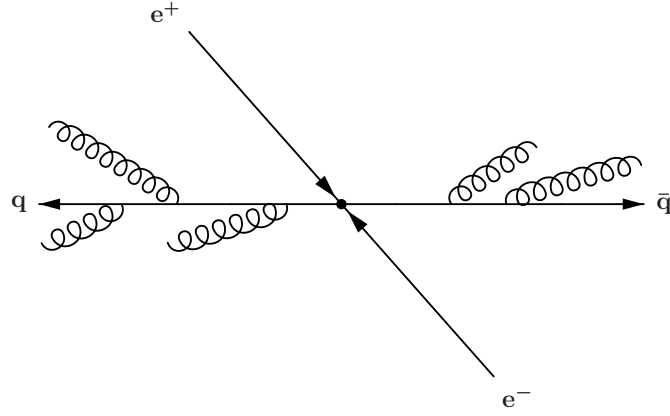
Figure 1.10: Multiple low-angle gluon emission near the two jet limit

on a set of "splitting kernels" $P_{a \to bc}(\alpha_S, z)$, which define the probability of a parton a splitting to produce partons b and c with momentum fractions z and $(1 - z)$ respectively. One can then derive a Sudakov form factor $\Delta(t, t_0)$, describing the probability for a parton to evolve from a mass scale Q_0 to a lower scale Q with no detectable emissions:[18]

$$\mathcal{P}_{\text{no emission}} = \Delta(t, t_0) = \exp\left[- \int_{t_0}^{t} dt' \sum_{b,c} \int dz \frac{\alpha_S}{2\pi} P_{a \to bc}(\alpha_S, z) \right] \quad , \qquad (1.44)$$

where $t \equiv \ln(Q^2/\Lambda^2)$ for some arbitrary scale Λ, and the sum $\sum_{b,c}$ runs over all possible branchings for a given parton a. The running coupling α_S is evaluated at a scale which depends on t'. This Sudakov form factor is analogous to the well-known exponential probability distribution for an unstable particle to exist for a time t; in this case, however, the "decay rate" is dependent on the scale parameter t.

Using these form factors, theorists have systematically collected together the terms containing factors $(-\ln y)^n$ in the event shape distributions $R(y)$. The result is a new series expansion, in which each term is characterised by the power of α_S minus the power of $L \equiv -\ln y$:

$$R(y) = C(\alpha_S)\Sigma(\alpha_S, y) + D(\alpha_S, y) \quad ,$$

$$\text{where} \quad \ln\Sigma = Lg_1(\alpha_S L) + g_2(\alpha_S L) + \alpha_S g_3(\alpha_S L) + \dots \quad . \qquad (1.45)$$

The functions $g_1(x)$, $g_2(x)$, ... are properties of the event shape y, which "resum"

---

[18]Since there is an infinite probability of emitting arbitrarily soft or collinear gluons, an "infrared cut-off" must be applied when defining an emission.

the large logarithms L to all orders in α_S. The term $Lg_1(\alpha_S L)$ resums the leading logarithms (LL), while $g_2(\alpha_S L)$ resums next-to-leading logarithms (NLL). Together, they give a prediction for $R(y)$ in the "Next-to-Leading Logarithmic Approximation" (NLLA). Although the function $D(\alpha_S, y)$ also contains some dependence on the event shape y, it is constrained to vanish at every order in α_S as $y \to 0$.

Expressions for $g_1(x)$ and $g_2(x)$ have been calculated for the thrust and heavy jet mass [32], the wide and total jet broadenings [24, 33], the C-parameter [34] and the Durham y_{23} parameter [25, 35, 36]. Predictions for the function $C(\alpha_S)$ are also available, in the form

$$C(\alpha_S) \;=\; 1 \;+\; C_1\alpha_S \;+\; C_2\alpha_S^2 \;\;, \tag{1.46}$$

where the coefficients C_1 and C_2 are constants for each observable. The next-to-next-to-leading resummations $g_3(x)$ are not yet available.

Quarks are assumed to be massless in both the $\mathcal{O}(\alpha_S^2)$ and NLLA predictions used in this work. Although perturbative predictions do exist for heavy quark production at $\mathcal{O}(\alpha_S^2)$ [37], there are no corresponding NLLA calculations.[19] In the interests of consistency, we will therefore use only the massless predictions.

1.6.3   Combining $\mathcal{O}(\alpha_S^2)$ and NLLA predictions

So far, we have described two separate predictions for each event shape distribution: an order-by-order perturbation expansion in the strong coupling, valid in the 3- and 4-jet regime, and a resummation of large logarithms, valid in the limit $y \to 0$. In a study of experimental data, however, we need a prediction covering the complete spectrum of multihadronic events. In this section we discuss the methods used to combine the $\mathcal{O}(\alpha_S^2)$ and NLLA predictions.

---

[19]Recently an NLLA prediction has become available for jet rate observables, including the Durham y_{23} parameter, in the presence of quark masses [38]. However, it does not have the same form as the massless calculations, and has not yet been combined with the $\mathcal{O}(\alpha_S^2)$ prediction.

	$\widehat{A}(y)\alpha_S$	$\widehat{B}(y)\alpha_S^2$	$\widehat{C}(y)\alpha_S^3$	$\ldots$
$L\,g_1(\alpha_S L)$	$G_{12}\alpha_S L^2$	$G_{23}\alpha_S^2 L^3$	$G_{34}\alpha_S^3 L^4$	$\ldots$
$g_2(\alpha_S L)$	$G_{11}\alpha_S L$	$G_{22}\alpha_S^2 L^2$	$G_{33}\alpha_S^3 L^3$	$\ldots$
$\alpha_S\,g_3(\alpha_S L)$		$G_{21}\alpha_S^2 L$	$G_{32}\alpha_S^3 L^2$	$\ldots$
$\alpha_S^2\,g_4(\alpha_S L)$	$f_1(y)\,\alpha_S$		$G_{31}\alpha_S^3 L$	$\ldots$
$\vdots$		$f_2(y)\,\alpha_S^2$	$f_3(y)\,\alpha_S^3$	$\ddots$

Table 1.3: An expansion of $\ln R$ in powers of α_S and L. The sum of the first two rows corresponds to the NLLA resummation, while the first two columns together represent the $\mathcal{O}(\alpha_S^2)$ perturbative prediction. The functions $f_1(y)$, $f_2(y)$,... have been introduced merely for consistency, to represent non-logarithmic contributions to the distribution.

1.6.3.1 Log(R) matching scheme

We begin by writing the logarithm of the NLLA distribution, $R_{\text{NLLA}}(\alpha_S, y)$, as a two-variable power series in α_S and L $(\equiv -\ln y)$:[20]

$$
\begin{aligned}
\ln R_{\text{NLLA}}(\alpha_S, y) &= \ln \Sigma(\alpha_S, y) = Lg_1(\alpha_S L) + g_2(\alpha_S L) \\
&= \ln \sum_{n=1}^{\infty} \left(G_{n,n+1}\alpha_S^n L^{n+1} + G_{n,n}\alpha_S^n L^n \right) \ . \quad (1.47)
\end{aligned}
$$

The coefficients G_{nm} are easily calculated from series expansions of the functions $g_n(x)$. The above expression can be compared with the corresponding logarithm of the $\mathcal{O}(\alpha_S^2)$ prediction, $R_{\mathcal{O}(\alpha_S^2)}(\alpha_S, y)$:

$$
\begin{aligned}
\ln R_{\mathcal{O}(\alpha_S^2)}(\alpha_S, y) &= \ln\left[1 + \mathcal{A}(y)\alpha_S + \mathcal{B}(y)\alpha_S^2 + \mathcal{O}(\alpha_S^3) \right] \\
&= \mathcal{A}(y)\alpha_S + \left[\mathcal{B}(y) - \tfrac{1}{2}\mathcal{A}(y) \right]\alpha_S^2 + \mathcal{O}(\alpha_S^3) \\
&\equiv \widehat{A}(y)\alpha_S + \widehat{B}(y)\alpha_S^2 + \mathcal{O}(\alpha_S^3) \ . \quad (1.48)
\end{aligned}
$$

In Table 1.3, we have arranged the terms $G_{nm}\alpha_S^n L^m$ in an array, such that sum of the first two rows is equivalent to $\ln[R_{\text{NLLA}}(\alpha_S, y)]$, while the first two columns give $\ln[R_{\mathcal{O}(\alpha_S^2)}(\alpha_S, y)]$. To combine the $\mathcal{O}(\alpha_S^2)$ and NLLA predictions, we add them

---

[20]The "remainder function" $D(\alpha_S, y)$ is not included explicitly here. However, the matching of $\mathcal{O}(\alpha_S^2)$ and NLLA calculations can be viewed as a way of estimating it. Similarly the term $\ln C(\alpha_S)$ is dropped, since it is formally of the same order as the next term $\alpha_S g_3(\alpha_S L)$ in the resummation.

together and subtract the four double-counted terms indicated in red:

$$\ln R_{\text{matched}}(\alpha_{\text{S}}, y) \;=\; L g_1(\alpha_{\text{S}} L) + g_2(\alpha_{\text{S}} L) + \mathcal{A}(y)\alpha_{\text{S}} + \left[\mathcal{B}(y) - \tfrac{1}{2}\mathcal{A}(y)\right]\alpha_{\text{S}}^2$$
$$- \left(G_{12}L^2 + G_{11}L\right)\alpha_{\text{S}} - \left(G_{23}L^3 + G_{22}L^2\right)\alpha_{\text{S}}^2 \;. \qquad (1.49)$$

After exponentiating the entire expression, this gives the $\mathcal{O}(\alpha_{\text{S}}^2) + \text{NLLA}$ prediction for $R(y)$ in the $\text{Log}(R)$ matching scheme.

1.6.3.2 R matching scheme

In the derivation above, we expanded the expressions for $\ln\left[R(\alpha_{\text{S}}, y)\right]$ in powers of α_{S} and L, and identified the four terms which were common to both expressions. Unfortunately, however, this procedure has an ambiguity. We could instead have expanded the two expressions for $R(\alpha_{\text{S}}, y)$ itself, or indeed any other function of R; in each case, the double-counted terms would be slightly different.

In the R matching scheme, we have

$$R_{\text{matched}}(\alpha_{\text{S}}, y) \;=\; R_{\text{NLLA}}(\alpha_{\text{S}}, y) + R_{\mathcal{O}(\alpha_{\text{S}}^2)}(\alpha_{\text{S}}, y)$$
$$- \left[\alpha_{\text{S}} \text{ and } \alpha_{\text{S}}^2 \text{ terms in } R_{\text{NLLA}}(\alpha_{\text{S}}, y)\right] \;. \qquad (1.50)$$

Expanding $R_{\text{NLLA}}(\alpha_{\text{S}}, y)$ in powers of α_{S} eventually leads to:

$$R_{\text{matched}}(\alpha_{\text{S}}, y) \;=\; \left[1 + C_1\alpha_{\text{S}} + C_2\alpha_{\text{S}}^2\right]\exp\left(L g_1(\alpha_{\text{S}} L) + g_2(\alpha_{\text{S}} L) + G_{21}\alpha_{\text{S}}^2 L\right)$$
$$+ \left[\mathcal{A}(y) - C_1 - G_{11}L - G_{12}L^2\right]\alpha_{\text{S}}$$
$$+ \left[\mathcal{B}(y) - C_2 - C_1(G_{11}L + G_{12}L^2) - \tfrac{1}{2}(G_{11}L + G_{12}L^2)^2\right.$$
$$\left. - G_{21}L - G_{22}L^2 - G_{23}L^3\right]\alpha_{\text{S}}^2 \;. \qquad (1.51)$$

This expression explicitly includes the coefficients C_1 and C_2, and also G_{21} which formally belongs to the sub-leading function $g_3(\alpha_{\text{S}} L)$ of the resummation. The coefficients C_2 and G_{21} cannot be derived analytically, and have been estimated numerically by comparing the NLLA and $\mathcal{O}(\alpha_{\text{S}}^2)$ expressions. Theorists generally advocate the $\text{Log}(R)$ matching scheme in preference to the R scheme, because the former does not depend on these numerical coefficients; however, it should be emphasised that both schemes are formally valid at both $\mathcal{O}(\alpha_{\text{S}}^2)$ and NLLA accuracy. We will use the difference between the two schemes as part of our estimate for the theoretical uncertainty in $R(y)$.

1.6.4 Kinematic constraints

Each of the event shapes y is constrained on kinematic grounds to lie within a certain range; the thrust, for example, must satisfy $\frac{1}{2} \leq T \leq 1$. Outside this range, the perturbative expansion for $\mathrm{d}R/\mathrm{d}y$ must vanish at every order in α_S. In the NLLA prediction, however, there is nothing to prevent the missing sub-leading terms from contributing a finite cross section outside the allowed range. To enforce the kinematic constraint $y \leq y_\mathrm{max}$, the logarithm $L = -\ln y$ can be replaced with

$$\widetilde{L} = \frac{1}{p} \ln \left[\frac{1}{y^p} - \frac{1}{y_\mathrm{max}^p} + 1 \right] \quad . \tag{1.52}$$

This substitution does not alter the formal NLLA accuracy of the predictions, and is valid for any $p \geq 1$. In the $\mathrm{Log}(R)$ matching scheme, we then have

$$\ln R(y_\mathrm{max}) = 0 \quad , \quad \text{and} \quad \left. \frac{\mathrm{d}R}{\mathrm{d}y} \right|_{y=y_\mathrm{max}} \equiv R \left. \frac{\mathrm{d}L}{\mathrm{d}y} \frac{\mathrm{d}(\ln R)}{\mathrm{d}L} \right|_{y=y_\mathrm{max}} = 0 \quad , \tag{1.53}$$

so the cumulative distribution $R(y)$ smoothly approaches unity at the kinematic boundary y_max. The parameter p determines the 'sharpness' with which the constraint is applied. For large values of p, the distribution is modified drastically in the region immediately below the cutoff, and almost unchanged elsewhere. In the past, however, all experimental analyses have implicitly taken $p = 1$, which gives a more smooth modification.[21] In this work we will continue to use $p = 1$, but will consider this ambiguity in our estimate of the theoretical uncertainty.

In the R matching scheme, a similar approach can be taken: the same substitution $L \to \widetilde{L}$ is valid, but the condition $\mathrm{d}R/\mathrm{d}y \to 0$ is not automatically satisfied at $y = y_\mathrm{max}$. Starting from Equation (1.51), and expanding $R_\mathrm{matched}(y)$ in powers of the logarithm L, one eventually obtains

$$R(y) = 1 + \left[C_2 \alpha_\mathrm{S}^3 G_{11} + \left(C_1 \alpha_\mathrm{S}^3 + C_2 \alpha_\mathrm{S}^4 \right) G_{21} \right] L + \mathcal{O}(L^2) \quad . \tag{1.54}$$

After substituting $L \to \widetilde{L}$, we immediately have $R(y_\mathrm{max}) = 1$, but we must also impose the smoothness criterion $\mathrm{d}R/\mathrm{d}\widetilde{L} = 0$ at the boundary. This is achieved by modifying the the coefficients G_{11} and G_{21}, and also the function $g_2(\alpha_\mathrm{S}\widetilde{L})$ which

---

[21]Some analyses, including previous OPAL publications, have omitted the kinematic constraint altogether. This corresponds to the limit $p \to \infty$, in the region $y < y_\mathrm{max}$.

implicitly contains the term $G_{11}\alpha_{\mathrm{S}}\widetilde{L}$:

$$
\begin{aligned}
G_{11} &\rightarrow \widetilde{G}_{11}(y) = \left[1 - \left(\frac{y}{y_{\mathrm{max}}}\right)^{p}\right] G_{11} \\
G_{21} &\rightarrow \widetilde{G}_{21}(y) = \left[1 - \left(\frac{y}{y_{\mathrm{max}}}\right)^{p}\right] G_{21} \\
g_{2}(\alpha_{\mathrm{S}}L) &\rightarrow \widetilde{g}_{2}(\alpha_{\mathrm{S}}\widetilde{L}) = g_{2}(\alpha_{\mathrm{S}}\widetilde{L}) - \left(\frac{y}{y_{\mathrm{max}}}\right)^{p} G_{11}\alpha_{\mathrm{S}}\widetilde{L} \quad .
\end{aligned}
\tag{1.55}
$$

Values for the kinematic boundaries y_{max}, and also for the matching coefficients G_{nm} and C_n, can be found in Ref. [12].

1.7   Recent advances in the NLLA predictions

Over the time since the first NLLA resummations were published, several improvements and corrections have followed:

- In Ref. [35], a more complete NLLA resummation was found for y_{23}, replacing the earlier predictions in Ref. [25]. These updated calculations were applied to LEP2 data in recent OPAL publications [11], but have now been superseded by a further improvement (see below).

- In Ref. [33], a problem was identified in the resummations of the total and wide jet broadening distributions, originally published in Ref. [24]. When the recoil effects in quark-gluon splittings were correctly taken into account, the distribution became 'shifted' slightly: $R_{\mathrm{new}}(B) = R_{\mathrm{old}}(\lambda B)$. The shift has not yet been implemented in OPAL publications, but in this work the new calculations are used throughout.

- In Ref. [36], a new approach to resummation was developed; this led to a further improvement in the y_{23} distribution, and also some new NLLA predictions for observables which had not been resummed previously. Given the probability density $R'_{\mathrm{s}}(y_s)$ for a 'simple' observable y_s, one can write down the distribution $R'(y)$ for any other observable in terms of the conditional probability density $P(y|y_s)$:

$$
R'(y) = \int R'_{\mathrm{s}}(y_s)\, P(y|y_s)\, \mathrm{d}y_s \quad .
\tag{1.56}
$$

Provided the observables y and y_s are suitably similar, it has been shown that the conditional probability $P(y|y_s)$ can be calculated quite straightforwardly. This leads to a relationship between the two NLLA resummed distributions, of the form

$$R'(y) \;=\; R'_\mathrm{s}(y) \;\times\; \mathcal{F}\left(-\frac{\mathrm{d}(\ln \Sigma)}{\mathrm{d}L}\right) \quad, \tag{1.57}$$

where $\Sigma(\alpha_\mathrm{S}, L)$ is the exponentiated part of the NLLA expression, defined in Equation (1.45). The numerical values of the functions $\mathcal{F}(\lambda)$ have been tabulated for three observables y, given in each case a corresponding observable y_s whose resummation is already known:

- The Durham y_{23} parameter

- The thrust major, $T_\mathrm{maj.}$

- The oblateness, O

It was shown that certain next-to-leading logarithmic contributions had been omitted from the previous y_{23} calculations in Ref. [35], and are now included in the new 'semi-numerical' result. In this work, we have implemented the improved calculations for the first time in the analysis of OPAL data.

The NLLA predictions for the thrust major and oblateness are completely new, and have not yet been compared with OPAL measurements.

- Resummed distributions have recently become available for some 'four-jet' observables, which provide sensitivity to the three-gluon vertex. In Ref. [39], a full NLLA calculation was presented for the light hemisphere mass M_L, and the narrow jet broadening B_N. The D-parameter was similarly treated in Ref. [40]. Since these observables vanish for all planar events, their perturbative distributions are of the form

$$R(y) \;=\; 1 \;+\; \mathcal{B}(y)\alpha_\mathrm{S}^2 \;+\; \mathcal{C}(y)\alpha_\mathrm{S}^3 \;+\; \dots \quad. \tag{1.58}$$

Monte Carlo programs analogous to EVENT2 are now available [41–44] to calculate the coefficients $\mathcal{B}(y)$ and $\mathcal{C}(y)$, using QCD matrix elements with up to one loop. Matching schemes have also been defined [39], to combine the $\mathcal{O}(\alpha_\mathrm{S}^3)$ and NLLA predictions.

Although it has not been possible to implement these calculations in the work presented here, we considered it worthwhile to measure the distributions themselves, at all LEP centre-of-mass energies. Future measurements using these NLLA predictions should yield substantial improvements over existing studies of four-jet events based on matrix elements alone.

1.8   Theoretical uncertainties

We consider here the sources of uncertainty in our perturbative predictions for the event shape distributions, and their effect on the values of α_S obtained in experimental measurements. The new methods presented here have been developed in collaboration with the LEP QCD Working Group, and are documented in Ref. [12].

1.8.1   Uncertainties in the event shape distributions

Owing to the truncation of both the $\mathcal{O}(\alpha_S^2)$ perturbation series and the NLLA resummed expressions, our predicted event shape distributions are not exact. Many techniques have been proposed to estimate the effect of the missing higher-order terms: one of the simplest would be to use the last known term of the perturbation expansion, proportional to α_S^2, as an estimate of remaining uncalculated terms. This approach is likely to overestimate the uncertainty, however, since the sum of the unknown terms is expected to be of order α_S^3. Instead we will identify several arbitrary assumptions which are made in our $\mathcal{O}(\alpha_S^2) + \text{NLLA}$ predictions; the variation of our results with respect to changes in these assumptions will give a measure of the theoretical uncertainty.

1.8.1.1   The renormalisation scale parameter, x_μ

As we explained in Section 1.3, a characteristic energy scale μ must be chosen at which to renormalise the QCD couplings.[22] It is generally agreed that the most appropriate choice for μ is the characteristic energy scale of the hard interaction (in our case, the e^+e^- centre-of-mass energy), but a review of other possible choices is

---

[22]In practice one must also choose a "renormalisation scheme," which specifies the detailed method of renormalisation; all of the predictions used in this work have been calculated in the modified minimal subtraction ($\overline{\text{MS}}$) scheme. However, the choice of scheme does not affect the first-order scale dependence of the predictions, and will therefore be neglected.

given in Ref. [13].

In general, our perturbation expansion for the cumulative distribution of an event shape y will be

$$R\left(y, \alpha_{\mathrm{S}}(Q), x_\mu\right) \; = \; 1 \; + \; \mathcal{A}\left(y\right) \alpha_{\mathrm{S}}(\mu) \; + \; \mathcal{B}\left(y, x_\mu\right) \alpha_{\mathrm{S}}^2(\mu) \; + \; \mathcal{C}\left(y, x_\mu\right) \alpha_{\mathrm{S}}^3(\mu) \; + \; \ldots \quad ,$$

(1.59)

where we have defined $x_\mu = \mu/Q$. The coupling $\alpha_{\mathrm{S}}(\mu)$ is a function of $\alpha_{\mathrm{S}}(Q)$, as described by the Renormalisation Group Equation (RGE) given in Equation (1.16). Since the renormalisation scale is an unphysical parameter, the *complete* prediction for the observable R cannot depend on μ; therefore the x_μ-dependence of the coefficients $\mathcal{B}, \mathcal{C}, \ldots$ must exactly cancel the variation of $\alpha_{\mathrm{S}}(\mu)$. However, as we discussed briefly in Section 1.3, the QCD prediction for R will no longer be independent of μ when truncated to $\mathcal{O}(\alpha_{\mathrm{S}}^2)$. This dependence, which should decrease as more terms are added to the series, can be used to estimate the effect of the higher-order terms.

Using the RGE, we find that the variation of $\alpha_{\mathrm{S}}(\mu)$ with respect to small deviations from our chosen scale $\mu = Q$ is given to first order by [23]

$$\alpha_{\mathrm{S}}(\mu) \; = \; \alpha_{\mathrm{S}}(Q) \; - \; \frac{\beta_0 \ln x_\mu}{\pi} \, \alpha_{\mathrm{S}}^2(Q) \; + \; \ldots \quad .$$

(1.60)

Inserting this into Equation (1.59), and requiring $\mathrm{d}R/\mathrm{d}\mu = 0$ when summed to all orders, we find that

$$\mathcal{B}(y, x_\mu) \; = \; \mathcal{B}(y, 1) \; + \; \frac{\beta_0 \ln x_\mu}{\pi} \, \mathcal{A}(y) \quad .$$

(1.61)

Conventionally, and somewhat arbitrarily, the theoretical uncertainty of the distribution is defined by varying x_μ in the range $1/2 < x_\mu < 2$.

1.8.1.2   The resummation parameter, x_L

For each event shape observable y, we have defined a resummation which collects the logarithms $L = -\ln y$ into a series of terms with the form $L g_1(\alpha_{\mathrm{S}} L)$, $g_2(\alpha_{\mathrm{S}} L)$, $\alpha_{\mathrm{S}} g_3(\alpha_{\mathrm{S}} L)$, $\ldots$, where only the first two functions g_1 and g_2 are currently known. However, it has been noted recently [45] that the choice of logarithm L is not unique. Suppose, for example, that we defined a new event shape observable $y = x_L B_{\mathrm{T}}$,

---

[23]This formula, together with certain others in this chapter, is often expressed in the literature in terms of $\overline{\alpha_{\mathrm{S}}} \equiv \alpha_{\mathrm{S}}/2\pi$.

where B_T is the total jet broadening and x_L is some arbitrary constant. Our re-summed distribution for this observable would be expressed in terms of the 'shifted' logarithm $L = -\ln B_T - \ln x_L$.

The new parameter x_L plays a rôle analogous to that of the renormalisation scale parameter x_μ. If the complete resummation were known, the overall dependence on x_L would vanish; however, while we only have the first two terms, some residual ambiguity will remain. Just as the coefficient functions of the perturbation series acquire a dependence on x_μ to cancel the variation of $\alpha_S(\mu)$, the functions $g_n(\alpha_S L)$ become dependent on x_L. Writing the modified logarithm as $\widehat{L} = L - \ln x_L$, our old NLLA resummation is given by

$$
\begin{aligned}
\ln R_{\text{NLLA}} &= L g_1(\alpha_S L) + g_2(\alpha_S L) \\
&\approx \left[\widehat{L} + \ln x_L\right]\left[g_1(\alpha_S \widehat{L}) + g_1'(\alpha_S \widehat{L})\alpha_S \ln x_L\right] \\
&\quad + g_2(\alpha_S \widehat{L}) + g_2'(\alpha_S \widehat{L})\alpha_S \ln x_L \quad,
\end{aligned}
\tag{1.62}
$$

where $g_n'(\lambda) \equiv \mathrm{d}g_n/\mathrm{d}\lambda$. Regrouping the terms of this expression, we can now write

$$
\ln R_{\text{NLLA}} = \widehat{L}\hat{g}_1(\alpha_S \widehat{L}) + \hat{g}_2(\alpha_S \widehat{L}) + \text{subleading terms} \quad,
\tag{1.63}
$$

where

$$
\begin{aligned}
\hat{g}_1(\alpha_S \widehat{L}) &= g_1(\alpha_S \widehat{L}) \\
\text{and} \quad \hat{g}_2(\alpha_S \widehat{L}) &= g_2(\alpha_S \widehat{L}) + \left[g_1(\alpha_S \widehat{L}) + g_1'(\alpha_S \widehat{L})\alpha_S \widehat{L}\right]\ln x_L \quad.
\end{aligned}
\tag{1.64}
$$

The "subleading terms" here represent an estimate of the theoretical uncertainty in the resummation. Similar transformation laws can be derived for the matching coefficients G_{nm} and C_n; these are listed in Ref. [12].

We must now choose a nominal value and a range of variation for the parameter x_L, to define our resummed prediction and its associated uncertainty. In the past, event shape distributions have always been calculated using the implicit assumption $x_L = 1$. This is, in fact, the most natural choice. The six event shape observables y have been defined such that they approach the form

$$
\ln y = a \ln\left(\frac{k_T}{Q}\right) - b\eta
\tag{1.65}
$$

in the case of a single soft and collinear gluon emission; k_T and η are respectively

the transverse momentum and rapidity of the emitted gluon with respect to the $q\bar{q}$ axis, and a and b are integers. When we perform the transformation $y \to x_L y$ an additional constant is introduced in the above expression. We will therefore continue to use $x_L = 1$ as our nominal choice, to preserve this simple relationship between the logarithm L and the physical properties of the event. The range of variation in x_L used to define our theoretical uncertainties, however, is a more complicated and subjective issue: we discuss this point in Ref. [12]. We will use the range $4/9 < x_L < 9/4$ for the Durham y_{23} parameter, and $2/3 < x_L < 3/2$ for all other observables.

1.8.1.3 The kinematic constraint parameters, p and y_{max}

In Section 1.6.4 we introduced a modified form for the logarithm L, to impose the kinematic constraint $R(y_{\text{max}}) = 1$ on our NLLA predictions. Including both the x_L parameter and the kinematic constraint, the logarithm is now given by

$$\widetilde{L} = \frac{1}{p} \ln \left[\frac{1}{(x_L y)^p} - \frac{1}{(x_L y_{\text{max}})^p} + 1 \right] \tag{1.66}$$

The parameter p, which determines the sharpness with which the constraint is applied, will be varied over the range $1 < p < 2$ to determine the theoretical uncertainty; for our nominal distribution, we will continue to use $p = 1$.

An ambiguity also exists in the choice of kinematic boundaries y_{max}. Although a well-defined limit may exist for each observable—for example $T > 0.5$ in the case of thrust—this may correspond to a very improbable state containing a large number of partons. Also, no analytical expressions exist for y_{max} in some cases, so they must be estimated using Monte Carlo simulations. In Ref. [12] we define ranges of variation for y_{max}, to be used as contributions to our theoretical uncertainty. This is, however, a negligible effect in comparison to the x_μ and x_L variations.

1.8.1.4 Matching scheme dependence

The $\text{Log}(R)$ and R matching schemes, defined in Sections 1.6.3.1 and 1.6.3.2, provide two alternative methods for combining the $\mathcal{O}(\alpha_S^2)$ and NLLA predictions. We have chosen to use the $\text{Log}(R)$ scheme as our nominal theory prediction, and the difference between the two schemes as an estimate of the theoretical uncertainty. Again, this is usually a negligible contribution when compared with the x_μ and x_L variations.

1.8.1.5   Quark mass effects

As we noted in Section 1.6.2, the perturbative predictions used in this work do not take account of quark masses. After averaging over all accessible quark flavours, the influence of heavy quark effects on the fitted value of α_S is expected to be $\sim 1\%$ at $\sqrt{s} = 91$ GeV [12]. When new NLLA predictions become available, a consistent $\mathcal{O}(\alpha_S^2) + \text{NLLA}$ mass correction can be applied to our results; meanwhile the size of the uncertainty is much smaller than other contributions such as the x_μ dependence, and will be neglected.

1.8.2   Uncertainties in α_S

The aim of our experimental analysis will be to measure the strong coupling α_S by fitting theoretical predictions to the observed event shape distributions. We now investigate the effects of our theoretical uncertainties on the extracted values of α_S; at this stage, we will consider separately the effects of the x_μ, x_L and p variations.

For each variant of the perturbative prediction, we define two distributions:

- The variant distribution, calculated at a fixed value of α_S.
  Example: $R'(B_W)$ with $x_\mu = 1$, $x_L = 3/2$, $p = 1$, $\alpha_S = 0.12$.

- The nominal distribution, calculated at an alternative value of α_S.
  Example: $R'(B_W)$ with $x_\mu = 1$, $x_L = 1$, $p = 1$, $\alpha_S = 0.12 + \Delta\alpha_S$.

We then fit the nominal distribution to the variant distribution, with α_S as a free parameter; the deviation $\Delta\alpha_S$ estimates the theoretical uncertainty in an experimental determination of α_S. Our fits are calculated using the method of least squares, with the statistical 'uncertainty' of each bin proportional to the square root of its contents.[24] The ranges of the fits for each observable are the same as those used in the OPAL analysis, as listed in Section 3.5.2. Our results are shown in Figure 1.11, for a nominal value of α_S=0.12. The total jet broadening consistently gives the largest theoretical uncertainties, while the Durham y_{23} parameter and heavy jet mass give comparatively small uncertainties. The deviations in α_S due to variation of p are much smaller than those due to x_μ and x_L.

---

[24]We do not consider the effects of background and detector biases, which will in practice alter the statistical weights slightly from a simple Poisson distribution.
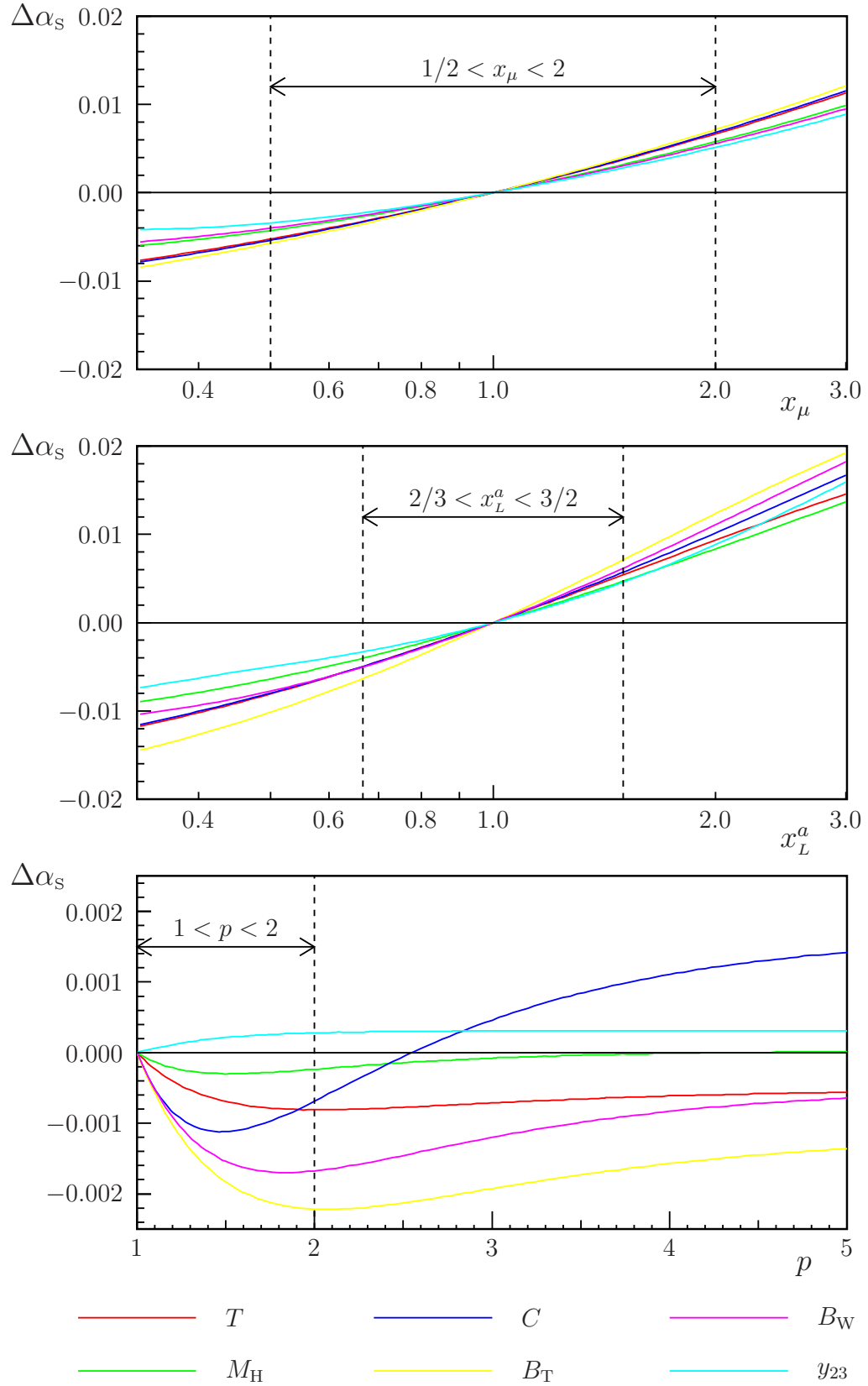
Figure 1.11: Deviations in α_S corresponding to variation of the parameters x_μ, x_L and p, in the perturbative predictions for the thrust, heavy jet mass, C-parameter, total jet broadening, wide jet broadening and Durham y_{23} parameter. The power a is equal to $1/2$ in the case of y_{23}, and 1 for all other observables.

1.8.3   Combining the theoretical uncertainty estimates

We would now like to calculate an overall theoretical uncertainty, combining each of the contributions listed in Section 1.8.1. One must remember, however, that the various contributions do not represent distinct *sources* of uncertainty, in the conventional sense: the sources here are simply the uncalculated terms of the order-by-order and resummed predictions. Our calculated uncertainties represent the sensitivity of the distributions to various subsets of the missing terms. Since those subsets are likely to overlap, we should not merely add the contributions in quadrature. Furthermore, different regions of the event shape distributions will be dominated by different types of uncertainty; generally the x_μ variation gives the largest uncertainty at the two-jet end of the fit range (small y), and the x_L variation dominates the region of multiple gluon emissions (large y). It is therefore appropriate to combine our theoretical uncertainty estimates at the distribution level, rather than combining deviations in the α_S fits.

Figure 1.12 shows the deviations in the thrust distribution corresponding to each of the uncertainty contributions (excluding quark mass effects). In the case of the upper x_L variation, for example, we plot the fractional difference between the distributions predicted for $x_L = 3/2$ and $x_L = 1$. The outer envelope of all these variations defines an "uncertainty band," indicated by yellow shading.

Just as we have done for the individual variations in the previous section, this combined uncertainty band can be translated into a deviation in α_S. We once again define a variant distribution, corresponding to the edge of the band, and a nominal distribution. While fixing $\alpha_S = \alpha_S^0$ in the variant distributions, we change α_S in the nominal distribution; the upper and lower uncertainties $\sigma^\pm$ are defined by the range of values $\alpha_S^0 - \sigma^- < \alpha_S < \alpha_S^0 + \sigma^+$ for which the nominal distribution lies completely inside the uncertainty band, within the standard fit range.[25]

---

[25]Alternatively, one could simply fit the nominal distributions to the variant distributions, with α_S as a free parameter, as we have done in Section 1.8.2. This approach would give slightly larger uncertainty estimates (an increase of $\sim 15\%$ in the theoretical uncertainty of the combined LEP α_S measurement presented in Chapter 4).
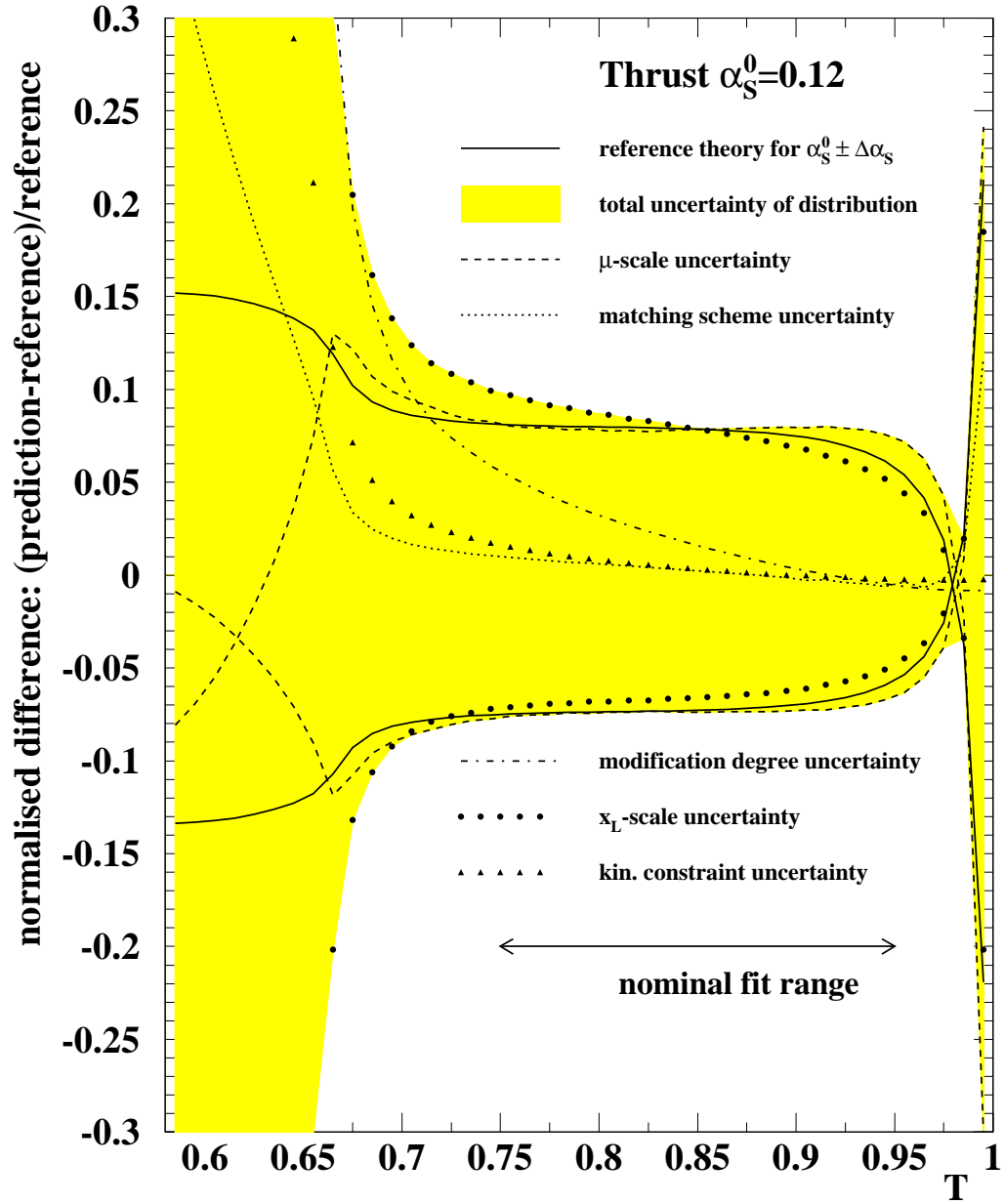
Figure 1.12: The uncertainty band for the thrust distribution *(Figure prepared by H. Stenzel, and published in Ref. [12])*

1.9   Monte Carlo models

So far, the QCD predictions we have discussed have been concerned with free quarks and gluons. Before reaching our detector, however, these partons must 'fragment' into bound colourless states. This final phase of the QCD interaction, which occurs at a low characteristic energy scale, cannot be predicted by perturbation theory. Instead, we must use numerical simulations based on semi-empirical models. The Monte Carlo programs used in our analysis to simulate multihadronic events are $\mathcal{KK}$2f 4.01/4.13 [46], PYTHIA 6.125 [47], HERWIG 6.2 [48] and ARIADNE 4.11 [49].

The simulation of each event proceeds in four distinct stages, which are illustrated schematically in Figure 1.13:

- Generation of a q$\bar{\text{q}}$ system from the initial e$^+$e$^-$ state, possibly with initial-state radiation

- A "parton shower," in which gluons are radiated from the q$\bar{\text{q}}$ pair; the gluons may then radiate other gluons, or split to form new q$\bar{\text{q}}$ pairs. This stage should reproduce as closely as possible the predictions of perturbative QCD.

- Fragmentation of the parton system into hadrons

- Decays of short-lived hadrons such as the π^0 and K$_{\text{S}}^0$ mesons

We will briefly describe the implementation of these stages in the Monte Carlo programs; not all stages are implemented by all programs.

1.9.1   Generation of the q$\bar{\text{q}}$ system

The first stage of the event is simulated most accurately by $\mathcal{KK}$2f, which provides a detailed treatment of multiple photon emission from the initial e$^+$e$^-$ state. The resulting q$\bar{\text{q}}$ system can then be passed as an input to the parton shower models in PYTHIA, HERWIG or ARIADNE. When simulating events without initial-state radiation, however, we can use PYTHIA or HERWIG in place of $\mathcal{KK}$2f.

1.9.2   The parton shower

In the PYTHIA [47] and HERWIG [48] programs, the perturbative stage of the event is simulated using a numerical implementation of the DGLAP equations [31],
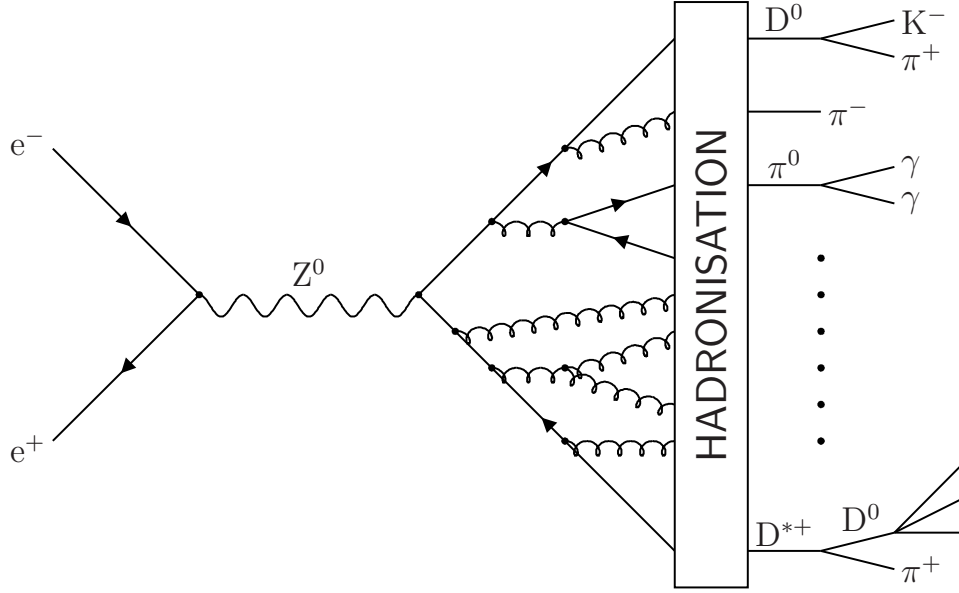
Figure 1.13: A schematic view of the stages to be simulated in an hadronic decay of the Z^0 boson at LEP

which were also used in the derivation of the NLLA analytical predictions. The progress of each parton in the cascade is parameterised by an "evolution variable," $t = \ln(Q^2/\Lambda^2)$, where Q^2 is related to the virtuality of the parton, and Λ is some arbitrary fixed scale. The probability $\mathcal{P}$ for a parton a of virtuality Q^2 to split into two partons b and c, carrying momentum fractions z and $(1 - z)$ respectively, can then be written in the form

$$\frac{\mathrm{d}\mathcal{P}}{\mathrm{d}t} \propto \int_0^1 \mathrm{d}z \, \frac{\alpha_{\mathrm{S}}}{2\pi} P_{a \to bc}(z) \qquad [0 < t < t_0] \quad , \tag{1.67}$$

where t_0 and t are the evolution variables before and after the splitting, and $P_{\mathrm{a \to bc}}$ are the Altarelli-Parisi splitting kernels for the processes $\mathrm{q \to qg}$, $\mathrm{g \to gg}$, $\mathrm{g \to q\bar{q}}$ and $\mathrm{q \to q\gamma}$. The precise definition of the scale Q^2 varies between models: PYTHIA uses $Q^2 = m_a^2$, while HERWIG uses $Q^2 \approx m_a^2/2z(1 - z)$, where m_a^2 is the invariant mass-squared of the parton a.

The models include various features to incorporate coherence effects,[26] the simplest of which is the property of *angular ordering*: the opening angle θ_{bc} of each branching $a \to bc$ is required to be less than that of the previous branch in the cascade. This result can be explained [4] in terms of the Uncertainty Principle. Other

---

[26]The acronym 'HERWIG' stands for "Hadron Emission Reactions With *Interfering Gluons*".

effects include correlations between the azimuthal branching angles, due to gluon polarisation.

The shower is continued until the virtuality of the partons reaches some lower limit $Q_0 \sim 1$ GeV, which is a tunable parameter of the model. The final parton configuration is then passed to the non-perturbative hadronisation stage. More detailed discussions of parton shower physics are given in Refs. [4] and [21].

The ARIADNE Monte Carlo [49] uses an alternative formalism: the Colour Dipole Model [50, 51]. In this paradigm, new partons are radiated by the colour fields between the existing quarks and gluons, and not by the partons themselves. The q$\bar{\text{q}}$ system represents a single dipole, capable of radiating a gluon; after the first branching has occurred, the q$\bar{\text{q}}$g system is described by two independent q–g and g–$\bar{\text{q}}$ dipoles, and so forth.

Since ARIADNE simulates only the parton shower stage, the quarks and gluons are then passed to PYTHIA for hadronisation.

1.9.3 Fragmentation

Hadronisation is simulated in PYTHIA using the *Lund string model* [52]. Unlike the electromagnetic field patterns formed by distributions of charges and currents, the corresponding fields in QCD are expected to be confined in narrow regions stretched between the colour charges; this is a result of the gluon's self-coupling property. According to the string model, the field lines will eventually 'break' at several points to form new q$\bar{\text{q}}$ or diquark-antidiquark pairs which lead to meson and baryon production. The model has many tunable parameters, which have been chosen to give optimal agreement with the LEP data.

HERWIG uses the alternative *cluster model* [53], motivated by the property of preconfinement [54] in perturbative QCD. It has been shown that partons naturally tend to group themselves into colourless low-mass clusters of quarks and gluons, during the perturbative shower evolution. Herwig simulates the production of hadrons through the decay of these 'preconfined' clusters. Any gluons remaining at the end of the parton shower are first divided non-perturbatively into q$\bar{\text{q}}$ pairs, which are then paired with neighbouring quarks and antiquarks to produce colourless clusters.

1.9.4 Decays

Some of the hadrons produced in e^+e^- collisions at LEP are expected to decay very close the interaction point; the experiments will then measure event shape observables based on the daughter particles. For convenience, we consider all particles with lifetimes less than 3×10^{-10} s to be unstable. PYTHIA and HERWIG simulate the decays of these particles based on standard branching ratios supplied by the Particle Data Group [13].

1.10 Other experimental studies of QCD

Our measurements of event shape observables in e^+e^- collisions represent just one of the experimental methods used to study QCD. Reviews of other tests and measurements can be found in Refs. [13] and [55]; only a very brief overview will be given here, focusing mainly on OPAL measurements. The results can be divided broadly into two categories: those which measure the free parameter α_S, and those which test the structure of the theory. Although the value of $\alpha_S(M_Z)$ is not predicted by the Standard Model, the consistency of measurements obtained from different physical processes at a variety of energy scales is itself a further success for perturbative QCD.

1.10.1 Measurements of α_S

The current world average of α_S at the Z^0 mass scale is $\alpha_S(M_Z) = 0.1172 \pm 0.0020$ [13]; a breakdown of the contributions from different physics processes is shown in Figure 1.14. The most precise determinations of $\alpha_S(M_Z)$ using LEP data are those from the hadronic decays of the τ lepton (for example, in Ref. [56]), and those from the ratio of hadronic and leptonic partial decay widths of the Z^0 boson [6]. These methods have two distinct advantages over the event shape fits: firstly they have negligible sensitivity to non-perturbative effects, and secondly the theory predictions are available to three orders of perturbation theory. Since the measurements themselves are single numbers rather than a fits to a distribution, however, they do not additionally provide a test of the QCD gauge structure.

The strong coupling has also been determined at LEP using a variety of jet multiplicity observables [57], similar to the y_{23} variable used in our own measure-
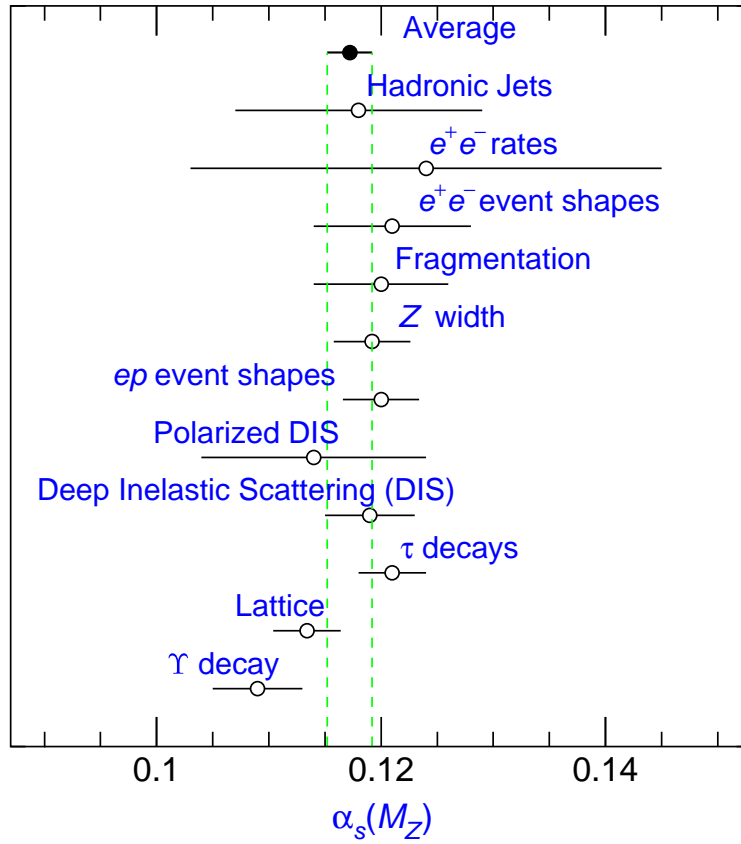
Figure 1.14: Contributions to the world average measurement of $\alpha_{\rm S}(M_{\rm Z})$
(Figure taken from Ref. [13])

ments; some of these distributions have only $\mathcal{O}(\alpha_{\rm S}^2)$ predictions, while others also have NLLA resummations.

A new determination of $\alpha_{\rm S}$ has recently been performed using the photon structure function F_2^γ in e^+e^- data from PETRA, TRISTAN and LEP [58]. By combining data at different centre-of-mass energies, one can also measure $\alpha_{\rm S}$ from the energy-dependence of the parton fragmentation functions [59].

In the last ten years, a new approach has been developed to account for non-perturbative effects in event shape distributions. In these "power correction" models [60–65], the distributions and their moments are predicted to be shifted by some factor proportional to $1/Q^n$, where Q is the energy scale of the hard interaction and n is an integer. The use of power corrections in experimental analyses (for example, Ref. [66]) is supposed to remove the need for a Monte Carlo model to simulate hadronisation corrections,[27] but also introduces a new free parameter α_0 which must be determined from the data.

---

[27]This point is perhaps debatable, since power corrections do not contain detailed information about resonances, hadron masses and decays.

Outside of e^+e^- physics, one of the most precise measurements of α_S has been obtained as part of a global determination of parton distribution functions in electron-proton and proton-antiproton collisions [67].

1.10.2 Tests of the QCD gauge structure

In addition to measuring the parameter α_S, experimental data can be used to test the validity of the SU(3) gauge theory as a description of the strong interaction. Predictions in perturbative QCD are often expressed in terms of three "colour factors," $C_A = 3$, $C_F = 4/3$ and $T_F = 1/2$, which roughly correspond to the relative strengths of the $g \to gg$, $q \to qg$ and $g \to q\bar{q}$ vertices respectively. These factors are fundamental properties of the symmetry group, and can be compared against the corresponding factors in other groups. One can determine C_A, C_F and T_F in e^+e^- annihilation [68], using four-jet events of the types $e^+e^- \to Z^0/\gamma \to q\bar{q}q\bar{q}$ and $e^+e^- \to Z^0/\gamma \to q\bar{q}gg$. The measurements use next-to-leading order QCD predictions, for the four-jet rate R_4 and several angular correlation variables. The results are in good agreement with the standard QCD values.

The QCD colour factors can also be measured using the three-jet e^+e^- event shape observables from which we determine α_S in this work. The results [69], although rather imprecise, are in agreement with the SU(3) gauge structure.

1.10.3 Flavour independence

QCD makes no distinction between the couplings of the six flavours. The quarks do have different masses and electric charges, but these are expected to have a negligible effect, when the energy scale probed is much higher than the quark masses. The proton and neutron masses, for example, which are dominated by QCD interaction potentials, differ by only 0.1%. At the energy scales of LEP, the perturbative behaviour of b quarks should differ slightly from that of the lighter flavours, but we do not expect to observe differences in the gluon radiation from u, d, s and c quarks. By tagging hadronic Z^0 decays as either u/d/s, c or b flavoured, based on the hadrons identified in the final state, one can demonstrate using OPAL data that the corresponding values of α_S do not differ by more than a few percent [70, 71]. Measurements of charged particle multiplicities in Z^0 decays have also been consistent with the flavour-independence of QCD [72, 73].

Chapter 2

The OPAL detector at LEP

The work described in this dissertation is based on data from the Large Electron-Positron Collider (LEP), which operated at CERN between the years 1989 and 2000. Interactions were studied at centre-of-mass energies in the range 91–209 GeV, using four detectors spaced around the circular collider. Our detailed event shape measurements, presented in Chapter 3, are derived from collisions observed in the OPAL detector. In Chapter 4 we combine our measurements of the strong coupling α_S with those from the other three LEP experiments: ALEPH, DELPHI and L3. This chapter outlines the main features of the LEP collider and the OPAL detector, with a focus on the components most relevant to our measurements. Details of the ALEPH, DELPHI and L3 experiments may be found in Refs. [74], [75] and [76] respectively; further information on the OPAL detector is given in Ref. [77].

2.1   The LEP collider

2.1.1   Historical background

In 1973 the Gargamelle bubble chamber at CERN delivered the world's first experimental evidence for "neutral currents," mediated by the Z^0 boson. A beam of muon neutrinos was observed to scatter from heavy nuclei, without any production of charged muons [78]. This confirmed the predictions of the Glashow-Weinberg-Salam electroweak gauge theory, and provoked further experiments to investigate the properties of the Z^0 and $W^\pm$ bosons. Ten years later, in 1983, the UA1 and UA2 experiments both reported direct evidence for the production of Z^0 [79,80] and $W^\pm$ [81,82] bosons in $p\bar{p}$ interactions at the CERN SPS collider.

Planning had already commenced in 1976 for the building a circular high energy e^+e^- collider, which would act as a 'factory' for Z^0 and $W^\pm$ bosons. Inelastic collisions between leptons are phenomenologically much simpler than those between composite hadrons, so extremely precise measurements could then be made at well-defined energy scales. Due to its low mass, an electron emits many times more energy in the form of synchrotron radiation than a proton would when travelling with the same energy.[1] It would therefore be necessary to build an accelerator with the largest feasible radius, in order to minimise the centripetal acceleration of the beam particles.

A LEP Study Group was formed, and published an initial design report in August 1977 [83] for a collider with eight experimental interaction points and a circumference of 51 km; after several revisions, the CERN Council in December 1981 approved a proposal for a 26.7 km accelerator with four experiments. The machine was designed to run initially with an energy of up to 50 GeV per beam, which was expected to be sufficient for the production of real Z^0 bosons. A later phase (LEP2) was also anticipated, with energies of up to 100 GeV per beam. LEP was to be installed in a tunnel approximately 100 m below the surface of the plain lying between Lake Geneva and the Jura mountains: a schematic view of the tunnel is shown in Figure 2.1. Construction began in 1983, and the first beams were injected in 1989. The final designs were published in Refs. [84–86].

LEP operated successfully with a beam energy of 45.6 GeV, exactly half of the Z^0 mass, from 1989 to 1995. Millions of Z^0 decays were observed by each of the four experiments, yielding precision tests of the Standard Model. During the winter shutdown of 1995–6, various hardware upgrades took place [87] including the installation of new superconducting cavities; these enabled LEP to start its second phase of running, with energies above the threshold for W^+W^- pair production. The beam energies were gradually increased over following five years, reaching a maximum of 104.5 GeV per beam during 2000. LEP was finally closed to make way for construction of the Large Hadron Collider (LHC), in November 2000.

---

[1]The energy loss per turn of a circular accelerator of radius R, for a particle of mass m, charge q, speed βc and energy $E = \gamma mc^2$, is

$$\Delta E \;=\; \frac{q^2 \beta^3 \gamma^4}{3\epsilon_0 R} \;=\; \frac{q^2 \beta^3 E^4}{3\epsilon_0 c^8 m^4 R} \;\;,$$

where c is the speed of light and ϵ_0 is the permittivity of free space.
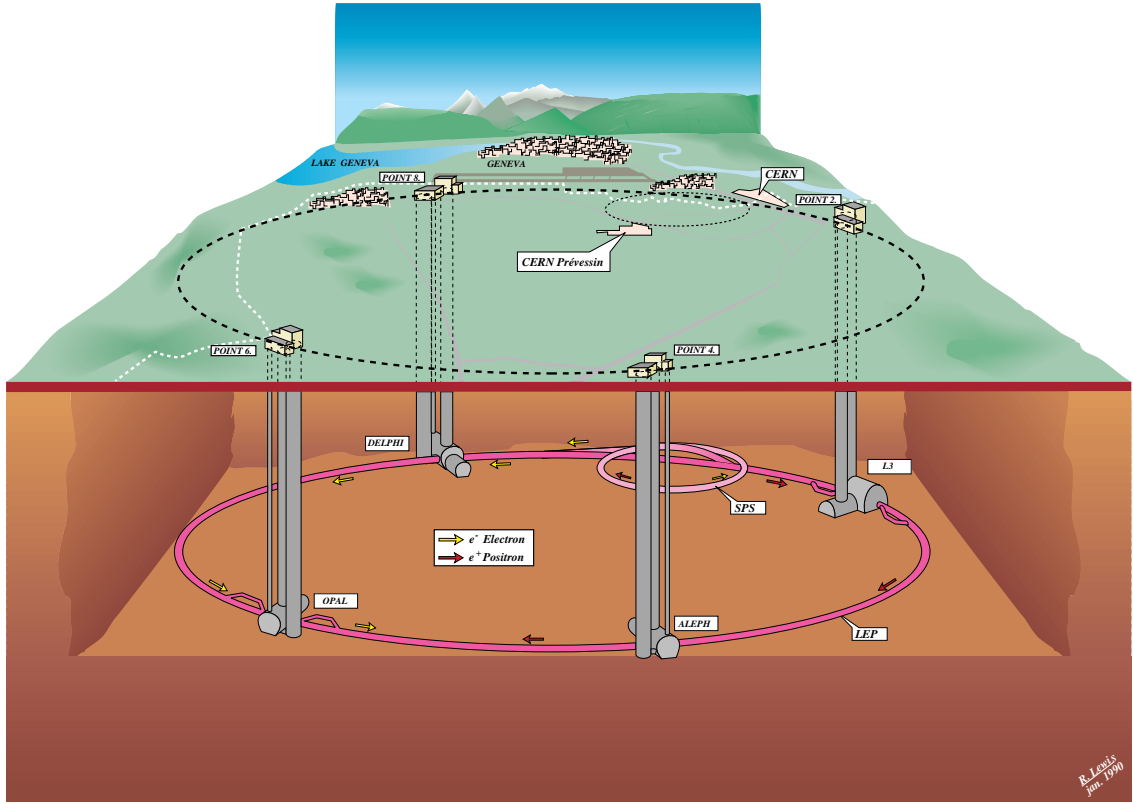
Figure 2.1: A schematic cut-away impression of the LEP collider and its geographical location; the Swiss-French border is indicated in white, with the city of Geneva and its airport in the background. The horizontal and vertical scales are not equal.

2.1.2   The LEP injector chain

A complex sequence of accelerators and storage rings were used to supply electrons and positrons to the LEP beampipe; Figure 2.2 shows a diagram of the complete CERN accelerator complex (some of which does not relate to LEP). The electrons and positrons were produced in pairs from a fixed tungsten target, using a beam of 200 MeV electrons from the LEP Injector Linac (LIL). The beams were separated, and accelerated to 600 MeV, before injection into the Electron-Positron Accumulator (EPA) and thence into the Proton Synchrotron (PS) ring. At an energy of 3.5 GeV, the particle bunches were transferred to the Super Proton Synchrotron (SPS), which finally accelerated them to 20 GeV for injection into LEP.

2.1.3   The main ring

The LEP main ring comprised eight circular arcs joined by straight sections of length 119 m; its total circumference was 26659 m, exactly 27/7 times larger that of the
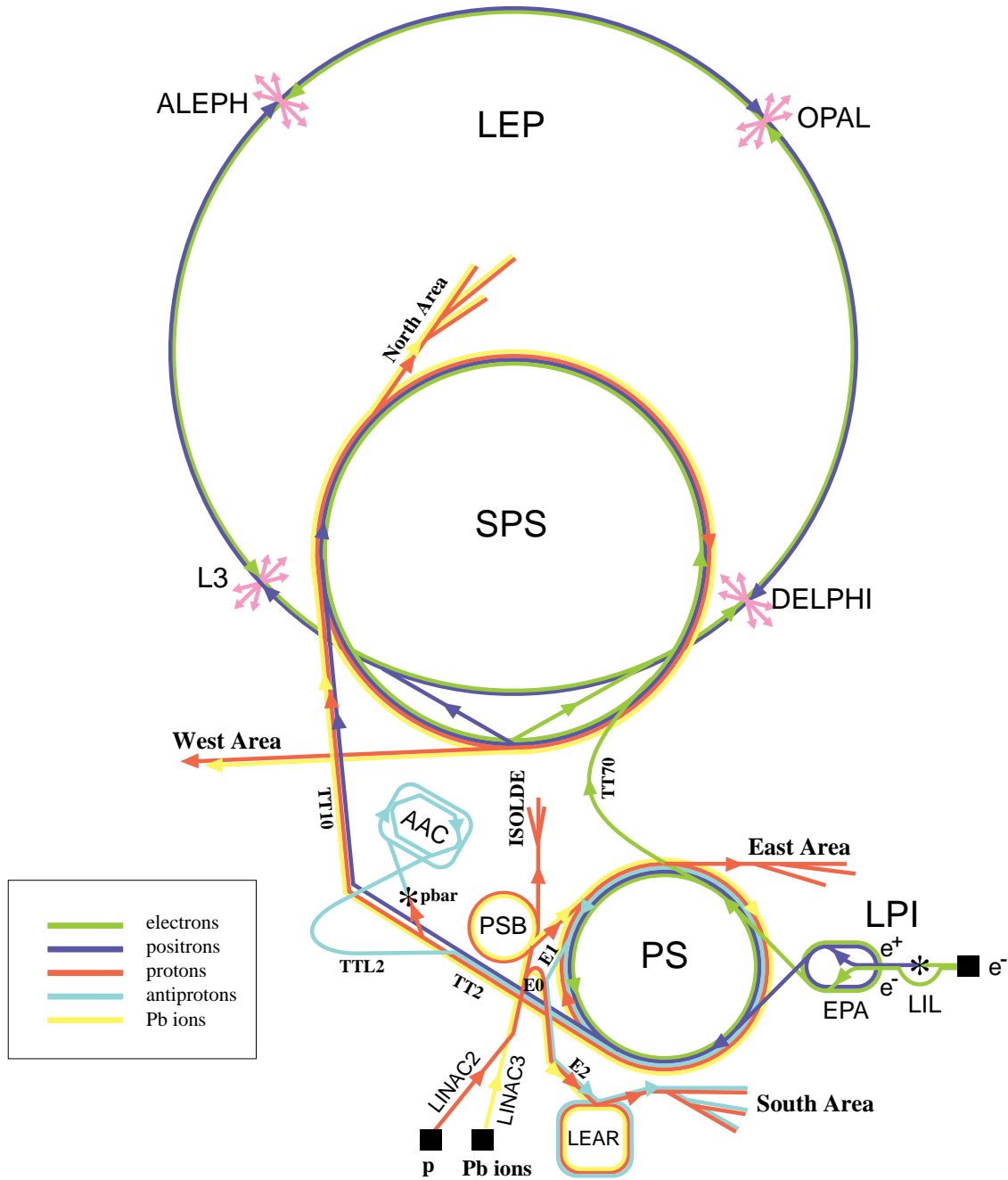
LEP: Large Electron-Positron collider   LPI: LEP Pre-Injector
SPS: Super Proton Synchrotron   EPA: Electron-Positron Accumulator
AAC: Antiproton Accumulator Complex   LIL: LEP Injector LINAC
ISOLDE: Isotope Separator OnLine DEvice   LINAC: LINear ACcelerator
PSB: Proton Synchrotron Booster   LEAR: Low Energy Antiproton Ring
PS: Proton Synchrotron

Figure 2.2: A plan of the CERN accelerator complex during the operation of LEP

SPS. For geological reasons the tunnel was constructed with a 1.4% tilt, resulting in an altitude difference of 120 m between the highest and lowest points.

Dipole magnets were installed at approximately 50 m intervals around the ring, providing a field of up to 0.135 T to bend the beams. These were interspersed with quadrupole and sextupole magnets, which focused the beam using linear and quadratic field gradients. Other magnets were used to correct the beam orbit in the vicinity of the straight sections.

Physics experiments were installed in four of the straight sections, at 90° intervals around the ring. In the same sections, either side of each experiment, a system of radio-frequency (RF) cavities provided the acceleration needed to reach and maintain the final beam energy. Initially only copper cavities were used, but these were gradually replaced by superconducting niobium cavities, cooled by liquid helium. All of the cavities operated at a frequency of 352.21 MHz, corresponding to the 31320$^{\text{th}}$ harmonic of the LEP revolution frequency.

LEP could be operated with either 4+4 or 8+8 bunches of electrons and positrons; the timing of the bunches was such that they crossed one another at the centres of the straight sections. A system of electrostatic separators was used to prevent the beams from interacting before reaching a stable orbit at their final energy; the bunches could then be brought into collision at the centre of each experiment, with a vertical precision of about 4 μm. When 8+8 bunches were used, the beams were kept separated at the non-experimental crossing points.

An extremely high vacuum was needed, to keep the beams circulating close to the speed of light for several hours. Synchrotron radiation from the beam stimulated the production of electron-positron pairs in the wall of the aluminium beampipe, and hence the desorption of gas molecules; continuous pumping was therefore required to maintain a pressure below 10^{-9} torr. Low pressures were especially important in the vicinity of the interaction points, where unwanted beam scattering could contribute to the experimental background. LEP was the first accelerator to use non-evaporable getter (NEG) strips for its main pumping system: these act by chemically adsorbing the majority of gases found inside the beampipe. Conventional rotary vane pumps were also used, to establish a pressure low enough for the NEG strips to become effective.

2.2   The OPAL detector

OPAL[2] was a multi-purpose experiment, designed to detect and identify nearly all of the possible processes occurring in e^+e^- collisions at LEP. The detector provided a high acceptance and accurate reconstruction for every type of event, with the exception of very low angle scattering processes ($\theta < 40$ mrad) and those producing only neutrinos.

The overall structure of the OPAL detector was similar to that of the other three LEP experiments. Each of the major subdetectors formed a cylindrical layer around the interaction point, offering the most complete feasible solid angle coverage in each case; a three-dimensional drawing and two cross sections of these layers are shown in Figures 2.3 and 2.4. At the centre, a silicon microvertex detector provided excellent spatial resolution for charged particles passing through the wall of the beampipe. This was surrounded by a system of pressurised drift chambers in a strong magnetic field, which measured the directions, momenta and energy losses of the charged particles. Outside the drift chambers and the magnet, a system of scintillation counters was used to determine the flight times of particles from the interaction region. An electromagnetic calorimeter then measured the energies of photons, electrons and positrons; hadrons were subsequently absorbed by the return yoke of the magnet, which functioned as an hadronic calorimeter. Finally, a layer of thin drift chambers identified muons, which were usually the only detectable particles to escape the calorimeters. A system of "forward detectors" was used to detect particles travelling nearly parallel to the beampipe, such as the electrons and positrons in Bhabha or two-photon events.

OPAL literature conventionally uses a Cartesian coordinate system, centred on the nominal interaction point. The z-axis points along the e^- beam direction, which is inclined above the horizontal at an angle of 13.9 mrad. The x-axis is precisely horizontal, and points approximately towards the centre of the LEP ring, while the y-axis is approximately vertical. The polar angle θ and azimuthal angle ϕ are defined in the usual way with respect to the Cartesian axes.

A more detailed description of the detector components will be given in the sections that follow; we focus particularly on those subdetectors most relevant to our analysis. Further details may be found in Ref. [77], which describes the original

---

[2]**O**mni-**P**urpose **A**pparatus at **LEP**

Electromagnetic calorimeters

Muon detectors

Hadron calorimeters and return yoke

Jet chamber

Vertex detector

Microvertex detector

Z chambers

y

θ   φ

z   x

Solenoid and Pressure Vessel

Presamplers

Time of flight detector

Original forward detector

Silicon-tungsten forward detector
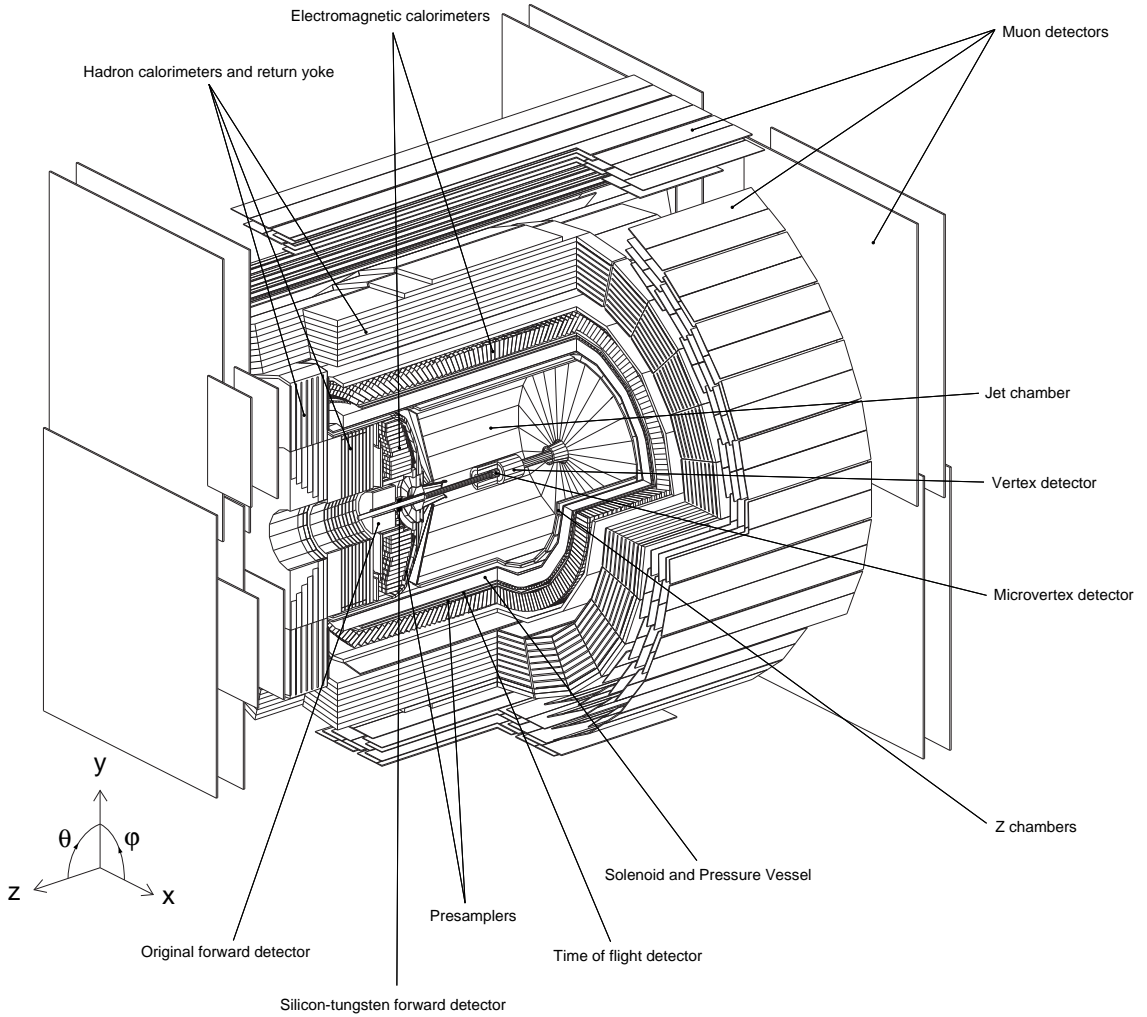
Figure 2.3: A cut-away drawing of the OPAL detector

detector as it was in 1989. The silicon microvertex detector [88–90], tile endcaps [91], silicon-tungsten luminometers [92] and pretrigger system [93] were added later.

2.2.1   Central tracking and microvertex detectors

The colliding beams at the centre of the OPAL detector were contained in an airtight beryllium pipe with a thickness of 1.1 mm and a minimum inner radius of 53 mm. Outside the beampipe, a second cylindrical tube of inner radius 80 mm formed the inner wall of a 4 bar pressure vessel, which contained the drift chambers of the central tracking system. A silicon microvertex detector was located in the narrow annular region between these two pipes.

a)

Barrel

Muon detector

Hadron calorimeter and return yoke

Electromagnetic calorimeter
Presampler
Time of flight detector
Solenoid and Pressure Vessel

Z chambers
Jet chamber
Vertex detector
Microvertex detector

Interaction region

b)

Endcap

Microvertex detector
Vertex detector
Jet chamber
Z chambers

Silicon-tungsten forward detector
Original forward detector

Presampler
Electromagnetic calorimeter
Pole tip hadron calorimeter
Hadron calorimeter
Muon detector

Figure 2.4: Section views of the OPAL detector, in planes (a) perpendicular and (b) parallel to the beam axis.

2.2.1.1   Silicon microvertex detector

The OPAL microvertex detector was first installed in 1991 [88], and was subse-
quently upgraded in 1993 [89] and 1995 [90]. The beampipe was surrounded by two
layers of slightly overlapping silicon 'ladders'. The two faces of each ladder were
divided perpendicularly into narrow strips, to give a two-dimensional readout when
a charged particle passed through the ladder. By combining spatial position data
from the two layers of the microvertex detector, one could extrapolate tracks back to
the interaction point with high precision. It was therefore possible, in many cases,
to resolve the secondary decay vertices associated with τ leptons and b flavoured
hadrons. One could also distinguish pairs of high energy particles produced almost
parallel to one another, which would appear as a single track in the drift chambers.

The resolution of the vertex position was approximately 20–50 μm in the z di-
rection and 15 μm in the r-ϕ plane; the azimuthal coverage of the detector was
made almost complete in the most recent upgrade, while the angular coverage in
the polar direction was increased to $|\cos\theta| < 0.89$.

2.2.1.2   Central vertex detector, jet chamber and z-chambers

A system of drift chambers provided the principal momentum measurement for
charged particles. The chambers were contained in a sealed cylindrical vessel around
the beam axis, filled with 88.2% argon, 9.8% methane and 2.0% isobutane at 4 bar
pressure. A solenoidal magnet surrounded the curved outer surface of the pressure
vessel, providing a field of 0.435 T; the field was uniform at the 0.5% level, and was
parallel to the beam axis, so that the beam itself was unperturbed.

The **central vertex detector** [94] formed the inner part of the tracking system,
and originally fulfilled the same purpose as the new silicon microvertex detector by
extrapolating tracks back to the interaction point. The chamber was 1 m long with
a 470 mm diameter, and was divided into two layers, each containing 36 identical
sectors, as shown in Figure 2.5. The inner 'axial' layer contained radial planes of
high-voltage wires aligned parallel to the beam axis; the electric field was directed
perpendicular to the anode planes. By measuring the drift times of electrons released
by the passage of a charged particle, one could determine the position of the ionised
gas molecule with a precision of about 50 μm in the r-ϕ plane. A crude measurement
of the z coordinate was also possible, by comparing the arrival times of the signal
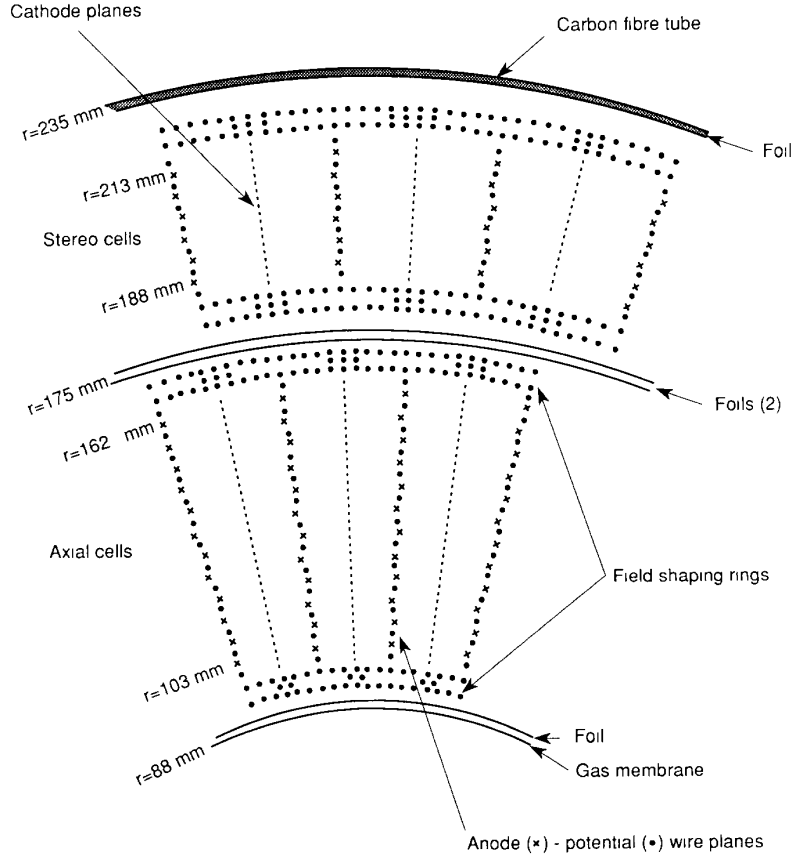
Figure 2.5: A cross section through the OPAL central vertex detector

at each end of the wire. This method was used for making fast real-time trigger decisions, but was inadequate for offline analysis purposes. A second 'stereo' layer was therefore constructed, in which the anode and cathode wires were not parallel to the beam; instead one of the endplates was rotated by approximately 4° about the beam axis. By combining the drift times from the axial and stereo layers, it was possible to reconstruct the trajectory of a particle in three dimensions.

The **jet chamber** [95] was similar to the axial part of the central vertex detector, but was 4 m long with an outer diameter of 3.7 m, and was divided into 24 sectors. By determining a large number of points on the curved trajectory of a charged particle in a known magnetic field, one could make a precise measurement of its transverse momentum. The fractional resolution was estimated to be $\sigma_{p_T}/p_T = 0.018 \oplus 0.0016\,p_T$, where the transverse momentum p_T is in units of GeV. The first term of the uncertainty is due to multiple scattering, and the second is due to the spatial resolution. The rate of energy loss due to ionisation, $\mathrm{d}E/\mathrm{d}x$, could also be calculated, from the charge depositions recorded on the wires. According to

the Bethe-Bloch formula, dE/dx is directly related to the speed v/c of the particle; by combining the momentum and speed, one obtains an estimate of the mass, and hence the identity of the particle. Such identification was only possible for particles of relatively low energy ($p \lesssim 10$ GeV), and is not directly relevant to our event shape measurements, which are fully inclusive quantities.

Of the three drift chamber systems, the jet chamber provided the most complete angular coverage, with all polar angles in the range $|\cos\theta| < 0.98$ being covered by at least eight sense wires.

Around the jet chamber was a cylindrical layer of 24 **z-chambers** [96], designed specifically to measure the z coordinates of the tracks. Each chamber was 50 cm wide and 59 mm thick, and covered the full 4 m length of the jet chamber. The maximum drift distance was about 25 cm in the z direction, corresponding to a resolution of approximately 200 μm.

In both the jet chamber and the z-chambers, it was possible to obtain track coordinates in the direction parallel to the wires by measuring the ratio of charges received at the two ends. However, far more precise reconstruction was possible by combining the transverse measurements from the jet chamber and z-chambers.

2.2.2 Electromagnetic calorimeters

For the purposes of our analysis, the data provided by the central tracking chambers are supplemented most importantly by energy measurements from the electromagnetic calorimeters.

The solenoid was surrounded by a cylindrical array of 9440 lead glass blocks, which formed the barrel section of the electromagnetic calorimeter system. Each block was $\sim$10$\times$10 cm in cross section and 37 cm in depth, providing 24.6 radiation lengths for photons travelling from the interaction point; the blocks were oriented approximately towards the centre of the detector, with a slight tilt to prevent particles escaping through the gaps. Two further arrays, each comprising 1132 lead glass blocks, formed the endcap electromagnetic calorimeters [97]: these blocks varied in depth, but provided a minimum of 20.5 radiation lengths. Together, the barrel and endcap sections offered complete azimuthal coverage over the polar range $|\cos\theta| < 0.98$.

When a high-energy electron or positron entered the lead glass, it would ra-

diate bremsstrahlung photons due to the nuclear Coulomb fields of the material; its energy would be reduced by a factor e^{-1} for each radiation length of material. Some of the emitted photons would then be converted to electron-positron pairs by further interaction with the material: the mean free path for this process is 9/7 of the radiation length. The result was an electromagnetic shower comprising electrons, positrons and photons. The electrons and positrons would also lose energy due to ionisation and Čerenkov radiation, until eventually the entire shower had been converted to low-energy radiation and heat. Each block was wrapped with a reflective aluminium layer, and was connected via a lightguide to a photomultiplier tube, which detected the Čerenkov photons. The number of observed photons was proportional to the total track length contained in the calorimeter, which in turn was proportional to the energy deposited.

Although the depth of the lead glass blocks ensured total absorption of electrons, positrons and photons, a considerable fraction of the initial energy carried by these particles was lost before they entered the electromagnetic calorimeter. Approximately two radiation lengths of material lay between the interaction point and the calorimeter, mostly due to the solenoid and pressure vessel. A system of **presamplers** [98] was therefore installed in front of the calorimeters, to measure the numbers and positions of particles produced through showering in this intervening material; the number of particles present in the shower at this stage provided a rough estimate of the energy already deposited. The presamplers in the barrel region comprised two layers of streamer tubes, while those in the endcaps consisted of thin high-gain multiwire chambers.

The energy resolution of the electromagnetic calorimeters was estimated to be $\sigma_E/E \approx 0.2\% \oplus 6.3\%/\sqrt{E[\text{GeV}]}$ in the barrel region, and $\sigma_E/E \approx 5\%/\sqrt{E[\text{GeV}]}$ in the endcaps; the $E^{-1/2}$ factors arise from statistical fluctuations in the number of Čerenkov photons, whose expected value is proportional to the incident energy. The resolution for shower positions measured in the presamplers was approximately 5 mm in the barrel and 2–5 mm in the endcaps.

2.2.3   Hadron calorimeters

Outside the electromagnetic calorimeters, the return yoke of the magnet absorbed the vast majority of hadrons emerging from the lead glass, through nuclear interac-

tions. In the barrel region, the yoke was divided into eight concentric iron layers of thickness 100 mm, with 25 mm spaces: these gaps contained streamer tubes [99], which sampled the energy of the shower. The toroidal endcaps of the magnet were similarly divided into seven layers of iron, with 35 mm spaces containing streamer tubes. In the forward regions, the magnet yoke was implemented as a poletip hadron calorimeter, which extended angular coverage to $|\cos\theta| < 0.99$.

Since approximately two interaction lengths of material lay in front of the hadron calorimeters, most hadronic showers were initiated in the electromagnetic calorimeters. In order to measure the energy of an incident hadron, one therefore needed to combine the energies recorded by both calorimeter systems. The intrinsic energy resolution of the hadron calorimeters was considerably lower than that of the electromagnetic calorimeters: in all three sections (barrel, endcap and poletip), the fractional uncertainty was $\sigma_E/E \approx 120\%/\sqrt{E[\text{GeV}]}$.

2.2.4 Muon detectors

Muons were not absorbed significantly by the electromagnetic calorimeter, due to their mass being far greater than that of the electron. They could also penetrate the hadron calorimeters, since muons do not couple to the strong interaction in nuclei. A further layer of detectors was therefore constructed outside the return yoke of the magnet, to measure the positions of muons and to distinguish them from other particles.

Isolated high-energy muons, such as those produced in $\text{e}^+\text{e}^- \to \mu^+\mu^-$ events, could be identified without the aid of dedicated muon detectors: the signature consisted of a continuous charged track in each subdetector, including the hadron calorimeters. Such events were useful for studying the response of the muon detector. However, the muons produced indirectly through decays of heavy hadrons or τ-leptons are perhaps of greater interest; these had to be distinguished from a background of other particles. Although the hadron calorimeter could still assist in the identification of these muons, the principal signal was based on extrapolation of tracks from the central drift chambers to the muon detectors.

The muon detectors comprised a cylindrical arrangement of 110 drift chambers surrounding the barrel [100], and two orthogonal layers of streamer tubes on each endcap [101]. The combined barrel and endcap muon detectors covered 93% of

4π solid angle, with gaps for the beampipe, cables and support structures. Within this region of coverage, the acceptance for isolated muons with an energy greater than 3 GeV was essentially 100%. The probability of misidentifying a 5 GeV pion as a muon was estimated to be less than 1%.

2.2.5   Time-of-flight detector

Between the jet chamber and the electromagnetic presamplers, a further subdetector was installed to measure the arrival times of charged particles. By comparing these times against the LEP bunch crossings, which occurred every 22 μs,[3] it was possible for the trigger system to reject cosmic ray backgrounds. To some extent one could also perform particle identification, in the energy range 0.6–2.5 GeV, by measuring deviations from the speed of light.

The barrel time-of-flight system, which was installed before OPAL began taking data, consisted of 160 scintillation counters. Each of these counters formed a strip of length 6.8 m, parallel to the beam axis. Light was collected by phototubes at both ends; a positive trigger required the two signals to arrive within 50 ns of each other, and within 50 ns of the expected arrival time of a relativistic particle from the beam interaction. The time resolution was estimated to be 280 ps at the centre of the counters, and 350 ps at the ends.

When searching for rare signatures of new particles at LEP2, it was especially important to eliminate spurious triggers caused by cosmic rays. An endcap time-of-flight system [91] was therefore added in 1996, between the end of the pressure vessel and the electromagnetic presamplers, to improve rejection of particles arriving out-of-time with the beam crossing. This comprised an array of thin scintillating tiles connected to remote photo-transducers via optical fibres. A further set of tiles, closer to the beampipe, formed a "minimum ionising particle (MIP) plug": this complemented the poletip hadron calorimeter, by extending the acceptance region for particles such as muons down to a polar angle of 43 mrad.

---

[3]LEP was designed to operate with either 4+4 or 8+8 bunches of electrons and positrons, corresponding respectively to periods of 22 μs and 11 μs between bunch crossings. In practice, however, the 8+8 bunch mode was not used extensively.

2.2.6 Forward detectors and silicon-tungsten luminometers

When measuring the cross section for a process such as Z^0 production, it is essential to determine the luminosity of the machine. In e^+e^- collisions, this is typically achieved by observing low-angle Bhabha scattering of the beam particles; the differential cross section for this process has been calculated with high precision in QED, so it can be used as a calibration reference when studying other processes. A pair of "forward detectors" was therefore placed in the regions close to the beampipe at either end of the detector. Each forward detector comprised several components, including calorimeters, drift chambers and tube chambers: these are described in Ref. [77].

A more precise silicon-tungsten calorimeter [92] was added in 1993, consisting of 18 tungsten plates interleaved with 19 silicon sampling wafers. While LEP was operating at 45 GeV per beam, this detector could determine the positions of Bhabha electrons to a precision of 0.2 mm, and their energies to $\pm 4\%$. The precision of the resulting luminosity measurements was limited by a theoretical systematic uncertainty of 0.05% [102].

2.2.7 Trigger system

After each bunch crossing, a real-time trigger system [103] was needed to decide within 22 μs whether an 'interesting' event had occurred. If so, a signal was sent to each subdetector requesting a full read-out of data collected from the event. No further triggers could then be received until the read-out had been completed, approximately 20 ms or 1000 bunch crossings later. It was therefore essential to keep the trigger rate below about 5 Hz, so that the detector would be responsive more than 90% of the time; when running at the Z^0 energy with a typical luminosity of about 1×10^{31} cm^{-2}s^{-1}, the production rate of Z^0 bosons was $\sim$0.4 Hz.

The first stage of triggering was performed by the electronics of the individual subdetectors. Each subdetector, or group of subdetectors, computed a set of binary trigger outputs based on various characteristics of the event. These signals were then combined in a programmable central trigger logic, which decided whether the event was to be accepted.

The trigger signals provided by the subdetectors fell into two categories, as follows:

The θ–ϕ matrix The detector was divided into a grid of overlapping bins of solid angle, in the θ and ϕ directions; the number of bins varied between subdetectors, up to a maximum of 6 bins in θ and 24 bins in ϕ. Every subdetector made a trigger decision for each individual bin, with a relatively low threshold. The central trigger logic could then test for spatial correlations between layers of the detector. The θ–ϕ matrix is shown schematically in Figure 2.6.

Direct trigger signals These were based on global properties of the event, such as total energies or track multiplicities; they generally had higher thresholds than the θ–ϕ matrix inputs. A full list of the direct signals from each subdetector is given in Ref. [103].

The trigger signals from the central vertex and jet chambers were generated by a sophisticated "track trigger" [104]. The z-coordinate of each hit was measured rapidly by comparing the charges or times of signals received at the two ends of the sense wire.[4] The ratio $z/r \equiv \cot\theta$ was then calculated to determine the polar angle of the hit. A genuine track originating at the interaction point would be expected to have the same z/r value for all hits, since the force due to the magnetic field acted in the ϕ direction.

An additional pretrigger system [93] was introduced in 1992: this was primarily intended to speed up the decisions of the central trigger logic, since it was planned that LEP should begin operating in the 8+8 bunch configuration.

2.2.8   Data acquisition, event builder and filter

After a positive trigger decision had been made, the data from the subdetectors were collected and merged by a central computer called the "event builder"; the hardware and software required to store, process and transmit data from the digitisers of the subdetectors to the event builder are described in Ref. [105].

Each complete event was then processed by an online software filter [106], which acted as a second-level trigger. The events were partially reconstructed, and classified into several categories such as multihadron events or lepton pairs; events

---

[4]As described in Section 2.2.1.2, a slower but more precise measurement of the z-coordinate was obtained for offline analysis purposes by combining data from the jet chamber and z-chambers.
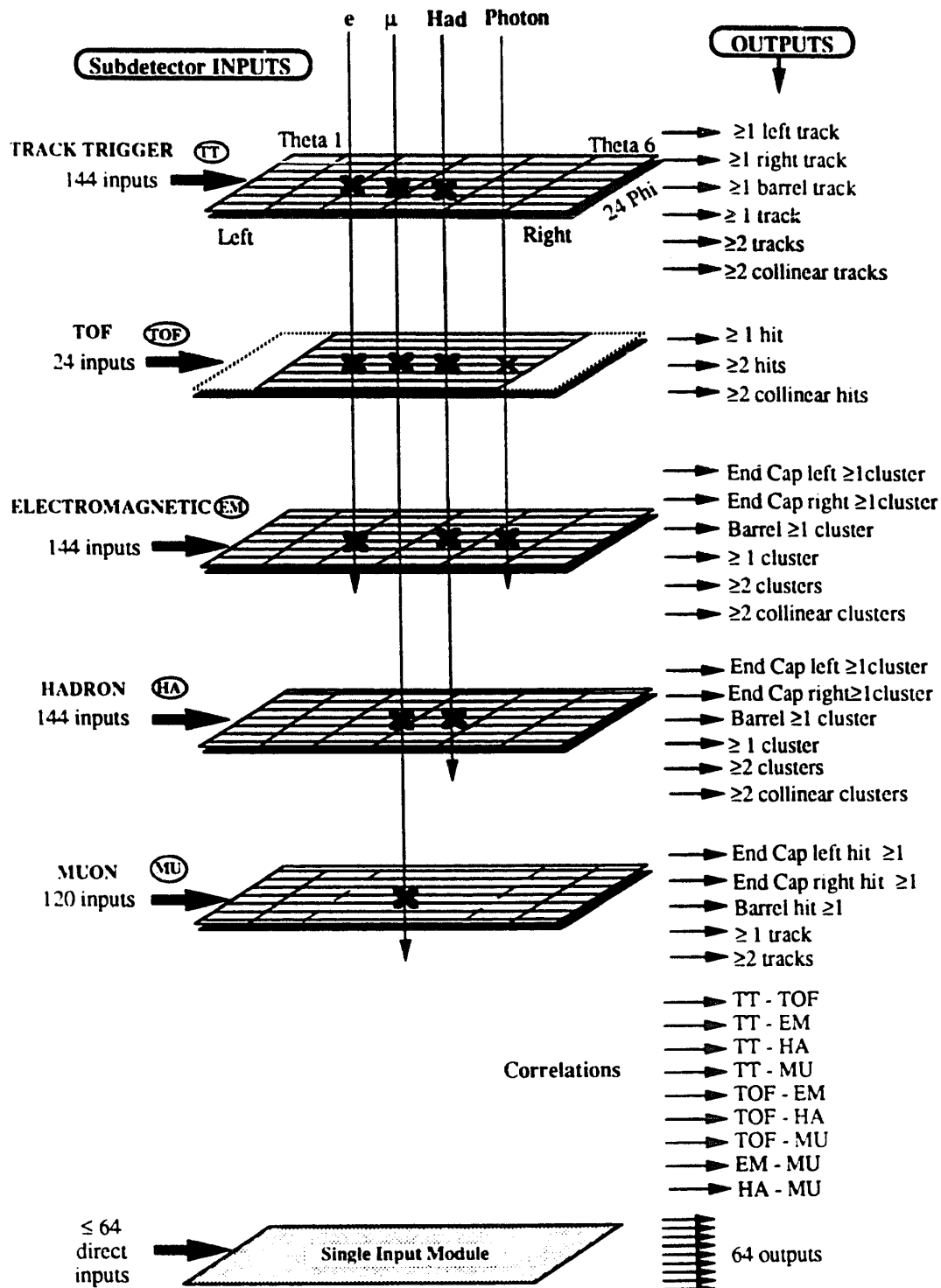
Figure 2.6: A schematic view of the θ–ϕ matrix used by the OPAL trigger system. Crosses on the vertical lines represent sensitivity of each subdetector to the various types of particle. The matrix input bits were combined by the central trigger logic to give the binary output signals listed in the right-hand column.

classified as background were rejected. The filter software also provided an online event display, and enabled real-time monitoring of the detector performance. Events passed by the filter were stored on disk to await offline reconstruction.

2.3   Reconstruction of OPAL events

Before an event could be used for physics analysis, the raw data from the subdetectors had to be converted into useful quantities such as energies, momenta and particle identities. This process was performed by a program called ROPE ("Reconstruction of OPAL Physics Events"), which also provides the standard framework for accessing stored data. The software contains a kernel and a collection of modules associated with individual tasks and subdetectors; the modules were developed, maintained and documented independently by their individual authors. ROPE uses a database of calibration constants, which was regularly updated to maintain accurate reconstruction; the raw data were generally reprocessed several times to incorporate improvements in the software and calibration.

The final reconstructed events were stored on data summary tapes (DST), where they could be accessed for further offline analysis. Lists were compiled of the events satisfying various criteria, to enable faster access to specific classes of event. For some analyses, such as the event shape measurements presented in this work, the relevant properties of each event are stored in databases called 'ntuples': these are conveniently accessed using the HBOOK package of the CERN program library, and can be shared between users with similar data requirements.

Chapter 3

Measurements of α_S using event shape distributions at OPAL

In Chapter 1, we defined a set of "event shape observables," which provide sensitivity to QCD interactions in e^+e^- annihilation. As discussed in Section 1.6, the distributions of certain observables have been predicted in perturbation theory at $\mathcal{O}(\alpha_S^2) + \text{NLLA}$ precision. Our aim is to measure these distributions experimentally, thereby testing the validity of the predictions and permitting a measurement of the coupling parameter α_S.

The OPAL Collaboration has previously published event shape distributions and α_S measurements using data collected at centre-of-mass energies in the range 91–189 GeV [8–11]. In this work, we have extended this set of measurements to include the full range of LEP collision energies up to 209 GeV. We have also reprocessed the data recorded at lower energies, to incorporate various experimental and theoretical developments which have taken place during the lifetime of LEP. This unification permits a more robust and consistent comparison between the results presented at different energies. The main improvements with respect to the published OPAL results can be summarised as follows:

- Improvements have been made in the NLLA theory predictions for the total jet broadening B_T, the wide jet broadening B_W, and the Durham y_{23} parameter. These were discussed in Section 1.7, and are used throughout this work.

- No measurements of the C-parameter were presented in the original analysis of LEP1 data. Distributions were published at $\sqrt{s} =$130–136 GeV [9] and

67

161 GeV [10], but α_S measurements were not performed using this observable until the NLLA resummation became available in 1998 [34]. Here we present distributions and α_S fits for the C-parameter at all LEP energy scales.

- The NLLA resummations do not automatically force each event shape distribution to vanish at the edge of phase space; missing subleading terms can result in a non-zero prediction outside the kinematically allowed range of the observable. In Section 1.6.4 we discussed a remedy for this situation, involving the substitution

$$ L = \ln\left(\frac{1}{y}\right) \;\; \rightarrow \;\; \widetilde{L} = \ln\left(\frac{1}{y} - \frac{1}{y_{\max}} + 1\right) \quad . $$

This method was known [32] at the time of the original LEP1 analysis [8], and was investigated as an alternative to the unmodified NLLA prediction. However, it was never adopted as the standard for α_S measurements by the OPAL Collaboration. In this work, we introduce the above substitution in our fits to all OPAL data; this approach is now advocated by most theorists, and has been adopted by the other three LEP experiments.

- In 1996, the EVENT2 Monte Carlo program [30] became available, for the computation of event shape distributions at $\mathcal{O}(\alpha_S^2)$ in perturbation theory, as described in Section 1.6.1. This superseded an earlier program, EVENT [17], which was used to generate the coefficient functions $\mathcal{A}(y)$ and $\mathcal{B}(y)$ [107] for previous LEP analyses. The two algorithms are ultimately equivalent, but EVENT2 is more efficient; coupled with the availability of much faster computers, this has led to a more precise determination of the coefficients. We therefore use these new $\mathcal{O}(\alpha_S^2)$ predictions throughout this work.

- The PYTHIA, HERWIG and ARIADNE Monte Carlo programs have evolved considerably since the first OPAL event shape analyses were published. In this work we use PYTHIA 6.1 for our central analysis, and HERWIG 6.2 and ARIADNE 4.11 as alternatives in the estimation of our systematic uncertainties. In each case we use the most recent parameter set tuned to OPAL data.

- A new event selection has been introduced to exclude the background of four-fermion events from our analysis. This replaces a cut used by OPAL in pre-

vious LEP2 publications, and significantly increases the purity of our sample. We present an analysis and justification of this selection in Section 3.3.6.

- Before 1996, no satisfactory algorithm existed for relating the charged tracks observed in the central detector with the energy depositions recorded in the electromagnetic calorimeters. The `MT` package ("Matching Tracks and clusters," [108]) was then developed to combine tracks and clusters, and reduce double-counted energy.

- The handling of statistical uncertainties in both the event shape distributions and the α_S measurements has changed. In the past, the uncertainties of the distributions were estimated directly from the data, and no statistical correlations were calculated between different bins. We now compute a full covariance matrix for each distribution, using Monte Carlo simulations, and then use this matrix when fitting for α_S.

The remainder of this chapter is organised as follows: in Section 3.1 we define our signal, and list the dominant background processes. Section 3.2 lists the OPAL data and Monte Carlo samples to be used in the analysis. In Section 3.3 we describe our event selection criteria, and list the numbers of events selected at each centre-of-mass energy. Section 3.4 discusses our event shape measurements, and compares the resulting distributions with those predicted by Monte Carlo models; the complete results are in Appendix B. In Section 3.5, we fit theoretical predictions to our data, and discuss the resulting measurements of α_S, which are tabulated in Appendix C. Finally, in Section 3.6, we discuss the combination of OPAL results obtained at different energy scales and from different observables.

3.1 Signal definition

The aim of this analysis is to compare measured event shape distributions with those predicted by perturbative QCD. Our experimental signal definition must therefore match, as closely as possible, the class of processes included in the theoretical calculations.

In Section 1.4, we described the basic $e^+e^- \rightarrow (Z^0/\gamma)^* \rightarrow q\bar{q}$ process, and an associated class of higher-order diagrams involving gluon radiation from the $q\bar{q}$ pair. The set of resulting final states defines a statistical population for the event shape
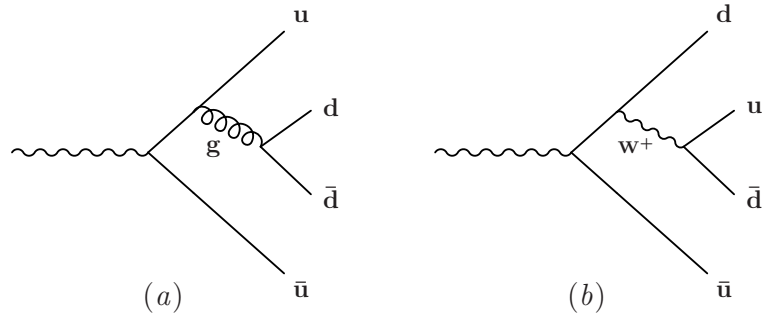
Figure 3.1: Two Feynman diagrams contributing to the $u\bar{u}d\bar{d}$ final state

distributions discussed in Section 1.6. All electroweak physics is "factored out" from these predictions, through normalisation of the distributions.

In reality, of course, one can never define processes or observables that depend *only* on strong interactions. Quarks are charged particles, which can radiate real or virtual photons, and also $W^{\pm}$ and Z^0 bosons.[1] Diagrams involving electroweak gauge bosons may in principle interfere with the "pure QCD" diagrams, so even statistical separation is not strictly possible. Figure 3.1, for example, shows two of the diagrams contributing to the $u\bar{u}d\bar{d}$ final state: diagram (a) is included in the QCD event shape predictions, while diagram (b) is not. Fortunately, however, there is negligible interference between these processes. The $W^{\pm}$ and Z^0 bosons are narrow high-energy resonances, with total widths of 2.1 GeV and 2.5 GeV respectively [13]; their decay products tend to be well-separated, with large invariant masses. Gluons, in contrast, are usually emitted at a low angle with respect to the parent quark, and carry a small momentum transfer. Hence there is very little overlap in phase space between the two processes shown in Figure 3.1. Furthermore, the vast majority of four-jet final states arising from QCD processes are $q\bar{q}gg$, rather than $q\bar{q}q\bar{q}$; there is no electroweak correction to these processes at tree level. We therefore claim that the set of QCD 'multihadron' processes described in Section 1.4 constitutes a valid signal definition, and that electroweak four-fermion processes such as Figure 3.1(b) form a separable background.

For experimental reasons, we will also include events with final-state photon radiation in our signal. An example is shown in Figure 3.2. Such photons tend to be radiated at low angles, and often cannot be distinguished from the decay products of the corresponding quark jet. We therefore make no attempt to identify

---

[1]In principle, H^0 bosons may also be exchanged. However, direct searches have found no conclusive evidence for Higgs production at LEP [109].
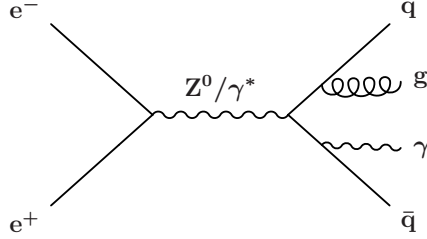
Figure 3.2: Multihadronic event with final-state photon radiation (FSR)

these events as background. Their influence is expected to be small, since the electromagnetic coupling α_{em} is much smaller than α_S, and the angular distribution of FSR photons is similar to that of gluons at lowest order.

3.2 Event samples

3.2.1 OPAL data

Our analysis will use all available data recorded in OPAL physics runs at centre-of-mass energies $\sqrt{s} \geq 130$ GeV, during the years 1995–2000. In most cases, the data are concentrated densely around well-defined energy points, as reflected by the ranges listed in Table 3.1. It is natural to treat each of these ranges separately, so that the running coupling $\alpha_S(Q)$ can be regarded as constant within each data sample. However, the data at 130.1 and 136.1 GeV will be merged into a single sample with mean $\sqrt{s} = 133.3$ GeV, to reduce statistical uncertainties.

In addition, several "calibration runs" were made during the same period, at the Z^0 energy $\sqrt{s} = M_Z = 91$ GeV. These primarily served to provide calibration constants for the experiments' reconstruction software, and to test the response of the detectors in a known physics environment with a large annihilation cross section. However, these new data at 91 GeV can also be used for physics analysis. Since the detector configuration was unchanged between the calibration runs and the high-energy runs, we expect a large degree of correlation between the experimental systematic uncertainties; this is extremely beneficial when measuring the energy-dependence of a quantity such as $\alpha_S(Q)$. Our analysis of the calibration data will therefore supersede previous measurements performed at LEP1.

Year	Range of $\sqrt{s}$ (GeV)	Mean $\sqrt{s}$ (GeV)	Integrated luminosity (pb^{-1})
1996–2000	91.0 – 91.5	91.3	14.7
1995, 1997	129.9 – 130.3	130.1	5.31
1995, 1997	135.7 – 136.3	136.1	5.95
1996	161.2 – 161.6	161.3	10.06
1996	170.2 – 172.5	172.1	10.38
1997	180.8 – 184.2	182.7	57.72
1998	188.3 – 189.1	188.6	185.2
1999	191.4 – 192.1	191.6	29.53
1999	195.4 – 196.1	195.5	76.67
1999, 2000	199.1 – 200.2	199.5	79.27
1999, 2000	201.3 – 202.1	201.6	37.75
2000	202.5 – 205.5	204.9	82.01
2000	205.5 – 208.9	206.6	138.8

Table 3.1: The OPAL data samples used for our analysis

3.2.2   Monte Carlo events

In order to optimise our selection cuts, and to correct for biases in our measurements, we require a faithful simulation of the entire experiment. Standard event generators are used to simulate the various types of signal and background processes, using parameters tuned to OPAL data at LEP1. Where necessary, the full response of the OPAL detector is estimated for each event using the GOPAL simulation program [110], and the simulated events are then reconstructed using ROPE, as described in Section 2.3. The event generators to be used in this analysis are as follows:

- $q\bar{q}$ events are generated using $\mathcal{KK}$2f linked with PYTHIA 6.125, as described in Section 1.9. Events involving photon radiation from the initial or final states are included. Some of the default PYTHIA parameters are replaced with optimised values, based on OPAL data at the Z^0 peak [111]. When testing the model-dependence of our analysis, and estimating systematic uncertainties, we use HERWIG 6.2 and ARIADNE 4.11 as alternative models to simulate parton showering; the HERWIG cluster model also provides an alternative to the PYTHIA string model for fragmentation. These two programs were also described in Section 1.9. The corresponding OPAL parameter sets were listed

in Ref. [112]. The same initial q$\bar{\text{q}}$ states, simulated by $\mathcal{KK}$2f, are used in the PYTHIA, HERWIG and ARIADNE event samples.

- For certain purposes, such as the prediction of hadronisation effects, we do not require simulation of the OPAL detector, nor the inclusion of initial-state radiation. In these cases we generate much larger samples of non-radiative q$\bar{\text{q}}$ events, using the OPAL-tuned versions of PYTHIA 6.158 [2], HERWIG 6.2 and ARIADNE 4.11. We do not use $\mathcal{KK}$2f to generate the initial q$\bar{\text{q}}$ systems, since this is only beneficial for radiative events.

- As we shall see in Section 3.3.6, a significant background arises from W$^+$W$^-$ and ZZ pair production, at energies $\sqrt{s} \geq 161$ GeV: the two on-shell gauge bosons decay to produce a four-fermion final state.

    - For all **q$\bar{\text{q}}$q$\bar{\text{q}}$**, **q$\bar{\text{q}}\ell^{\pm}\nu_\ell$**, **q$\bar{\text{q}}\ell^+\ell^-$** and **q$\bar{\text{q}}\nu\bar{\nu}$** background final states at $\sqrt{s} \geq 183$ GeV (except q$\bar{\text{q}}$e$^+$e$^-$), we use the KoralW [113] generator, version 1.42 [114]. This uses four-fermion matrix elements calculated with grc4f [115] version 2.1, including interference between W$^+$W$^-$ and ZZ diagrams. KoralW also features accurate predictions for initial- and final-state photon radiation, which may interfere with one another.

    - For **q$\bar{\text{q}}$e$^+$e$^-$** final states, and for all four-fermion processes at $\sqrt{s} = 161$ GeV and 172 GeV, no KoralW samples are available. We instead use grc4f 2.1. The simulation of q$\bar{\text{q}}$e$^+$e$^-$ processes excludes 'multiperipheral' diagrams such as two-photon processes, which will be rejected efficiently by the selection cuts.

    Hadronisation of the four-fermion final states is simulated using JETSET 7.4, which contains a slightly older version of the string fragmentation model used by PYTHIA 6.1.

---

[2]The OPAL parameter set for PYTHIA version 6.158 is the same as that for version 6.125, except that the parameter `PARJ(55)` describing b-quark fragmentation has been changed from -0.0038 to -0.0020.

3.3   Event selection

We now describe in turn each of the selection criteria applied to our data. For each case, we indicate the class of background events to be removed.

3.3.1   Detector status

To ensure the best possible precision, we require that all relevant components of the detector are fully operational:

- The status flags for the central jet chamber, and for both the barrel and endcap electromagnetic calorimeter systems, must indicate 'OK'.

- At least two out of the following three inputs to the trigger system must be working, to ensure near-perfect efficiency for detecting multihadronic events:

  (i) the track trigger

  (ii) the time-of-flight detector

  (iii) both the barrel and endcap electromagnetic calorimeter systems.

3.3.2   LEP2 multihadron selection (L2MH)[3]

This standard selection is used for many OPAL analyses. It efficiently eliminates background events with low multiplicities, such as electron or muon pair production, and also those with missing energy or momentum. Untagged and single-tagged two-photon events are rejected, because the electron or positron is usually not deflected sufficiently to be observed in the calorimeter.

- The event must include at least five good tracks in the central detector. A "good track" is defined as follows:

  - Momentum transverse to the beam axis: $p_{\mathrm{T}} \geq 50$ MeV$/c$

  - Number of hits in the jet chamber: $N_{\mathrm{hits}} \geq 20$

---

[3] For our analysis of calibration data at $\sqrt{s} = 91$ GeV, we use the Tokyo multihadron selection (TKMH) instead of L2MH. TKMH is defined in exactly the same way as L2MH, except that the cut on visible energy is slightly looser ($R_{\mathrm{vis}} \geq 0.10$), and the cut on energy balance is slightly tighter ($|R_{\mathrm{bal}}| \leq 0.65$). These values are chosen to optimise acceptance of multihadron events, in a regime where background processes and initial-state radiation can be neglected.

- The track is extrapolated to find the point P where it passes closest to the beam axis. The displacement of P from the nominal interaction point must satisfy the following conditions, when expressed in cylindrical polar coordinates:

$$r - \phi \text{ component (normal to the beam axis):} \quad d_0 \leq 2 \text{ cm}$$
$$z \text{ component (parallel to the beam axis):} \quad |z_0| \leq 25 \text{ cm}$$

- At least seven good energy clusters are required in the electromagnetic calorimeters. "Good clusters" are defined as those having raw energies of at least 100 MeV in the barrel region or 200 MeV in the endcap region.

- The visible energy ratio, R_{vis}, must satisfy

$$R_{\text{vis}} \equiv \frac{\sum E_{\text{raw}}}{2E_{\text{beam}}} \geq 0.14$$

- The energy balance ratio, R_{bal}, must satisfy

$$R_{\text{bal}} \equiv \left| \frac{\sum E_{\text{raw}} \cos\theta}{\sum E_{\text{raw}}} \right| \leq 0.75$$

3.3.3 Number of accepted tracks

As described above, the L2MH selection requires at least five "good tracks" to be observed in the central detector. For this analysis we increase the minimum number of tracks to seven, in order to reduce the remaining background from two-photon and $\tau^+\tau^-$ events to a negligible level. According to Monte Carlo simulations at $\sqrt{s} = 189$ GeV, we expect 98.5% of signal events passing the L2MH selection to satisfy this additional criterion.

3.3.4 Containment in the detector

For each event, we find the direction of the thrust axis $\hat{\boldsymbol{n}}_T$ as defined in Section 1.5.1. We require the angle between $\hat{\boldsymbol{n}}_T$ and the LEP beam axis, θ_T, to satisfy $|\cos\theta_T| \leq 0.9$. This reduces the probability of final-state hadrons being lost in the beampipe, which would bias the event shape observables.
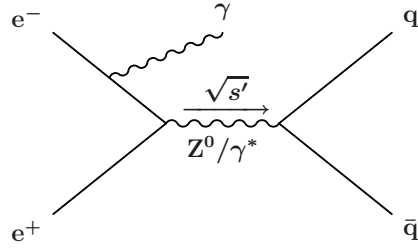
Figure 3.3: Multihadronic event with initial-state photon radiation (ISR)

3.3.5 Rejection of radiative events ($\sqrt{s'}$ cut)

At LEP2 collision energies, the majority of $q\bar{q}$ events include at least one photon radiated from the electron or positron in the initial state, as shown in Figure 3.3. In most cases, the photon carries an energy

$$E_\gamma \approx \frac{1}{2}\left(\sqrt{s} - \frac{M_{Z^0}^2}{\sqrt{s}}\right) \quad , \tag{3.1}$$

leaving an electron-positron pair with exactly the energy needed to create a Z^0 boson on the mass shell. Such events are regarded as background, because the quark-antiquark pairs are not created with the desired centre-of-mass energy, and would lead to a measurement of the running coupling $\alpha_S(Q)$ at the wrong energy scale.

An algorithm has been developed by the OPAL Collaboration [116] to determine whether an event contains initial-state radiation. Firstly, any isolated photons seen in the electromagnetic calorimeter are immediately identified as ISR. The remaining charged tracks and calorimeter clusters are then formed into jets using the Durham algorithm. A kinematic fit is performed, allowing for up to two unseen ISR photons, and imposing energy-momentum conservation for the whole event. All ISR photons are then discarded from the event, and the invariant mass $\sqrt{s'}$ of the remaining hadronic system computed. Events are selected only if

$$\sqrt{s} - \sqrt{s'} \leq 10 \text{ GeV} \quad . \tag{3.2}$$

This algorithm is compared in Ref. [116] with an older method, which is still used in the present analysis to estimate systematic uncertainties. In addition to eliminating radiative multihadronic events, the above cut removes the vast majority of the remaining two-photon and $q\bar{q}e^+e^-$ events. The isolated electrons and positrons in these events are identified as converted ISR photons by our $\sqrt{s'}$ algorithm.

In principle, the cross section for the process $e^+e^- \rightarrow q\bar{q}\gamma$ will include contributions from both initial- and final-state radiation. ISR diagrams such as Figure 3.3 will interfere with FSR diagrams such as Figure 3.2. Fortunately, however, final-state radiation is much rarer than ISR at LEP2 energies, and tends to occupy a different region of phase space; most FSR photons have low momenta, and are detected close to a quark jet. A detailed investigation [117] has shown that ignoring ISR/FSR interference leads to an error of order 0.1% in measurements of the non-radiative multihadron cross section at LEP2 energies.

3.3.6 Four-fermion rejection cuts

After imposing the criteria described in Sections 3.3.1–3.3.5, Monte Carlo simulations show that about 65–70% of selected events at the highest LEP2 energies fall within our signal definition. Nearly all of the remaining events are due to 'four-fermion' processes involving the production of an on-shell W^+W^- or ZZ pair. Such events can closely resemble our signal, especially when both of the $W^\pm$ or Z^0 bosons decay hadronically, as occurs in about 50% of cases. Fortunately however, as we have discussed in Section 3.1, the $q\bar{q}$ and four-fermion processes tend to populate different regions of phase space. Hence there is little interference, and we have some possibility of separating them on an event-by-event basis.

The main four-fermion backgrounds are $q\bar{q}q\bar{q}$, $q\bar{q}\ell^\pm\nu_\ell$ and $q\bar{q}\ell^+\ell^-$ final states, produced via the processes shown in Figure 3.4. In addition, there are some extra t-channel exchange diagrams, shown in Figure 3.5, which lead to $q\bar{q}e^+e^-$ final states. The latter are already excluded to a satisfactory level by our $\sqrt{s'}$ cut, along with two-photon events, because the final-state electron or positron tends to pass undetected into the beampipe. For convenience, we will use the term "$qq\ell\nu$ background" to imply both $q\bar{q}\ell^\pm\nu_\ell$ and $q\bar{q}\ell^+\ell^-$ states, of which the former is a more significant contribution.

In previous studies of QCD event shapes at LEP2 [11], the following procedure has been used to estimate the compatibility of each event with our signal definition. The event is first forced into a four-jet configuration using the Durham algorithm, as described in Section 1.5.5. The EVENT2 [30] program is then used to compute the matrix element $\mathcal{M}(p_1, p_2, p_3, p_4)$ for each of the possible processes $e^+e^- \rightarrow q\bar{q}q\bar{q}, q\bar{q}gg$. Since there is no identification of quark and gluon jets, the
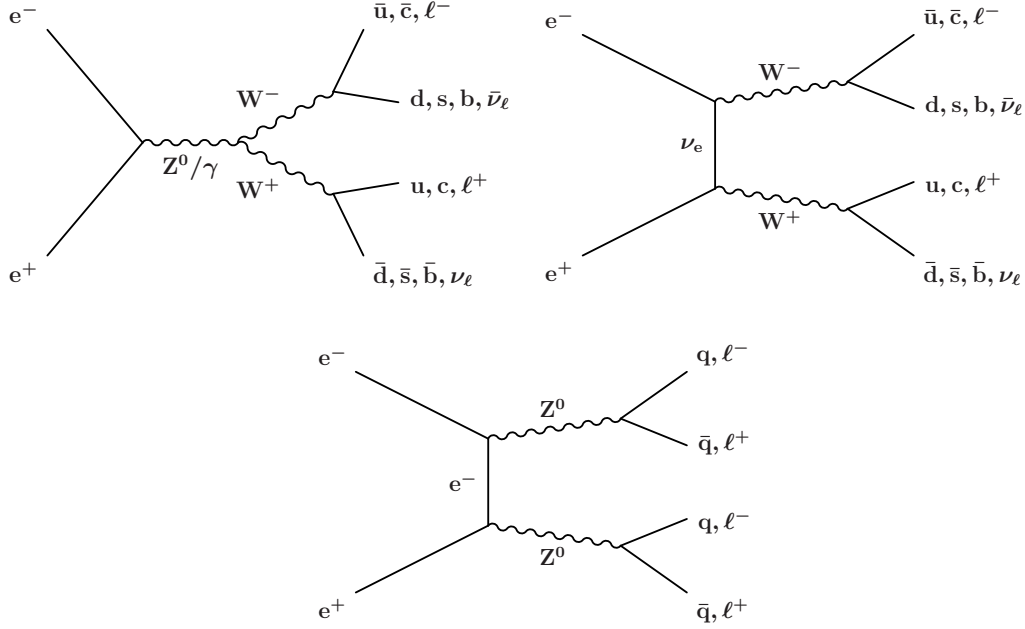
Figure 3.4: Principal four-fermion background diagrams
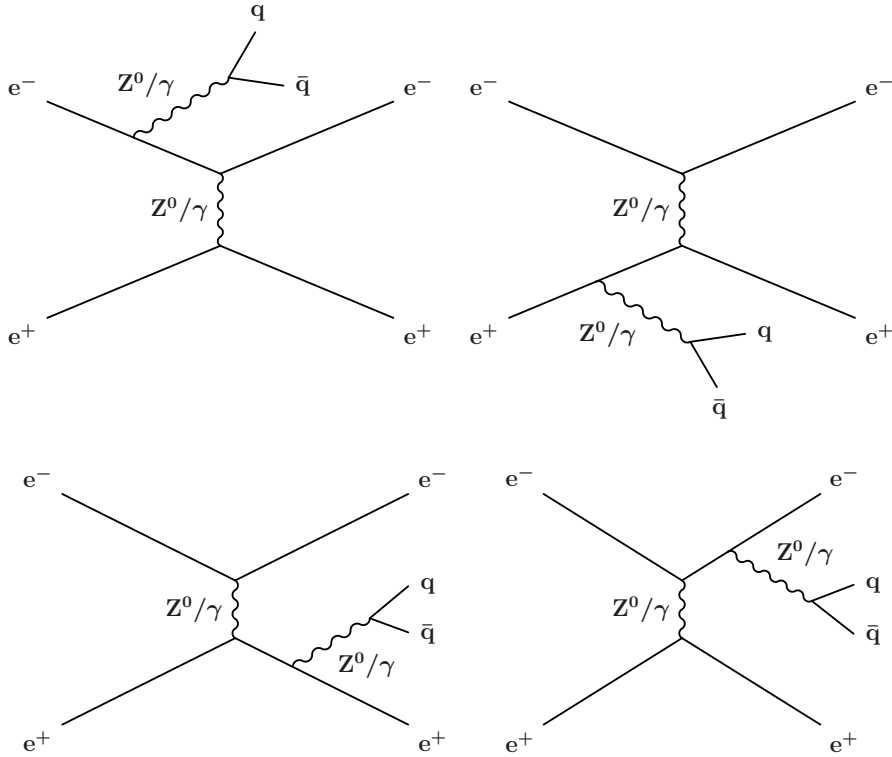
Figure 3.5: t-channel exchange diagrams leading to $q\bar{q}e^+e^-$ final states

matrix elements for all permutations of jet momenta $\{p_1, p_2, p_3, p_4\}$ are considered. We define the discriminator variable W_{QCD} as the largest of these: [4]

$$W_{\text{QCD}} = \max_{\{p_1, p_2, p_3, p_4\}} \left[\left| \mathcal{M}(p_1, p_2, p_3, p_4) \right|^2 \right] \quad . \tag{3.3}$$

The expected and measured distributions of this observable are shown in Figure 3.6, for events which have passed the selection criteria defined in Sections 3.3.1–3.3.5. The W_{QCD} values for signal events are generally higher than those for four-fermion events. Although most events to be selected are not four-jet processes of the type used to compute W_{QCD}, the final state particles can nonetheless be resolved into four jets, of which some pairs are nearly parallel. Since the probability of collinear gluon emission is high, the matrix element for this four-jet state will be closely related to that for the 'true' two- or three-jet state. The cut

$$\log_{10}(W_{\text{QCD}}) > -0.5 \tag{3.4}$$

is imposed to complete the event selection. After all cuts have been applied we would then expect 77% of genuine signal events to be selected, and 88% of selected events to be $q\bar{q}$ processes (including those with ISR).[5]

In a recent OPAL publication [119], however, it has been suggested that the above selection can be improved. While the W_{QCD} variable is an effective measure of compatibility with our signal definition, it does not contain any information about an event's consistency with the four-fermion background processes. In an OPAL measurement of the W^+W^- production cross section and branching fractions [118], two likelihood variables were used to select $e^+e^- \to W^+W^-/ZZ \to q\bar{q}q\bar{q}$ and $e^+e^- \to W^+W^- \to q\bar{q}\ell^\pm\nu_\ell$ events. These discriminators, called L_{qqqq} and $L_{\text{qq}\ell\nu}$ respectively, are based on several input variables. L_{qqqq}, which is defined in Ref. [118], uses both W_{QCD} and the corresponding matrix elements for four-fermion processes; $L_{\text{qq}\ell\nu}$ is based primarily on the identification of isolated leptons [120]. The following cuts were adopted in Ref. [119] to reject four-fermion background:

$$L_{\text{qqqq}} < 0.25 \,, \qquad L_{\text{qq}\ell\nu} < 0.5 \,, \qquad \log_{10}(W_{\text{QCD}}) > -0.5 \quad . \tag{3.5}$$

---

[4] W_{QCD} is sometimes called W_{420}, for example in Ref. [118].
[5] These statistics are calculated at $\sqrt{s} = 207$ GeV using the PYTHIA, KoralW and grc4f event generators, and a full simulation of the OPAL detector.
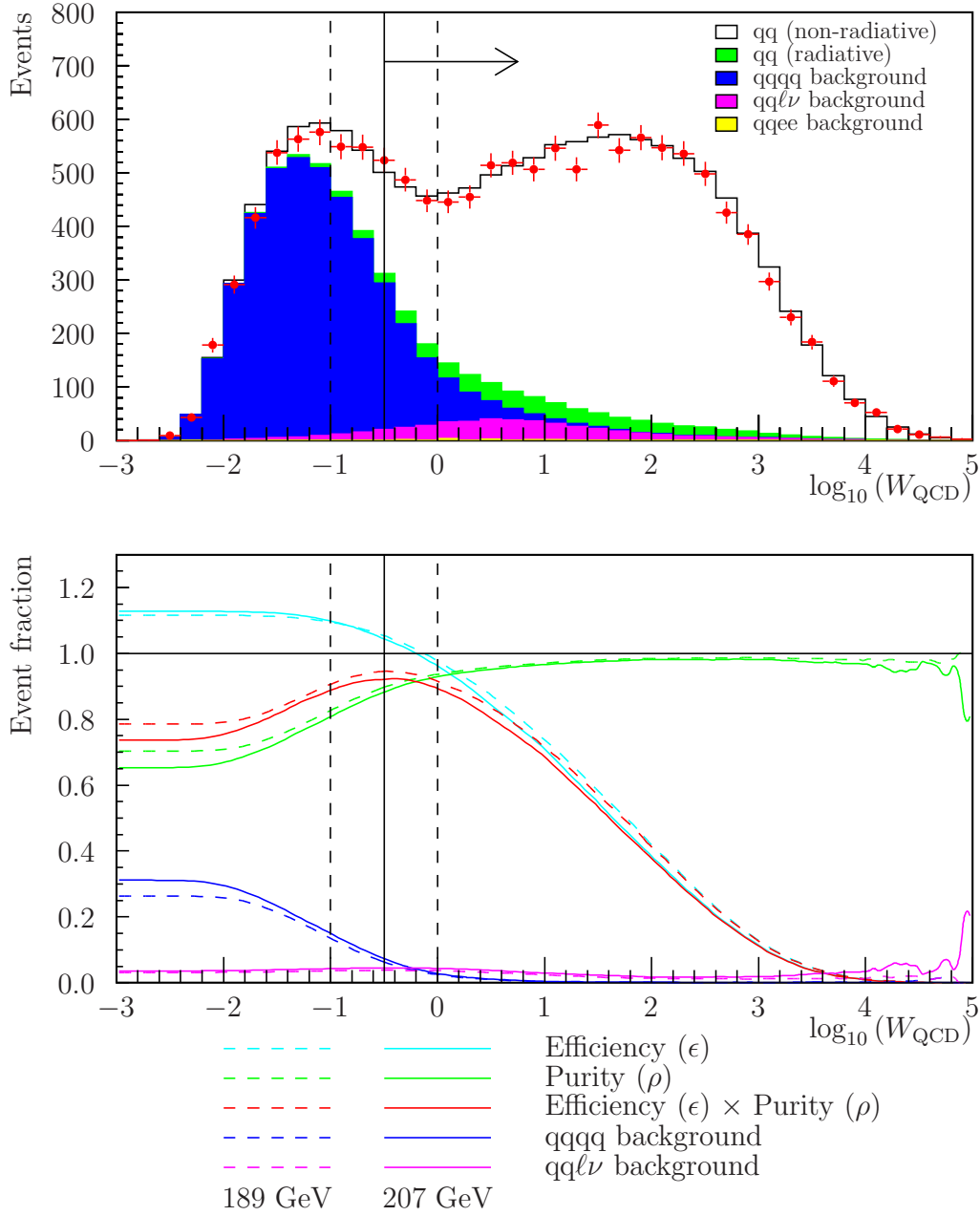
Figure 3.6: Distribution and event selection properties for the W_{QCD} observable used in previous OPAL event shape analyses. In the upper plot, OPAL data are compared with MC predictions for the distribution; the data points represent all selected OPAL events at energies $\sqrt{s} \geq 189$ GeV, after imposing the cuts defined in Sections 3.3.1–3.3.5. The solid histograms represent Monte Carlo predictions, using KK2f/PYTHIA 6.15 for the $q\bar{q}$ events, KoralW for the qqqq and qq$\ell\nu$ backgrounds, and grc4f 2.1 for the qqee background. The "hadron level" events predicted by each Monte Carlo program have been subjected to a full simulation of the OPAL detector. In the lower plot, we show the efficiency and purity of the selection as a function of the cut position, calculated using Monte Carlo simulations at $\sqrt{s} = 189$ GeV and 207 GeV. Also shown are the numbers of qqqq and qq$\ell\nu$ events expected to pass the selection, as fractions of the total selected events. The chosen position for the cut is indicated by a solid vertical line; the dashed lines indicate alternative cuts, which are used to estimate systematic uncertainties.

In the remainder of this section, we will discuss the implementation of these new cuts. First, however, we will describe in general terms a criterion for optimising selection algorithms.

3.3.6.1 Minimisation of the statistical uncertainty

We wish to choose our selection cuts such that the uncertainty in our final measurements will be minimised. Unfortunately it is difficult to calculate reliably the dependence of our systematic uncertainties on the cut parameters; however, the treatment of statistical uncertainties is straightforward.

Suppose we expect the following numbers of events to be produced at our interaction point, in a given time interval:

- N_{nr} non-radiative q$\bar{\mathrm{q}}$ events ($\sqrt{s} - \sqrt{s'} \leq 1$ GeV)

- N_{r} radiative q$\bar{\mathrm{q}}$ events ($\sqrt{s} - \sqrt{s'} > 1$ GeV)

- N_{b} background events

The efficiencies for observing these events in our detector, and selecting them as signal, are ϵ_{nr}, ϵ_{r} and ϵ_{b} respectively. The total number of selected events N_{data}, and its associated standard deviation, is therefore [6]

$$N_{\mathrm{data}} = \epsilon_{\mathrm{nr}} N_{\mathrm{nr}} + \epsilon_{\mathrm{r}} N_{\mathrm{r}} + \epsilon_{\mathrm{b}} N_{\mathrm{b}} \pm \sqrt{\epsilon_{\mathrm{nr}} N_{\mathrm{nr}} + \epsilon_{\mathrm{r}} N_{\mathrm{r}} + \epsilon_{\mathrm{b}} N_{\mathrm{b}}} \quad . \tag{3.6}$$

After subtracting the expected background,[7] we have

$$N_{\mathrm{data}} - \epsilon_{\mathrm{b}} N_{\mathrm{b}} = \epsilon_{\mathrm{nr}} N_{\mathrm{nr}} + \epsilon_{\mathrm{r}} N_{\mathrm{r}} \pm \sqrt{\epsilon_{\mathrm{nr}} N_{\mathrm{nr}} + \epsilon_{\mathrm{r}} N_{\mathrm{r}} + \epsilon_{\mathrm{b}} N_{\mathrm{b}}} \quad . \tag{3.7}$$

We now multiply this result by a "detector correction," such that the expected value

---

[6] N_{nr}, N_{r} and N_{b} are *constants*, representing the mean number of events in each category, while N_{data} is a random variable with a statistical distribution.

[7] The background subtraction and detector correction will be discussed in the next section.

is equal to the original number of non-radiative signal events, N_{nr}:

$$
\begin{aligned}
N_{\text{corr.}} &= \frac{N_{nr}\left(N_{\text{data}} - \epsilon_b N_b\right)}{\epsilon_{nr}N_{nr} + \epsilon_r N_r} = N_{nr} \pm \frac{N_{nr}\sqrt{\epsilon_{nr}N_{nr} + \epsilon_r N_r + \epsilon_b N_b}}{\epsilon_{nr}N_{nr} + \epsilon_r N_r} \\
&= N_{nr} \pm \sqrt{N_{nr}\left(\frac{N_{nr}}{\epsilon_{nr}N_{nr} + \epsilon_r N_r}\right)\left(\frac{\epsilon_{nr}N_{nr} + \epsilon_r N_r + \epsilon_b N_b}{\epsilon_{nr}N_{nr} + \epsilon_r N_r}\right)} \\
&\equiv N_{nr} \pm \sqrt{\frac{N_{nr}}{\epsilon\rho}} \quad ,
\end{aligned}
\tag{3.8}
$$

where we have defined

$$
\text{Efficiency:} \quad \epsilon = \frac{\epsilon_{nr}N_{nr} + \epsilon_r N_r}{N_{nr}}
\tag{3.9}
$$

$$
\text{Purity:} \quad \rho = \frac{\epsilon_{nr}N_{nr} + \epsilon_r N_r}{\epsilon_{nr}N_{nr} + \epsilon_r N_r + \epsilon_b N_b}
\tag{3.10}
$$

To minimise the statistical uncertainty, we must therefore maximise the product of efficiency and purity, $\epsilon\rho$.

In the absence of radiative events ($N_r = 0$), our definitions for ϵ and ρ reduce to their familiar form: the efficiency ϵ is the probability for a given signal event to be selected, and the purity ρ is the probability for a given selected event to be signal. In this analysis, however, the 'efficiency' is not constrained to satisfy $0 \leq \epsilon \leq 1$, and cannot be interpreted as a probability.[8] This anomaly arises because the residual contribution from radiative events is not removed from our measurements by subtraction; instead it is included in a multiplicative "detector correction" to be described in Section 3.4. When interpreting our results, we will use ϵ_{nr}, which is a more conventional measure of efficiency, involving only non-radiative $q\bar{q}$ events:

$$
\epsilon_{nr} = \lim_{\delta \to 0}\left[P\left(\text{ event is selected }\Big|\ \sqrt{s} - \sqrt{s'} < \delta\right)\right] \quad .
\tag{3.11}
$$

---

[8]If the denominator in Equation (3.9) were changed from N_{nr} to $N_{nr} + N_r$, we could interpret ϵ as the average selection probability of a $q\bar{q}$ event, including those with initial-state radiation. With this definition, the statistical uncertainty of $N_{\text{corr.}}$ would still be minimised by maximising $\epsilon\rho$. However, the 'efficiency' ϵ would then be very small, because most radiative events are deliberately rejected by our cut on $\sqrt{s'}$.

3.3.6.2 The W_{QCD}, L_{qqqq} and $L_{\mathrm{qq\ell\nu}}$ selection cuts

In Figure 3.6, we have shown the distribution of the QCD event weight W_{QCD}, for events passing the cuts defined in Sections 3.3.1–3.3.5. Also shown are the efficiency ϵ, the purity ρ, and their product $\epsilon\rho$, as a function of the cut position. The left-hand side of the plot corresponds to a very 'loose' cut passed by every event, while the right-hand side represents a 'tight' cut which rejects all events. As the cut is tightened, the efficiency ϵ decreases and the purity ρ rises. The product $\epsilon\rho$ reaches a maximum when $W_{\mathrm{QCD}}^{\mathrm{cut}} \approx -0.5$, as indicated by the solid vertical line. This optimised cut value is in agreement with the choice made in previous OPAL analyses [11].

Treating the $\mathrm{q\bar{q}q\bar{q}}$ likelihood variable L_{qqqq} in the same way, we obtain the distribution shown in Figure 3.7. Some events, which fail a 'preselection' in the calculation of L_{qqqq}, are given the value $L_{\mathrm{qqqq}} = -1$. After applying the cuts listed in Sections 3.3.1–3.3.5, we estimate that the events in this category amount to 83% of remaining $\mathrm{q\bar{q}}$ events, and 81% of remaining $\mathrm{qq\ell\nu}$ background events, but only 4% of remaining $\mathrm{q\bar{q}q\bar{q}}$ events. These events are omitted from Figure 3.7. The peak of $\epsilon\rho$ with respect to L_{qqqq} is much broader than in the W_{QCD} case; the selection would be well optimised by any cut in the range $L_{\mathrm{qqqq}} < 0.1$ to $L_{\mathrm{qqqq}} < 0.5$. For consistency with previous analyses, we choose the cut $L_{\mathrm{qqqq}} < 0.25$.

We now consider a selection based on the $\mathrm{q\bar{q}\ell^{\pm}\nu_{\ell}}$ likelihood variable, $L_{\mathrm{qq\ell\nu}}$. After imposing the L_{qqqq} cut, the distribution of $L_{\mathrm{qq\ell\nu}}$ is as shown in Figure 3.8. Once again, some events which fail a preselection are given the value $L_{\mathrm{qq\ell\nu}} = -1$; in this case, however, such events are included in the $L_{\mathrm{qq\ell\nu}} = 0$ bin of the histogram. For most events, $L_{\mathrm{qq\ell\nu}}$ is then very close to zero or one, while a small minority are scattered evenly in the central range. Any cut in the range $L_{\mathrm{qq\ell\nu}} < 0.01$ to $L_{\mathrm{qq\ell\nu}} < 0.99$ would give an almost optimal selection; we again follow the convention of Ref. [119], and select events with $L_{\mathrm{qq\ell\nu}} < 0.5$.

When these new likelihood cuts are used at $\sqrt{s} = 207$ GeV, the predicted efficiency ϵ_{nr} for selecting non-radiative signal events is 76%, and the purity ρ is 94%. The four-fermion background has been halved when compared with the original W_{QCD} selection, while leaving the efficiency almost unchanged.

Finally, we investigate whether any improvement can be achieved by applying a cut on W_{QCD} in addition to the likelihood selection. Figure 3.9 shows the distri-

bution of W_{QCD} for events satisfying the cuts defined thus far. We find that the product of efficiency and purity, $\epsilon\rho$, cannot be increased significantly by excluding further events. This result is to be expected, since the information contained in W_{QCD} has been used in the calculation of L_{qqqq}. We therefore place no explicit cut on W_{QCD}.

In summary, we will use the following two selection criteria to reject four-fermion events:

- $L_{\mathrm{qqqq}} < 0.25$

- $L_{\mathrm{qq}\ell\nu} < 0.5$.

For our analysis of data at $\sqrt{s} = 91$ GeV and 130–136 GeV we do not apply these cuts, because the background from four-fermion processes is negligible below the W^+W^- pair production threshold.

3.3.6.3   Aside: a useful cross-check for the position of a cut

To choose the cut position for a continuous variable such as W_{QCD} or L_{qqqq}, we have maximised the product of efficiency (ϵ) and purity (ρ). Our selection criterion takes the form

$$\lambda \; < \; \lambda_{\mathrm{cut}}   , \tag{3.12}$$

for some some cut variable λ,[9] and the probabilities ϵ_{nr}, ϵ_{r} and ϵ_{b} defined in Section 3.3.6.1 are functions of the cut position λ_{cut}. Intuitively, one expects that the optimal value of λ_{cut} will be at a position where the differential cross sections $\mathrm{d}\sigma/\mathrm{d}\lambda$ for signal and background processes are roughly equal; examples of this can be seen in Figures 3.6 and 3.7. It turns out that a general theorem exists for the proportions of signal and background events at the cut threshold.

The product of efficiency and purity can be written as

$$\epsilon\rho \; = \; \frac{1}{N} \frac{s^2}{s+b}   , \tag{3.13}$$

where s and b are the expected numbers of signal and background events passing the selection, and N is the expected number of signal events before any cuts are applied. In the presence of initial-state radiation, the selected radiative events are

---

[9]For cuts of the form $\lambda > \lambda_{\mathrm{cut}}$, we can transform to a new cut variable $\tilde{\lambda} = -\lambda$.
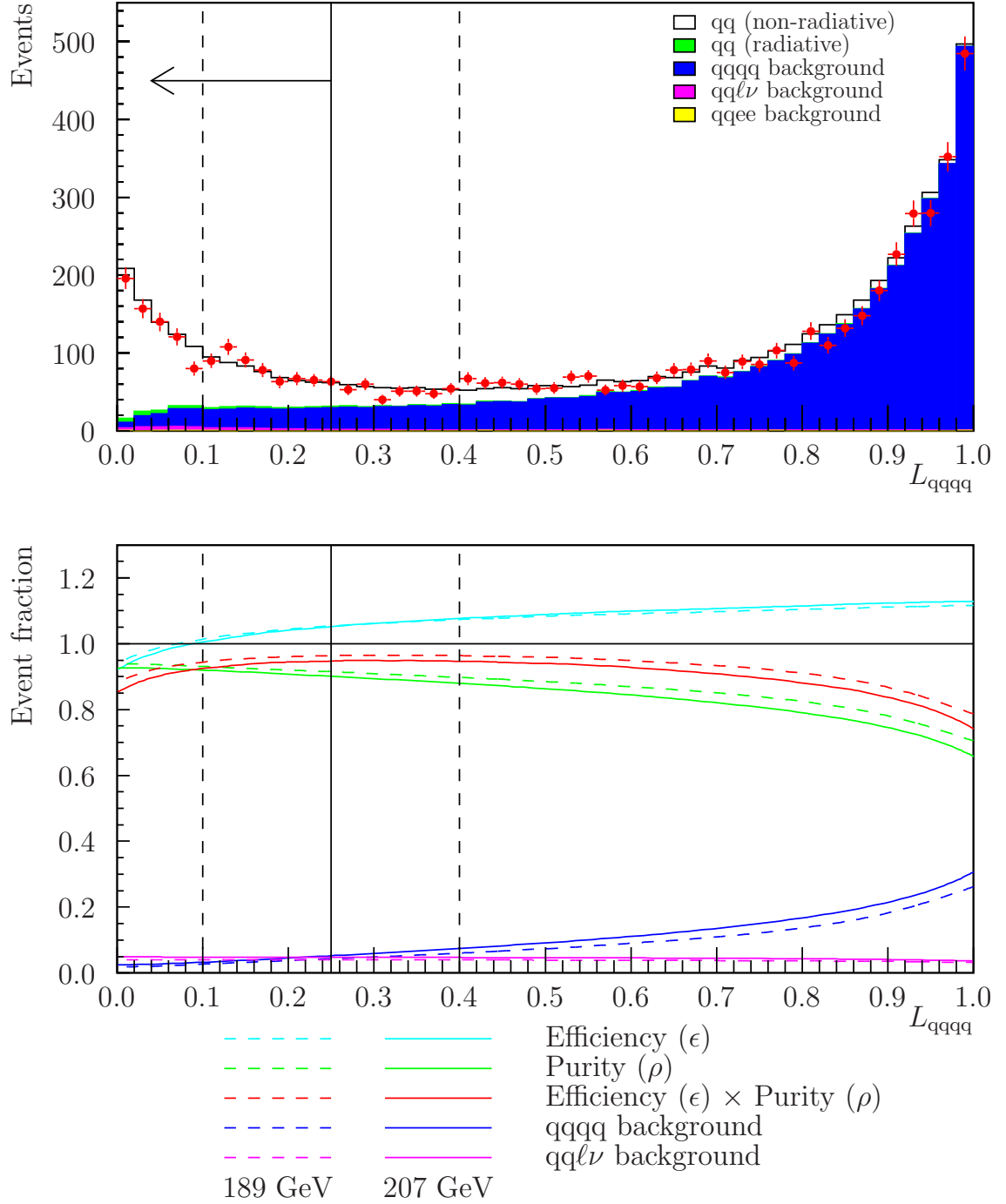
Figure 3.7: Distribution and event selection properties for the L_{qqqq} likelihood observable. Events with $L_{qqqq} = -1$ have been excluded from the upper plot. See the caption of Figure 3.6 for further details.
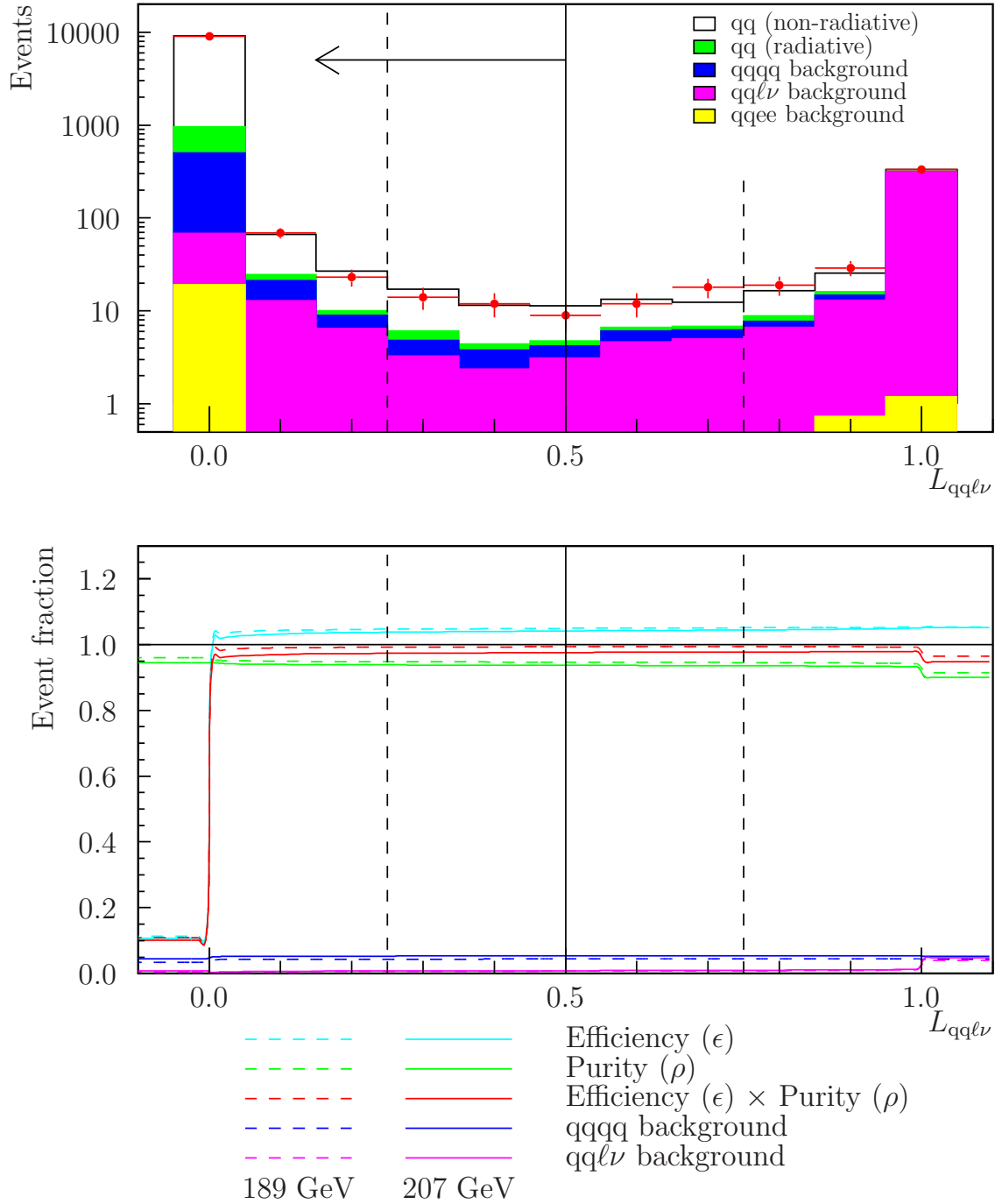
Figure 3.8: Distribution and event selection properties for the $L_{qq\ell\nu}$ likelihood observable. In the upper plot, events with $L_{qq\ell\nu} = -1$ have been redefined to have $L_{qq\ell\nu} = 0$. See the caption of Figure 3.6 for further details.
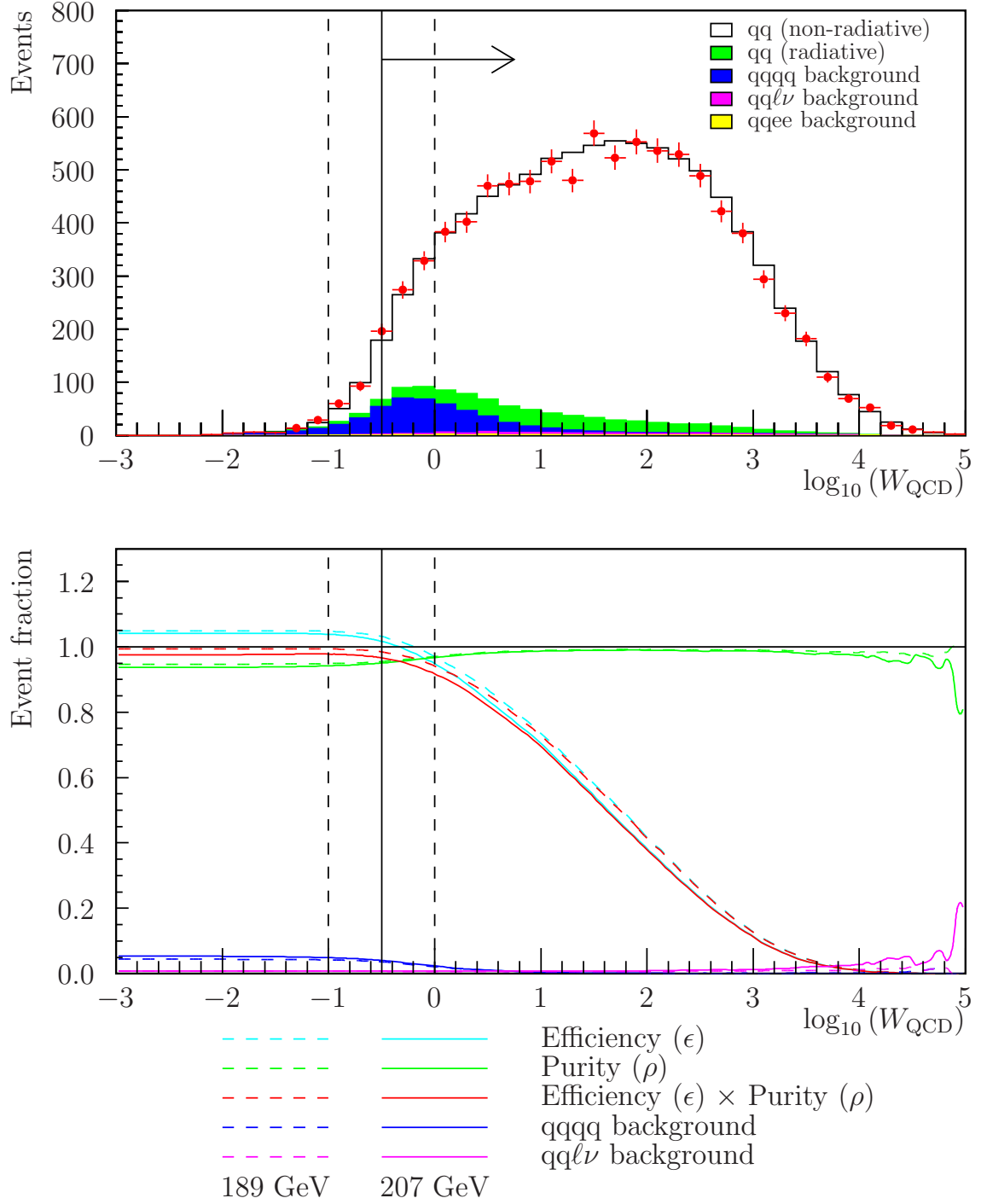
Figure 3.9: Distribution and event selection properties for the W_{QCD} observable, after imposing the cuts $L_{qqqq} < 0.25$ and $L_{qq\ell\nu} < 0.5$. The vertical lines indicate the original position of the W_{QCD} cut, and its alternative variations. See the caption of Figure 3.6 for a full explanation.

included as signal. Using the notation of Section 3.3.6.1, the numbers s, b and N
correspond to

$$
\begin{aligned}
s &= \epsilon_{\mathrm{nr}} N_{\mathrm{nr}} + \epsilon_{\mathrm{r}} N_{\mathrm{r}} \\
b &= \epsilon_{\mathrm{b}} N_{\mathrm{b}} \\
N &= N_{\mathrm{nr}} \qquad\qquad .
\end{aligned}
\tag{3.14}
$$

At the maximum of $\epsilon\rho$, we have

$$
\frac{\partial(\epsilon\rho)}{\partial s}\frac{\mathrm{d}s}{\mathrm{d}\lambda_{\mathrm{cut}}} + \frac{\partial(\epsilon\rho)}{\partial b}\frac{\mathrm{d}b}{\mathrm{d}\lambda_{\mathrm{cut}}} = 0 \quad .
\tag{3.15}
$$

Evaluating the partial derivatives and multiplying the above equation by $N(s+b)^2/s$,
we find

$$
(s+2b)\frac{\mathrm{d}s}{\mathrm{d}\lambda_{\mathrm{cut}}} - s\frac{\mathrm{d}b}{\mathrm{d}\lambda_{\mathrm{cut}}} = 0 \quad .
\tag{3.16}
$$

We now determine the fraction of events at the cut threshold $\lambda = \lambda_{\mathrm{cut}}$ that are
signal:

$$
\frac{\mathrm{d}s/\mathrm{d}\lambda_{\mathrm{cut}}}{\mathrm{d}s/\mathrm{d}\lambda_{\mathrm{cut}} + \mathrm{d}b/\mathrm{d}\lambda_{\mathrm{cut}}} = \frac{s}{2(s+b)} \equiv \frac{\rho}{2} \quad .
\tag{3.17}
$$

Thus for a reasonably pure selection ($\rho \approx 1$), we expect signal events to contribute
just under half the combined differential cross section at the optimal cut value.
This result is confirmed by the W_{QCD} and L_{qqqq} distributions, shown in Figures 3.6
and 3.7 respectively. Equation (3.17) cannot be applied to the $L_{\mathrm{qq\ell\nu}}$ cut, because
the distribution for this observable is not sufficiently smooth; the vast majority of
events fall into one of three bins, at $L_{\mathrm{qq\ell\nu}} = -1$, 0 or 1.

3.3.7   Results of the event selection

In Tables 3.2–3.4, we list the numbers of events passing each stage of the selection
procedure, at each centre-of-mass energy. To confirm that the final quantities of
events selected from OPAL data are consistent with Monte Carlo predictions, we
perform a χ^2 test: the results are given in Table 3.5. We find $\chi^2 = 17.2$ for 11 degrees
of freedom, corresponding to a P-value of 0.90. At $\sqrt{s} = 91$ GeV, the predicted and
observed numbers of selected events differ by 8 standard deviations, and are not
included in the χ^2 test; the luminosity of our data sample has not been calculated
with sufficient precision to make a meaningful comparison at this energy.

Energy and cut	Data events	Events predicted by MC sims.			Efficiency (ϵ_{nr})
		$q\bar{q}$ (non-rad.)	$q\bar{q}$ (radiative)	Total	
91 GeV					
All MC events	–	441590	–	441590	1.000
TKMH	426193	420817	–	420817	0.953
$N_{\mathrm{tracks}} \geq 7$	419922	414362	–	414362	0.938
$|\cos\theta_{\mathrm{T}}| < 0.9$	**395695**	**390438**	–	**390438**	**0.884**
133 GeV					
All MC events	–	560	2815	3376	1.000
L2MH	3178	535	2546	3081	0.955
$N_{\mathrm{tracks}} \geq 7$	3132	530	2508	3038	0.946
$|\cos\theta_{\mathrm{T}}| < 0.9$	2929	499	2363	2863	0.891
ISR cut	**630**	**479**	**205**	**684**	**0.854**

Table 3.2: Numbers of selected events at $\sqrt{s} = 91$ GeV and 133 GeV. Each selection cut is applied to events passing all previous cuts, and the lines printed in bold indicate the final selection. The 'TKMH' and 'L2MH' lines include an extra cut on the thrust axis: $|\cos\theta_{\mathrm{T}}| < 0.95$. At 133 GeV, the Monte Carlo predictions have been re-scaled from samples much larger than the data. The efficiency ϵ_{nr} is calculated using only non-radiative $q\bar{q}$ events, which are defined in this table by $\sqrt{s} - \sqrt{s'} < 1$ GeV.

Finally, in Figure 3.10, we present the distribution of centre-of-mass energies for all selected events at $\sqrt{s} \geq 130$ GeV.

3.4 Measurement of the event shape distributions

Using data from the tracking chambers and the electromagnetic calorimeters, we now compute the event shape observables defined in Section 1.5, for each selected event.

Charged particles normally produce both a curved track in the central detector and a cluster of energy deposition in the calorimeters, while neutral particles are seen only in the calorimeters. To avoid double-counting of energy, an association must be made between the charged tracks and the energy clusters; this is not trivial, however, because the clusters from two neighbouring particles can often overlap in a high-multiplicity event. To solve this problem a matching algorithm, MT [108], has been developed. For each charged track of momentum $\boldsymbol{p}$, the expected energy response $\widehat{E}(\boldsymbol{p})$ of the calorimeters is estimated. If the measured energy E of the matched cluster is less than $\widehat{E}(\boldsymbol{p}) + \Delta E$, where ΔE is the assumed resolution of the calorimeter, then the cluster is not used. If $E > \widehat{E}(\boldsymbol{p}) + \Delta E$, however, then

Energy and cut	Data events	Events predicted by MC simulations						Efficiency (ϵ_{nr})	Purity (ρ)
		$q\bar{q}$ (non-rad.)	$q\bar{q}$ (radiative)	qqqq	qq$\ell\nu$	qqee	Total		
161 GeV									
All MC events	–	244	1327	21	27	52	1671	1.000	0.941
L2MH	1395	231	1141	20	21	6	1419	0.945	0.967
$N_{\mathrm{tracks}} \geq 7$	1369	229	1123	20	21	5	1398	0.938	0.967
$|\cos\theta_{\mathrm{T}}| < 0.9$	1287	215	1059	19	20	4	1317	0.879	0.967
ISR cut	304	204	77	15	3	1	300	0.834	0.938
$L_{\mathrm{qqqq}} < 0.25$	283	196	74	4	3	1	278	0.802	0.972
$L_{\mathrm{qq}\ell\nu} < 0.5$	**281**	**196**	**74**	**4**	**1**	**1**	**275**	**0.800**	**0.979**
172 GeV									
All MC events	–	205	1130	63	65	49	1512	1.000	0.883
L2MH	1311	194	950	61	58	6	1268	0.946	0.902
$N_{\mathrm{tracks}} \geq 7$	1285	193	934	61	57	5	1250	0.941	0.901
$|\cos\theta_{\mathrm{T}}| < 0.9$	1218	181	880	59	56	5	1181	0.881	0.899
ISR cut	280	171	62	50	7	1	290	0.833	0.803
$L_{\mathrm{qqqq}} < 0.25$	228	164	59	9	6	1	238	0.798	0.936
$L_{\mathrm{qq}\ell\nu} < 0.5$	**218**	**163**	**59**	**9**	**1**	**0**	**232**	**0.796**	**0.956**
183 GeV									
All MC events	–	955	5336	464	468	1543	8941	1.000	0.704
L2MH	6146	903	4350	452	417	131	6253	0.946	0.840
$N_{\mathrm{tracks}} \geq 7$	6027	897	4270	451	413	126	6157	0.940	0.839
$|\cos\theta_{\mathrm{T}}| < 0.9$	5682	842	4018	437	401	116	5815	0.882	0.836
ISR cut	1456	793	282	358	43	3	1479	0.830	0.727
$L_{\mathrm{qqqq}} < 0.25$	1111	757	270	52	40	3	1122	0.792	0.916
$L_{\mathrm{qq}\ell\nu} < 0.5$	**1077**	**754**	**269**	**51**	**7**	**2**	**1084**	**0.790**	**0.945**
189 GeV									
All MC events	–	2793	15608	1588	1630	4726	26345	1.000	0.698
L2MH	18946	2651	12460	1541	1450	404	18505	0.949	0.817
$N_{\mathrm{tracks}} \geq 7$	18559	2634	12216	1539	1438	384	18212	0.943	0.815
$|\cos\theta_{\mathrm{T}}| < 0.9$	17457	2473	11469	1489	1391	363	17185	0.886	0.811
ISR cut	4448	2320	829	1202	139	7	4498	0.830	0.700
$L_{\mathrm{qqqq}} < 0.25$	3217	2189	783	144	128	7	3251	0.784	0.914
$L_{\mathrm{qq}\ell\nu} < 0.5$	**3086**	**2181**	**779**	**141**	**23**	**6**	**3130**	**0.781**	**0.945**
192 GeV									
All MC events	–	427	2374	258	266	1223	4548	1.000	0.616
L2MH	2911	405	1876	251	236	62	2830	0.950	0.806
$N_{\mathrm{tracks}} \geq 7$	2866	403	1839	251	234	59	2785	0.943	0.805
$|\cos\theta_{\mathrm{T}}| < 0.9$	2696	378	1723	242	225	56	2624	0.887	0.801
ISR cut	717	353	127	195	22	1	698	0.827	0.687
$L_{\mathrm{qqqq}} < 0.25$	530	332	119	21	20	1	493	0.778	0.915
$L_{\mathrm{qq}\ell\nu} < 0.5$	**514**	**330**	**118**	**20**	**4**	**1**	**473**	**0.773**	**0.947**

Table 3.3: Numbers of selected events at $\sqrt{s} = $ 161–192 GeV. Each selection cut is applied to events passing all previous cuts, and the lines printed in bold indicate the final selection. The 'L2MH' line includes an extra cut on the thrust axis: $|\cos\theta_{\mathrm{T}}| < 0.95$. The Monte Carlo predictions have been re-scaled from samples much larger than the data, and rounded to the nearest integer. The efficiency ϵ_{nr} is calculated using only non-radiative $q\bar{q}$ events, which are defined in this table by $\sqrt{s} - \sqrt{s'} < 1$ GeV. The purity ρ includes all two-fermion multihadron events as signal.

Energy and cut	Data events	Events predicted by MC simulations						Efficiency (ϵ_{nr})	Purity (ρ)
		$q\bar{q}$ (non-rad.)	$q\bar{q}$ (radiative)	qqqq	$qq\ell\nu$	qqee	Total		
196 GeV									
All MC events	–	1044	5863	684	704	3105	11400	1.000	0.606
L2MH	7213	991	4546	662	625	171	6995	0.949	0.792
$N_{\mathrm{tracks}} \geq 7$	7078	985	4454	662	620	161	6882	0.943	0.790
$|\cos\theta_{\mathrm{T}}| < 0.9$	6622	924	4171	637	597	151	6480	0.884	0.786
ISR cut	1732	863	313	510	57	3	1747	0.826	0.674
$L_{\mathrm{qqqq}} < 0.25$	1187	809	293	56	52	3	1213	0.774	0.908
$L_{\mathrm{qq}\ell\nu} < 0.5$	**1137**	**803**	**290**	**55**	**10**	**3**	**1161**	**0.769**	**0.942**
200 GeV									
Total MC	–	1007	5775	715	739	3130	11366	1.000	0.597
L2MH	6807	956	4407	690	654	164	6871	0.949	0.781
$N_{\mathrm{tracks}} \geq 7$	6676	949	4315	690	648	156	6757	0.942	0.779
$|\cos\theta_{\mathrm{T}}| < 0.9$	6217	891	4033	660	622	145	6352	0.885	0.775
ISR cut	1636	832	309	516	57	3	1718	0.826	0.664
$L_{\mathrm{qqqq}} < 0.25$	1145	779	290	56	52	3	1179	0.773	0.906
$L_{\mathrm{qq}\ell\nu} < 0.5$	**1090**	**775**	**288**	**56**	**9**	**3**	**1131**	**0.769**	**0.940**
202 GeV									
All MC events	–	469	2678	341	355	1474	5317	1.000	0.592
L2MH	3292	445	2021	328	313	79	3186	0.947	0.774
$N_{\mathrm{tracks}} \geq 7$	3225	441	1978	328	310	75	3132	0.941	0.772
$|\cos\theta_{\mathrm{T}}| < 0.9$	3021	413	1846	313	297	70	2940	0.880	0.768
ISR cut	806	385	143	244	29	2	802	0.821	0.658
$L_{\mathrm{qqqq}} < 0.25$	538	361	134	26	26	1	549	0.770	0.902
$L_{\mathrm{qq}\ell\nu} < 0.5$	**519**	**360**	**134**	**26**	**5**	**1**	**527**	**0.768**	**0.938**
205 GeV									
All MC events	–	983	5685	749	772	3144	11607	1.000	0.575
L2MH	6861	932	4209	720	680	166	6706	0.948	0.767
$N_{\mathrm{tracks}} \geq 7$	6721	926	4116	719	675	158	6593	0.942	0.765
$|\cos\theta_{\mathrm{T}}| < 0.9$	6260	868	3842	685	645	147	6186	0.883	0.761
ISR cut	1687	810	295	530	57	3	1695	0.824	0.652
$L_{\mathrm{qqqq}} < 0.25$	1187	756	274	57	51	3	1143	0.770	0.902
$L_{\mathrm{qq}\ell\nu} < 0.5$	**1130**	**750**	**272**	**56**	**9**	**3**	**1090**	**0.763**	**0.938**
207 GeV									
All MC events	–	1626	9392	1255	1317	5290	19343	1.000	0.570
L2MH	11239	1545	6852	1202	1155	287	11040	0.950	0.761
$N_{\mathrm{tracks}} \geq 7$	10987	1535	6699	1202	1144	270	10850	0.944	0.759
$|\cos\theta_{\mathrm{T}}| < 0.9$	10221	1441	6242	1145	1091	251	10169	0.886	0.755
ISR cut	2713	1345	488	876	96	3	2808	0.827	0.653
$L_{\mathrm{qqqq}} < 0.25$	1806	1255	454	96	86	3	1895	0.772	0.902
$L_{\mathrm{qq}\ell\nu} < 0.5$	**1717**	**1244**	**449**	**94**	**15**	**3**	**1804**	**0.765**	**0.938**

Table 3.4: Numbers of selected events at $\sqrt{s} = 196$–207 GeV. For details see the caption of Figure 3.3.

$\sqrt{s}$ (GeV)	Integrated luminosity (pb^{-1})	Observed events	Predicted events	Difference (standard deviations)
133.3	11.26	630	684 ± 26	-2.1
161.3	10.06	281	275 ± 17	$+0.4$
172.1	10.38	218	232 ± 15	-0.9
182.7	57.72	1077	1084 ± 33	-0.2
188.6	185.2	3086	3130 ± 56	-0.8
191.6	29.53	514	473 ± 22	$+1.9$
195.5	76.67	1137	1161 ± 34	-0.7
199.5	79.27	1090	1131 ± 34	-1.2
201.6	37.75	519	527 ± 23	-0.3
204.8	82.01	1130	1090 ± 33	$+1.2$
206.6	138.8	1717	1804 ± 42	-2.0

Table 3.5: Differences between observed and predicted numbers of selected events at each centre-of-mass energy, excluding 91 GeV. The uncertainties indicated are statistical, and are based on a Poisson distribution (they do not represent uncertainties in the predicted mean of the distribution). Combining the squared deviations gives $\chi^2 = 17.2$ with 11 degrees of freedom. The data are therefore consistent with Monte Carlo expectations at the 90% confidence level.

two particles are deemed to have contributed to the cluster: a charged particle of momentum $\boldsymbol{p}$, and a neutral particle of energy $E - \widehat{E}(\boldsymbol{p})$. This algorithm ensures that high-resolution data from the tracking chambers are given preference over less precise information from the calorimeters.[10] The four-momentum of each particle is then computed, by assuming masses equal to the pion mass $m_{\pi^\pm}$ for charged particles, and zero for neutral electromagnetic clusters.

For each event shape observable, we construct a histogram of about ten bins. The bin boundaries, listed in Appendix B, have been taken from previous OPAL publications where possible. For the narrow jet broadening (B_N), light jet mass (M_L) and D-parameter, however, the choice of binning is new. At the peak of each distribution the bin width is determined by the resolution of the detector, while in the tail we use wider bins to reduce the statistical uncertainty.

---

[10]As noted in Ref. [108], the resolution of the electromagnetic calorimeters is usually less than that of the tracking chambers. The only common exception is for very high energy electrons, which are not generally produced in multihadronic events.
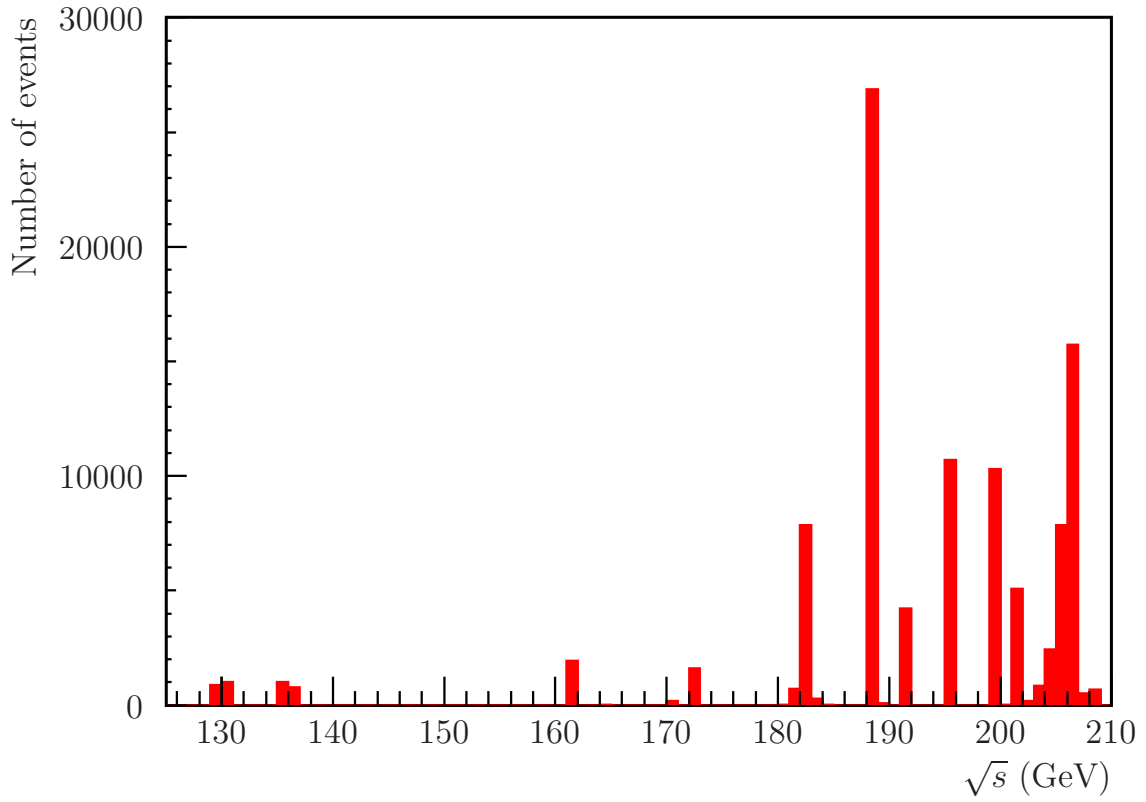
Figure 3.10: Distribution of centre-of-mass energies for selected non-radiative q$\bar{\text{q}}$ events (calibration data at $\sqrt{s} = 91$ GeV is not shown).

3.4.1 Estimation of background

The selection algorithm discussed in Section 3.3 is not perfectly efficient, and does not remove all of the four-fermion background events present. Although it was claimed in Tables 3.3 and 3.4 that only 6% of selected events at the highest energies are background, this statistic does not apply to individual bins of the event shape distributions. Among signal events, it is inevitable that three- and four-jet QCD processes will be the least distinguishable from four-fermion background events. It is therefore essential to estimate the expected background selected within each bin of the distributions, and subtract it from the number of events selected in the data.

Our predictions for four-fermion background processes are based on the standard OPAL Monte Carlo runs described in Section 3.2.2. A full simulation of the detector response has been performed for each event. After applying our selection algorithm to the simulated events, which have been reconstructed with ROPE in the same way as for real data, we compute the event shape distributions of the selected background events. These are then subtracted from the corresponding data histograms.

In this analysis, we have not considered every possible source of background;

other classes of event, such as two-photon processes and $\tau^+\tau^-$ production, will very occasionally pass our selection. These rare backgrounds are beyond the scope of this work, but a detailed study [117] has shown their contribution to be negligible in a measurement of the non-radiative $e^+e^- \to q\bar{q}$ cross section.

3.4.2   Detector correction

After the subtraction of four-fermion background, our distributions must be 'unfolded' to correct for three remaining sources of bias:

- Only 75–80% of non-radiative $q\bar{q}$ events pass the event selection at energies above the W^+W^- production threshold.

- Some of the selected $q\bar{q}$ events include initial-state radiation. Their contribution cannot be subtracted with other backgrounds, since our measurements would then rely on accurate simulation of the QCD processes which we are aiming to measure; instead we will include them in a multiplicative "detector correction," which is less sensitive to the Monte Carlo model.

- Biases will be present in our measurement of the actual event shape observables, due to the limitations of the detector. For example, the spreading of energy clusters within the calorimeters will tend to increase the apparent width of jets.

To accomplish this correction, we use the simulated $q\bar{q}$ event samples described in Section 3.2.2. Two sets of normalised event shape distributions are computed, using the same set of Monte Carlo events in each case:

Detector-level distributions, which include a full simulation of the OPAL detector, and are subjected to the same selection criteria as the real data.

Hadron-level distributions, computed using the true particle momenta predicted by PYTHIA, without simulation of the detector. Particles with mean lifetimes longer than 3×10^{-10} s are treated as stable, while others are forced to decay. Radiative events are removed by applying the cut

$$\left[\sqrt{s} - \sqrt{s'}\right]_\mathrm{true} < 1 \text{ GeV} \quad , \tag{3.18}$$

but no further selection criteria are applied.

The ratio of these two distributions gives a numerical correction factor for each bin. We apply this to our measured distributions using a simple bin-by-bin multiplication, and finally normalise the result.

3.4.3   Results from the detector simulation

We have already listed, in Tables 3.3 and 3.4, the expected numbers of signal and background events passing our selection. In this section, we present a more detailed analysis of the predicted signal and background contributions to each event shape distribution.

In Figures 3.11–3.15, the selection purity ρ and the non-radiative efficiency ϵ_{nr} are given as functions of each event shape observable y,[11] at $\sqrt{s} = 189$ GeV. The legend for these plots can be found in Figure 3.16. In most cases we find that the selection is extremely pure for events at low values of y, which represent the two-jet regime. As y increases towards the region of multiple hard gluon emissions, the purity ρ decreases monotonically in every case. This effect is especially pronounced in the distributions of the 'four-jet' variables M_L, B_N and D, for which only 10–20% of selected events in the last bin are signal. The efficiency ϵ_{nr} also drops with increasing y, as QCD processes become more compatible with four-fermion background. However, the efficiency does not approach 100% in the two-jet region, since events are rejected if the thrust axis lies within 26° of the beam axis; the largest values of ϵ_{nr} are approximately 0.85.

In the same figures, we have shown the probabilities $P(D|H)$ for hadron-level events to be observed in the correct bin by the detector, and $P(H|D)$ for detector-level events to have originated at hadron-level in the observed bin. These probabilities usually lie in the range $0.4 < P < 0.8$, with no common trend across the distributions; we can conclude that the bin widths are of the same order of magnitude as the detector resolution. The exception, once again, is in the bins of largest M_L, B_N and D, for which the probability of observing an event in the correct bin is below 10%. We suggest that this is due to the limited volume of phase space within the bin.

In the right-hand columns of Figures 3.11–3.15, we present the bin-by-bin "de-

---

[11]Recall that the dimensionless variable y represents a generic event shape observable. In all cases, a final state comprising two back-to-back particles is assigned the value $y = 0$; in the case of thrust, we must therefore define $y = 1 - T$. Further examples were listed in Section 1.6.
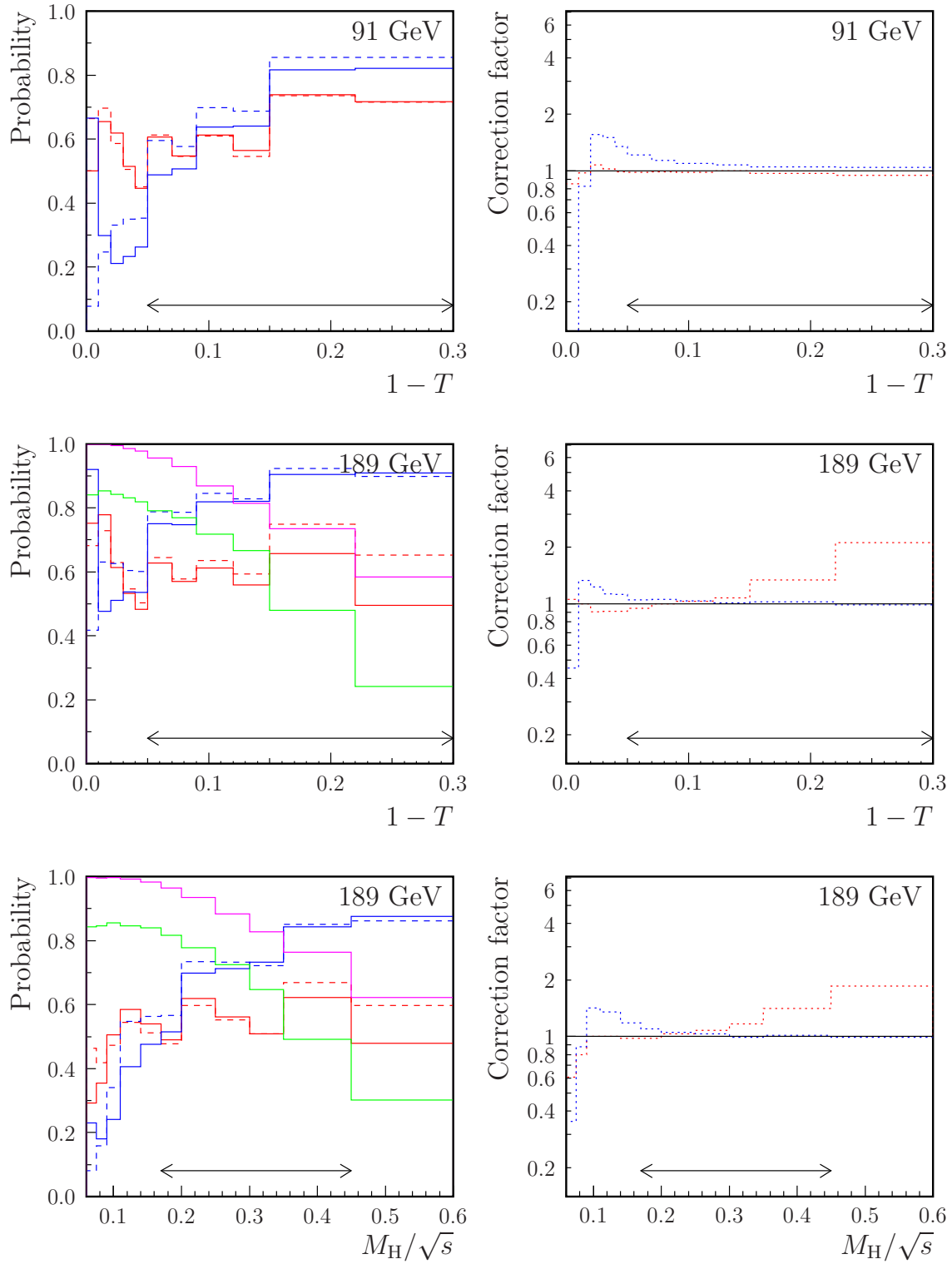
Figure 3.11: Efficiencies, purities, correction factors and bin migration probabilities for the thrust distribution at $\sqrt{s} = 91$ GeV and 189 GeV, and for the heavy jet mass distribution at 189 GeV. See Figure 3.16 for a full explanation.
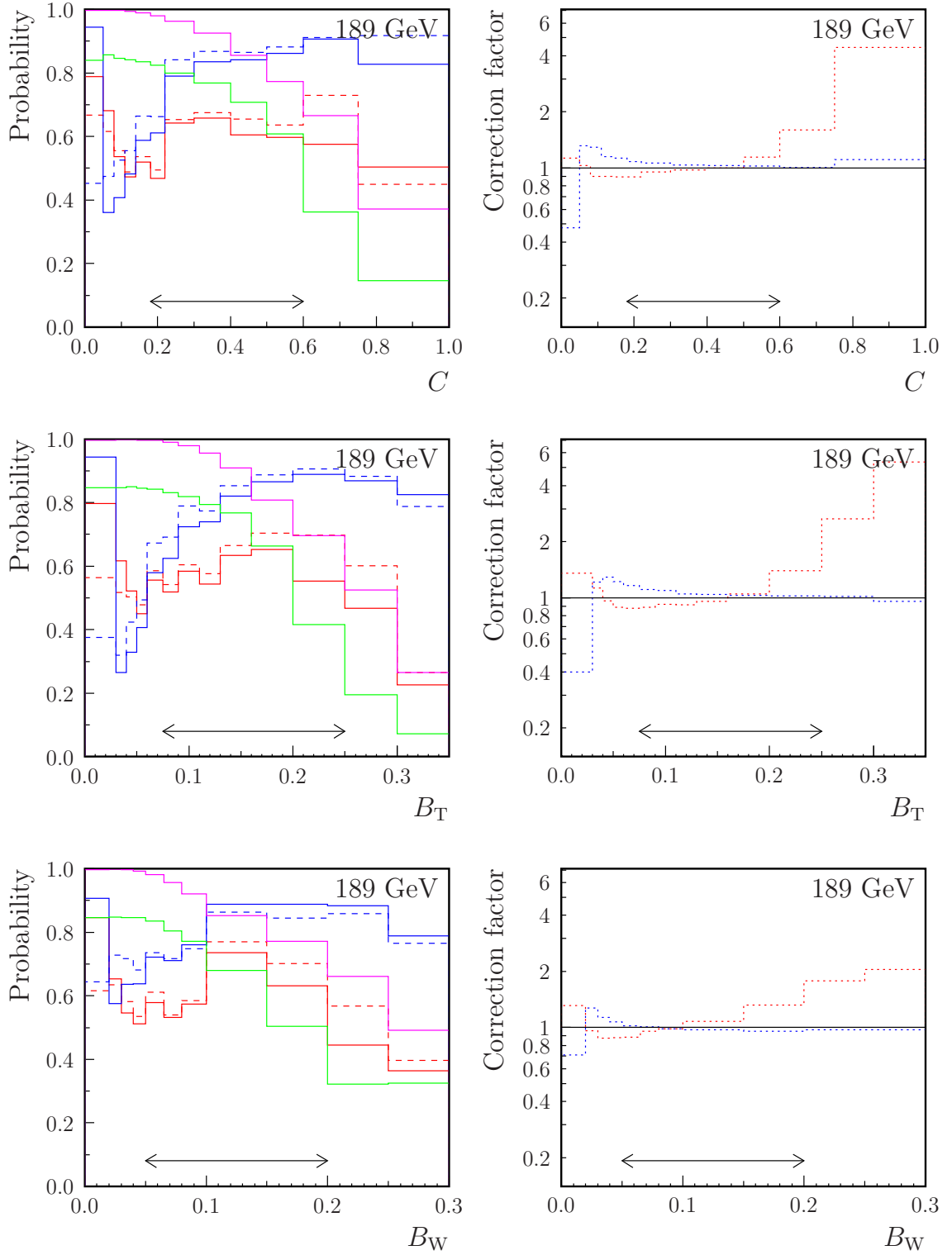
Figure 3.12: Efficiencies, purities, correction factors and bin migration probabilities for the C-parameter and for the total and wide jet broadenings at $\sqrt{s} = 189$ GeV. See Figure 3.16 for a full explanation.
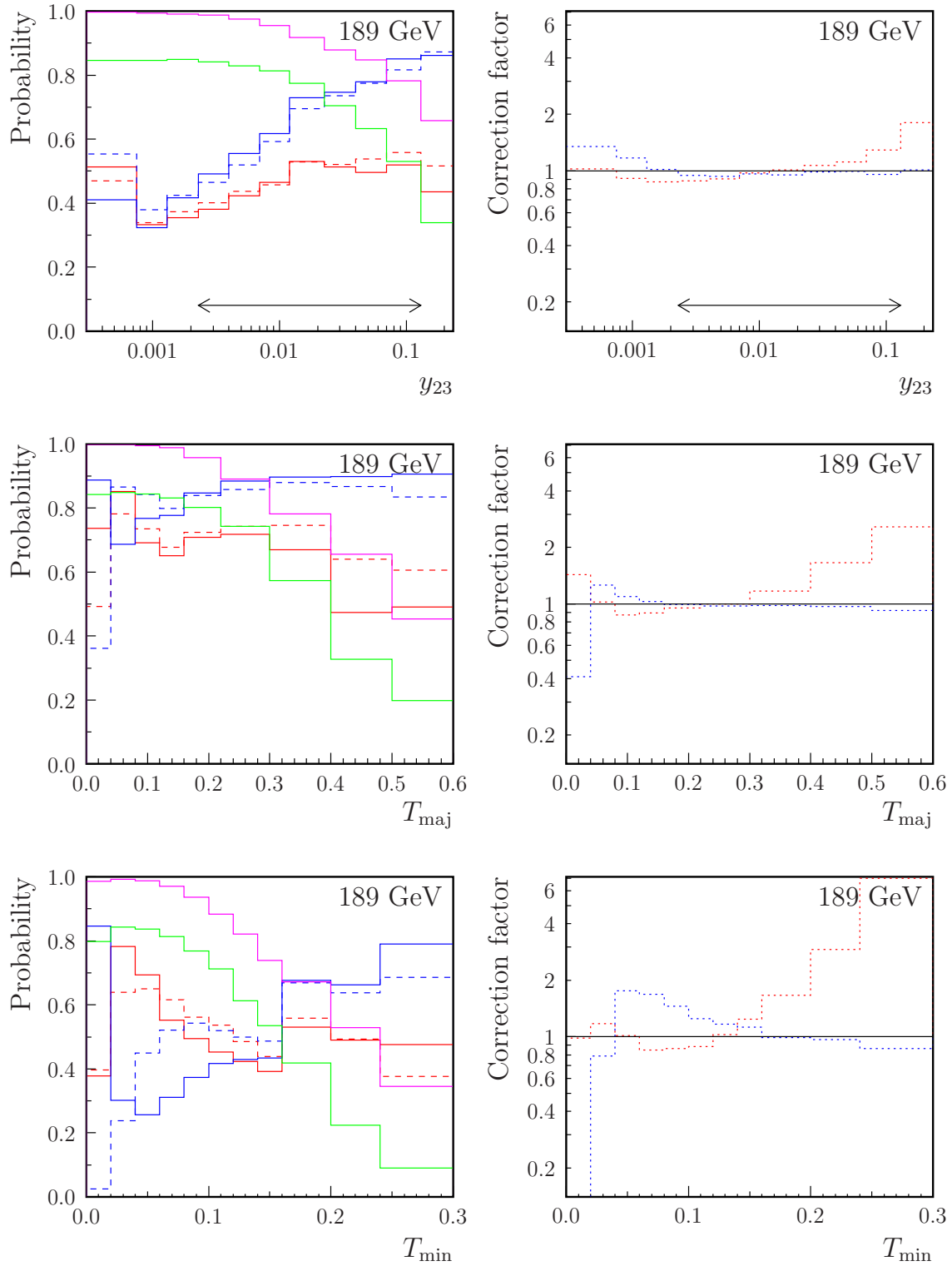
Figure 3.13: Efficiencies, purities, correction factors and bin migration probabilities for the Durham y_{23}parameter, thrust major and thrust minor at $\sqrt{s} = 189$ GeV. See Figure 3.16 for a full explanation.
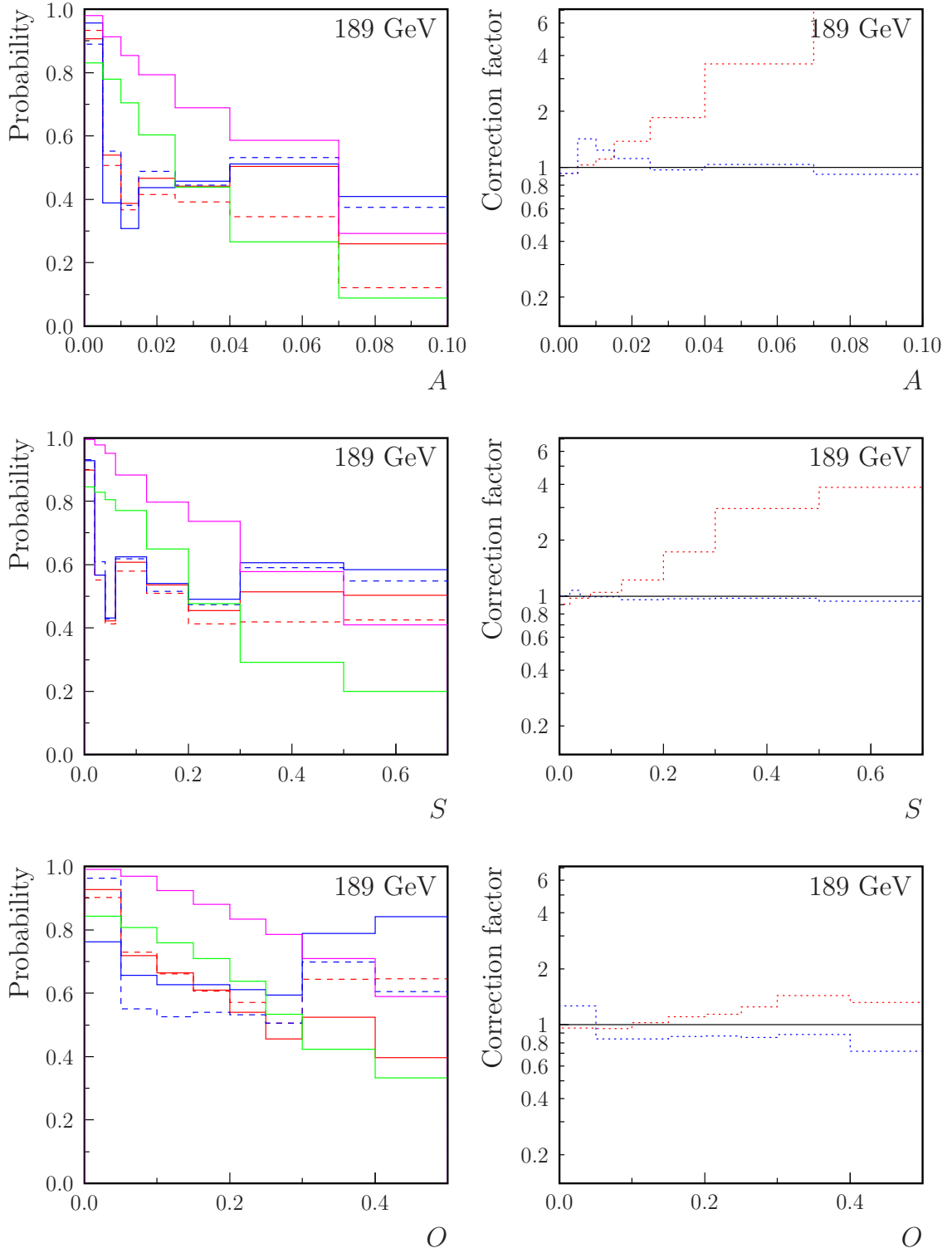
Figure 3.14: Efficiencies, purities, correction factors and bin migration probabilities for the aplanarity, sphericity and oblateness at $\sqrt{s} = 189$ GeV. See Figure 3.16 for a full explanation.
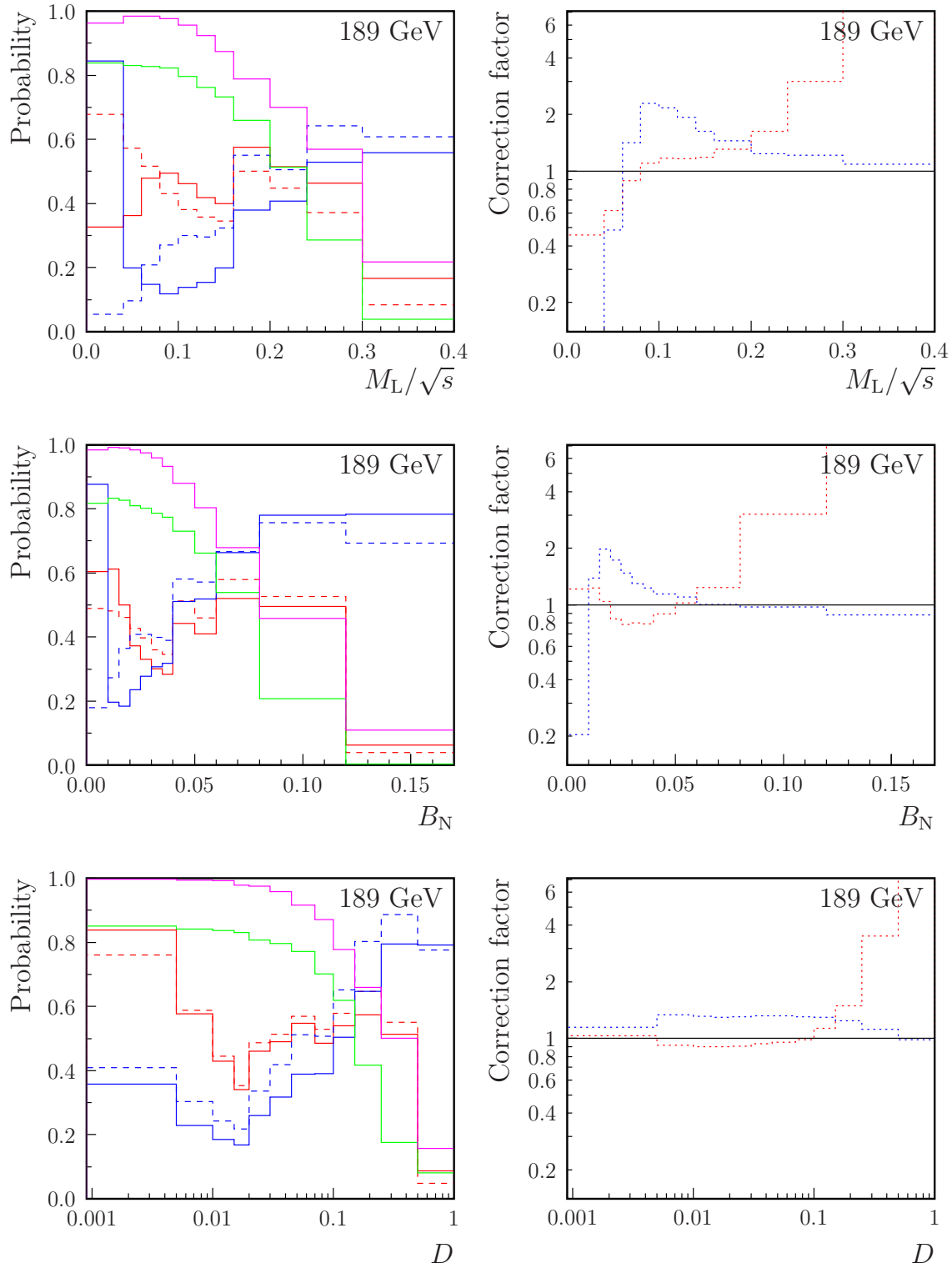
Figure 3.15: Efficiencies, purities, correction factors and bin migration probabilities for the light jet mass, narrow jet broadening and D-parameter at $\sqrt{s} = 189$ GeV. See Figure 3.16 for a full explanation.

Figure 3.16: Legend for Figures 3.11–3.15

tector corrections" defined in Section 3.4.2.[12] These compensate for selection inefficiencies, initial-state radiation and bin migrations. For the observables T, M_H, C, B_T, B_W, y_{23}, $T_\mathrm{maj.}$, O and D, we find a central range of several bins for which the correction is uniform and close to unity. For $T_\mathrm{min.}$, M_L, B_N, and most notably A and S, the detector correction is larger and varies significantly across the distribution. In the case of the aplanarity and sphericity, the poor resolution of the detector may be attributed to the sphericity tensor being non-infrared-safe, as discussed in Section 1.5.2; its quadratic dependence on the particle momenta implies that an error will be incurred if two overlapping calorimeter clusters are assigned to a single particle.

In Figure 3.11, we have compared the detector corrections for the thrust distribution at $\sqrt{s} = 91$ GeV and 189 GeV. We find that the response of the detector does not differ significantly between these two energies, for our purposes.

In many similar analyses, such as the OPAL measurement of event shapes at LEP1 [8], detector corrections have been performed using a complete response matrix. This takes account of the migration probabilities between bins, and attempts to

---

[12]The hadronisation corrections, plotted in blue, will be discussed in Section 3.5.1.

'invert' the detector simulation as accurately as possible. Although mathematically elegant, however, the inversion of the response matrix can lead to an unacceptable amplification of statistical fluctuations [121]; it also transfers systematic uncertainties between bins, by mixing data from regions of different purity. For these reasons, we have instead adopted the simpler bin-by-bin approach. As noted in Ref. [121], there may be a bias associated with the correction, due to imperfect modelling of the underlying hadron-level distribution.[13] We will estimate the size of this systematic error by calculating an alternative set of detector corrections based on events generated with HERWIG.

To give an indication of the off-diagonal elements in the response matrix, we have calculated joint distributions for the hadron- and detector-level observables at $\sqrt{s} = 189$ GeV; these are presented in Figures 3.17 and 3.18. The distributions are not perfectly diagonal, but the vast majority of events do not migrate by more than one bin from their true hadron-level position. In most, but not all, cases the probabilities of upward and downward migrations are roughly equal; this implies that we do not waste a significant amount of information by using bin-by-bin correction factors.

3.4.4   Estimation of uncertainties

The statistical uncertainties of the distributions are obtained using the method described in Appendix A.1. In previous OPAL publications, this uncertainty has been estimated by treating the raw number of events in each bin as an independent Poisson variable; the corresponding uncertainty was then rescaled according to the detector correction and normalisation. This is a very good approximation in the case of a narrow bin, but it fails when the relative uncertainty of the total number of events is comparable with that of the individual bin contents. Other authors, such as the ALEPH Collaboration [122], have assumed a multinomial distribution which takes into account correlations between the bin contents and the normalisation. When the bin contents are corrected for background and detector effects before normalisation, however, the multinomial distribution is no longer a perfect description; the precise covariance matrix for a corrected and normalised histogram

---

[13]This error would still be present, though perhaps smaller, in the case of the matrix method. The response matrix itself depends on the complete structure of the hadron-level event population, and not simply on the event shape distribution. It would be meaningless to refer to a "migration probability" from one bin to another without specifying the full kinematics of the events involved.

is derived in Appendix A.1.

To estimate the systematic uncertainty, we repeat the complete measurements using several variants of our standard method. In each case the difference with respect our central result is taken as a contribution to the uncertainty:

- To determine the uncertainty due to modelling of the event selection, we vary some of the cuts for both data and Monte Carlo samples:

  - The containment cut is tightened to $|\cos\theta_T| < 0.7$.

  - The $q\bar{q}q\bar{q}$ rejection cut is tightened to $L_{qqqq} < 0.1$ and loosened to $L_{qqqq} < 0.4$. The larger of the two absolute differences is taken as a systematic uncertainty.

  - The $q\bar{q}\ell^{\pm}\nu_\ell$ rejection cut is tightened to $L_{qq\ell\nu} < 0.25$ and loosened to $L_{qq\ell\nu} < 0.75$. The larger of the two absolute differences is taken as a systematic uncertainty.

  - An simpler algorithm is used to identify initial-state radiation, allowing only one ISR photon per event [116]. This gives an alternative value of $\sqrt{s'}$, which we use for the ISR rejection cut.

- The uncertainty due to background modelling is estimated by varying the subtracted background in each bin by $\pm 5\%$. This range of variation has been investigated by fitting Monte Carlo predictions for the W_{QCD} distribution to the observed data, with the total background cross section as a free parameter [117]. Our systematic uncertainty is taken as the larger of the upper and lower deviations in the event shape distribution.

- To estimate the bias due to the bin-by-bin detector correction, we re-calculate the correction factors using events simulated with HERWIG 6.2 instead of PYTHIA 6.1. As discussed in Section 3.2.2, the PYTHIA and HERWIG samples both use the same initial $q\bar{q}$ pairs, generated by $\mathcal{KK}$2f.

- Instead of using the MT algorithm to match charged tracks and electromagnetic energy clusters, we simply add all tracks and clusters without compensation for double-counting.

The ranges of variation for the cuts are essentially arbitrary, and have been chosen for consistency with other OPAL analyses.
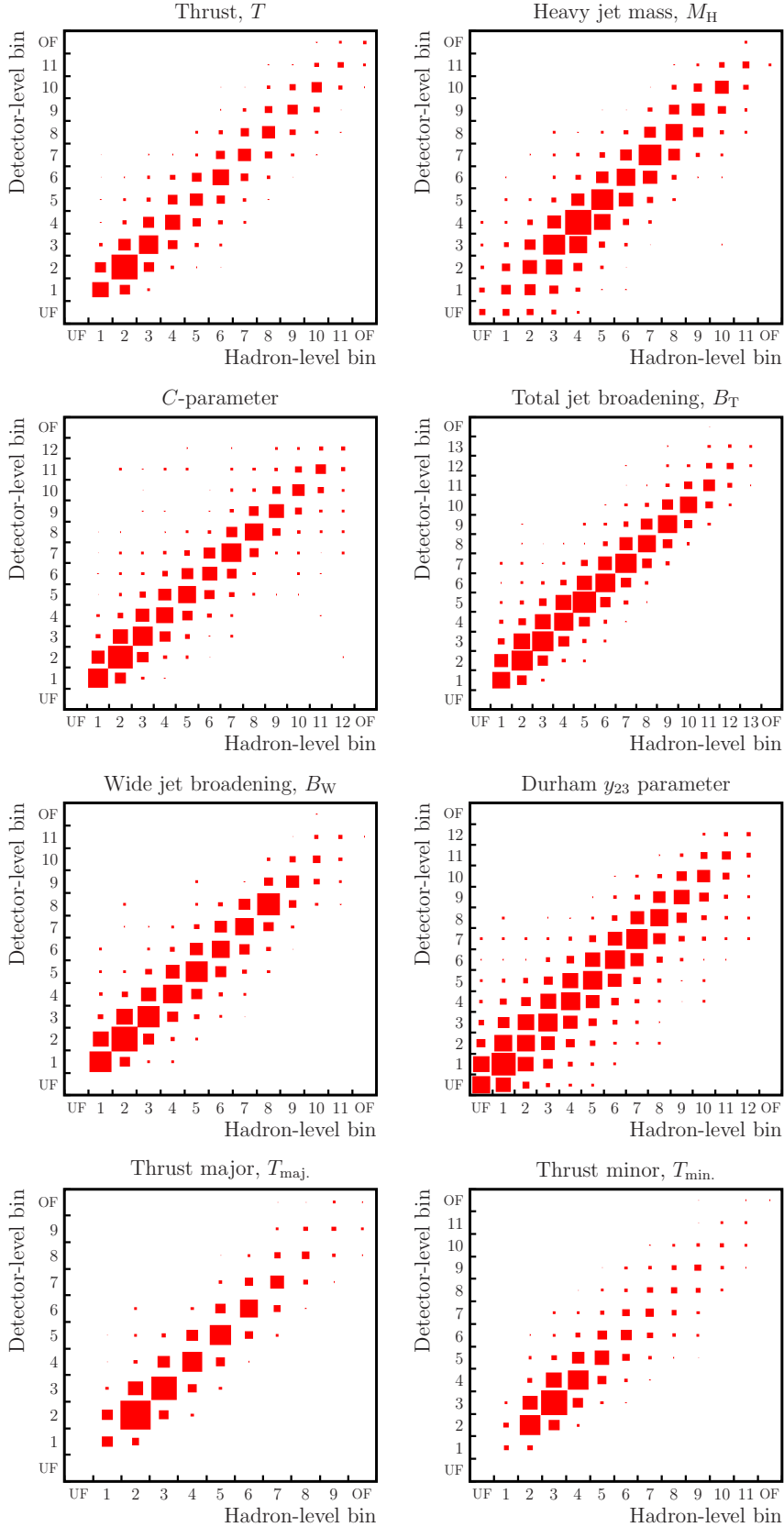
Figure 3.17: Joint hadron- and detector-level distributions predicted for T, M_H, C, B_T, B_W, y_{23}, $T_{maj.}$ and $T_{min.}$ at $\sqrt{s} = 189$ GeV. The area of each box represents the expected number of events within the given pair of bins. The underflow and overflow bins are denoted by UF and OF respectively.
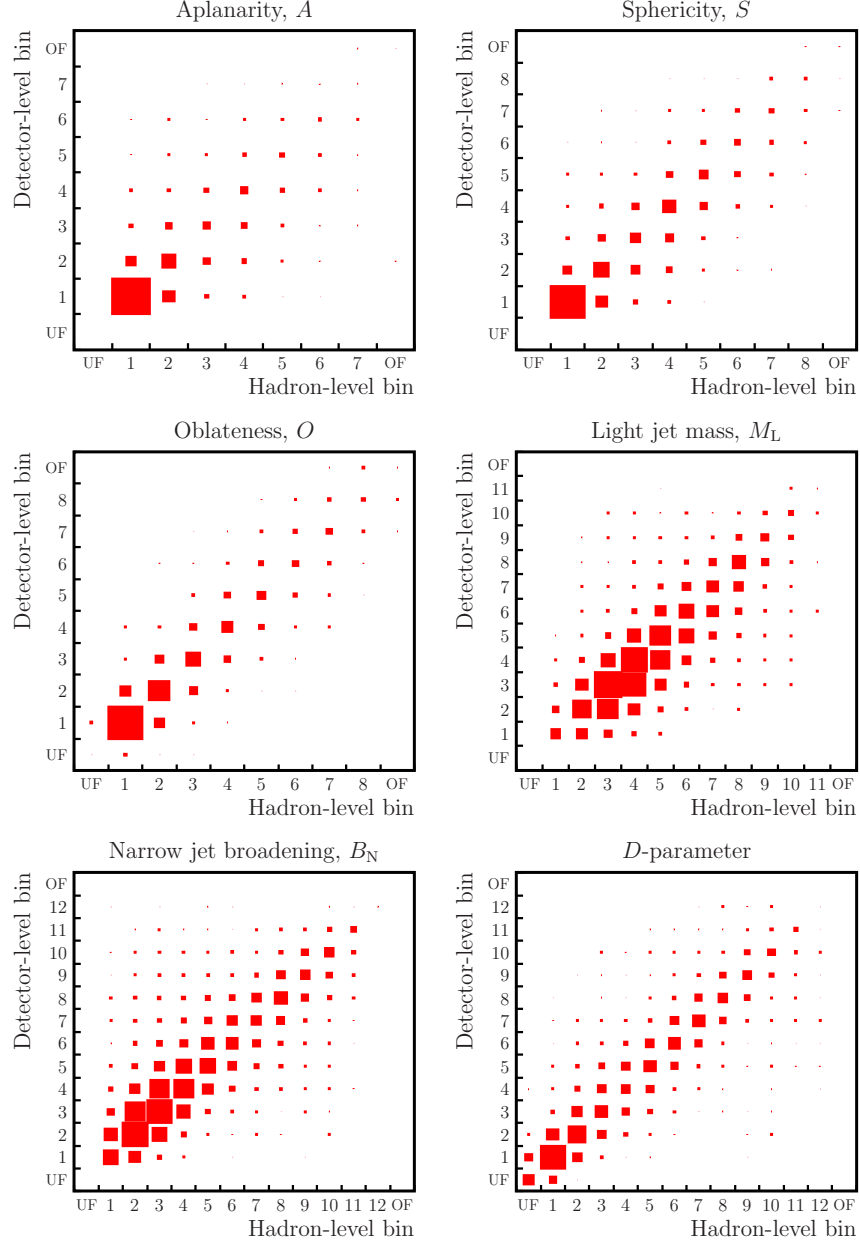
Figure 3.18: Joint hadron- and detector-level distributions predicted for A, S, O, M_L, B_N and D at $\sqrt{s} = 189$ GeV. The area of each box represents the expected number of events within the given pair of bins. The underflow and overflow bins are denoted by UF and OF respectively.

In addition to these systematic variations, we estimate the statistical uncertainty due to the finite numbers of Monte Carlo events used to calculate the background subtraction and detector correction. A complete analysis would involve determining the statistical correlation between the numbers of hadron- and detector-level Monte Carlo events in each bin; for our purposes, however, we have conservatively assumed that the numerator and denominator of the detector correction have uncorrelated statistical uncertainties. We include the result as a contribution to the *systematic* uncertainty of our event shape distributions, though this classification is debatable.

The total systematic uncertainty within each bin is obtained by summing all of the above contributions in quadrature.

3.4.5   Results of the event shape measurements

Our complete event shape measurements at each centre-of-mass energy are presented in Appendix B. Results are quoted as estimates of the probability density $R'(y)$, which satisfies the normalisation condition $\int_0^{y_{\max}} R'(y)\,\mathrm{d}y = 1$.

The distributions are shown graphically in Figures B.1–B.28, and are compared against predictions from three hadron-level Monte Carlo generators: PYTHIA 6.1, HERWIG 6.2 and ARIADNE 4.11. In each case, we have generated finely-binned histograms using a sample of five million events[14] with the standard OPAL choice of parameters.

As an example of the background subtraction, detector correction and systematic uncertainty composition, we will give detailed breakdowns of four distributions: the thrust and light jet mass measurements are presented for $\sqrt{s} = 91$ GeV and 189 GeV in Tables 3.6–3.9. The relative systematic uncertainties are generally found to be larger at high energies. This difference is mainly due to the presence of four-fermion background, but is also caused by statistical fluctuations in the "systematic deviations" used to estimate the uncertainty.

Our detector correction factors are particularly large at the extremities of the light jet mass distribution, at $\sqrt{s} = 189$ GeV. The corrections are estimated from Monte Carlo models, which do not always provide an accurate description of four-jet observables such as M_{L}; the relative systematic uncertainties in these bins are therefore considerably larger than those in the extremities of the thrust distribution.

---

[14]These hadron-level Monte Carlo samples are much larger than the standard OPAL runs used to compute the detector corrections. The size of the OPAL samples is limited by the speed of the GOPAL detector simulation.

3.4.6   Comparison with Monte Carlo models

To assess the level of agreement between Monte Carlo models and OPAL data, we have performed a set of crude χ^2 calculations, which are illustrated in Figures 3.19–3.23. For each bin of the measured distributions, we have calculated a corresponding hadron-level prediction using the large PYTHIA, HERWIG and ARIADNE samples. The differences between Monte Carlo distributions and OPAL data are displayed as multiples of the total uncertainty in the OPAL measurement. A χ^2 value is then calculated by summing the squared deviations across the distribution, assuming no correlation of uncertainties between bins; this approximation is not accurate, but provides a rudimentary statistic with which to compare the performance of different generators.

At $\sqrt{s} = 91$ GeV, where the uncertainties of the OPAL measurements are smallest, we observe significant discrepancies in the modelling of some distributions: all three generators appear to overestimate the cross section in the extreme two-jet region of certain observables.[15] HERWIG sometimes underestimates the distributions in the peak region, as does ARIADNE to a lesser extent. Since the distributions are normalised, however, it is to be expected that deviations of opposite sign will appear in different regions of the observables. In the three-jet regions of the observables used for our α_S fits (T, M_H, C, B_T, B_W and y_{23}), PYTHIA and ARIADNE both tend to give slightly better predictions than HERWIG. We do not find significant evidence to discriminate between the quality of PYTHIA and ARIADNE, for these observables.

All three models generally give less accurate descriptions for four-jet observables ($T_{\min}$, A, M_L, B_N and D) than for three-jet quantities; the models also do not agree well with one another, which implies that the fault cannot not lie entirely in the data. For all five of these observables, ARIADNE gives the lowest χ^2.

At LEP2, we have combined the OPAL data at all centre-of-mass energies $\sqrt{s} \geq 189$ GeV, to reduce statistical uncertainties; this should also have the effect of reducing fluctuations in our estimates of the systematic uncertainties. Nonetheless, our measurements do not have sufficient precision to detect significant deviations

---

[15]These large discrepancies between data and Monte Carlo, for example in the first bin of thrust, could also indicate that our systematic uncertainties have been underestimated. We aim to measure the model-dependence of our detector corrections by taking the differences between results obtained using PYTHIA- and HERWIG-based correction factors; however, the uncertainty obtained by this method is subject to fluctuations, and may happen to give an unrealistically low value in certain bins. This effect will need to be investigated further, prior to publication of the final OPAL results.

$1 - T$	Selected events	Detector correction	$\frac{\mathrm{d}R}{\mathrm{d}(1-T)}$	$\sigma_{\text{stat.}}$
$0.000 - 0.010$	5893	0.85	1.273	± 0.019
$0.010 - 0.020$	49730	0.98	12.26	± 0.05
$0.020 - 0.030$	67777	1.07	18.38	± 0.07
$0.030 - 0.040$	53616	1.02	13.86	± 0.06
$0.040 - 0.050$	39244	0.99	9.80	± 0.05
$0.050 - 0.070$	52393	0.98	6.502	± 0.027
$0.070 - 0.090$	33228	0.98	4.133	± 0.022
$0.090 - 0.120$	31949	0.98	2.649	± 0.014
$0.120 - 0.150$	20205	1.00	1.705	± 0.012
$0.150 - 0.220$	26117	0.97	0.913	± 0.006
$0.220 - 0.300$	12382	0.95	0.3704	± 0.0033

$1 - T$	Systematic deviations in $\mathrm{d}R/\mathrm{d}(1-T)$				Total $\sigma_{\text{syst.}}$
	No MT algorithm	$\|\cos\theta_{\text{T}}\|$ < 0.7	Alt. MC (HERWIG)	MC stats	
$0.000 - 0.010$	$+0.014$	-0.035	-0.005	± 0.021	± 0.043
$0.010 - 0.020$	-0.06	-0.05	$+0.39$	± 0.07	± 0.40
$0.020 - 0.030$	-0.17	-0.02	-0.20	± 0.10	± 0.28
$0.030 - 0.040$	$+0.09$	$+0.06$	$+0.06$	± 0.08	± 0.15
$0.040 - 0.050$	$+0.04$	$+0.10$	$+0.13$	± 0.07	± 0.18
$0.050 - 0.070$	$+0.015$	$+0.030$	$+0.068$	± 0.040	± 0.086
$0.070 - 0.090$	$+0.010$	$+0.016$	-0.002	± 0.032	± 0.037
$0.090 - 0.120$	$+0.015$	-0.008	-0.052	± 0.021	± 0.058
$0.120 - 0.150$	$+0.004$	-0.039	-0.061	± 0.017	± 0.075
$0.150 - 0.220$	-0.002	-0.003	-0.018	± 0.008	± 0.020
$0.220 - 0.300$	-0.0024	$+0.0009$	-0.0072	± 0.0047	± 0.0090

Table 3.6: The thrust distribution measured at $\sqrt{s} = 91$ GeV. In the first table, the "detector correction" represents the ratio of two *normalised* distributions of Monte Carlo events, at hadron level and detector level; the number of events selected in each bin is multiplied by this detector correction, then normalised, to give the measured distribution $\mathrm{d}R/\mathrm{d}(1-T)$. In the second table, the total systematic uncertainty for each bin is obtained by summing in quadrature the four contributions shown.

$1 - T$	Selected events	Estimated background	Detector correction	$\dfrac{\mathrm{d}R}{\mathrm{d}(1-T)}$	$\sigma_{\text{stat.}}$
$0.000 - 0.010$	260	0.7	1.05	9.36	± 0.55
$0.010 - 0.020$	642	1.9	1.00	21.93	± 0.80
$0.020 - 0.030$	497	2.5	0.90	15.35	± 0.64
$0.030 - 0.040$	319	4.7	0.91	9.82	± 0.54
$0.040 - 0.050$	234	5.4	0.91	7.15	± 0.47
$0.050 - 0.070$	346	14.2	0.94	5.38	± 0.28
$0.070 - 0.090$	184	15.0	1.00	2.89	± 0.24
$0.090 - 0.120$	236	28.0	1.03	2.44	± 0.16
$0.120 - 0.150$	136	25.6	1.08	1.36	± 0.14
$0.150 - 0.220$	151	41.9	1.34	0.72	± 0.08
$0.220 - 0.300$	76	23.2	2.12	0.479	± 0.065

$1 - T$	Systematic deviations in $\mathrm{d}R/\mathrm{d}(1-T)$					
	Alt. $\sqrt{s'}$ algorithm	No MT algorithm	$\lvert\cos\theta_{\text{T}}\rvert < 0.7$	Alternative MC		MC stats
				HERWIG	ARIADNE	
$0.000 - 0.010$	-0.01	-0.54	$+0.03$	$+0.09$	-0.04	± 0.16
$0.010 - 0.020$	$+0.07$	$+0.30$	$+0.45$	$+0.68$	$+0.15$	± 0.23
$0.020 - 0.030$	$+0.03$	$+0.57$	$+0.18$	$+0.61$	-0.20	± 0.20
$0.030 - 0.040$	-0.11	-0.63	$+0.06$	$+0.14$	$+0.05$	± 0.16
$0.040 - 0.050$	$+0.06$	$+0.12$	$+0.13$	$+0.45$	-0.03	± 0.13
$0.050 - 0.070$	-0.03	$+0.03$	-0.15	$+0.21$	-0.17	± 0.09
$0.070 - 0.090$	$+0.06$	$+0.03$	-0.02	-0.10	-0.14	± 0.06
$0.090 - 0.120$	-0.01	-0.03	-0.01	-0.05	-0.13	± 0.05
$0.120 - 0.150$	$+0.00$	-0.10	$+0.04$	-0.04	$+0.06$	± 0.04
$0.150 - 0.220$	$+0.01$	$+0.04$	$+0.01$	$+0.04$	-0.02	± 0.02
$0.220 - 0.300$	$+0.014$	-0.059	-0.001	-0.042	$+0.106$	± 0.021

$1 - T$	Systematic deviations in $\mathrm{d}R/\mathrm{d}(1-T)$						Total $\sigma_{\text{syst.}}$
	Background		L_{qqqq} cut		$L_{\text{qq}\ell\nu}$ cut		
	$+5\%$	-5%	< 0.10	< 0.40	< 0.25	< 0.75	
$0.000 - 0.010$	-0.04	$+0.04$	$+0.01$	$+0.06$	$+0.00$	$+0.01$	± 0.58
$0.010 - 0.020$	-0.08	$+0.09$	$+0.02$	$+0.13$	$+0.00$	-0.05	± 0.91
$0.020 - 0.030$	-0.06	$+0.06$	$+0.02$	$+0.09$	-0.09	$+0.01$	± 0.89
$0.030 - 0.040$	-0.03	$+0.03$	$+0.04$	$+0.06$	$+0.01$	$+0.00$	± 0.68
$0.040 - 0.050$	-0.02	$+0.02$	$+0.02$	$+0.03$	$+0.02$	-0.03	± 0.51
$0.050 - 0.070$	-0.01	$+0.01$	$+0.00$	-0.01	$+0.02$	-0.03	± 0.28
$0.070 - 0.090$	$+0.00$	$+0.00$	-0.02	-0.07	$+0.01$	$+0.03$	± 0.16
$0.090 - 0.120$	$+0.01$	-0.01	$+0.01$	$+0.01$	-0.01	-0.01	± 0.08
$0.120 - 0.150$	$+0.01$	-0.01	$+0.03$	-0.07	-0.01	$+0.01$	± 0.14
$0.150 - 0.220$	$+0.01$	-0.01	-0.09	$+0.02$	$+0.00$	-0.01	± 0.11
$0.220 - 0.300$	$+0.008$	-0.009	$+0.040$	-0.057	$+0.004$	$+0.003$	± 0.096

Table 3.7: The thrust distribution measured at $\sqrt{s} = 189$ GeV. In the first table, the measured distribution $\mathrm{d}R/\mathrm{d}(1-T)$ is obtained by subtracting the expected background from the number of selected events in each bin, then applying the detector correction and normalisation as described in Table 3.6. In the second and third tables, the total systematic uncertainty for each bin is calculated by summing in quadrature the eight contributions shown. For the background variation and the L_{qqqq} and $L_{\text{qq}\ell\nu}$ cut variations, the larger of the two absolute deviations is used; for the alternative Monte Carlo generators, only HERWIG is used.

$M_{\mathrm{L}}/\sqrt{s}$	Selected events	Detector correction	$\frac{\mathrm{d}R}{\mathrm{d}(M_{\mathrm{L}}/\sqrt{s})}$	$\sigma_{\mathrm{stat.}}$
$0.000 - 0.040$	4372	0.46	0.124	± 0.002
$0.040 - 0.060$	20627	0.43	1.108	± 0.008
$0.060 - 0.080$	53790	0.55	3.72	± 0.02
$0.080 - 0.100$	79765	0.83	8.22	± 0.03
$0.100 - 0.120$	76525	1.12	10.73	± 0.04
$0.120 - 0.140$	55519	1.31	9.11	± 0.04
$0.140 - 0.160$	36503	1.37	6.22	± 0.03
$0.160 - 0.200$	39726	1.27	3.150	± 0.015
$0.200 - 0.240$	17750	1.21	1.343	± 0.010
$0.240 - 0.300$	9140	1.18	0.450	± 0.005
$0.300 - 0.400$	1975	1.24	0.0610	± 0.0013

$M_{\mathrm{L}}/\sqrt{s}$	Systematic deviations in $\mathrm{d}R/\mathrm{d}(M_{\mathrm{L}}/\sqrt{s})$				Total $\sigma_{\mathrm{syst.}}$
	No MT algorithm	$|\cos\theta_{\mathrm{T}}|$ < 0.7	Alt. MC (HERWIG)	MC stats	
$0.000 - 0.040$	$+0.000$	-0.003	-0.038	± 0.003	± 0.038
$0.040 - 0.060$	-0.006	-0.004	-0.088	± 0.013	± 0.089
$0.060 - 0.080$	-0.05	-0.01	$+0.55$	± 0.03	± 0.55
$0.080 - 0.100$	$+0.00$	$+0.00$	$+0.56$	± 0.04	± 0.56
$0.100 - 0.120$	-0.10	-0.01	-0.36	± 0.05	± 0.37
$0.120 - 0.140$	$+0.07$	$+0.04$	-0.53	± 0.05	± 0.54
$0.140 - 0.160$	$+0.00$	$+0.03$	-0.21	± 0.04	± 0.22
$0.160 - 0.200$	$+0.027$	-0.010	$+0.074$	± 0.021	± 0.083
$0.200 - 0.240$	$+0.008$	-0.016	$+0.023$	± 0.014	± 0.033
$0.240 - 0.300$	$+0.002$	$+0.002$	-0.015	± 0.007	± 0.017
$0.300 - 0.400$	$+0.0026$	$+0.0017$	-0.0001	± 0.0019	± 0.0037

Table 3.8: The light jet mass distribution measured at $\sqrt{s} = 91$ GeV. See Table 3.6 for further explanation.

$M_{\mathrm{L}}/\sqrt{s}$	Selected events	Estimated background	Detector correction	$\dfrac{\mathrm{d}R}{\mathrm{d}(M_{\mathrm{L}}/\sqrt{s})}$	$\sigma_{\mathrm{stat.}}$
$0.000 - 0.040$	109	5.0	0.46	0.402	± 0.044
$0.040 - 0.060$	422	6.5	0.62	4.35	± 0.22
$0.060 - 0.080$	741	12.0	0.89	11.02	± 0.39
$0.080 - 0.100$	640	15.0	1.10	11.71	± 0.43
$0.100 - 0.120$	441	18.4	1.17	8.38	± 0.38
$0.120 - 0.140$	261	20.4	1.17	4.76	± 0.31
$0.140 - 0.160$	186	21.3	1.19	3.31	± 0.25
$0.160 - 0.200$	184	37.9	1.30	1.62	± 0.14
$0.200 - 0.240$	69	21.0	1.63	0.66	± 0.11
$0.240 - 0.300$	30	10.7	3.01	0.328	± 0.084
$0.300 - 0.400$	3	2.4	12.13	0.03	± 0.07

$M_{\mathrm{L}}/\sqrt{s}$	Systemic deviations in $\mathrm{d}R/\mathrm{d}(M_{\mathrm{L}}/\sqrt{s})$					MC stats
	Alt. $\sqrt{s'}$ algorithm	No MT algorithm	$\|\cos\theta_{\mathrm{T}}\|$ < 0.7	Alternative MC		
				HERWIG	ARIADNE	
$0.000 - 0.040$	-0.013	$+0.007$	-0.009	-0.054	-0.123	± 0.013
$0.040 - 0.060$	$+0.00$	-0.03	$+0.07$	$+0.12$	-0.82	± 0.07
$0.060 - 0.080$	-0.01	-0.24	-0.04	$+0.16$	-0.32	± 0.12
$0.080 - 0.100$	-0.06	-0.21	$+0.38$	-0.43	-0.04	± 0.12
$0.100 - 0.120$	-0.16	$+0.40$	-0.21	$+0.00$	$+0.25$	± 0.11
$0.120 - 0.140$	$+0.05$	-0.18	-0.09	$+0.14$	$+0.27$	± 0.08
$0.140 - 0.160$	-0.02	-0.30	$+0.13$	$+0.10$	$+0.23$	± 0.07
$0.160 - 0.200$	$+0.05$	$+0.11$	$+0.07$	$+0.03$	$+0.01$	± 0.04
$0.200 - 0.240$	-0.06	$+0.04$	$+0.02$	-0.05	$+0.01$	± 0.03
$0.240 - 0.300$	$+0.019$	$+0.027$	-0.008	-0.045	$+0.098$	± 0.022
$0.300 - 0.400$	$+0.04$	$+0.03$	-0.08	$+0.04$	$+0.07$	± 0.01

$M_{\mathrm{L}}/\sqrt{s}$	Systemic deviations in $\mathrm{d}R/\mathrm{d}(M_{\mathrm{L}}/\sqrt{s})$						Total $\sigma_{\mathrm{syst.}}$
	Background		L_{qqqq} cut		$L_{\mathrm{qq}\ell\nu}$ cut		
	$+5\%$	-5%	< 0.10	< 0.40	< 0.25	< 0.75	
$0.000 - 0.040$	-0.001	$+0.001$	-0.006	$+0.001$	$+0.001$	$+0.004$	± 0.059
$0.040 - 0.060$	-0.01	$+0.02$	-0.02	$+0.02$	-0.01	$+0.01$	± 0.16
$0.060 - 0.080$	-0.04	$+0.04$	$+0.04$	$+0.08$	-0.02	$+0.03$	± 0.33
$0.080 - 0.100$	-0.03	$+0.04$	$+0.01$	$+0.06$	-0.01	-0.01	± 0.63
$0.100 - 0.120$	-0.02	$+0.02$	$+0.04$	$+0.00$	$+0.02$	$+0.00$	± 0.50
$0.120 - 0.140$	$+0.00$	$+0.00$	$+0.07$	$+0.09$	-0.01	-0.02	± 0.28
$0.140 - 0.160$	$+0.01$	-0.01	-0.02	-0.07	$+0.01$	$+0.05$	± 0.36
$0.160 - 0.200$	$+0.01$	-0.01	-0.10	-0.05	$+0.00$	$+0.00$	± 0.18
$0.200 - 0.240$	$+0.01$	-0.01	$+0.02$	-0.03	-0.01	$+0.00$	± 0.10
$0.240 - 0.300$	$+0.007$	-0.008	-0.014	$+0.055$	$+0.003$	-0.008	± 0.082
$0.300 - 0.400$	$+0.00$	-0.01	$+0.02$	-0.03	$+0.00$	-0.01	± 0.11

Table 3.9: The light jet mass distribution measured at $\sqrt{s} = 189$ GeV. See Table 3.7 for further explanation.

between Monte Carlo and data. This may in part be due to the scaling proper-
ties of non-perturbative QCD; at higher energies, predictions are less sensitive to
the accurate modelling of non-perturbative effects, since the effects themselves are
smaller.

3.4.7   A note on the horizontal positioning of data points

All of our event shape histograms include some wide bins, which span a substantial
range of the observable. The predicted value of the distribution dR/dy may vary
significantly across the width of such bins, and its gradient may not be constant.
When fitting perturbative QCD predictions to the data, we integrate the predicted
distribution across the width of the bin, thereby avoiding the need to choose a
specific value for the observable y. However, when presenting the distributions
graphically, we must take care in the horizontal positioning of data points, to ensure
a valid comparison with the predicted functions.

Instead of plotting points at the centre of each bin, it is common practice to
plot them at the barycentre; this is the "centre of mass," or mean value of the
observable y within the bin. However, it has been shown [123] that there is a better
solution. We can write our measured distribution in a given bin $y_i < y < y_{i+1}$ as

$$R'_i = \frac{N_i^{\text{corr.}} / \sum_j N_j^{\text{corr.}}}{y_{i+1} - y_i} \quad , \tag{3.19}$$

where $N_i^{\text{corr.}}$ is the number of events observed in the bin, after the background
subtraction and detector correction. The summation over bins j in the normalisation
must include the 'underflow' and 'overflow' bins at the extremities of the histogram.
The expected value of R'_i is

$$\langle R'_i \rangle = \frac{\int_{y_i}^{y_{i+1}} R'(y)\, dy}{y_{i+1} - y_i} \equiv \frac{R(y_{i+1}) - R(y_i)}{y_{i+1} - y_i} \quad , \tag{3.20}$$

where $R'(y)$ is the true distribution. We wish to make a graphical comparison
between the measurements R'_i and the distributions $R'(y)$ predicted by Monte Carlo
models and by perturbative QCD. If our measurements are in agreement with the
predictions, we would like their expected values to lie on the curve $R'(y)$. Adopting
the notation of Ref. [123] for bins of "large width," we therefore choose to plot our
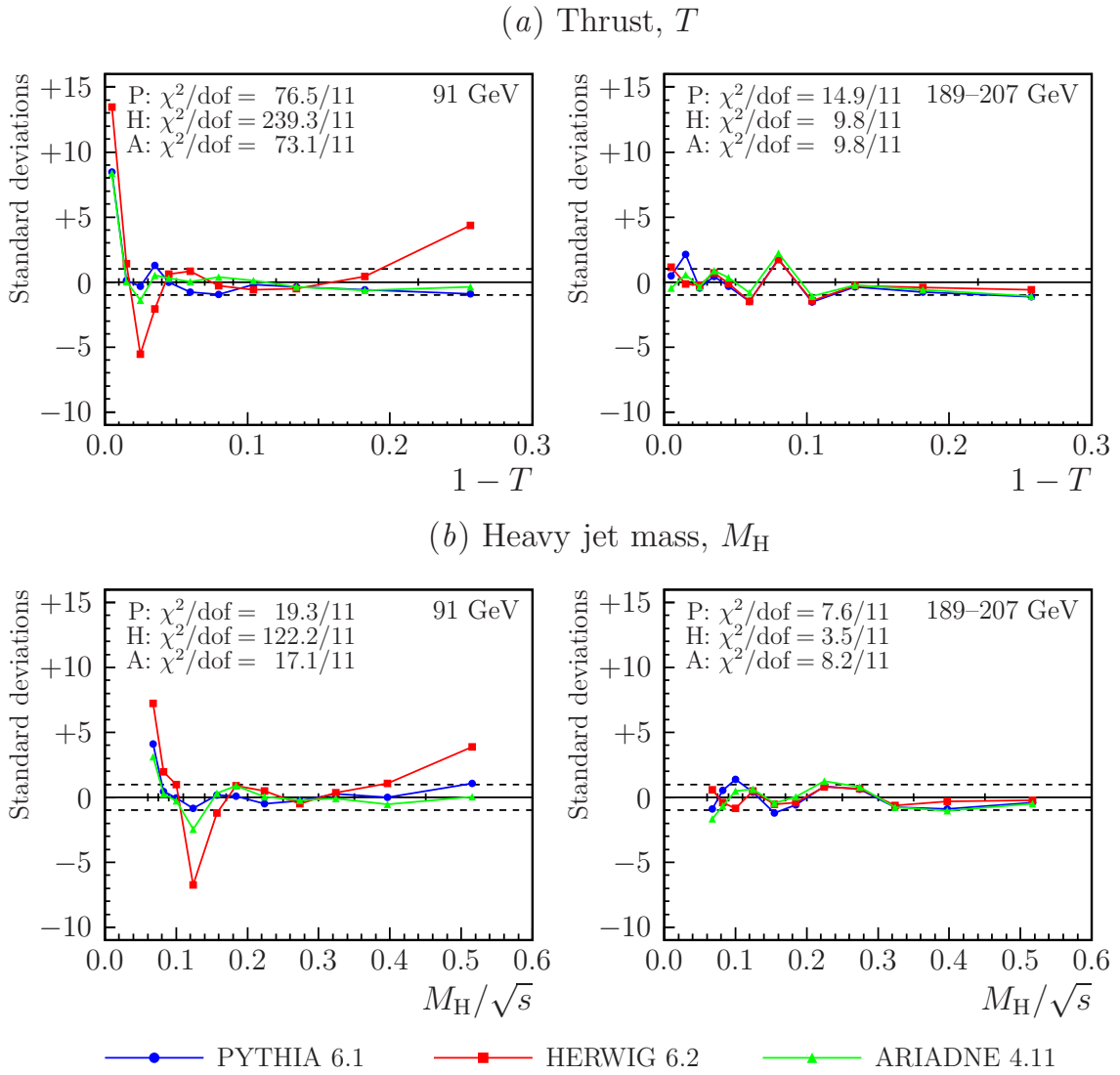
Figure 3.19: Deviations between Monte Carlo predictions and OPAL data, for the thrust and heavy jet mass distributions. In each bin, we show the Monte Carlo prediction minus the OPAL measurement, expressed in units of the total uncertainty in the data; the pairs of dashed horizontal lines represent a difference of one standard deviation. Bin edges are indicated by small tick-marks on the central axis. The χ^2 values for PYTHIA (P), HERWIG (H) and ARIADNE (A) are based on the total uncertainty of the data, assuming no correlation between bins. Points for each generator are connected by coloured lines for clarity, though no interpolation is implied.

(*a*) *C*-parameter
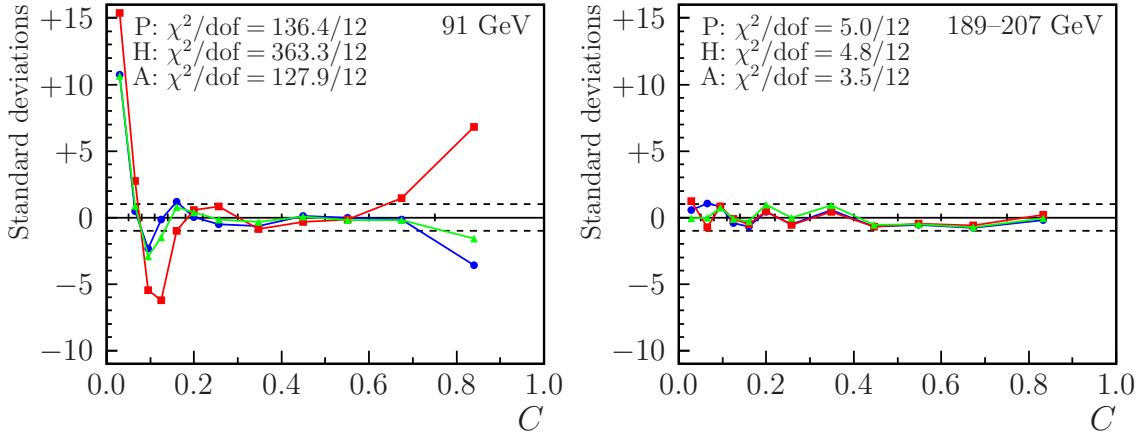
(*b*) Total jet broadening, B_T

(*c*) Wide jet broadening, B_W

PYTHIA 6.1   HERWIG 6.2   ARIADNE 4.11
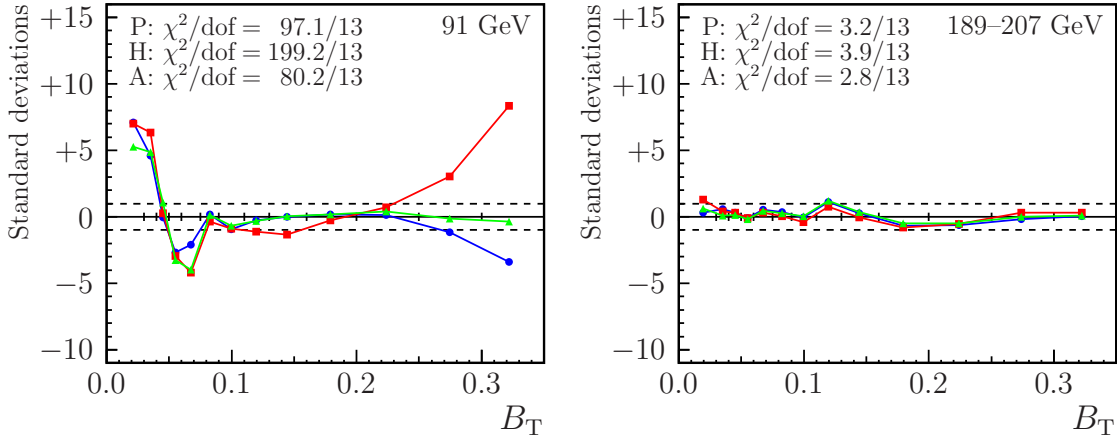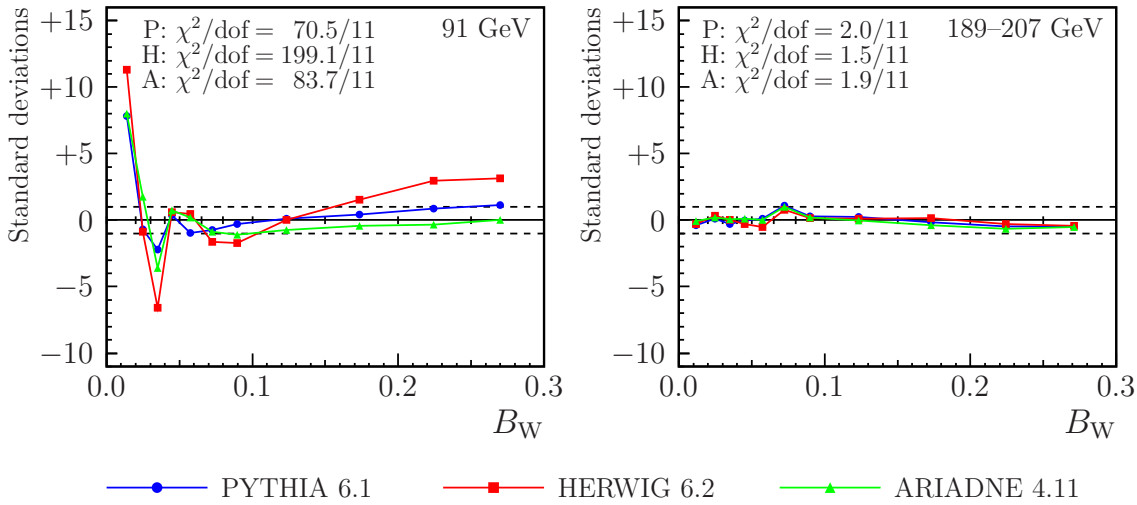
Figure 3.20: Deviations of Monte Carlo predictions from OPAL data, for the *C*-parameter, total jet broadening and wide jet broadening. See Figure 3.19 for full details.

(*a*) Durham y_{23} parameter
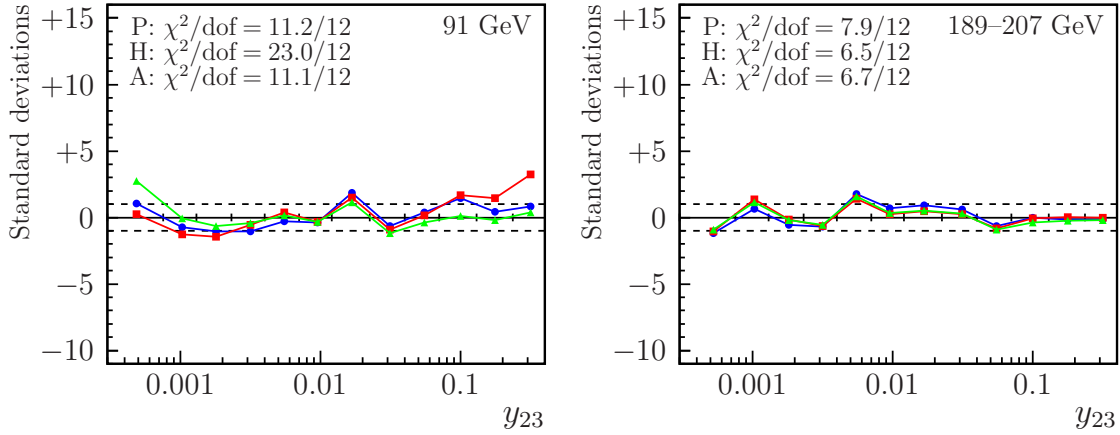
(*b*) Thrust major, $T_{\mathrm{maj.}}$
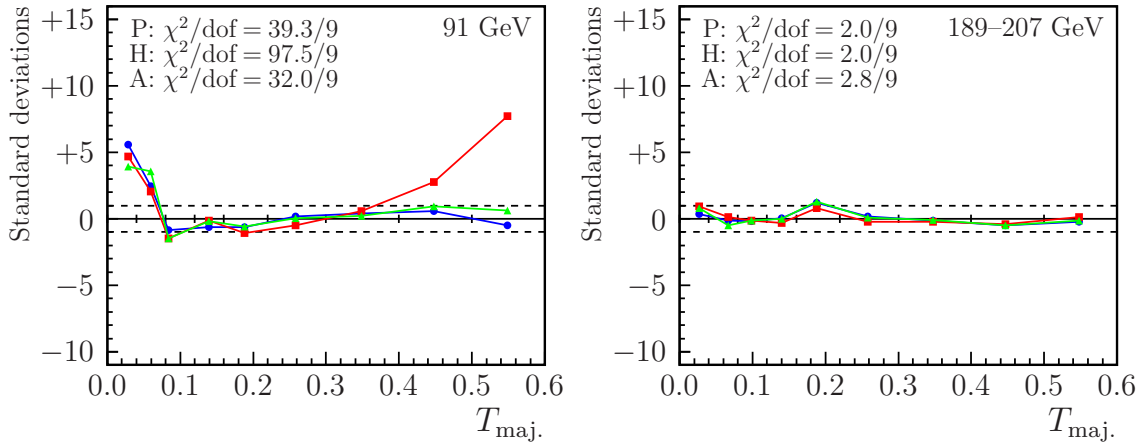
(*c*) Thrust minor, $T_{\mathrm{min.}}$
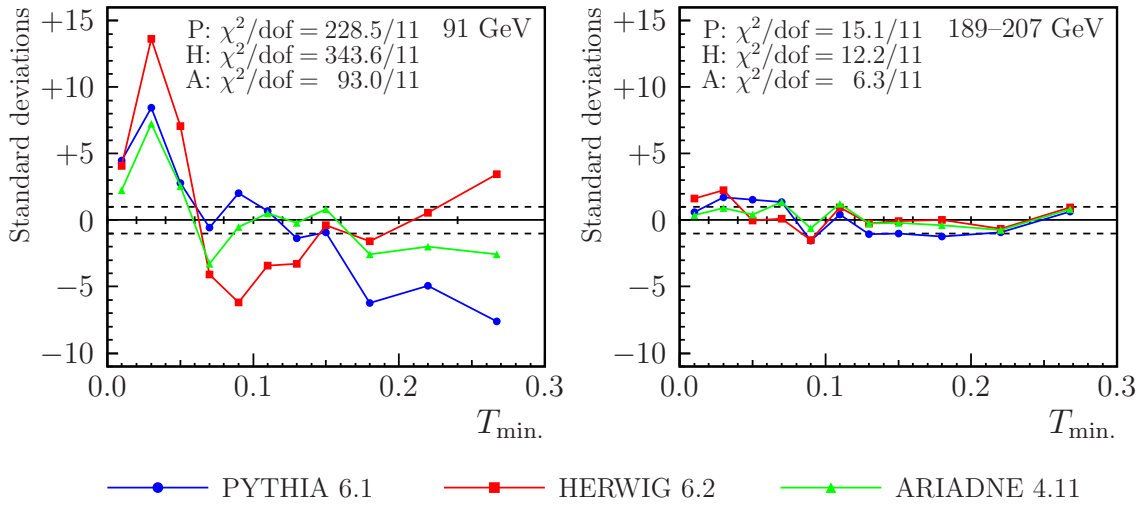
Figure 3.21: Deviations of Monte Carlo predictions from OPAL data, for the Durham y_{23} parameter, thrust major and thrust minor. See Figure 3.19 for full details.

(a) Aplanarity, A
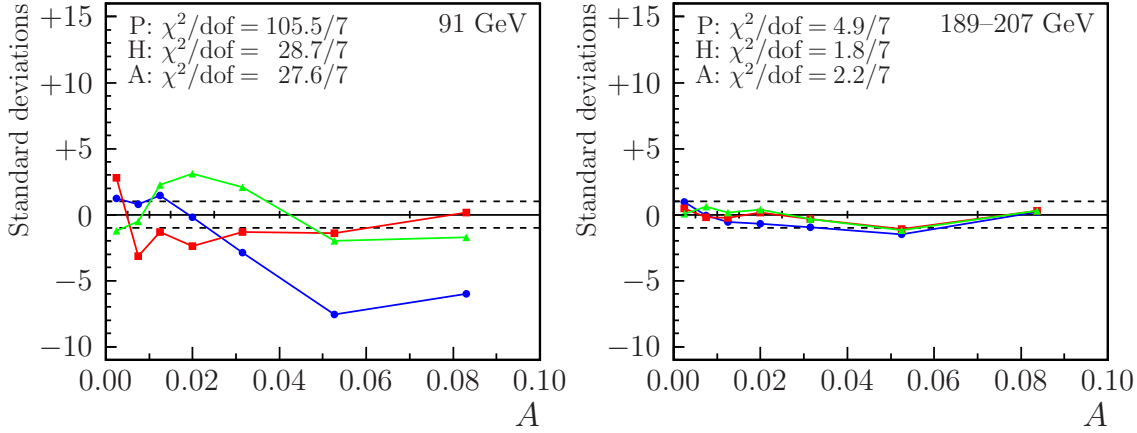
(b) Sphericity, S
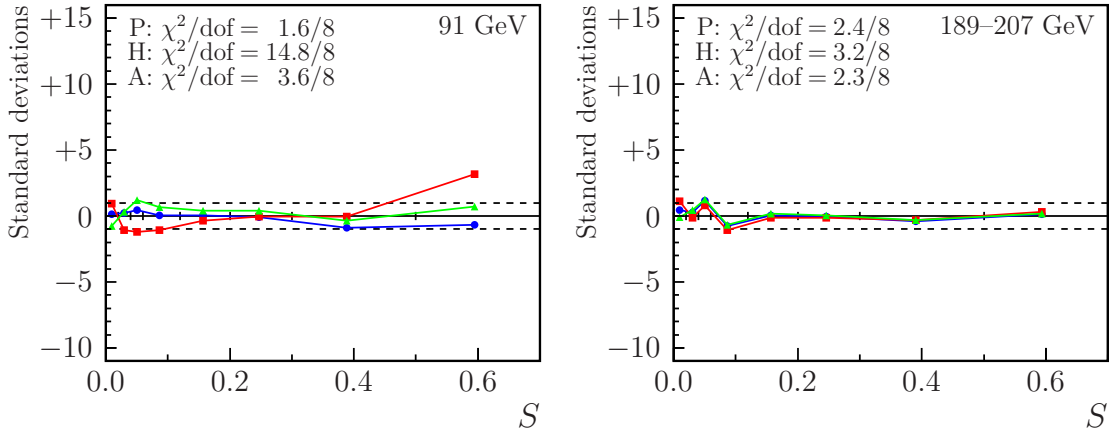
(c) Oblateness, O
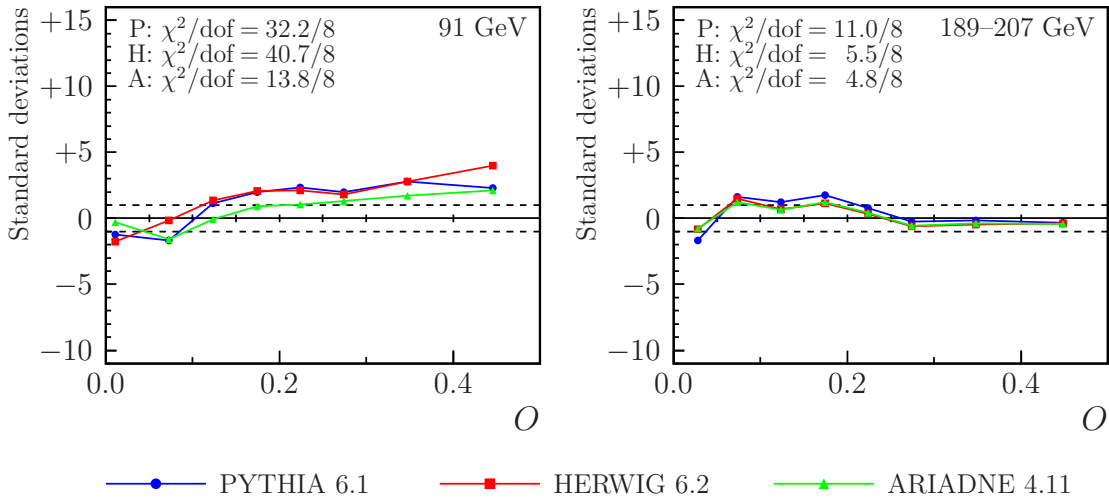
Figure 3.22: Deviations of Monte Carlo predictions from OPAL data, for the aplanarity, sphericity and oblateness. See Figure 3.19 for full details.

(a) Light jet mass, M_{L}
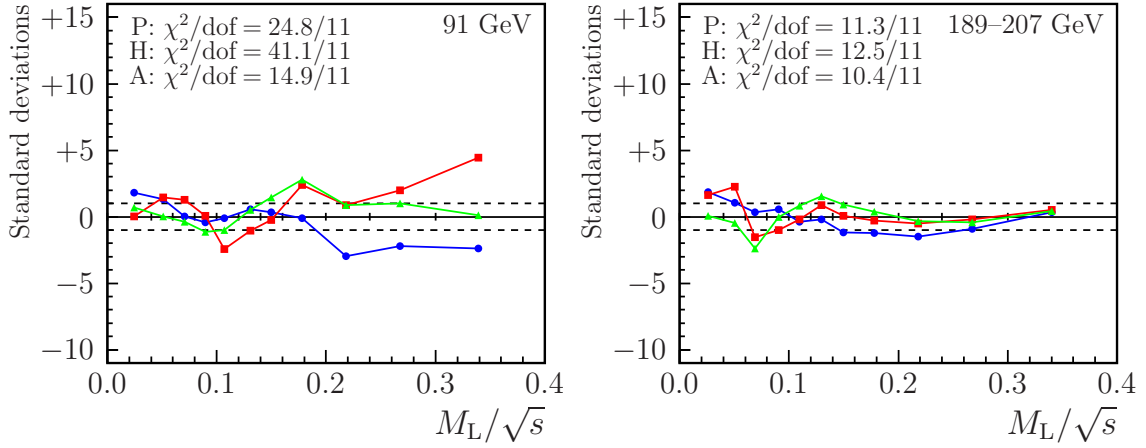
(b) Narrow jet broadening, B_{N}
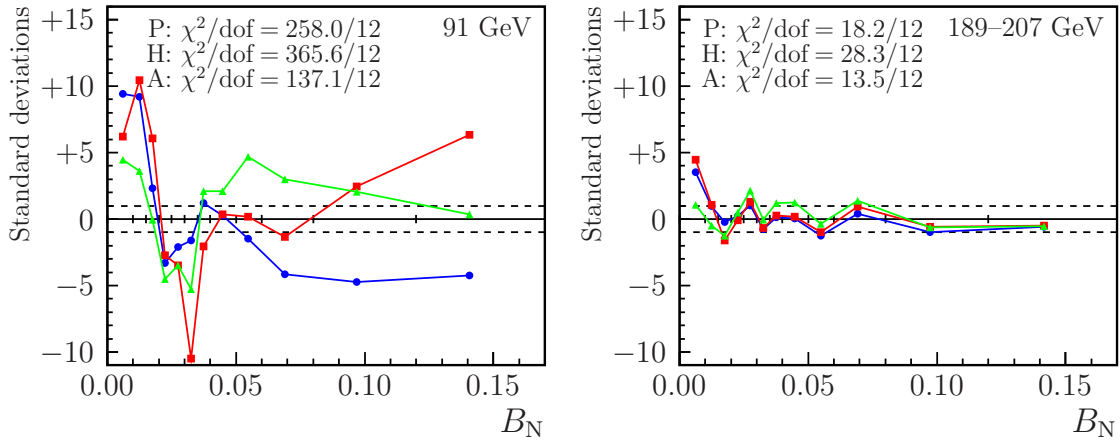
(c) D-parameter
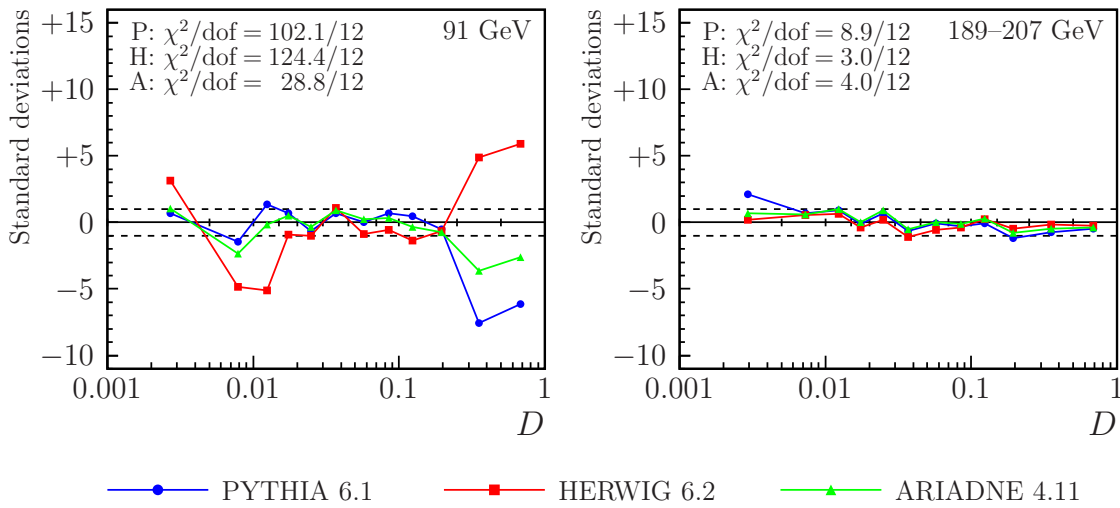
Figure 3.23: Deviations of Monte Carlo predictions from OPAL data, for the light jet mass, narrow jet broadening and D-parameter. See Figure 3.19 for full details.

$1 - T$	Bin centre	y_i^{lw}
$0.0000 - 0.0100$	0.0050	–
$0.0100 - 0.0200$	0.0150	–
$0.0200 - 0.0300$	0.0250	–
$0.0300 - 0.0400$	0.0350	–
$0.0400 - 0.0500$	0.0450	–
$0.0500 - 0.0700$	0.0600	–
$0.0700 - 0.0900$	0.0800	–
$0.0900 - 0.1200$	0.1050	0.1039
$0.1200 - 0.1500$	0.1350	0.1343
$0.1500 - 0.2200$	0.1850	0.1823
$0.2200 - 0.3000$	0.2600	0.2565

D	Bin centre	y_i^{lw}
$0.0010 - 0.0050$	0.0030	0.0030
$0.0050 - 0.0100$	0.0075	0.0073
$0.0100 - 0.0150$	0.0125	0.0124
$0.0150 - 0.0200$	0.0175	–
$0.0200 - 0.0300$	0.0250	–
$0.0300 - 0.0450$	0.0375	0.0370
$0.0450 - 0.0700$	0.0575	–
$0.0700 - 0.1000$	0.0850	–
$0.1000 - 0.1500$	0.1250	0.1230
$0.1500 - 0.2500$	0.2000	0.1943
$0.2500 - 0.5000$	0.3750	0.3523
$0.5000 - 1.0000$	0.7500	0.6859

Table 3.10: Horizontal positions y_i^{lw} for data points, calculated from Equation (3.21) for the thrust and D-parameter distributions at $\sqrt{s} = 189$ GeV. Where less than five bins of the Monte Carlo distribution are contained within a single bin of the measured distribution (indicated by '–'), our data points are plotted at the centre.

data points at the horizontal position y_i^{lw}, such that

$$\frac{\int_{y_i}^{y_{i+1}} R'(y) \, \mathrm{d}y}{y_{i+1} - y_i} = R'(y_i^{\mathrm{lw}}) \quad . \tag{3.21}$$

We solve Equation (3.21) numerically at each centre-of-mass energy, using our PYTHIA hadron-level Monte Carlo samples. The five million events are placed in histograms comprising 100 bins of equal width.[16] Where a bin of the measured distribution spans at least five bins of the Monte Carlo distribution, we compute the horizontal position of the data point using Equation (3.21); the function $R'(y)$ is estimated by linear interpolation between the centres of the Monte Carlo bins. For narrower bins, we plot our data points at the centre.

In Table 3.10, we show the horizontal positions of data points for the thrust and D-parameter distributions. We find that there is usually very little difference between the centres of the bins and the calculated positions y_i^{lw}.

---

[16]In the case of y_{23} and the D-parameter, the bins were evenly distributed in $\log y_{23}$ and $\log D$ respectively.

3.5 Measurements of α_S

We discussed in Section 1.6 the prediction of event shape distributions by perturbative QCD. The distribution of each observable is dependent on the dimensionless coupling strength α_S, which in turn is predicted to depend on the energy scale Q of the hard interaction. By fitting perturbative predictions to each of our measured distributions, we can determine α_S and test its energy dependence.

Throughout this section, we use the $\mathcal{O}(\alpha_S^2)$+NLLA prediction for the cumulative distributions $R(y)$, with the Log(R) matching scheme; a kinematic constraint is applied as discussed in Section 1.6.4. The renormalisation scale μ is assumed equal to the centre-of-mass energy $\sqrt{s}$, and the parameters x_L and p defined in Section 1.8.1 are set to unity. Variation of these assumptions will form the basis for our estimate of the theoretical uncertainty.

3.5.1 Predictions at the hadron level

Perturbative QCD does not describe the complete process by which an electron-positron system annihilates to form hadrons; instead it gives us an intermediate "parton level" prediction, for a state comprised of quarks and gluons. In Section 1.9, we discussed various models for the non-perturbative fragmentation of quarks into bound colourless objects. Some of these hadrons may then decay to produce more stable particles, which are finally observed by our detector. Before theory and data can be compared, one of these models must be used to simulate the effects of hadronisation and decays on the event shape distributions. By default we will use PYTHIA 6.1 with the OPAL parameter set, as we have done for the detector correction. Since no simulation of the OPAL detector is required in this case, it is possible to generate larger samples: we use five million events at each centre-of-mass energy. Also, since we do not include initial-state radiation at the hadron and parton levels, there is no need to simulate interference between initial- and final-state photons emissions; we therefore generate the q$\bar{\text{q}}$ pairs using PYTHIA in place of $\mathcal{KK}$2f.

Conventionally, the OPAL Collaboration performs the hadronisation correction by applying a multiplicative factor to the integrated parton-level theory predic-

tion $R_{\text{part.}}(y)$:

$$R_{\text{hadr.}}(y) \;=\; \frac{R_{\text{hadr.}}^{\text{MC}}(y)}{R_{\text{part.}}^{\text{MC}}(y)} \, R_{\text{part.}}(y) \quad , \tag{3.22}$$

where $R_{\text{part.}}^{\text{MC}}(y)$ and $R_{\text{hadr.}}^{\text{MC}}(y)$ are results of the same Monte Carlo simulation at the parton and hadron levels. Many other authors apply a correction factor to the differential distribution $R'(y)$, or use a full matrix-based unfolding method:

$$R'_{\text{hadr.}}(y) \;=\; \frac{R'^{\,\text{MC}}_{\text{hadr.}}(y)}{R'^{\,\text{MC}}_{\text{part.}}(y)} \, R'_{\text{part.}}(y) \tag{3.23}$$

$$\text{or} \quad R'_{\text{hadr.}}(y_i) \;=\; \sum_j A_{ij} R'_{\text{part.}}(y_j) \quad . \tag{3.24}$$

It can be shown that Equations (3.22) and (3.23) are almost equivalent, provided the simulation gives a good description of the data, and the correction factor does not vary rapidly across the distribution. Studies by the LEP QCD Working Group have shown that hadronisation corrections do differ between the experiments, but that this difference is largely due to the tuning of Monte Carlo models rather than the method by which the correction is applied: details of this comparison will be given in Section 4.1.3. It is open to question which method is most accurate and reliable; however, for consistency with other OPAL work, we will continue to use the correction defined in Equation (3.22).

3.5.2   Fitting the distributions

Our fits to the data are based on the method of least squares, with the coupling α_S being the only free parameter of the theory. We use a χ^2 variable which includes only the statistical uncertainties of the data; experimental systematic uncertainties in the fitted value of α_S will be evaluated separately, by fitting several variants of the measured distributions.[17]

As we have seen from Figures 3.11–3.15, certain bins of the event shape dis-

---

[17]Inclusion of systematic uncertainties in the χ^2 variable would in principle give a more reliable estimate of α_S, because the bins with smallest total uncertainties would be given the greatest weight. However, the construction of such a χ^2 would require detailed understanding of the covariance matrix relating uncertainties in different bins. As we shall see in Chapter 4, an inappropriate choice of correlation coefficients can result in a fit which bears little connection to the data; to avoid such dangers, we will accept a possible small bias by neglecting systematic uncertainties in our central fit.

tributions have a low efficiency or purity, or a high probability of bin migration. These are usually the bins at largest y, corresponding to multiple gluon emissions. Furthermore, the bins at low y tend to offer a poor sensitivity to α_S, because the form of the peak in this region is determined primarily by non-perturbative physics. We therefore restrict our fit to an intermediate range of bins, for which both our experimental measurements and the theoretical predictions are sufficiently precise. The choice of fit range is a trade-off between statistical and systematic uncertainties, and the four LEP Collaborations have made different decisions. The OPAL philosophy has been to adopt the same fit ranges at all energy scales, regardless of variation in the selection purity; this ensures a high correlation between the theoretical systematic uncertainties at different energies.[18] We therefore use the ranges chosen for previous LEP2 analyses in Refs. [9–11, 124], which are as follows:

$$
\begin{aligned}
0.05 &< 1-T &&< 0.30 \\
0.17 &< M_{\mathrm{H}}/\sqrt{s} &&< 0.45 \\
0.18 &< C &&< 0.60 \\
0.075 &< B_{\mathrm{T}} &&< 0.250 \\
0.05 &< B_{\mathrm{W}} &&< 0.20 \\
0.0023 &< y_{23} &&< 0.1300
\end{aligned} \qquad .
$$

The fit includes statistical correlations between bins of the normalised distribution, by using the full covariance matrix V derived in Appendix A.1. The best fit is given by the value of α_S which minimises the following χ^2 expression:

$$
\chi^2 = \sum_{i,j \,\in\, \mathrm{fit}} \left[\widetilde{N}_i - \widetilde{N}_i^{\mathrm{theo}}(\alpha_S) \right] \left(\widehat{V}^{-1} \right)_{ij} \left[\widetilde{N}_j - \widetilde{N}_j^{\mathrm{theo}}(\alpha_S) \right] \quad , \qquad (3.25)
$$

where $\widetilde{N}_i$ and $\widetilde{N}_i^{\mathrm{theo}}(\alpha_S)$ are the measured and predicted numbers of signal events in bin i, and $\widehat{V}^{-1}$ is the inverse of the sub-covariance matrix within the fit range, defined by

$$
\sum_{j \,\in\, \mathrm{fit}} V_{ij} \left(\widehat{V}^{-1} \right)_{jk} = \delta_{ik} \qquad (i, k \in \mathrm{fit}) \quad . \qquad (3.26)
$$

---

[18]Slightly different ranges were used in the original analysis of 91 GeV data [8], because four-fermion background events were not considered. In our new 91 GeV measurement, we will use the standard LEP2 fit ranges.

	Diagonal covariance matrix			Full covariance matrix		
	Fitted α_S	$\sigma_{\text{stat.}}$ from $\chi^2 = \chi^2_{\text{min}}+1$	$\sigma_{\text{stat.}}$ from subsamples	$\sigma_{\text{stat.}}$ from Ref. [11]	Fitted α_S	$\sigma_{\text{stat.}}$ from $\chi^2 = \chi^2_{\text{min}}+1$	$\sigma_{\text{stat.}}$ from subsamples
T	0.11396	± 0.00261	± 0.00222	± 0.0016	0.11469	± 0.00212	± 0.00224
M_{H}	0.10678	± 0.00251	± 0.00194	± 0.0017	0.10690	± 0.00191	± 0.00198
C	0.10840	± 0.00241	± 0.00195	± 0.0018	0.10844	± 0.00207	± 0.00195
B_{T}	0.11271	± 0.00238	± 0.00195	± 0.0014	0.11284	± 0.00198	± 0.00197
B_{W}	0.10311	± 0.00213	± 0.00170	± 0.0013	0.10301	± 0.00162	± 0.00171
y_{23}	0.10672	± 0.00228	± 0.00171	± 0.0017	0.10671	± 0.00159	± 0.00169

Table 3.11: A comparison of the fitted α_S values and statistical uncertainties $\sigma_{\text{stat.}}$ obtained by different methods at $\sqrt{s} = 189$ GeV. The covariance matrix is calculated using Equation (A.7) in Appendix A.1; in the 'diagonal' case, we substitute $V_{ij} = 0$ for all elements $i \neq j$. We use two different methods to calculate $\sigma_{\text{stat.}}$: in the first case we measure the width of the minimum in the χ^2 fit, and in the second we find the standard deviation of 100 fits to simulated data samples.

3.5.3   Statistical uncertainties

We consider here two possible methods for the estimation of statistical uncertainties in our α_S measurements.

3.5.3.1   Width of the χ^2 minimum

In a least-squares fit, the uncertainty of the fitted parameter α_S can be estimated from the width of the minimum in χ^2:

$$\chi^2(\alpha_S \pm \sigma_{\text{stat.}}) \;=\; \chi^2_{\text{min.}} + 1 \;\; , \qquad \text{where} \quad \chi^2_{\text{min.}} = \chi^2(\alpha_S) \;\; . \qquad (3.27)$$

This formula makes a justified assumption that the predicted contents of each bin varies linearly with α_S, over the range of the corresponding statistical uncertainty.

To obtain a reliable estimate using this method, χ^2 must be calculated using the full covariance matrix given in Equation A.7. If only the diagonal elements were used, we would fail to take into account the anti-correlation between bins, which is introduced by the normalisation; this would result in an overestimate of the statistical uncertainty, as shown in Table 3.11.

3.5.3.2   Monte Carlo subsample method

In previous OPAL measurements, an exact statistical covariance matrix has not been calculated for the measured event shape histograms. Instead, fits have been

performed using a diagonal covariance matrix, and a Monte Carlo technique has been used to estimate the statistical uncertainties.

In this method, we create 100 samples of simulated data at each centre-of-mass energy. We first calculate the quantity of each event type expected to occur at each energy; a Poisson random number generator is then used to determine the numbers of signal and background events in each sample. The simulated events are drawn randomly from the appropriate OPAL Monte Carlo sample. Selection is performed "with replacement," so the same event may appear more than once in any given sample.

The Monte Carlo subsamples are then processed in exactly the same way as the real data; our standard selection criteria are applied to the simulated events, based on the reconstructed output of the OPAL detector simulation. Finally, we obtain a set of α_S measurements from each sample. The standard deviation of the 100 simulated measurements for each event shape observable gives an estimate of the statistical uncertainty $\sigma_{\text{stat.}}$. Assuming a Gaussian distribution of α_S values, the fractional uncertainty in our determination of $\sigma_{\text{stat.}}$ from N subsamples is $(2N+2)^{-1/2} \approx 7\%$.

Given $\mathcal{N}$ Monte Carlo events from which to construct subsamples of size n, one might naïvely expect that the maximum number of useful subsamples would be $N = \mathcal{N}/n$. If one were using the subsamples to estimate the *mean* of the statistical distribution of α_S values, this statement would be true; in that case, we would not allow re-sampling of simulated events. However, it has been shown [125] that the uncertainty in the *standard deviation* estimated from N subsamples is proportional to

$$\sqrt{\frac{1}{N} + \rho^2} \quad ,$$

where ρ is the correlation coefficient between measurements from different samples. Assuming that this correlation is roughly equal to the fractional overlap in the event samples, $\rho = n/\mathcal{N}$, our precision in $\sigma_{\text{stat.}}$ will therefore saturate when

$$N \sim \frac{1}{\rho^2} = \left(\frac{\mathcal{N}}{n}\right)^2 \quad . \tag{3.28}$$

Therefore, provided we have at least ten times more simulated events than data events, we are justified in using 100 subsamples. This condition is satisfied at

all centre-of-mass energies except 91 GeV, for which the integrated luminosity of the Monte Carlo sample is roughly twice that of the data. At $\sqrt{s} = 91$ GeV we therefore generate each of the 100 subsamples with one tenth of the data luminosity, and multiply the resulting statistical uncertainties by $1/\sqrt{10}$.

3.5.3.3   Comparing the χ^2 and subsample methods

We conclude from Table 3.11 that the two methods for estimating $\sigma_{\text{stat.}}$ give compatible results when the full covariance matrix is used. If we include only the diagonal elements of V_{ij}, so that

$$\chi^2 = \sum_{i \in \text{fit}} \left[\frac{\widetilde{N}_i - \widetilde{N}_i^{\text{theo}}(\alpha_S)}{\sigma_i^{\text{stat.}}} \right]^2 \;\;, \tag{3.29}$$

then the width of the χ^2 minimum gives an overestimate of the statistical uncertainty in α_S, as expected; this is because we are ignoring the effect of the normalisation, which tends to "average out" statistical fluctuations across the fit range. The Monte Carlo subsample method, however, yields similar results regardless of whether correlations are included in the covariance matrix. It was claimed in Ref. [11] that the statistical uncertainties in the OPAL α_S measurements at $\sqrt{s} = 172$–189 GeV had been estimated using the Monte Carlo subsample method with a diagonal covariance matrix. Our own results in Table 3.11 suggest that the published uncertainties were usually underestimated; we believe that this problem was caused by ignoring fluctuations in the number of background events in the subsamples.

Since the full statistical covariance matrix is now known, we will use it in the calculation of χ^2 for our α_S fits. A choice still remains, however, as to whether one should use the subsample method or the width of the χ^2 minimum to estimate the uncertainties. The subsamples have the advantage that they are based entirely on Monte Carlo simulations, so the uncertainty will not vary between one data sample and another.[19] However, when we calculate $\sigma_{\text{stat.}}$ using the width of the

---

[19]A Bayesian statistician might argue that it is *right* for an uncertainty to depend on the observed data; a lucky observation will provide more information than an unlucky one. However, it is conventional in High Energy Physics to use a purely frequentist interpretation of probability, in which an uncertainty is defined by the standard deviation of the predicted distribution of measurements. In an OPAL measurement of the W boson mass [126], a similar study based on Monte Carlo subsamples concluded that the statistical uncertainty returned by a χ^2 fit to data can sometimes be misleading; among the simulated data samples returning the lowest uncertainties, the spread of fitted W mass values was not in fact smaller than average.

χ^2 minimum for each of the 100 subsamples, we find that the relative variations in our estimates are of order ± 1–2%, whereas the uncertainty in our determination of $\sigma_\mathrm{stat.}$ from the standard deviation of the 100 α_S fits is around 7%. We will therefore take our statistical uncertainties from the width of the χ^2 minimum observed in the data. The subsamples will be used later, in Section 3.6.1, when we combine α_S measurements obtained from the six observables.

3.5.4 Systematic uncertainties

The systematic uncertainties in our measurements of α_S are attributed to three independent sources:

- An **experimental systematic uncertainty**, corresponding to the systematic uncertainty of the measured distribution

- A **hadronisation uncertainty**, due to imperfect simulation of non-perturbative effects by the Monte Carlo model (PYTHIA, in this case)

- A **theoretical uncertainty**, relating to missing higher-order contributions to the event shape predictions in perturbative QCD

3.5.4.1 Experimental systematic uncertainties

In Section 3.4.4 we described several variants of our standard analysis procedure, which were used to assess the systematic uncertainties of our event shape measurements. We would now like to propagate these uncertainties through to our α_S fits. An analytical "propagation of errors" would be difficult in these circumstances, as it would require detailed knowledge of the correlation between bins of the distributions. We instead compute a set of alternative distributions using each of the variant analyses described in Section 3.4.4, and repeat the fit to determine α_S in each case; the difference between the α_S values obtained from the variant and standard distributions gives a contribution to the systematic uncertainty. We then combine these uncertainties in exactly the same way as for the distributions themselves, taking for example the larger of the two deviations in α_S when the subtracted background is varied by ± 5%.

3.5.4.2   Hadronisation uncertainties

To estimate the uncertainties due to modelling of non-perturbative physics, we repeat our α_S fits using two alternative hadronisation corrections calculated using HERWIG 6.2 and ARIADNE 4.11 in place of PYTHIA 6.1; in each case, we use the parameter sets tuned to OPAL data. We generate independent samples of five million events using each Monte Carlo model at each centre-of-mass energy. In accordance with the current convention within the OPAL Collaboration, we define the uncertainty in α_S to be the larger of the two absolute deviations with respect to the PYTHIA result.

In previous OPAL analyses [8–11], some additional contributions to the hadronisation uncertainty have been estimated by variation of the PYTHIA parameter set. However, it was proposed recently by the LEP QCD Working Group that such uncertainties in the parameters are already included, to a large extent, by considering differences between independently tuned models. Although this point may be debatable, we have adopted the LEP convention by removing these uncertainties, which were anyhow much smaller in most cases than the differences between models.

3.5.4.3   Theoretical uncertainties

Each of the six event shape distributions has been predicted in perturbative QCD using $\mathcal{O}\left(\alpha_\mathrm{S}^2\right) + \mathrm{NLLA}$ calculations. As we have discussed in Section 1.8, a variety of possible methods exist to estimate the uncertainty due to missing higher orders in the calculation. In previous OPAL measurements, the renormalisation scale μ has been varied over the range from $\frac{1}{2}\sqrt{s}$ to $2\sqrt{s}$; we now use the "uncertainty band" method, developed in collaboration with the LEP QCD Working Group [12], which aims to incorporate a wider range of possible higher-order contributions.

3.5.5   Results of the α_S fits

In Figure 3.24, we present our measurements of α_S using each of the six observables at each centre-of-mass energy; previous OPAL measurements are indicated by open circles, where they exist. Our results are also tabulated with a full breakdown of uncertainties in Appendix C.

Given that a high degree of correlation is expected between the systematic uncertainties at different energy scales, our fits provide strong evidence for the evolution
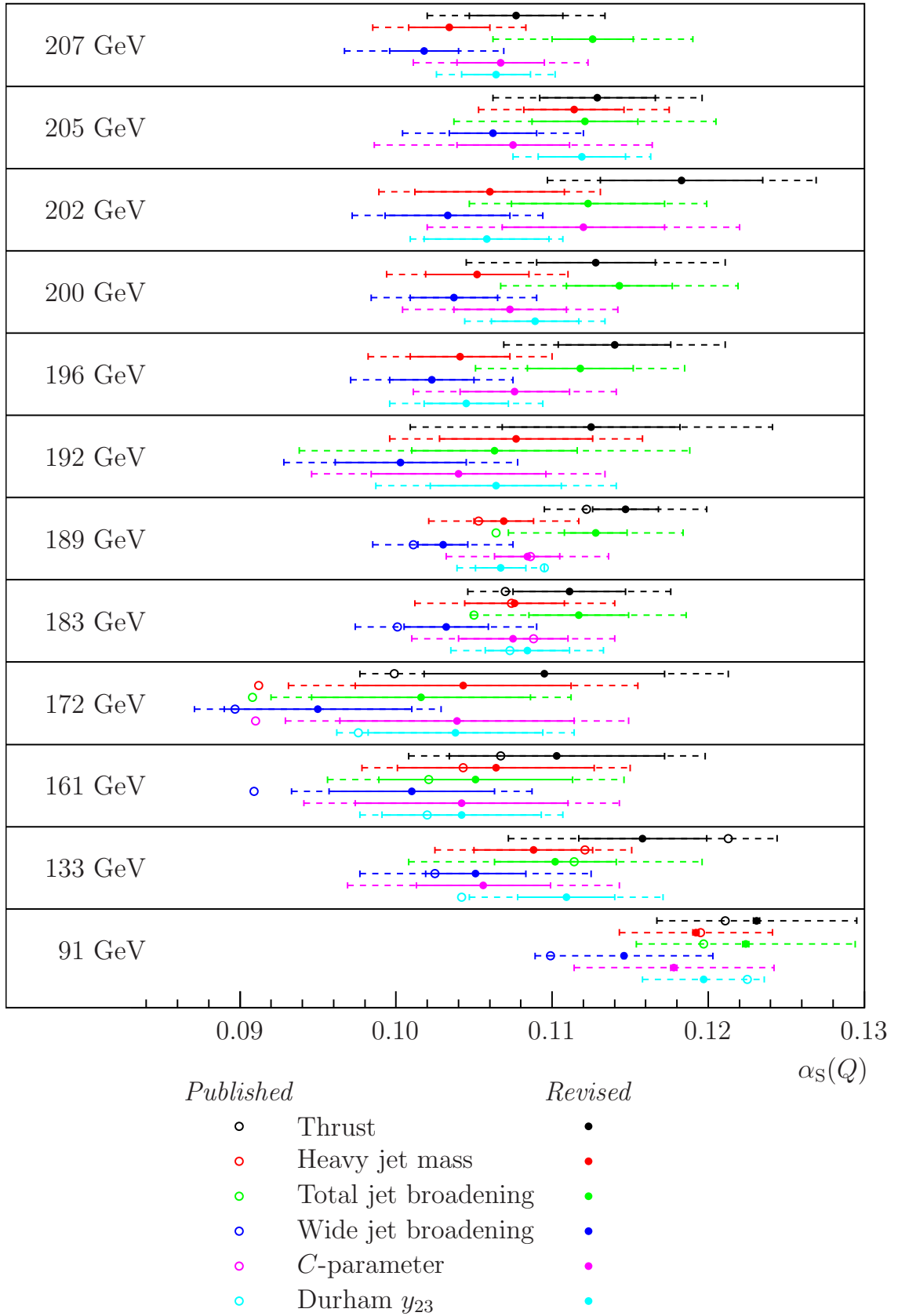
Figure 3.24: Measurements of $\alpha_{\rm S}$ using fits to six event shape observables. The inner (solid) error bars represent statistical uncertainties. The open circles indicate previously published OPAL measurements, which are superseded by our new results.

of α_S between $\sqrt{s} = 91$ GeV and the highest LEP2 energies.[20] We find that the α_S values obtained from the thrust and total jet broadening distributions tend to be higher than the average at each energy, while those from the wide jet broadening are consistently lower: this effect is due to the missing higher orders in the perturbative predictions, which differ between observables, and are highly correlated between energy scales.

We also see that the statistical uncertainties are correlated between observables at each energy; at $\sqrt{s} = 161$ GeV, for example, the scatter of the six α_S measurements less than one might expect from the size of the statistical error-bars. This should not be surprising, when one recalls the physical interpretations of the event shape variables: each observable measures the amount of 'branching' in an event, on some positive scale where zero is defined to represent a perfectly linear two-jet event. The event shape distributions are all sensitive to the number and character of the three- and four-jet signal events present in a given sample. If we have a significant upward fluctuation in the number of such events (or in the number of background events passing our selection), we expect an upward fluctuation in each of the event shape distributions within our fit ranges, and hence an increase in the fitted values of α_S from all six observables. Correlations between the event shapes will be discussed further in Chapter 4.

Our new α_S fits differ in some cases by up to about ± 0.01 with respect to those previously published by the OPAL Collaboration, though in most cases the differences are less than 0.004. In the introduction to this chapter, we listed the main improvements that have been applied to the analysis since these original results were published; the observed differences are due to a combination of these. For comparison, the intermediate results presented at $\sqrt{s} \leq 189$ GeV in Refs. [124, 127] were obtained by fitting the new theory predictions to previously published experimental distributions.[21]

The large differences seen at $\sqrt{s} = 172$ GeV are mainly due to a statistical effect. In the past, the statistical uncertainties of the distributions were computed from the data, and not from the Monte Carlo predictions; a downward fluctuation

---

[20]To quantify this evidence in the form of a χ^2 statistic would be difficult, due to complicated nature of the covariance matrix; this issue will be discussed in greater detail in Chapter 4.

[21]These are the measurements to be used for the LEP α_S combination presented in Chapter 4, and are tabulated in Appendix D.

in the distribution could therefore lead to an underestimation of the statistical uncertainty. This effect is especially significant when the expected number of events is small. The bin $0.85 < T < 0.87$ at 172 GeV, for example, is predicted by Monte Carlo to contain 10.9 events, but only 4 events are observed in the data. When the statistical uncertainty is measured from the Monte Carlo, this represents a difference of 2.1 standard deviations, but using the data it is 3.5 standard deviations. The α_S fits were consequently "dragged down" in the previous analysis, by excessive χ^2 contributions from bins with downward fluctuations.[22]

At some energies we have cross-checked our distributions with other members of the OPAL Collaboration [128], and we have also verified our theory predictions and fitting algorithms with other members the LEP QCD Working Group, as we will discuss in Section 4.1. We therefore have good faith in our new α_S measurements.

The figures in Appendix C present a comparison between the measured and fitted event shape distributions at each centre-of-mass energy. Each data point represents the ratio of the measured hadron-level bin contents to the integral of the fitted prediction over the width of the bin. The statistical and experimental uncertainties are indicated by the error bars of the data points, while the hadronisation and theory uncertainties are shown by the horizontal yellow bands. The fit ranges are represented by arrows. At $\sqrt{s} = 91$ GeV, there is clear evidence of deviations between theory and data outside the fit ranges, except perhaps in the case of thrust and the Durham y_{23} parameter; in some cases there is also some evidence of a slope within the fit range, which is likely to be caused by the missing higher orders of the perturbative prediction. Our sensitivity to these higher orders suggests that we have potential not only to improve our measurements of α_S, but also to test the validity of the $\mathcal{O}(\alpha_S^3)$ predictions when they become available. At the higher centre-of-mass energies, where our statistical uncertainties are much larger, no conclusive deviations are seen between data and theory, except in the extreme two-jet regions of some distributions.

---

[22]One can imagine an extreme case in which *no* events are observed in certain bin. In this case the fit would fail altogether, due to an infinite χ^2, if the uncertainty is estimated from the data.

3.6   Combined α_S measurements

By combining some of the α_S fits shown in Figure 3.24, it should be possible to obtain a smaller number of results, each with smaller uncertainties. In Section 3.6.1 we will combine results from the six observables at each energy point, and in Section 3.6.2 we will attempt to combine all of our OPAL results to give a single measurement of $\alpha_\mathrm{S}(M_\mathrm{Z})$. In Chapter 4, we proceed to combine our OPAL measurements with those from the other LEP experiments.

3.6.1   Combining the six observables

We would like to calculate a single measurement of α_S at each energy point, using all six of the event shape observables for which perturbative predictions exist. There are two possible ways to proceed:

- Perform a simultaneous fit to the six measured event shape distributions, with α_S as a single free parameter.

- Combine the six existing fits by forming a weighted mean.

Ideally, the simultaneous fit would be the more accurate method: it uses a single χ^2 statistic, depending explicitly on each individual bin within the fit ranges of all six distributions. As we have discussed, however, our fits to the individual observables are based only on statistical uncertainties; we do not have reliable estimates for the bin-to-bin correlations of the systematic uncertainties. When combining results from the six event shapes, we would like to give larger weights to those observables which have smaller systematic uncertainties. This is not possible using a purely statistical covariance matrix. We therefore use the second of the two methods proposed above: we calculate a weighted mean of the six fits to individual observables, of the form

$$\alpha_\mathrm{S}(Q)_\mathrm{comb.} = \sum_{i=1}^{6} w_i \, \alpha_\mathrm{S}(Q)_i \quad . \tag{3.30}$$

The calculation of the weights w_i will be discussed in detail in the next chapter. In summary, they are given by the expression

$$w_i = \frac{\sum_j \left(V^{-1}\right)_{ij}}{\sum_{j,k} \left(V^{-1}\right)_{jk}} \quad , \tag{3.31}$$

where V_{ij} is the 6×6 covariance matrix relating the uncertainties of the six measurements. The diagonal elements of this matrix include all four contributions to the total variance: statistical, experimental, hadronisation and theory. The off-diagonal elements, however, which represent correlations between the uncertainties of different measurements, include only statistical components.[23] Although we know that the systematic uncertainties *are* correlated between measurements, we do not include them in the covariance matrix, for reasons to be discussed in the next chapter. The correlation coefficients ρ between the six statistical uncertainties are estimated using the Monte Carlo subsamples described in Section 3.5.3.2; most are found to be about 0.7. Table 4.3 in the next chapter lists the correlations determined for the 207 GeV measurements.

The calculation of uncertainties in the weighted mean will also be discussed in the next chapter. Even though we ignore the correlation of systematic uncertainties when calculating the weights w_i, we will attempt to re-introduce them when determining the combined uncertainty.

Our combined results at each energy, and the weights given to each observable, are tabulated in Appendix C. Generally the Durham y_{23} parameter has the largest weight, due to the small theoretical uncertainties in its distribution.

3.6.2 Combining OPAL measurements at all energies

Finally, we present a global combination of all our 72 measurements of the strong coupling. Since they have been determined at a range of different energy scales, the first step is to convert each measurement to a value of α_S at the Z^0 mass scale. We then calculate a weighted mean of all the results, to obtain a combined value of $\alpha_S(M_Z)$. Once again, details of the procedure will be left for the next chapter.

Unlike our weighted means at the individual energies, the global combination will use standardised LEP definitions for the uncertainties: the hadronisation uncertainties used in the combined LEP analysis are slightly different from those used in OPAL, for example. We will also calculate our OPAL distributions in standard LEP

---

[23]For the LEP combination discussed in Chapter 4, and for the combination of all OPAL measurements in the next section, we include both statistical and experimental uncertainties in the off-diagonal elements of the covariance matrix. In the present six-variable combination, however, we find that the weights w_i are liable to fluctuate excessively between energies, or become negative, if correlations between experimental uncertainties are included. This problem is reduced in the LEP combination by averaging the experimental uncertainties between different experiments.

OPAL energy bin		LEP energy bin	
Mean $\sqrt{s}$ (GeV)	Integrated luminosity (pb^{-1})	Mean $\sqrt{s}$ (GeV)	Integrated luminosity (pb^{-1})
188.6 191.6	185.2 29.53	189.0	214.7
195.5 199.5 201.6	76.67 79.27 37.75	198.5 (200.0 nominal)	193.7
204.9 206.6	82.01 138.8	206.0	220.8

Table 3.12: Centre-of-mass energy bins used for the OPAL analysis and for the LEP α_S combination

energy bins, instead of the twelve OPAL bins used elsewhere in this chapter. For energies $\sqrt{s} \leq 183$ GeV, the OPAL and LEP bins coincide. At the highest energies, however, seven of the OPAL bins are combined to give three LEP energy ranges; these are shown in Table 3.12. Background subtractions and detector corrections are calculated using a weighted average of the OPAL Monte Carlo samples within each LEP energy bin. The α_S measurements obtained at $\langle \sqrt{s} \rangle = 198.5$ GeV are converted to the nominal LEP energy point of 200.0 GeV (a difference of $\Delta\alpha_S \approx -0.0001$).

Our result is as follows:

$$
\begin{aligned}
\alpha_S(M_Z) &= 0.1189 \pm 0.0005 \text{ (stat.)} \pm 0.0010 \text{ (exp.)} \pm 0.0006 \text{ (hadr.)} \, {}^{+0.0039}_{-0.0040} \text{ (theo.)} \\
&= 0.1189 \pm 0.0005 \text{ (stat.)} \pm 0.0041 \text{ (syst.)} \\
&= 0.1189 \pm 0.0042 \text{ (total)}
\end{aligned}
$$

We have also calculated combinations for other subsets of the OPAL measurements. Tables 3.13 gives α_S values for individual observables, and Table 3.14 gives separate results for LEP1[24] and LEP2 data. In both cases, a breakdown of the weights w_i is shown. Figures 3.25 and 3.26 present the same results, and also show the $\alpha_S(M_Z)$ values obtained from each of the eight LEP energy bins. Figure 3.27 shows the running of α_S predicted by the Renormalisation Group Equation for our measured value of $\alpha_S(M_Z)$. The OPAL results are found to be in good agreement

---

[24]'LEP1' here refers to measurements at $\sqrt{s} = 91$ GeV, which in this case were performed during calibration runs with the LEP2 detector.

with the QCD prediction, although we do not calculate a χ^2 value, due to the complications of correlated uncertainties.

The results given here may be compared with Tables 4.9 and 4.10, and Figures 4.24–4.26 in the next chapter, which show the corresponding results for all four LEP experiments combined. Counter-intuitively, the total uncertainty of the overall LEP combination is slightly larger than that of our OPAL combination. The least-squares method should ordinarily lead to a combination with the lowest possible uncertainty, but we shall see in the next chapter that such a combination would not be reliable in this case. The combined OPAL α_S measurement is more precise than the corresponding combinations of DELPHI and L3 results, because the latter do not include fits to the y_{23} distribution, which has the smallest theoretical uncertainty of the six observables.

The LEP combination does not currently use the newest set of OPAL measurements presented here. Instead, we use the most recent set of preliminary measurements approved by the OPAL Collaboration. These can be found in Refs. [124, 127], and are reproduced in Appendix D, together with measurements from the other experiments. The final LEP result will be published after final measurements have become available from all four Collaborations.

	T only	M_H only	C only	B_T only	B_W only	y_{23} only	All
Fit results							
$\alpha_s(M_Z)$	0.1249	0.1185	0.1188	0.1235	0.1137	0.1194	0.1189
Stat. error	±0.0011	±0.0008	±0.0010	±0.0010	±0.0009	±0.0007	±0.0005
Exp. error	±0.0017	±0.0017	±0.0019	±0.0020	±0.0015	±0.0012	±0.0010
Hadr. error	±0.0014	±0.0009	±0.0016	±0.0014	±0.0005	±0.0004	±0.0006
Theory (upper)	+0.0053	+0.0041	+0.0054	+0.0065	+0.0050	+0.0026	+0.0039
Theory (lower)	−0.0052	−0.0042	−0.0052	−0.0060	−0.0051	−0.0028	−0.0040
Syst. error	±0.0057	±0.0046	±0.0058	±0.0067	±0.0053	±0.0030	±0.0041
Total error	±0.0058	±0.0047	±0.0059	±0.0068	±0.0054	±0.0031	±0.0042
χ^2 / d.o.f.	1.3/ 7	0.8/ 7	1.2/ 7	3.3/ 7	1.9/ 7	2.2/ 7	27.7/ 47
Weights by observable							
T	100 %	–	–	–	–	–	8.3 %
M_H	–	100 %	–	–	–	–	14.8 %
C	–	–	100 %	–	–	–	7.1 %
B_T	–	–	–	100 %	–	–	5.3 %
B_W	–	–	–	–	100 %	–	15.9 %
y_{23}	–	–	–	–	–	100 %	48.6 %
Weights by c.m. energy							
91.2 GeV	24.8 %	37.7 %	27.4 %	25.9 %	20.1 %	30.3 %	49.0 %
133.0 GeV	4.9 %	8.8 %	4.8 %	4.7 %	5.4 %	2.1 %	2.3 %
161.0 GeV	3.5 %	2.4 %	2.4 %	4.2 %	4.2 %	2.0 %	1.0 %
172.0 GeV	1.6 %	1.2 %	1.8 %	4.3 %	4.4 %	0.7 %	0.7 %
183.0 GeV	9.7 %	5.1 %	10.2 %	9.4 %	8.6 %	3.9 %	2.9 %
189.0 GeV	17.9 %	14.4 %	22.5 %	22.2 %	19.6 %	26.2 %	18.7 %
200.0 GeV	13.3 %	14.1 %	12.4 %	9.9 %	17.8 %	18.6 %	12.0 %
206.0 GeV	24.4 %	16.2 %	18.6 %	19.5 %	19.9 %	16.2 %	13.5 %
Other weight statistics							
Total +ve	100.0 %	100.0 %	100.0 %	100.0 %	100.0 %	100.0 %	101.0 %
Total −ve	0.0 %	0.0 %	0.0 %	0.0 %	0.0 %	0.0 %	−1.0 %
Maximum	24.8 %	37.7 %	27.4 %	25.9 %	20.1 %	30.3 %	17.8 %
Minimum	0.0 %	0.0 %	0.0 %	0.0 %	0.0 %	0.0 %	−0.6 %

Table 3.13: Combined $\alpha_S(M_Z)$ fit results for different observables, using OPAL data. These results may be compared with Table 4.9 in the next chapter, which includes data from all four LEP experiments.

	LEP1 $(Q = M_\mathrm{Z})$	**LEP2** $(Q > M_\mathrm{Z})$	**All**
Fit results			
$\alpha_\mathrm{s}(M_\mathrm{Z})$	0.1194	0.1184	0.1189
Stat. error	±0.0001	±0.0011	±0.0005
Exp. error	±0.0008	±0.0014	±0.0010
Hadr. error	±0.0010	±0.0003	±0.0006
Theory (upper)	+0.0044	+0.0034	+0.0039
Theory (lower)	−0.0043	−0.0036	−0.0040
Syst. error	±0.0045	±0.0038	±0.0041
Total error	±0.0045	±0.0039	±0.0042
χ^2 / d.o.f.	1.4/ 5	26.1/ 41	27.7/ 47
Weights by observable			
T	10.1 %	7.6 %	8.3 %
M_H	20.6 %	6.2 %	14.8 %
C	10.5 %	3.1 %	7.1 %
B_T	8.5 %	1.6 %	5.3 %
B_W	11.8 %	21.1 %	15.9 %
y_{23}	38.5 %	60.4 %	48.6 %
Weights by c.m. energy			
91.2 GeV	100 %	–	49.0 %
133.0 GeV	–	4.4 %	2.3 %
161.0 GeV	–	2.0 %	1.0 %
172.0 GeV	–	1.4 %	0.7 %
183.0 GeV	–	5.6 %	2.9 %
189.0 GeV	–	36.7 %	18.7 %
200.0 GeV	–	23.4 %	12.0 %
206.0 GeV	–	26.5 %	13.5 %
Other weight statistics			
Total +ve	100.0 %	101.9 %	101.0 %
Total −ve	0.0 %	−1.9 %	−1.0 %
Maximum	38.5 %	26.1 %	17.8 %
Minimum	0.0 %	−1.1 %	−0.6 %

Table 3.14: Combined $\alpha_\mathrm{S}(M_\mathrm{Z})$ fit results at LEP1 and LEP2 centre-of-mass energies, using OPAL data. These results may be compared with Table 4.10 in the next chapter, which includes data from all four LEP experiments.
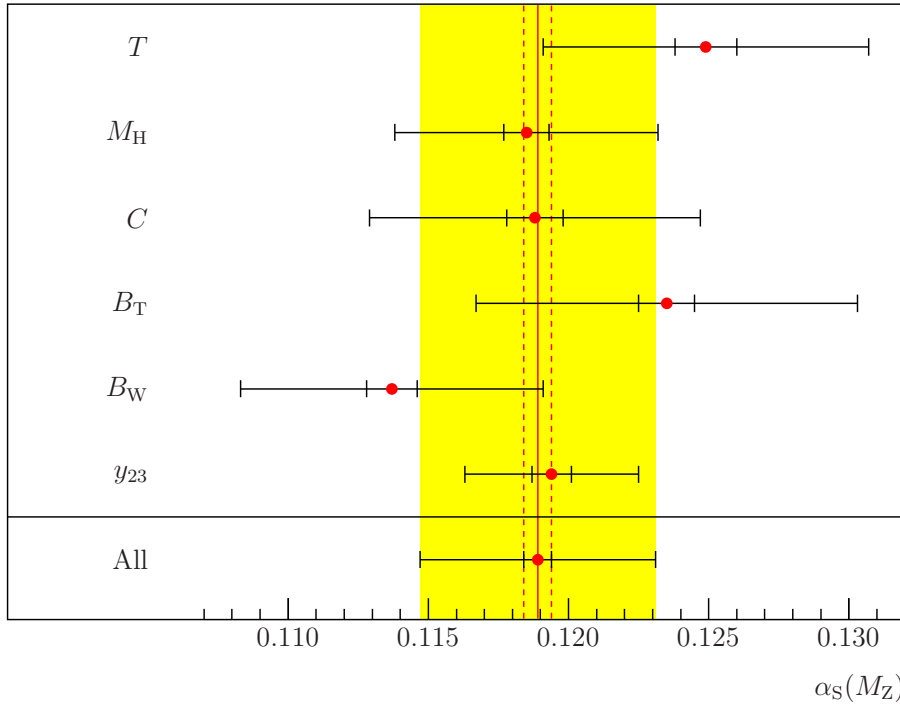
Figure 3.25: OPAL $\alpha_{\mathrm{S}}(M_{\mathrm{Z}})$ combinations for individual event shape observables. The inner error bars are statistical, while the outer bars represent total uncertainties.
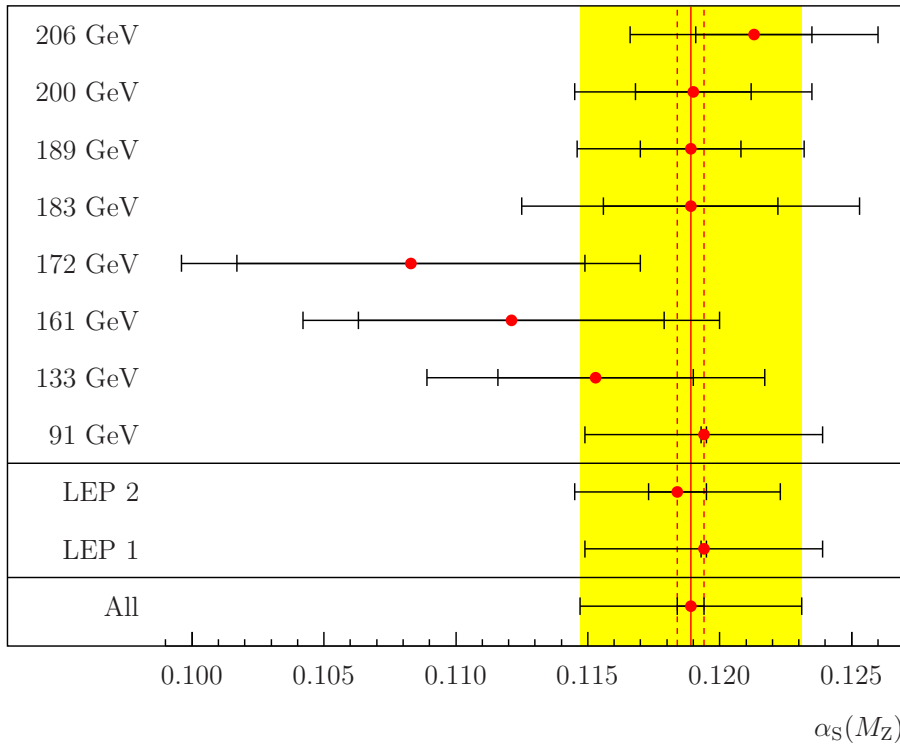
Figure 3.26: OPAL $\alpha_{\mathrm{S}}(M_{\mathrm{Z}})$ combinations for individual centre-of-mass energies. The inner error bars are statistical, while the outer bars represent total uncertainties.
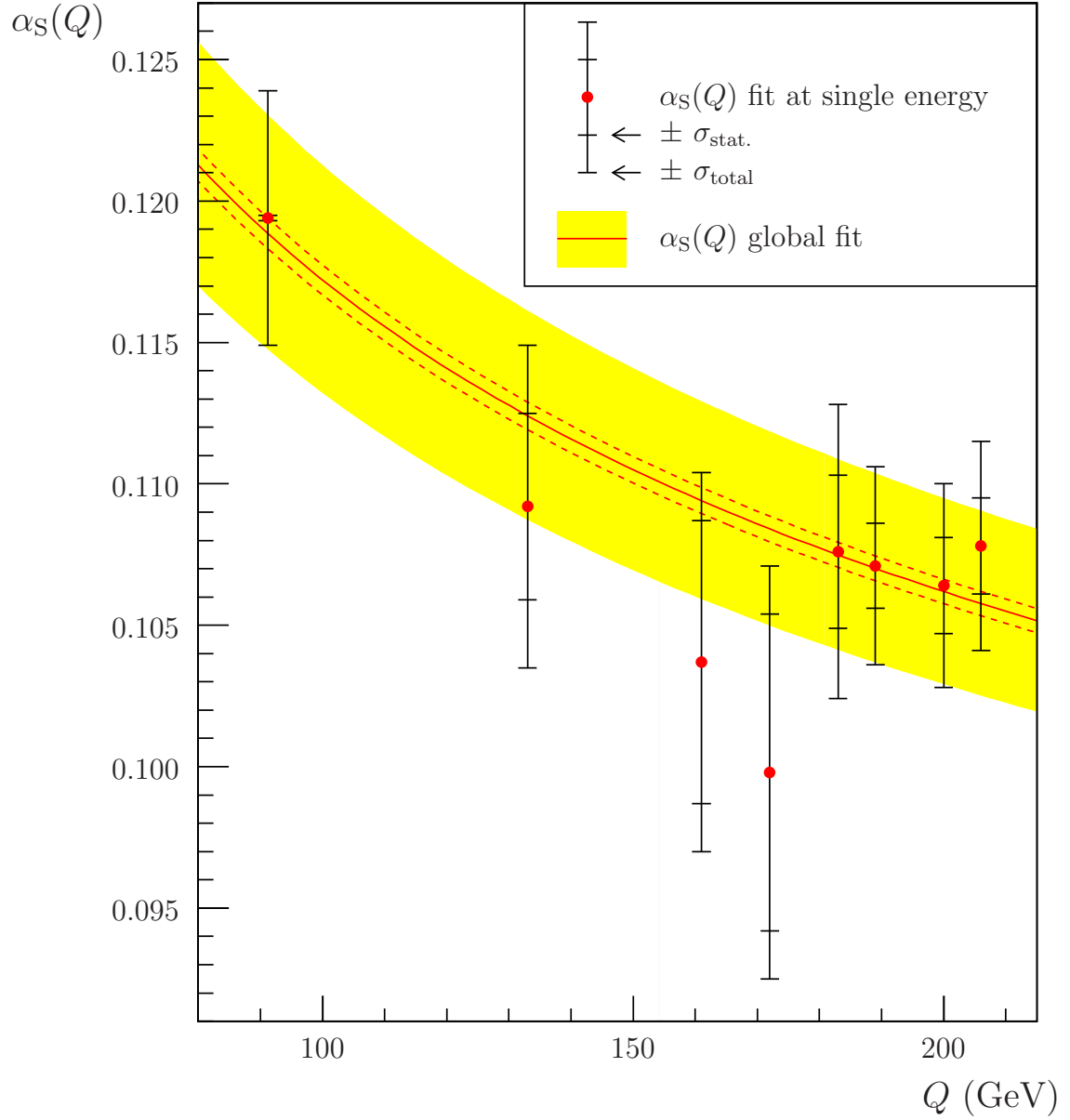
Figure 3.27: A global QCD running fit to the OPAL α_S measurements. Each point represents a fit to the six measurements at an individual centre-of-mass energy, while the curve represents a global fit to all measurements. The form of the curve is determined by the Renormalisation Group Equation of QCD, with $\alpha_S(M_Z)$ as a free parameter. The yellow band corresponds to the total uncertainty of the fitted $\alpha_S(M_Z)$ value, and the dotted curves indicate the statistical uncertainty.

Chapter 4

A combined measurement of α_S by the four LEP Collaborations

All four of the LEP Collaborations have presented measurements of the strong coupling derived from e^+e^- event shape observables, over the full range of LEP centre-of-mass energies [8–11, 66, 124, 129–136]. The L3 Collaboration has also published measurements at energy scales lower than the Z^0 mass,[1] using events with final-state photon radiation at LEP1 [138]. In this chapter, we describe a method developed with the LEP QCD Working Group to combine all of these results into a single measurement. Such a combination should allow a more precise measurement of $\alpha_S(M_Z)$, and a more sensitive test for the energy-evolution of $\alpha_S(Q)$, than is possible with one experiment alone.

4.1 Preliminary consistency tests

When combining results from more than one experiment, it is essential to ensure that the same quantity is being measured in each case. Furthermore, when estimating uncertainties in the combined result, it is desirable that the same analysis methods should be followed by all Collaborations. Several preliminary tests and comparisons were therefore performed, before the combination itself. These consistency checks served not only to improve the reliability of the combined LEP α_S measurement, but also to eliminate problems in the internal procedures of the Collaborations.

---

[1]Preliminary measurements at $Q < M_Z$ have also been performed using radiative events from OPAL [137]. These are not currently included in the LEP α_S combination.

It was agreed that some minor differences could remain between the methods used by different experiments. For example, the ALEPH and L3 Collaborations currently use a matrix unfolding method to apply hadronisation corrections to the perturbative predictions [130, 136]; OPAL instead uses a bin-by-bin correction based on the ratios of integrated distributions, as described in Section 3.5.1, while DEL-PHI uses ratios of differential distributions [133]. Furthermore, each Collaboration has chosen its own ranges in which to fit the event shape distributions. However, since significant differences exist between possible 'variants' of the perturbative theory predictions, it was decided that all Collaborations should use $\mathcal{O}(\alpha_S^2)$ matrix elements matched with the most recent NLLA resummations, using the $\text{Log}(R)$ matching scheme, as described in Section 1.6. The kinematic constraints defined in Section 1.6.4 were also adopted, so that the NLLA prediction is forced to vanish in unphysical regions.

In the following sections, we outline the investigations performed by the LEP QCD Working Group to test the consistency of our theory predictions, fitting procedures and hadronisation corrections.

4.1.1   Theoretical predictions

Figure 4.1 illustrates a comparison between the perturbative theory predictions used by the four Collaborations at the start of our investigation. Differences are shown relative to the differential cross sections used by OPAL at the time. As a measure of the effect these deviations had on our α_S fits, we also show bands indicating fractional variations of the OPAL prediction with respect to changes in α_S; the widths of the bands correspond to the statistical and total uncertainties of the OPAL α_S measurements at $\sqrt{s} \geq 203$ GeV. Some of the differences between our distributions were found to be substantial. Although all four Collaborations were using $\mathcal{O}(\alpha_S^2)+$NLLA calculations with the $\text{Log}(R)$ matching scheme, the OPAL and L3 Collaborations had not yet adopted the latest NLLA calculations for the total and wide jet broadenings [33], and were also not using the kinematic constraints described in Section 1.6.4.

After detailed discussion and documentation of the theoretical predictions and matching schemes, satisfactory agreement was reached. Figure 4.2 compares the $\text{Log}(R)$-matched predictions now implemented in the ALEPH, DELPHI and OPAL software. The L3 predictions were not included in this figure, but were also found

to be in good agreement. The small statistical fluctuations between bins are due to the finite number of $\mathcal{O}(\alpha_\mathrm{S}^2)$ 'events' generated in EVENT2, when estimating the $\mathcal{A}(y)$ and $\mathcal{B}(y)$ coefficient functions.

4.1.2 Fitting procedures

As a further cross-check on fits to LEP data, a set of event shape distributions from a parton shower Monte Carlo program was distributed to the Collaborations. Fits were then performed to determine α_S from the simulated parton-level 'data', using two different $\mathcal{O}(\alpha_\mathrm{S}^2) + \mathrm{NLLA}$ matching schemes, and also using pure $\mathcal{O}(\alpha_\mathrm{S}^2)$ matrix element predictions. The same fit ranges were used by ALEPH, DELPHI and OPAL for the purposes of this test (L3 did not take part), and no hadronisation effects were included. The results, shown in Figure 4.3, show that the fitted α_S values do not differ by more than about ± 0.001. The residual discrepancies are much smaller than the theoretical uncertainties of the α_S measurements, which are partially reflected in the differences between matching schemes. The level of agreement between experiments in this test is again limited in principle by the size of the EVENT2 samples.

4.1.3 Hadronisation corrections

When fitting theoretical predictions to real data, one of the Monte Carlo models described in Section 1.9 must be used to propagate the predicted parton-level distributions to the hadron level. Although the models themselves are universal, the Collaborations must choose values for various parameters. The string fragmentation model of PYTHIA, for example, is dependent on many quantities which can be 'tuned' to give the best possible fit to experimental data. As part of our programme of consistency checks, we have therefore compared the hadronisation corrections calculated with each tuned version of PYTHIA, HERWIG and ARIADNE. Our results for the thrust distribution are shown in Figure 4.4. For OPAL, we also compare hadronisation corrections based on the differential and integrated distributions $R(y)$ and $R'(y)$, as we described in Section 3.5.1.[2] The discrepancies between hadroni-

---

[2]In notation of Section 3.5.1, the functions "OPAL (diff)" and "OPAL (int)" displayed in Figure 4.4 are given respectively by:

$$\text{``OPAL (diff)''} = \frac{\mathrm{d}R_\mathrm{hadr.}^\mathrm{MC}/\mathrm{d}y}{\mathrm{d}R_\mathrm{part.}^\mathrm{MC}/\mathrm{d}y} \quad , \qquad \text{``OPAL (int)''} = \frac{1}{\mathrm{d}R_\mathrm{part.}/\mathrm{d}y}\left[\frac{\mathrm{d}}{\mathrm{d}y}\left(\frac{R_\mathrm{hadr.}^\mathrm{MC}(y)}{R_\mathrm{part.}^\mathrm{MC}(y)}\,R_\mathrm{part.}(y)\right)\right]$$
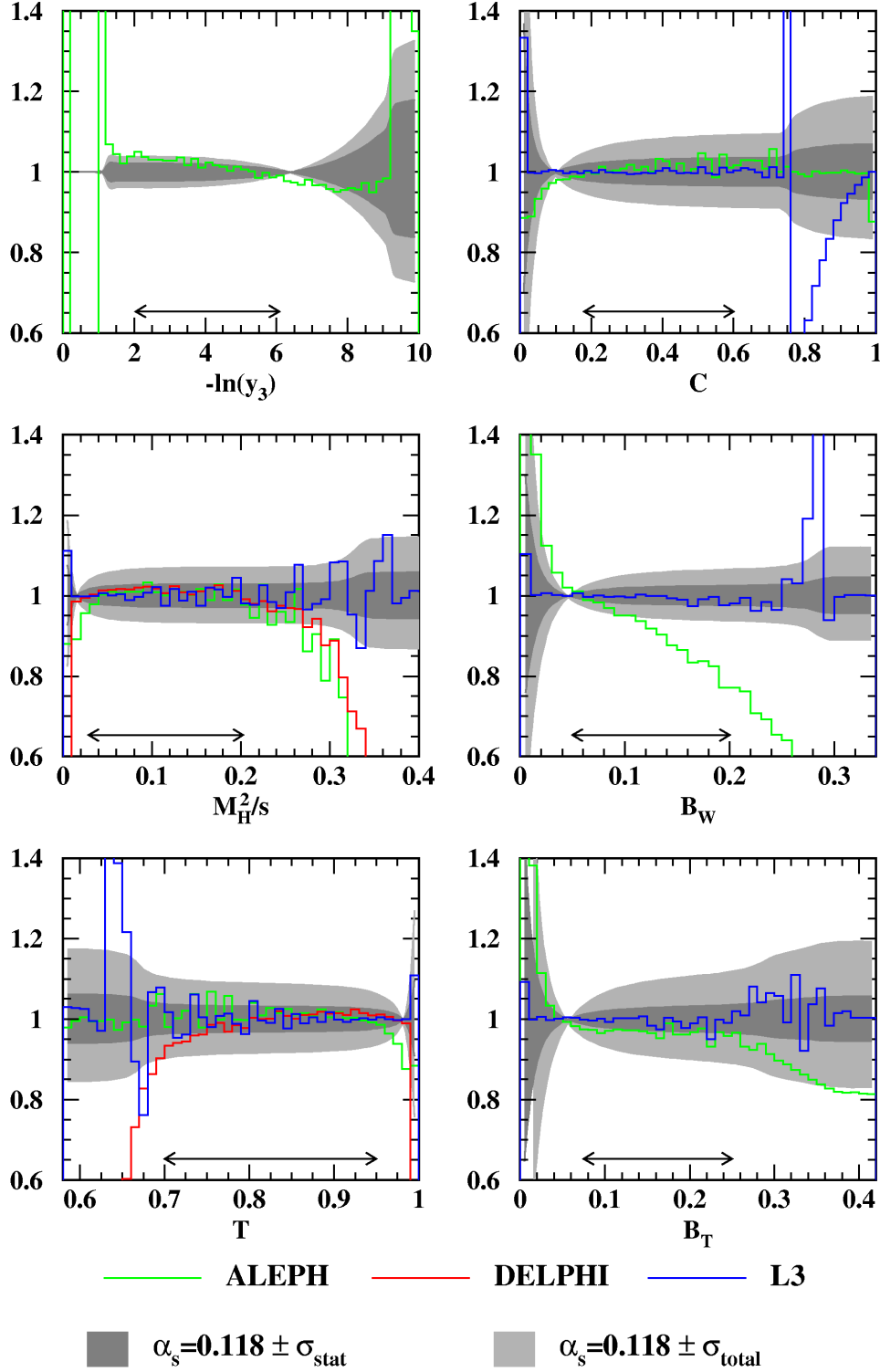
Figure 4.1: A comparison between the theory predictions used for α_S fits by the LEP Collaborations, in February 2001. The differential cross sections dR/dy used by ALEPH, DELPHI and L3 are shown as multiples of that used by OPAL. The grey bands indicate fractional variations of the OPAL prediction with respect to changes in α_S: the dark and light bands correspond to the statistical and total uncertainties of the α_S measurements using all OPAL data at $\sqrt{s} \geq 203$ GeV. The fit ranges used by OPAL are indicated by arrows.
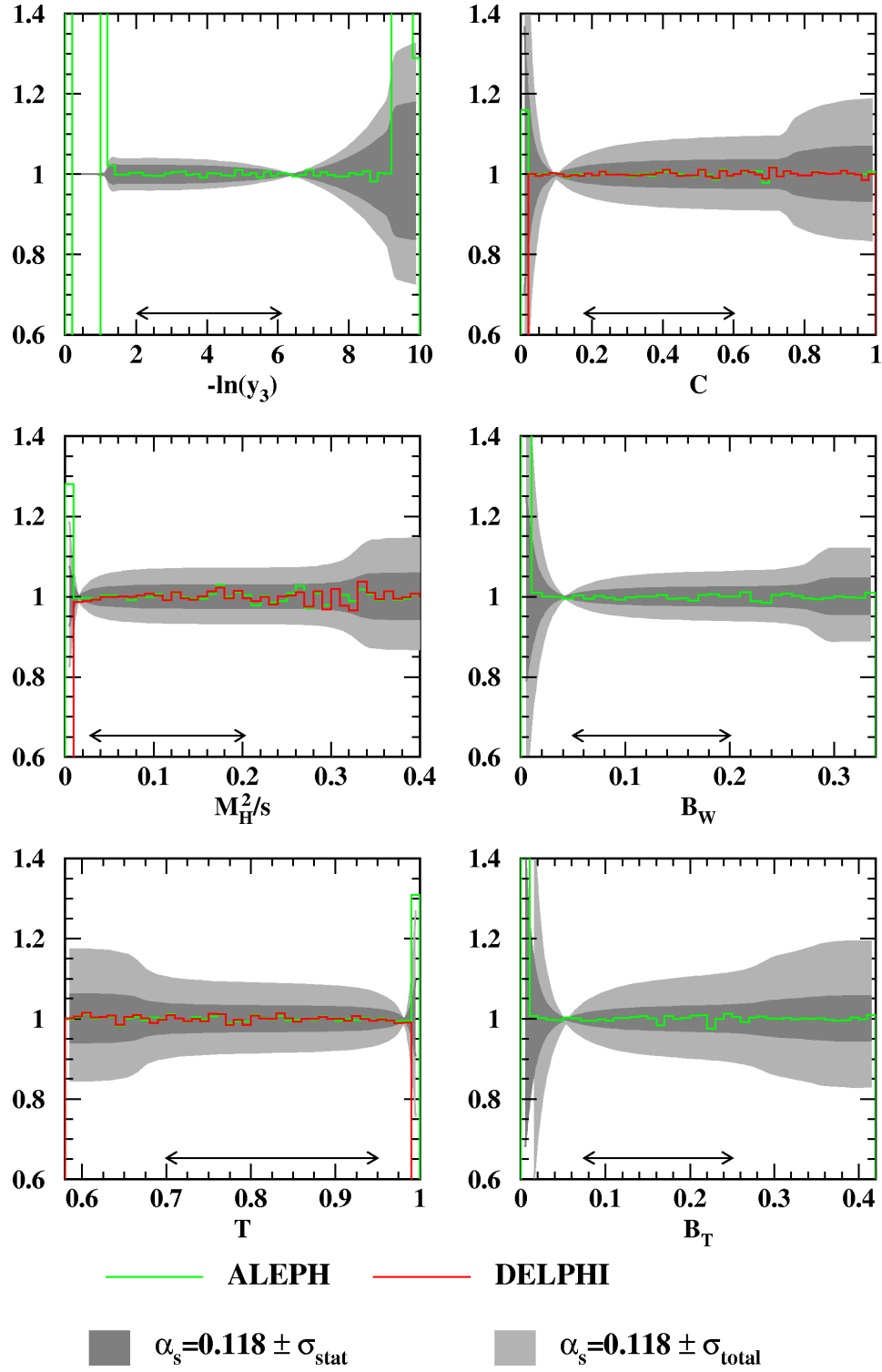
Figure 4.2: A updated comparison between the theory predictions used for α_S fits by ALEPH, DELPHI and OPAL, in June 2001. See the caption of Figure 4.1 for further details.
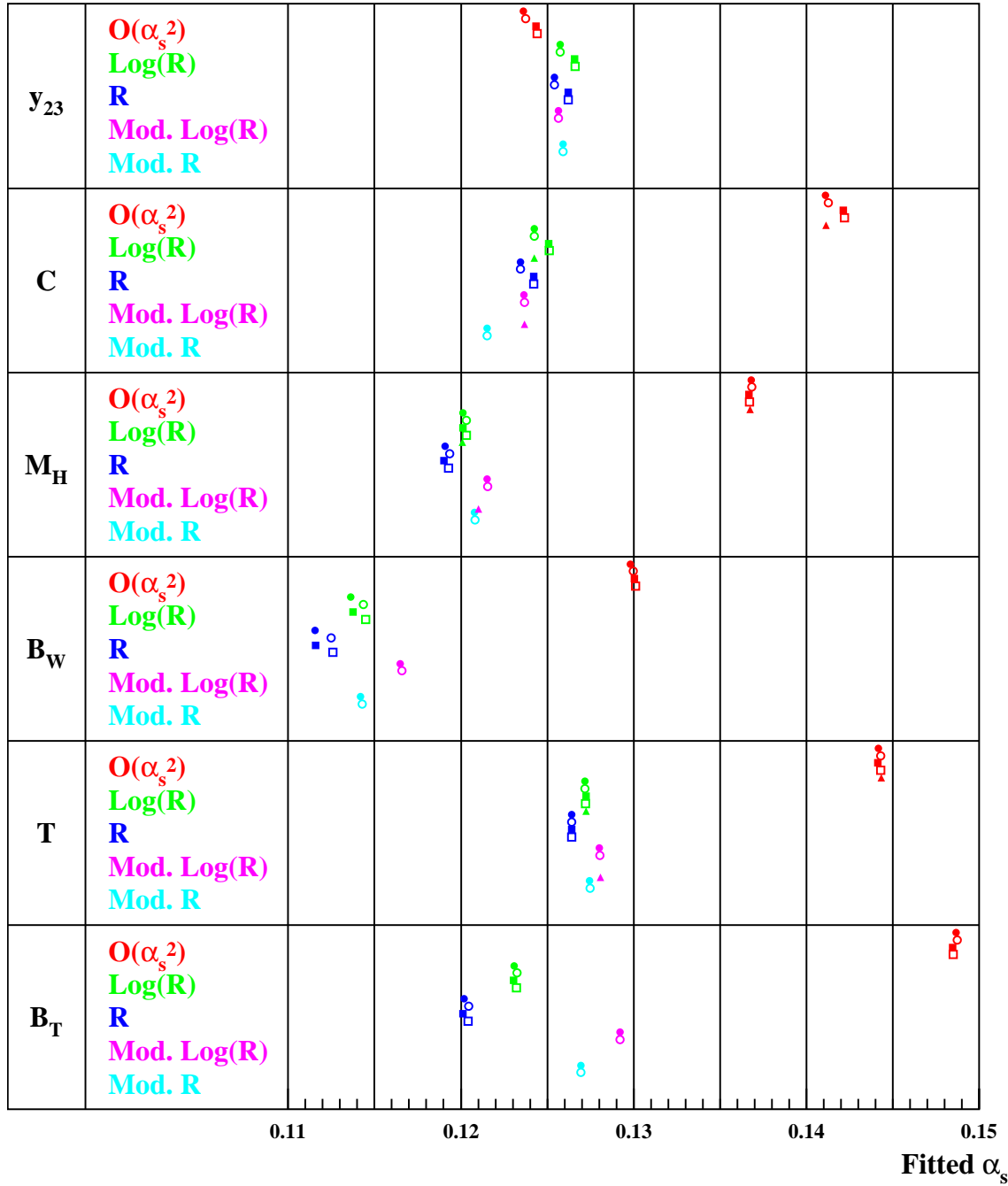
Figure 4.3: Fitted α_S values calculated by the OPAL, ALEPH and DELPHI software, from a single set of simulated parton-level events. The five colours indicate different theoretical predictions used in the fit ('Mod.' indicates that kinematic constraints were imposed), and the different symbols represent fits by different Collaborations or using different covariance matrices.

Q/GeV	T	M_H	B_W	B_T	C	y_{23}	
41.4	L	L	L	L	L		
55.3	L	L	L	L	L		
65.4	L	L	L	L	L		
75.7	L	L	L	L	L		
82.3	L	L	L	L	L		
85.1	L	L	L	L	L		
91.2	ADLO	ADLO	ADLO	ADLO	ADL	A	O
133.0	ADLO	ADLO	A LO	A LO	A L	A	O
161.0	ADLO	ADLO	A LO	A LO	A L	A	O
172.0	ADLO	ADLO	A LO	A LO	A LO	A	O
183.0	ADLO	ADLO	ADLO	ADLO	ADLO	A	O
189.0	ADLO	ADLO	ADLO	ADLO	ADLO	A	O
200.0	ADLO	ADLO	ADLO	ADLO	ADLO	A	O
206.0	ADLO	ADLO	ADLO	ADLO	ADLO	A	O

Table 4.1: Measurements of $\alpha_\text{S}(Q)$ contributing to the LEP combination. Each letter in the table indicates a fit to the event shape distribution indicated in the column heading. The letters themselves indicate the experimental Collaborations ('A'=ALEPH, 'D'=DELPHI, 'L'=L3, 'O'=OPAL).

sation corrections used by the four experiments are far more significant at 91 GeV than at 189 GeV. In the three-jet region at 91 GeV, the differences are typically of order 3%, although L3 shows slightly larger deviations relative to the other three experiments. The two OPAL correction methods agree to better than 1% within the OPAL fit range; the methods become formally equivalent if the parton shower model gives a perfect description of the perturbative theory. Our OPAL analysis described in Chapter 3 uses the 'integral' form of the correction, described in 3.5.1.

4.2 The input measurements and their uncertainties

Table 4.1 lists the 194 available α_S measurements contributing to the LEP combination. The measurements themselves are tabulated for reference in Appendix D. Not all of the results are published, but all have been approved by the individual Collaborations for use in a preliminary LEP average. In the case of OPAL, we will use the preliminary results listed in Refs. [124, 127], and not the most recent measurements presented in Chapter 3.

The uncertainty of each measurement has four uncorrelated contributions: a
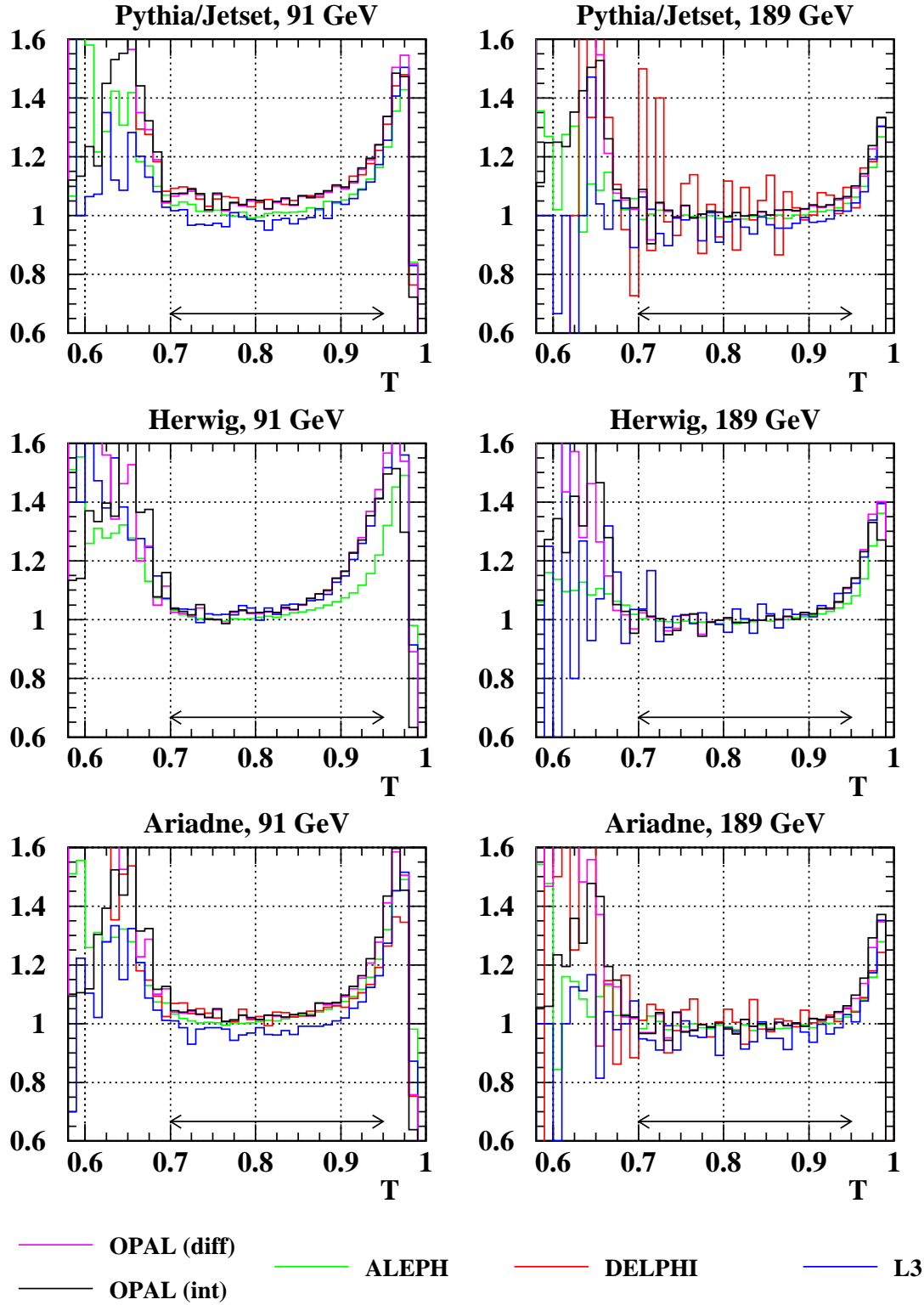
Figure 4.4: Ratios of the hadron- and parton-level differential thrust distributions, $(\mathrm{d}R_{\mathrm{had}}/\mathrm{d}T)/(\mathrm{d}R_{\mathrm{part}}/\mathrm{d}T)$, predicted by the tuned PYTHIA, HERWIG and ARIADNE Monte Carlo programs at $\sqrt{s} = 91$ GeV and 189 GeV. In the case of OPAL, we also show the effective bin-by-bin correction factors "OPAL (int)" based on the *integrated* distribution of $(1-T)$, as described in Section 3.5.1. The arrows indicate OPAL fit ranges for the α_S measurements.

statistical uncertainty, an experimental systematic uncertainty, a hadronisation uncertainty, and a theoretical uncertainty:

$$\sigma^2_\mathrm{total} \;=\; \sigma^2_\mathrm{stat.} \;+\; \sigma^2_\mathrm{exp.} \;+\; \sigma^2_\mathrm{hadr.} \;+\; \sigma^2_\mathrm{theo.} \quad . \tag{4.1}$$

All four Collaborations have decomposed their quoted uncertainties in this way.

One can define a 194×194 covariance matrix V_{ij}, relating the uncertainties of all input measurements. The diagonal elements of this matrix are the variances σ^2 of the individual measurements, while the off-diagonal terms relate to correlations between measurements from different experiments, energy scales, or observables. For example, one of the single elements V_{ij} would be

$$\mathrm{Cov}\left(\alpha_\mathrm{S}^{[189\ \mathrm{GeV},T,\mathrm{OPAL}]}, \; \alpha_\mathrm{S}^{[161\ \mathrm{GeV},M_\mathrm{H},\mathrm{ALEPH}]} \right) \quad .$$

Since the four uncertainty contributions are independent, the entire covariance matrix can be expressed as a sum of four parts,

$$
\begin{aligned}
V_{ij}^\mathrm{total} \;&=\; V_{ij}^\mathrm{stat.} \;+\; V_{ij}^\mathrm{exp.} \;+\; V_{ij}^\mathrm{hadr.} \;+\; V_{ij}^\mathrm{theo.} \\
&=\; \begin{cases} (\sigma_i^2)_\mathrm{stat.} \;+\; (\sigma_i^2)_\mathrm{exp.} \;+\; (\sigma_i^2)_\mathrm{hadr.} \;+\; (\sigma_i^2)_\mathrm{theo.} & i=j \\ (\rho_{ij}\sigma_i\sigma_j)_\mathrm{stat.} + (\rho_{ij}\sigma_i\sigma_j)_\mathrm{exp.} + (\rho_{ij}\sigma_i\sigma_j)_\mathrm{hadr.} + (\rho_{ij}\sigma_i\sigma_j)_\mathrm{theo.} & i \neq j \end{cases}
\end{aligned}
\tag{4.2}
$$

where the correlation coefficients ρ_{ij} must be estimated for each class of uncertainty.

4.3 Methods for combining α_S measurements

Before further discussion of the uncertainties σ_i, and their correlations, ρ_{ij}, we first outline our basic combination method.

4.3.1 The least-squares method for $\alpha_\mathrm{S}(Q)$

Given the value of the strong coupling $\alpha_\mathrm{S}(Q_0)$, at one arbitrary energy scale Q_0, the Renormalisation Group Equation (RGE) will predict the running coupling $\alpha_\mathrm{S}(Q)$ at all other scales, as described in Section 1.3. Our task, therefore, is to find a value for the parameter $\lambda = \alpha_\mathrm{S}(Q_0)$, such that the function $\alpha_\mathrm{S}(Q; \lambda)$ makes the best possible fit to the data $y_i = [\alpha_\mathrm{S}(Q)]_i$. We perform this fit by applying the principle of least

squares, which implies minimisation of the following expression with respect to λ: [3]

$$\chi^2 \; = \; \sum_{i,j} \left(y_i - \alpha_{\mathrm{S}}(Q_i; \lambda) \right) \left(V^{-1} \right)_{ij} \left(y_j - \alpha_{\mathrm{S}}(Q_j; \lambda) \right) \quad . \tag{4.3}$$

Our statistical estimator, $\hat{\lambda} = \hat{\alpha}_{\mathrm{S}}(Q_0)$, is the value of λ corresponding to the minimum of χ^2. By convention, we set the arbitrary energy scale Q_0 equal to the Z^0 mass, so our parameter λ becomes $\alpha_{\mathrm{S}}(M_{\mathrm{Z}})$. This is a sensible choice, since the most statistically precise measurements of α_{S} were performed at this scale, where the cross section for multihadron production is highest. After estimating the covariance matrix V, we can use a numerical minimisation program such as MINUIT to perform the fit. A numerical solution of the RGE provides the running coupling $\alpha_{\mathrm{S}}(Q_i; \lambda)$ to three-loop accuracy, and a routine from the CERN program library inverts the 194×194 matrix V. The uncertainty on $\hat{\alpha}_{\mathrm{S}}(M_{\mathrm{Z}})$ can be estimated using variations of χ^2 around its minimum:

$$\chi^2(\hat{\lambda} \pm \sigma_\lambda) = \chi^2(\hat{\lambda}) + 1 \quad . \tag{4.4}$$

This numerical implementation of the least squares method, however, has several disadvantages:

- It would be useful to know the 'weight' of each input measurement contributing to the combination. We expect the more precise measurements to carry a higher weight, and we do not expect any measurements to carry an unduly large (or negative) weight, which could destabilise the combination. However, the numerical minimisation technique does not allow such weights to be calculated easily.

- The uncertainty determined from Equation (4.4) cannot be decomposed into distinct sources; only the total uncertainty can be calculated by this method.

- Equation (4.4) assumes that the function $\alpha_{\mathrm{S}}(Q_i; \lambda)$ varies linearly with λ, so that the minimum of χ^2 is perfectly parabolic. Although true to leading order, this condition is not strictly satisfied.

---

[3]This is a standard formula for χ^2, to be used in the case where the input measurements have correlated uncertainties. A brief explanation for this formula is given in Appendix A.2.

4.3.2 The weighted mean method

Fortunately, there are conditions under which the minimum of χ^2 may be found analytically. Instead of fitting the set of measurements $y_i \equiv [\alpha_S(Q)]_i$ to the predicted running function, we can convert each of them into a measurement y_i' of $\alpha_S(M_Z)$. Letting $f_i(\alpha_S)$ be the function which maps a value of $\alpha_S(Q_i)$ on to a corresponding value of $\alpha_S(M_Z)$, we have

$$y_i' \;=\; f_i(y_i) \tag{4.5}$$

$$\text{and} \quad \sigma_{y_i'} \;\approx\; \frac{f_i(y_i + \sigma_{y_i}) - f_i(y_i - \sigma_{y_i})}{2} \quad, \tag{4.6}$$

where Equation (4.6) applies individually to the statistical, experimental and hadronisation uncertainties of y_i'.[4] Equation (4.3) then simplifies to

$$\chi^2 \;=\; \sum_{i,j} \left(y_i' - \lambda\right) \left(V'^{\,-1}\right)_{ij} \left(y_j' - \lambda\right) \quad, \tag{4.7}$$

where V' is the full covariance matrix relating the measurements y_i'. To find the minimum of χ^2, we simply differentiate the above expression with respect the parameter λ, and exploit the symmetry of the covariance matrix V':

$$\frac{\mathrm{d}\chi^2}{\mathrm{d}\lambda} \;=\; -2\sum_{i,j} \left(V'^{\,-1}\right)_{ij} \left(y_j' - \lambda\right) \quad. \tag{4.8}$$

Setting this derivative to zero at the minimum $\lambda = \hat{\lambda}$ gives

$$\sum_{i,j} \left(V'^{\,-1}\right)_{ij} y_j' \;=\; \hat{\lambda}\sum_{i,j} \left(V'^{\,-1}\right)_{ij} \quad. \tag{4.9}$$

Hence our estimator for $\alpha_S(M_Z)$ becomes a linear combination of the measurements y_i',

$$\hat{\alpha}_S(M_Z) \;=\; \hat{\lambda} \;=\; \sum_i w_i\, y_i' \quad, \tag{4.10}$$

---

[4]Treating each σ_i formally as the standard deviation of some distribution, Equation (4.6) will be precisely valid only in the case when $f_i(y_i)$ is a linear function of y_i. That is to say, the shape of the probability distribution for $\alpha_S(Q_i)$ must be preserved (up to a scale factor) when running measurements to the scale Q_0. Although this condition is only approximately satisfied, the uncertainties σ_{y_i} are not estimated with sufficient precision for the effects of non-linearity to be significant.

where the weights w_i are given by

$$w_i = \frac{\sum_j \left(V'^{-1}\right)_{ij}}{\sum_{j,k} \left(V'^{-1}\right)_{jk}} \quad . \tag{4.11}$$

4.3.3 The uncertainties of the combined measurement

Since we now have an explicit expression for our combined measurement of $\alpha_{\mathrm{S}}(M_{\mathrm{Z}})$ in terms of the 'converted' inputs y_i', we can now find corresponding expressions for the uncertainties. The variance of λ is given by

$$\sigma^2 = \left\langle \left(\lambda - \langle\lambda\rangle\right)^2 \right\rangle = \left\langle \left[\sum_i w_i \left(y_i' - \langle y_i'\rangle\right)\right]^2 \right\rangle \quad . \tag{4.12}$$

Expanding the square of the sum yields

$$\begin{aligned}
\sigma^2 &= \sum_{i,j} w_i\, w_j \left\langle \left(y_i' - \langle y_i'\rangle\right)\left(y_j' - \langle y_j'\rangle\right)\right\rangle \\
&= \sum_{i,j} w_i\, V_{ij}'\, w_j \\
&\equiv w^{\mathrm{T}}\, V'\, w \quad ,
\end{aligned} \tag{4.13}$$

where w represents a vector of weights in the last line. We have already noted in Equation (4.2), however, that the covariance matrix V (and hence V'), can be expressed as a sum of four independent contributions. Hence we can now deduce the statistical, experimental, hadronisation and theory uncertainties of our combined measurement λ: [5]

$$\sigma^2_{\left\{\begin{smallmatrix}\text{stat.}\\\text{exp.}\\\text{hadr.}\\\text{theo.}\end{smallmatrix}\right\}} = w^{\mathrm{T}}\, V'_{\left\{\begin{smallmatrix}\text{stat.}\\\text{exp.}\\\text{hadr.}\\\text{theo.}\end{smallmatrix}\right\}}\, w \quad . \tag{4.14}$$

4.3.4 Minimisation of the total uncertainty

An interesting property of our weighted mean formula, Equation (4.10), is that it automatically minimises the total uncertainty given in Equation (4.13) for our combined result, in addition to minimising χ^2. A proof of this result is given in Appendix A.3. We will return to this property later, in Section 4.12, when considering our numerical results.

---

[5]We will return to this point in Section 4.9. For our final combined $\alpha_{\mathrm{S}}(M_{\mathrm{Z}})$ measurement, we will use Equation 4.14 to estimate only our statistical and experimental uncertainties.

4.4 The covariance matrix

Given the formulae presented in the previous section, all that remains for a measurement of $\alpha_S(M_Z)$ is to specify the covariance matrix V (or V'). We will first discuss the uncertainties, which form the leading diagonal of the matrix, and then their correlations.

4.4.1 The uncertainties

In previous LEP combinations of α_S measurements, the four uncertainties $\sigma_{stat.}$, $\sigma_{exp.}$, $\sigma_{had.}$ and $\sigma_{theo.}$ were taken directly from values quoted by the Collaborations. However, there are differences in the methods used to estimate these uncertainties; undue weight could therefore be given to one Collaboration's results, simply because they used a less conservative error estimate. We therefore attempt to re-evaluate the uncertainties independently wherever possible, or to smooth differences between the experiments. Our treatments of the four error types are explained in the sections that follow.

4.4.1.1 Statistical uncertainties, $\sigma_{stat.}$

Unlike the three systematic uncertainties, $\sigma_{stat.}$ is a well-defined and calculable quantity: it is the standard deviation of the ensemble of results obtained, if the complete experiment were repeated indefinitely.[6] As explained in Section 3.5.3, we have investigated two possible methods to determine the statistical uncertainty for OPAL measurements, and found them to be in good agreement. The methods used by other Collaborations vary, but should in principle be equivalent. We therefore insert the quoted statistical uncertainties into the covariance matrix without modification.

4.4.1.2 Experimental systematic uncertainties, $\sigma_{exp.}$

The experimental systematic uncertainties account for unknown biases which are largely unique to a specific experiment or analysis. It is therefore impossible for the LEP QCD Working Group to estimate them independently. However, the problem remains that certain experiments consistently make more conservative estimates

---

[6]There is, however, an ambiguity as to whether the uncertainty due to the finite sizes of Monte Carlo samples should be included in $\sigma_{stat.}$ or in $\sigma_{exp.}$. With the exception of LEP1 results, this contribution is generally small in comparison to both $\sigma_{stat.}$ and $\sigma_{exp.}$.

	T	M_H	B_W	B_T	C	y_{23}
ALEPH	0.0008	0.0009	0.0006	0.0007	0.0007	0.0010
DELPHI	0.0012	0.0019	0.0021	0.0019	0.0022	–
L3	0.0023	0.0011	0.0018	0.0019	0.0016	–
OPAL	0.0024	0.0017	0.0027	0.0034	–	0.0042

Table 4.2: Experimental systematic uncertainties in the α_S measurements quoted by the four Collaborations at LEP1

than others. Consider, for example, the LEP1 measurements shown in Table 4.2, which suggest that the experimental systematic uncertainties quoted by ALEPH are consistently lower than those for the other Collaborations. Experiments do, of course, have their own unique strengths and weaknesses, which should be manifest in the systematic uncertainties; however, it was felt that such extreme differences as seen in Table 4.2 were not justified, and would lead to unfair weighting in the combined measurement. We have therefore averaged the experimental systematic uncertainties between all contributing experiments, for each variable and centre-of-mass energy.

4.4.1.3   Hadronisation uncertainties, $\sigma_{\text{had.}}$

As described in Section 3.5.4.2, the uncertainties due to non-perturbative modelling are estimated using three different Monte Carlo programs (PYTHIA[7], HERWIG and ARIADNE) to calculate hadronisation corrections to the event shape distributions. The differences between the α_S values obtained in the three cases should give an indication of the uncertainty. However, the exact definitions vary between Collaborations: some have taken the largest deviation from the PYTHIA result, while others have taken the standard deviation of the three results, for example. In the past, OPAL has also considered variations of certain parameters within the individual models [8–11].

For the combined LEP measurement, we have agreed a universal definition for the hadronisation uncertainty. The Collaborations each provided three sets of α_S measurements, corresponding to the three Monte Carlo event generators; the PYTHIA result is taken as the central value, and the standard deviation of the

---

[7]For some of the earlier LEP results, the hadronisation corrections were performed using JETSET, which has since merged with PYTHIA.

three results gives the uncertainty. The hadronisation uncertainties published individually by the Collaborations were not used.

4.4.1.4 Perturbative theory uncertainties, $\sigma_{\mathrm{theo.}}$

Until recently, all four Collaborations have estimated the uncertainty associated with the perturbative QCD predictions by varying the renormalisation scale μ from $\frac{1}{2}\sqrt{s}$ to $2\sqrt{s}$. As we described in Section 1.8 and in Ref. [12], however, we have now developed a more sophisticated "uncertainty band" method, involving several parameter variations. The perturbative theory uncertainties are now estimated independently by the LEP QCD Working Group, and the values quoted by the Collaborations are ignored.

4.4.2 Correlation terms in the covariance matrix

To determine the off-diagonal parts of the covariance matrix V, certain assumptions must be made about the correlation of uncertainties between different measurements. The results provided by the Collaborations do not explicitly include information on these correlations, so we must make our own estimates. We shall see later, in Section 4.5, that our initial naïve choice of correlations will lead to somewhat unexpected results. However, we will proceed in this section with a description of our *a priori* expectations for the off-diagonal part of the covariance matrix.

As with the uncertainties themselves, the covariances V_{ij} can be written as a sum of four contributions, and these will be treated separately.

4.4.2.1 Correlation of statistical uncertainties

The statistical uncertainties for measurements at different centre-of-mass energies or different experiments are completely uncorrelated. However, fits to different event shape distributions measured by the same experiment at the same centre-of-mass energy will be statistically correlated. For example, an upward fluctuation in the number of three- or four-jet events may increase the measured values of α_{S} from all six event shape variables.

The correlation coefficients between pairs of fits to different variables may be estimated using simulated data samples. A large number of detector-level Monte Carlo subsamples were generated at each centre-of-mass energy, with the same inte-

	T	M_{H}	B_{W}	B_{T}	C	y_{23}
T	1.00 1.00	0.79 0.77	0.77 0.62	0.80 0.64	0.86 0.66	0.75 0.53
M_{H}		1.00 1.00	0.86 0.76	0.81 0.76	0.78 0.75	0.79 0.61
B_{W}			1.00 1.00	0.84 0.81	0.80 0.67	0.83 0.81
B_{T}				1.00 1.00	0.82 0.80	0.79 0.68
C					1.00 1.00	0.70 0.60
y_{23}						1.00 1.00

Table 4.3: Statistical correlation coefficients between α_{S} measurements using different event shape observables at 206 GeV. The top coefficients of each pair were estimated using ALEPH Monte Carlo samples, while the lower coefficients were estimated by OPAL. Both sets of fits were performed using the OPAL fit ranges.

grated luminosity as the data, as explained in Section 3.5.3.2. The six event shape distributions were calculated for each subsample, and 'unfolded' back to the hadron level in the same way as the data. A set of six α_{S} measurements was hence obtained from each simulated data sample. Finally, the fifteen correlation coefficients were calculated between pairs of α_{S} values from different observables.

The statistical correlation coefficients used in our LEP α_{S} combination were evaluated by the ALEPH Collaboration, using simulated ALEPH data [139]. Separate correlation coefficients were estimated for each experiment, however, due to differing choices of fit range. We have independently cross-checked the correlations calculated for OPAL measurements at $\sqrt{s} = 206$ GeV, using OPAL Monte Carlo samples: the results of this comparison are shown in Table 4.3. The uncertainties in the ALEPH and OPAL values for the correlation coefficients are estimated to be approximately ± 0.03 and ± 0.04 respectively. There is some evidence of a slight discrepancy (the ALEPH coefficients are all larger than our OPAL estimates, by an average of 0.10), but tests have shown that a difference at this level will not affect our results significantly.

4.4.2.2 Correlation of experimental systematic uncertainties

We do not expect the experimental systematic uncertainties to be correlated between measurements from different Collaborations. However, there should be a partial correlation between the experimental uncertainties for measurements from the same experiment, using different observables or different centre-of-mass energies. It is impossible to calculate precise correlation coefficients for these uncertainties, since we do not have a well-defined statistical ensemble; we would need to simulate an infinite set of *detectors* and *analyses*, with calibration constants and cut values varied according according to some arbitrary distribution. This is in contrast to the correlation of statistical uncertainties, for which our ensemble is an infinite set of *events* occurring with well-defined probabilities.

A notable feature of the experimental uncertainty is that it contains several independent contributions, some of which apply only at certain centre-of-mass energies. For example, the estimation and subtraction of four-fermion background does not contribute an uncertainty at energies below the W^+W^- pair threshold. Similarly, biases related to the response of the detector may change from year to year, and will affect different observables in different ways. With this in mind, we will adopt a "minimum overlap" convention for the correlation of experimental systematic uncertainties; the covariance for a pair of measurements from the same experiment is defined as the smaller of the two corresponding variances:

$$V_{ij}^{\text{exp.}} = \min\left\{ (\sigma_i^{\text{exp.}})^2, (\sigma_j^{\text{exp.}})^2 \right\} \quad . \tag{4.15}$$

This is probably a slight overestimate, since it assumes that *all* of the contributions to the smaller of the two variances are fully correlated with corresponding equal-sized contributions to the larger variance. However, it is felt that an overestimate of the covariance will be 'safer' than an underestimate, since it should lead to a more conservative total uncertainty in the weighted mean.

4.4.2.3 Correlation of hadronisation uncertainties

Without a complete understanding of non-perturbative QCD, we cannot precisely calculate the correlations between our hadronisation uncertainties. Such a calculation would require us to define a large ensemble of alternative hadronisation models, *and* to know their relationship to true non-perturbative physics.

However, we can make very rough estimates of these correlations, using the three Monte Carlo programs available to us. If the fitted α_S results from the three generators always differ by the same amounts, and in the same directions, we can deduce that the hadronisation uncertainties are highly correlated; if the pattern of the three generators' results is different for each measurement, however, the uncertainties will be uncorrelated. This is based on the (perhaps naïve) assumption that true non-perturbative QCD can be regarded as a fourth independent 'generator', so that the mutual differences between PYTHIA, HERWIG and ARIADNE can be used to model the difference between PYTHIA and true physics.

Correlations between observables

Figure 4.5 compares OPAL α_S measurements using the three generators, for each of the six event shape observables. For LEP2 data, we observe a similar pattern for all observables: in most cases we have

$$\alpha_\mathrm{S}^\mathrm{HERWIG} \ < \ \alpha_\mathrm{S}^\mathrm{PYTHIA} \ < \ \alpha_\mathrm{S}^\mathrm{ARIADNE} \quad .$$

The distribution of 91 GeV fits is somewhat more random. However, for the majority of our results, we deduce that the hadronisation uncertainties are highly, but not fully, correlated between fits to different observables. As a crude estimate of these correlations, we will make the same "minimum overlap" assumption as defined in Equation 4.15 for the experimental systematic uncertainties. [8]

Correlations between energy scales

In Figure 4.6, we compare differences between the three generators at eight centre-of-mass energies. We observe a high degree of correlation between the hadronisation uncertainties at neighbouring energy scales. As the energy gap increases, the pattern of the three generators is seen to change more significantly; however, between most pairs of LEP energy scales, we can safely assume that the uncertainties are highly correlated. Once again, we apply the minimum overlap assumption.

---

[8]The minimum overlap assumption is not so easily justified for hadronisation uncertainties, because they are not derived from several independent contributions added in quadrature. However, we will see later (Section 4.9) that precise estimates of these correlations are not needed for our final combination. The crude simplifications made in this discussion will not, therefore, compromise our results.

Correlations between experiments

Finally, in Figure 4.7, we make the same comparison between the four LEP experiments. In this case, we see very little correlation between the patterns of the three generators in each Collaboration. As we demonstrated in Section 4.1.3, the independent tuning of Monte Carlo event generators by the four Collaborations has led to significant differences between the predicted hadronisation corrections. This suggests that the correlation between hadronisation uncertainties for different experiments can be neglected.

4.4.2.4 Correlation of perturbative theory uncertainties

Correlations between experiments

As we discussed in Section 4.1.1, we have taken care to ensure that all four Collaborations are using the same perturbative theory predictions for the event shape distributions. Thus the uncertainties due to uncomputed higher-order terms should be strongly correlated between measurements from different experiments. They will not be *fully* correlated in reality, because each Collaboration has chosen its own fit ranges; however, the extent of the overlap in these ranges suggests that we can treat the correlations as 100% in practice.

Correlations between energy scales

Between different energy scales, we also expect the theory uncertainties to be highly correlated. Setting the renormalisation scale $\mu = Q$, our order-by-order theory prediction for the cumulative distribution of the event shape y is given by

$$R(y, Q) \;=\; 1 \;+\; \mathcal{A}(y)\,\alpha_{\mathrm{S}}(Q) \;+\; \mathcal{B}(y)\,\alpha_{\mathrm{S}}^2(Q) \;+\; \underbrace{\mathcal{C}(y)\,\alpha_{\mathrm{S}}^3(Q) \;+\; \mathcal{D}(y)\,\alpha_{\mathrm{S}}^4(Q) \;+\; \ldots}_{\text{unknown higher orders}}$$

$$(4.16)$$

If the unknown coefficient functions $\mathcal{C}(y), \mathcal{D}(y), \ldots$ in this expansion are of similar magnitudes, which we intuitively expect, our theoretical error will be dominated by the first unknown term:

$$\mathcal{C}(y)\,\alpha_{\mathrm{S}}^3(Q) \;\gg\; \mathcal{D}(y)\,\alpha_{\mathrm{S}}^4(Q) \;\gg\; \mathcal{E}(y)\,\alpha_{\mathrm{S}}^5(Q) \;\ldots \quad . \qquad (4.17)$$
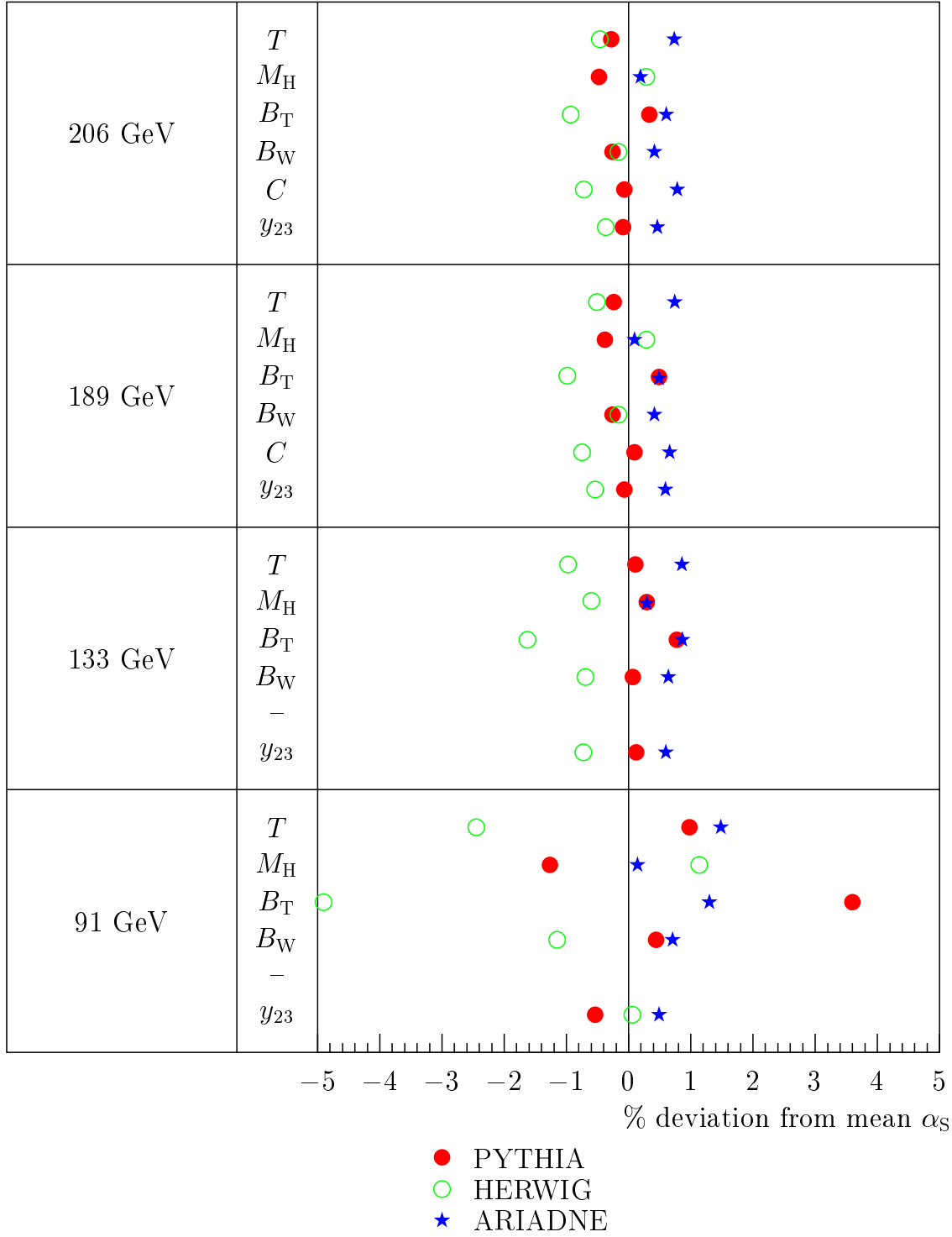
Figure 4.5: The spread of α_S fit results using PYTHIA, HERWIG and ARIADNE hadronisation corrections, for fits to T, M_H, B_T, B_W, C and y_{23}. This comparison uses OPAL data, at centre-of-mass energies of 91, 133, 189 and 206 GeV. In each case, the three results are plotted as percentage deviations from their mean value. *(Note, however, that the "central value" used in our analyses is the PYTHIA result, not the mean result.)*
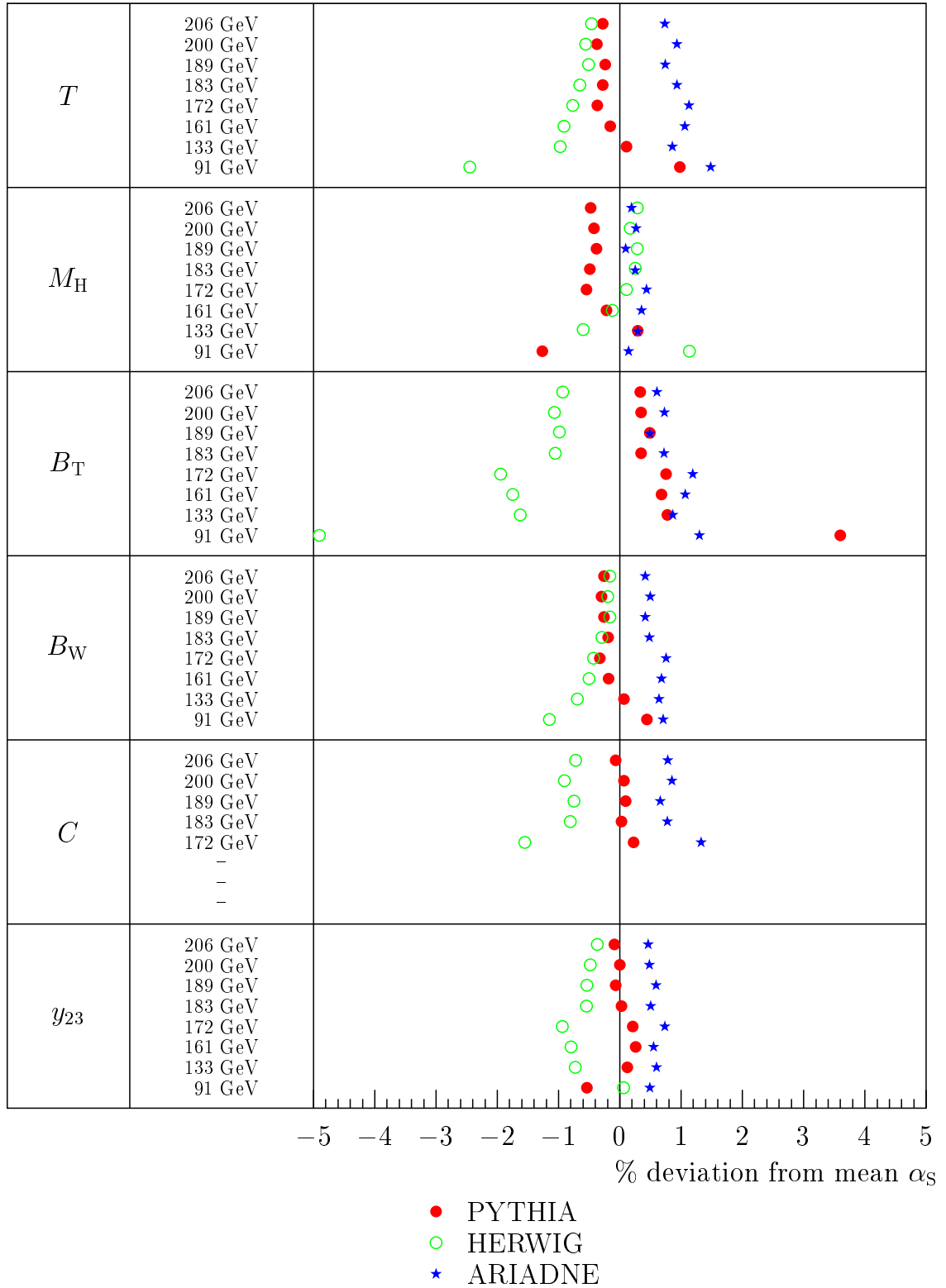
Figure 4.6: The spread of α_S fit results using PYTHIA, HERWIG and ARIADNE hadronisation corrections, at centre-of-mass energies in the range 91–206 GeV. This comparison uses the six observables T, M_H, B_T, B_W, C and y_{23}, measured by OPAL. In each case, the three results are plotted as percentage deviations from their mean value.
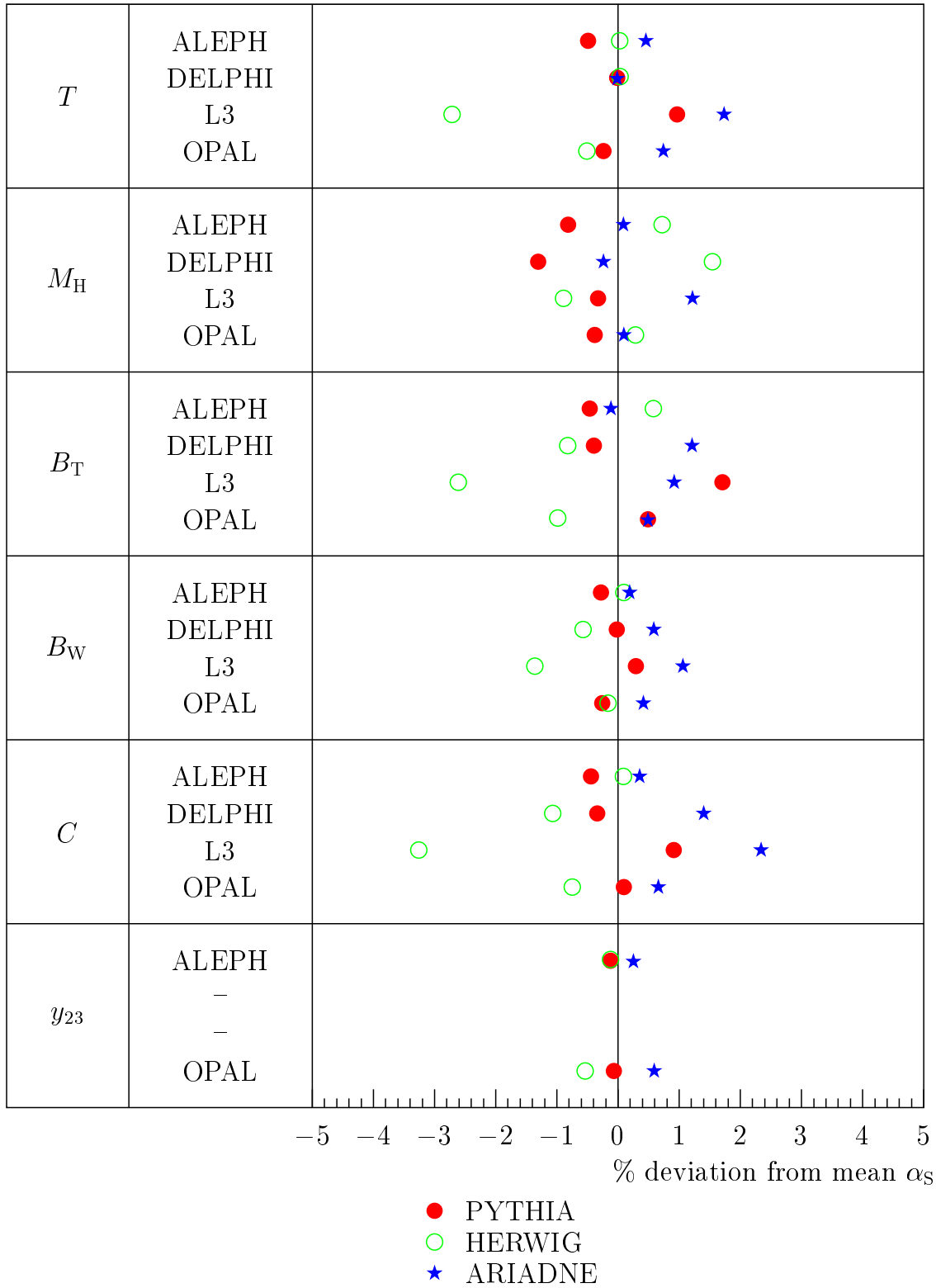
Figure 4.7: The spread of α_S fit results using PYTHIA, HERWIG and ARIADNE hadronisation corrections, from ALEPH, DELPHI, L3 and OPAL. This comparison uses the six observables T, M_H, B_T, B_W, C and y_{23}, measured at 189 GeV centre-of-mass energy. In each case, the three results are plotted as percentage deviations from their mean value.

Since $\mathcal{C}(y)$ does not depend on the energy scale Q, our uncertainty on this first term will be fully correlated between energy scales. To see the effect of the second unknown term, let us consider the functions $\mathcal{C}(y)$ and $\mathcal{D}(y)$ to be independent random variables. We can calculate the covariance between the cumulative distributions $R(y, Q_i)$ at two different energy scales Q_1 and Q_2, as follows:

$$
\begin{aligned}
\mathrm{Cov}&\big[R(y,Q_1), R(y,Q_2)\big] \\
&= \ \mathrm{Cov}\left[\mathcal{C}(y)\,\alpha_\mathrm{S}^3(Q_1) + \mathcal{D}(y)\,\alpha_\mathrm{S}^4(Q_1)\ ,\ \mathcal{C}(y)\,\alpha_\mathrm{S}^3(Q_2) + \mathcal{D}(y)\,\alpha_\mathrm{S}^4(Q_2)\right] \\
&= \ \left(\,\alpha_\mathrm{S}(Q_1)\,\alpha_\mathrm{S}(Q_2)\,\right)^3 \mathrm{Var}\left[\mathcal{C}(y)\right] \ + \ \left(\,\alpha_\mathrm{S}(Q_1)\,\alpha_\mathrm{S}(Q_2)\,\right)^4 \mathrm{Var}\left[\mathcal{D}(y)\right] \\
&\equiv \ (\,\alpha_1\alpha_2\,)^3\,\sigma_\mathcal{C}^2 \ + \ (\,\alpha_1\alpha_2\,)^4\,\sigma_\mathcal{D}^2 \quad,
\end{aligned}
\tag{4.18}
$$

where we have defined $\sigma_\mathcal{C}^2 \equiv \mathrm{Var}\left[\mathcal{C}(y)\right]$, $\sigma_\mathcal{D}^2 \equiv \mathrm{Var}\left[\mathcal{D}(y)\right]$ and $\alpha_i \equiv \alpha_\mathrm{S}(Q_i)$. The corresponding correlation coefficient ρ, between $R(y, Q_1)$ and $R(y, Q_2)$, is then given by

$$
\begin{aligned}
\rho \ &= \ \frac{(\,\alpha_1\alpha_2\,)^3\,\sigma_\mathcal{C}^2 \ + \ (\,\alpha_1\alpha_2\,)^4\,\sigma_\mathcal{D}^2}{\sqrt{\left((\,\alpha_1^3\,\sigma_\mathcal{C}\,)^2 \ + \ (\,\alpha_1^4\,\sigma_\mathcal{D}\,)^2\right)\left((\,\alpha_2^3\,\sigma_\mathcal{C}\,)^2 \ + \ (\,\alpha_2^4\,\sigma_\mathcal{D}\,)^2\right)}} \\
&= \ \frac{\sigma_\mathcal{C}^2 \ + \ \alpha_1\alpha_2\sigma_\mathcal{D}^2}{\sqrt{\left(\sigma_\mathcal{C}^2 \ + \ \alpha_1^2\,\sigma_\mathcal{D}^2\right)\left(\sigma_\mathcal{C}^2 \ + \ \alpha_2^2\,\sigma_\mathcal{D}^2\right)}} \\
&\approx \ 1 \ - \ \frac{\sigma_\mathcal{D}^2}{2\,\sigma_\mathcal{C}^2}\,(\alpha_1 - \alpha_2)^2 \quad.
\end{aligned}
\tag{4.19}
$$

Over the full range of LEP energy scales, including those of radiative events used by the L3 Collaboration, we have

$$
|\alpha_1 - \alpha_2| \ \leq \ \alpha_\mathrm{S}(206\ \mathrm{GeV}) - \alpha_\mathrm{S}(41\ \mathrm{GeV}) \ \approx \ 0.03 \quad,
$$

so that

$$
\rho \ \gtrsim \ 1 \ - \ 0.0005\,\frac{\sigma_\mathcal{D}^2}{\sigma_\mathcal{C}^2} \quad.
$$

Therefore, provided the uncertainties $\sigma_\mathcal{C}$ and $\sigma_\mathcal{D}$ on the two coefficient functions are of similar magnitude, the correlation coefficient ρ will be very close to unity. Since we have no reason to suspect *a priori* that $\mathcal{C}(y)$ and $\mathcal{D}(y)$ should be of vastly differing magnitude, we thus assert that the uncertainties of our perturbative theory predictions $R(y, Q)$ are fully correlated between energy scales. Assuming that

changes in our fit-ranges are negligible, this also implies that the corresponding theoretical uncertainties in our measurements of α_S are fully correlated.

Correlations between observables

We must also consider the correlation of theory uncertainties between measurements using different observables. We know that the observables themselves are statistically correlated, and that their perturbative QCD calculations have much in common. Therefore it should be expected that the uncalculated higher-order corrections to these calculations will also be correlated. However, the extent of this correlation is difficult to estimate.

The LEP QCD Working Group has attempted to study the correlation of theory uncertainties between observables in the following way. We define an "ensemble of theories," by varying the parameters x_μ, x_L and p.[9] Our ensemble comprises an $N_1 \times N_2 \times N_3$ grid, with each point representing a particular set of values for these three parameters. At every point on the grid, we fit the distributions of the six event shape distributions, using the same (arbitrarily chosen) sample of events in each case. We can then measure the correlation coefficient between fits to each pair of observables. This method has two drawbacks, however:

- The results will depend on the size, density and metric of the grid, along its three axes. For example, a grid spaced evenly with respect to x_μ may give different results from a grid spaced evenly with respect to $\ln x_\mu$.

- Without justification, we are varying the parameters x_μ, x_L and p *simultaneously* for all six event shape observables. In reality, the true higher-order corrections to these six distributions may be best represented by *different* sets of values for these parameters.

Nonetheless, all the results [140] obtained by this method indicated high degrees of correlation, of the order $\rho \gtrsim 0.9$.

Based on the conclusions of this section, it is tempting to define a 100% correlation between all pairs of theoretical uncertainties in our covariance matrix. However, this would imply that every theoretical error[10] can be expressed in terms of a single

---

[9]These are the same parameters used in the "uncertainty band" method to estimate our theoretical uncertainties, as described in Section 1.8.

[10]The word 'error' here refers strictly to the unknown deviation between the true and measured values of α_S; the 'uncertainty' is the RMS of the error distribution.

	Different experiments	Different energies	Different observables
$V_{ij}^{\text{stat.}}$	0	0	$\rho_{ij}^{\text{stat.}}\sigma_i\sigma_j$
$V_{ij}^{\text{exp.}}$	0	$\min(\sigma_i^2, \sigma_j^2)$	$\min(\sigma_i^2, \sigma_j^2)$
$V_{ij}^{\text{hadr.}}$	0	$\min(\sigma_i^2, \sigma_j^2)$	$\min(\sigma_i^2, \sigma_j^2)$
$V_{ij}^{\text{theo.}}$	$\sigma_i\sigma_j$	$\sigma_i\sigma_j$	$0.90\,\sigma_i\sigma_j$

Table 4.4: The approximate values expected for off-diagonal elements of the covariance matrix V

unknown random variable δ, with zero expectation and unit variance:

$$\left[\, \alpha_i^{\text{measured}} - \alpha_i^{\text{true}} \,\right]^{\text{theo.}} = \sigma_i^{\text{theo.}}\,\delta \quad . \tag{4.20}$$

If the measurements α_i are combined in a weighted mean $\alpha_S = \sum w_i\alpha_i$, such that the weights w_i satisfy

$$\sum_i w_i\,\sigma_i^{\text{theo.}} = 0 \quad , \tag{4.21}$$

then the theoretical uncertainty of our combined α_S will be zero. This phenomenon has been observed numerically in our weighted means, and is clearly unrealistic.

We therefore modify our ansatz, for the moment, by defining the correlation coefficient ρ between theoretical uncertainties for different observables to be 0.9 instead of 1. Later we will see that even this assumption is unsatisfactory; however, it does avoid the immediate difficulty described above, and the resulting α_S is reasonably stable with respect to small changes in ρ.

4.4.2.5 Summary

The anticipated off-diagonal elements of the covariance matrix, as discussed in Sections 4.4.2.1–4.4.2.4, are summarised in Table 4.4.

Where more than one of the three column-headings applies in this table, the covariance is taken to be the smallest of the entries in the corresponding columns. For example in the case

$$i = [\,\text{OPAL},\ 189\ \text{GeV},\ T\,] \quad , \quad j = [\,\text{OPAL},\ 133\ \text{GeV},\ B_{\text{W}}\,] \quad ,$$

we take the smaller of the two covariances listed in the "different energies" and

"different observables" columns:

$$V_{ij}^{\text{stat.}} = 0 \ , \quad V_{ij}^{\text{exp.}} = \min(\sigma_i^2, \sigma_j^2) \ , \quad V_{ij}^{\text{hadr.}} = \min(\sigma_i^2, \sigma_j^2) \ , \quad V_{ij}^{\text{theo.}} = 0.90 \, \sigma_i \, \sigma_j \quad .$$

The uncertainties σ_i here refer to the corresponding contribution $\sigma_i^{\text{exp.}}$, $\sigma_i^{\text{hadr.}}$ or $\sigma_i^{\text{theo.}}$.

4.5   A naïve measurement of $\alpha_{\mathrm{S}}(M_{\mathrm{Z}})$

Using the input measurements tabulated in Appendix D, and the covariance matrix defined in the previous section, we can apply the "weighted mean" method described in Section 4.3.2 to obtain the following measurement:

$$
\begin{aligned}
\alpha_{\mathrm{S}}(M_{\mathrm{Z}}) \ &= \ 0.1162 \ \pm \ 0.0008 \ \text{(stat.)} \ \pm \ 0.0008 \ \text{(exp.)} \ \pm \ 0.0003 \ \text{(hadr.)} \ \pm \ 0.0017 \ \text{(theo.)} \\
&= \ 0.1162 \ \pm \ 0.0008 \ \text{(stat.)} \ \pm \ 0.0019 \ \text{(syst.)} \\
&= \ 0.1162 \ \pm \ 0.0021 \ \text{(total)}
\end{aligned}
$$

with $\chi^2/\text{d.o.f.} = 432/193$. As a cross-check, we also performed a numerical minimisation of χ^2 as described in Section 4.3.1; the result was identical, except that no breakdown of the total uncertainty was possible.

Our measurement suffers three obvious problems:

- The χ^2 value indicates unreasonably poor agreement between the weighted average and its contributing measurements.

- The statistical uncertainty of the combined value is larger than that of several contributing measurements.

- The current world average quoted by the Particle Data Group [13] is $\alpha_{\mathrm{S}}(M_{\mathrm{Z}}) = 0.1172 \pm 0.0020$. Although our own central result is in good numerical agreement with this value,[11] we would expect our result to have a much larger total uncertainty than that of the PDG; the PDG average includes α_{S} measurements from many different processes, including τ decays and deep inelastic scattering, which are more precise than those from $\mathrm{e}^+\mathrm{e}^-$ event shapes.

These problems stem from our poor knowledge of certain parts of the covariance matrix. Various attempts have been made in the past by the LEP QCD Working

---

[11]$\Delta\alpha_{\mathrm{S}}(M_{\mathrm{Z}}) = -0.0010 \pm 0.0029$, assuming no correlation between the respective uncertainties.

Group, to reduce our sensitivity to fluctuations in the covariance matrix. These are described in a previous report by the group [141], and have led to results with more reasonable uncertainties and χ^2 values.

However, further investigation revealed severe internal inconsistencies in these results. Figure 4.8 shows a fit to all LEP α_S measurements derived from the total jet broadening, B_T, using the covariance matrix defined in Section 4.4. The global fit in this case predicts $\alpha_S(Q)$ to be higher than *all* of the fits at individual centre-of-mass energies. Such pathological fits have been confirmed independently by another member of the LEP QCD Working Group [142]. In the sections that follow, we discuss the symptoms, cause and remedy for these unacceptable fits.

4.6 Dependence on the correlation coefficients

When defining the correlations between uncertainties in different measurements, many imprecise and subjective assumptions were made. We should therefore ensure that our combined $\alpha_S(M_Z)$ measurement is not excessively sensitive to any reasonable variation of these estimates. In Figure 4.9, we show the dependence of our fitted $\alpha_S(M_Z)$ values on various subsets of the correlation coefficients between systematic uncertainties. For the purposes of this plot, we define five independent groups of coefficients:

1. Correlations of statistical uncertainties between measurements from different observables, using the same experiments at the same centre-of-mass energy: these correlations are not varied, as they are known to about 10% precision, as described in Section 4.4.2.1.

2. Correlations of experimental systematic uncertainties, between pairs of measurements from the same experiment

3. Correlations of hadronisation uncertainties, between pairs of measurements from the same experiment

4. Correlations of theory uncertainties, between measurements using the same observable

5. Correlations of theory uncertainties, between measurements using different observables
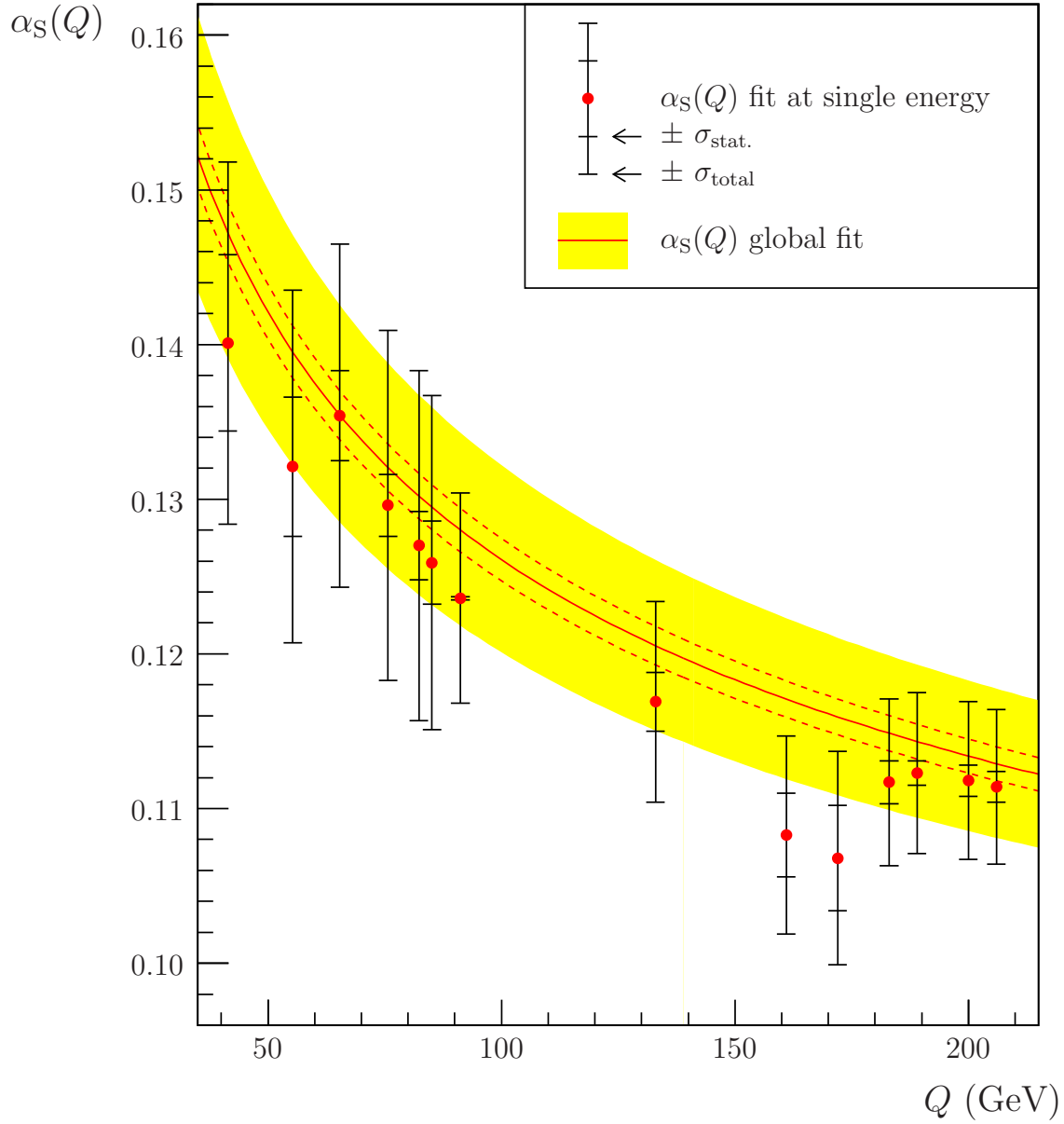
Figure 4.8: A pathological combination of 35 $\alpha_S(Q)$ measurements derived from the total jet broadening, B_T, using the 'naïve' covariance matrix described in Section 4.4. Each point represents a combination of all available measurements at a single energy, while the curve represents a simultaneous fit at all energies.

To study the effects of these correlations on our α_S fits, we vary them in three different ways:

- Switch the correlations 'on', one at a time, leaving the other types of correlation switched 'off'. This mode of variation is indicated in Figure 4.9 by the solid red, green, blue and magenta curves.

- Switch the correlations 'off', one at a time, leaving the other types of correlation fixed at their default values. This mode of variation is indicated by the dashed red, green, blue and magenta curves.

- Switch all correlations 'on' simultaneously. This mode of variation is indicated by the solid cyan curve.

These variations have been applied to fits to each individual event shape observable, in Figures 4.9(a)–(f), and also for global fits to all observables, in Figure 4.9(g). In all cases, the variable r is used as a "switching parameter" for the correlations which are to be varied: $r = 0$ corresponds to zero correlation, while $r = 1$ corresponds to the correlation assumed in Section 4.4.2.

With the exception of B_T, shown in Figure 4.9(d), we find that the fits using single observables are relatively insensitive to variation of the correlation coefficients. Generally the range of variation in the combined $\alpha_S(M_Z)$ value is much smaller than the systematic uncertainties of the input measurements. When all observables are used simultaneously in a global fit, however, as shown in Figure 4.9(g), we find a more pronounced dependence on the covariance matrix. Several pieces of evidence in Figure 4.9 suggest that this dependence can be attributed to the correlation of theory uncertainties between measurements using different observables ('type 5'):

- Correlation type 5 is only present in the global fit, where more than one observable is involved. This is also the only case in which a substantial variation is seen in the $\alpha_S(M_Z)$ fit.

- When correlation type 5 remains switched off, the $\alpha_S(M_Z)$ fit shows very little dependence on the other correlation types; this is indicated by the solid red, green and blue curves in Figure 4.9(g).

- When correlation type 5 is switched on *alone*, we find a large amplitude of variation in the $\alpha_S(M_Z)$ fit, with some apparently chaotic behaviour. For
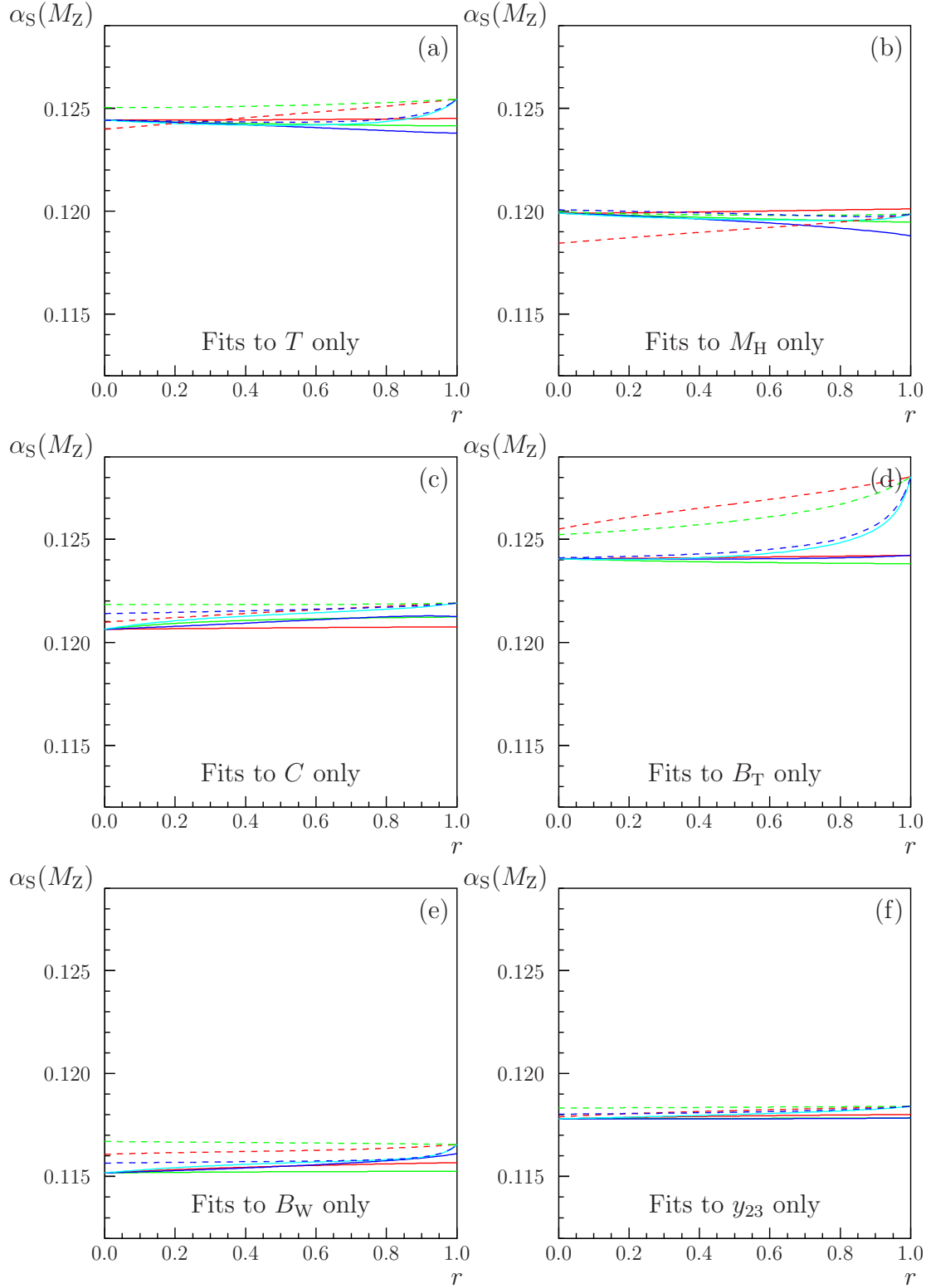
Figure 4.9: Variation of the fitted $\alpha_S(M_Z)$ value with respect to certain subsets of terms in the covariance matrix V. Each colour and line-style in the legend (shown on the next page) represents a different variation of the covariance matrix with respect to the parameter r; only the off-diagonal terms $(V_{ij} : i \neq j)$ are varied. For clarity, the covariance terms which depend on r are highlighted in red. The same legend applies to all seven plots.

	$V_{ij}^{\text{stat.}}$	$V_{ij}^{\text{exp.}}$	$V_{ij}^{\text{hadr.}}$	$V_{ij}^{\text{theo.}}$	$V_{ij}^{\text{theo.}}$
	Same expt. and energy	Same expt.	Same expt.	Same observables	Different observables
—— (red)	$\rho_{ij}^{\text{stat.}}\,\sigma_i\,\sigma_j$	$r\min(\sigma_i^2,\sigma_j^2)$	0	0	0
—— (black)	$\rho_{ij}^{\text{stat.}}\,\sigma_i\,\sigma_j$	0	$r\min(\sigma_i^2,\sigma_j^2)$	0	0
—— (blue)	$\rho_{ij}^{\text{stat.}}\,\sigma_i\,\sigma_j$	0	0	$r\,\sigma_i\,\sigma_j$	0
—— (dark blue)	$\rho_{ij}^{\text{stat.}}\,\sigma_i\,\sigma_j$	0	0	0	$0.9\,r\,\sigma_i\,\sigma_j$
- - - - (black)	$\rho_{ij}^{\text{stat.}}\,\sigma_i\,\sigma_j$	$r\min(\sigma_i^2,\sigma_j^2)$	$\min(\sigma_i^2,\sigma_j^2)$	$\sigma_i\,\sigma_j$	$0.9\,\sigma_i\,\sigma_j$
- - - - (green)	$\rho_{ij}^{\text{stat.}}\,\sigma_i\,\sigma_j$	$\min(\sigma_i^2,\sigma_j^2)$	$r\min(\sigma_i^2,\sigma_j^2)$	$\sigma_i\,\sigma_j$	$0.9\,\sigma_i\,\sigma_j$
- - - - (black)	$\rho_{ij}^{\text{stat.}}\,\sigma_i\,\sigma_j$	$\min(\sigma_i^2,\sigma_j^2)$	$\min(\sigma_i^2,\sigma_j^2)$	$r\,\sigma_i\,\sigma_j$	$0.9\,\sigma_i\,\sigma_j$
- - - - (magenta)	$\rho_{ij}^{\text{stat.}}\,\sigma_i\,\sigma_j$	$\min(\sigma_i^2,\sigma_j^2)$	$\min(\sigma_i^2,\sigma_j^2)$	$\sigma_i\,\sigma_j$	$0.9\,r\,\sigma_i\,\sigma_j$
—— (cyan)	$\rho_{ij}^{\text{stat.}}\,\sigma_i\,\sigma_j$	$r\min(\sigma_i^2,\sigma_j^2)$	$r\min(\sigma_i^2,\sigma_j^2)$	$r\,\sigma_i\,\sigma_j$	$0.9\,r\,\sigma_i\,\sigma_j$

Figure 4.9 (contd.)

$r \gtrsim 0.3$, the weighted mean contains only measurements using thrust (T), and the weights w_i for all other measurements vanish; therefore no further dependence on r is observed. This is indicated by the solid magenta curve in Figure 4.9(g).

- A large amplitude of variation is also seen when correlations of theory uncertainties between measurements using the *same* observable ('type 4') are switched off, while leaving type-5 correlations switched on. Switching off the type-4 correlations in this case allows the type-5 correlations to dominate the off-diagonal part of the covariance matrix. This is indicated by the dashed blue curve in Figure 4.9(g).

We must therefore seek to explain why the fits are so sensitive to this type of correlation, and attempt to stabilise them.

4.7 The problem of negative weights

In our formulation of the weighted mean method, in Section 4.3.2, we did not place any restriction on the signs of the weights w_i; the only constraint was that their sum should be unity. However, one intuitively expects that a weighted mean of N measurements should move in the "right direction" if one of the contributing measurements changes:[12]

$$\frac{\partial \hat{\lambda}}{\partial y_i'} \geq 0 \quad \forall i \quad . \tag{4.22}$$

Recalling that $\hat{\lambda}$, our measurement of $\alpha_S(M_Z)$, is given by $\sum_i w_i y_i'$, this implies

$$w_i \geq 0 \quad \forall i \quad . \tag{4.23}$$

Requiring the weights w_i to be non-negative also implies that the weighted mean will be *bounded* by the range of the input measurements, as one expects.

The weights contributing to the combination in Section 4.5 do not satisfy the above condition. The 194 weights vary in this case between -30.5% and $+53.6\%$,[13] with a total positive weight of $+400.8\%$ being balanced by a total negative weight

---

[12]As in Section 4.3.2, each input measurement has been converted to the Z^0 mass scale, and denoted by $y_i' \equiv [\alpha_S(M_Z)]_i$.

[13]The minimum and maximum weights are those for the OPAL B_W and ALEPH y_{23} measurements respectively, both at 91 GeV.

of -300.8%. This explains why the global fit presented in Figure 4.8 appears inconsistent with the fits at individual energy points; it also explains the large statistical uncertainty of the combined value.

We therefore wish to reformulate our combination algorithm, such that the weights w_i are constrained to be positive. One approach to this problem would be to vary the 194 weights, subject to the constraints $0 \leq w_i \leq 1$, such that χ^2 is minimised. This would lead to two difficulties:

- The practical implementation of this constrained minimisation would not be straightforward. We would need to minimise over the volume of a 194-dimensional hypercube, which has an enormous number of 'edges' and 'surfaces'.

- More importantly, our χ^2 would still be defined by inverting the same poorly-known covariance matrix which led to our unstable 'naïve' combination. A small change in our correlation assumptions could therefore lead to a dramatic change in our combined result, even if the weights are constrained to be positive.

Since the weights are functions of the covariance matrix V, as defined by Equation (4.11), we will instead attempt to eliminate the negative weights by modifying V. As we shall see later, this does inevitably lead to some compromises; however it will not prevent us from taking full account of the uncertainties in our final results.

4.8 Criteria for the avoidance of negative weights

As we derived in Section 4.3.2, the weights w_i can be expressed as a function of the covariance matrix V: [14]

$$w_i = \frac{\sum_j \left(V^{-1}\right)_{ij}}{\sum_{j,k} \left(V^{-1}\right)_{jk}} \quad . \tag{4.24}$$

We wish to find some conditions on the matrix V, to ensure that none of the weights are negative. In the general case, it is difficult to define any necessary or sufficient conditions under which this requirement is satisfied. However, there are some special cases in which the covariance matrix can be inverted analytically to obtain simple expressions for the weights w_i.

---

[14] Here V is the covariance matrix relating measurements of α_S at the Z^0 mass scale. We have dropped the notation V', used in Section 4.3.2.

4.8.1 The trivial case: uncorrelated measurements

When all correlations are removed from the covariance matrix, including those between statistical uncertainties, V and its inverse are both diagonal:

$$V_{ij} = \sigma_i^2 \, \delta_{ij} \tag{4.25}$$

$$\left(V^{-1}\right)_{ij} = \frac{1}{\sigma_i^2} \, \delta_{ij} \quad . \tag{4.26}$$

The weights in this case are guaranteed be positive, and are inversely proportional to the squares of the total uncertainties:

$$w_i = \frac{1/\sigma_i^2}{\sum_j 1/\sigma_j^2} \quad . \tag{4.27}$$

4.8.2 The weighted mean of two correlated measurements

Given two measurements y_1 and y_2, with variances σ_1^2 and σ_2^2 respectively, the covariance matrix and its inverse are given by

$$V = \begin{pmatrix} \sigma_1^2 & \mathrm{Cov}(y_1, y_2) \\ \mathrm{Cov}(y_1, y_2) & \sigma_2^2 \end{pmatrix} \tag{4.28}$$

$$V^{-1} = \frac{1}{\sigma_1^2 \sigma_2^2 - [\mathrm{Cov}(y_1, y_2)]^2} \begin{pmatrix} \sigma_2^2 & -\mathrm{Cov}(y_1, y_2) \\ -\mathrm{Cov}(y_1, y_2) & \sigma_1^2 \end{pmatrix} \quad , \tag{4.29}$$

and hence the ratio of weights contributing to the least-squares fit is

$$\frac{w_1}{w_2} = \frac{\sigma_2^2 - \mathrm{Cov}(y_1, y_2)}{\sigma_1^2 - \mathrm{Cov}(y_1, y_2)} \quad . \tag{4.30}$$

Both weights will therefore be positive, if and only if the covariance of y_1 and y_2 is less than both of the two variances: [15]

$$\mathrm{Cov}(y_1, y_2) < \sigma_\mathrm{min}^2 \tag{4.31}$$

When Condition (4.31) is violated, one of the two weights will become negative, and the weighted mean $w_1 y_1 + w_2 y_2$ may not lie between the measurements y_1 and

---

[15]It is impossible for both weights to be negative, as their sum is constrained to be unity.

y_2. This does not *necessarily* imply that the weighted mean is unreliable; it simply means that the uncertainties are dominated by a correlated systematic contribution. For example, if we have two measurements with fully correlated uncertainties, $y_1 \pm \sigma_1$ and $y_2 \pm \sigma_2$, we could write

$$
\begin{aligned}
y_1 &= y_{\text{true}} + \sigma_1 \delta \\
y_2 &= y_{\text{true}} + \sigma_2 \delta \quad ,
\end{aligned}
\tag{4.32}
$$

for some single unknown quantity δ with zero expectation and unit variance. As we described in Section 4.4.2.4, we could then deduce

$$
y_{\text{true}} = \frac{\sigma_1 y_2 - \sigma_2 y_1}{\sigma_1 - \sigma_2} \quad ,
\tag{4.33}
$$

with *no uncertainty*. A negative weight has been used in this example to cancel out completely the systematic uncertainty. There is nothing improper about this, provided the ratio of uncertainties σ_1/σ_2, and their correlation coefficient ($\rho = 1$ in this example), are known with sufficiently high precision. A legitimate physical example of this is discussed in Ref. [121]. In the case of our $\alpha_S(M_Z)$ combination, however, we do not have sufficient knowledge of the covariance matrix to "cancel out" systematic uncertainties in this way.

For cases with more than two measurements, it is difficult to find criteria analogous to Condition (4.31) to prevent negative weights. We can, of course, still write out the inverse covariance matrix explicitly, and determine relationships between the variances and covariances to ensure positive weights. However, even in the 3×3 case, it is difficult to interpret the constraints in meaningful terms. We will therefore consider another special case in which the covariance matrix may be inverted analytically.

4.8.3   A single fully-correlated source of systematic error, and uncorrelated statistical errors

Suppose each measurement y_i is subject to a statistical uncertainty σ_i and a *single* systematic error s_i. Suppose further that the systematic errors are fully correlated

between all measurements. The covariance matrix is therefore

$$
\begin{aligned}
V_{ij} &= \sigma_i \sigma_j \, \delta_{ij} + s_i s_j \\
       &= \sigma_i \sigma_j \, (\delta_{ij} + \beta_i \beta_j) \qquad \text{[no summation]} \ ,
\end{aligned}
\tag{4.34}
$$

where $\beta_i \equiv s_i/\sigma_i$. For example in the case of two measurements, we have

$$
V = \begin{pmatrix} \sigma_1^2 + s_1^2 & s_1 s_2 \\ s_1 s_2 & \sigma_2^2 + s_2^2 \end{pmatrix} \ .
\tag{4.35}
$$

As shown in Ref. [143], this covariance matrix may be inverted analytically:[16]

$$
\left(V^{-1}\right)_{ij} = \frac{1}{\sigma_i \sigma_j} \left(\delta_{ij} - \frac{\beta_i \beta_j}{1 + \sum_k \beta_k^2} \right) \ .
\tag{4.36}
$$

Substituting this into Equation (4.24), we obtain the weights.

$$
\begin{aligned}
w_i &= \frac{1}{\sum_{j,k} \left(V^{-1}\right)_{jk}} \left[\sum_j \frac{1}{\sigma_i \sigma_j} \left(\delta_{ij} - \frac{(s_i/\sigma_i)(s_j/\sigma_j)}{1 + \sum_k (s_k^2/\sigma_k^2)} \right) \right] \\
    &= \frac{1}{\sigma_i^2 \sum_{j,k} \left(V^{-1}\right)_{jk}} \left(1 - \frac{s_i \sum_j (s_j/\sigma_j^2)}{1 + \sum_j (s_j^2/\sigma_j^2)} \right)
\end{aligned}
\tag{4.37}
$$

To avoid negative weights, we therefore require

$$
1 - \frac{s_i \sum_j (s_j/\sigma_j^2)}{1 + \sum_j (s_j^2/\sigma_j^2)} > 0 \quad \forall i \ ,
\tag{4.38}
$$

so

$$
\sum_j \frac{s_j(s_i - s_j)}{\sigma_j^2} < 1 \quad \forall i \ .
\tag{4.39}
$$

Choosing s_i to be the largest of the systematic uncertainties $s_{\max}$, we arrive at the following necessary and sufficient condition for all weights w_i to be positive:

$$
\boxed{\sum_j \frac{s_j(s_{\max} - s_j)}{\sigma_j^2} < 1} \ .
\tag{4.40}
$$

---

[16]It is straightforward to verify that this expression satisfies $V^{-1}V = I$.

In the case of only two measurements, this inequality simplifies to

$$s_1 s_2 < \sigma_1^2 + s_1^2 \quad , \qquad \text{where} \quad s_1 < s_2 \quad , \qquad (4.41)$$

in agreement with our earlier result, Condition (4.31).[17] One obvious situation in which Condition (4.40) will be satisfied is the case in which all the systematic uncertainties are equal. In this case, the left-hand side of the inequality is zero, and the weights are identical to those in the uncorrelated case:

$$w_i = \frac{1/\sigma_i^2}{\sum_j 1/\sigma_j^2} \quad . \qquad (4.42)$$

4.8.4 Examples

Table 4.5 illustrates four hypothetical weighted means, with dominant but variable systematic uncertainties. In each case, the middle column shows the terms contributing to the sum in Equation (4.40).

In Example (a), we have

$$\sum_{i=1}^{5} \frac{s_i(s_{\max} - s_i)}{\sigma_i^2} = 0.96 \quad , \qquad \text{where} \quad s_{\max} = 8.0 \quad ,$$

so Condition (4.40) is satisfied; therefore, all five weights w_i are positive.

In Example (b), one of the systematic uncertainties (printed in boldface) has been modified from $s = 7.9$ to $s = 7.8$. Since this measurement has a small statistical uncertainty ($\sigma = 2.0$), the effect of this change is sufficient to violate Condition (4.40):

$$\sum_{i=1}^{5} \frac{s_i(s_{\max} - s_i)}{\sigma_i^2} = 1.15 \quad , \qquad \text{where} \quad s_{\max} = 8.0 \quad .$$

We now find that one of the weights w_i (the weight corresponding to the measurement with the largest systematic uncertainty $s_{\max}$) has become negative.

In Example (c), the largest systematic uncertainty $s_{\max}$ (also printed in boldface) has been modified from $s = 8.0$ to $s = 8.1$; all other uncertainties are identical to those in Example (a). In this case we have violated Condition (4.40) more severely

---

[17]The smallest total uncertainty $\sigma_{\min}$ in Condition (4.31) corresponds to the expression $\sqrt{\sigma_1^2 + s_1^2}$ in Condition (4.41).

Example (a)

| Uncertainties | | $\frac{s_i(s_{\max}-s_i)}{\sigma_i^2}$ | Weight |
σ_i (stat.)	s_i (syst.)		w_i
2.0	**7.9**	0.20	0.202
2.0	**8.0**	0.00	0.012
3.0	7.7	0.26	0.258
3.0	7.9	0.09	0.090
3.5	7.3	0.42	0.438
		Total: 0.96	Total: 1.000

Example (b)

| Uncertainties | | $\frac{s_i(s_{\max}-s_i)}{\sigma_i^2}$ | Weight |
σ_i (stat.)	s_i (syst.)		w_i
2.0	**7.8**	0.39	0.333
2.0	**8.0**	0.00	-0.046
3.0	7.7	0.26	0.232
3.0	7.9	0.09	0.064
3.5	7.3	0.42	0.417
		Total: 1.15	Total: 1.000

Example (c)

| Uncertainties | | $\frac{s_i(s_{\max}-s_i)}{\sigma_i^2}$ | Weight |
σ_i (stat.)	s_i (syst.)		w_i
2.0	**7.9**	0.39	0.261
2.0	**8.1**	0.00	-0.116
3.0	7.7	0.34	0.284
3.0	7.9	0.18	0.116
3.5	7.3	0.48	0.455
		Total: 1.39	Total: 1.000

Example (d)

| Uncertainties | | $\frac{s_i(s_{\max}-s_i)}{\sigma_i^2}$ | Weight |
σ_i (stat.)	s_i (syst.)		w_i
2.0	**7.9**	0.20	0.050
2.0	**7.9**	0.20	0.050
2.0	**8.0**	0.00	-0.134
2.0	**8.0**	0.00	-0.134
3.0	7.7	0.26	0.186
3.0	7.7	0.26	0.186
3.0	7.9	0.09	0.022
3.0	7.9	0.09	0.022
3.5	7.3	0.42	0.376
3.5	7.3	0.42	0.376
		Total: 1.92	Total: 1.000

Table 4.5: Examples illustrating the application of Condition (4.40), in combinations of hypothetical measurements.

than in Example (b), because the largest systematic uncertainty contributes to every term in the summation:

$$\sum_{i=1}^{5} \frac{s_i(s_{\max} - s_i)}{\sigma_i^2} = 1.39 \quad, \quad \text{where} \quad s_{\max} = 8.1 \quad .$$

We now have a negative weight of -11.6% in our hypothetical combination, compared with -4.6% in Example (b).

In Example (d), we have repeated each of the five measurements used in Example (a). The new measurements have uncorrelated statistical uncertainties, but their systematic uncertainties remain fully correlated with the original measurements. Condition (4.40) is now violated, since each term of the summation has been duplicated:

$$\sum_{i=1}^{10} \frac{s_i(s_{\max} - s_i)}{\sigma_i^2} = 2 \times 0.96 = 1.92 \quad, \quad \text{where} \quad s_{\max} = 8.0 \quad .$$

Once again, we have a negative weight. It is worth noting, in particular, that the weights in Example (d) are *not* equal to half of the corresponding weights in Example (a).

4.8.5 Application to the LEP $\alpha_\text{S}(M_\text{Z})$ combination

Our calculations discussed in the preceding sections are not strictly applicable to the combination of LEP $\alpha_\text{S}(M_\text{Z})$ measurements. Condition (4.40) is only valid in the case where *all* systematic uncertainties are *fully* correlated with all others; it does not allow for four independent sources of systematic uncertainty, nor for the detailed correlation assumptions discussed in Section 4.4.2. However, we can expect some of the same principles to apply. We have seen that the following factors influence the tendency toward negative weights:

- **Relative magnitudes of systematic and statistical uncertainties:**
  Measurements with systematically dominated uncertainties are most prone to negative weights. Previous combinations of statistically limited LEP measurements, such as the $W^{\pm}$ boson mass [144], have not suffered from negative weights.

- **Spread in the magnitudes of systematic uncertainties:**

  When systematic uncertainties have the same magnitude for all measurements, they do not influence the weights; they simply "carry through" as an uncertainty in the weighted mean. If the magnitudes vary, however, their spread must be small in comparison to the statistical uncertainties if negative weights are to be avoided.

- **Largest systematic uncertainty:**

  In Condition (4.40), the 'spread' of systematic uncertainties is measured in relation to the largest of them, s_max. As we saw in Example (c) of the preceding section, an increase in the largest uncertainty has a much greater effect than a decrease in one of the others.

- **Number of measurements:**

  The left-hand side of Condition (4.40) scales in proportion to the number of measurements. As we increase the number of terms contributing to the sum, as in Example (d), we must decrease the average size of each term to prevent the inequality being violated. For N measurements, the condition can be rewritten as

$$\left\langle \frac{s_i(s_\mathrm{max} - s_i)}{\sigma_i^2} \right\rangle < \frac{1}{N} \quad . \tag{4.43}$$

  When the uncertainties of all measurements are roughly equal, and are dominated by systematics,

$$\langle s_\mathrm{max} - s_i \rangle \lesssim \frac{\langle \sigma \rangle^2}{N \langle s \rangle} < \frac{\langle \sigma \rangle}{N} \quad . \tag{4.44}$$

  For our 194 measurements of $\alpha_\mathrm{S}(M_\mathrm{Z})$, which have $\sigma_\mathrm{stat.} \sim 0.002$ and $s = \sigma_\mathrm{syst.} \sim 0.005$, the fractional range of our systematic uncertainties would need to satisfy

$$\left\langle \frac{s_\mathrm{max} - s_i}{s_i} \right\rangle \lesssim \frac{0.002^2}{194 \times 0.005^2} = 0.08\,\% \quad .$$

  This condition is obviously not satisfied, so our naïve combination presented in Section 4.5 inevitably had large negative weights.

To ensure that our $\alpha_\mathrm{S}(M_\mathrm{Z})$ combination has only positive weights, we therefore have three options.

1. Remove the systematic uncertainties from the covariance matrix altogether, and instead apply an 'averaged' systematic uncertainty to the final weighted mean. The weights will then be proportional to the inverse squares of the statistical uncertainties.

2. Artificially set the systematic uncertainties for different measurements equal to one another.

3. Remove some, or all, of the *correlations* between systematic uncertainties, but leave the diagonal elements of the covariance matrix unchanged.

The first option is undesirable, as it does not give extra weight to measurements with the smallest systematic uncertainties: for example, measurements at LEP2 are less sensitive to the effects of non-perturbative QCD than those at LEP1. The second option is mathematically equivalent to the first, and will not be considered further. The third option is preferable, as it allows the weights to be influenced by systematic uncertainties, without permitting them to become negative. In the next section, we determine which correlations need to be removed from the covariance matrix to avoid negative weights.

4.8.6 Effects of correlations on the $\alpha_S(M_Z)$ weights

In Section 4.6, we studied the dependence of our fitted $\alpha_S(M_Z)$ values on the correlation coefficients between systematic uncertainties. We now perform a similar investigation, but focusing on the distribution of weights, w_i.

In each of Figures 4.10–4.13, we show the variation of the following quantities with respect to certain correlation coefficients in the covariance matrix:

(a) the fitted $\alpha_S(M_Z)$ values derived from individual event shape observables, and from a global fit to all measurements.

(b) the total weights assigned to each event shape observable, and the sum of the negative weights, in the global fit.

The legend for these plots is given in Figure 4.14; note that the vertical scales for the weight variations differ between the four plots. We will discuss separately the effects of correlations in the four types of uncertainty.

Figure 4.10: Variation of $\alpha_{\rm S}(M_{\rm Z})$ fits (Fig. (a)), and weights (Fig. (b)), for the six observables, as the correlations of experimental systematic uncertainties are "switched on". The hadronisation and theory uncertainties remain uncorrelated. See Fig. 4.14 for the legend.

Figure 4.11: Variation of $\alpha_{\rm S}(M_{\rm Z})$ fits (Fig. (a)), and weights (Fig. (b)), for the six observables, as the correlations of hadronisation uncertainties are "switched on". The experimental systematic uncertainties have a "minimum overlap" correlation, while the theory uncertainties remain uncorrelated. See Fig. 4.14 for the legend.
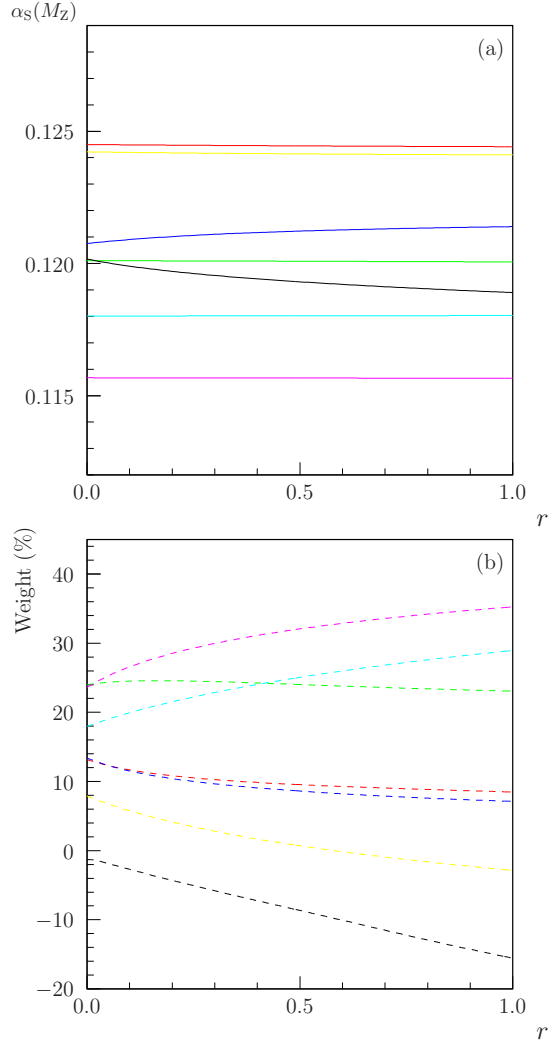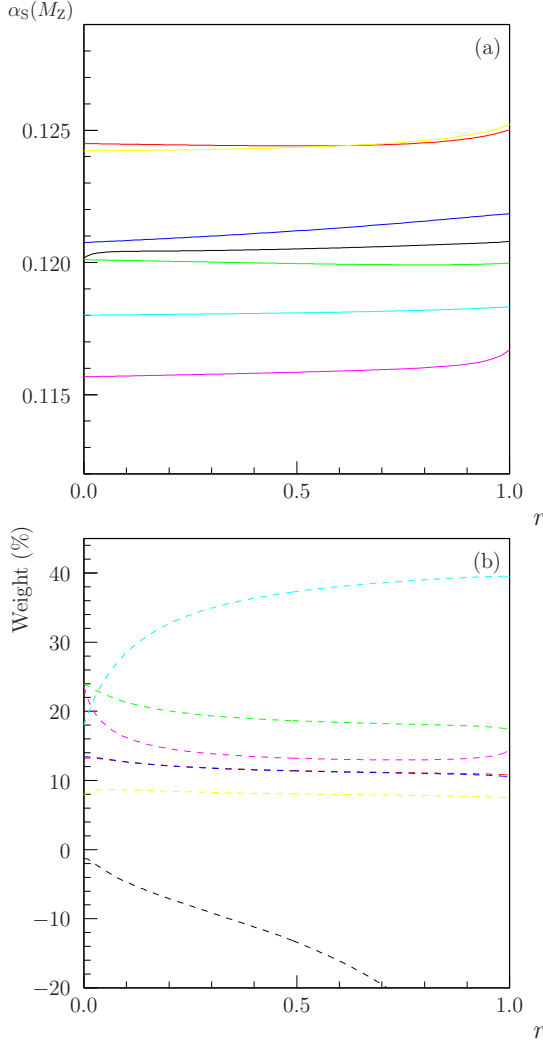
Off-diagonal elements of V:

$$V_{ij}^{\text{stat.}} = \rho_{ij}^{\text{stat.}}\,\sigma_i\,\sigma_j$$
(same energy and experiment)

$$V_{ij}^{\text{exp.}} = \min(\sigma_i^2, \sigma_j^2)$$
(same experiment)

$$V_{ij}^{\text{hadr.}} = 0$$
(same experiment)

$$V_{ij}^{\text{theo.}} = r\,\sigma_i\,\sigma_j$$
(same observable)

$$V_{ij}^{\text{theo.}} = 0$$
(different observables)

Off-diagonal elements of V:

$$V_{ij}^{\text{stat.}} = \rho_{ij}^{\text{stat.}}\,\sigma_i\,\sigma_j$$
(same energy and experiment)

$$V_{ij}^{\text{exp.}} = \min(\sigma_i^2, \sigma_j^2)$$
(same experiment)

$$V_{ij}^{\text{hadr.}} = 0$$
(same experiment)

$$V_{ij}^{\text{theo.}} = r\,\sigma_i\,\sigma_j$$
(same observable)

$$V_{ij}^{\text{theo.}} = 0.9\,r\,\sigma_i\,\sigma_j$$
(different observables)

Figure 4.12: Variation of $\alpha_{\text{S}}(M_{\text{Z}})$ fits (Fig. (a)) and weights (Fig. (b)) for the six observables, as the correlations of theory uncertainties are "switched on" between measurements using the same observables. The experimental systematic uncertainties have a "minimum overlap" correlation, while the hadronisation uncertainties remain uncorrelated. See Fig. 4.14 for the legend.

Figure 4.13: Variation of $\alpha_{\text{S}}(M_{\text{Z}})$ fits (Fig. (a)) and weights (Fig. (b)) for the six observables, as the correlations between all theory uncertainties are "switched on," including those between measurements derived from different observables. The experimental systematic uncertainties have a "minimum overlap" correlation, while the hadronisation uncertainties remain uncorrelated. See Fig. 4.14 for the legend.

————	Combined value of $\alpha_\mathrm{S}(M_\mathrm{Z})$, using T alone
————	Combined value of $\alpha_\mathrm{S}(M_\mathrm{Z})$, using M_H alone
————	Combined value of $\alpha_\mathrm{S}(M_\mathrm{Z})$, using C alone
————	Combined value of $\alpha_\mathrm{S}(M_\mathrm{Z})$, using B_T alone
————	Combined value of $\alpha_\mathrm{S}(M_\mathrm{Z})$, using B_W alone
————	Combined value of $\alpha_\mathrm{S}(M_\mathrm{Z})$, using y_{23} alone
————	Combined value of $\alpha_\mathrm{S}(M_\mathrm{Z})$, using all observables
- - - - - - -	Total weight for T, in the fit using all observables
- - - - - - -	Total weight for M_H, in the fit using all observables
- - - - - - -	Total weight for C, in the fit using all observables
- - - - - - -	Total weight for B_T, in the fit using all observables
- - - - - - -	Total weight for B_W, in the fit using all observables
- - - - - - -	Total weight for y_{23}, in the fit using all observables
- - - - - - -	Total negative weight, in the fit using all observables

Figure 4.14: Legend for Figures 4.10–4.13.

Statistical uncertainties: As in Section 4.6, we do not vary the correlations of statistical uncertainties, as they are well understood.

Experimental systematic uncertainties: In Figure 4.10, we smoothly switch on the correlation of experimental systematic uncertainties, starting from a covariance matrix with only statistical correlations. The right-hand side of the plot corresponds to a "minimum overlap" correlation between measurements within the same experiment, as described in Section 4.4.2. We observe very little variation in the fitted $\alpha_\mathrm{S}(M_\mathrm{Z})$ values, and also no significant negative weights. With correlations fully switched on, the total negative weight is only -1.3%. Furthermore, the distribution of weights among the six observables is rather insensitive to small variations of the correlation from its maximum value. We will therefore continue to apply the minimum overlap assumption in the covariance matrix.

Hadronisation uncertainties: In Figure 4.11, we switch on the correlation of hadronisation uncertainties, while leaving the statistical and experimental uncertainties correlated as described above. The right-hand side of the plot corresponds to a "minimum overlap" correlation between measurements within the same experiment. When the correlation is fully switched on, we find a sig-

nificant total negative weight (-15.6%). This also leads to a stronger variation of the weight distributions than was seen in the case of experimental uncertainties. These observations can be attributed to the energy-dependence of the hadronisation uncertainties, which is far greater than that of the experimental systematics. As we saw in Section 4.8.5, a wider spread in the magnitudes of systematic uncertainties leads to an increased tendency towards negative weights. In order to prevent an unreasonable increase in negative weights, we will therefore consider hadronisation uncertainties to be uncorrelated.[18]

Theory uncertainties: In Section 4.6, we distinguished between two types of correlations between theoretical uncertainties: those between fits to the same observable, and those between measurements using different observables. We will maintain this distinction here. In Figure 4.12, we switch on the correlation of theory uncertainties between fits to the same observable, while leaving the statistical and experimental uncertainties correlated as described above. In this case, the right-hand side of the plot corresponds to 100% correlation. Although the $\alpha_{\mathrm{S}}(M_{\mathrm{Z}})$ fit results do not change significantly, there is a rapid increase in negative weights as the correlation is switched on: when the correlation reaches 100%, the total negative weight is -79%. In Figure 4.13, we simultaneously switch on *all* correlations between theory uncertainties, including those between measurements derived from different observables; as before, the maximum correlation coefficient between fits to different observables is taken to be 0.9. We now see a dramatic increase in the negative weights, reaching -179% when the correlations are fully switched on. The total weight assigned to the observable y_{23} increases to $+144\%$, leaving overall negative weights assigned to T, C, B_{T} and B_{W}. This result supports the conclusions of Section 4.6, that the instability of our naïve combination can be attributed primarily to the correlation of theoretical uncertainties between different observables. These uncertainties are large, and differ more significantly between observables than between experiments or centre-of-mass energies, so such correlations are highly prone to introduce negative weights. As with hadronisation uncertainties, we therefore choose to remove all correlations between theory uncertainties from the covariance matrix.

---

[18]This assumption will necessitate a modification in our definition of the combined uncertainty, which will be discussed in Section 4.9.

In summary, our covariance matrix will contain all uncertainties in the diagonal terms, but only statistical and experimental uncertainties in the off-diagonal terms.

4.9   The combined uncertainty revisited

In the previous section, we have discussed the need to modify the covariance matrix, thereby eliminating large negative weights from the combination. This will not bias our estimator, $\hat{\alpha}_{\mathrm{S}}(M_{\mathrm{Z}}) = \sum w_i \alpha_i$, but will certainly change the variance of the combination, $\sigma^2 = \sum w_i V_{ij} w_j$, defined in Section 4.3.3. Regarding the hadronisation and theory uncertainties as uncorrelated between measurements would reduce the combined uncertainty. To take account of correlations, we instead use the following method:

Statistical and experimental uncertainties: The covariance matrices associated with these uncertainties, $V_{\mathrm{stat.}}$ and $V_{\mathrm{exp.}}$, are unaltered by our new combination algorithm. We can therefore still apply Equation (4.14) to estimate the corresponding uncertainties $\sigma_{\mathrm{stat.}}$ and $\sigma_{\mathrm{exp.}}$.

Combined hadronisation uncertainties: We repeat the entire combination procedure three times, using different sets of input measurements y_i. Each set uses a different Monte Carlo event generator to estimate hadronisation corrections:

- $y_{i,\mathrm{P}} \equiv \left[\, \alpha_{\mathrm{S}}(Q)^{\mathrm{PYTHIA}} \,\right]_i$
- $y_{i,\mathrm{H}} \equiv \left[\, \alpha_{\mathrm{S}}(Q)^{\mathrm{HERWIG}} \,\right]_i$
- $y_{i,\mathrm{A}} \equiv \left[\, \alpha_{\mathrm{S}}(Q)^{\mathrm{ARIADNE}} \,\right]_i$

The covariance matrix V, and hence the weights w_i, are the same in all three cases. Our hadronisation uncertainty for the combined measurement is then defined as the standard deviation of the three resulting estimators: $\hat{\alpha}_{\mathrm{S}}(M_{\mathrm{Z}})_{\mathrm{P}}$, $\hat{\alpha}_{\mathrm{S}}(M_{\mathrm{Z}})_{\mathrm{H}}$ and $\hat{\alpha}_{\mathrm{S}}(M_{\mathrm{Z}})_{\mathrm{A}}$. This definition is analogous to that of the hadronisation uncertainties for the individual measurements, discussed in Section 4.4.1.3.

Combined theory uncertainties: We again repeat the combination with three sets of input values:

- 'Central' values, $y_i^0 \equiv [\, \alpha_S(Q) \,]_i$

- 'Raised' values, at the upper extremity of the theory error-bar, [19]
  $$y_i^+ \equiv [\, \alpha_S(Q) \,]_i + \sigma_{i,\,\text{theo.}}^+$$

- 'Lowered' values, at the lower extremity of the theory error-bar,
  $$y_i^- \equiv [\, \alpha_S(Q) \,]_i + \sigma_{i,\,\text{theo.}}^-$$

The upper and lower uncertainties for the combined result are then given by the differences $\hat{\alpha}_S(M_Z)^+ - \hat{\alpha}_S(M_Z)^0$ and $\hat{\alpha}_S(M_Z)^0 - \hat{\alpha}_S(M_Z)^-$.

4.9.1 A minor caveat

It is sometimes claimed that this treatment described above takes full account of correlations between the systematic uncertainties. This is not strictly true, unless the uncertainties are 100% correlated. For example, our combined upper theory uncertainty is given by

$$\sigma_{\text{theo.}} = \sum_i w_i \, (y_i'^+ - y_i'^0) \quad , \tag{4.45}$$

where y_i' are the individual input measurements after 'running' to the Z^0 mass. The corresponding variance is therefore

$$\sigma_{\text{theo.}}^2 = \sum_{i,j} w_i \, [(y_i'^+ - y_i'^0)(y_j'^+ - y_j'^0)] \, w_j \quad , \tag{4.46}$$

where the term in square brackets is equivalent to the covariance matrix $(V_{ij}')^{\text{theo.}}$ for a theory uncertainty which is *fully* correlated between the input measurements. Our combined hadronisation uncertainty can similarly be written as

$$\sigma_{\text{hadr.}}^2 = \frac{1}{9} \left((\hat{\alpha}_{S,P} - \hat{\alpha}_{S,H})^2 + (\hat{\alpha}_{S,H} - \hat{\alpha}_{S,A})^2 + (\hat{\alpha}_{S,A} - \hat{\alpha}_{S,P})^2 \right)$$

$$= \frac{1}{9} \left(\left[\sum_i w_i \, (y_{i,P}' - y_{i,H}') \right]^2 + \left[\sum_i w_i \, (y_{i,H}' - y_{i,A}') \right]^2 + \left[\sum_i w_i \, (y_{i,A}' - y_{i,P}') \right]^2 \right) . \tag{4.47}$$

---

[19] The theory uncertainties predicted by the "uncertainty band" method are generally asymmetric. We denote the upper and lower uncertainties by $\sigma_{\text{theo.}}^+$ and $\sigma_{\text{theo.}}^-$ respectively.

This expression can be regarded as a quadratic sum of three fully-correlated 'uncertainties', provided the signs of the differences $(y'_{i,\mathrm{P}} - y'_{i,\mathrm{H}})$, $(y'_{i,\mathrm{H}} - y'_{i,\mathrm{A}})$ and $(y'_{i,\mathrm{A}} - y'_{i,\mathrm{P}})$ do not vary between measurements.[20]

Our algorithm therefore includes no information about the *true* correlations of hadronisation and theory uncertainties between measurements, except in the signs of the differences between measurements using different event generators.

4.10   Fitting the hadronisation uncertainties

The uncertainties in our hadronisation corrections should vary smoothly with the energy scale, provided the same models, parameters and fit ranges are used. However, as discussed in Section 4.4.2.3, there are significant differences between the tuned parameters used by the four Collaborations, which lead to variations in the estimated hadronisation uncertainties. Figure 4.15 illustrates the fits obtained for $\alpha_\mathrm{S}(Q)$ at each centre-of-mass energy, and also the global running fits, using each of the three generators. The differences between generators clearly do not vary smoothly between energies, especially between $Q = 91$ GeV and the lower-energy measurements from L3 data.[21]   To prevent these fluctuations from affecting the weights, it is desirable to smooth them out.

Various theoretical models [60–65] have predicted that non-perturbative contributions to the moments and distributions of the event shapes should scale as $1/Q^n$ for some n. For the observables involved in our combination, we expect $n = 1$ for T, M_H C, B_T and B_W and $n = 2$ for y_{23}. A recent review of these "power correction" models, and of their experimental tests, can be found in Ref. [145].

We would intuitively expect that the uncertainties should depend linearly on the correction itself, which in turn scales as $1/Q^n$. We therefore adopt the form

$$\sigma'_\mathrm{hadr.} = \frac{A_y}{Q} + B_y \quad , \tag{4.48}$$

for our new hadronisation uncertainty, where the constants A and B are fitted to the data. A separate fit is calculated for each observable y, since the event shapes differ

---

[20] As we saw in Section 4.4.2.3, a high proportion of our measurements satisfy $y'_{i,\mathrm{H}} < y'_{i,\mathrm{P}} < y'_{i,\mathrm{A}}$.
[21] Much of this variation is due to differing contributions from the four experiments entering into our combination at different energies.
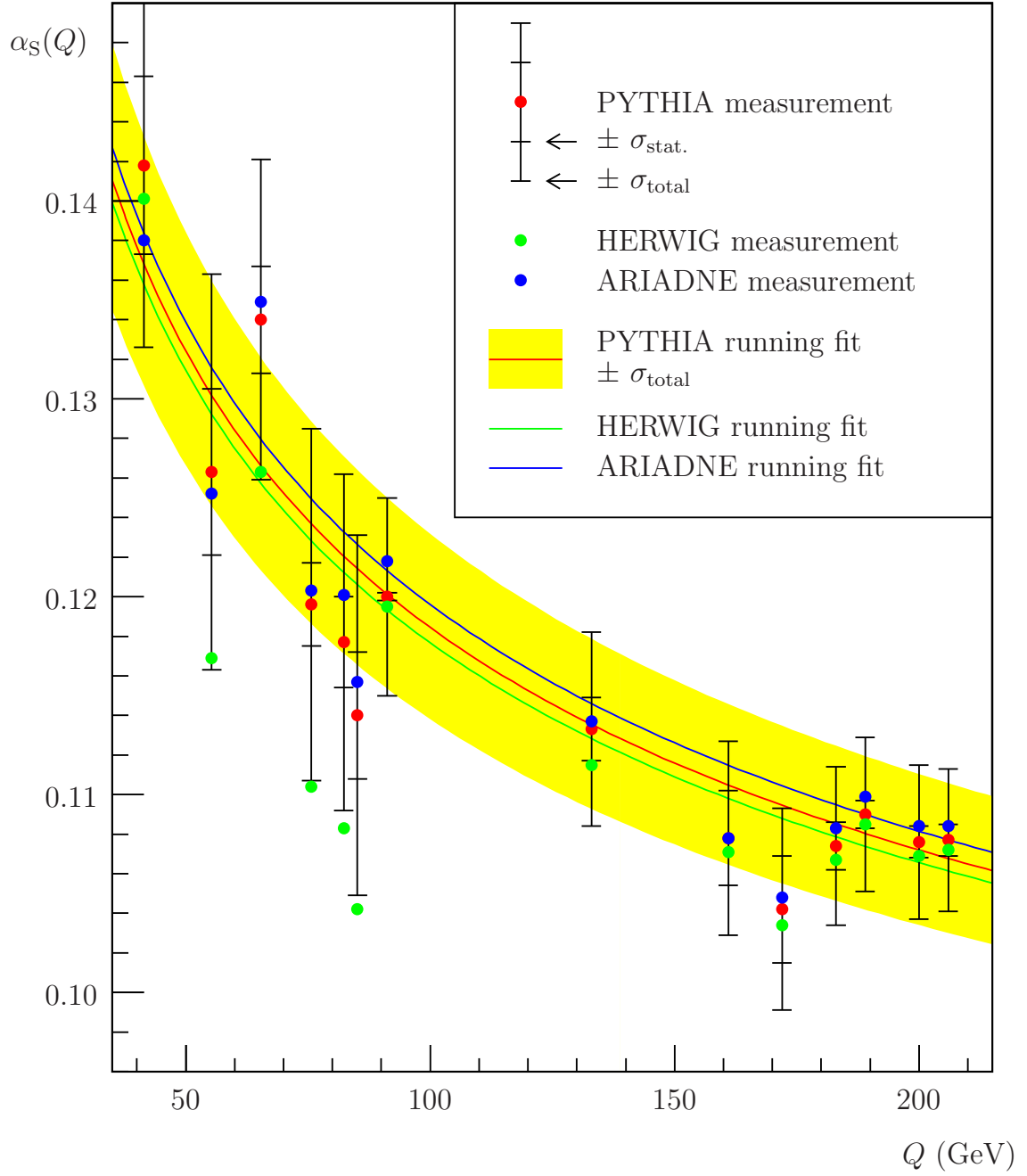
Figure 4.15: Fits to LEP α_S measurements using PYTHIA, HERWIG and ARIADNE hadronisation corrections. Each point is a weighted average of measurements derived from all available experiments and event-shape observables at the given centre-of-mass energy. The curves are obtained by fitting all measurements from a given generator, after conversion to the M_Z scale.

in their sensitivity to non-perturbative effects.[22] The fit is performed with weights w_i equal to those used in the $\alpha_S(M_Z)$ fit itself. We minimise the following expression, where $(\sigma_{\text{hadr.}})_i$ is the original hadronisation uncertainty defined in Section 4.4.1.3, and the summation runs over all measurements using a single observable y:

$$\chi^2 \;=\; \sum_i w_i \left(\frac{A_y}{Q} + B_y - (\sigma_{\text{hadr.}})_i \right)^2 \tag{4.49}$$

Since the weights vary as functions of covariance matrix, which includes the hadronisation uncertainty, we must iterate the fit until the coefficients are stable. The results of our iterated fit are as follows:

$$
\begin{aligned}
\text{Thrust, } T: \quad & \sigma_{\text{hadr.}} = 0.29/Q - 0.00067 \\
\text{Heavy Jet mass, } M_{\text{H}}: \quad & \sigma_{\text{hadr.}} = 0.25/Q - 0.00063 \\
\text{C-parameter, } C: \quad & \sigma_{\text{hadr.}} = 0.42/Q - 0.00093 \\
\text{Total jet broadening, } B_{\text{T}}: \quad & \sigma_{\text{hadr.}} = 0.17/Q + 0.00041 \\
\text{Wide jet broadening, } B_{\text{W}}: \quad & \sigma_{\text{hadr.}} = 0.13/Q - 0.00009 \\
\text{Durham } y_{23}: \quad & \sigma_{\text{hadr.}} = 0.05/Q + 0.00009
\end{aligned}
$$

Note that we cannot specify the precision of these coefficients, because the hadronisation uncertainties entering in the fit do not have well-defined uncertainties of their own.

Our fitted hadronisation uncertainties for each observable are illustrated in Figures 4.16 and 4.17. The fits do not describe the data well, because there are large differences between hadronisation uncertainties from different experiments. In particular, the measurements from L3 tend to suggest a much steeper energy-dependence than those from other experiments; this causes an apparent anomaly in the fit for y_{23}, which is not measured by L3. However, the fits do provide a satisfactory smoothing algorithm to remove unwanted fluctuations between energies, so we will adopt them in our covariance matrix V.

At present, the hadronisation uncertainties on our *combined* results continue to be evaluated as described in Section 4.9, by repeating the entire combination for

---

[22]It could be argued that the uncertainty for y_{23} measurements should include a $1/Q^2$ term; however, it was decided that the input uncertainties are not sufficiently precise to distinguish between different scaling laws, and that the two terms of the fit would be sufficient to mimic any significant $1/Q^2$ behaviour in the 91–206 GeV energy range.

Covariance element		Matrix 1	Matrix 2	Matrix 3	Matrix 4
Statistical	Diagonal	●	●	●	●
	Off-diagonal	●		●	●
Experimental	Diagonal	●	●	●	●
	Off-diagonal	●		●	●
Hadronisation	Diagonal	●	●		●
	Off-diagonal	●			
Theory	Diagonal	●	●		●
	Off-diagonal	●			

Table 4.6: The diagonal and off-diagonal components of the four alternative covariance matrices compared in Table 4.7 and in Figures 4.19–4.22. Matrix 4 corresponds to the covariances used in our final LEP $\alpha_S(M_Z)$ combination.

each generator. For the final LEP results, however, it is planned that the smoothed hadronisation uncertainties should be used throughout, both for the weights and for the combined uncertainty.

4.11 Weight distributions

Our complete combination procedure is summarised in Figure 4.18. Up to this point, our main criterion for choosing the covariance matrix V has been the prevention of negative weights. Before presenting our final results, however, we will investigate the distribution of weights allocated to the various input measurements. We define four alternative covariance matrices, as follows:

Matrix 1: The 'naïve' covariance matrix, containing all the uncertainties and correlations discussed in Section 4.4.

Matrix 2: A matrix containing all four types of uncertainty, but regarding them as uncorrelated.

Matrix 3: A matrix containing only statistical and experimental uncertainties, including their correlations.

Matrix 4: The matrix chosen for our LEP $\alpha_S(M_Z)$ combination. All uncertainties are included in the diagonal terms of the covariance matrix, but only statistical and experimental uncertainties are regarded as correlated.

Thrust, T

Heavy jet mass, M_{H}

C-parameter

- ● ALEPH
- ■ DELPHI
- ▲ L3
- ★ OPAL
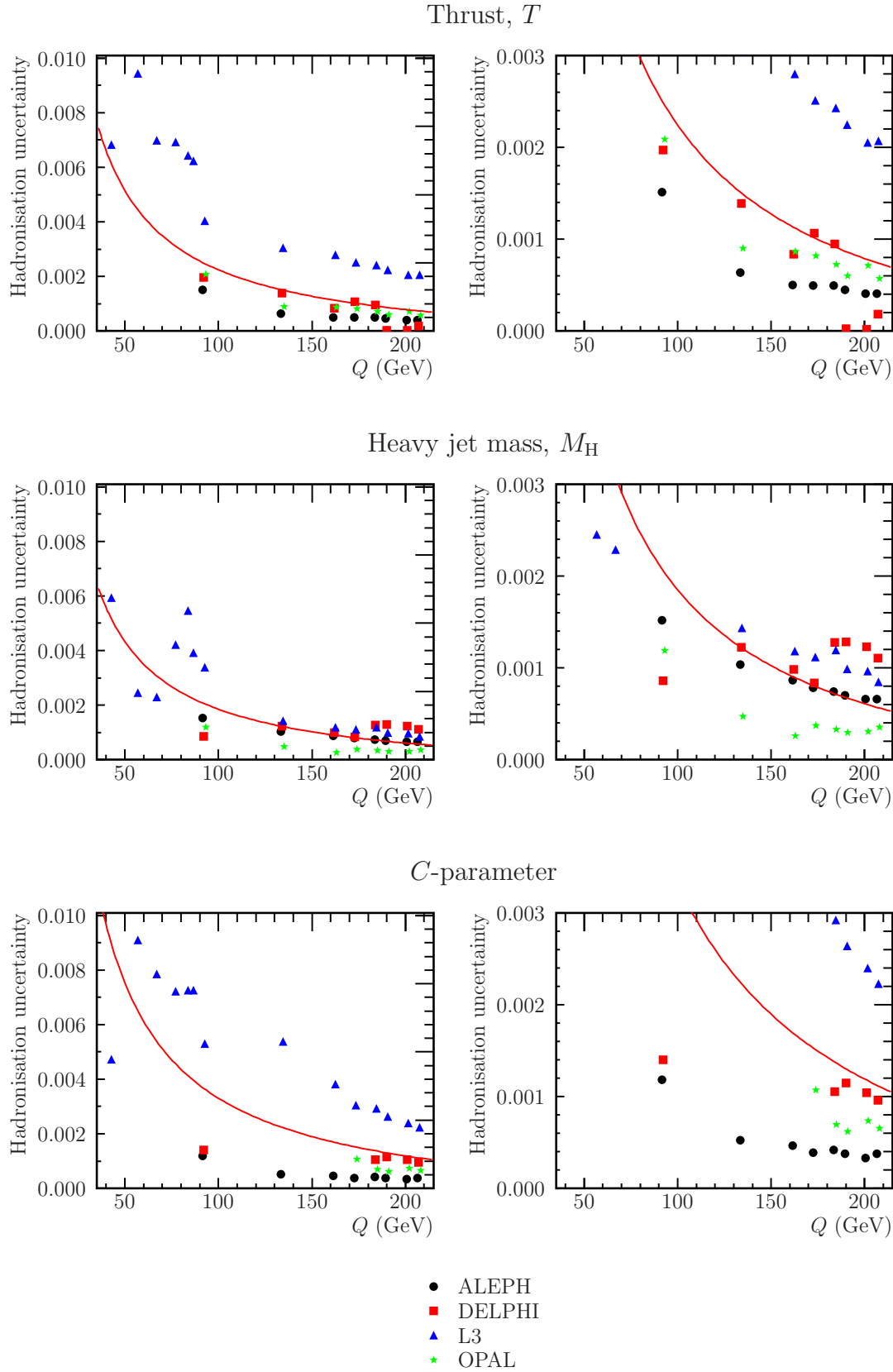
Figure 4.16: Fitted hadronisation uncertainties for T, M_{H} and C. Each point represents the standard deviation of three results using PYTHIA, HERWIG and ARIADNE hadronisation corrections, for an individual LEP α_S measurement. The left and right plots contain the same data on different scales.

Total jet broadening, B_T
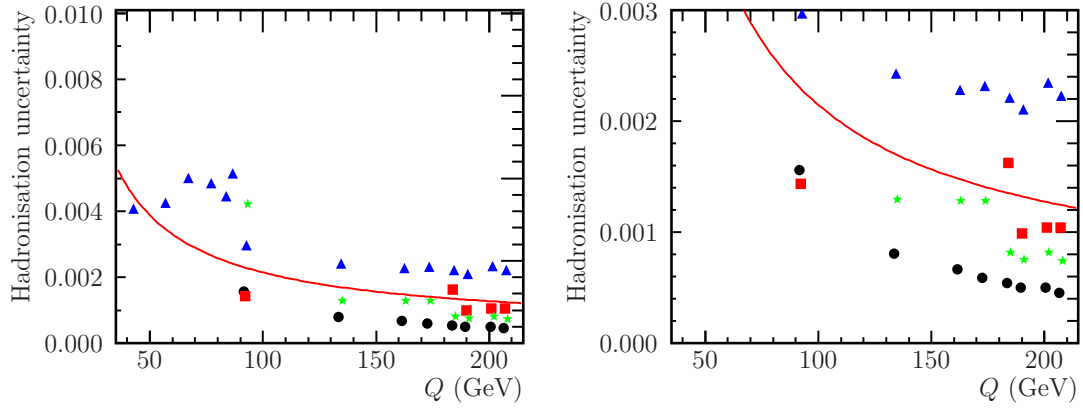
Wide jet broadening, B_W
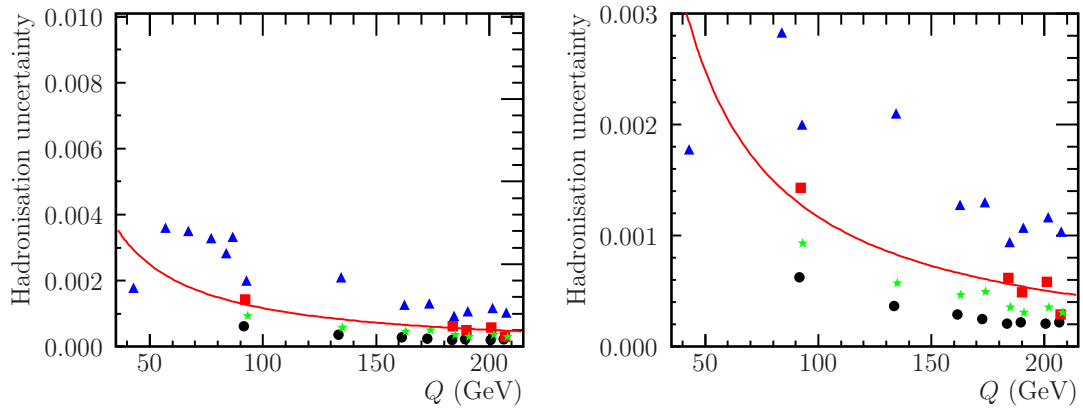
Durham y_{23}
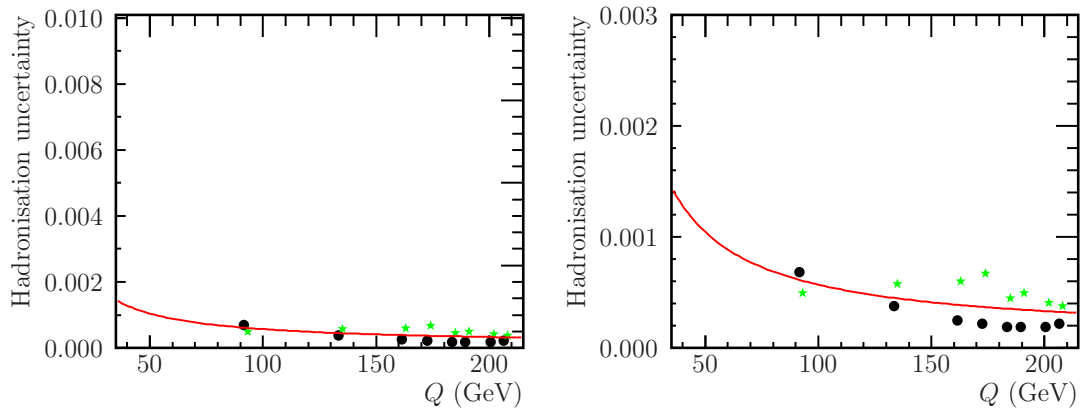
● ALEPH
■ DELPHI
▲ L3
★ OPAL

Figure 4.17: Fitted hadronisation uncertainties for B_T, B_W and y_{23}. Each point represents the standard deviation of three results using PYTHIA, HERWIG and ARIADNE hadronisation corrections, for an individual LEP α_S measurement. The left and right plots contain the same data on different scales.
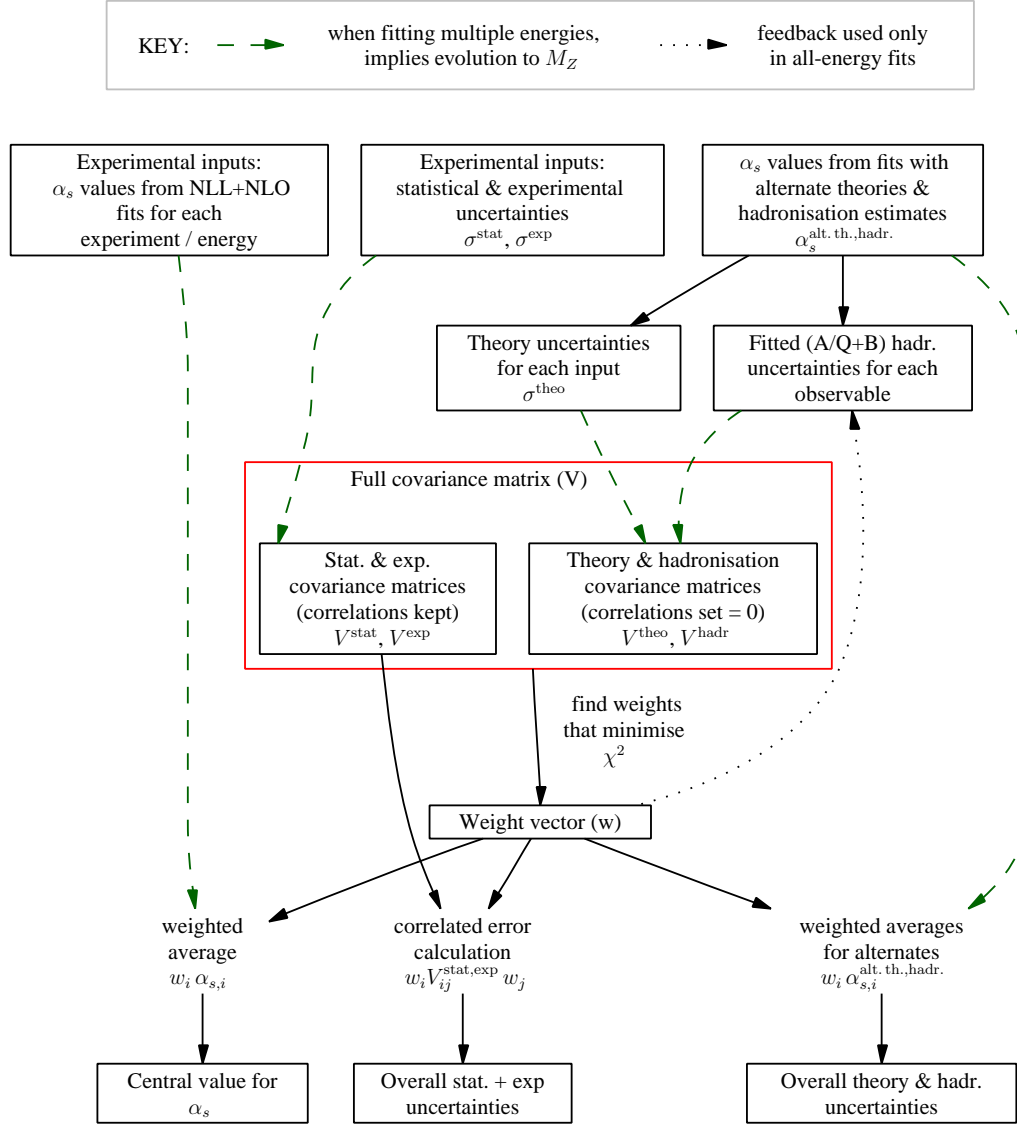
Figure 4.18: Summary of the LEP $\alpha_\mathrm{S}(M_\mathrm{Z})$ combination method *(Figure prepared by G.P. Salam)*.

The diagonal and off-diagonal parts of these matrices are summarised in Table 4.6. The resulting fits and weight distributions are presented in Table 4.7, and in Figures 4.19–4.22. We will discuss in turn each of the plots (a)–(f) within these figures.

(a) **Running α_S fit:** This plot shows the combined $\alpha_\mathrm{S}(Q)$ measurement at each energy point, and the QCD running curve predicted from a global $\alpha_\mathrm{S}(M_\mathrm{Z})$ fit at all energies. The inner error-bars and dotted red curves show the statistical uncertainty, while the outer bars and yellow band show the total uncertainty. The running curve describes the $\alpha_\mathrm{S}(Q)$ points satisfactorily for all matrices except Matrix 3.

(b) **Weight distribution:** This histogram shows the distribution of weights assigned to individual α_S measurements. The number of measurements in each bin is multiplied by the weight itself, so the histogram is automatically normalised. We require the contribution from negative weights to be negligible, and the size of each positive weight to be reasonably small. These conditions are satisfied only by matrices 2 and 4 (negative weights cannot arise from Matrix 2, since there are no correlations).

(c) **Weights per energy point:** This bar-chart shows the total weight assigned to measurements at each centre-of-mass energy. We expect a large weight for measurements at 91 GeV, which have very small statistical uncertainties, but also a significant weight for higher-energy LEP2 data, where the theory and hadronisation uncertainties are smaller. These conditions are satisfied best by Matrices 1 and 4. An uncorrelated fit (Matrix 2) does not give sufficient weight to LEP1 measurements, while a fit which omits theory and hadronisation uncertainties (Matrix 3) does not give sufficient weight to LEP2.

(d) **Weights per OPAL event:** Here we present the weight for each centre-of-mass energy divided by the number of selected signal events used. Since this information is not readily available for other LEP experiments, the fit is restricted to OPAL data; as with all OPAL measurements used in this chapter, the results at $\sqrt{s} \leq 200$ GeV are based on previously published or approved distributions, and not on those presented in Chapter 3. In a fit based entirely on statistical uncertainties, we would expect the weight per event to

be roughly constant,[23] except at 91 GeV, where Monte Carlo statistics form a significant contribution to the uncertainty.

(*e*) **Weight per observable:** The perturbative predictions have different uncertainties, which should be reflected in the total weights assigned to each observable. Based on the theoretical uncertainty estimates discussed in Section 1.8, we would expect y_{23} to carry the most weight, followed by M_H. B_T should carry the least weight. This is confirmed in the fit using Matrix 4, except that the weight for y_{23} is suppressed, because only two experiments have measured it.

(*f*) **Weight per experiment:** We would expect the total weights for each experiment to be roughly equal, although differences will arise from the availability of input measurements. Once again, Matrix 4 provides the most even distribution between the experiments.

In Figure 4.23, we repeat the combination with Matrix 4, but apply the smoothing of hadronisation uncertainties described in Section 4.10. This smoothing was not applied in Figures 4.19–4.22. Comparing the fits and weight distributions in Figures 4.22 and 4.23, we find the effect of this smoothing to be negligible.

In conclusion, the distribution of weights derived from for our chosen covariance matrix (Matrix 4) is satisfactory. All weights assigned to individual input measurements are between -0.5% and $+4.5\%$, with a total negative weight of only -1.3%. Although a significant weight (37%) is allocated to measurements at 91 GeV, these are complemented in the combination by measurements at higher energy scales, which have smaller systematic uncertainties. The balance of weights among the six observables reflects the relative theoretical uncertainties and the number of available input measurements; all observables contribute between 7% and 24% to the combination. The weight distribution among the four experiments is roughly equal, though the DELPHI Collaboration has a slightly smaller contribution since they have measured α_S neither from y_{23} nor from radiative ($Q < 91$ GeV) events.

---

[23]This assumes that the same set of observables is used at all energies. In fact, the C-parameter is omitted at 91–161 GeV, which should reduce the weight at these energies by $\sim$20%.

	Matrix 1	Matrix 2	Matrix 3	Matrix 4 without $A/Q+B$ fit	Matrix 4 with $A/Q+B$ fit
Fit results					
$\alpha_{\mathrm{s}}(M_{\mathrm{Z}})$	0.1162	0.1201	0.1197	0.1202	0.1201
Stat. error	±0.0008	±0.0002	±0.0001	±0.0003	±0.0003
Exp. error	±0.0008	±0.0002	±0.0007	±0.0009	±0.0009
Hadr. error	±0.0005	±0.0010	±0.0010	±0.0008	±0.0009
Theory (upper)	+0.0004	+0.0048	+0.0044	+0.0047	+0.0046
Theory (lower)	−0.0013	−0.0048	−0.0044	−0.0047	−0.0047
Syst. error	±0.0013	±0.0049	±0.0046	±0.0048	±0.0048
Total error	±0.0015	±0.0049	±0.0046	±0.0048	±0.0048
χ^2 / d.o.f.	431.6/193	125.8/193	2618.3/193	119.4/193	128.5/193
Weights by observable					
T	−16.5 %	16.5 %	−6.5 %	13.2 %	13.2 %
M_{H}	26.2 %	22.6 %	84.5 %	24.0 %	23.6 %
C	−15.1 %	14.0 %	19.3 %	13.4 %	13.3 %
B_{T}	−32.1 %	13.2 %	−5.4 %	7.9 %	7.9 %
B_{W}	−6.0 %	19.4 %	4.6 %	23.6 %	23.6 %
y_{23}	143.5 %	14.4 %	3.5 %	18.0 %	18.4 %
Weights by c.m. energy					
41.4 GeV	−3.6 %	1.8 %	0.2 %	1.7 %	1.6 %
55.3 GeV	−2.3 %	1.4 %	0.1 %	0.3 %	0.3 %
65.4 GeV	−2.2 %	1.8 %	0.3 %	1.1 %	1.2 %
75.7 GeV	−4.0 %	1.4 %	0.3 %	0.3 %	0.4 %
82.3 GeV	−5.0 %	1.4 %	0.4 %	0.6 %	0.9 %
85.1 GeV	−1.1 %	1.3 %	0.2 %	0.4 %	0.5 %
91.2 GeV	31.1 %	16.6 %	90.4 %	38.2 %	37.1 %
133.0 GeV	0.9 %	7.4 %	0.4 %	4.3 %	4.5 %
161.0 GeV	1.1 %	5.1 %	0.1 %	1.5 %	1.5 %
172.0 GeV	1.1 %	4.1 %	0.1 %	0.9 %	0.9 %
183.0 GeV	13.4 %	12.2 %	1.4 %	9.5 %	9.6 %
189.0 GeV	26.4 %	16.0 %	2.7 %	15.8 %	16.0 %
200.0 GeV	20.6 %	13.9 %	1.5 %	9.7 %	9.9 %
206.0 GeV	23.7 %	15.6 %	1.9 %	15.6 %	15.8 %
Weights by experiment					
ALEPH	24.3 %	26.8 %	25.8 %	26.2 %	25.6 %
DELPHI	25.1 %	16.9 %	25.8 %	22.9 %	22.2 %
L3	24.6 %	29.7 %	24.5 %	24.6 %	26.1 %
OPAL	26.0 %	26.6 %	23.9 %	26.3 %	26.2 %
Other weight statistics					
Total +ve	400.8 %	100.0 %	124.0 %	101.3 %	101.3 %
Total −ve	−300.8 %	0.0 %	−24.0 %	−1.3 %	−1.3 %
Maximum	53.6 %	1.6 %	23.8 %	4.4 %	4.5 %
Minimum	−30.5 %	0.0 %	−4.8 %	−0.3 %	−0.2 %

Table 4.7: Combined α_{S} fit results and weights for the four different correlation assumptions
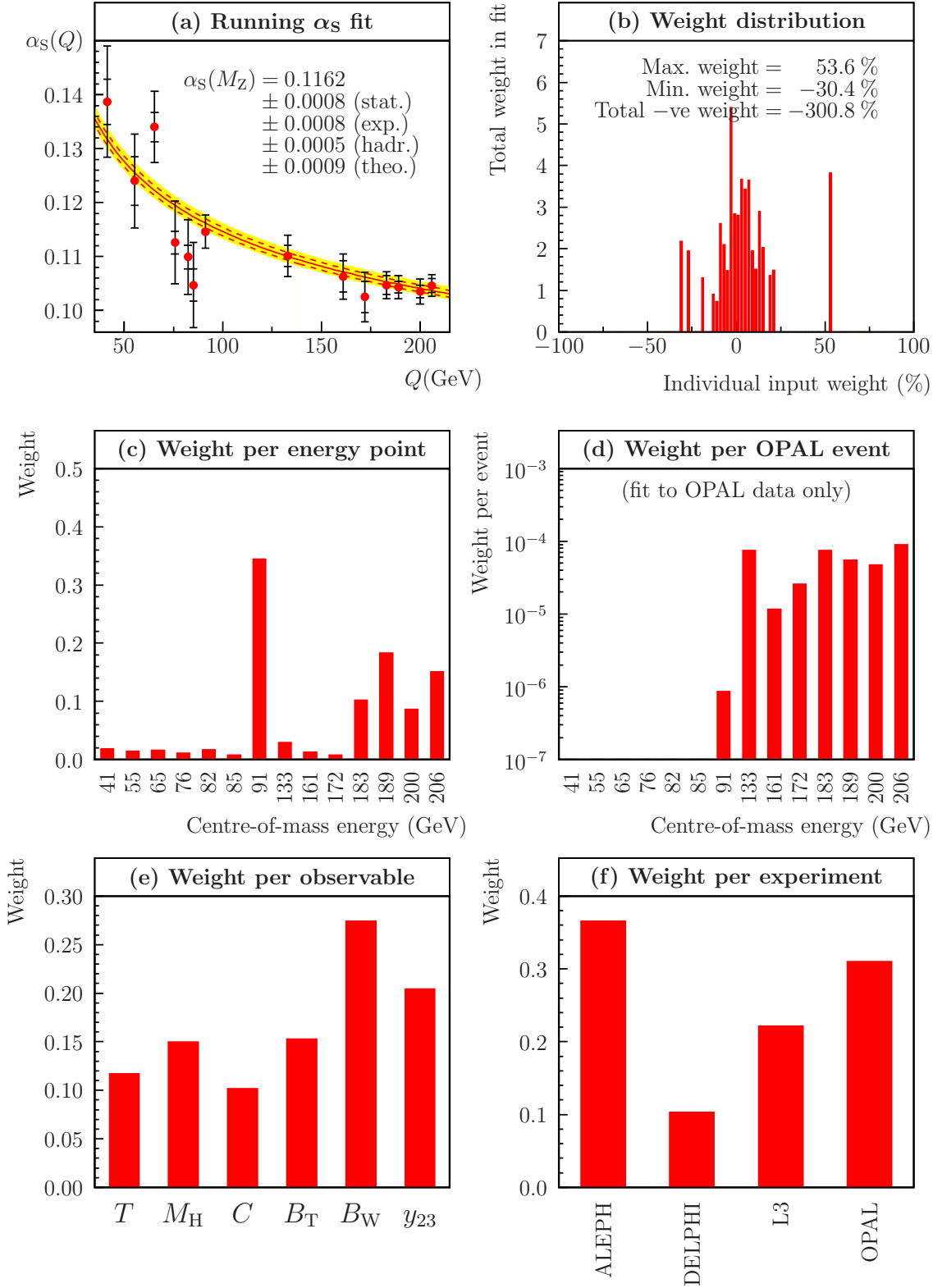
Figure 4.19: Fit results and distributions of weights, using **covariance matrix 1**, the naïve method discussed in Section 4.5. In this method, all of the uncertainties and correlations described in Section 4.4 are included in the covariance matrix.
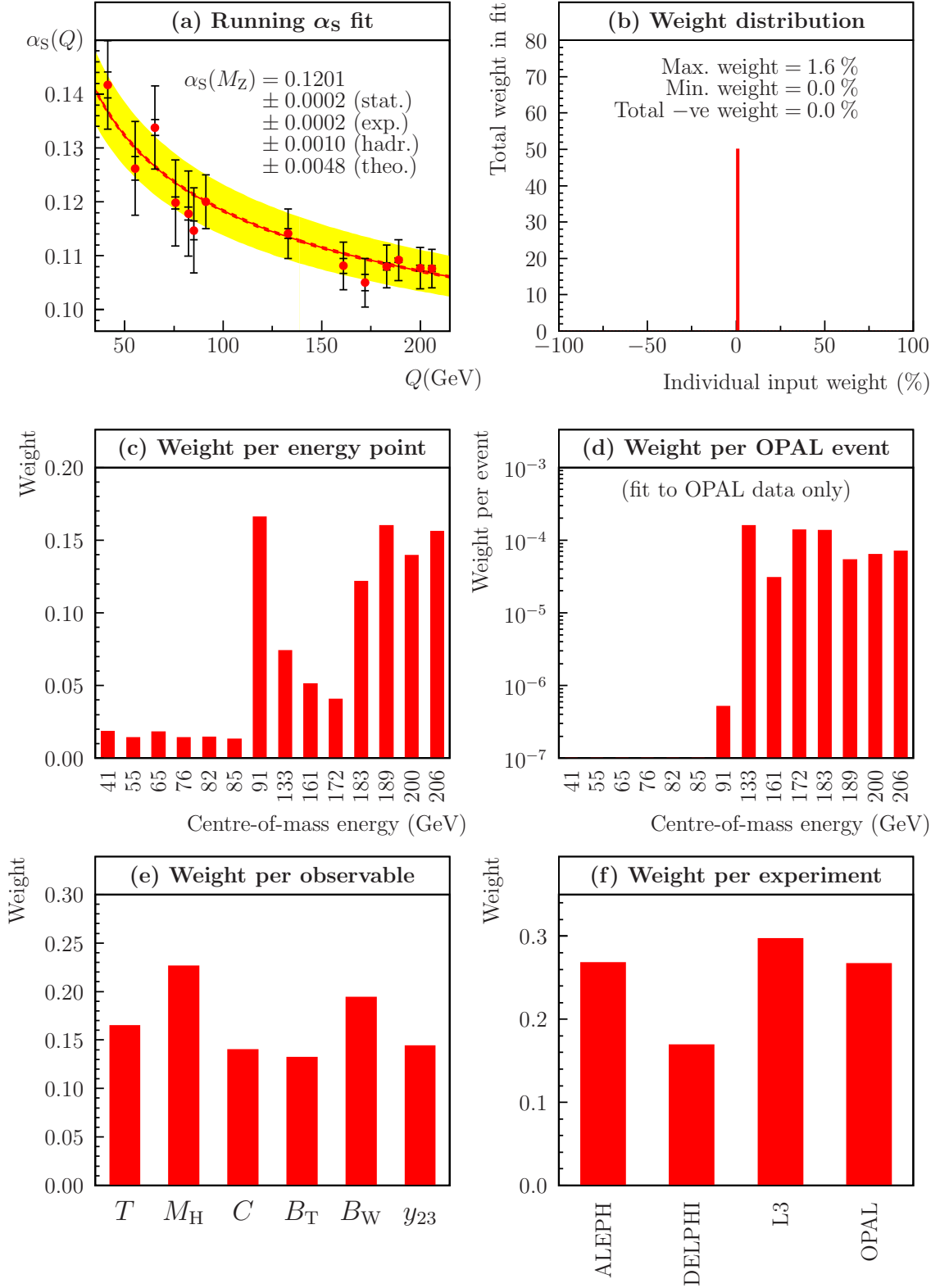
Figure 4.20: Fit results and distributions of weights, using **covariance matrix 2**. In this method, all of the uncertainties defined in Section 4.4.1 are included in the covariance matrix, but they are treated as uncorrelated.
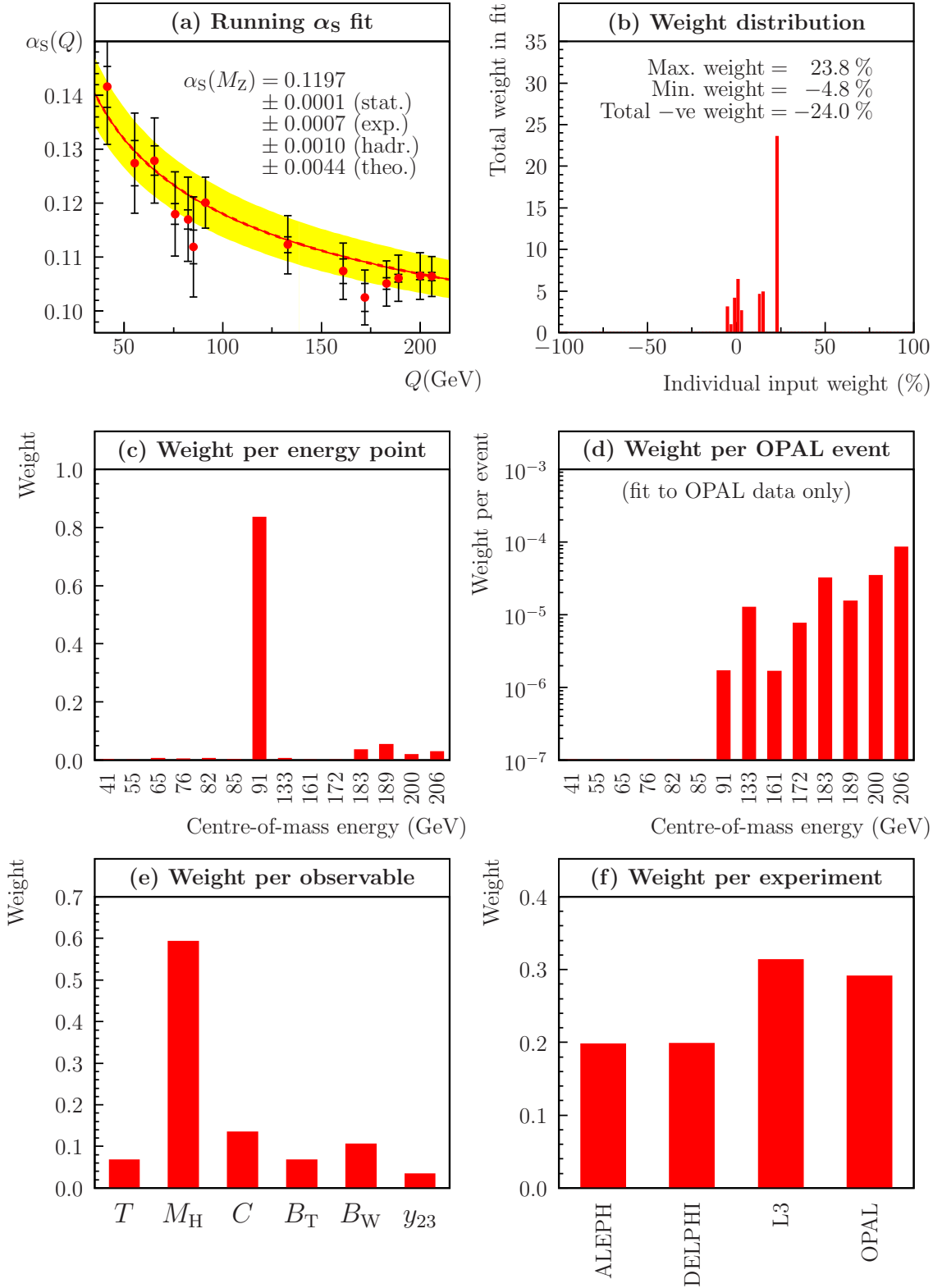
Figure 4.21: Fit results and distributions of weights, using **covariance matrix 3**. In this method, only statistical and experimental uncertainties are included in the covariance matrix. Correlations for these uncertainties are included, as defined in Section 4.4.2.
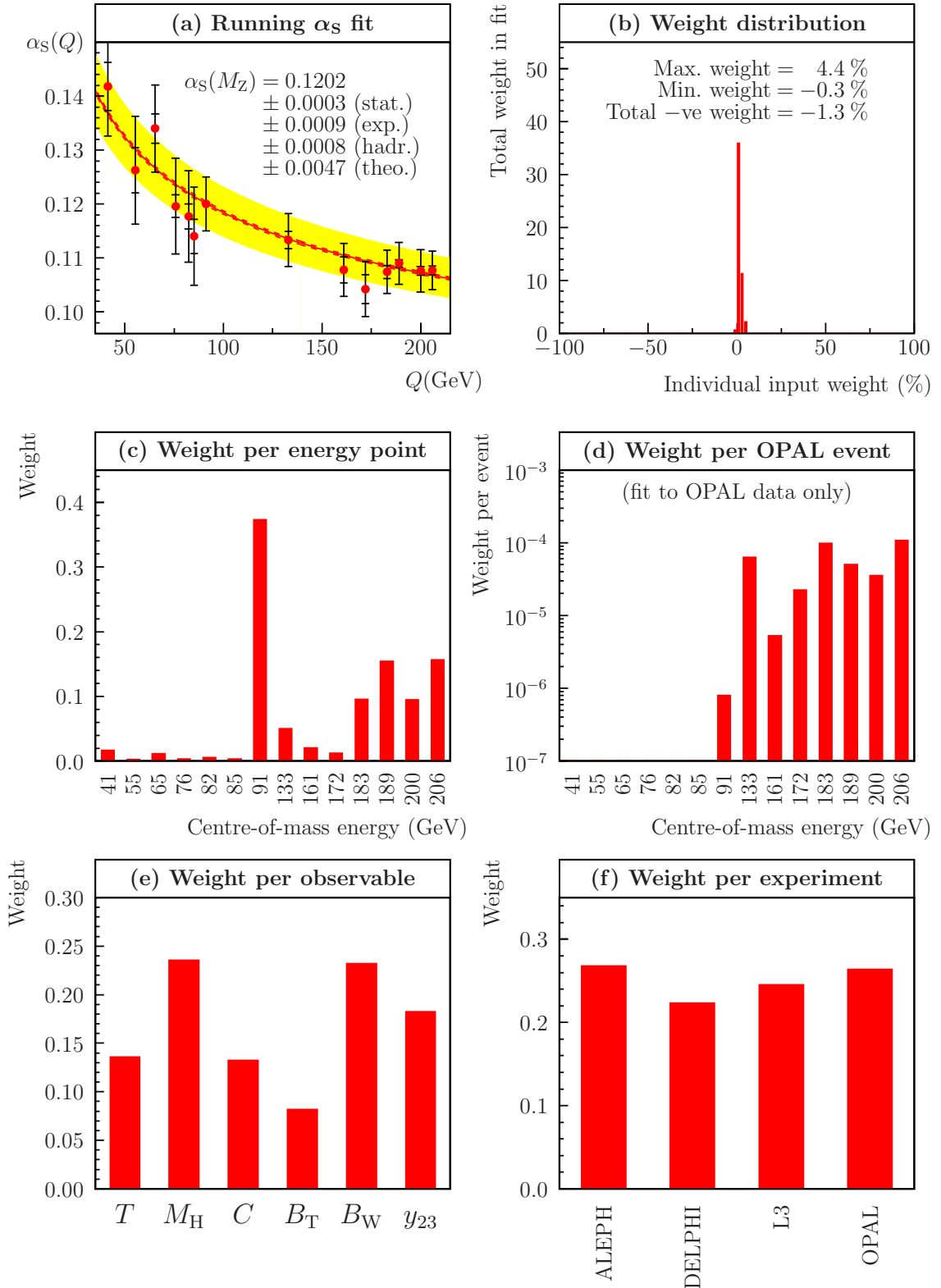
Figure 4.22: Fit results and distributions of weights, using **covariance matrix 4**, the method adopted for our final combination. In this method, all of the uncertainties defined in Section 4.4.1 are included in the diagonal terms of the covariance matrix, but only the statistical and experimental uncertainties are regarded as correlated.
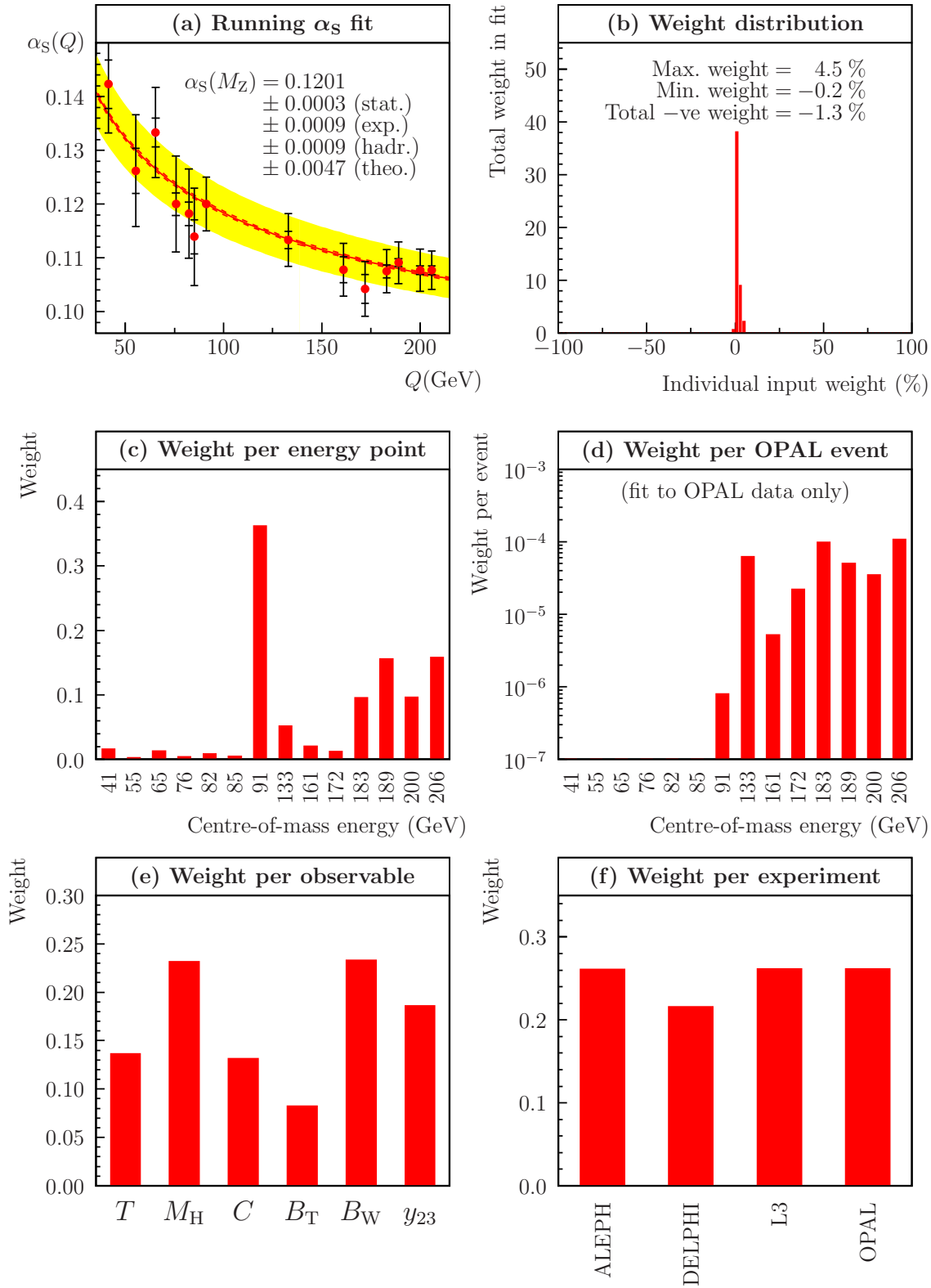
Figure 4.23: Fit results and distributions of weights, using **covariance matrix 4**, after smoothing of the hadronisation uncertainties as described in Section 4.10.

4.12 $\alpha_S(M_Z)$ fit results

Our final combined measurement of $\alpha_S(M_Z)$, using all available measurements, is:

$$
\begin{aligned}
\alpha_S(M_Z) \;&=\; 0.1201 \pm 0.0003 \text{ (stat.)} \pm 0.0009 \text{ (exp.)} \pm 0.0009 \text{ (hadr.)} \; ^{+0.0046}_{-0.0047} \text{ (theo.)} \\
&=\; 0.1201 \pm 0.0003 \text{ (stat.)} \pm 0.0048 \text{ (syst.)} \\
&=\; 0.1201 \pm 0.0048 \text{ (total)}
\end{aligned}
$$

The $\alpha_S(Q)$ results at individual energy points are presented in Table 4.8. These have been combined without conversion to the M_Z scale. Figure 4.24 illustrates these fits, together with the $\alpha_S(Q)$ running curve predicted from the global $\alpha_S(M_Z)$ combination.

In Tables 4.9–4.11 and Figures 4.25–4.27, we present combinations of $\alpha_S(M_Z)$ measurements based on individual observables, energy ranges, and experiments. The breakdown of weights by energy, by observable and by experiment is given for each combination. The value of the minimised χ^2 is also quoted for each fit; however, this is of limited use for judging the quality of the fit, since it is calculated using an incomplete covariance matrix. In almost all cases, the χ^2 value is "too small" for the number of degrees of freedom, indicating that the spread of measurements is inconsistent with the assumption of uncorrelated theory and hadronisation uncertainties. This should not concern us, however, since the correlations have been 're-included' in the uncertainties of our combined results, as described in Section 4.9.

All of the partial combinations are consistent with the global combination, within the appropriate uncertainties. However, it should be noted that some have smaller total uncertainties than that of the global combination. For example, when we fit LEP1 and LEP2[24] data alone, we obtain the following results:

$$
\text{LEP1}: \; \alpha_S(M_Z) \;=\; 0.1200 \pm 0.0002 \text{ (stat.)} \pm 0.0008 \text{ (exp.)} \pm 0.0010 \text{ (hadr.)} \; ^{+0.0048}_{-0.0048} \text{ (theo.)}
$$

$$
\text{LEP2}: \; \alpha_S(M_Z) \;=\; 0.1201 \pm 0.0005 \text{ (stat.)} \pm 0.0010 \text{ (exp.)} \pm 0.0007 \text{ (hadr.)} \; ^{+0.0044}_{-0.0045} \text{ (theo.)}
$$

The combined uncertainty for LEP2 measurements alone is less than that for the all-energies combination. Similarly the combinations of ALEPH and OPAL results, and also those using the observables M_H and y_{23} alone, have smaller uncertainties than the global LEP combination. Ordinarily this situation should not occur,

---

[24]LEP2 includes all centre-of-mass energies $\sqrt{s} \geq 133$ GeV in this context.

Energy scale Q (GeV)	$\alpha_\mathrm{s}(Q)$	$\sigma_\mathrm{stat.}$	$\sigma_\mathrm{exp.}$	$\sigma_\mathrm{hadr.}$	$\sigma_\mathrm{theo.}$
41.4	0.1423	±0.0045	±0.0025	±0.0015	$^{+0.0076}_{-0.0071}$
55.3	0.1262	±0.0042	±0.0049	±0.0049	$^{+0.0067}_{-0.0064}$
65.4	0.1333	±0.0027	±0.0030	±0.0044	$^{+0.0061}_{-0.0058}$
75.7	0.1200	±0.0021	±0.0050	±0.0046	$^{+0.0055}_{-0.0053}$
82.3	0.1182	±0.0022	±0.0031	±0.0053	$^{+0.0052}_{-0.0051}$
85.1	0.1139	±0.0032	±0.0037	±0.0054	$^{+0.0056}_{-0.0054}$
91.2	0.1200	±0.0002	±0.0008	±0.0010	$^{+0.0048}_{-0.0048}$
133.0	0.1133	±0.0016	±0.0012	±0.0011	$^{+0.0044}_{-0.0044}$
161.0	0.1078	±0.0024	±0.0015	±0.0003	$^{+0.0040}_{-0.0040}$
172.0	0.1042	±0.0027	±0.0017	±0.0006	$^{+0.0039}_{-0.0039}$
183.0	0.1075	±0.0012	±0.0009	±0.0007	$^{+0.0036}_{-0.0037}$
189.0	0.1091	±0.0007	±0.0009	±0.0006	$^{+0.0036}_{-0.0037}$
200.0	0.1077	±0.0008	±0.0010	±0.0006	$^{+0.0035}_{-0.0037}$
206.0	0.1077	±0.0008	±0.0008	±0.0005	$^{+0.0033}_{-0.0034}$

Table 4.8: Combined LEP $\alpha_\mathrm{S}(Q)$ measurements at individual energy scales

	T only	M_H only	C only	B_T only	B_W only	y_{23} only	All
Fit results							
$\alpha_s(M_Z)$	0.1245	0.1200	0.1206	0.1243	0.1157	0.1180	0.1201
Stat. error	±0.0006	±0.0005	±0.0006	±0.0005	±0.0005	±0.0008	±0.0003
Exp. error	±0.0011	±0.0010	±0.0011	±0.0012	±0.0010	±0.0014	±0.0009
Hadr. error	±0.0015	±0.0008	±0.0018	±0.0013	±0.0007	±0.0004	±0.0009
Theory (upper)	+0.0053	+0.0041	+0.0054	+0.0065	+0.0051	+0.0025	+0.0046
Theory (lower)	−0.0052	−0.0042	−0.0052	−0.0061	−0.0052	−0.0030	−0.0047
Syst. error	±0.0056	±0.0044	±0.0057	±0.0065	±0.0053	±0.0031	±0.0048
Total error	±0.0056	±0.0044	±0.0058	±0.0065	±0.0053	±0.0032	±0.0048
χ^2 / d.o.f.	20.7/ 37	19.8/ 37	15.0/ 31	10.5/ 34	12.8/ 34	6.0/ 15	128.5/193
Weights by observable							
T	100 %	–	–	–	–	–	13.2 %
M_H	–	100 %	–	–	–	–	23.6 %
C	–	–	100 %	–	–	–	13.3 %
B_T	–	–	–	100 %	–	–	7.9 %
B_W	–	–	–	–	100 %	–	23.6 %
y_{23}	–	–	–	–	–	100 %	18.4 %
Weights by c.m. energy							
41.4 GeV	1.8 %	2.9 %	1.1 %	2.7 %	1.5 %	–	1.6 %
55.3 GeV	0.8 %	0.5 %	0.5 %	1.1 %	0.6 %	–	0.3 %
65.4 GeV	0.8 %	1.8 %	2.9 %	0.8 %	0.7 %	–	1.2 %
75.7 GeV	0.6 %	0.7 %	0.7 %	0.5 %	0.4 %	–	0.4 %
82.3 GeV	0.7 %	2.7 %	1.0 %	0.4 %	0.4 %	–	0.9 %
85.1 GeV	0.7 %	0.5 %	2.2 %	0.6 %	0.3 %	–	0.5 %
91.2 GeV	19.9 %	26.8 %	14.6 %	19.0 %	18.0 %	23.2 %	37.1 %
133.0 GeV	10.7 %	6.2 %	8.3 %	5.5 %	5.9 %	2.2 %	4.5 %
161.0 GeV	5.0 %	3.2 %	4.4 %	4.2 %	2.7 %	1.9 %	1.5 %
172.0 GeV	2.8 %	2.5 %	2.8 %	2.4 %	3.3 %	0.5 %	0.9 %
183.0 GeV	11.7 %	12.1 %	12.4 %	13.2 %	15.6 %	13.9 %	9.6 %
189.0 GeV	19.0 %	17.8 %	18.8 %	16.1 %	18.0 %	13.4 %	16.0 %
200.0 GeV	12.4 %	8.1 %	14.5 %	16.8 %	16.0 %	13.2 %	9.9 %
206.0 GeV	13.0 %	14.3 %	15.8 %	16.7 %	16.6 %	31.6 %	15.8 %
Weights by experiment							
ALEPH	24.4 %	22.5 %	27.0 %	24.9 %	24.9 %	47.8 %	25.6 %
DELPHI	23.5 %	23.4 %	21.8 %	21.4 %	21.2 %	–	22.2 %
L3	28.2 %	30.2 %	33.0 %	28.7 %	28.0 %	–	26.1 %
OPAL	23.9 %	24.0 %	18.2 %	25.0 %	25.8 %	52.2 %	26.2 %
Other weight statistics							
Total +ve	100.0 %	100.0 %	100.0 %	100.0 %	100.0 %	100.0 %	101.3 %
Total −ve	0.0 %	0.0 %	0.0 %	0.0 %	0.0 %	0.0 %	−1.3 %
Maximum	5.3 %	7.0 %	5.5 %	5.1 %	4.9 %	17.3 %	4.5 %
Minimum	0.0 %	0.0 %	0.0 %	0.0 %	0.0 %	0.0 %	−0.2 %

Table 4.9: Combined α_S fit results for different observables

	Radiative ($Q < M_{\rm Z}$)	LEP1 ($Q = M_{\rm Z}$)	LEP2 ($Q > M_{\rm Z}$)	All
Fit results				
$\alpha_{\rm s}(M_{\rm Z})$	0.1208	0.1200	0.1201	0.1201
Stat. error	±0.0012	±0.0002	±0.0005	±0.0003
Exp. error	±0.0023	±0.0008	±0.0010	±0.0009
Hadr. error	±0.0032	±0.0010	±0.0007	±0.0009
Theory (upper)	+0.0052	+0.0048	+0.0044	+0.0046
Theory (lower)	−0.0050	−0.0048	−0.0045	−0.0047
Syst. error	±0.0064	±0.0050	±0.0046	±0.0048
Total error	±0.0066	±0.0050	±0.0047	±0.0048
χ^2 / d.o.f.	34.3/ 29	7.8/ 20	83.7/142	128.5/193
Weights by observable				
T	9.5 %	15.1 %	12.4 %	13.2 %
$M_{\rm H}$	54.8 %	26.1 %	15.8 %	23.6 %
C	22.4 %	10.3 %	12.9 %	13.3 %
$B_{\rm T}$	7.2 %	11.0 %	8.0 %	7.9 %
$B_{\rm W}$	6.0 %	17.2 %	28.5 %	23.6 %
y_{23}	–	20.3 %	22.5 %	18.4 %
Weights by c.m. energy				
41.4 GeV	26.8 %	–	–	1.6 %
55.3 GeV	8.5 %	–	–	0.3 %
65.4 GeV	23.2 %	–	–	1.2 %
75.7 GeV	10.6 %	–	–	0.4 %
82.3 GeV	20.0 %	–	–	0.9 %
85.1 GeV	10.8 %	–	–	0.5 %
91.2 GeV	–	100 %	–	37.1 %
133.0 GeV	–	–	7.9 %	4.5 %
161.0 GeV	–	–	2.9 %	1.5 %
172.0 GeV	–	–	1.8 %	0.9 %
183.0 GeV	–	–	16.2 %	9.6 %
189.0 GeV	–	–	27.4 %	16.0 %
200.0 GeV	–	–	17.8 %	9.9 %
206.0 GeV	–	–	26.0 %	15.8 %
Weights by experiment				
ALEPH	–	29.5 %	25.5 %	25.6 %
DELPHI	–	22.4 %	20.3 %	22.2 %
L3	100 %	21.3 %	25.4 %	26.1 %
OPAL	–	26.8 %	28.8 %	26.2 %
Other weight statistics				
Total +ve	100.5 %	100.0 %	101.0 %	101.3 %
Total −ve	−0.5 %	0.0 %	−1.0 %	−1.3 %
Maximum	18.0 %	10.3 %	6.6 %	4.5 %
Minimum	−0.4 %	0.0 %	−0.4 %	−0.2 %

Table 4.10: $\alpha_{\rm S}$ fit results for different LEP energy ranges

	ALEPH only	DELPHI only	L3 only	OPAL only	All
Fit results					
$\alpha_\mathrm{s}(M_\mathrm{Z})$	0.1200	0.1220	0.1222	0.1183	0.1201
Stat. error	±0.0007	±0.0010	±0.0006	±0.0007	±0.0003
Exp. error	±0.0008	±0.0016	±0.0014	±0.0020	±0.0009
Hadr. error	±0.0005	±0.0008	±0.0018	±0.0005	±0.0009
Theory (upper)	+0.0044	+0.0053	+0.0050	+0.0040	+0.0046
Theory (lower)	−0.0045	−0.0052	−0.0050	−0.0042	−0.0047
Syst. error	±0.0046	±0.0055	±0.0055	±0.0046	±0.0048
Total error	±0.0046	±0.0056	±0.0055	±0.0046	±0.0048
χ^2 / d.o.f.	25.4/ 47	9.3/ 30	64.4/ 69	21.0/ 44	128.5/193
Weights by observable					
T	10.0 %	21.2 %	10.0 %	9.8 %	13.2 %
M_H	13.3 %	31.2 %	39.8 %	15.5 %	23.6 %
C	9.6 %	10.7 %	13.1 %	3.5 %	13.3 %
B_T	7.1 %	26.5 %	12.1 %	1.5 %	7.9 %
B_W	29.6 %	10.4 %	25.1 %	32.7 %	23.6 %
y_{23}	30.3 %	–	–	36.9 %	18.4 %
Weights by c.m. energy					
41.4 GeV	–	–	3.9 %	–	1.6 %
55.3 GeV	–	–	1.0 %	–	0.3 %
65.4 GeV	–	–	3.1 %	–	1.2 %
75.7 GeV	–	–	1.4 %	–	0.4 %
82.3 GeV	–	–	2.5 %	–	0.9 %
85.1 GeV	–	–	1.4 %	–	0.5 %
91.2 GeV	40.0 %	38.0 %	18.5 %	27.8 %	37.1 %
133.0 GeV	7.0 %	10.9 %	6.1 %	0.8 %	4.5 %
161.0 GeV	3.0 %	5.5 %	1.7 %	0.8 %	1.5 %
172.0 GeV	2.1 %	3.9 %	1.6 %	0.4 %	0.9 %
183.0 GeV	7.3 %	6.8 %	18.9 %	9.6 %	9.6 %
189.0 GeV	14.1 %	13.1 %	19.9 %	20.5 %	16.0 %
200.0 GeV	13.3 %	11.7 %	8.6 %	8.7 %	9.9 %
206.0 GeV	13.1 %	10.1 %	11.5 %	31.5 %	15.8 %
Weights by experiment					
ALEPH	100 %	–	–	–	25.6 %
DELPHI	–	100 %	–	–	22.2 %
L3	–	–	100 %	–	26.1 %
OPAL	–	–	–	100 %	26.2 %
Other weight statistics					
Total +ve	101.0 %	100.0 %	101.4 %	104.7 %	101.3 %
Total −ve	−1.0 %	0.0 %	−1.4 %	−4.7 %	−1.3 %
Maximum	16.2 %	10.5 %	9.2 %	21.2 %	4.5 %
Minimum	−0.7 %	0.0 %	−0.5 %	−1.6 %	−0.2 %

Table 4.11: Combined α_S fit results for different experiments
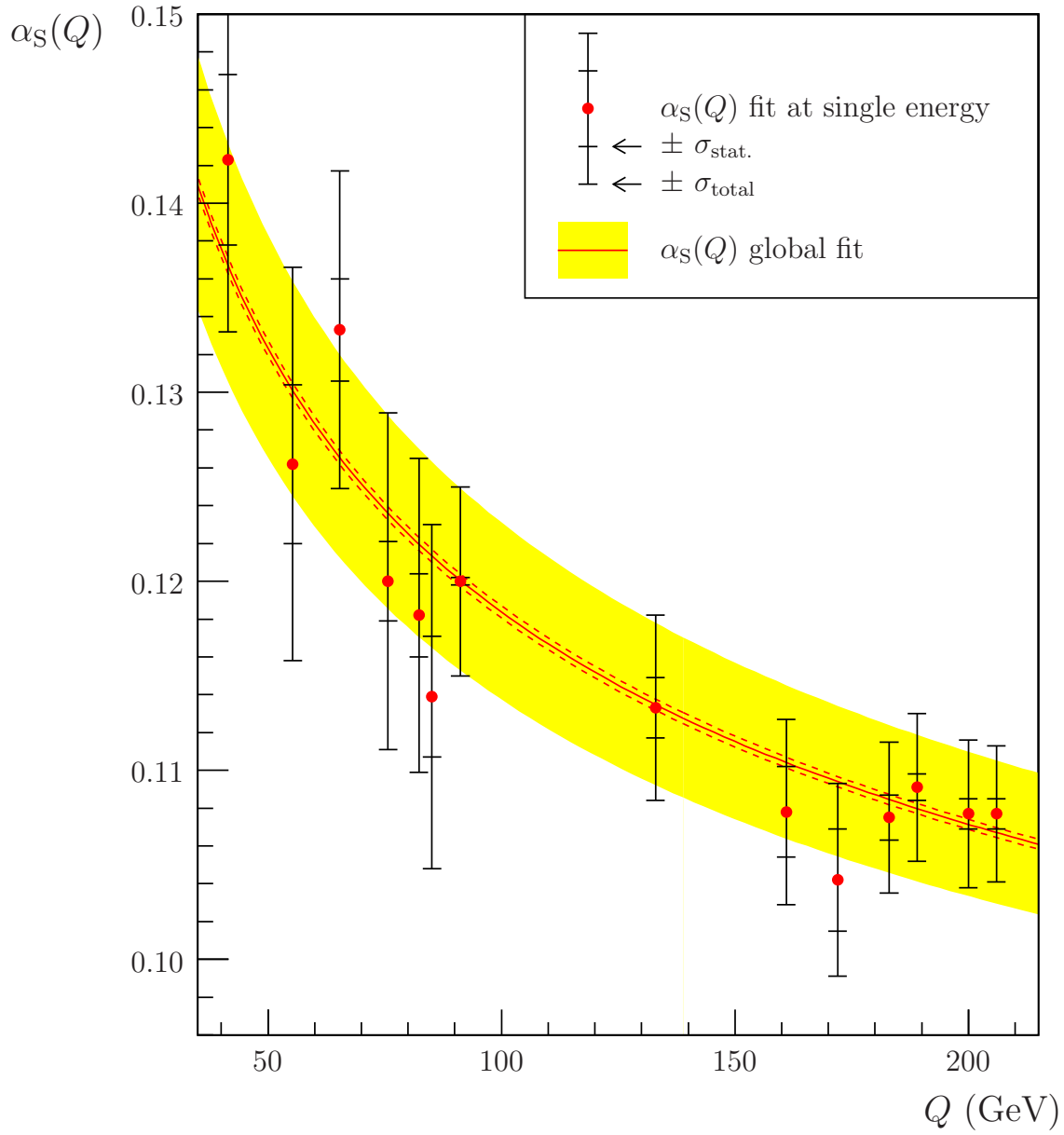
Figure 4.24: A global QCD running fit to the LEP α_{S} measurements. Each point represents a fit to the available measurements at an individual centre-of-mass energy, while the curve represents a global fit to all measurements. The form of the curve is determined by the Renormalisation Group Equation of QCD, with $\alpha_{\mathrm{S}}(M_{\mathrm{Z}})$ as a free parameter. The yellow band corresponds to the total uncertainty of the fitted $\alpha_{\mathrm{S}}(M_{\mathrm{Z}})$ value, and the dotted curves indicate the statistical uncertainty.
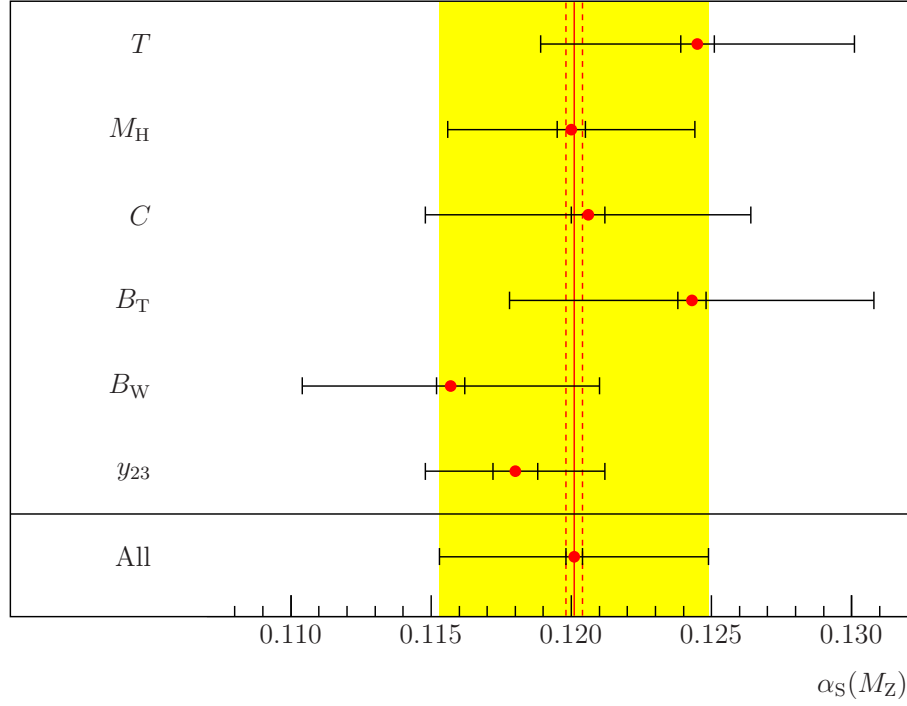
Figure 4.25: LEP $\alpha_\mathrm{S}(M_\mathrm{Z})$ combinations for individual event shape observables. The inner error bars are statistical, while the outer bars represent total uncertainties.
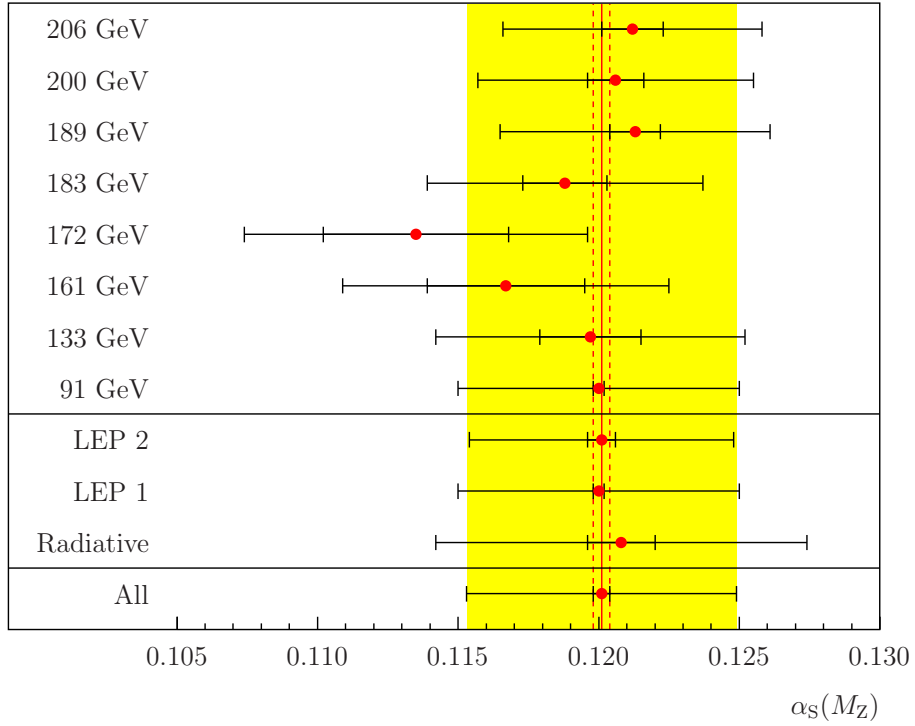
Figure 4.26: LEP $\alpha_\mathrm{S}(M_\mathrm{Z})$ combinations for individual centre-of-mass energies. The inner error bars are statistical, while the outer bars represent total uncertainties.
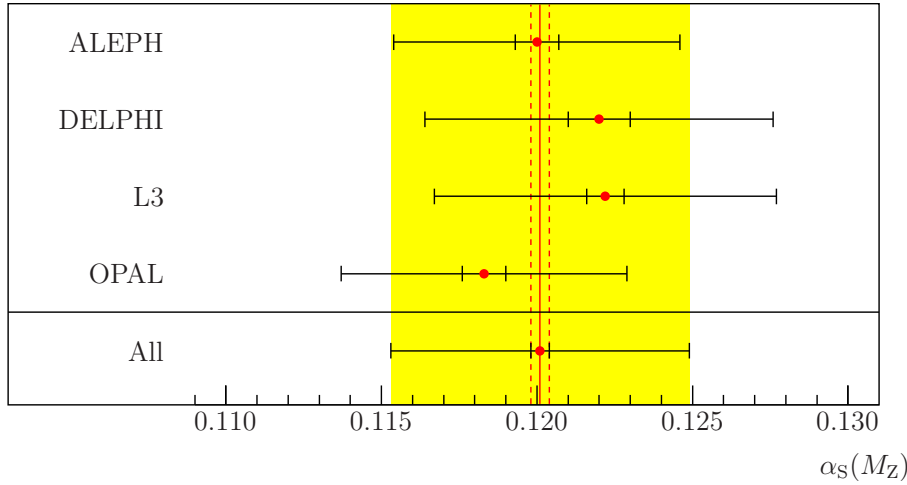
Figure 4.27: LEP $\alpha_S(M_Z)$ combinations for individual experiments. The inner error bars are statistical, while the outer bars represent total uncertainties.

since the minimisation of χ^2 should automatically select the same weights which minimise the total uncertainty: a proof of this result is given in Appendix A.3. As we have seen, however, the choice of weights which minimises the 'true' χ^2 is not acceptable, since the result depends strongly on our subjective estimates of the uncertainties and correlation coefficients. Also, many of the weights in such a combination are negative. We have therefore compromised by developing an alternative algorithm, which gives more reasonable weights, but does not minimise the uncertainty. It is debatable whether one should regard the global combination as our 'best' measurement of $\alpha_S(M_Z)$, when several of the partial combinations (and indeed several individual input measurements) have smaller uncertainties. However, we consider the global combination to be robust, since it takes input from a variety of observables, and does not rely excessively on any single assumption used in the construction of the covariance matrix. Although the 'uncertainty band' method presented in Section 1.8 represents an improvement over previous theoretical uncertainty estimates based exclusively on variation of the renormalisation scale μ, it cannot guarantee to reflect the true magnitude of the uncalculated terms in the perturbative predictions. Similarly, a high degree of arbitrariness remains in our estimation of the hadronisation uncertainties. It would therefore be inappropriate to focus *exclusively* on the measurements or observables which return the smallest uncertainties; instead we have performed a global combination, giving higher weight to the measurements which appear most precise.

The fits for individual observables, presented in Table 4.9 and Figure 4.25, provide an interesting test for our theory uncertainties. The spread of $\alpha_\mathrm{S}(M_\mathrm{Z})$ values among these six fits suggests that the correlation of theory uncertainties between observables may be lower than our previous crude estimate in Section 4.4.2.4.[25] It also indicates that the six central values agree with one another, within their total uncertainties. One could argue that the theory uncertainty for our global combination is too conservative, as it assumes 100% correlation of the theory uncertainty between observables. However, in the absence of firm evidence to the contrary, we continue to apply the method described in Section 4.9; to do otherwise would risk underestimating the dominant source of uncertainty in our combination.

---

[25]Alternatively, the theory uncertainty itself could have been drastically underestimated. This is unlikely, since all our results are in good agreement with independent measurements of $\alpha_\mathrm{S}(M_\mathrm{Z})$ from other sources.

Chapter 5

Summary and outlook

In this work, we have presented the culmination of a series of event shape measurements published by OPAL and the other LEP Collaborations.

Using a consistent set of theoretical predictions and experimental methods, we have re-analysed samples of $e^+e^- \to Z^0/\gamma \to q\bar{q}$ events collected with the OPAL detector in the energy range $\sqrt{s} = 91$–202 GeV, and have performed new measurements of event shape distributions and of the strong coupling at the highest LEP energies, up to 209 GeV. We have presented distributions of fourteen observables, including three 'four-jet' quantities which have not previously been measured from OPAL data.

Our measurements use a new event selection based on four-fermion likelihood variables, which have not been applied in previous OPAL event shape studies; the overall purities of our $q\bar{q}$ multihadronic event samples are predicted to be 94% at the highest collision energies. We have studied the efficiency and purity of this selection as functions of the event shape observables, and have also investigated the bin-to-bin response matrix of the detector. We conclude that the unfolding methods and fit ranges used in previous OPAL measurements are suitable for our own analysis.

A comparison was made between the measured event shape distributions and those predicted by Monte Carlo models. Significant discrepancies were found at $\sqrt{s} = 91$ GeV, where the measurements are statistically most precise; the modelling of observables sensitive to three-jet events, however, is superior to that for four-jet quantities. For the three-jet observables used in our α_S measurements, the modelling is satisfactory within the appropriate fit ranges: PYTHIA and ARIADNE generally give the best description. We therefore have reason to trust the hadronisation

corrections applied to perturbative predictions when measuring α_S. At energies above $\sqrt{s} = 91$ GeV, we do not have sufficient events to detect a deviation between the OPAL measurements and Monte Carlo predictions.

Fits have been performed to determine the strong coupling over the full range of LEP energy scales, based on the same six event shape observables used in previous OPAL publications. Our results strongly disfavour a constant α_S over this energy range, and are compatible with the 'running' predicted by perturbative QCD. Combining OPAL measurements from all observables and energy scales, we obtain the following weighted average of α_S at the Z^0 mass scale:

$$\alpha_S(M_Z) = 0.1189 \pm 0.0005 \text{ (stat.)} \pm 0.0041 \text{ (syst.)}   .$$

A new method was investigated to determine the statistical uncertainties of the event shape distributions and α_S measurements, using an exact analytical form for the covariance matrix; results were found to be compatible with previous estimates based on simulated data samples. The estimation of theoretical uncertainties in the fits has also been improved: an "uncertainty band" algorithm, which considers the variation of several arbitrary parameters in the theory, has been introduced in collaboration with the LEP QCD working group.

We have developed a successful method to combine α_S measurements obtained using different observables, experiments and energy scales. Detailed comparisons were made between the results and analysis methods of the four LEP Collaborations, to ensure consistent implementation of the perturbative theory predictions and fitting algorithms: the agreement was initially unsatisfactory, but is now almost perfect. Estimates were then made for the covariance matrix relating uncertainties of different measurements. The four contributions to the covariance (statistical, experimental, hadronisation and theory uncertainties) were treated separately, including correlations between all possible pairs of measurements.

Initial attempts to form a weighted mean of α_S measurements were unreliable, due to the appearance of negative weights in the combination. We have demonstrated that the negative weights arise from the presence of large correlated uncertainties with differing magnitudes in the covariance matrix. By removing the larger correlated uncertainties from the off-diagonal elements of the matrix, we were able to form a stable combination with reasonable weights. Our final combined result,

using all available measurements from event shape observables at LEP, is

$$\alpha_S(M_Z) = 0.1201 \pm 0.0003 \text{ (stat.)} \pm 0.0048 \text{ (syst.)} \quad .$$

We have also performed combinations of certain subsets of measurements, such as those for individual energies, observables or experiments. These results are all in good agreement with the global combination, and with the predicted running of α_S with energy. Some of the partial combinations, however, such as the OPAL result, have a smaller uncertainty than that of the complete LEP combination: this is a consequence of the incomplete correlations used in the covariance matrix.

The dominant uncertainty in our combined α_S measurement, and in many of the original input measurements, arises from the higher-order terms missing from the perturbative calculations; at $\sqrt{s} = 91$ GeV, the measured event shape distributions are sufficiently precise to observe significant deviations from the fitted $\mathcal{O}(\alpha_S^2)$ + NLLA theory predictions. When the next generation of QCD calculations become available, at $\mathcal{O}(\alpha_S^3)$ and next-to-next-to-leading logarithmic order, a more precise measurement of $\alpha_S(M_Z)$ will be possible using the existing LEP data. It is also likely that the data at 91 GeV will permit a test of the higher-order terms.

As we discussed in Section 1.7, several new resummations have recently become available at NLLA precision, including the distributions of the light jet mass, narrow jet broadening and D-parameter. Although we have not performed fits to these 'four-jet' observables ourselves, it is planned that OPAL data will be used to test these predictions, and to extract a corresponding measurement of α_S.

It is expected that the measurements presented in this dissertation will form the basis for two publications in the near future, containing the final measurement of α_S from event shapes at OPAL, and the final combination of published α_S results from the four LEP Collaborations. A small number of improvements may be made to the analysis presented here, prior to publication.

Appendix A

Explanations and proofs of some statistical results

In this appendix, we shall elaborate on some of the statistical methods applied in our analysis. With the possible exception of Section A.1, the results presented here are standard, and can be can be found in textbooks such as Ref. [121].

A.1 The statistical covariance matrix for a corrected and normalised histogram

In Chapter 3, we described measurements of $\alpha_S(Q)$ obtained by fitting theoretical predictions to several event shape distributions constructed from OPAL data. The best fit between the prediction and the data was determined by minimisation of a χ^2 variable, based only on statistical uncertainties.

When we construct a 'raw' histogram from the events seen in the detector, without normalisation, the statistical uncertainties are straightforward: the number of events, N_i, in each bin conforms to a Poisson distribution, and there is no correlation between bins.[1] Before making a fit, however, we apply three modifications to our data:

1. We subtract the expected background β_i from each bin:

$$N_i \;\; \to \;\; N_i - \beta_i \tag{A.1}$$

---

[1]There may be 'migrations' between bins, as discussed in Section 3.4.3, but these only introduce *systematic* correlations.

2. We multiply the remaining events by a "detector correction," α_i:

$$N_i - \beta_i \quad \rightarrow \quad \widetilde{N}_i = \alpha_i \left(N_i - \beta_i \right) \tag{A.2}$$

3. Finally we normalise the distribution, to obtain a measure P_i of the probability for a given event to occur in bin i:

$$P_i \;=\; \frac{\widetilde{N}_i}{\sum_k \widetilde{N}_k} \tag{A.3}$$

In practice we also divide the contents of each bin by the width Δy_i, to measure the probability density function. This factor will be omitted here, and can easily be applied to each element of our final covariance matrix.

In the final normalisation step above, we have introduced correlations between bins, since the contents of each bin now appears in the denominator of every other. For a trivial case of only two bins, their correlation coefficient ρ would be -1, because an upward fluctuation in one bin must be precisely compensated by a downward fluctuation in the other. Here we derive the general covariance matrix $V_{ij} = \text{Cov}\left[P_i, P_j\right]$, which is used in Section 3.5 to perform a least-squares fit to the distribution, and to determine the corresponding statistical uncertainty. The uncertainty can also be measured numerically by a Monte Carlo method, as we discussed in Section 3.5.3.2.

The covariance matrix for the corrected bin contents $\widetilde{N}_i$ is given by

$$\text{Cov}\left[\widetilde{N}_i, \widetilde{N}_j\right] \;=\; \alpha_i \alpha_j \, \text{Cov}\left[N_i, N_j\right] \;=\; \begin{cases} \alpha_i^2 N_i & i = j \\ 0 & i \neq j \end{cases} \tag{A.4}$$

We can propagate these uncertainties into a covariance matrix for P_i, as follows:

$$\begin{aligned} V_{ij} \;=\; \text{Cov}\left[P_i, P_j\right] \;&=\; \sum_{k,l} \frac{\partial P_i}{\partial \widetilde{N}_k} \frac{\partial P_j}{\partial \widetilde{N}_l} \, \text{Cov}\left[\widetilde{N}_k, \widetilde{N}_l\right] \\ &=\; \sum_k \frac{\partial P_i}{\partial \widetilde{N}_k} \frac{\partial P_j}{\partial \widetilde{N}_k} \, \alpha_k^2 N_k \quad . \end{aligned} \tag{A.5}$$

The partial derivatives here are obtained directly from Equation (A.3):

$$\frac{\partial P_i}{\partial \widetilde{N}_k} = \begin{cases} \dfrac{\sum_{l \neq i} \widetilde{N}_l}{\left[\sum_l \widetilde{N}_l\right]^2} & i = k \\[4ex] -\dfrac{\widetilde{N}_i}{\left[\sum_l \widetilde{N}_l\right]^2} & i \neq k \end{cases} \quad, \tag{A.6}$$

leading to the following expressions for the covariance matrix V_{ij}:

$$V_{ij} = \begin{cases} \dfrac{\alpha_i^2 N_i \left[\sum_{k \neq i} \widetilde{N}_k\right]^2 + \left[\sum_{k \neq i} \alpha_k^2 N_k\right] \widetilde{N}_i^2}{\left[\sum_k \widetilde{N}_k\right]^4} & i = j \\[5ex] \dfrac{\left[\sum_{k \neq i,j} \alpha_k^2 N_k\right] \widetilde{N}_i \widetilde{N}_j - \alpha_i^2 N_i \widetilde{N}_j \left[\sum_{k \neq i} \widetilde{N}_k\right] - \alpha_j^2 N_j \widetilde{N}_i \left[\sum_{k \neq j} \widetilde{N}_k\right]}{\left[\sum_k \widetilde{N}_k\right]^4} & i \neq j \end{cases} \tag{A.7}$$

In the case where no background subtraction or detector correction takes place, namely $\alpha_i = 1$ and $\widetilde{N}_i = N_i$, the above formulae simplify to

$$V_{ij} = \begin{cases} \dfrac{N_i \left[\sum_{k \neq i} N_k\right]}{\left[\sum_k N_k\right]^3} = \dfrac{P_i (1 - P_i)}{\sum_k N_k} & i = j \\[4ex] -\dfrac{N_i N_j}{\left[\sum_k N_k\right]^3} = -\dfrac{P_i P_j}{\sum_k N_k} & i \neq j \end{cases} \quad. \tag{A.8}$$

This is the standard covariance matrix for a normalised multinomial distribution (or binomial distribution, in the case of the diagonal elements).

In practice, we calculate the covariance matrix using the *expected* numbers of events N_i and $\widetilde{N}_i$, estimated from Monte Carlo samples, and not from the actual data. Using real data would allow a downward fluctuation in the observed number of events N_i to reduce the corresponding uncertainty, as described in Section 3.5.5.

It should be emphasised that it is *not* correct, as is sometimes suggested, to assume a multinomial covariance matrix for the bins N_i at the detector level and then propagate this matrix to the normalised hadron level. This approach would give covariances for a distribution which has been normalised at the detector level, and is no longer normalised after unfolding. The statistical properties of the nor-

malisation factor, which is responsible for the bin-to-bin correlations, can differ substantially between the detector and hadron levels. At the detector level, the bin contents are Poisson distributions, so the bins with the largest contents also have the largest absolute uncertainties; after unfolding to the detector level, however, the uncertainties in the tail of the distribution may be amplified by large detector corrections, and can even exceed those in the most highly populated bins. This effect is especially significant for 'four-jet' observables, such as the aplanarity, which are measured relatively poorly by the detector. One cannot, therefore, expect a matrix of correlation coefficients derived for a normalised *detector-level* distribution to be valid for an unfolded hadron-level distribution.

Table A.1 shows the predicted statistical uncertainties for the total jet broadening and aplanarity distributions, at 189 GeV. In the unfolded aplanarity distribution, we see that the largest contribution to the uncertainty of the normalisation factor is due to the overflow bin; this bin would be completely neglected if the uncertainty were derived by propagation from a normalised detector-level distribution.

Fortunately, most bins of our event shape distributions are 'narrow', so they behave approximately like a set of uncorrelated Poisson variables divided by a constant normalisation factor: this was the implicit assumption made in previous OPAL analyses. For wide bins such as the first bin of aplanarity, however, the uncertainty of the normalisation cannot be neglected. Furthermore, the correlations between bins can never be neglected when fitting a theoretical prediction to the distribution, if a significant proportion of events fall inside the fit range.[2] To calculate the uncertainty of the fit, one must either use a Monte Carlo 'subsample' method, as described in Section 3.5.3.2, or use a χ^2 parameter based on the full analytical covariance matrix.

---

[2]This statement is true even if the bins themselves are infinitesimally narrow. As the number of bins n within the fit range increases, the covariance between any pair of bins will fall as $1/n^2$ (and the correlation coefficient as $1/n$), but the number of entries in the covariance matrix will scale with n^2.

Total jet broadening, B_{T}	Detector level events $N_i \pm \sqrt{N_i}$	Background β_i	Detector correction α_i	Hadron-level events $\alpha_i(N_i - \beta_i) \pm \alpha_i\sqrt{N_i}$
$0.000 - 0.030$	147 ± 12	0	1.27	187 ± 15
$0.030 - 0.040$	297 ± 17	1	1.06	315 ± 18
$0.040 - 0.050$	351 ± 19	1	0.91	317 ± 17
$0.050 - 0.060$	327 ± 18	1	0.84	273 ± 15
$0.060 - 0.075$	405 ± 20	2	0.83	334 ± 17
$0.075 - 0.090$	313 ± 18	3	0.84	261 ± 15
$0.090 - 0.110$	324 ± 18	7	0.87	276 ± 16
$0.110 - 0.130$	248 ± 16	11	0.86	205 ± 14
$0.130 - 0.160$	278 ± 17	25	0.90	228 ± 15
$0.160 - 0.200$	237 ± 15	45	0.99	190 ± 15
$0.200 - 0.250$	144 ± 12	44	1.32	132 ± 16
$0.250 - 0.300$	46.7 ± 6.8	22.2	2.50	61 ± 17
$0.300 - 0.350$	10.4 ± 3.2	7.7	5.04	14 ± 16
Overflow	1.1 ± 1.0	1.0	18.0	1 ± 18
Total	$\sum_i N_i = 3130 \pm 56$	171	—	$\sum_i \widetilde{N}_i = 2793 \pm 60$

Aplanarity, A	Detector level events $N_i \pm \sqrt{N_i}$	Background β_i	Detector correction α_i	Hadron-level events $\alpha_i(N_i - \beta_i) \pm \alpha_i\sqrt{N_i}$
$0.000 - 0.005$	2260 ± 48	45	0.88	1945 ± 42
$0.005 - 0.010$	481 ± 22	42	0.97	429 ± 21
$0.010 - 0.015$	177 ± 13	26	1.05	158 ± 14
$0.015 - 0.025$	128 ± 11	26	1.30	132 ± 15
$0.025 - 0.040$	55.4 ± 7.4	17.2	1.75	67 ± 13
$0.040 - 0.070$	20.9 ± 4.6	8.7	3.40	42 ± 16
$0.070 - 0.100$	3.4 ± 1.8	2.4	11.7	12 ± 22
Overflow	3.8 ± 1.9	3.5	30.1	9 ± 58
Total	$\sum_i N_i = 3130 \pm 56$	171	—	$\sum_i \widetilde{N}_i = 2793 \pm 83$

Table A.1: Monte Carlo predictions for the total jet broadening and aplanarity distributions at 189 GeV, corresponding to the luminosity of the OPAL measurement. The expected number of events in each bin is shown without normalisation, at the detector and hadron levels; the detector level includes background. The predicted statistical uncertainties are those of the OPAL measurement (not of the Monte Carlo prediction itself), and are uncorrelated between bins in this unnormalised distribution.

A.2 χ^2 in the presence of correlations

In Section 4.3.1, we claimed that the following expression should be minimised with respect to the parameter λ to determine the best fit between theory and experiment:

$$
\begin{aligned}
\chi^2 &= \sum_{ij} \left(y_i - \alpha_\mathrm{S}(Q_i; \lambda)\right) \left(V^{-1}\right)_{ij} \left(y_j - \alpha_\mathrm{S}(Q_j; \lambda)\right) \\
&\equiv \sum_{ij} \delta y_i \left(V^{-1}\right)_{ij} \delta y_j
\end{aligned}
\tag{A.9}
$$

Here y_i is an experimental measurement at an energy scale Q_i, and $\alpha_\mathrm{S}(Q_i; \lambda)$ is a theoretical prediction for the measured quantity at the same energy scale. V is the covariance matrix relating the uncertainties of the measurements. λ is an unknown parameter of the theory, which we wish to measure (in our case, $\alpha_\mathrm{S}(M_\mathrm{Z})$).

Explanation:

It is well-known [121] that the following definition of χ^2 is a measure of the negative log-likelihood for data with *uncorrelated* Gaussian distributions:

$$
\chi^2 = \sum_i \frac{\left(u_i - f(x_i; \lambda)\right)^2}{\sigma_i^2} \equiv \frac{(\delta u_i)^2}{\sigma_i^2} \quad .
\tag{A.10}
$$

In this expression, $f(x_i; \lambda)$ is the predicted mean value for the measurement u_i, and σ_i is its standard deviation. Therefore δu_i, the difference between the measurement and its predicted mean, has an expectation value of zero, and a standard deviation of σ_i.

Equation (A.10) can be written in matrix form, by defining the covariance matrix W for the vector of deviations δu:

$$
W = \begin{pmatrix} \sigma_1^2 & 0 & 0 & \cdots \\ 0 & \sigma_2^2 & 0 & \cdots \\ 0 & 0 & \sigma_3^2 & \cdots \\ \vdots & \vdots & \vdots & \ddots \end{pmatrix} \quad \text{and} \quad W^{-1} = \begin{pmatrix} \frac{1}{\sigma_1^2} & 0 & 0 & \cdots \\ 0 & \frac{1}{\sigma_2^2} & 0 & \cdots \\ 0 & 0 & \frac{1}{\sigma_3^2} & \cdots \\ \vdots & \vdots & \vdots & \ddots \end{pmatrix} \quad ,
\tag{A.11}
$$

so that

$$
\chi^2 = (\delta u)^\mathrm{T} W^{-1} (\delta u) \quad .
\tag{A.12}
$$

Suppose we now apply a linear transformation represented by the matrix A:

$$
\begin{aligned}
\chi^2 &= \left(A\,\delta u\right)^{\mathrm{T}}\left(A\,W A^{\mathrm{T}}\right)^{-1}\left(A\,\delta u\right) \\
&\equiv \left(\delta u'\right)^{\mathrm{T}}\left(W'\right)^{-1}\left(\delta u'\right) \tag{A.13}
\end{aligned}
$$

Here each component of the vector $\delta u' = A\,\delta u$ represents a linear combination of the original elements δu_i defined in Equation (A.10). Furthermore, the matrix $W' = A\,W A^{\mathrm{T}}$ is the covariance matrix relating these linear combinations; this can be proven by the same method used in Section 4.3.3 to find the variance of a single linear combination.

We now wish to establish the validity of Equation (A.9), for a set of measurements y_i with covariance matrix V. This will be proven if we can find a set of uncorrelated quantities δu_i with covariance matrix W, and a matrix A, such that

$$
\delta y = A\,\delta u \tag{A.14}
$$

$$
\text{and} \quad V = A\,W A^{\mathrm{T}} \quad . \tag{A.15}
$$

The covariance matrix V is real and symmetric, by definition, so A is simply the orthonormal matrix which diagonalises it. The elements of the diagonal matrix W are the eigenvalues of V. Furthermore, the matrix A is non-singular (since $A^{\mathrm{T}} = A^{-1}$), so Equation (A.14) may be inverted to find δu. Each element δu_i is an uncorrelated linear combination of the correlated deviations δy.

Hence we have shown that χ^2, as defined in Equation (A.9), is a valid measure of the negative log-likelihood when the Gaussian uncertainties of the measurements y_i are correlated. Applying the principle of maximum likelihood, we should therefore minimise this quantity to estimate the parameter λ.

A.3 Minimisation of the total uncertainty in a weighted mean[3]

In Section 4.3.2 we chose the weights

$$w_i = \frac{\sum_j (V^{-1})_{ij}}{\sum_{jk} (V^{-1})_{jk}} \quad , \tag{A.16}$$

so as to minimise the following χ^2, which measures the likelihood of the data y_i for a weighted mean $\sum_k w_k y_k$:

$$\chi^2 = \sum_{ij} \left(y_i - \left[\sum_k w_k y_k\right]\right) (V^{-1})_{ij} \left(y_j - \left[\sum_k w_k y_k\right]\right) \quad . \tag{A.17}$$

But we claimed without proof, in Section 4.3.4, that that these same weights would also minimise the total variance σ^2 of the weighted mean:

$$\sigma^2 = \sum_{ij} w_i V_{ij} w_j \equiv w^{\mathrm{T}} V w \quad . \tag{A.18}$$

Proof:

We wish to minimise the variance σ^2, as defined in Equation (A.18), subject to the constraint that the sum of the weights w_i should be unity:

$$\sum_k w_k = 1 \quad . \tag{A.19}$$

This is achieved by introducing a Lagrange multiplier μ, and requiring the following set of partial derivatives to vanish:

$$\frac{\partial}{\partial w_i}\left(\sigma^2 - \mu \sum_k w_k\right) = 0 \, , \quad \forall i \quad . \tag{A.20}$$

Substituting σ^2 from Equation (A.18), and exploiting the symmetry of the covariance matrix V, we find

$$2\left(\sum_j V_{ij} w_j\right) - \mu = 0 \, , \quad \forall i \quad . \tag{A.21}$$

---

[3]The primed quantities y_i' and V' used in Equations (4.7), (4.11) and (4.13) will be denoted by y_i and V respectively in this section, for clarity.

In matrix notation, we have

$$2\,V w = \mu\,a \quad , \quad \text{where we have defined} \quad a = \begin{pmatrix} 1 \\ 1 \\ 1 \\ \vdots \end{pmatrix} \qquad \text{(A.22)}$$

Therefore, provided V is non-singular[4], we may invert this equation to find the vector of weights w:

$$w = \frac{\mu}{2} V^{-1} a \quad . \qquad \text{(A.23)}$$

Re-writing Equation (A.19) in vector notation, we have

$$a^{\mathrm{T}} w = 1 \quad , \qquad \text{(A.24)}$$

so we can now eliminate the Lagrange multiplier μ to find

$$w = \frac{V^{-1} a}{a^{\mathrm{T}} V^{-1} a} \quad . \qquad \text{(A.25)}$$

This is the same vector of weights given in Equation (A.16). We have therefore shown that our choice of weights simultaneously maximises the likelihood of the data, and minimises the total variance of the weighted mean.

---

[4]The statement that V is non-singular is equivalent to the requirement that no measurement can be predicted with absolute precision from the other measurements. If this condition were violated, a linear combination of measurements would exist with a variance of zero, and so one of the eigenvalues of V would vanish.

Appendix B

OPAL event shape distributions

In this appendix, we present the distributions of the following event shape observables, measured by OPAL at centre-of-mass energies $\sqrt{s} = 91 - 207$ GeV:

1. Thrust, T

2. Heavy jet mass, M_{H}

3. C-parameter

4. Total jet broadening, B_{T}

5. Wide jet broadening, B_{W}

6. Durham y_{23} parameter

7. Thrust major, $T_{\mathrm{maj.}}$

8. Thrust minor, $T_{\mathrm{min.}}$

9. Aplanarity, A

10. Sphericity, S

11. Oblateness, O

12. Light jet mass, M_{L}

13. Narrow jet broadening, B_{N}

14. D-parameter

Definitions of these observables can be found in Section 1.5, and a full discussion of the analysis procedure is given in Chapter 3.

B.1   Thrust, T

$1 - T$	$R'(1-T)$ at 91 GeV			$R'(1-T)$ at 133 GeV		
$0.00 - 0.01$	1.273	$\pm$ 0.019	$\pm$ 0.043	4.37	$\pm$ 0.82	$\pm$ 0.55
$0.01 - 0.02$	12.26	$\pm$ 0.05	$\pm$ 0.40	20.4	$\pm$ 1.6	$\pm$ 3.8
$0.02 - 0.03$	18.38	$\pm$ 0.07	$\pm$ 0.28	20.4	$\pm$ 1.5	$\pm$ 1.7
$0.03 - 0.04$	13.86	$\pm$ 0.06	$\pm$ 0.15	10.5	$\pm$ 1.2	$\pm$ 0.9
$0.04 - 0.05$	9.80	$\pm$ 0.05	$\pm$ 0.18	6.7	$\pm$ 1.0	$\pm$ 0.4
$0.05 - 0.07$	6.502	$\pm$ 0.027	$\pm$ 0.086	4.70	$\pm$ 0.58	$\pm$ 0.35
$0.07 - 0.09$	4.133	$\pm$ 0.022	$\pm$ 0.037	3.64	$\pm$ 0.51	$\pm$ 0.29
$0.09 - 0.12$	2.649	$\pm$ 0.014	$\pm$ 0.058	1.68	$\pm$ 0.32	$\pm$ 0.44
$0.12 - 0.15$	1.705	$\pm$ 0.012	$\pm$ 0.075	1.36	$\pm$ 0.24	$\pm$ 0.32
$0.15 - 0.22$	0.913	$\pm$ 0.006	$\pm$ 0.020	1.09	$\pm$ 0.12	$\pm$ 0.18
$0.22 - 0.30$	0.3704	$\pm$ 0.0033	$\pm$ 0.0090	0.467	$\pm$ 0.065	$\pm$ 0.066

$1 - T$	$R'(1-T)$ at 161 GeV			$R'(1-T)$ at 172 GeV		
$0.00 - 0.01$	8.9	$\pm$ 1.6	$\pm$ 1.3	11.3	$\pm$ 1.8	$\pm$ 3.0
$0.01 - 0.02$	23.0	$\pm$ 2.6	$\pm$ 1.2	20.9	$\pm$ 2.9	$\pm$ 2.1
$0.02 - 0.03$	16.5	$\pm$ 2.2	$\pm$ 1.5	19.0	$\pm$ 2.4	$\pm$ 4.6
$0.03 - 0.04$	11.8	$\pm$ 1.8	$\pm$ 1.7	8.5	$\pm$ 2.0	$\pm$ 1.0
$0.04 - 0.05$	5.4	$\pm$ 1.6	$\pm$ 1.4	4.5	$\pm$ 1.7	$\pm$ 0.5
$0.05 - 0.07$	3.82	$\pm$ 0.93	$\pm$ 0.64	6.0	$\pm$ 1.0	$\pm$ 1.2
$0.07 - 0.09$	2.51	$\pm$ 0.77	$\pm$ 0.96	4.0	$\pm$ 0.9	$\pm$ 1.3
$0.09 - 0.12$	2.77	$\pm$ 0.51	$\pm$ 0.38	1.14	$\pm$ 0.58	$\pm$ 0.57
$0.12 - 0.15$	1.60	$\pm$ 0.41	$\pm$ 0.68	0.42	$\pm$ 0.52	$\pm$ 0.34
$0.15 - 0.22$	0.80	$\pm$ 0.22	$\pm$ 0.20	1.08	$\pm$ 0.26	$\pm$ 0.27
$0.22 - 0.30$	0.40	$\pm$ 0.15	$\pm$ 0.21	0.22	$\pm$ 0.22	$\pm$ 0.24

$1 - T$	$R'(1-T)$ at 183 GeV			$R'(1-T)$ at 189 GeV		
$0.00 - 0.01$	8.08	$\pm$ 0.94	$\pm$ 0.61	9.36	$\pm$ 0.55	$\pm$ 0.58
$0.01 - 0.02$	23.0	$\pm$ 1.4	$\pm$ 1.9	21.93	$\pm$ 0.80	$\pm$ 0.91
$0.02 - 0.03$	15.6	$\pm$ 1.1	$\pm$ 1.7	15.35	$\pm$ 0.64	$\pm$ 0.89
$0.03 - 0.04$	9.6	$\pm$ 0.9	$\pm$ 1.6	9.82	$\pm$ 0.54	$\pm$ 0.68
$0.04 - 0.05$	7.7	$\pm$ 0.8	$\pm$ 1.1	7.15	$\pm$ 0.47	$\pm$ 0.51
$0.05 - 0.07$	5.06	$\pm$ 0.47	$\pm$ 0.48	5.38	$\pm$ 0.28	$\pm$ 0.28
$0.07 - 0.09$	3.21	$\pm$ 0.40	$\pm$ 0.63	2.89	$\pm$ 0.24	$\pm$ 0.16
$0.09 - 0.12$	2.05	$\pm$ 0.28	$\pm$ 0.25	2.44	$\pm$ 0.16	$\pm$ 0.08
$0.12 - 0.15$	1.36	$\pm$ 0.23	$\pm$ 0.16	1.36	$\pm$ 0.14	$\pm$ 0.14
$0.15 - 0.22$	0.77	$\pm$ 0.13	$\pm$ 0.11	0.72	$\pm$ 0.08	$\pm$ 0.11
$0.22 - 0.30$	0.34	$\pm$ 0.09	$\pm$ 0.14	0.479	$\pm$ 0.065	$\pm$ 0.096

Table B.1: Distributions for the thrust, T, measured by OPAL at centre-of-mass energies $\sqrt{s} = 91$–189 GeV. The first uncertainty is statistical, while the second is systematic.

Figure B.1: Distributions for the thrust, T, measured by OPAL at centre-of-mass energies $\sqrt{s} = 91$–189 GeV. The inner error bars indicate statistical uncertainties. Each curve is generated using five million non-radiative Monte Carlo events, after hadronisation.

Thrust, T (contd.)

$1 - T$	$R'(1 - T)$ at 192 GeV	$R'(1 - T)$ at 196 GeV
$0.00 - 0.01$	$9.0 \pm 1.5 \pm 1.6$	$8.70 \pm 0.95 \pm 0.53$
$0.01 - 0.02$	$22.6 \pm 2.1 \pm 3.0$	$23.6 \pm 1.4 \pm 1.4$
$0.02 - 0.03$	$13.2 \pm 1.7 \pm 1.4$	$15.3 \pm 1.1 \pm 1.2$
$0.03 - 0.04$	$9.3 \pm 1.4 \pm 1.8$	$9.86 \pm 0.85 \pm 0.94$
$0.04 - 0.05$	$7.0 \pm 1.2 \pm 0.9$	$7.13 \pm 0.78 \pm 0.95$
$0.05 - 0.07$	$5.67 \pm 0.73 \pm 0.85$	$5.21 \pm 0.46 \pm 0.22$
$0.07 - 0.09$	$3.16 \pm 0.60 \pm 0.83$	$2.59 \pm 0.39 \pm 0.48$
$0.09 - 0.12$	$1.84 \pm 0.41 \pm 0.30$	$2.54 \pm 0.26 \pm 0.16$
$0.12 - 0.15$	$1.55 \pm 0.36 \pm 0.48$	$1.42 \pm 0.23 \pm 0.18$
$0.15 - 0.22$	$0.81 \pm 0.20 \pm 0.39$	$0.70 \pm 0.14 \pm 0.28$
$0.22 - 0.30$	$0.19 \pm 0.18 \pm 0.17$	$0.54 \pm 0.13 \pm 0.24$

$1 - T$	$R'(1 - T)$ at 200 GeV	$R'(1 - T)$ at 202 GeV
$0.00 - 0.01$	$9.8 \pm 1.0 \pm 1.1$	$11.3 \pm 1.5 \pm 1.5$
$0.01 - 0.02$	$22.6 \pm 1.4 \pm 1.4$	$20.5 \pm 2.0 \pm 0.7$
$0.02 - 0.03$	$14.3 \pm 1.1 \pm 1.0$	$14.8 \pm 1.5 \pm 1.1$
$0.03 - 0.04$	$8.7 \pm 0.9 \pm 1.3$	$8.0 \pm 1.3 \pm 0.5$
$0.04 - 0.05$	$7.85 \pm 0.78 \pm 0.88$	$6.2 \pm 1.2 \pm 0.8$
$0.05 - 0.07$	$4.70 \pm 0.47 \pm 0.47$	$5.12 \pm 0.67 \pm 0.41$
$0.07 - 0.09$	$2.75 \pm 0.42 \pm 0.53$	$3.34 \pm 0.59 \pm 0.75$
$0.09 - 0.12$	$2.09 \pm 0.26 \pm 0.19$	$2.54 \pm 0.41 \pm 0.45$
$0.12 - 0.15$	$1.57 \pm 0.24 \pm 0.50$	$1.38 \pm 0.34 \pm 0.16$
$0.15 - 0.22$	$1.06 \pm 0.13 \pm 0.24$	$0.91 \pm 0.19 \pm 0.27$
$0.22 - 0.30$	$0.34 \pm 0.15 \pm 0.20$	$0.43 \pm 0.23 \pm 0.47$

$1 - T$	$R'(1 - T)$ at 205 GeV	$R'(1 - T)$ at 207 GeV
$0.00 - 0.01$	$10.4 \pm 1.0 \pm 1.0$	$11.61 \pm 0.79 \pm 0.69$
$0.01 - 0.02$	$21.6 \pm 1.4 \pm 1.2$	$23.7 \pm 1.1 \pm 0.9$
$0.02 - 0.03$	$14.8 \pm 1.1 \pm 2.5$	$15.03 \pm 0.85 \pm 0.69$
$0.03 - 0.04$	$10.4 \pm 0.9 \pm 1.5$	$9.53 \pm 0.71 \pm 0.77$
$0.04 - 0.05$	$7.12 \pm 0.78 \pm 0.94$	$7.51 \pm 0.62 \pm 0.27$
$0.05 - 0.07$	$6.19 \pm 0.47 \pm 0.48$	$4.68 \pm 0.36 \pm 0.15$
$0.07 - 0.09$	$2.75 \pm 0.40 \pm 0.43$	$2.93 \pm 0.31 \pm 0.32$
$0.09 - 0.12$	$1.95 \pm 0.27 \pm 0.22$	$2.23 \pm 0.21 \pm 0.17$
$0.12 - 0.15$	$1.37 \pm 0.25 \pm 0.28$	$1.35 \pm 0.19 \pm 0.16$
$0.15 - 0.22$	$0.81 \pm 0.15 \pm 0.15$	$0.73 \pm 0.11 \pm 0.15$
$0.22 - 0.30$	$0.17 \pm 0.17 \pm 0.26$	$0.20 \pm 0.13 \pm 0.15$

Table B.2: Distributions for the thrust, T, measured by OPAL at centre-of-mass energies $\sqrt{s} = 192$–207 GeV. The first uncertainty is statistical, while the second is systematic.

Figure B.2: Distributions for the thrust, T, measured by OPAL at centre-of-mass energies $\sqrt{s} = 192$–207 GeV. The inner error bars indicate statistical uncertainties. Each curve is generated using five million non-radiative Monte Carlo events, after hadronisation.

B.2   Heavy jet mass, M_{H}

$M_{\mathrm{H}}/\sqrt{s}$	$R'(M_{\mathrm{H}}/\sqrt{s})$ at 91 GeV	$R'(M_{\mathrm{H}}/\sqrt{s})$ at 133 GeV
$0.060 - 0.075$	$0.1185 \pm 0.0030 \pm 0.0098$	$0.38 \pm 0.16 \pm 0.13$
$0.075 - 0.090$	$0.55 \pm 0.01 \pm 0.13$	$1.56 \pm 0.35 \pm 0.36$
$0.090 - 0.110$	$2.17 \pm 0.01 \pm 0.38$	$4.7 \pm 0.5 \pm 1.3$
$0.110 - 0.140$	$5.729 \pm 0.020 \pm 0.057$	$8.2 \pm 0.5 \pm 1.0$
$0.140 - 0.170$	$6.65 \pm 0.02 \pm 0.35$	$4.99 \pm 0.48 \pm 0.82$
$0.170 - 0.200$	$4.88 \pm 0.02 \pm 0.15$	$3.92 \pm 0.43 \pm 0.28$
$0.200 - 0.250$	$3.30 \pm 0.01 \pm 0.11$	$2.47 \pm 0.27 \pm 0.30$
$0.250 - 0.300$	$2.105 \pm 0.010 \pm 0.051$	$1.41 \pm 0.23 \pm 0.22$
$0.300 - 0.350$	$1.353 \pm 0.008 \pm 0.042$	$1.35 \pm 0.18 \pm 0.23$
$0.350 - 0.450$	$0.703 \pm 0.004 \pm 0.030$	$0.758 \pm 0.088 \pm 0.075$
$0.450 - 0.600$	$0.1378 \pm 0.0016 \pm 0.0043$	$0.162 \pm 0.033 \pm 0.016$
$M_{\mathrm{H}}/\sqrt{s}$	$R'(M_{\mathrm{H}}/\sqrt{s})$ at 161 GeV	$R'(M_{\mathrm{H}}/\sqrt{s})$ at 172 GeV
$0.060 - 0.075$	$1.54 \pm 0.32 \pm 0.64$	$1.21 \pm 0.42 \pm 0.60$
$0.075 - 0.090$	$3.9 \pm 0.8 \pm 1.8$	$4.96 \pm 0.89 \pm 0.92$
$0.090 - 0.110$	$5.4 \pm 1.0 \pm 2.6$	$5.1 \pm 1.1 \pm 0.5$
$0.110 - 0.140$	$7.4 \pm 0.8 \pm 1.6$	$7.3 \pm 0.9 \pm 1.4$
$0.140 - 0.170$	$4.67 \pm 0.71 \pm 0.79$	$4.0 \pm 0.8 \pm 1.4$
$0.170 - 0.200$	$2.85 \pm 0.63 \pm 0.42$	$4.9 \pm 0.7 \pm 1.3$
$0.200 - 0.250$	$2.28 \pm 0.43 \pm 0.63$	$2.51 \pm 0.47 \pm 0.30$
$0.250 - 0.300$	$1.94 \pm 0.34 \pm 0.63$	$1.09 \pm 0.43 \pm 0.21$
$0.300 - 0.350$	$1.27 \pm 0.31 \pm 0.40$	$0.47 \pm 0.35 \pm 0.25$
$0.350 - 0.450$	$0.72 \pm 0.17 \pm 0.22$	$0.76 \pm 0.20 \pm 0.29$
$0.450 - 0.600$	$0.068 \pm 0.066 \pm 0.099$	$0.20 \pm 0.09 \pm 0.11$
$M_{\mathrm{H}}/\sqrt{s}$	$R'(M_{\mathrm{H}}/\sqrt{s})$ at 183 GeV	$R'(M_{\mathrm{H}}/\sqrt{s})$ at 189 GeV
$0.060 - 0.075$	$1.23 \pm 0.24 \pm 0.34$	$1.71 \pm 0.15 \pm 0.10$
$0.075 - 0.090$	$4.29 \pm 0.45 \pm 0.54$	$4.03 \pm 0.27 \pm 0.21$
$0.090 - 0.110$	$6.68 \pm 0.56 \pm 0.83$	$6.49 \pm 0.32 \pm 0.16$
$0.110 - 0.140$	$5.47 \pm 0.41 \pm 0.46$	$6.24 \pm 0.24 \pm 0.34$
$0.140 - 0.170$	$5.39 \pm 0.37 \pm 0.74$	$4.58 \pm 0.21 \pm 0.17$
$0.170 - 0.200$	$3.34 \pm 0.32 \pm 0.74$	$3.54 \pm 0.19 \pm 0.24$
$0.200 - 0.250$	$2.62 \pm 0.21 \pm 0.37$	$2.50 \pm 0.13 \pm 0.13$
$0.250 - 0.300$	$1.50 \pm 0.19 \pm 0.28$	$1.52 \pm 0.11 \pm 0.17$
$0.300 - 0.350$	$1.41 \pm 0.18 \pm 0.22$	$1.28 \pm 0.10 \pm 0.12$
$0.350 - 0.450$	$0.60 \pm 0.10 \pm 0.10$	$0.625 \pm 0.059 \pm 0.065$
$0.450 - 0.600$	$0.112 \pm 0.040 \pm 0.066$	$0.146 \pm 0.029 \pm 0.030$

Table B.3: Distributions for the heavy jet mass, M_{H}, measured by OPAL at centre-of-mass energies $\sqrt{s} = 91$–189 GeV. The first uncertainty is statistical, while the second is systematic.

Figure B.3: Distributions for the heavy jet mass, M_{H}, measured by OPAL at centre-of-mass energies $\sqrt{s} = 91$–189 GeV. The inner error bars indicate statistical uncertainties. Each curve is generated using five million non-radiative Monte Carlo events, after hadronisation.

Heavy jet mass, M_H (contd.)

$M_H/\sqrt{s}$	$R'(M_H/\sqrt{s})$ at 192 GeV	$R'(M_H/\sqrt{s})$ at 196 GeV
$0.060 - 0.075$	$1.44 \pm 0.37 \pm 0.54$	$1.55 \pm 0.25 \pm 0.22$
$0.075 - 0.090$	$4.96 \pm 0.72 \pm 0.84$	$4.30 \pm 0.48 \pm 0.46$
$0.090 - 0.110$	$6.85 \pm 0.83 \pm 0.83$	$7.11 \pm 0.53 \pm 0.63$
$0.110 - 0.140$	$5.31 \pm 0.61 \pm 0.88$	$6.08 \pm 0.39 \pm 0.54$
$0.140 - 0.170$	$4.47 \pm 0.55 \pm 0.52$	$4.38 \pm 0.35 \pm 0.59$
$0.170 - 0.200$	$4.36 \pm 0.49 \pm 0.54$	$3.23 \pm 0.30 \pm 0.27$
$0.200 - 0.250$	$2.23 \pm 0.34 \pm 0.34$	$2.30 \pm 0.21 \pm 0.18$
$0.250 - 0.300$	$1.81 \pm 0.28 \pm 0.16$	$1.72 \pm 0.19 \pm 0.22$
$0.300 - 0.350$	$0.87 \pm 0.26 \pm 0.27$	$1.15 \pm 0.16 \pm 0.26$
$0.350 - 0.450$	$0.61 \pm 0.15 \pm 0.19$	$0.62 \pm 0.10 \pm 0.11$
$0.450 - 0.600$	$0.22 \pm 0.08 \pm 0.19$	$0.23 \pm 0.06 \pm 0.12$

$M_H/\sqrt{s}$	$R'(M_H/\sqrt{s})$ at 200 GeV	$R'(M_H/\sqrt{s})$ at 202 GeV
$0.060 - 0.075$	$1.81 \pm 0.26 \pm 0.27$	$2.17 \pm 0.40 \pm 0.57$
$0.075 - 0.090$	$5.75 \pm 0.51 \pm 0.97$	$5.8 \pm 0.8 \pm 1.2$
$0.090 - 0.110$	$6.27 \pm 0.54 \pm 0.28$	$6.08 \pm 0.79 \pm 0.49$
$0.110 - 0.140$	$5.30 \pm 0.39 \pm 0.30$	$5.04 \pm 0.58 \pm 0.59$
$0.140 - 0.170$	$4.89 \pm 0.35 \pm 0.43$	$4.61 \pm 0.50 \pm 0.52$
$0.170 - 0.200$	$3.28 \pm 0.31 \pm 0.25$	$3.43 \pm 0.46 \pm 0.32$
$0.200 - 0.250$	$2.19 \pm 0.21 \pm 0.23$	$1.73 \pm 0.32 \pm 0.53$
$0.250 - 0.300$	$1.49 \pm 0.20 \pm 0.37$	$2.26 \pm 0.27 \pm 0.50$
$0.300 - 0.350$	$1.35 \pm 0.17 \pm 0.14$	$1.44 \pm 0.26 \pm 0.43$
$0.350 - 0.450$	$0.76 \pm 0.10 \pm 0.13$	$0.49 \pm 0.14 \pm 0.26$
$0.450 - 0.600$	$0.184 \pm 0.060 \pm 0.071$	$0.28 \pm 0.09 \pm 0.12$

$M_H/\sqrt{s}$	$R'(M_H/\sqrt{s})$ at 205 GeV	$R'(M_H/\sqrt{s})$ at 207 GeV
$0.060 - 0.075$	$2.29 \pm 0.29 \pm 0.58$	$2.53 \pm 0.22 \pm 0.58$
$0.075 - 0.090$	$4.36 \pm 0.52 \pm 0.65$	$4.92 \pm 0.41 \pm 0.24$
$0.090 - 0.110$	$5.95 \pm 0.55 \pm 0.44$	$6.91 \pm 0.43 \pm 0.58$
$0.110 - 0.140$	$5.85 \pm 0.40 \pm 0.60$	$5.63 \pm 0.31 \pm 0.36$
$0.140 - 0.170$	$4.77 \pm 0.36 \pm 0.29$	$4.88 \pm 0.28 \pm 0.26$
$0.170 - 0.200$	$3.90 \pm 0.32 \pm 0.29$	$3.44 \pm 0.25 \pm 0.10$
$0.200 - 0.250$	$2.66 \pm 0.21 \pm 0.21$	$2.35 \pm 0.17 \pm 0.17$
$0.250 - 0.300$	$1.40 \pm 0.19 \pm 0.31$	$1.56 \pm 0.15 \pm 0.18$
$0.300 - 0.350$	$1.15 \pm 0.17 \pm 0.21$	$1.15 \pm 0.14 \pm 0.20$
$0.350 - 0.450$	$0.81 \pm 0.11 \pm 0.23$	$0.563 \pm 0.082 \pm 0.081$
$0.450 - 0.600$	$-0.02 \pm 0.06 \pm 0.14$	$0.105 \pm 0.051 \pm 0.054$

Table B.4: Distributions for the heavy jet mass, M_H, measured by OPAL at centre-of-mass energies $\sqrt{s} = 192$–207 GeV. The first uncertainty is statistical, while the second is systematic.

Figure B.4: Distributions for the heavy jet mass, M_H, measured by OPAL at centre-of-mass energies $\sqrt{s} = 192$–207 GeV. The inner error bars indicate statistical uncertainties. Each curve is generated using five million non-radiative Monte Carlo events, after hadronisation.

B.3 C-parameter

C	$R'(C)$ at 91 GeV	$R'(C)$ at 133 GeV
$0.00 - 0.05$	$0.2177 \pm 0.0038 \pm 0.0068$	$0.83 \ \pm 0.17 \ \pm 0.11$
$0.05 - 0.08$	$2.07 \ \ \pm 0.01 \ \ \ \pm 0.10$	$4.1 \ \ \pm 0.5 \ \ \ \pm 1.2$
$0.08 - 0.11$	$4.033 \ \pm 0.018 \ \pm 0.049$	$5.70 \ \pm 0.46 \ \pm 0.51$
$0.11 - 0.14$	$4.154 \ \pm 0.019 \ \pm 0.053$	$3.86 \ \pm 0.39 \ \pm 0.41$
$0.14 - 0.18$	$3.224 \ \pm 0.014 \ \pm 0.046$	$2.55 \ \pm 0.29 \ \pm 0.14$
$0.18 - 0.22$	$2.418 \ \pm 0.012 \ \pm 0.060$	$1.65 \ \pm 0.25 \ \pm 0.19$
$0.22 - 0.30$	$1.705 \ \pm 0.007 \ \pm 0.020$	$1.22 \ \pm 0.15 \ \pm 0.07$
$0.30 - 0.40$	$1.114 \ \pm 0.005 \ \pm 0.013$	$0.93 \ \pm 0.11 \ \pm 0.06$
$0.40 - 0.50$	$0.746 \ \pm 0.004 \ \pm 0.017$	$0.43 \ \pm 0.09 \ \pm 0.12$
$0.50 - 0.60$	$0.537 \ \pm 0.004 \ \pm 0.025$	$0.73 \ \pm 0.08 \ \pm 0.15$
$0.60 - 0.75$	$0.3685 \pm 0.0024 \pm 0.0073$	$0.334 \pm 0.051 \pm 0.061$
$0.75 - 1.00$	$0.0983 \pm 0.0009 \pm 0.0022$	$0.101 \pm 0.018 \pm 0.021$

C	$R'(C)$ at 161 GeV	$R'(C)$ at 172 GeV
$0.00 - 0.05$	$1.98 \ \ \pm 0.34 \ \ \ \pm 0.41$	$2.56 \ \pm 0.38 \ \pm 0.17$
$0.05 - 0.08$	$4.77 \ \ \pm 0.77 \ \ \ \pm 0.74$	$4.16 \ \pm 0.85 \ \pm 0.89$
$0.08 - 0.11$	$4.98 \ \ \pm 0.67 \ \ \ \pm 0.33$	$5.22 \ \pm 0.73 \ \pm 0.96$
$0.11 - 0.14$	$3.19 \ \ \pm 0.58 \ \ \ \pm 0.61$	$4.18 \ \pm 0.62 \ \pm 0.70$
$0.14 - 0.18$	$2.55 \ \ \pm 0.44 \ \ \ \pm 0.49$	$1.21 \ \pm 0.49 \ \pm 0.49$
$0.18 - 0.22$	$1.75 \ \ \pm 0.39 \ \ \ \pm 0.40$	$1.60 \ \pm 0.43 \ \pm 0.24$
$0.22 - 0.30$	$0.89 \ \ \pm 0.23 \ \ \ \pm 0.25$	$1.58 \ \pm 0.26 \ \pm 0.25$
$0.30 - 0.40$	$0.78 \ \ \pm 0.18 \ \ \ \pm 0.08$	$0.96 \ \pm 0.20 \ \pm 0.23$
$0.40 - 0.50$	$0.78 \ \ \pm 0.15 \ \ \ \pm 0.13$	$0.19 \ \pm 0.18 \ \pm 0.06$
$0.50 - 0.60$	$0.62 \ \ \pm 0.13 \ \ \ \pm 0.23$	$0.49 \ \pm 0.16 \ \pm 0.15$
$0.60 - 0.75$	$0.26 \ \ \pm 0.10 \ \ \ \pm 0.11$	$0.30 \ \pm 0.12 \ \pm 0.16$
$0.75 - 1.00$	$0.051 \ \pm 0.054 \ \pm 0.042$	$0.070 \pm 0.071 \pm 0.075$

C	$R'(C)$ at 183 GeV	$R'(C)$ at 189 GeV
$0.00 - 0.05$	$1.81 \ \ \pm 0.20 \ \ \ \pm 0.13$	$1.90 \ \pm 0.12 \ \pm 0.11$
$0.05 - 0.08$	$5.29 \ \ \pm 0.39 \ \ \ \pm 0.34$	$5.10 \ \pm 0.23 \ \pm 0.27$
$0.08 - 0.11$	$3.98 \ \ \pm 0.34 \ \ \ \pm 0.42$	$3.91 \ \pm 0.20 \ \pm 0.37$
$0.11 - 0.14$	$3.09 \ \ \pm 0.30 \ \ \ \pm 0.27$	$3.31 \ \pm 0.17 \ \pm 0.17$
$0.14 - 0.18$	$2.44 \ \ \pm 0.22 \ \ \ \pm 0.32$	$2.43 \ \pm 0.13 \ \pm 0.13$
$0.18 - 0.22$	$1.76 \ \ \pm 0.20 \ \ \ \pm 0.12$	$1.75 \ \pm 0.12 \ \pm 0.11$
$0.22 - 0.30$	$1.38 \ \ \pm 0.12 \ \ \ \pm 0.10$	$1.385 \pm 0.071 \pm 0.051$
$0.30 - 0.40$	$0.854 \ \pm 0.092 \ \pm 0.060$	$0.825 \pm 0.054 \pm 0.050$
$0.40 - 0.50$	$0.593 \ \pm 0.082 \ \pm 0.088$	$0.658 \pm 0.047 \pm 0.027$
$0.50 - 0.60$	$0.450 \ \pm 0.079 \ \pm 0.059$	$0.444 \pm 0.046 \pm 0.052$
$0.60 - 0.75$	$0.341 \ \pm 0.062 \ \pm 0.094$	$0.352 \pm 0.039 \pm 0.057$
$0.75 - 1.00$	$0.076 \ \pm 0.039 \ \pm 0.054$	$0.048 \pm 0.031 \pm 0.045$

Table B.5: Distributions for the C-parameter, measured by OPAL at centre-of-mass energies $\sqrt{s} = 91$–189 GeV. The first uncertainty is statistical, while the second is systematic.

Figure B.5: Distributions for the C-parameter, measured by OPAL at centre-of-mass energies $\sqrt{s} = 91$–189 GeV. The inner error bars indicate statistical uncertainties. Each curve is generated using five million non-radiative Monte Carlo events, after hadronisation.

C-parameter (contd.)

C	$R'(C)$ at 192 GeV	$R'(C)$ at 196 GeV
$0.00 - 0.05$	$1.79 \pm 0.31 \pm 0.31$	$1.78 \pm 0.20 \pm 0.13$
$0.05 - 0.08$	$5.1 \pm 0.6 \pm 1.0$	$5.39 \pm 0.39 \pm 0.45$
$0.08 - 0.11$	$3.92 \pm 0.51 \pm 0.70$	$4.12 \pm 0.32 \pm 0.48$
$0.11 - 0.14$	$2.99 \pm 0.43 \pm 0.64$	$3.08 \pm 0.29 \pm 0.24$
$0.14 - 0.18$	$2.20 \pm 0.34 \pm 0.24$	$2.28 \pm 0.21 \pm 0.46$
$0.18 - 0.22$	$1.72 \pm 0.30 \pm 0.21$	$1.88 \pm 0.19 \pm 0.20$
$0.22 - 0.30$	$1.32 \pm 0.19 \pm 0.26$	$1.23 \pm 0.12 \pm 0.12$
$0.30 - 0.40$	$0.87 \pm 0.14 \pm 0.15$	$0.97 \pm 0.09 \pm 0.13$
$0.40 - 0.50$	$0.53 \pm 0.12 \pm 0.08$	$0.572 \pm 0.080 \pm 0.084$
$0.50 - 0.60$	$0.38 \pm 0.12 \pm 0.12$	$0.40 \pm 0.08 \pm 0.13$
$0.60 - 0.75$	$0.45 \pm 0.10 \pm 0.11$	$0.369 \pm 0.069 \pm 0.079$
$0.75 - 1.00$	$0.16 \pm 0.10 \pm 0.20$	$0.08 \pm 0.07 \pm 0.15$

C	$R'(C)$ at 200 GeV	$R'(C)$ at 202 GeV
$0.00 - 0.05$	$2.02 \pm 0.20 \pm 0.16$	$2.37 \pm 0.31 \pm 0.22$
$0.05 - 0.08$	$5.58 \pm 0.40 \pm 0.42$	$5.27 \pm 0.59 \pm 0.43$
$0.08 - 0.11$	$3.46 \pm 0.33 \pm 0.46$	$2.81 \pm 0.47 \pm 0.18$
$0.11 - 0.14$	$2.83 \pm 0.28 \pm 0.21$	$3.32 \pm 0.41 \pm 0.24$
$0.14 - 0.18$	$2.43 \pm 0.21 \pm 0.23$	$2.01 \pm 0.31 \pm 0.28$
$0.18 - 0.22$	$1.74 \pm 0.19 \pm 0.11$	$1.41 \pm 0.28 \pm 0.13$
$0.22 - 0.30$	$1.24 \pm 0.12 \pm 0.12$	$1.38 \pm 0.18 \pm 0.11$
$0.30 - 0.40$	$0.81 \pm 0.10 \pm 0.12$	$0.76 \pm 0.13 \pm 0.13$
$0.40 - 0.50$	$0.594 \pm 0.078 \pm 0.084$	$0.82 \pm 0.12 \pm 0.19$
$0.50 - 0.60$	$0.588 \pm 0.078 \pm 0.089$	$0.65 \pm 0.11 \pm 0.20$
$0.60 - 0.75$	$0.40 \pm 0.07 \pm 0.11$	$0.26 \pm 0.10 \pm 0.17$
$0.75 - 1.00$	$0.07 \pm 0.07 \pm 0.12$	$0.13 \pm 0.10 \pm 0.18$

C	$R'(C)$ at 205 GeV	$R'(C)$ at 207 GeV
$0.00 - 0.05$	$2.23 \pm 0.22 \pm 0.27$	$2.54 \pm 0.17 \pm 0.17$
$0.05 - 0.08$	$5.22 \pm 0.40 \pm 0.61$	$5.12 \pm 0.31 \pm 0.27$
$0.08 - 0.11$	$3.46 \pm 0.33 \pm 0.42$	$4.10 \pm 0.26 \pm 0.33$
$0.11 - 0.14$	$2.87 \pm 0.29 \pm 0.41$	$2.89 \pm 0.22 \pm 0.10$
$0.14 - 0.18$	$2.61 \pm 0.22 \pm 0.40$	$2.34 \pm 0.17 \pm 0.11$
$0.18 - 0.22$	$1.71 \pm 0.20 \pm 0.19$	$1.84 \pm 0.15 \pm 0.10$
$0.22 - 0.30$	$1.48 \pm 0.12 \pm 0.11$	$1.239 \pm 0.094 \pm 0.039$
$0.30 - 0.40$	$0.82 \pm 0.09 \pm 0.14$	$0.875 \pm 0.071 \pm 0.045$
$0.40 - 0.50$	$0.568 \pm 0.082 \pm 0.093$	$0.619 \pm 0.062 \pm 0.078$
$0.50 - 0.60$	$0.403 \pm 0.083 \pm 0.089$	$0.405 \pm 0.062 \pm 0.052$
$0.60 - 0.75$	$0.29 \pm 0.08 \pm 0.19$	$0.274 \pm 0.064 \pm 0.070$
$0.75 - 1.00$	$0.11 \pm 0.07 \pm 0.19$	$0.049 \pm 0.053 \pm 0.093$

Table B.6: Distributions for the C-parameter, measured by OPAL at centre-of-mass energies $\sqrt{s} = 192$–207 GeV. The first uncertainty is statistical, while the second is systematic.
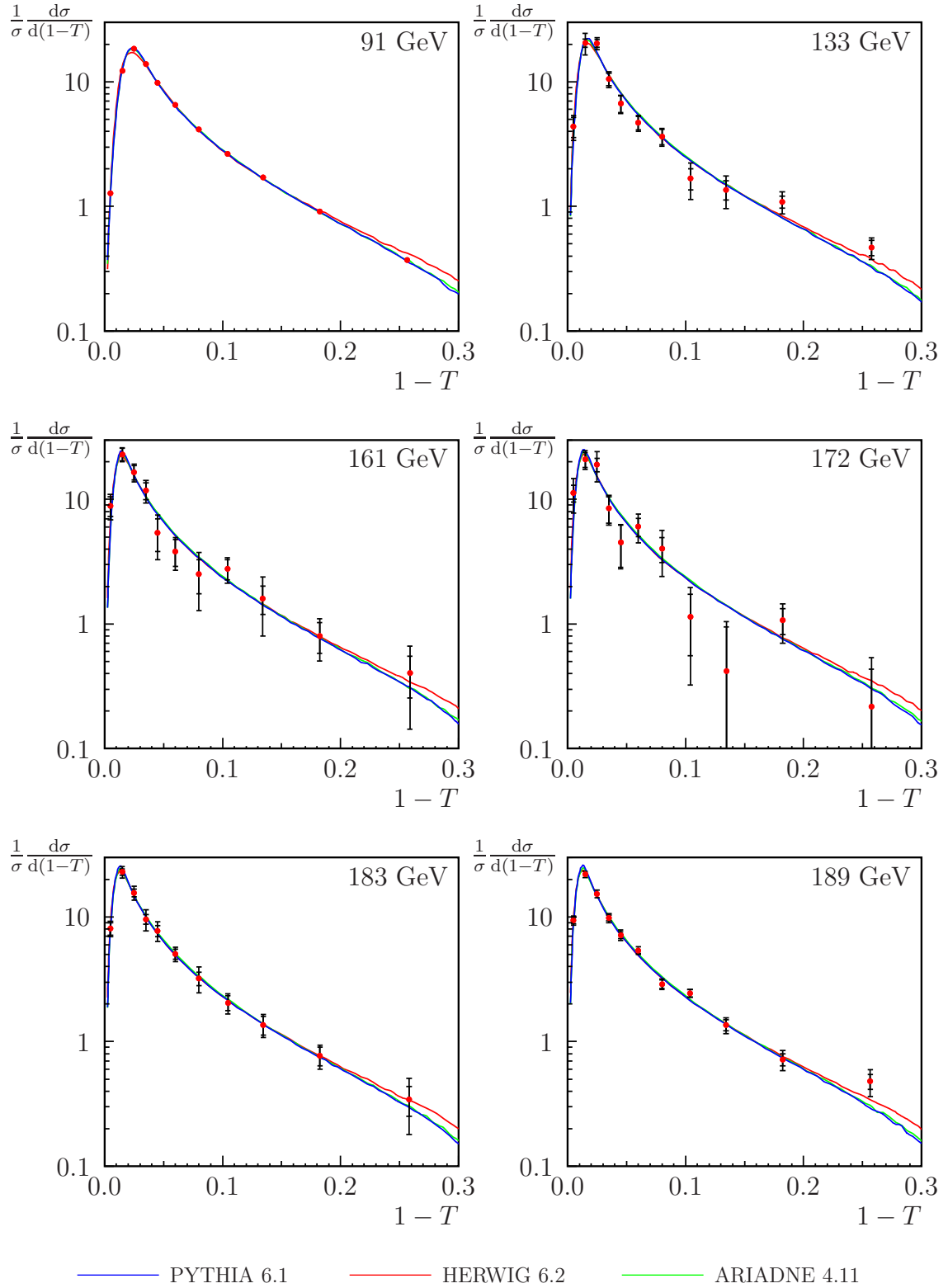
Figure B.6: Distributions for the C-parameter, measured by OPAL at centre-of-mass energies $\sqrt{s}$ = 192–207 GeV. The inner error bars indicate statistical uncertainties. Each curve is generated using five million non-radiative Monte Carlo events, after hadronisation.

B.4   Total jet broadening, B_{T}

B_{T}	$R'(B_{\mathrm{T}})$ at 91 GeV			$R'(B_{\mathrm{T}})$ at 133 GeV		
$0.000 - 0.030$	0.116	± 0.005	± 0.013	0.58	± 0.26	± 0.16
$0.030 - 0.040$	2.49	± 0.03	± 0.12	10.2	± 1.1	± 1.3
$0.040 - 0.050$	6.98	± 0.05	± 0.16	9.6	± 1.3	± 1.9
$0.050 - 0.060$	9.780	± 0.051	± 0.083	11.9	± 1.2	± 0.9
$0.060 - 0.075$	10.755	± 0.041	± 0.098	10.06	± 0.86	± 0.52
$0.075 - 0.090$	8.77	± 0.04	± 0.24	6.31	± 0.76	± 0.36
$0.090 - 0.110$	6.595	± 0.026	± 0.072	4.35	± 0.59	± 0.82
$0.110 - 0.130$	4.830	± 0.023	± 0.077	4.36	± 0.52	± 0.41
$0.130 - 0.160$	3.392	± 0.016	± 0.048	2.43	± 0.36	± 0.25
$0.160 - 0.200$	2.130	± 0.011	± 0.050	1.71	± 0.24	± 0.22
$0.200 - 0.250$	1.185	± 0.007	± 0.022	1.25	± 0.16	± 0.30
$0.250 - 0.300$	0.566	± 0.005	± 0.015	0.72	± 0.10	± 0.09
$0.300 - 0.350$	0.1556	± 0.0025	± 0.0045	0.128	± 0.042	± 0.059

B_{T}	$R'(B_{\mathrm{T}})$ at 161 GeV			$R'(B_{\mathrm{T}})$ at 172 GeV		
$0.000 - 0.030$	1.84	± 0.49	± 0.20	2.24	± 0.54	± 0.88
$0.030 - 0.040$	11.5	± 2.1	± 2.8	13.3	± 2.2	± 4.7
$0.040 - 0.050$	11.0	± 2.0	± 1.7	8.7	± 2.2	± 1.1
$0.050 - 0.060$	13.5	± 1.7	± 2.0	14.7	± 1.9	± 3.0
$0.060 - 0.075$	8.8	± 1.3	± 1.0	7.5	± 1.4	± 0.8
$0.075 - 0.090$	6.1	± 1.2	± 1.0	4.9	± 1.3	± 0.7
$0.090 - 0.110$	3.76	± 0.91	± 0.33	4.6	± 1.0	± 0.3
$0.110 - 0.130$	2.13	± 0.80	± 0.29	4.87	± 0.86	± 0.78
$0.130 - 0.160$	2.99	± 0.56	± 0.58	2.43	± 0.65	± 0.48
$0.160 - 0.200$	2.03	± 0.39	± 0.34	1.05	± 0.47	± 0.33
$0.200 - 0.250$	1.01	± 0.30	± 0.45	0.55	± 0.37	± 0.27
$0.250 - 0.300$	0.47	± 0.24	± 0.17	1.01	± 0.32	± 0.43
$0.300 - 0.350$	-0.03	± 0.17	± 0.02	-0.09	± 0.22	± 0.52

B_{T}	$R'(B_{\mathrm{T}})$ at 183 GeV			$R'(B_{\mathrm{T}})$ at 189 GeV		
$0.000 - 0.030$	1.64	± 0.29	± 0.15	2.05	± 0.18	± 0.11
$0.030 - 0.040$	12.1	± 1.1	± 1.2	10.42	± 0.63	± 0.68
$0.040 - 0.050$	12.2	± 1.0	± 1.3	12.32	± 0.59	± 0.44
$0.050 - 0.060$	9.66	± 0.91	± 0.65	9.46	± 0.53	± 0.87
$0.060 - 0.075$	8.40	± 0.67	± 0.46	8.04	± 0.39	± 0.57
$0.075 - 0.090$	5.80	± 0.57	± 0.39	6.51	± 0.35	± 0.30
$0.090 - 0.110$	4.54	± 0.45	± 0.46	4.82	± 0.27	± 0.25
$0.110 - 0.130$	3.83	± 0.41	± 0.58	3.76	± 0.24	± 0.25
$0.130 - 0.160$	2.81	± 0.29	± 0.29	2.47	± 0.17	± 0.17
$0.160 - 0.200$	1.45	± 0.22	± 0.30	1.83	± 0.13	± 0.12
$0.200 - 0.250$	1.30	± 0.19	± 0.28	0.98	± 0.11	± 0.13
$0.250 - 0.300$	0.29	± 0.16	± 0.22	0.52	± 0.12	± 0.14
$0.300 - 0.350$	0.11	± 0.12	± 0.18	0.08	± 0.12	± 0.15

Table B.7: Distributions for the total jet broadening, B_{T}, measured by OPAL at centre-of-mass energies $\sqrt{s} = 91$–189 GeV. The first uncertainty is statistical, while the second is systematic.

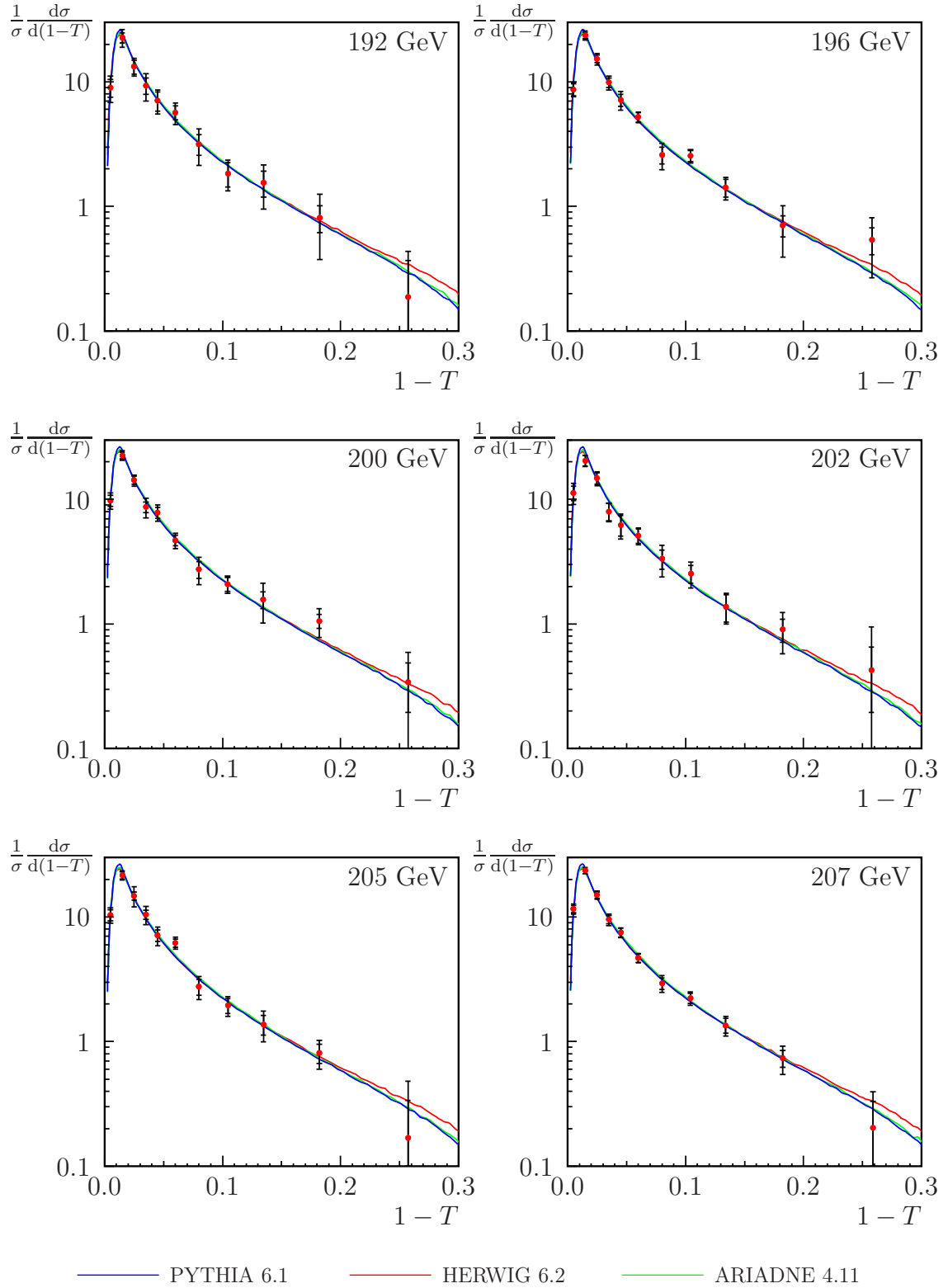Figure B.7: Distributions for the total jet broadening, B_T, measured by OPAL at centre-of-mass energies $\sqrt{s}$ = 91–189 GeV. The inner error bars indicate statistical uncertainties. Each curve is generated using five million non-radiative Monte Carlo events, after hadronisation.

Total jet broadening, B_T (contd.)

B_T	$R'(B_T)$ at 192 GeV	$R'(B_T)$ at 196 GeV
0.000 − 0.030	2.40 ± 0.47 ± 0.26	2.12 ± 0.31 ± 0.45
0.030 − 0.040	10.5 ± 1.6 ± 2.7	10.9 ± 1.0 ± 1.7
0.040 − 0.050	10.3 ± 1.5 ± 1.0	11.9 ± 0.9 ± 1.3
0.050 − 0.060	10.0 ± 1.4 ± 1.3	12.1 ± 0.9 ± 1.2
0.060 − 0.075	8.6 ± 1.0 ± 1.2	7.62 ± 0.64 ± 0.97
0.075 − 0.090	4.58 ± 0.87 ± 0.62	6.10 ± 0.57 ± 0.57
0.090 − 0.110	5.3 ± 0.7 ± 1.4	4.70 ± 0.44 ± 0.32
0.110 − 0.130	2.92 ± 0.63 ± 0.97	3.03 ± 0.41 ± 0.41
0.130 − 0.160	2.61 ± 0.43 ± 0.47	2.92 ± 0.28 ± 0.20
0.160 − 0.200	1.44 ± 0.34 ± 0.38	1.78 ± 0.23 ± 0.26
0.200 − 0.250	1.24 ± 0.27 ± 0.26	1.05 ± 0.19 ± 0.26
0.250 − 0.300	0.36 ± 0.38 ± 0.26	0.66 ± 0.24 ± 0.47
0.300 − 0.350	0.9 ± 0.4 ± 1.7	−0.34 ± 0.33 ± 0.58

B_T	$R'(B_T)$ at 200 GeV	$R'(B_T)$ at 202 GeV
0.000 − 0.030	2.21 ± 0.31 ± 0.32	2.37 ± 0.46 ± 0.25
0.030 − 0.040	12.2 ± 1.1 ± 1.6	12.3 ± 1.6 ± 0.6
0.040 − 0.050	11.2 ± 1.0 ± 1.0	9.0 ± 1.4 ± 0.8
0.050 − 0.060	9.26 ± 0.87 ± 0.71	9.1 ± 1.3 ± 0.9
0.060 − 0.075	7.53 ± 0.64 ± 0.62	7.83 ± 0.91 ± 0.69
0.075 − 0.090	6.15 ± 0.58 ± 0.22	5.26 ± 0.86 ± 0.35
0.090 − 0.110	4.56 ± 0.45 ± 0.25	5.08 ± 0.66 ± 0.58
0.110 − 0.130	3.52 ± 0.41 ± 0.69	3.25 ± 0.59 ± 0.98
0.130 − 0.160	2.44 ± 0.29 ± 0.20	2.85 ± 0.43 ± 0.63
0.160 − 0.200	1.96 ± 0.22 ± 0.20	2.27 ± 0.32 ± 0.38
0.200 − 0.250	1.38 ± 0.21 ± 0.41	0.61 ± 0.28 ± 0.44
0.250 − 0.300	0.24 ± 0.26 ± 0.43	1.23 ± 0.38 ± 0.53
0.300 − 0.350	0.15 ± 0.31 ± 0.58	−0.10 ± 0.33 ± 0.25

B_T	$R'(B_T)$ at 205 GeV	$R'(B_T)$ at 207 GeV
0.000 − 0.030	2.97 ± 0.34 ± 0.29	3.14 ± 0.26 ± 0.19
0.030 − 0.040	11.5 ± 1.1 ± 1.1	12.70 ± 0.84 ± 0.96
0.040 − 0.050	9.20 ± 0.97 ± 0.83	10.6 ± 0.8 ± 1.1
0.050 − 0.060	9.0 ± 0.9 ± 1.1	9.80 ± 0.68 ± 0.40
0.060 − 0.075	8.18 ± 0.66 ± 0.83	7.28 ± 0.50 ± 0.38
0.075 − 0.090	6.1 ± 0.6 ± 1.3	6.69 ± 0.46 ± 0.48
0.090 − 0.110	5.37 ± 0.47 ± 0.59	4.91 ± 0.36 ± 0.35
0.110 − 0.130	3.38 ± 0.40 ± 0.36	3.46 ± 0.32 ± 0.33
0.130 − 0.160	2.79 ± 0.29 ± 0.31	2.65 ± 0.22 ± 0.17
0.160 − 0.200	1.44 ± 0.23 ± 0.44	1.68 ± 0.17 ± 0.26
0.200 − 0.250	1.01 ± 0.21 ± 0.36	0.91 ± 0.17 ± 0.25
0.250 − 0.300	0.30 ± 0.29 ± 0.90	0.12 ± 0.21 ± 0.31
0.300 − 0.350	0.38 ± 0.28 ± 0.53	−0.01 ± 0.17 ± 0.19

Table B.8: Distributions for the total jet broadening, B_T, measured by OPAL at centre-of-mass energies $\sqrt{s} = 192$–207 GeV. The first uncertainty is statistical, while the second is systematic.
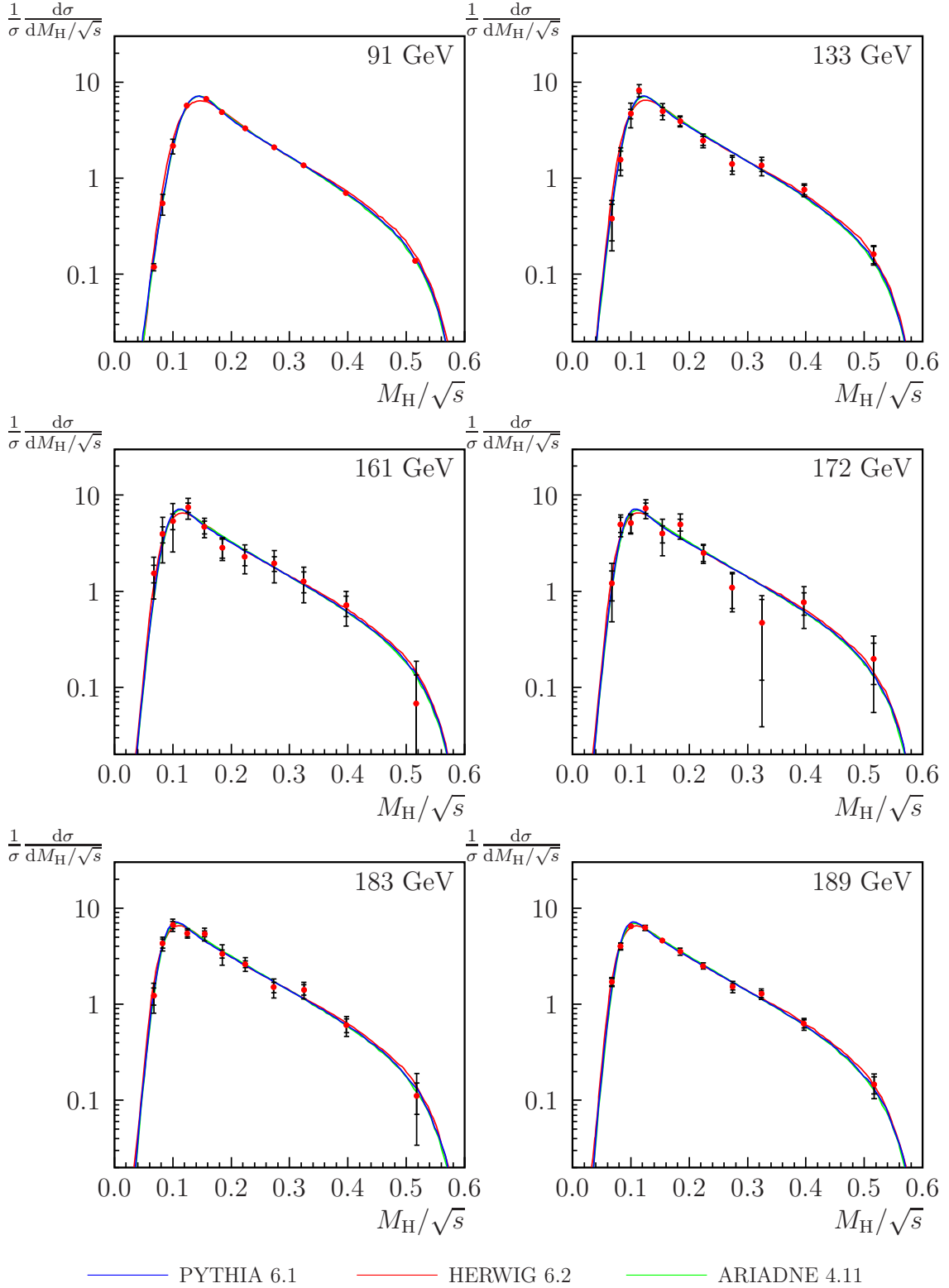
Figure B.8: Distributions for the total jet broadening, B_{T}, measured by OPAL at centre-of-mass energies $\sqrt{s} = 192$–207 GeV. The inner error bars indicate statistical uncertainties. Each curve is generated using five million non-radiative Monte Carlo events, after hadronisation.

B.5   Wide jet broadening, B_W

B_W	$R'(B_W)$ at 91 GeV			$R'(B_W)$ at 133 GeV		
$0.000 - 0.020$	0.557	$\pm$ 0.011	$\pm$ 0.021	3.15	$\pm$ 0.53	$\pm$ 0.83
$0.020 - 0.030$	10.39	$\pm$ 0.06	$\pm$ 0.17	16.4	$\pm$ 1.5	$\pm$ 2.5
$0.030 - 0.040$	16.50	$\pm$ 0.06	$\pm$ 0.12	14.6	$\pm$ 1.3	$\pm$ 0.6
$0.040 - 0.050$	13.34	$\pm$ 0.05	$\pm$ 0.63	10.7	$\pm$ 1.1	$\pm$ 0.7
$0.050 - 0.065$	9.82	$\pm$ 0.04	$\pm$ 0.13	9.47	$\pm$ 0.84	$\pm$ 0.84
$0.065 - 0.080$	7.16	$\pm$ 0.03	$\pm$ 0.15	5.44	$\pm$ 0.72	$\pm$ 0.40
$0.080 - 0.100$	5.067	$\pm$ 0.024	$\pm$ 0.062	3.96	$\pm$ 0.54	$\pm$ 0.45
$0.100 - 0.150$	2.844	$\pm$ 0.011	$\pm$ 0.062	2.44	$\pm$ 0.27	$\pm$ 0.24
$0.150 - 0.200$	1.239	$\pm$ 0.008	$\pm$ 0.043	1.19	$\pm$ 0.16	$\pm$ 0.25
$0.200 - 0.250$	0.465	$\pm$ 0.005	$\pm$ 0.016	0.63	$\pm$ 0.11	$\pm$ 0.07
$0.250 - 0.300$	0.0625	$\pm$ 0.0018	$\pm$ 0.0027	0.077	$\pm$ 0.033	$\pm$ 0.057

B_W	$R'(B_W)$ at 161 GeV			$R'(B_W)$ at 172 GeV		
$0.000 - 0.020$	4.4	$\pm$ 1.0	$\pm$ 0.3	6.8	$\pm$ 1.1	$\pm$ 1.1
$0.020 - 0.030$	19.0	$\pm$ 2.3	$\pm$ 1.6	17.5	$\pm$ 2.5	$\pm$ 1.8
$0.030 - 0.040$	13.2	$\pm$ 1.9	$\pm$ 2.4	14.0	$\pm$ 2.1	$\pm$ 2.4
$0.040 - 0.050$	11.9	$\pm$ 1.8	$\pm$ 2.0	10.2	$\pm$ 1.9	$\pm$ 1.0
$0.050 - 0.065$	8.5	$\pm$ 1.3	$\pm$ 0.7	6.9	$\pm$ 1.4	$\pm$ 0.6
$0.065 - 0.080$	3.9	$\pm$ 1.2	$\pm$ 1.3	6.8	$\pm$ 1.3	$\pm$ 2.0
$0.080 - 0.100$	2.47	$\pm$ 0.86	$\pm$ 0.97	3.70	$\pm$ 0.99	$\pm$ 0.62
$0.100 - 0.150$	2.96	$\pm$ 0.42	$\pm$ 0.40	1.54	$\pm$ 0.49	$\pm$ 0.57
$0.150 - 0.200$	1.38	$\pm$ 0.32	$\pm$ 0.39	1.17	$\pm$ 0.37	$\pm$ 0.28
$0.200 - 0.250$	0.30	$\pm$ 0.21	$\pm$ 0.22	0.41	$\pm$ 0.28	$\pm$ 0.35
$0.250 - 0.300$	0.07	$\pm$ 0.10	$\pm$ 0.12	0.21	$\pm$ 0.12	$\pm$ 0.26

B_W	$R'(B_W)$ at 183 GeV			$R'(B_W)$ at 189 GeV		
$0.000 - 0.020$	5.15	$\pm$ 0.57	$\pm$ 0.27	5.10	$\pm$ 0.33	$\pm$ 0.24
$0.020 - 0.030$	16.1	$\pm$ 1.1	$\pm$ 2.0	16.57	$\pm$ 0.67	$\pm$ 0.83
$0.030 - 0.040$	13.1	$\pm$ 1.0	$\pm$ 0.8	13.30	$\pm$ 0.59	$\pm$ 0.46
$0.040 - 0.050$	11.11	$\pm$ 0.91	$\pm$ 0.92	10.18	$\pm$ 0.53	$\pm$ 0.44
$0.050 - 0.065$	7.65	$\pm$ 0.66	$\pm$ 0.74	7.77	$\pm$ 0.38	$\pm$ 0.48
$0.065 - 0.080$	4.99	$\pm$ 0.57	$\pm$ 0.74	5.56	$\pm$ 0.35	$\pm$ 0.25
$0.080 - 0.100$	4.82	$\pm$ 0.45	$\pm$ 0.31	4.13	$\pm$ 0.27	$\pm$ 0.32
$0.100 - 0.150$	2.53	$\pm$ 0.23	$\pm$ 0.16	2.53	$\pm$ 0.14	$\pm$ 0.10
$0.150 - 0.200$	1.02	$\pm$ 0.19	$\pm$ 0.19	1.08	$\pm$ 0.11	$\pm$ 0.10
$0.200 - 0.250$	0.53	$\pm$ 0.13	$\pm$ 0.31	0.58	$\pm$ 0.09	$\pm$ 0.15
$0.250 - 0.300$	0.08	$\pm$ 0.07	$\pm$ 0.12	0.11	$\pm$ 0.05	$\pm$ 0.13

Table B.9: Distributions for the wide jet broadening, B_W, measured by OPAL at centre-of-mass energies $\sqrt{s} = 91$–189 GeV. The first uncertainty is statistical, while the second is systematic.
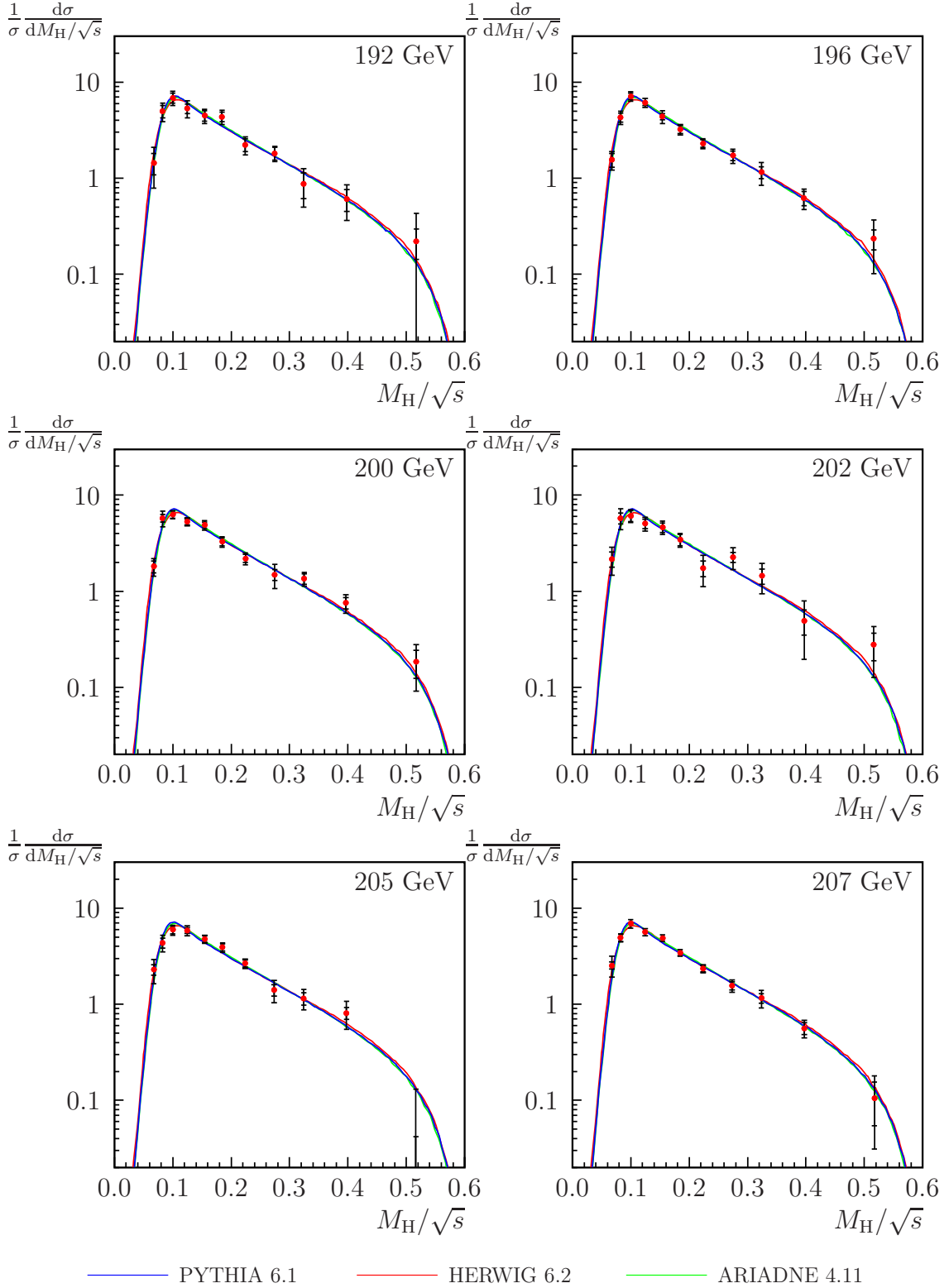
Figure B.9: Distributions for the wide jet broadening, B_{W}, measured by OPAL at centre-of-mass energies $\sqrt{s} = 91\text{--}189$ GeV. The inner error bars indicate statistical uncertainties. Each curve is generated using five million non-radiative Monte Carlo events, after hadronisation.

Wide jet broadening, B_W (contd.)

B_W	$R'(B_W)$ at 192 GeV			$R'(B_W)$ at 196 GeV		
$0.000 - 0.020$	6.42	± 0.85	± 0.59	5.45	± 0.55	± 0.40
$0.020 - 0.030$	14.8	± 1.7	± 2.6	15.1	± 1.1	± 1.7
$0.030 - 0.040$	14.2	± 1.5	± 2.1	14.1	± 1.0	± 1.2
$0.040 - 0.050$	10.0	± 1.4	± 1.5	10.2	± 0.9	± 1.1
$0.050 - 0.065$	7.52	± 0.97	± 0.45	7.22	± 0.63	± 0.69
$0.065 - 0.080$	6.15	± 0.93	± 0.82	5.57	± 0.56	± 0.39
$0.080 - 0.100$	3.68	± 0.69	± 0.75	4.91	± 0.46	± 0.74
$0.100 - 0.150$	2.28	± 0.34	± 0.22	2.18	± 0.22	± 0.20
$0.150 - 0.200$	1.09	± 0.29	± 0.35	1.20	± 0.19	± 0.13
$0.200 - 0.250$	0.58	± 0.23	± 0.33	0.66	± 0.16	± 0.23
$0.250 - 0.300$	0.12	± 0.12	± 0.25	0.10	± 0.09	± 0.12
B_W	$R'(B_W)$ at 200 GeV			$R'(B_W)$ at 202 GeV		
$0.000 - 0.020$	5.77	± 0.56	± 0.39	6.54	± 0.85	± 0.63
$0.020 - 0.030$	16.2	± 1.1	± 1.2	15.0	± 1.6	± 2.0
$0.030 - 0.040$	12.4	± 1.0	± 1.0	9.8	± 1.4	± 1.7
$0.040 - 0.050$	9.22	± 0.88	± 0.80	11.5	± 1.3	± 1.7
$0.050 - 0.065$	7.26	± 0.63	± 0.28	8.04	± 0.92	± 0.61
$0.065 - 0.080$	5.92	± 0.58	± 0.41	4.1	± 0.9	± 1.2
$0.080 - 0.100$	4.01	± 0.46	± 0.46	3.98	± 0.67	± 0.94
$0.100 - 0.150$	2.38	± 0.23	± 0.24	3.00	± 0.33	± 0.28
$0.150 - 0.200$	1.44	± 0.19	± 0.24	1.04	± 0.28	± 0.29
$0.200 - 0.250$	0.48	± 0.17	± 0.29	0.56	± 0.23	± 0.51
$0.250 - 0.300$	0.26	± 0.12	± 0.32	0.30	± 0.16	± 0.48
B_W	$R'(B_W)$ at 205 GeV			$R'(B_W)$ at 207 GeV		
$0.000 - 0.020$	6.56	± 0.59	± 0.60	7.13	± 0.45	± 0.35
$0.020 - 0.030$	15.0	± 1.1	± 1.1	15.8	± 0.9	± 1.0
$0.030 - 0.040$	11.01	± 0.99	± 0.63	12.5	± 0.8	± 1.1
$0.040 - 0.050$	10.8	± 0.9	± 2.0	9.70	± 0.70	± 0.36
$0.050 - 0.065$	8.85	± 0.65	± 0.30	7.86	± 0.51	± 0.53
$0.065 - 0.080$	5.3	± 0.6	± 1.1	5.68	± 0.46	± 0.46
$0.080 - 0.100$	4.70	± 0.45	± 0.54	3.84	± 0.35	± 0.31
$0.100 - 0.150$	2.36	± 0.23	± 0.23	2.42	± 0.18	± 0.23
$0.150 - 0.200$	1.16	± 0.20	± 0.33	1.09	± 0.15	± 0.14
$0.200 - 0.250$	0.27	± 0.18	± 0.27	0.36	± 0.14	± 0.14
$0.250 - 0.300$	0.075	± 0.082	± 0.091	0.080	± 0.078	± 0.082

Table B.10: Distributions for the wide jet broadening, B_W, measured by OPAL at centre-of-mass energies $\sqrt{s} = 192$–207 GeV. The first uncertainty is statistical, while the second is systematic.
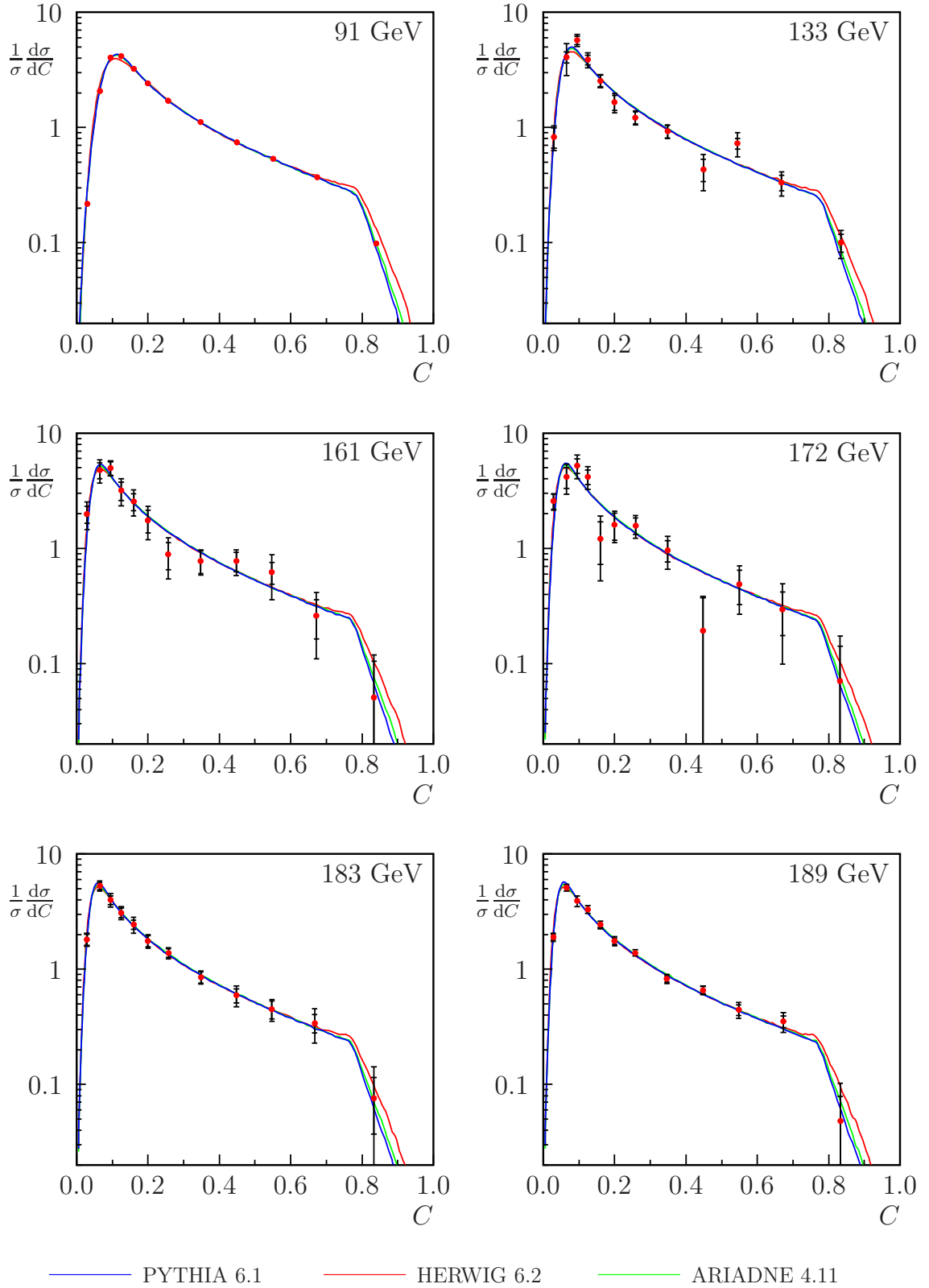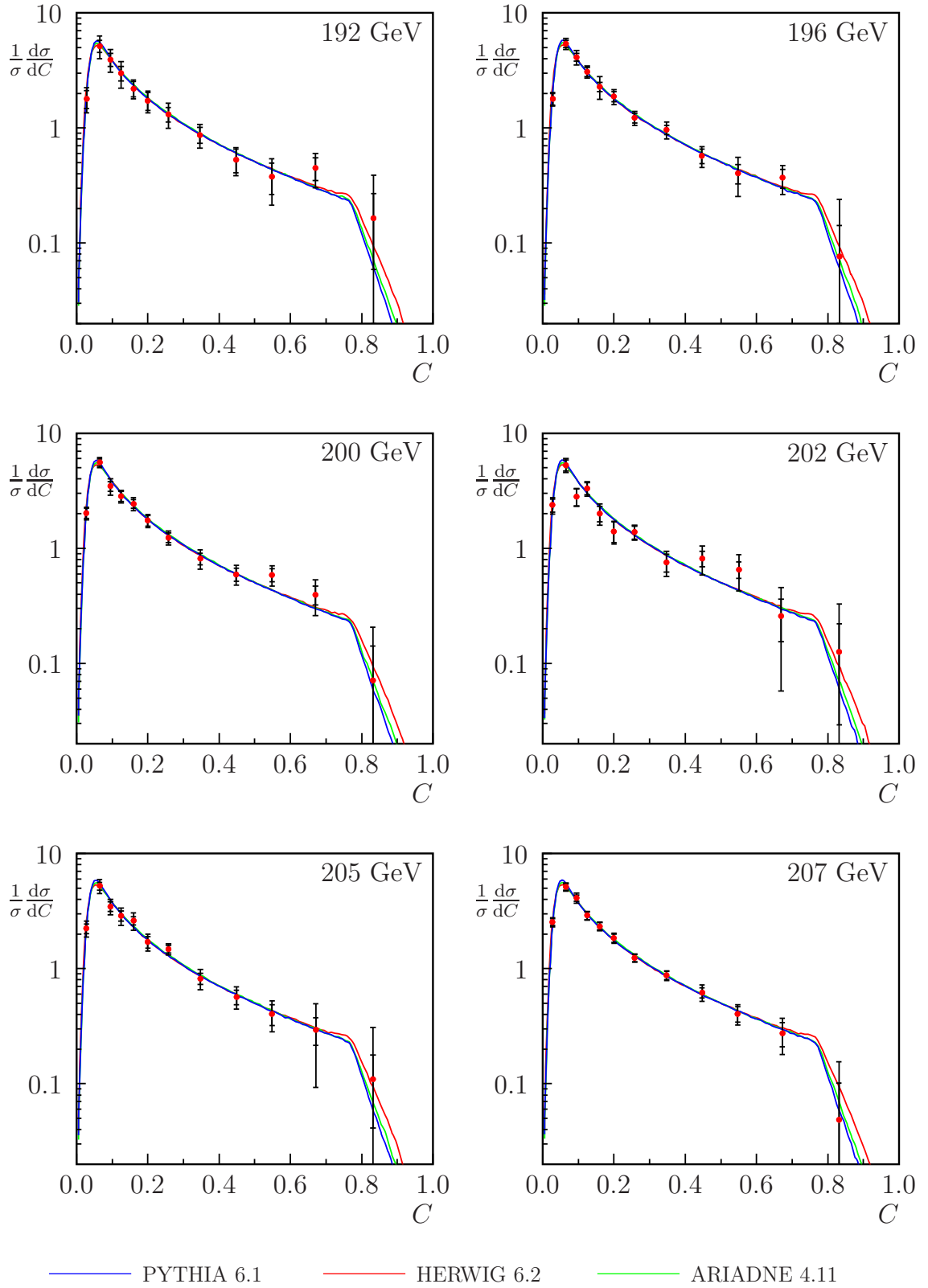
Figure B.10: Distributions for the wide jet broadening, $B_{\rm W}$, measured by OPAL at centre-of-mass energies $\sqrt{s} = 192$–207 GeV. The inner error bars indicate statistical uncertainties. Each curve is generated using five million non-radiative Monte Carlo events, after hadronisation.

B.6   Durham y_{23} parameter

y_{23}	$R'(y_{23})$ at 91 GeV			$R'(y_{23})$ at 133 GeV		
$0.00030 - 0.00075$	146.5	$\pm$ 1.0	$\pm$ 2.8	299.	$\pm$ 30.	$\pm$ 41.
$0.00075 - 0.00130$	183.1	$\pm$ 0.9	$\pm$ 5.5	201.	$\pm$ 22.	$\pm$ 21.
$0.00130 - 0.00230$	141.5	$\pm$ 0.6	$\pm$ 2.8	116.	$\pm$ 12.	$\pm$ 22.
$0.00230 - 0.00400$	81.7	$\pm$ 0.3	$\pm$ 1.5	62.6	$\pm$ 6.7	$\pm$ 8.4
$0.00400 - 0.00700$	39.5	$\pm$ 0.2	$\pm$ 1.2	33.0	$\pm$ 3.9	$\pm$ 5.1
$0.00700 - 0.01200$	19.92	$\pm$ 0.09	$\pm$ 0.22	19.9	$\pm$ 2.2	$\pm$ 3.1
$0.01200 - 0.02250$	9.73	$\pm$ 0.05	$\pm$ 0.20	6.9	$\pm$ 1.1	$\pm$ 0.4
$0.02250 - 0.04000$	4.57	$\pm$ 0.03	$\pm$ 0.19	3.72	$\pm$ 0.60	$\pm$ 0.50
$0.04000 - 0.07000$	2.104	$\pm$ 0.013	$\pm$ 0.094	2.30	$\pm$ 0.29	$\pm$ 0.35
$0.07000 - 0.13000$	0.825	$\pm$ 0.006	$\pm$ 0.024	0.93	$\pm$ 0.12	$\pm$ 0.25
$0.13000 - 0.23500$	0.265	$\pm$ 0.003	$\pm$ 0.014	0.315	$\pm$ 0.058	$\pm$ 0.069
$0.23500 - 0.40000$	0.0303	$\pm$ 0.0008	$\pm$ 0.0019	0.020	$\pm$ 0.016	$\pm$ 0.011

y_{23}	$R'(y_{23})$ at 161 GeV			$R'(y_{23})$ at 172 GeV		
$0.00030 - 0.00075$	323.	$\pm$ 48.	$\pm$ 24.	357.	$\pm$ 53.	$\pm$ 84.
$0.00075 - 0.00130$	262.	$\pm$ 33.	$\pm$ 54.	224.	$\pm$ 35.	$\pm$ 40.
$0.00130 - 0.00230$	97.	$\pm$ 18.	$\pm$ 38.	83.	$\pm$ 19.	$\pm$ 45.
$0.00230 - 0.00400$	52.	$\pm$ 9.	$\pm$ 12.	57.	$\pm$ 11.	$\pm$ 9.
$0.00400 - 0.00700$	33.3	$\pm$ 6.3	$\pm$ 6.1	26.3	$\pm$ 6.6	$\pm$ 2.9
$0.00700 - 0.01200$	14.7	$\pm$ 3.5	$\pm$ 6.1	19.0	$\pm$ 4.0	$\pm$ 3.3
$0.01200 - 0.02250$	7.5	$\pm$ 1.8	$\pm$ 1.5	9.4	$\pm$ 2.0	$\pm$ 1.2
$0.02250 - 0.04000$	4.5	$\pm$ 0.9	$\pm$ 1.1	3.6	$\pm$ 1.1	$\pm$ 2.2
$0.04000 - 0.07000$	2.42	$\pm$ 0.50	$\pm$ 0.75	2.0	$\pm$ 0.6	$\pm$ 1.2
$0.07000 - 0.13000$	0.58	$\pm$ 0.24	$\pm$ 0.38	0.52	$\pm$ 0.29	$\pm$ 0.42
$0.13000 - 0.23500$	0.31	$\pm$ 0.12	$\pm$ 0.21	0.20	$\pm$ 0.15	$\pm$ 0.14
$0.23500 - 0.40000$	-0.007	$\pm$ 0.034	$\pm$ 0.046	0.048	$\pm$ 0.050	$\pm$ 0.077

y_{23}	$R'(y_{23})$ at 183 GeV			$R'(y_{23})$ at 189 GeV		
$0.00030 - 0.00075$	316.	$\pm$ 25.	$\pm$ 38.	338.	$\pm$ 14.	$\pm$ 28.
$0.00075 - 0.00130$	212.	$\pm$ 17.	$\pm$ 33.	160.	$\pm$ 10.	$\pm$ 26.
$0.00130 - 0.00230$	94.3	$\pm$ 9.0	$\pm$ 8.9	109.8	$\pm$ 5.3	$\pm$ 3.3
$0.00230 - 0.00400$	52.	$\pm$ 5.	$\pm$ 12.	56.9	$\pm$ 3.1	$\pm$ 3.9
$0.00400 - 0.00700$	34.0	$\pm$ 3.1	$\pm$ 7.1	29.1	$\pm$ 1.7	$\pm$ 2.7
$0.00700 - 0.01200$	16.7	$\pm$ 1.8	$\pm$ 1.6	18.1	$\pm$ 1.1	$\pm$ 1.2
$0.01200 - 0.02250$	8.8	$\pm$ 0.9	$\pm$ 1.0	9.41	$\pm$ 0.55	$\pm$ 0.81
$0.02250 - 0.04000$	4.75	$\pm$ 0.51	$\pm$ 0.34	3.87	$\pm$ 0.31	$\pm$ 0.48
$0.04000 - 0.07000$	1.77	$\pm$ 0.29	$\pm$ 0.40	2.12	$\pm$ 0.16	$\pm$ 0.32
$0.07000 - 0.13000$	0.85	$\pm$ 0.14	$\pm$ 0.15	0.686	$\pm$ 0.081	$\pm$ 0.070
$0.13000 - 0.23500$	0.23	$\pm$ 0.07	$\pm$ 0.11	0.258	$\pm$ 0.046	$\pm$ 0.061
$0.23500 - 0.40000$	0.015	$\pm$ 0.028	$\pm$ 0.030	0.059	$\pm$ 0.018	$\pm$ 0.052

Table B.11: Distributions for the Durham y_{23} parameter, measured by OPAL at centre-of-mass energies $\sqrt{s} = 91$–189 GeV. The first uncertainty is statistical, while the second is systematic.

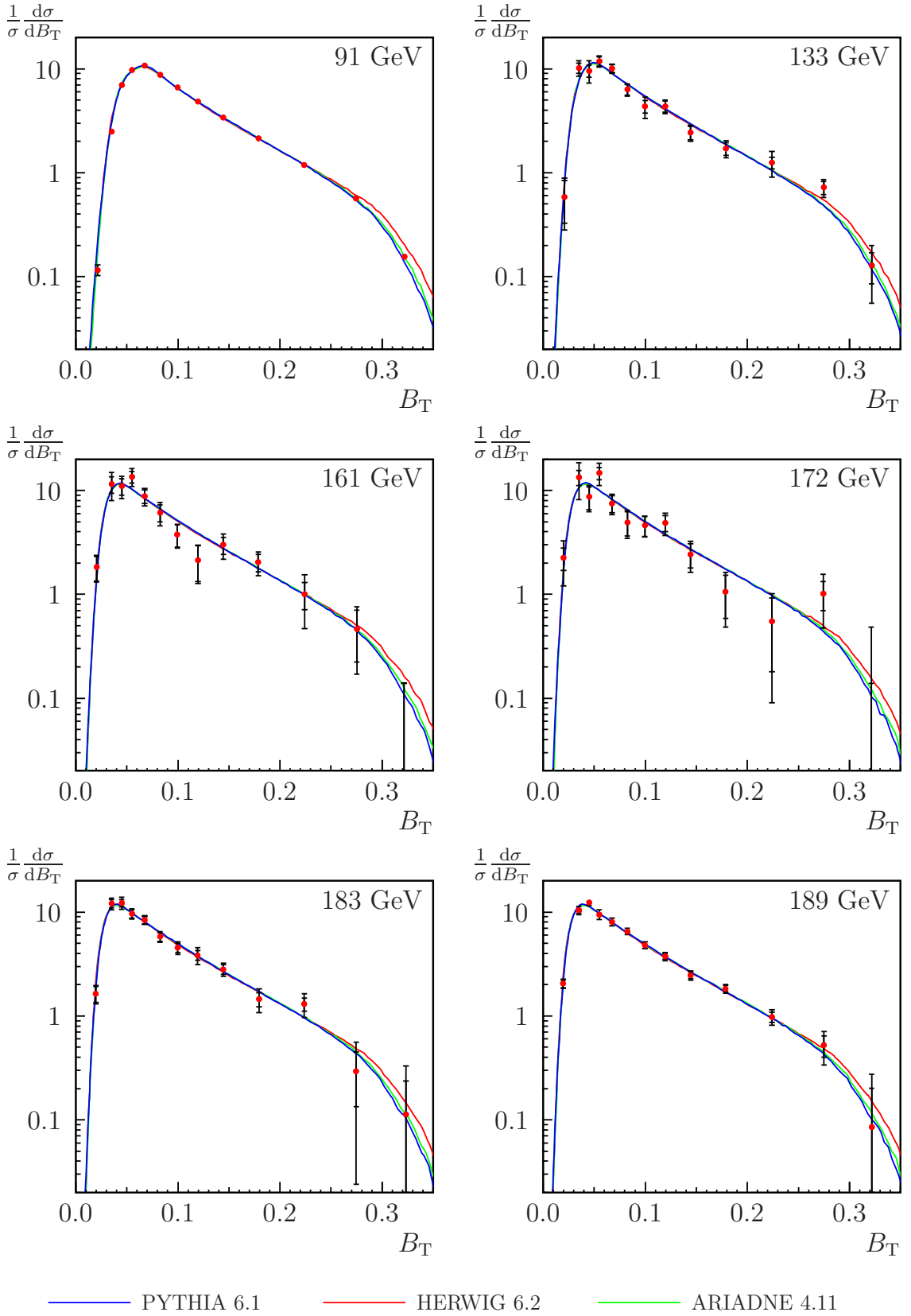Figure B.11: Distributions for the Durham y_{23} parameter, measured by OPAL at centre-of-mass energies $\sqrt{s} = 91$–189 GeV. The inner error bars indicate statistical uncertainties. Each curve is generated using five million non-radiative Monte Carlo events, after hadronisation.

Durham y_{23} parameter (contd.)

y_{23}	$R'(y_{23})$ at 192 GeV			$R'(y_{23})$ at 196 GeV		
$0.00030 - 0.00075$	283.	$\pm$ 37.	$\pm$ 88.	325.	$\pm$ 24.	$\pm$ 30.
$0.00075 - 0.00130$	194.	$\pm$ 24.	$\pm$ 37.	195.	$\pm$ 15.	$\pm$ 14.
$0.00130 - 0.00230$	106.	$\pm$ 13.	$\pm$ 11.	102.5	$\pm$ 8.6	$\pm$ 5.0
$0.00230 - 0.00400$	66.0	$\pm$ 7.9	$\pm$ 8.4	54.5	$\pm$ 5.2	$\pm$ 2.5
$0.00400 - 0.00700$	27.8	$\pm$ 4.6	$\pm$ 5.2	31.1	$\pm$ 2.8	$\pm$ 5.5
$0.00700 - 0.01200$	17.8	$\pm$ 2.8	$\pm$ 2.5	19.3	$\pm$ 1.8	$\pm$ 1.9
$0.01200 - 0.02250$	8.8	$\pm$ 1.4	$\pm$ 1.6	7.70	$\pm$ 0.91	$\pm$ 0.99
$0.02250 - 0.04000$	4.0	$\pm$ 0.8	$\pm$ 1.2	3.78	$\pm$ 0.50	$\pm$ 0.58
$0.04000 - 0.07000$	1.82	$\pm$ 0.43	$\pm$ 0.40	1.83	$\pm$ 0.27	$\pm$ 0.43
$0.07000 - 0.13000$	0.75	$\pm$ 0.20	$\pm$ 0.17	0.83	$\pm$ 0.14	$\pm$ 0.19
$0.13000 - 0.23500$	0.28	$\pm$ 0.12	$\pm$ 0.13	0.39	$\pm$ 0.08	$\pm$ 0.22
$0.23500 - 0.40000$	0.03	$\pm$ 0.08	$\pm$ 0.14	0.033	$\pm$ 0.036	$\pm$ 0.059

y_{23}	$R'(y_{23})$ at 200 GeV			$R'(y_{23})$ at 202 GeV		
$0.00030 - 0.00075$	335.	$\pm$ 24.	$\pm$ 41.	320.	$\pm$ 36.	$\pm$ 18.
$0.00075 - 0.00130$	167.	$\pm$ 16.	$\pm$ 12.	187.	$\pm$ 24.	$\pm$ 38.
$0.00130 - 0.00230$	97.9	$\pm$ 8.5	$\pm$ 8.7	90.	$\pm$ 13.	$\pm$ 13.
$0.00230 - 0.00400$	57.2	$\pm$ 5.2	$\pm$ 4.3	60.4	$\pm$ 7.5	$\pm$ 5.2
$0.00400 - 0.00700$	31.8	$\pm$ 3.0	$\pm$ 4.4	25.8	$\pm$ 4.4	$\pm$ 2.7
$0.00700 - 0.01200$	15.2	$\pm$ 1.8	$\pm$ 1.8	15.7	$\pm$ 2.7	$\pm$ 3.1
$0.01200 - 0.02250$	10.0	$\pm$ 0.9	$\pm$ 1.8	8.2	$\pm$ 1.4	$\pm$ 2.0
$0.02250 - 0.04000$	3.58	$\pm$ 0.51	$\pm$ 0.75	4.43	$\pm$ 0.73	$\pm$ 0.72
$0.04000 - 0.07000$	2.47	$\pm$ 0.28	$\pm$ 0.25	2.12	$\pm$ 0.42	$\pm$ 0.50
$0.07000 - 0.13000$	0.85	$\pm$ 0.15	$\pm$ 0.17	0.97	$\pm$ 0.20	$\pm$ 0.32
$0.13000 - 0.23500$	0.26	$\pm$ 0.09	$\pm$ 0.15	0.32	$\pm$ 0.12	$\pm$ 0.18
$0.23500 - 0.40000$	0.039	$\pm$ 0.051	$\pm$ 0.042	0.03	$\pm$ 0.07	$\pm$ 0.10

y_{23}	$R'(y_{23})$ at 205 GeV			$R'(y_{23})$ at 207 GeV		
$0.00030 - 0.00075$	300.	$\pm$ 24.	$\pm$ 25.	374.	$\pm$ 19.	$\pm$ 18.
$0.00075 - 0.00130$	151.	$\pm$ 16.	$\pm$ 18.	166.	$\pm$ 12.	$\pm$ 5.
$0.00130 - 0.00230$	98.	$\pm$ 9.	$\pm$ 11.	93.	$\pm$ 7.	$\pm$ 11.
$0.00230 - 0.00400$	62.9	$\pm$ 5.3	$\pm$ 9.2	61.7	$\pm$ 4.0	$\pm$ 2.7
$0.00400 - 0.00700$	32.8	$\pm$ 3.1	$\pm$ 2.4	31.2	$\pm$ 2.4	$\pm$ 3.3
$0.00700 - 0.01200$	19.1	$\pm$ 1.8	$\pm$ 1.7	16.7	$\pm$ 1.4	$\pm$ 0.9
$0.01200 - 0.02250$	9.04	$\pm$ 0.93	$\pm$ 0.96	8.55	$\pm$ 0.73	$\pm$ 0.59
$0.02250 - 0.04000$	3.71	$\pm$ 0.52	$\pm$ 0.79	4.24	$\pm$ 0.40	$\pm$ 0.45
$0.04000 - 0.07000$	2.41	$\pm$ 0.29	$\pm$ 0.53	1.80	$\pm$ 0.23	$\pm$ 0.22
$0.07000 - 0.13000$	0.79	$\pm$ 0.15	$\pm$ 0.22	0.79	$\pm$ 0.11	$\pm$ 0.13
$0.13000 - 0.23500$	0.17	$\pm$ 0.09	$\pm$ 0.25	0.160	$\pm$ 0.069	$\pm$ 0.057
$0.23500 - 0.40000$	-0.001	$\pm$ 0.037	$\pm$ 0.049	-0.023	$\pm$ 0.035	$\pm$ 0.060

Table B.12: Distributions for the Durham y_{23} parameter, measured by OPAL at centre-of-mass energies $\sqrt{s} = 192$–207 GeV. The first uncertainty is statistical, while the second is systematic.
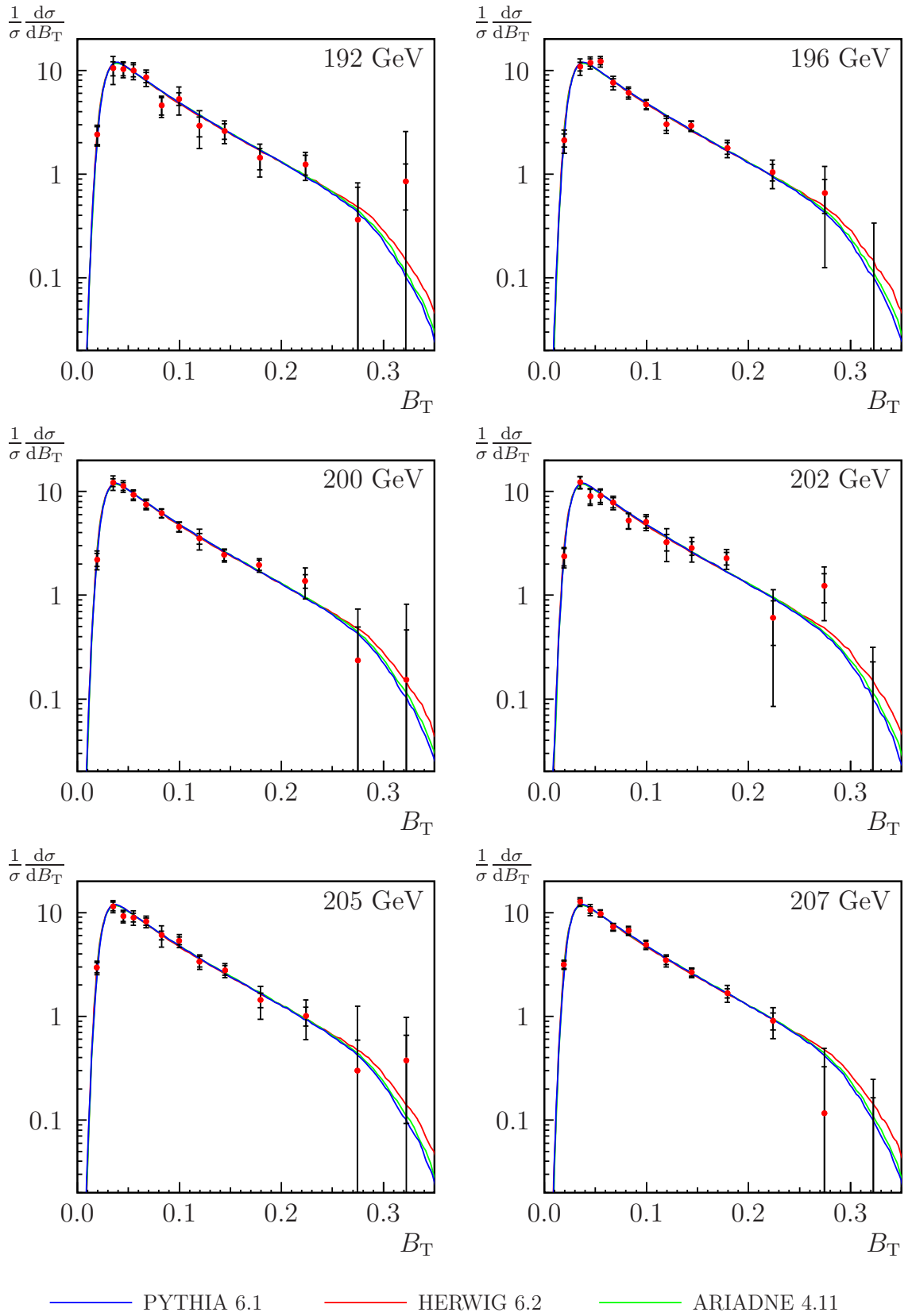
Figure B.12: Distributions for the Durham y_{23} parameter, measured by OPAL at centre-of-mass energies $\sqrt{s} = 192$–207 GeV. The inner error bars indicate statistical uncertainties. Each curve is generated using five million non-radiative Monte Carlo events, after hadronisation.

B.7   Thrust major, $T_{\text{maj.}}$

$T_{\text{maj.}}$	$R'\,(T_{\text{maj.}})$ at 91 GeV	$R'\,(T_{\text{maj.}})$ at 133 GeV
$0.00 - 0.04$	$0.0356 \pm 0.0028 \pm 0.0067$	$0.27 \pm 0.15 \pm 0.18$
$0.04 - 0.08$	$3.374 \pm 0.016 \pm 0.046$	$6.00 \pm 0.44 \pm 0.60$
$0.08 - 0.12$	$6.50 \pm 0.02 \pm 0.12$	$5.93 \pm 0.39 \pm 0.16$
$0.12 - 0.16$	$4.417 \pm 0.015 \pm 0.069$	$3.32 \pm 0.33 \pm 0.40$
$0.16 - 0.22$	$2.755 \pm 0.010 \pm 0.048$	$2.29 \pm 0.23 \pm 0.18$
$0.22 - 0.30$	$1.578 \pm 0.007 \pm 0.025$	$1.12 \pm 0.15 \pm 0.16$
$0.30 - 0.40$	$0.825 \pm 0.004 \pm 0.021$	$0.94 \pm 0.10 \pm 0.11$
$0.40 - 0.50$	$0.3868 \pm 0.0030 \pm 0.0083$	$0.363 \pm 0.064 \pm 0.059$
$0.50 - 0.60$	$0.1344 \pm 0.0017 \pm 0.0029$	$0.220 \pm 0.038 \pm 0.046$

$T_{\text{maj.}}$	$R'\,(T_{\text{maj.}})$ at 161 GeV	$R'\,(T_{\text{maj.}})$ at 172 GeV
$0.00 - 0.04$	$1.12 \pm 0.31 \pm 0.56$	$1.00 \pm 0.34 \pm 0.29$
$0.04 - 0.08$	$6.34 \pm 0.69 \pm 0.45$	$7.94 \pm 0.76 \pm 0.39$
$0.08 - 0.12$	$6.06 \pm 0.59 \pm 0.42$	$4.66 \pm 0.65 \pm 0.20$
$0.12 - 0.16$	$3.11 \pm 0.51 \pm 0.35$	$3.36 \pm 0.56 \pm 0.38$
$0.16 - 0.22$	$1.71 \pm 0.35 \pm 0.17$	$1.98 \pm 0.38 \pm 0.20$
$0.22 - 0.30$	$1.15 \pm 0.24 \pm 0.17$	$1.13 \pm 0.28 \pm 0.29$
$0.30 - 0.40$	$0.98 \pm 0.17 \pm 0.17$	$0.48 \pm 0.21 \pm 0.15$
$0.40 - 0.50$	$0.32 \pm 0.14 \pm 0.08$	$0.36 \pm 0.16 \pm 0.16$
$0.50 - 0.60$	$0.107 \pm 0.083 \pm 0.099$	$0.10 \pm 0.13 \pm 0.26$

$T_{\text{maj.}}$	$R'\,(T_{\text{maj.}})$ at 183 GeV	$R'\,(T_{\text{maj.}})$ at 189 GeV
$0.00 - 0.04$	$0.85 \pm 0.19 \pm 0.10$	$1.01 \pm 0.11 \pm 0.09$
$0.04 - 0.08$	$6.96 \pm 0.36 \pm 0.40$	$6.68 \pm 0.21 \pm 0.10$
$0.08 - 0.12$	$5.06 \pm 0.30 \pm 0.23$	$4.84 \pm 0.18 \pm 0.17$
$0.12 - 0.16$	$3.30 \pm 0.26 \pm 0.25$	$3.22 \pm 0.15 \pm 0.16$
$0.16 - 0.22$	$2.12 \pm 0.18 \pm 0.23$	$2.27 \pm 0.11 \pm 0.09$
$0.22 - 0.30$	$1.31 \pm 0.13 \pm 0.10$	$1.285 \pm 0.076 \pm 0.084$
$0.30 - 0.40$	$0.72 \pm 0.10 \pm 0.16$	$0.721 \pm 0.058 \pm 0.055$
$0.40 - 0.50$	$0.374 \pm 0.081 \pm 0.075$	$0.389 \pm 0.053 \pm 0.056$
$0.50 - 0.60$	$0.14 \pm 0.06 \pm 0.11$	$0.174 \pm 0.048 \pm 0.068$

Table B.13: Distributions for the thrust major, $T_{\text{maj.}}$, measured by OPAL at centre-of-mass energies $\sqrt{s} = 91$–189 GeV. The first uncertainty is statistical, while the second is systematic.
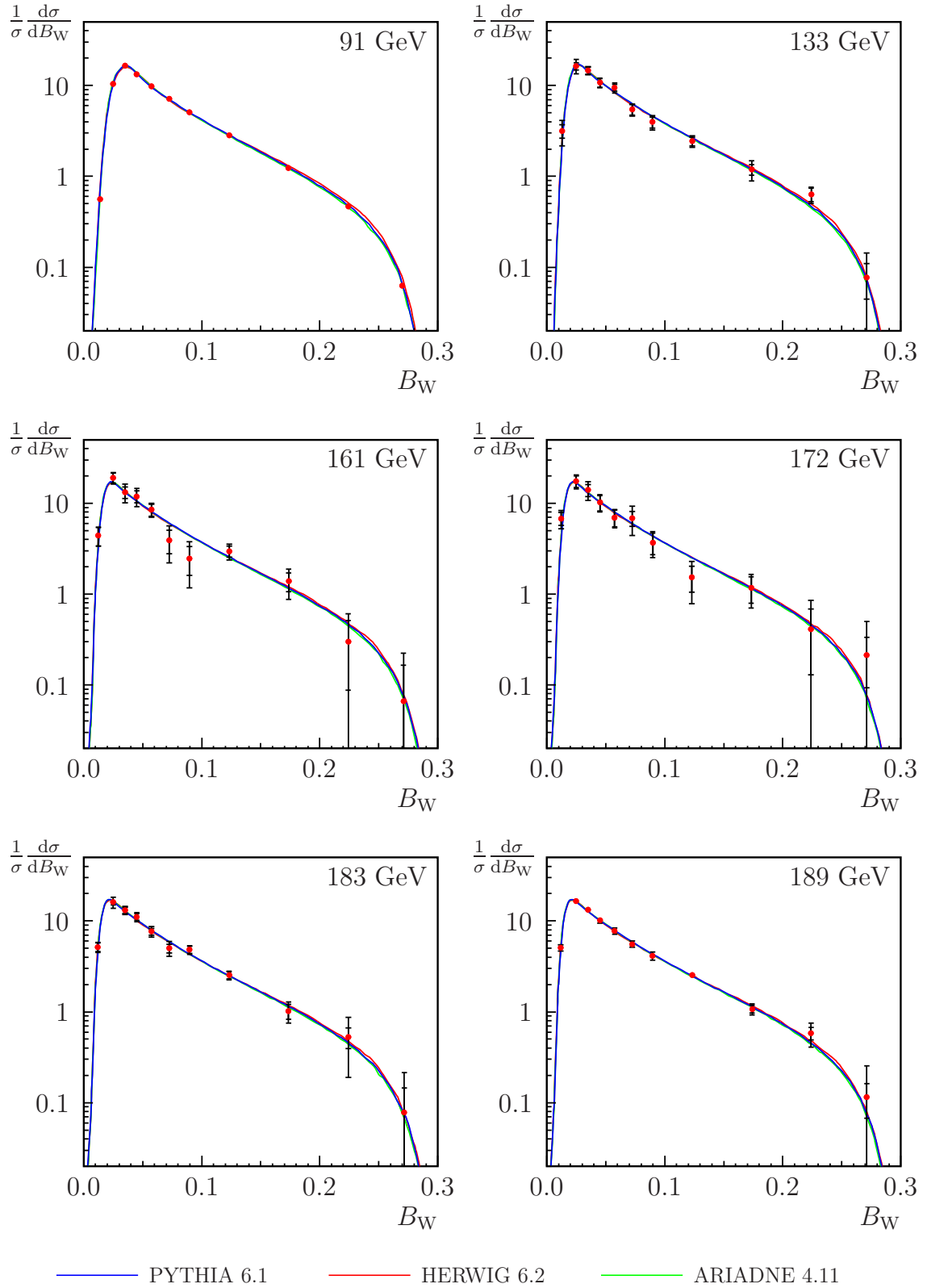
Figure B.13: Distributions for the thrust major, $T_{\mathrm{maj.}}$, measured by OPAL at centre-of-mass energies $\sqrt{s} = 91$–189 GeV. The inner error bars indicate statistical uncertainties. Each curve is generated using five million non-radiative Monte Carlo events, after hadronisation.

Thrust major, $T_{\mathrm{maj.}}$ (contd.)

$T_{\mathrm{maj.}}$	$R'(T_{\mathrm{maj.}})$ at 192 GeV	$R'(T_{\mathrm{maj.}})$ at 196 GeV
$0.00 - 0.04$	$1.07 \pm 0.30 \pm 0.16$	$1.06 \ \pm 0.19 \ \pm 0.31$
$0.04 - 0.08$	$6.62 \pm 0.54 \pm 0.73$	$6.78 \ \pm 0.35 \ \pm 0.34$
$0.08 - 0.12$	$5.30 \pm 0.45 \pm 0.54$	$4.86 \ \pm 0.29 \ \pm 0.28$
$0.12 - 0.16$	$3.05 \pm 0.39 \pm 0.49$	$3.37 \ \pm 0.25 \ \pm 0.27$
$0.16 - 0.22$	$2.06 \pm 0.28 \pm 0.22$	$2.11 \ \pm 0.18 \ \pm 0.14$
$0.22 - 0.30$	$1.48 \pm 0.20 \pm 0.10$	$1.21 \ \pm 0.13 \ \pm 0.13$
$0.30 - 0.40$	$0.42 \pm 0.15 \pm 0.20$	$0.79 \ \pm 0.10 \ \pm 0.16$
$0.40 - 0.50$	$0.65 \pm 0.13 \pm 0.26$	$0.31 \ \pm 0.09 \ \pm 0.21$
$0.50 - 0.60$	$0.11 \pm 0.16 \pm 0.17$	$0.27 \ \pm 0.10 \ \pm 0.20$
$T_{\mathrm{maj.}}$	$R'(T_{\mathrm{maj.}})$ at 200 GeV	$R'(T_{\mathrm{maj.}})$ at 202 GeV
$0.00 - 0.04$	$1.18 \pm 0.20 \pm 0.11$	$1.00 \ \pm 0.31 \ \pm 0.41$
$0.04 - 0.08$	$6.73 \pm 0.36 \pm 0.37$	$6.53 \ \pm 0.53 \ \pm 0.34$
$0.08 - 0.12$	$4.92 \pm 0.30 \pm 0.27$	$4.72 \ \pm 0.43 \ \pm 0.42$
$0.12 - 0.16$	$3.00 \pm 0.25 \pm 0.11$	$3.48 \ \pm 0.38 \ \pm 0.31$
$0.16 - 0.22$	$1.99 \pm 0.18 \pm 0.19$	$1.85 \ \pm 0.26 \ \pm 0.17$
$0.22 - 0.30$	$1.46 \pm 0.13 \pm 0.11$	$1.36 \ \pm 0.19 \ \pm 0.11$
$0.30 - 0.40$	$0.75 \pm 0.10 \pm 0.16$	$0.97 \ \pm 0.14 \ \pm 0.13$
$0.40 - 0.50$	$0.46 \pm 0.10 \pm 0.23$	$0.31 \ \pm 0.14 \ \pm 0.16$
$0.50 - 0.60$	$0.01 \pm 0.10 \pm 0.17$	$0.17 \ \pm 0.16 \ \pm 0.07$
$T_{\mathrm{maj.}}$	$R'(T_{\mathrm{maj.}})$ at 205 GeV	$R'(T_{\mathrm{maj.}})$ at 207 GeV
$0.00 - 0.04$	$1.42 \pm 0.21 \pm 0.20$	$1.53 \ \pm 0.16 \ \pm 0.08$
$0.04 - 0.08$	$6.42 \pm 0.36 \pm 0.25$	$6.95 \ \pm 0.28 \ \pm 0.16$
$0.08 - 0.12$	$4.81 \pm 0.30 \pm 0.57$	$4.53 \ \pm 0.23 \ \pm 0.28$
$0.12 - 0.16$	$3.47 \pm 0.26 \pm 0.36$	$3.71 \ \pm 0.20 \ \pm 0.34$
$0.16 - 0.22$	$2.26 \pm 0.18 \pm 0.27$	$1.97 \ \pm 0.14 \ \pm 0.10$
$0.22 - 0.30$	$1.31 \pm 0.13 \pm 0.10$	$1.36 \ \pm 0.10 \ \pm 0.06$
$0.30 - 0.40$	$0.68 \pm 0.10 \pm 0.17$	$0.705 \pm 0.079 \pm 0.074$
$0.40 - 0.50$	$0.38 \pm 0.11 \pm 0.23$	$0.28 \ \pm 0.09 \ \pm 0.15$
$0.50 - 0.60$	$0.06 \pm 0.09 \pm 0.16$	$0.06 \ \pm 0.07 \ \pm 0.11$

Table B.14: Distributions for the thrust major, $T_{\mathrm{maj.}}$, measured by OPAL at centre-of-mass energies $\sqrt{s} = 192$–207 GeV. The first uncertainty is statistical, while the second is systematic.
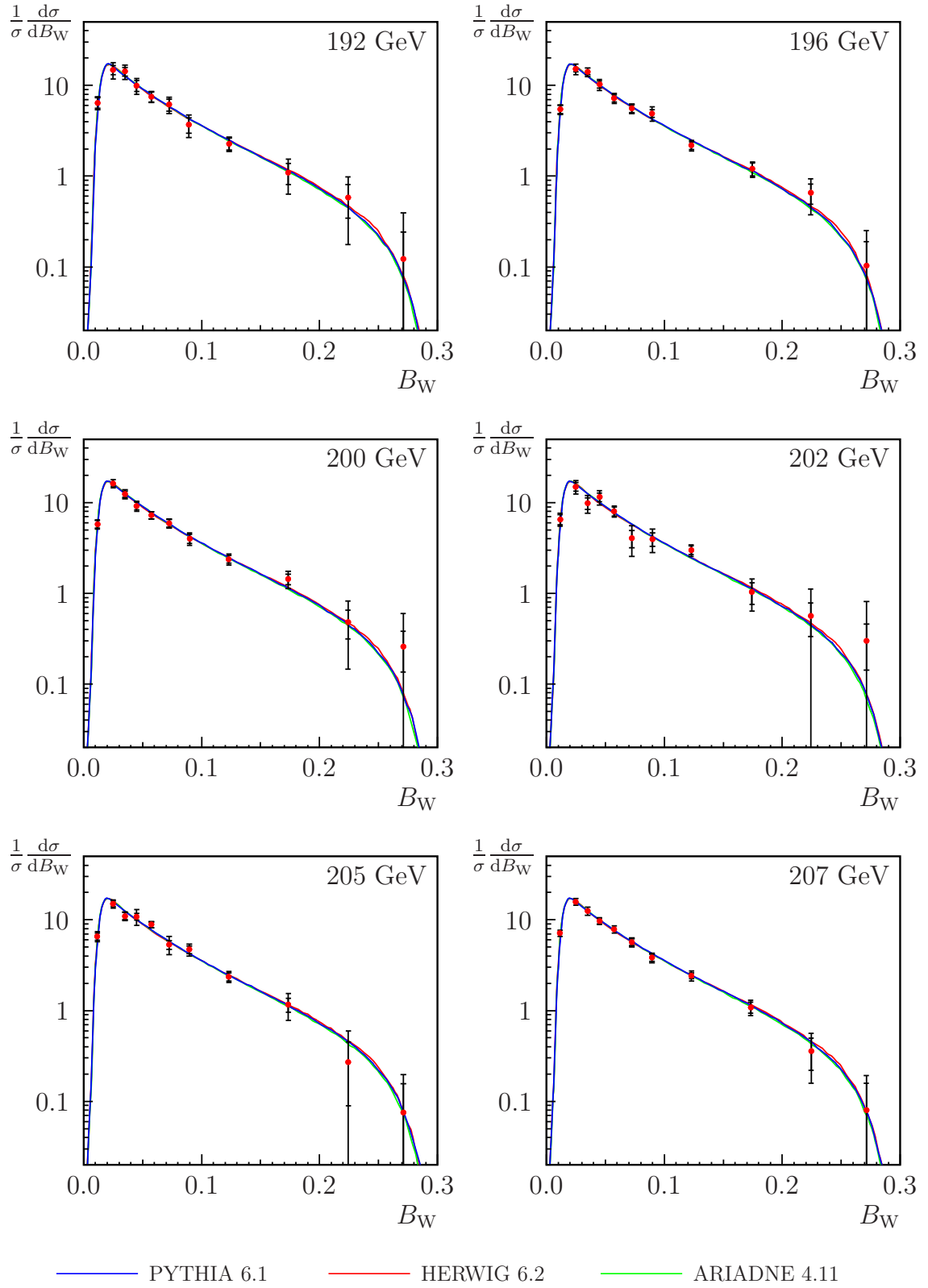
Figure B.14: Distributions for the thrust major, $T_{\mathrm{maj.}}$, measured by OPAL at centre-of-mass energies $\sqrt{s} = 192$–207 GeV. The inner error bars indicate statistical uncertainties. Each curve is generated using five million non-radiative Monte Carlo events, after hadronisation.

B.8   Thrust minor, $T_{\text{min.}}$

$T_{\text{min.}}$	$R'(T_{\text{min.}})$ at 91 GeV	$R'(T_{\text{min.}})$ at 133 GeV
$0.00 - 0.02$	$0.0229 \pm 0.0029 \pm 0.0038$	$0.07 \pm 0.08 \pm 0.19$
$0.02 - 0.04$	$1.386 \pm 0.016 \pm 0.045$	$5.13 \pm 0.62 \pm 0.44$
$0.04 - 0.06$	$8.147 \pm 0.032 \pm 0.070$	$13.9 \pm 0.9 \pm 1.8$
$0.06 - 0.08$	$12.413 \pm 0.036 \pm 0.097$	$12.1 \pm 0.8 \pm 1.7$
$0.08 - 0.10$	$10.335 \pm 0.033 \pm 0.056$	$6.9 \pm 0.7 \pm 1.1$
$0.10 - 0.12$	$6.850 \pm 0.027 \pm 0.065$	$4.69 \pm 0.49 \pm 0.62$
$0.12 - 0.14$	$4.195 \pm 0.021 \pm 0.046$	$2.75 \pm 0.38 \pm 0.69$
$0.14 - 0.16$	$2.434 \pm 0.016 \pm 0.054$	$1.59 \pm 0.31 \pm 0.38$
$0.16 - 0.20$	$1.253 \pm 0.008 \pm 0.022$	$0.94 \pm 0.16 \pm 0.35$
$0.20 - 0.24$	$0.499 \pm 0.005 \pm 0.017$	$0.217 \pm 0.095 \pm 0.049$
$0.24 - 0.30$	$0.1733 \pm 0.0023 \pm 0.0044$	$0.145 \pm 0.046 \pm 0.029$

$T_{\text{min.}}$	$R'(T_{\text{min.}})$ at 161 GeV	$R'(T_{\text{min.}})$ at 172 GeV
$0.00 - 0.02$	$0.17 \pm 0.19 \pm 0.20$	$-0.00 \pm 0.20 \pm 0.00$
$0.02 - 0.04$	$10.2 \pm 1.2 \pm 1.4$	$9.0 \pm 1.4 \pm 2.1$
$0.04 - 0.06$	$14.6 \pm 1.5 \pm 2.0$	$14.2 \pm 1.8 \pm 2.9$
$0.06 - 0.08$	$9.8 \pm 1.3 \pm 1.1$	$7.0 \pm 1.5 \pm 2.3$
$0.08 - 0.10$	$5.97 \pm 0.99 \pm 0.86$	$5.4 \pm 1.1 \pm 1.1$
$0.10 - 0.12$	$3.10 \pm 0.75 \pm 0.42$	$2.9 \pm 0.9 \pm 1.8$
$0.12 - 0.14$	$1.39 \pm 0.56 \pm 0.54$	$2.24 \pm 0.67 \pm 0.72$
$0.14 - 0.16$	$1.63 \pm 0.49 \pm 0.69$	$0.96 \pm 0.64 \pm 0.68$
$0.16 - 0.20$	$0.87 \pm 0.30 \pm 0.52$	$0.70 \pm 0.33 \pm 0.38$
$0.20 - 0.24$	$0.27 \pm 0.23 \pm 0.33$	$-0.17 \pm 0.34 \pm 0.09$
$0.24 - 0.30$	$0.30 \pm 0.21 \pm 0.25$	$-0.07 \pm 0.21 \pm 0.07$

$T_{\text{min.}}$	$R'(T_{\text{min.}})$ at 183 GeV	$R'(T_{\text{min.}})$ at 189 GeV
$0.00 - 0.02$	$0.19 \pm 0.12 \pm 0.05$	$0.297 \pm 0.075 \pm 0.042$
$0.02 - 0.04$	$9.80 \pm 0.69 \pm 0.63$	$8.87 \pm 0.43 \pm 0.63$
$0.04 - 0.06$	$14.70 \pm 0.81 \pm 0.82$	$15.91 \pm 0.54 \pm 0.48$
$0.06 - 0.08$	$10.30 \pm 0.65 \pm 0.72$	$10.00 \pm 0.40 \pm 0.69$
$0.08 - 0.10$	$5.13 \pm 0.48 \pm 0.60$	$5.88 \pm 0.30 \pm 0.20$
$0.10 - 0.12$	$3.70 \pm 0.39 \pm 0.33$	$3.10 \pm 0.23 \pm 0.19$
$0.12 - 0.14$	$2.68 \pm 0.34 \pm 0.61$	$2.02 \pm 0.20 \pm 0.38$
$0.14 - 0.16$	$1.48 \pm 0.28 \pm 0.30$	$1.10 \pm 0.18 \pm 0.41$
$0.16 - 0.20$	$0.41 \pm 0.18 \pm 0.16$	$0.67 \pm 0.11 \pm 0.12$
$0.20 - 0.24$	$0.02 \pm 0.16 \pm 0.13$	$0.38 \pm 0.11 \pm 0.20$
$0.24 - 0.30$	$0.32 \pm 0.16 \pm 0.33$	$-0.05 \pm 0.10 \pm 0.16$

Table B.15: Distributions for the thrust minor, $T_{\text{min.}}$, measured by OPAL at centre-of-mass energies $\sqrt{s} = 91$–189 GeV. The first uncertainty is statistical, while the second is systematic.

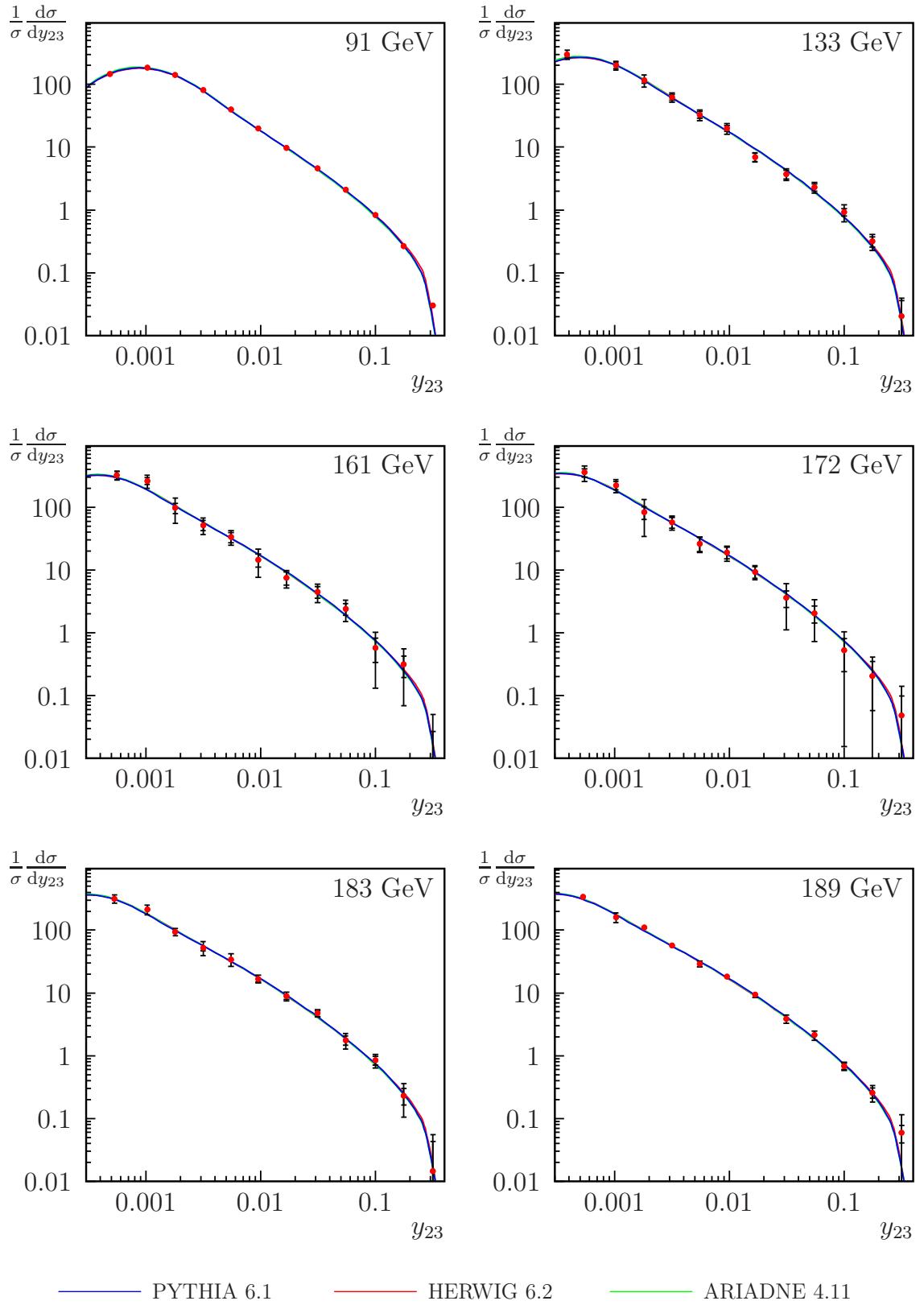Figure B.15: Distributions for the thrust minor, $T_{\mathrm{min.}}$, measured by OPAL at centre-of-mass energies $\sqrt{s} = 91$–189 GeV. The inner error bars indicate statistical uncertainties. Each curve is generated using five million non-radiative Monte Carlo events, after hadronisation.

Thrust minor, $T_{\mathrm{min.}}$ (contd.)

$T_{\mathrm{min.}}$	$R'(T_{\mathrm{min.}})$ at 192 GeV	$R'(T_{\mathrm{min.}})$ at 196 GeV
$0.00 - 0.02$	$0.14 \pm 0.18 \pm 0.17$	$0.28 \pm 0.15 \pm 0.08$
$0.02 - 0.04$	$8.4 \;\pm 1.2 \;\pm 2.9$	$9.1 \;\pm 0.7 \;\pm 1.1$
$0.04 - 0.06$	$12.8 \;\pm 1.5 \;\pm 3.5$	$16.4 \;\pm 0.8 \;\pm 2.2$
$0.06 - 0.08$	$7.6 \;\pm 1.1 \;\pm 1.5$	$8.93 \pm 0.61 \pm 0.62$
$0.08 - 0.10$	$5.2 \;\pm 0.8 \;\pm 1.4$	$5.87 \pm 0.47 \pm 0.58$
$0.10 - 0.12$	$2.89 \pm 0.61 \pm 0.66$	$3.14 \pm 0.37 \pm 0.51$
$0.12 - 0.14$	$1.43 \pm 0.52 \pm 0.31$	$2.63 \pm 0.35 \pm 0.53$
$0.14 - 0.16$	$1.58 \pm 0.48 \pm 0.69$	$1.46 \pm 0.30 \pm 0.58$
$0.16 - 0.20$	$0.73 \pm 0.28 \pm 0.62$	$0.78 \pm 0.18 \pm 0.23$
$0.20 - 0.24$	$0.49 \pm 0.29 \pm 0.39$	$0.20 \pm 0.21 \pm 0.49$
$0.24 - 0.30$	$1.2 \;\pm 0.6 \;\pm 1.9$	$0.16 \pm 0.24 \pm 0.44$

$T_{\mathrm{min.}}$	$R'(T_{\mathrm{min.}})$ at 200 GeV	$R'(T_{\mathrm{min.}})$ at 202 GeV
$0.00 - 0.02$	$0.28 \pm 0.15 \pm 0.15$	$0.53 \pm 0.21 \pm 0.20$
$0.02 - 0.04$	$11.2 \;\pm 1.2 \;\pm 1.2$	$10.1 \;\pm 1.1 \;\pm 0.5$
$0.04 - 0.06$	$17.5 \;\pm 1.7 \;\pm 2.4$	$13.1 \;\pm 1.2 \;\pm 0.7$
$0.06 - 0.08$	$9.9 \;\pm 1.1 \;\pm 0.7$	$10.3 \;\pm 0.9 \;\pm 1.0$
$0.08 - 0.10$	$6.7 \;\pm 0.7 \;\pm 1.2$	$6.12 \pm 0.66 \pm 0.48$
$0.10 - 0.12$	$3.14 \pm 0.48 \pm 0.42$	$3.73 \pm 0.56 \pm 0.78$
$0.12 - 0.14$	$1.87 \pm 0.37 \pm 0.66$	$2.63 \pm 0.48 \pm 0.62$
$0.14 - 0.16$	$1.45 \pm 0.31 \pm 0.75$	$1.76 \pm 0.41 \pm 0.23$
$0.16 - 0.20$	$0.95 \pm 0.19 \pm 0.31$	$0.83 \pm 0.33 \pm 0.54$
$0.20 - 0.24$	$1.54 \pm 0.23 \pm 0.87$	$0.57 \pm 0.29 \pm 0.45$
$0.24 - 0.30$	$-0.25 \pm 0.18 \pm 0.36$	$0.04 \pm 0.23 \pm 0.22$

$T_{\mathrm{min.}}$	$R'(T_{\mathrm{min.}})$ at 205 GeV	$R'(T_{\mathrm{min.}})$ at 207 GeV
$0.00 - 0.02$	$0.61 \pm 0.15 \pm 0.19$	$0.31 \pm 0.13 \pm 0.09$
$0.02 - 0.04$	$10.64 \pm 0.74 \pm 0.65$	$10.5 \;\pm 0.9 \;\pm 1.7$
$0.04 - 0.06$	$14.81 \pm 0.81 \pm 0.64$	$13.0 \;\pm 1.1 \;\pm 2.8$
$0.06 - 0.08$	$9.74 \pm 0.62 \pm 0.65$	$8.5 \;\pm 0.7 \;\pm 1.5$
$0.08 - 0.10$	$6.04 \pm 0.48 \pm 0.70$	$4.7 \;\pm 0.5 \;\pm 1.2$
$0.10 - 0.12$	$2.23 \pm 0.36 \pm 0.78$	$2.51 \pm 0.34 \pm 0.70$
$0.12 - 0.14$	$1.92 \pm 0.32 \pm 0.50$	$1.76 \pm 0.29 \pm 0.47$
$0.14 - 0.16$	$0.99 \pm 0.32 \pm 0.44$	$1.22 \pm 0.25 \pm 0.30$
$0.16 - 0.20$	$0.67 \pm 0.20 \pm 0.26$	$0.47 \pm 0.16 \pm 0.21$
$0.20 - 0.24$	$0.57 \pm 0.24 \pm 0.56$	$0.10 \pm 0.19 \pm 0.18$
$0.24 - 0.30$	$0.18 \pm 0.29 \pm 0.43$	$-0.08 \pm 0.20 \pm 0.29$

Table B.16: Distributions for the thrust minor, $T_{\mathrm{min.}}$, measured by OPAL at centre-of-mass energies $\sqrt{s} = 192$–207 GeV. The first uncertainty is statistical, while the second is systematic.
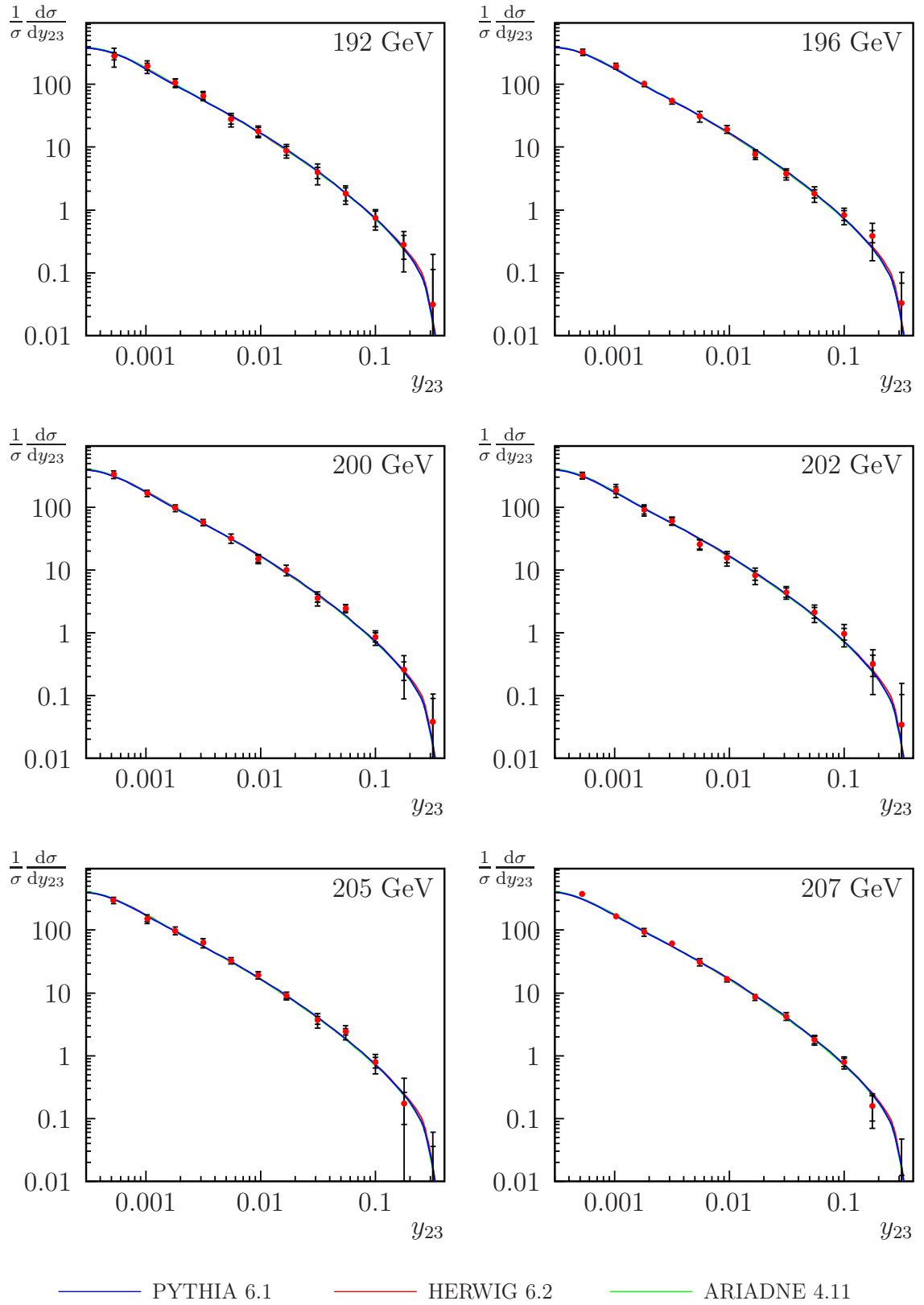
Figure B.16: Distributions for the thrust minor, $T_{\mathrm{min.}}$, measured by OPAL at centre-of-mass energies $\sqrt{s} = 192$–207 GeV. The inner error bars indicate statistical uncertainties. Each curve is generated using five million non-radiative Monte Carlo events, after hadronisation.

B.9   Aplanarity, *A*

A	$R'(A)$ at 91 GeV	$R'(A)$ at 133 GeV
$0.000 - 0.005$	$76.9 \quad \pm 0.2 \quad \pm 1.2$	$115.0 \quad \pm \quad 3.8 \quad \pm \quad 7.4$
$0.005 - 0.010$	$54.66 \quad \pm 0.15 \quad \pm 0.55$	$38.3 \quad \pm \quad 3.1 \quad \pm \quad 2.7$
$0.010 - 0.015$	$25.50 \quad \pm 0.11 \quad \pm 0.41$	$16.8 \quad \pm \quad 2.0 \quad \pm \quad 1.9$
$0.015 - 0.025$	$10.90 \quad \pm 0.05 \quad \pm 0.14$	$7.7 \quad \pm \quad 0.9 \quad \pm \quad 1.7$
$0.025 - 0.040$	$3.708 \pm 0.023 \pm 0.064$	$2.60 \quad \pm \quad 0.47 \quad \pm \quad 0.24$
$0.040 - 0.070$	$1.108 \pm 0.008 \pm 0.022$	$0.76 \quad \pm \quad 0.17 \quad \pm \quad 0.16$
$0.070 - 0.100$	$0.320 \pm 0.005 \pm 0.011$	$0.204 \pm \quad 0.076 \pm \quad 0.072$

A	$R'(A)$ at 161 GeV	$R'(A)$ at 172 GeV
$0.000 - 0.005$	$133.0 \quad \pm 8.8 \quad \pm 8.2$	$111. \quad \pm 14. \quad \pm 49.$
$0.005 - 0.010$	$30.3 \quad \pm 5.1 \quad \pm 8.4$	$27. \quad \pm \quad 6. \quad \pm 14.$
$0.010 - 0.015$	$13.0 \quad \pm 3.2 \quad \pm 2.1$	$12.2 \quad \pm \quad 3.6 \quad \pm \quad 9.1$
$0.015 - 0.025$	$6.7 \quad \pm 1.4 \quad \pm 1.4$	$6.7 \quad \pm \quad 1.8 \quad \pm \quad 3.0$
$0.025 - 0.040$	$2.5 \quad \pm 0.8 \quad \pm 1.2$	$0.7 \quad \pm \quad 1.1 \quad \pm \quad 0.8$
$0.040 - 0.070$	$0.73 \quad \pm 0.42 \quad \pm 0.57$	$-0.27 \quad \pm \quad 0.53 \quad \pm \quad 0.23$
$0.070 - 0.100$	$-0.05 \quad \pm 0.32 \quad \pm 0.02$	$-0.09 \quad \pm \quad 0.38 \quad \pm \quad 0.13$

A	$R'(A)$ at 183 GeV	$R'(A)$ at 189 GeV
$0.000 - 0.005$	$126.3 \quad \pm 5.4 \quad \pm 9.2$	$135.7 \quad \pm \quad 3.7 \quad \pm \quad 9.8$
$0.005 - 0.010$	$32.1 \quad \pm 2.6 \quad \pm 3.7$	$31.3 \quad \pm \quad 1.6 \quad \pm \quad 2.7$
$0.010 - 0.015$	$13.1 \quad \pm 1.7 \quad \pm 1.4$	$11.7 \quad \pm \quad 1.0 \quad \pm \quad 1.3$
$0.015 - 0.025$	$5.7 \quad \pm 0.9 \quad \pm 1.1$	$4.58 \quad \pm \quad 0.52 \quad \pm \quad 0.61$
$0.025 - 0.040$	$1.53 \quad \pm 0.51 \quad \pm 0.80$	$1.96 \quad \pm \quad 0.31 \quad \pm \quad 0.48$
$0.040 - 0.070$	$0.61 \quad \pm 0.27 \quad \pm 0.48$	$0.79 \quad \pm \quad 0.18 \quad \pm \quad 0.26$
$0.070 - 0.100$	$0.34 \quad \pm 0.31 \quad \pm 0.67$	$0.1 \quad \pm \quad 0.3 \quad \pm \quad 1.1$

Table B.17: Distributions for the aplanarity, A, measured by OPAL at centre-of-mass energies $\sqrt{s}$ = 91–189 GeV. The first uncertainty is statistical, while the second is systematic.

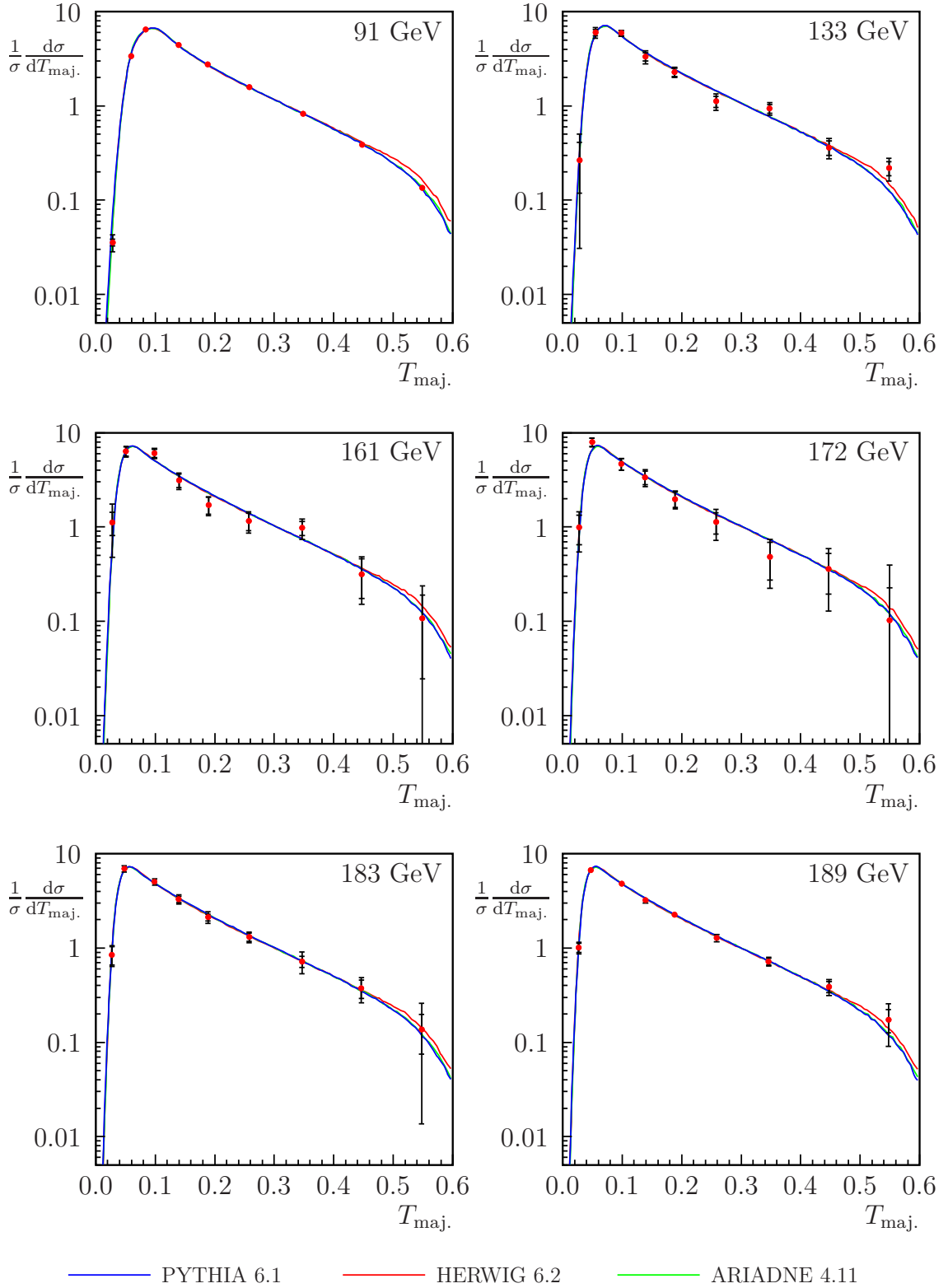Figure B.17: Distributions for the aplanarity, A, measured by OPAL at centre-of-mass energies $\sqrt{s} = 91$–189 GeV. The inner error bars indicate statistical uncertainties. Each curve is generated using five million non-radiative Monte Carlo events, after hadronisation.

Aplanarity, A (contd.)

A	$R'(A)$ at 192 GeV	$R'(A)$ at 196 GeV
$0.000 - 0.005$	$123. \pm 12. \pm 13.$	$136.1 \pm 4.8 \pm 9.7$
$0.005 - 0.010$	$29.2 \pm 4.2 \pm 6.6$	$32.6 \pm 2.4 \pm 3.0$
$0.010 - 0.015$	$12.0 \pm 2.7 \pm 7.0$	$12.1 \pm 1.6 \pm 1.9$
$0.015 - 0.025$	$5.0 \pm 1.4 \pm 1.7$	$5.98 \pm 0.87 \pm 0.96$
$0.025 - 0.040$	$3.3 \pm 0.8 \pm 1.4$	$1.59 \pm 0.53 \pm 0.50$
$0.040 - 0.070$	$0.4 \pm 0.5 \pm 1.1$	$0.68 \pm 0.36 \pm 0.73$
$0.070 - 0.100$	$0.92 \pm 0.49 \pm 0.87$	$-0.03 \pm 0.46 \pm 0.67$
A	$R'(A)$ at 200 GeV	$R'(A)$ at 202 GeV
$0.000 - 0.005$	$160. \pm 19. \pm 42.$	$127. \pm 7. \pm 12.$
$0.005 - 0.010$	$32.8 \pm 4.4 \pm 8.5$	$31.4 \pm 3.4 \pm 7.7$
$0.010 - 0.015$	$14.8 \pm 2.2 \pm 6.6$	$15.5 \pm 2.4 \pm 5.0$
$0.015 - 0.025$	$6.0 \pm 1.1 \pm 2.2$	$6.6 \pm 1.3 \pm 2.1$
$0.025 - 0.040$	$2.6 \pm 0.6 \pm 1.2$	$2.05 \pm 0.81 \pm 0.98$
$0.040 - 0.070$	$1.6 \pm 0.4 \pm 1.2$	$1.10 \pm 0.53 \pm 0.83$
$0.070 - 0.100$	$0.1 \pm 0.5 \pm 1.1$	$-0.28 \pm 0.51 \pm 0.78$
A	$R'(A)$ at 205 GeV	$R'(A)$ at 207 GeV
$0.000 - 0.005$	$130. \pm 20. \pm 22.$	$118. \pm 23. \pm 33.$
$0.005 - 0.010$	$23.6 \pm 4.5 \pm 4.6$	$26.1 \pm 4.7 \pm 7.8$
$0.010 - 0.015$	$10.2 \pm 2.2 \pm 1.8$	$9.4 \pm 2.1 \pm 3.2$
$0.015 - 0.025$	$3.8 \pm 1.0 \pm 1.3$	$3.7 \pm 0.9 \pm 1.2$
$0.025 - 0.040$	$1.8 \pm 0.6 \pm 1.1$	$1.4 \pm 0.5 \pm 1.2$
$0.040 - 0.070$	$1.38 \pm 0.38 \pm 0.67$	$0.56 \pm 0.31 \pm 0.44$
$0.070 - 0.100$	$-1.2 \pm 1.5 \pm 2.9$	$-0.1 \pm 0.4 \pm 1.3$

Table B.18: Distributions for the aplanarity, A, measured by OPAL at centre-of-mass energies $\sqrt{s} = 192$–207 GeV. The first uncertainty is statistical, while the second is systematic.
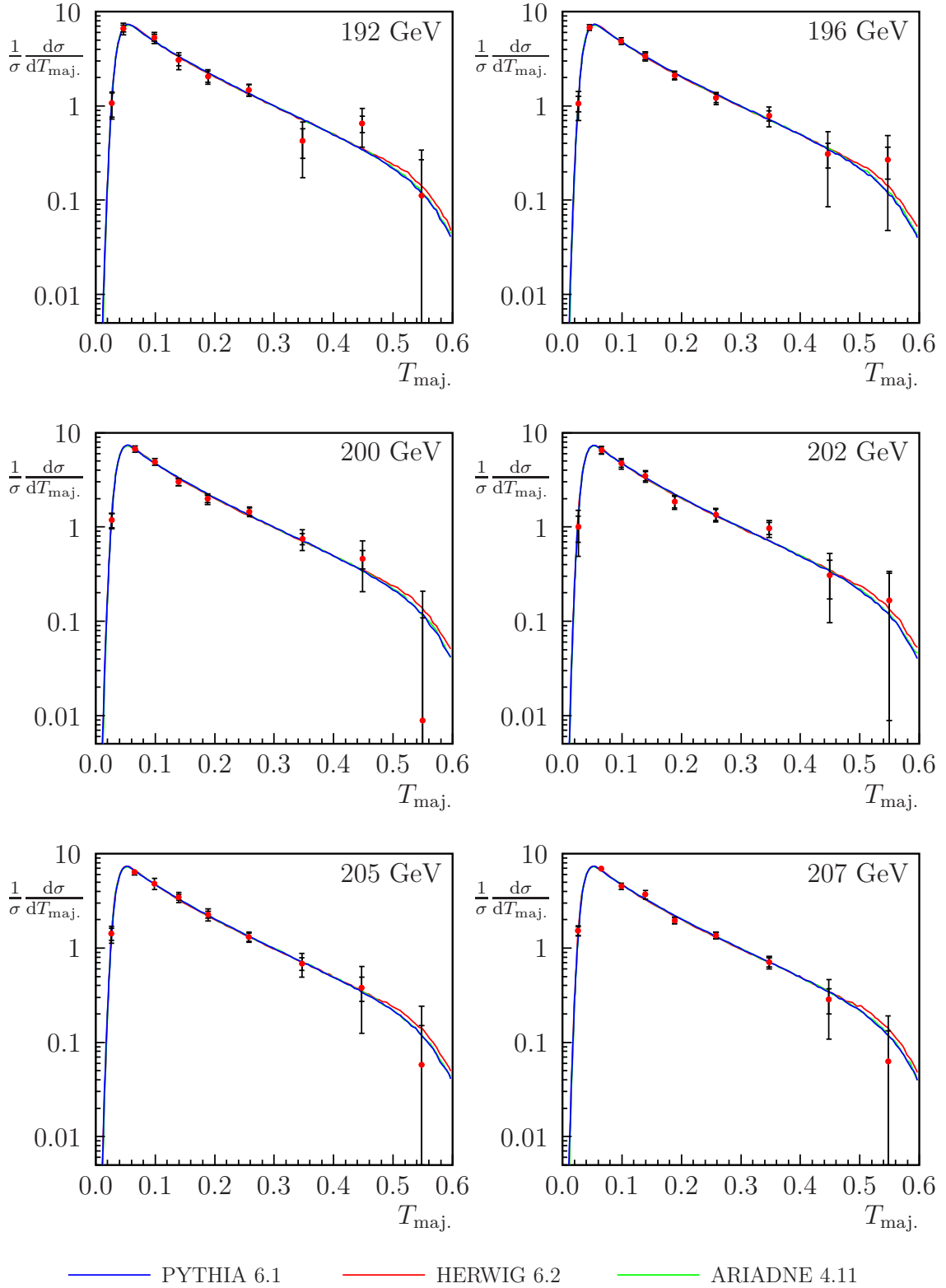
Figure B.18: Distributions for the aplanarity, A, measured by OPAL at centre-of-mass energies $\sqrt{s} = 192$–207 GeV. The inner error bars indicate statistical uncertainties. Each curve is generated using five million non-radiative Monte Carlo events, after hadronisation.

B.10   Sphericity, S

S	$R'(S)$ at 91 GeV			$R'(S)$ at 133 GeV		
$0.00 - 0.02$	18.06	$\pm\ 0.04$	$\pm\ 0.41$	23.6	$\pm\ 1.0$	$\pm\ 1.8$
$0.02 - 0.04$	10.56	$\pm\ 0.03$	$\pm\ 0.16$	8.15	$\pm\ 0.72$	$\pm\ 0.77$
$0.04 - 0.06$	5.185	$\pm\ 0.024$	$\pm\ 0.068$	4.07	$\pm\ 0.53$	$\pm\ 0.28$
$0.06 - 0.12$	2.408	$\pm\ 0.009$	$\pm\ 0.051$	1.65	$\pm\ 0.22$	$\pm\ 0.13$
$0.12 - 0.20$	0.989	$\pm\ 0.005$	$\pm\ 0.033$	0.93	$\pm\ 0.12$	$\pm\ 0.22$
$0.20 - 0.30$	0.467	$\pm\ 0.003$	$\pm\ 0.015$	0.377	$\pm\ 0.068$	$\pm\ 0.048$
$0.30 - 0.50$	0.200	$\pm\ 0.002$	$\pm\ 0.011$	0.293	$\pm\ 0.034$	$\pm\ 0.033$
$0.50 - 0.70$	0.0613	$\pm\ 0.0009$	$\pm\ 0.0024$	0.068	$\pm\ 0.016$	$\pm\ 0.013$

S	$R'(S)$ at 161 GeV			$R'(S)$ at 172 GeV		
$0.00 - 0.02$	27.2	$\pm\ 1.6$	$\pm\ 0.9$	26.0	$\pm\ 1.8$	$\pm\ 1.1$
$0.02 - 0.04$	5.9	$\pm\ 1.1$	$\pm\ 0.6$	8.5	$\pm\ 1.2$	$\pm\ 0.5$
$0.04 - 0.06$	3.29	$\pm\ 0.86$	$\pm\ 0.80$	3.92	$\pm\ 0.93$	$\pm\ 0.56$
$0.06 - 0.12$	2.00	$\pm\ 0.33$	$\pm\ 0.35$	1.70	$\pm\ 0.38$	$\pm\ 0.30$
$0.12 - 0.20$	0.81	$\pm\ 0.20$	$\pm\ 0.36$	0.72	$\pm\ 0.24$	$\pm\ 0.19$
$0.20 - 0.30$	0.40	$\pm\ 0.14$	$\pm\ 0.17$	0.16	$\pm\ 0.18$	$\pm\ 0.13$
$0.30 - 0.50$	0.203	$\pm\ 0.077$	$\pm\ 0.080$	0.13	$\pm\ 0.10$	$\pm\ 0.15$
$0.50 - 0.70$	0.031	$\pm\ 0.053$	$\pm\ 0.049$	0.16	$\pm\ 0.07$	$\pm\ 0.16$

S	$R'(S)$ at 183 GeV			$R'(S)$ at 189 GeV		
$0.00 - 0.02$	25.2	$\pm\ 0.9$	$\pm\ 1.1$	25.06	$\pm\ 0.53$	$\pm\ 0.59$
$0.02 - 0.04$	6.80	$\pm\ 0.56$	$\pm\ 0.35$	7.82	$\pm\ 0.34$	$\pm\ 0.45$
$0.04 - 0.06$	3.96	$\pm\ 0.42$	$\pm\ 0.62$	3.72	$\pm\ 0.25$	$\pm\ 0.12$
$0.06 - 0.12$	2.38	$\pm\ 0.18$	$\pm\ 0.25$	1.94	$\pm\ 0.11$	$\pm\ 0.19$
$0.12 - 0.20$	0.73	$\pm\ 0.11$	$\pm\ 0.12$	0.83	$\pm\ 0.07$	$\pm\ 0.12$
$0.20 - 0.30$	0.361	$\pm\ 0.090$	$\pm\ 0.087$	0.388	$\pm\ 0.053$	$\pm\ 0.085$
$0.30 - 0.50$	0.118	$\pm\ 0.052$	$\pm\ 0.060$	0.152	$\pm\ 0.036$	$\pm\ 0.042$
$0.50 - 0.70$	0.054	$\pm\ 0.041$	$\pm\ 0.056$	0.060	$\pm\ 0.028$	$\pm\ 0.048$

Table B.19: Distributions for the sphericity, S, measured by OPAL at centre-of-mass energies $\sqrt{s} = 91$–189 GeV. The first uncertainty is statistical, while the second is systematic.
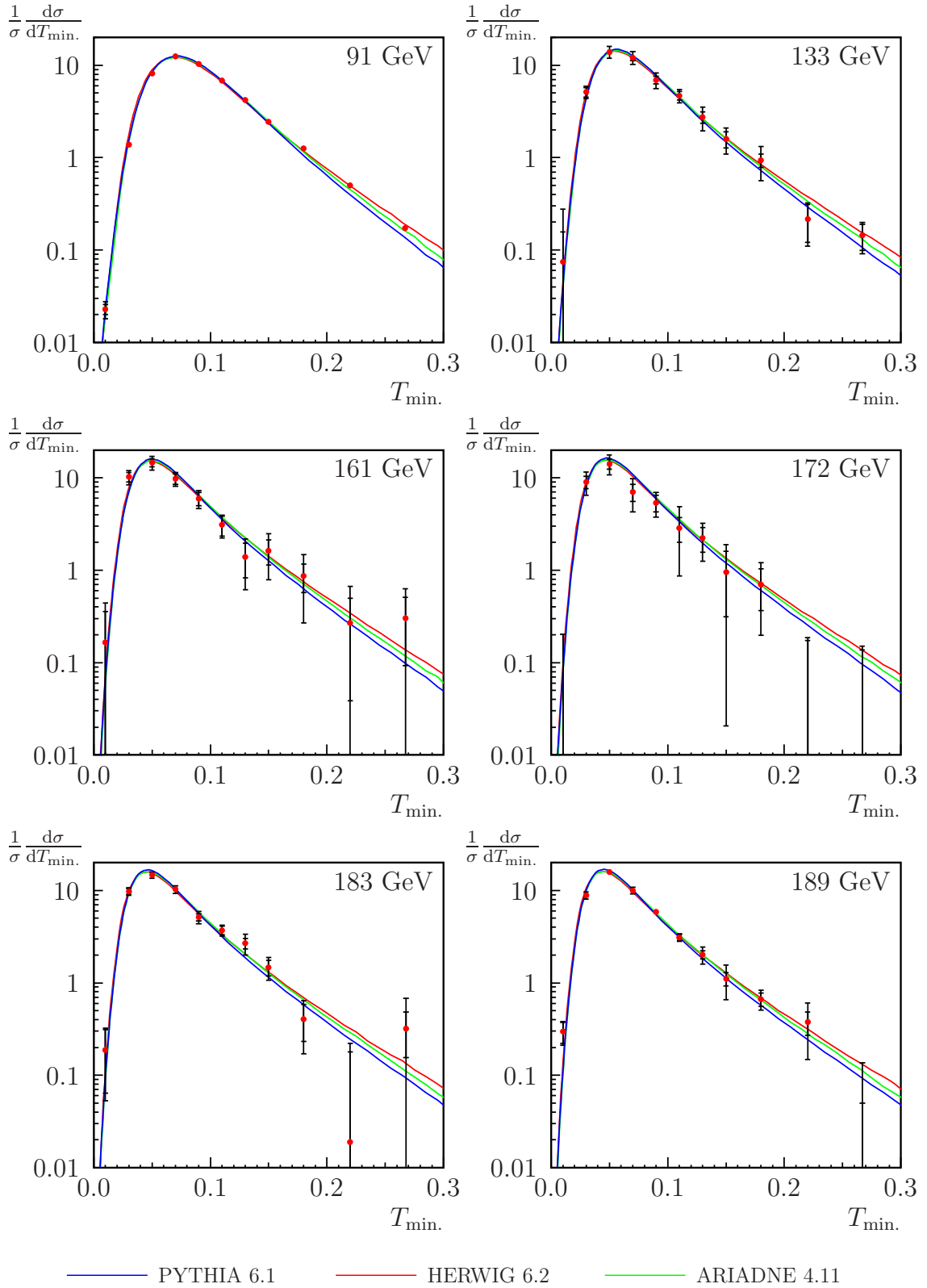
Figure B.19: Distributions for the sphericity, S, measured by OPAL at centre-of-mass energies $\sqrt{s} = 91$–189 GeV. The inner error bars indicate statistical uncertainties. Each curve is generated using five million non-radiative Monte Carlo events, after hadronisation.

Sphericity, S (contd.)

S	$R'(S)$ at 192 GeV			$R'(S)$ at 196 GeV		
$0.00 - 0.02$	25.1	± 1.4	± 1.9	26.3	± 1.0	± 1.1
$0.02 - 0.04$	6.42	± 0.85	± 0.49	6.44	± 0.56	± 0.41
$0.04 - 0.06$	3.93	± 0.70	± 0.76	3.42	± 0.43	± 0.72
$0.06 - 0.12$	1.76	± 0.27	± 0.24	2.07	± 0.18	± 0.27
$0.12 - 0.20$	0.98	± 0.19	± 0.28	0.83	± 0.12	± 0.18
$0.20 - 0.30$	0.25	± 0.13	± 0.17	0.373	± 0.092	± 0.070
$0.30 - 0.50$	0.31	± 0.09	± 0.14	0.155	± 0.061	± 0.087
$0.50 - 0.70$	0.10	± 0.11	± 0.29	0.03	± 0.06	± 0.12

S	$R'(S)$ at 200 GeV			$R'(S)$ at 202 GeV		
$0.00 - 0.02$	24.7	± 0.9	± 1.0	25.5	± 1.4	± 1.7
$0.02 - 0.04$	7.14	± 0.57	± 0.85	6.61	± 0.83	± 0.71
$0.04 - 0.06$	3.74	± 0.43	± 0.46	3.56	± 0.60	± 0.56
$0.06 - 0.12$	1.97	± 0.18	± 0.21	1.90	± 0.27	± 0.36
$0.12 - 0.20$	0.80	± 0.12	± 0.16	0.95	± 0.17	± 0.24
$0.20 - 0.30$	0.25	± 0.10	± 0.13	0.60	± 0.13	± 0.26
$0.30 - 0.50$	0.30	± 0.07	± 0.14	0.28	± 0.10	± 0.16
$0.50 - 0.70$	0.09	± 0.07	± 0.11	-0.10	± 0.09	± 0.19

S	$R'(S)$ at 205 GeV			$R'(S)$ at 207 GeV		
$0.00 - 0.02$	26.3	± 1.0	± 1.3	27.00	± 0.75	± 0.41
$0.02 - 0.04$	7.70	± 0.58	± 0.58	7.67	± 0.45	± 0.19
$0.04 - 0.06$	3.36	± 0.45	± 0.76	3.80	± 0.34	± 0.37
$0.06 - 0.12$	2.41	± 0.18	± 0.38	1.87	± 0.15	± 0.15
$0.12 - 0.20$	0.61	± 0.12	± 0.26	0.65	± 0.09	± 0.11
$0.20 - 0.30$	0.50	± 0.11	± 0.13	0.335	± 0.081	± 0.063
$0.30 - 0.50$	0.052	± 0.073	± 0.098	0.16	± 0.06	± 0.16
$0.50 - 0.70$	0.03	± 0.06	± 0.11	0.02	± 0.05	± 0.10

Table B.20: Distributions for the sphericity, S, measured by OPAL at centre-of-mass energies $\sqrt{s} = 192$–207 GeV. The first uncertainty is statistical, while the second is systematic.
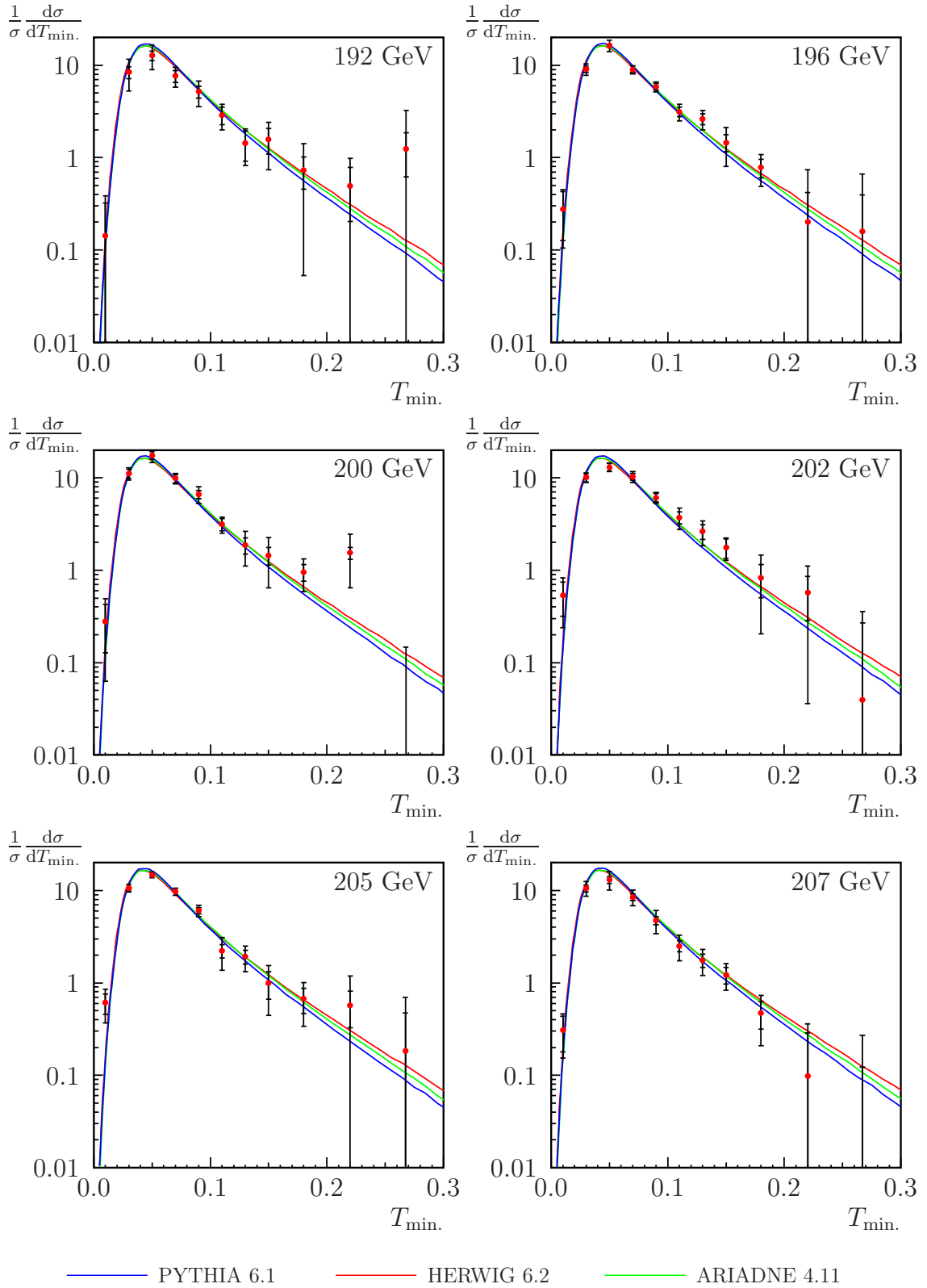
Figure B.20: Distributions for the sphericity, S, measured by OPAL at centre-of-mass energies $\sqrt{s} = 192$–207 GeV. The inner error bars indicate statistical uncertainties. Each curve is generated using five million non-radiative Monte Carlo events, after hadronisation.

B.11   Oblateness, *O*

O	$R'(O)$ at 91 GeV	$R'(O)$ at 133 GeV
$0.00 - 0.05$	$9.93 \pm 0.02 \pm 0.14$	$9.71 \pm 0.38 \pm 0.20$
$0.05 - 0.10$	$4.579 \pm 0.013 \pm 0.041$	$4.52 \pm 0.31 \pm 0.24$
$0.10 - 0.15$	$2.273 \pm 0.010 \pm 0.037$	$2.17 \pm 0.25 \pm 0.13$
$0.15 - 0.20$	$1.307 \pm 0.008 \pm 0.031$	$1.20 \pm 0.19 \pm 0.13$
$0.20 - 0.25$	$0.811 \pm 0.007 \pm 0.016$	$0.82 \pm 0.15 \pm 0.07$
$0.25 - 0.30$	$0.489 \pm 0.005 \pm 0.022$	$0.65 \pm 0.11 \pm 0.13$
$0.30 - 0.40$	$0.2364 \pm 0.0025 \pm 0.0078$	$0.318 \pm 0.062 \pm 0.045$
$0.40 - 0.50$	$0.0519 \pm 0.0011 \pm 0.0024$	$0.150 \pm 0.028 \pm 0.059$
O	$R'(O)$ at 161 GeV	$R'(O)$ at 172 GeV
$0.00 - 0.05$	$9.82 \pm 0.62 \pm 0.33$	$10.42 \pm 0.69 \pm 0.56$
$0.05 - 0.10$	$4.62 \pm 0.50 \pm 0.60$	$4.97 \pm 0.56 \pm 0.59$
$0.10 - 0.15$	$2.01 \pm 0.41 \pm 0.43$	$1.86 \pm 0.46 \pm 0.34$
$0.15 - 0.20$	$1.01 \pm 0.32 \pm 0.38$	$0.86 \pm 0.38 \pm 0.49$
$0.20 - 0.25$	$1.23 \pm 0.26 \pm 0.43$	$0.54 \pm 0.34 \pm 0.29$
$0.25 - 0.30$	$0.56 \pm 0.22 \pm 0.21$	$0.45 \pm 0.25 \pm 0.18$
$0.30 - 0.40$	$0.22 \pm 0.12 \pm 0.11$	$0.43 \pm 0.15 \pm 0.32$
$0.40 - 0.50$	$0.12 \pm 0.06 \pm 0.13$	$0.02 \pm 0.08 \pm 0.14$
O	$R'(O)$ at 183 GeV	$R'(O)$ at 189 GeV
$0.00 - 0.05$	$10.06 \pm 0.32 \pm 0.35$	$10.00 \pm 0.19 \pm 0.23$
$0.05 - 0.10$	$4.13 \pm 0.26 \pm 0.27$	$3.93 \pm 0.15 \pm 0.23$
$0.10 - 0.15$	$2.20 \pm 0.22 \pm 0.31$	$2.43 \pm 0.12 \pm 0.15$
$0.15 - 0.20$	$1.54 \pm 0.18 \pm 0.33$	$1.27 \pm 0.11 \pm 0.05$
$0.20 - 0.25$	$0.82 \pm 0.15 \pm 0.17$	$0.861 \pm 0.089 \pm 0.085$
$0.25 - 0.30$	$0.46 \pm 0.12 \pm 0.24$	$0.608 \pm 0.076 \pm 0.091$
$0.30 - 0.40$	$0.32 \pm 0.07 \pm 0.12$	$0.312 \pm 0.044 \pm 0.036$
$0.40 - 0.50$	$0.069 \pm 0.037 \pm 0.062$	$0.131 \pm 0.026 \pm 0.089$

Table B.21: Distributions for the oblateness, O, measured by OPAL at centre-of-mass energies $\sqrt{s} = 91$–189 GeV. The first uncertainty is statistical, while the second is systematic.
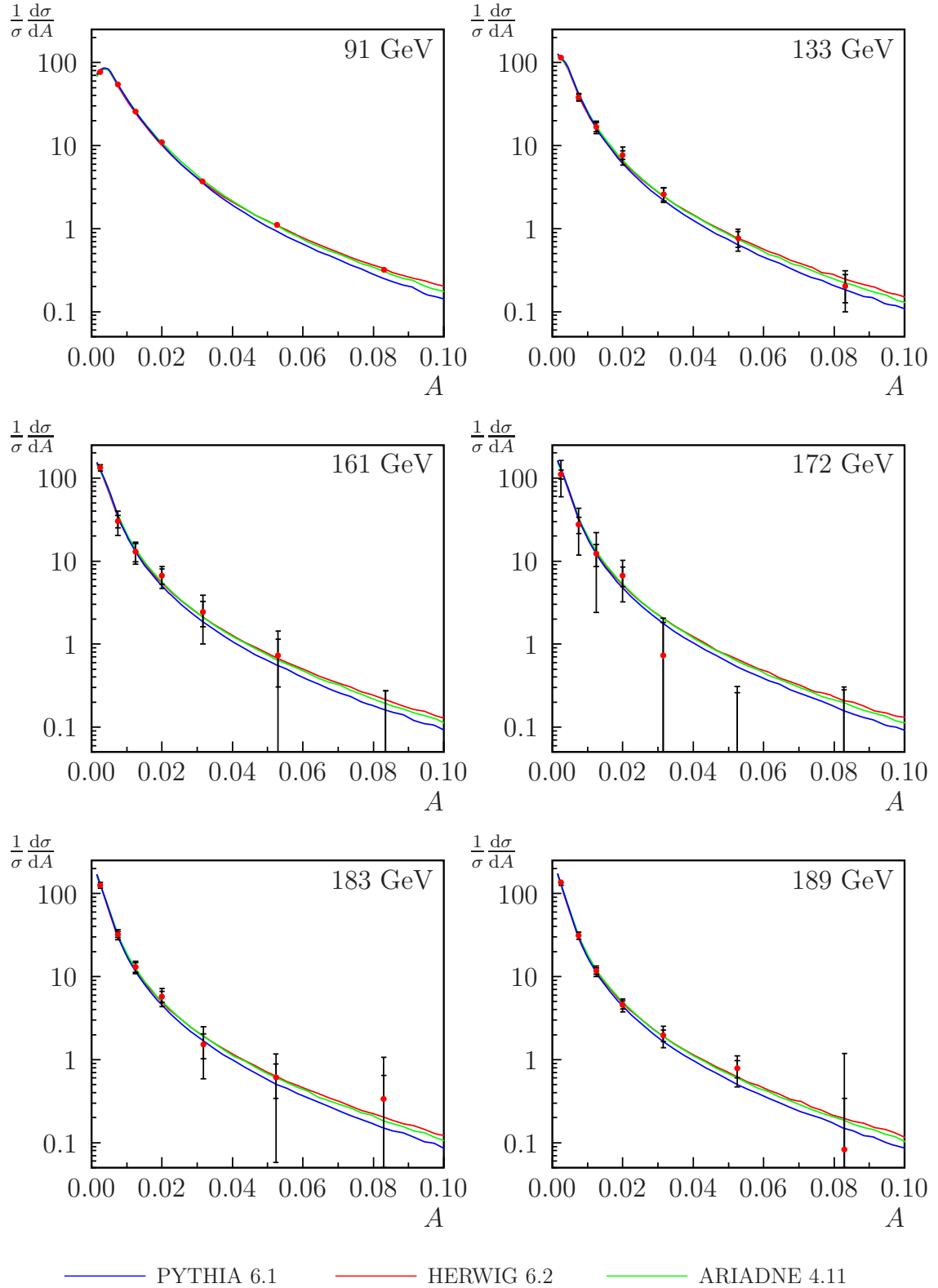
Figure B.21: Distributions for the oblateness, O, measured by OPAL at centre-of-mass energies $\sqrt{s} = 91\text{--}189$ GeV. The inner error bars indicate statistical uncertainties. Each curve is generated using five million non-radiative Monte Carlo events, after hadronisation.

Oblateness, O (contd.)

O	$R'(O)$ at 192 GeV	$R'(O)$ at 196 GeV
$0.00 - 0.05$	$10.37 \pm 0.49 \pm 0.65$	$10.00 \pm 0.31 \pm 0.40$
$0.05 - 0.10$	$4.24 \pm 0.40 \pm 0.48$	$4.41 \pm 0.25 \pm 0.39$
$0.10 - 0.15$	$2.36 \pm 0.32 \pm 0.19$	$2.06 \pm 0.21 \pm 0.07$
$0.15 - 0.20$	$1.15 \pm 0.27 \pm 0.41$	$1.21 \pm 0.17 \pm 0.26$
$0.20 - 0.25$	$0.64 \pm 0.24 \pm 0.21$	$0.72 \pm 0.15 \pm 0.23$
$0.25 - 0.30$	$0.52 \pm 0.19 \pm 0.13$	$0.71 \pm 0.13 \pm 0.22$
$0.30 - 0.40$	$0.26 \pm 0.12 \pm 0.14$	$0.26 \pm 0.07 \pm 0.12$
$0.40 - 0.50$	$0.092 \pm 0.050 \pm 0.045$	$0.16 \pm 0.05 \pm 0.11$
O	$R'(O)$ at 200 GeV	$R'(O)$ at 202 GeV
$0.00 - 0.05$	$9.89 \pm 0.32 \pm 0.33$	$9.72 \pm 0.47 \pm 0.46$
$0.05 - 0.10$	$4.15 \pm 0.25 \pm 0.17$	$4.06 \pm 0.38 \pm 0.32$
$0.10 - 0.15$	$2.07 \pm 0.21 \pm 0.11$	$1.95 \pm 0.31 \pm 0.25$
$0.15 - 0.20$	$1.42 \pm 0.18 \pm 0.08$	$1.43 \pm 0.25 \pm 0.41$
$0.20 - 0.25$	$0.82 \pm 0.15 \pm 0.13$	$1.30 \pm 0.23 \pm 0.38$
$0.25 - 0.30$	$0.53 \pm 0.14 \pm 0.17$	$0.63 \pm 0.19 \pm 0.26$
$0.30 - 0.40$	$0.45 \pm 0.08 \pm 0.14$	$0.29 \pm 0.11 \pm 0.15$
$0.40 - 0.50$	$0.098 \pm 0.047 \pm 0.060$	$0.08 \pm 0.07 \pm 0.13$
O	$R'(O)$ at 205 GeV	$R'(O)$ at 207 GeV
$0.00 - 0.05$	$9.54 \pm 0.33 \pm 0.26$	$10.24 \pm 0.25 \pm 0.22$
$0.05 - 0.10$	$4.61 \pm 0.26 \pm 0.24$	$4.29 \pm 0.20 \pm 0.12$
$0.10 - 0.15$	$2.29 \pm 0.21 \pm 0.20$	$2.22 \pm 0.17 \pm 0.18$
$0.15 - 0.20$	$1.33 \pm 0.18 \pm 0.15$	$1.26 \pm 0.14 \pm 0.19$
$0.20 - 0.25$	$0.82 \pm 0.16 \pm 0.24$	$0.81 \pm 0.12 \pm 0.09$
$0.25 - 0.30$	$0.59 \pm 0.15 \pm 0.20$	$0.55 \pm 0.10 \pm 0.09$
$0.30 - 0.40$	$0.34 \pm 0.08 \pm 0.12$	$0.238 \pm 0.060 \pm 0.080$
$0.40 - 0.50$	$0.064 \pm 0.048 \pm 0.083$	$0.064 \pm 0.043 \pm 0.046$

Table B.22: Distributions for the oblateness, O, measured by OPAL at centre-of-mass energies $\sqrt{s} = $ 192–207 GeV. The first uncertainty is statistical, while the second is systematic.
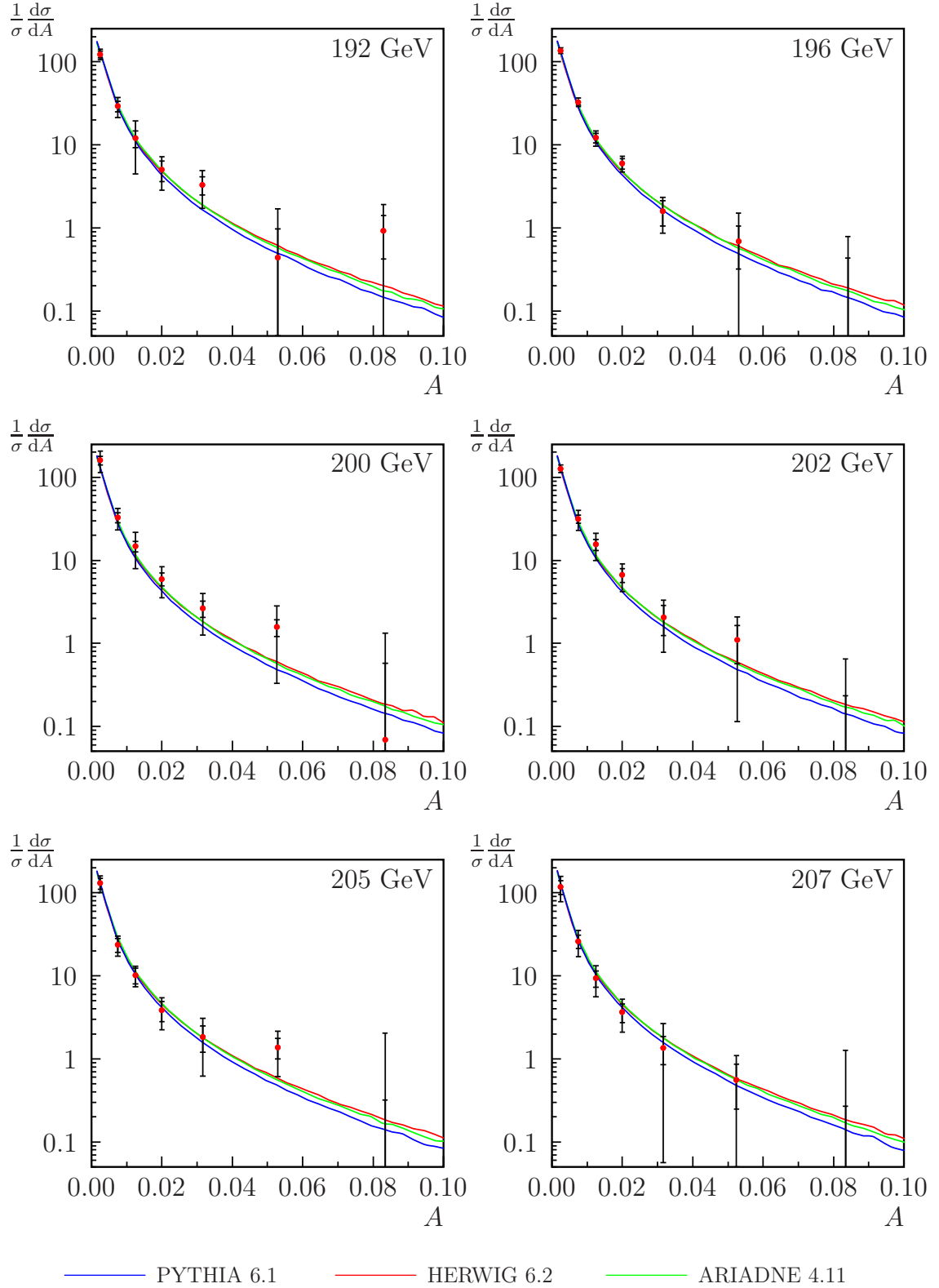
Figure B.22: Distributions for the oblateness, O, measured by OPAL at centre-of-mass energies $\sqrt{s} = 192$–207 GeV. The inner error bars indicate statistical uncertainties. Each curve is generated using five million non-radiative Monte Carlo events, after hadronisation.

B.12   Light jet mass, M_L

$M_L/\sqrt{s}$	$R'(M_L/\sqrt{s})$ at 91 GeV	$R'(M_L/\sqrt{s})$ at 133 GeV
$0.00 - 0.04$	$0.124 \pm 0.002 \pm 0.038$	$0.292 \pm 0.067 \pm 0.080$
$0.04 - 0.06$	$1.108 \pm 0.008 \pm 0.089$	$2.29 \pm 0.29 \pm 0.57$
$0.06 - 0.08$	$3.72 \pm 0.02 \pm 0.55$	$7.5 \pm 0.6 \pm 1.4$
$0.08 - 0.10$	$8.22 \pm 0.03 \pm 0.56$	$11.1 \pm 0.8 \pm 1.7$
$0.10 - 0.12$	$10.73 \pm 0.04 \pm 0.37$	$10.3 \pm 0.8 \pm 1.1$
$0.12 - 0.14$	$9.11 \pm 0.04 \pm 0.54$	$6.2 \pm 0.7 \pm 1.0$
$0.14 - 0.16$	$6.22 \pm 0.03 \pm 0.22$	$4.7 \pm 0.6 \pm 1.1$
$0.16 - 0.20$	$3.150 \pm 0.015 \pm 0.083$	$1.85 \pm 0.28 \pm 0.27$
$0.20 - 0.24$	$1.343 \pm 0.010 \pm 0.033$	$1.03 \pm 0.18 \pm 0.15$
$0.24 - 0.30$	$0.450 \pm 0.005 \pm 0.017$	$0.461 \pm 0.085 \pm 0.089$
$0.30 - 0.40$	$0.0610 \pm 0.0013 \pm 0.0037$	$0.038 \pm 0.025 \pm 0.024$

$M_L/\sqrt{s}$	$R'(M_L/\sqrt{s})$ at 161 GeV	$R'(M_L/\sqrt{s})$ at 172 GeV
$0.00 - 0.04$	$0.19 \pm 0.12 \pm 0.13$	$0.28 \pm 0.13 \pm 0.07$
$0.04 - 0.06$	$4.24 \pm 0.61 \pm 0.87$	$5.62 \pm 0.74 \pm 0.37$
$0.06 - 0.08$	$10.5 \pm 1.1 \pm 1.5$	$9.5 \pm 1.3 \pm 1.9$
$0.08 - 0.10$	$11.9 \pm 1.4 \pm 1.4$	$10.4 \pm 1.5 \pm 0.6$
$0.10 - 0.12$	$7.6 \pm 1.3 \pm 1.2$	$6.7 \pm 1.4 \pm 1.2$
$0.12 - 0.14$	$5.7 \pm 1.1 \pm 0.9$	$7.1 \pm 1.2 \pm 0.9$
$0.14 - 0.16$	$2.70 \pm 0.83 \pm 0.62$	$3.10 \pm 0.95 \pm 0.88$
$0.16 - 0.20$	$1.85 \pm 0.45 \pm 0.55$	$2.27 \pm 0.52 \pm 0.96$
$0.20 - 0.24$	$0.96 \pm 0.31 \pm 0.80$	$0.36 \pm 0.38 \pm 0.27$
$0.24 - 0.30$	$0.48 \pm 0.19 \pm 0.51$	$0.09 \pm 0.26 \pm 0.12$
$0.30 - 0.40$	$-0.006 \pm 0.082 \pm 0.009$	$0.29 \pm 0.13 \pm 0.54$

$M_L/\sqrt{s}$	$R'(M_L/\sqrt{s})$ at 183 GeV	$R'(M_L/\sqrt{s})$ at 189 GeV
$0.00 - 0.04$	$0.339 \pm 0.070 \pm 0.067$	$0.402 \pm 0.044 \pm 0.059$
$0.04 - 0.06$	$4.78 \pm 0.37 \pm 0.35$	$4.35 \pm 0.22 \pm 0.16$
$0.06 - 0.08$	$9.93 \pm 0.63 \pm 0.46$	$11.02 \pm 0.39 \pm 0.33$
$0.08 - 0.10$	$12.2 \pm 0.7 \pm 1.7$	$11.71 \pm 0.43 \pm 0.63$
$0.10 - 0.12$	$9.1 \pm 0.7 \pm 2.1$	$8.38 \pm 0.38 \pm 0.50$
$0.12 - 0.14$	$4.64 \pm 0.50 \pm 0.77$	$4.76 \pm 0.31 \pm 0.28$
$0.14 - 0.16$	$3.05 \pm 0.43 \pm 0.40$	$3.31 \pm 0.25 \pm 0.36$
$0.16 - 0.20$	$1.74 \pm 0.24 \pm 0.18$	$1.62 \pm 0.14 \pm 0.18$
$0.20 - 0.24$	$0.43 \pm 0.20 \pm 0.39$	$0.66 \pm 0.11 \pm 0.10$
$0.24 - 0.30$	$0.37 \pm 0.11 \pm 0.32$	$0.328 \pm 0.084 \pm 0.082$
$0.30 - 0.40$	$0.03 \pm 0.06 \pm 0.14$	$0.03 \pm 0.07 \pm 0.11$

Table B.23: Distributions for the light jet mass, M_L, measured by OPAL at centre-of-mass energies $\sqrt{s} = 91$–189 GeV. The first uncertainty is statistical, while the second is systematic.
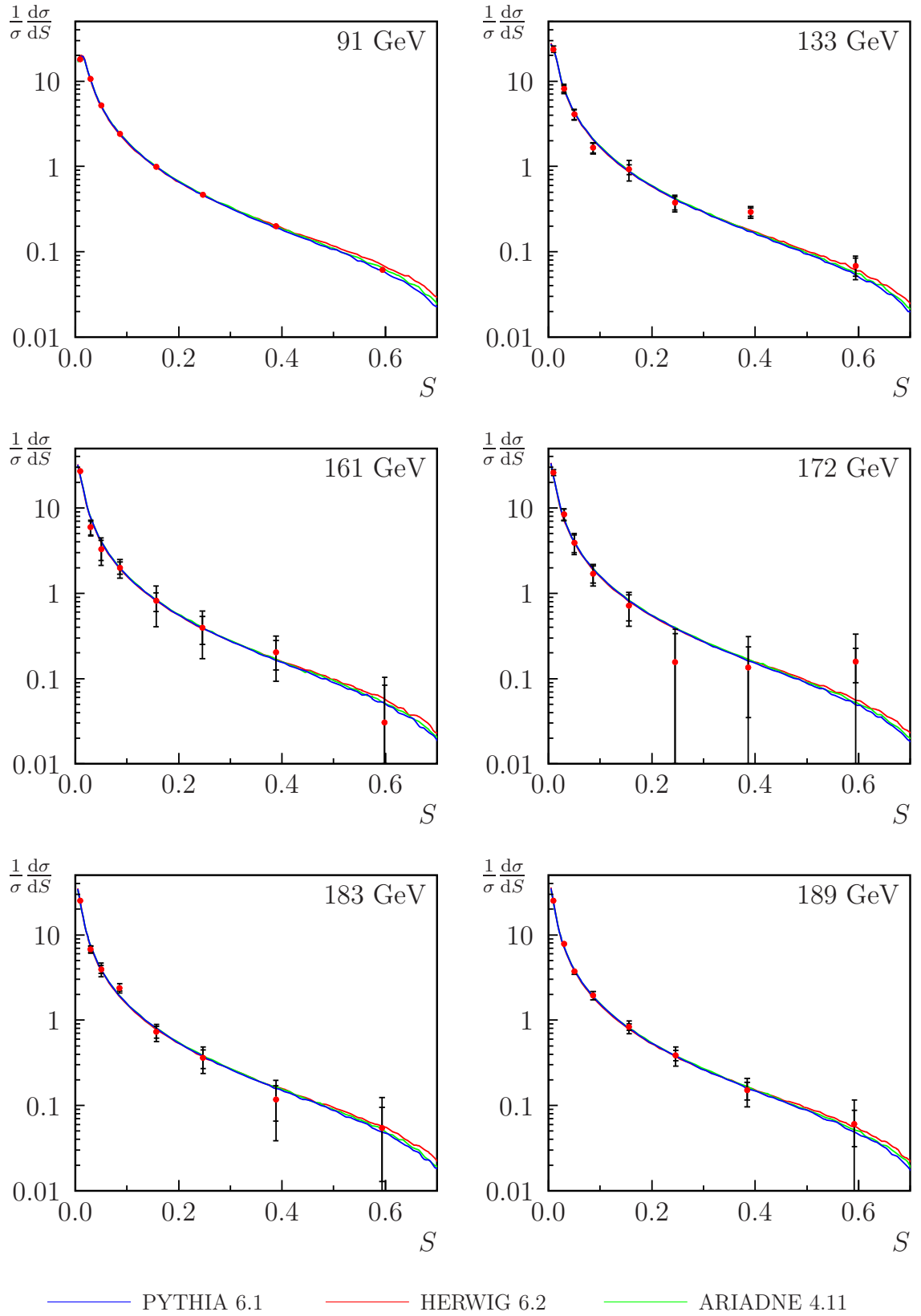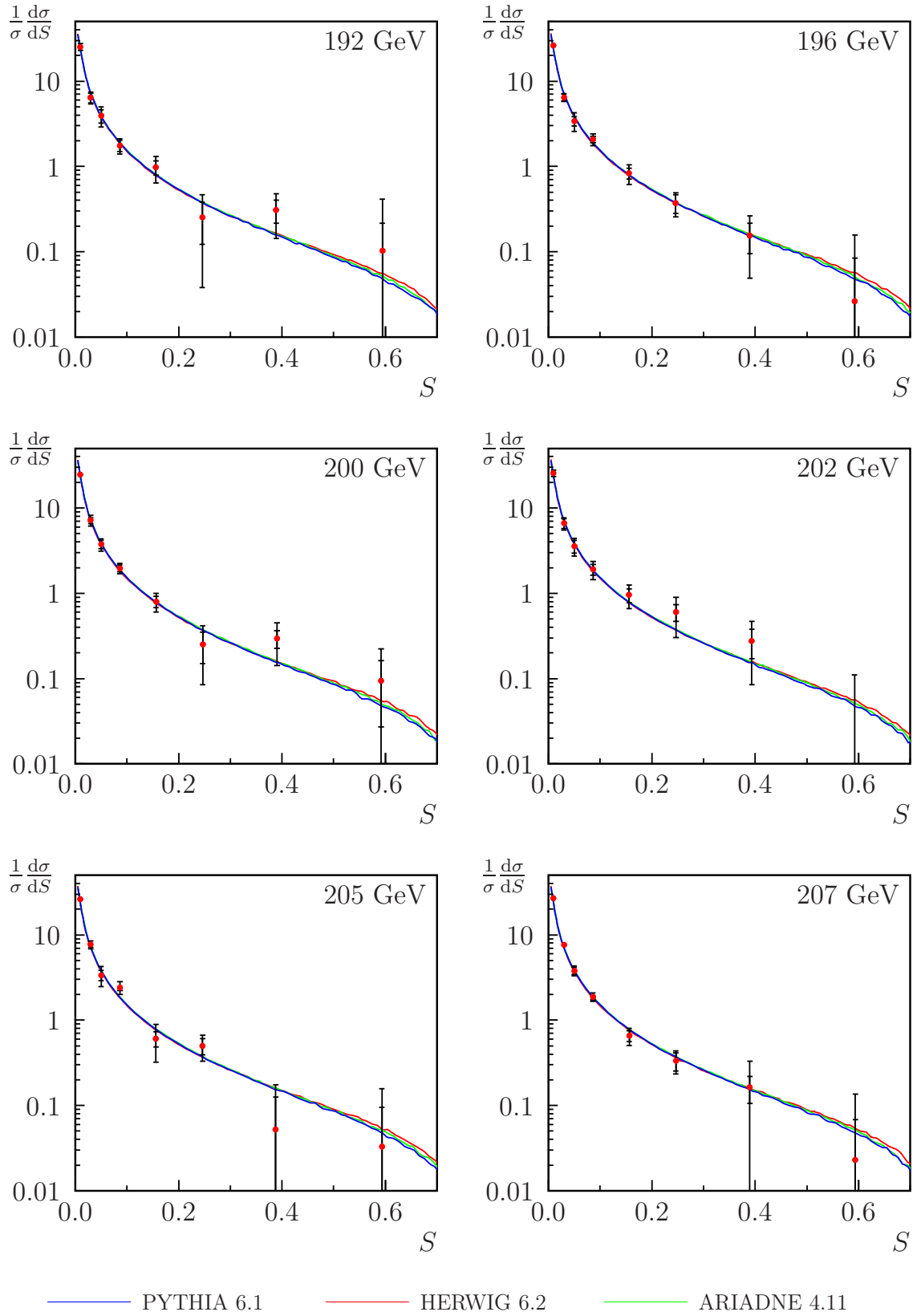
Figure B.23: Distributions for the light jet mass, M_{L}, measured by OPAL at centre-of-mass energies $\sqrt{s} = 91$–189 GeV. The inner error bars indicate statistical uncertainties. Each curve is generated using five million non-radiative Monte Carlo events, after hadronisation.

Light jet mass, M_{L} (contd.)

$M_{\mathrm{L}}/\sqrt{s}$	$R'\,(M_{\mathrm{L}}/\sqrt{s})$ at 192 GeV	$R'\,(M_{\mathrm{L}}/\sqrt{s})$ at 196 GeV
$0.00 - 0.04$	$0.26 \pm 0.12 \pm 0.06$	$0.48 \pm 0.07 \pm 0.11$
$0.04 - 0.06$	$3.94 \pm 0.57 \pm 0.55$	$4.59 \pm 0.40 \pm 0.64$
$0.06 - 0.08$	$9.27 \pm 0.97 \pm 0.75$	$11.10 \pm 0.73 \pm 0.65$
$0.08 - 0.10$	$12.2 \pm 1.1 \pm 1.4$	$12.65 \pm 0.79 \pm 0.86$
$0.10 - 0.12$	$8.4 \pm 0.9 \pm 1.4$	$7.96 \pm 0.65 \pm 0.42$
$0.12 - 0.14$	$4.7 \pm 0.8 \pm 1.4$	$4.51 \pm 0.51 \pm 0.57$
$0.14 - 0.16$	$4.44 \pm 0.67 \pm 0.55$	$2.89 \pm 0.42 \pm 0.28$
$0.16 - 0.20$	$1.84 \pm 0.36 \pm 0.20$	$1.74 \pm 0.25 \pm 0.24$
$0.20 - 0.24$	$0.80 \pm 0.28 \pm 0.40$	$0.82 \pm 0.19 \pm 0.17$
$0.24 - 0.30$	$0.40 \pm 0.20 \pm 0.32$	$0.07 \pm 0.13 \pm 0.17$
$0.30 - 0.40$	$0.00 \pm 0.00 \pm 0.30$	$0.01 \pm 0.31 \pm 0.33$
$M_{\mathrm{L}}/\sqrt{s}$	$R'\,(M_{\mathrm{L}}/\sqrt{s})$ at 200 GeV	$R'\,(M_{\mathrm{L}}/\sqrt{s})$ at 202 GeV
$0.00 - 0.04$	$0.397 \pm 0.078 \pm 0.080$	$0.25 \pm 0.11 \pm 0.10$
$0.04 - 0.06$	$4.70 \pm 0.40 \pm 0.59$	$4.82 \pm 0.60 \pm 0.78$
$0.06 - 0.08$	$12.6 \pm 0.7 \pm 1.5$	$11.24 \pm 0.99 \pm 0.41$
$0.08 - 0.10$	$11.26 \pm 0.75 \pm 1.00$	$9.9 \pm 1.0 \pm 1.8$
$0.10 - 0.12$	$8.35 \pm 0.63 \pm 0.99$	$8.5 \pm 0.9 \pm 2.1$
$0.12 - 0.14$	$4.36 \pm 0.49 \pm 0.52$	$4.8 \pm 0.7 \pm 1.2$
$0.14 - 0.16$	$2.22 \pm 0.43 \pm 0.62$	$4.14 \pm 0.61 \pm 0.64$
$0.16 - 0.20$	$1.99 \pm 0.24 \pm 0.27$	$1.82 \pm 0.35 \pm 0.46$
$0.20 - 0.24$	$0.92 \pm 0.19 \pm 0.46$	$0.99 \pm 0.31 \pm 0.45$
$0.24 - 0.30$	$0.29 \pm 0.16 \pm 0.27$	$0.31 \pm 0.23 \pm 0.37$
$0.30 - 0.40$	$-0.19 \pm 0.18 \pm 0.50$	$-0.08 \pm 0.12 \pm 0.22$
$M_{\mathrm{L}}/\sqrt{s}$	$R'\,(M_{\mathrm{L}}/\sqrt{s})$ at 205 GeV	$R'\,(M_{\mathrm{L}}/\sqrt{s})$ at 207 GeV
$0.00 - 0.04$	$0.490 \pm 0.083 \pm 0.057$	$0.539 \pm 0.064 \pm 0.047$
$0.04 - 0.06$	$4.73 \pm 0.44 \pm 0.55$	$4.52 \pm 0.33 \pm 0.66$
$0.06 - 0.08$	$11.90 \pm 0.79 \pm 0.66$	$12.02 \pm 0.58 \pm 0.72$
$0.08 - 0.10$	$12.1 \pm 0.8 \pm 1.9$	$11.63 \pm 0.60 \pm 0.60$
$0.10 - 0.12$	$6.61 \pm 0.67 \pm 0.56$	$7.56 \pm 0.49 \pm 0.66$
$0.12 - 0.14$	$4.09 \pm 0.50 \pm 0.40$	$5.21 \pm 0.39 \pm 0.43$
$0.14 - 0.16$	$3.21 \pm 0.44 \pm 0.21$	$2.52 \pm 0.33 \pm 0.52$
$0.16 - 0.20$	$1.70 \pm 0.25 \pm 0.23$	$1.51 \pm 0.19 \pm 0.26$
$0.20 - 0.24$	$0.99 \pm 0.20 \pm 0.45$	$0.66 \pm 0.16 \pm 0.22$
$0.24 - 0.30$	$0.34 \pm 0.18 \pm 0.23$	$0.35 \pm 0.13 \pm 0.36$
$0.30 - 0.40$	$-0.00 \pm 0.32 \pm 0.39$	$0.01 \pm 0.18 \pm 0.27$

Table B.24: Distributions for the light jet mass, M_{L}, measured by OPAL at centre-of-mass energies $\sqrt{s} = 192\text{--}207$ GeV. The first uncertainty is statistical, while the second is systematic.
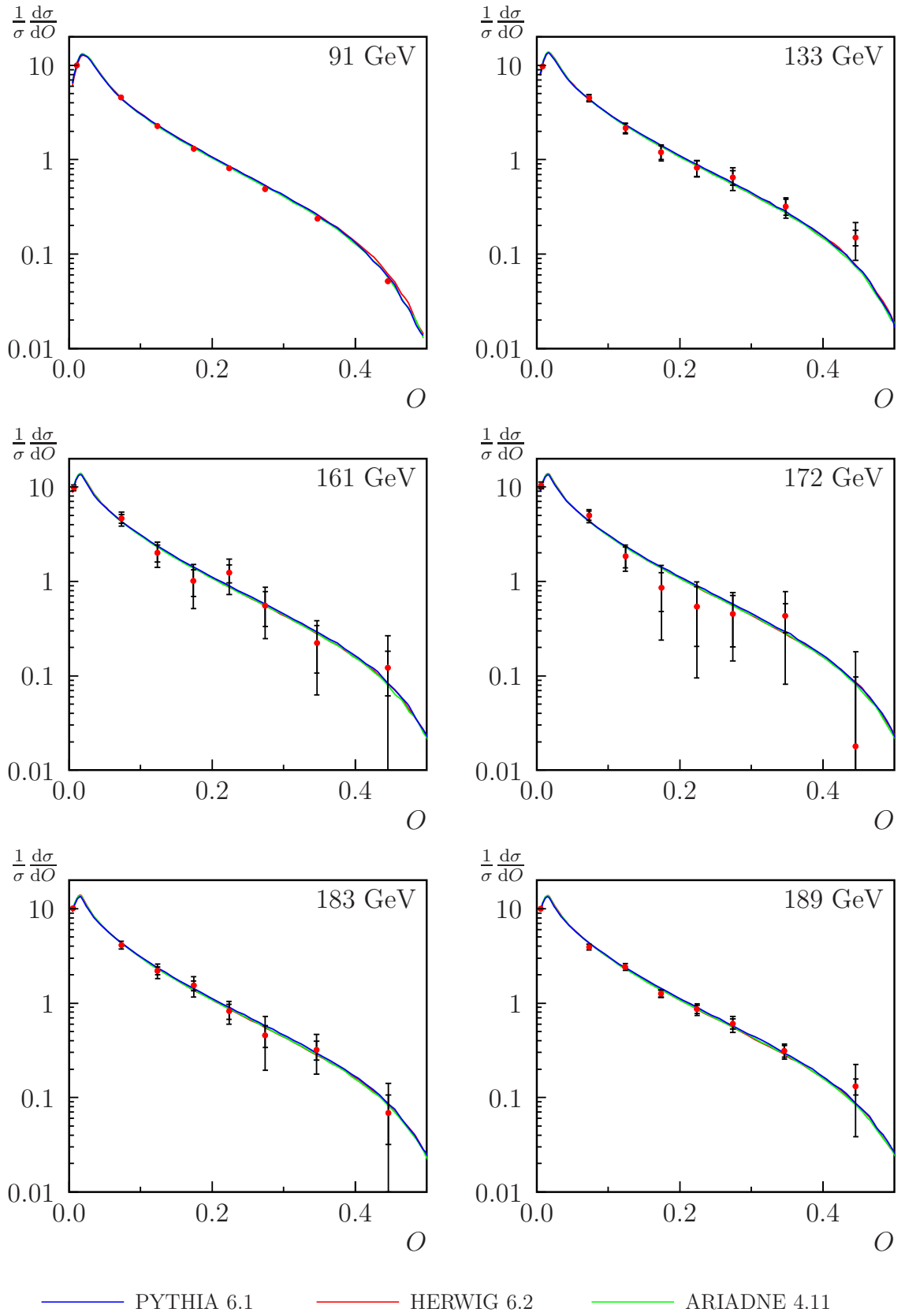
Figure B.24: Distributions for the light jet mass, M_{L}, measured by OPAL at centre-of-mass energies $\sqrt{s} = 192$–207 GeV. The inner error bars indicate statistical uncertainties. Each curve is generated using five million non-radiative Monte Carlo events, after hadronisation.

B.13   Narrow jet broadening, B_N

B_N	$R'(B_N)$ at 91 GeV			$R'(B_N)$ at 133 GeV		
$0.000 - 0.010$	0.693	$\pm$ 0.020	$\pm$ 0.081	1.83	$\pm$ 0.71	$\pm$ 1.00
$0.010 - 0.015$	8.00	$\pm$ 0.08	$\pm$ 0.23	30.0	$\pm$ 2.8	$\pm$ 1.6
$0.015 - 0.020$	21.56	$\pm$ 0.11	$\pm$ 0.35	37.7	$\pm$ 3.2	$\pm$ 4.9
$0.020 - 0.025$	32.43	$\pm$ 0.12	$\pm$ 0.46	34.1	$\pm$ 3.2	$\pm$ 6.9
$0.025 - 0.030$	33.64	$\pm$ 0.13	$\pm$ 0.70	26.3	$\pm$ 2.5	$\pm$ 3.7
$0.030 - 0.035$	28.37	$\pm$ 0.11	$\pm$ 0.17	15.6	$\pm$ 2.0	$\pm$ 1.0
$0.035 - 0.040$	19.99	$\pm$ 0.09	$\pm$ 0.29	10.3	$\pm$ 1.7	$\pm$ 1.2
$0.040 - 0.050$	11.48	$\pm$ 0.05	$\pm$ 0.42	8.2	$\pm$ 0.9	$\pm$ 2.4
$0.050 - 0.060$	6.052	$\pm$ 0.035	$\pm$ 0.088	4.15	$\pm$ 0.68	$\pm$ 0.85
$0.060 - 0.080$	2.914	$\pm$ 0.017	$\pm$ 0.040	2.81	$\pm$ 0.35	$\pm$ 0.23
$0.080 - 0.120$	0.836	$\pm$ 0.006	$\pm$ 0.015	0.68	$\pm$ 0.14	$\pm$ 0.12
$0.120 - 0.170$	0.1204	$\pm$ 0.0021	$\pm$ 0.0042	0.094	$\pm$ 0.042	$\pm$ 0.035

B_N	$R'(B_N)$ at 161 GeV			$R'(B_N)$ at 172 GeV		
$0.000 - 0.010$	3.0	$\pm$ 1.5	$\pm$ 1.9	5.5	$\pm$ 1.7	$\pm$ 0.8
$0.010 - 0.015$	38.3	$\pm$ 5.1	$\pm$ 2.3	36.2	$\pm$ 5.6	$\pm$ 7.9
$0.015 - 0.020$	52.3	$\pm$ 5.3	$\pm$ 5.1	51.9	$\pm$ 6.0	$\pm$ 4.8
$0.020 - 0.025$	32.6	$\pm$ 4.6	$\pm$ 3.0	25.0	$\pm$ 4.8	$\pm$ 7.1
$0.025 - 0.030$	15.1	$\pm$ 3.6	$\pm$ 1.7	22.9	$\pm$ 3.9	$\pm$ 4.4
$0.030 - 0.035$	12.3	$\pm$ 2.8	$\pm$ 2.0	9.3	$\pm$ 3.1	$\pm$ 2.9
$0.035 - 0.040$	10.1	$\pm$ 2.4	$\pm$ 5.5	6.3	$\pm$ 2.6	$\pm$ 1.8
$0.040 - 0.050$	6.3	$\pm$ 1.4	$\pm$ 1.9	7.7	$\pm$ 1.6	$\pm$ 2.1
$0.050 - 0.060$	2.9	$\pm$ 1.1	$\pm$ 1.1	3.4	$\pm$ 1.2	$\pm$ 1.6
$0.060 - 0.080$	1.61	$\pm$ 0.60	$\pm$ 0.67	2.70	$\pm$ 0.80	$\pm$ 0.81
$0.080 - 0.120$	1.09	$\pm$ 0.33	$\pm$ 0.54	-0.10	$\pm$ 0.50	$\pm$ 0.61
$0.120 - 0.170$	-0.02	$\pm$ 0.20	$\pm$ 0.03	0.54	$\pm$ 0.34	$\pm$ 0.85

B_N	$R'(B_N)$ at 183 GeV			$R'(B_N)$ at 189 GeV		
$0.000 - 0.010$	5.1	$\pm$ 0.9	$\pm$ 1.1	5.77	$\pm$ 0.53	$\pm$ 0.87
$0.010 - 0.015$	38.8	$\pm$ 2.8	$\pm$ 2.3	39.9	$\pm$ 1.8	$\pm$ 2.9
$0.015 - 0.020$	50.4	$\pm$ 2.8	$\pm$ 2.8	47.6	$\pm$ 1.7	$\pm$ 3.4
$0.020 - 0.025$	30.2	$\pm$ 2.1	$\pm$ 3.5	28.4	$\pm$ 1.3	$\pm$ 2.0
$0.025 - 0.030$	20.0	$\pm$ 1.7	$\pm$ 1.8	17.70	$\pm$ 1.00	$\pm$ 0.90
$0.030 - 0.035$	11.7	$\pm$ 1.4	$\pm$ 1.7	14.3	$\pm$ 0.8	$\pm$ 2.0
$0.035 - 0.040$	8.0	$\pm$ 1.2	$\pm$ 1.2	8.92	$\pm$ 0.70	$\pm$ 0.88
$0.040 - 0.050$	6.80	$\pm$ 0.71	$\pm$ 0.48	5.74	$\pm$ 0.44	$\pm$ 0.51
$0.050 - 0.060$	3.29	$\pm$ 0.60	$\pm$ 0.85	3.44	$\pm$ 0.38	$\pm$ 0.70
$0.060 - 0.080$	1.74	$\pm$ 0.40	$\pm$ 0.57	1.52	$\pm$ 0.22	$\pm$ 0.15
$0.080 - 0.120$	0.46	$\pm$ 0.23	$\pm$ 0.42	0.73	$\pm$ 0.17	$\pm$ 0.25
$0.120 - 0.170$	-0.01	$\pm$ 0.20	$\pm$ 0.34	0.14	$\pm$ 0.26	$\pm$ 0.42

Table B.25: Distributions for the narrow jet broadening, B_N, measured by OPAL at centre-of-mass energies $\sqrt{s}$ = 91–189 GeV. The first uncertainty is statistical, while the second is systematic.

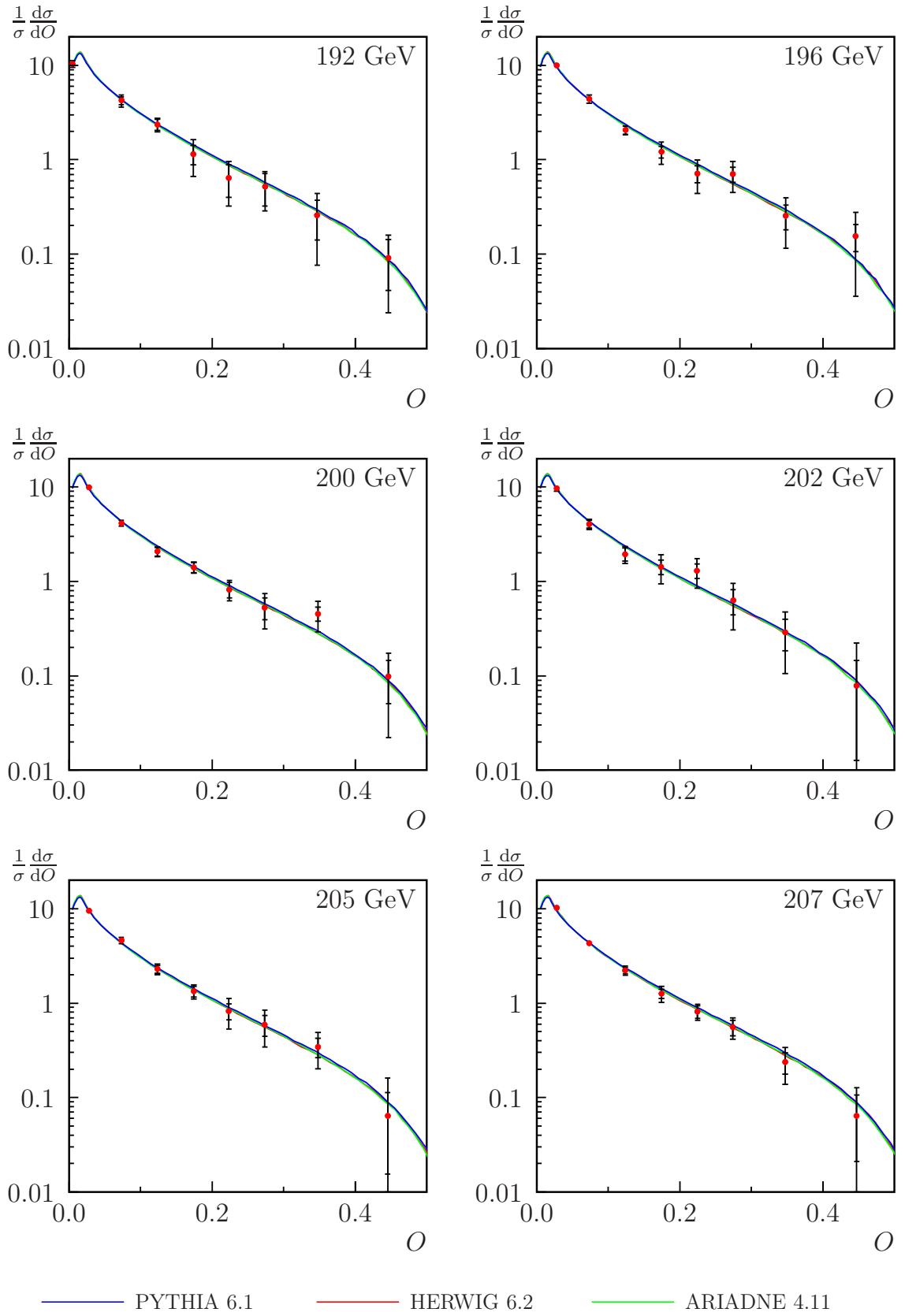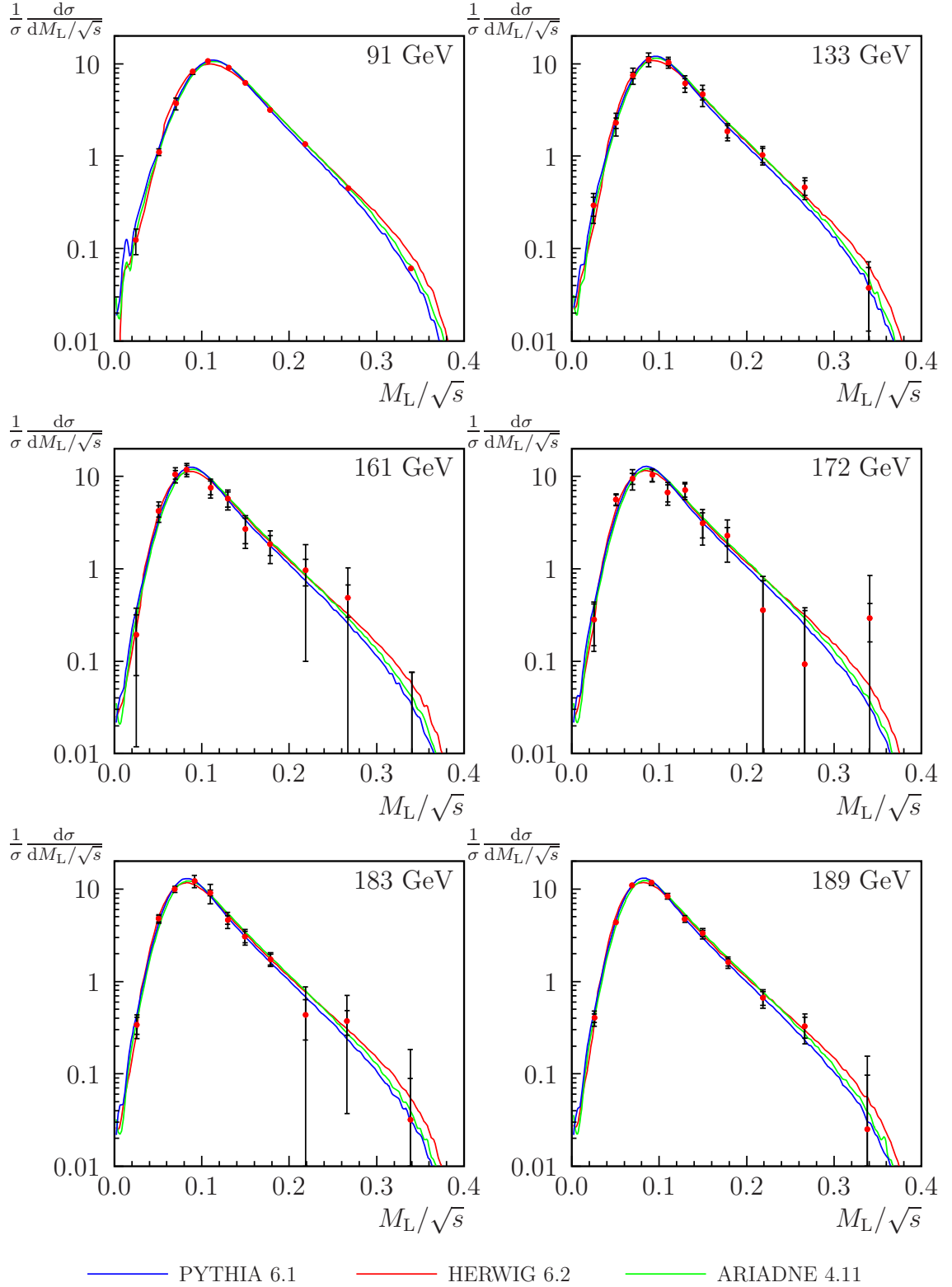Figure B.25: Distributions for the narrow jet broadening, B_N, measured by OPAL at centre-of-mass energies $\sqrt{s} = 91$–189 GeV. The inner error bars indicate statistical uncertainties. Each curve is generated using five million non-radiative Monte Carlo events, after hadronisation.

Narrow jet broadening, B_N (contd.)

B_N	$R'(B_N)$ at 192 GeV	$R'(B_N)$ at 196 GeV
$0.000 - 0.010$	$4.6 \pm 1.5 \pm 0.9$	$6.3 \pm 1.0 \pm 1.8$
$0.010 - 0.015$	$35.2 \pm 4.8 \pm 4.8$	$41.6 \pm 3.7 \pm 8.7$
$0.015 - 0.020$	$36.5 \pm 4.6 \pm 6.4$	$45.8 \pm 3.6 \pm 9.8$
$0.020 - 0.025$	$26.5 \pm 3.4 \pm 3.8$	$29.6 \pm 2.5 \pm 7.6$
$0.025 - 0.030$	$20.2 \pm 2.7 \pm 2.8$	$16.1 \pm 1.8 \pm 3.9$
$0.030 - 0.035$	$15.1 \pm 2.0 \pm 2.7$	$11.5 \pm 1.5 \pm 2.3$
$0.035 - 0.040$	$9.9 \pm 1.8 \pm 2.2$	$6.8 \pm 1.2 \pm 1.2$
$0.040 - 0.050$	$6.1 \pm 1.1 \pm 1.7$	$4.80 \pm 0.77 \pm 0.91$
$0.050 - 0.060$	$3.4 \pm 1.0 \pm 0.9$	$4.3 \pm 0.7 \pm 1.1$
$0.060 - 0.080$	$2.40 \pm 0.60 \pm 0.88$	$1.36 \pm 0.40 \pm 0.61$
$0.080 - 0.120$	$1.06 \pm 0.44 \pm 0.60$	$0.72 \pm 0.28 \pm 0.49$
$0.120 - 0.170$	$1.0 \pm 0.9 \pm 1.5$	$0.7 \pm 1.1 \pm 3.3$

B_N	$R'(B_N)$ at 200 GeV	$R'(B_N)$ at 202 GeV
$0.000 - 0.010$	$5.61 \pm 0.95 \pm 0.50$	$5.1 \pm 1.4 \pm 0.5$
$0.010 - 0.015$	$49.7 \pm 3.1 \pm 2.4$	$42.0 \pm 4.6 \pm 7.0$
$0.015 - 0.020$	$45.7 \pm 2.9 \pm 4.4$	$37.3 \pm 4.2 \pm 3.7$
$0.020 - 0.025$	$26.4 \pm 2.1 \pm 2.5$	$26.9 \pm 3.0 \pm 2.7$
$0.025 - 0.030$	$16.0 \pm 1.6 \pm 1.9$	$16.3 \pm 2.4 \pm 1.4$
$0.030 - 0.035$	$12.7 \pm 1.4 \pm 2.0$	$9.9 \pm 1.9 \pm 1.6$
$0.035 - 0.040$	$8.8 \pm 1.2 \pm 1.9$	$10.8 \pm 1.8 \pm 2.1$
$0.040 - 0.050$	$4.35 \pm 0.73 \pm 1.00$	$9.0 \pm 1.1 \pm 1.5$
$0.050 - 0.060$	$4.6 \pm 0.6 \pm 1.3$	$2.45 \pm 0.87 \pm 0.54$
$0.060 - 0.080$	$2.06 \pm 0.38 \pm 0.94$	$1.41 \pm 0.62 \pm 0.74$
$0.080 - 0.120$	$0.53 \pm 0.30 \pm 0.37$	$0.79 \pm 0.44 \pm 0.34$
$0.120 - 0.170$	$-0.08 \pm 0.51 \pm 0.59$	$1.2 \pm 0.7 \pm 1.2$

B_N	$R'(B_N)$ at 205 GeV	$R'(B_N)$ at 207 GeV
$0.000 - 0.010$	$8.7 \pm 1.2 \pm 1.0$	$7.16 \pm 0.95 \pm 0.84$
$0.010 - 0.015$	$42.0 \pm 4.1 \pm 4.5$	$44.7 \pm 3.7 \pm 3.3$
$0.015 - 0.020$	$42.8 \pm 3.8 \pm 4.0$	$45.8 \pm 3.4 \pm 3.6$
$0.020 - 0.025$	$26.0 \pm 2.6 \pm 2.8$	$27.9 \pm 2.2 \pm 2.3$
$0.025 - 0.030$	$15.3 \pm 1.9 \pm 3.4$	$14.9 \pm 1.6 \pm 2.0$
$0.030 - 0.035$	$12.8 \pm 1.6 \pm 2.2$	$12.4 \pm 1.2 \pm 1.7$
$0.035 - 0.040$	$6.9 \pm 1.3 \pm 2.5$	$8.2 \pm 1.0 \pm 1.1$
$0.040 - 0.050$	$5.9 \pm 0.8 \pm 1.2$	$4.87 \pm 0.65 \pm 0.87$
$0.050 - 0.060$	$3.62 \pm 0.66 \pm 0.87$	$4.32 \pm 0.53 \pm 0.47$
$0.060 - 0.080$	$1.72 \pm 0.43 \pm 0.71$	$1.19 \pm 0.34 \pm 0.35$
$0.080 - 0.120$	$0.85 \pm 0.34 \pm 0.76$	$0.64 \pm 0.26 \pm 0.41$
$0.120 - 0.170$	$0.4 \pm 1.2 \pm 1.6$	$0.3 \pm 1.2 \pm 0.8$

Table B.26: Distributions for the narrow jet broadening, B_N, measured by OPAL at centre-of-mass energies $\sqrt{s} = 192$–207 GeV. The first uncertainty is statistical, while the second is systematic.
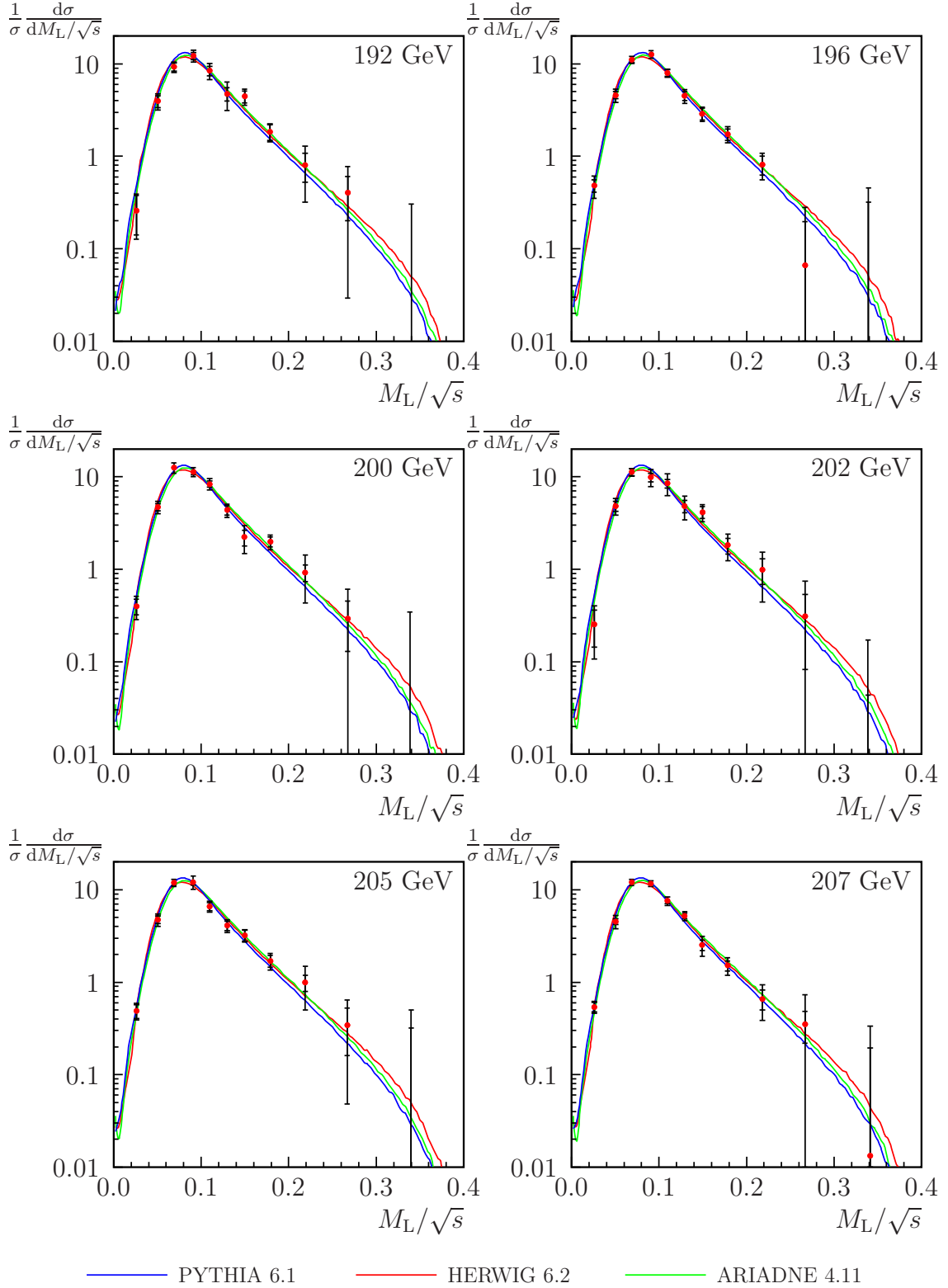
Figure B.26: Distributions for the narrow jet broadening, B_N, measured by OPAL at centre-of-mass energies $\sqrt{s} = 192$–207 GeV. The inner error bars indicate statistical uncertainties. Each curve is generated using five million non-radiative Monte Carlo events, after hadronisation.

B.14   *D*-parameter

D	$R'(D)$ at 91 GeV			$R'(D)$ at 133 GeV		
$0.001 - 0.005$	23.1	$\pm$ 0.1	$\pm$ 1.1	43.9	$\pm$ 3.9	$\pm$ 7.9
$0.005 - 0.010$	29.70	$\pm$ 0.12	$\pm$ 0.38	40.9	$\pm$ 2.9	$\pm$ 3.0
$0.010 - 0.015$	21.72	$\pm$ 0.10	$\pm$ 0.20	20.2	$\pm$ 2.2	$\pm$ 1.3
$0.015 - 0.020$	15.64	$\pm$ 0.09	$\pm$ 0.38	10.5	$\pm$ 1.9	$\pm$ 2.4
$0.020 - 0.030$	10.83	$\pm$ 0.05	$\pm$ 0.12	8.4	$\pm$ 1.1	$\pm$ 1.1
$0.030 - 0.045$	6.64	$\pm$ 0.03	$\pm$ 0.11	4.37	$\pm$ 0.72	$\pm$ 0.93
$0.045 - 0.070$	4.036	$\pm$ 0.019	$\pm$ 0.030	3.31	$\pm$ 0.43	$\pm$ 0.26
$0.070 - 0.100$	2.406	$\pm$ 0.014	$\pm$ 0.040	2.24	$\pm$ 0.30	$\pm$ 0.32
$0.100 - 0.150$	1.424	$\pm$ 0.008	$\pm$ 0.027	1.06	$\pm$ 0.17	$\pm$ 0.19
$0.150 - 0.250$	0.672	$\pm$ 0.004	$\pm$ 0.023	0.66	$\pm$ 0.08	$\pm$ 0.12
$0.250 - 0.500$	0.1660	$\pm$ 0.0012	$\pm$ 0.0020	0.122	$\pm$ 0.022	$\pm$ 0.024
$0.500 - 1.000$	0.0142	$\pm$ 0.0002	$\pm$ 0.0006	0.0042	$\pm$ 0.0036	$\pm$ 0.0020

D	$R'(D)$ at 161 GeV			$R'(D)$ at 172 GeV		
$0.001 - 0.005$	67.9	$\pm$ 6.7	$\pm$ 5.2	64.	$\pm$ 7.	$\pm$ 12.
$0.005 - 0.010$	32.2	$\pm$ 4.3	$\pm$ 2.6	34.0	$\pm$ 4.8	$\pm$ 4.7
$0.010 - 0.015$	12.9	$\pm$ 3.3	$\pm$ 5.2	14.8	$\pm$ 3.7	$\pm$ 2.5
$0.015 - 0.020$	13.4	$\pm$ 2.9	$\pm$ 6.3	5.6	$\pm$ 3.1	$\pm$ 3.8
$0.020 - 0.030$	6.5	$\pm$ 1.7	$\pm$ 3.2	6.7	$\pm$ 1.9	$\pm$ 1.5
$0.030 - 0.045$	6.0	$\pm$ 1.1	$\pm$ 0.7	6.6	$\pm$ 1.2	$\pm$ 2.3
$0.045 - 0.070$	1.97	$\pm$ 0.64	$\pm$ 0.49	3.3	$\pm$ 0.8	$\pm$ 1.7
$0.070 - 0.100$	1.24	$\pm$ 0.46	$\pm$ 0.54	1.12	$\pm$ 0.55	$\pm$ 0.25
$0.100 - 0.150$	1.64	$\pm$ 0.27	$\pm$ 0.33	0.76	$\pm$ 0.33	$\pm$ 0.32
$0.150 - 0.250$	0.41	$\pm$ 0.14	$\pm$ 0.20	0.30	$\pm$ 0.17	$\pm$ 0.21
$0.250 - 0.500$	0.117	$\pm$ 0.061	$\pm$ 0.072	0.161	$\pm$ 0.069	$\pm$ 0.071
$0.500 - 1.000$	-0.002	$\pm$ 0.020	$\pm$ 0.001	0.08	$\pm$ 0.04	$\pm$ 0.21

D	$R'(D)$ at 183 GeV			$R'(D)$ at 189 GeV		
$0.001 - 0.005$	61.7	$\pm$ 3.7	$\pm$ 4.8	59.6	$\pm$ 2.2	$\pm$ 2.0
$0.005 - 0.010$	27.7	$\pm$ 2.2	$\pm$ 3.0	31.1	$\pm$ 1.3	$\pm$ 1.3
$0.010 - 0.015$	19.1	$\pm$ 1.8	$\pm$ 3.4	17.5	$\pm$ 1.0	$\pm$ 0.5
$0.015 - 0.020$	8.6	$\pm$ 1.4	$\pm$ 3.3	13.15	$\pm$ 0.86	$\pm$ 0.94
$0.020 - 0.030$	8.71	$\pm$ 0.85	$\pm$ 0.59	7.90	$\pm$ 0.50	$\pm$ 0.85
$0.030 - 0.045$	5.39	$\pm$ 0.55	$\pm$ 0.53	5.51	$\pm$ 0.33	$\pm$ 0.27
$0.045 - 0.070$	2.93	$\pm$ 0.34	$\pm$ 0.26	2.86	$\pm$ 0.20	$\pm$ 0.09
$0.070 - 0.100$	1.42	$\pm$ 0.25	$\pm$ 0.26	1.86	$\pm$ 0.15	$\pm$ 0.20
$0.100 - 0.150$	1.27	$\pm$ 0.16	$\pm$ 0.22	1.05	$\pm$ 0.09	$\pm$ 0.11
$0.150 - 0.250$	0.35	$\pm$ 0.09	$\pm$ 0.14	0.399	$\pm$ 0.052	$\pm$ 0.079
$0.250 - 0.500$	0.133	$\pm$ 0.045	$\pm$ 0.069	0.068	$\pm$ 0.028	$\pm$ 0.046
$0.500 - 1.000$	0.042	$\pm$ 0.027	$\pm$ 0.050	0.019	$\pm$ 0.018	$\pm$ 0.020

Table B.27: Distributions for the *D*-parameter, measured by OPAL at centre-of-mass energies $\sqrt{s}$ = 91–189 GeV. The first uncertainty is statistical, while the second is systematic.

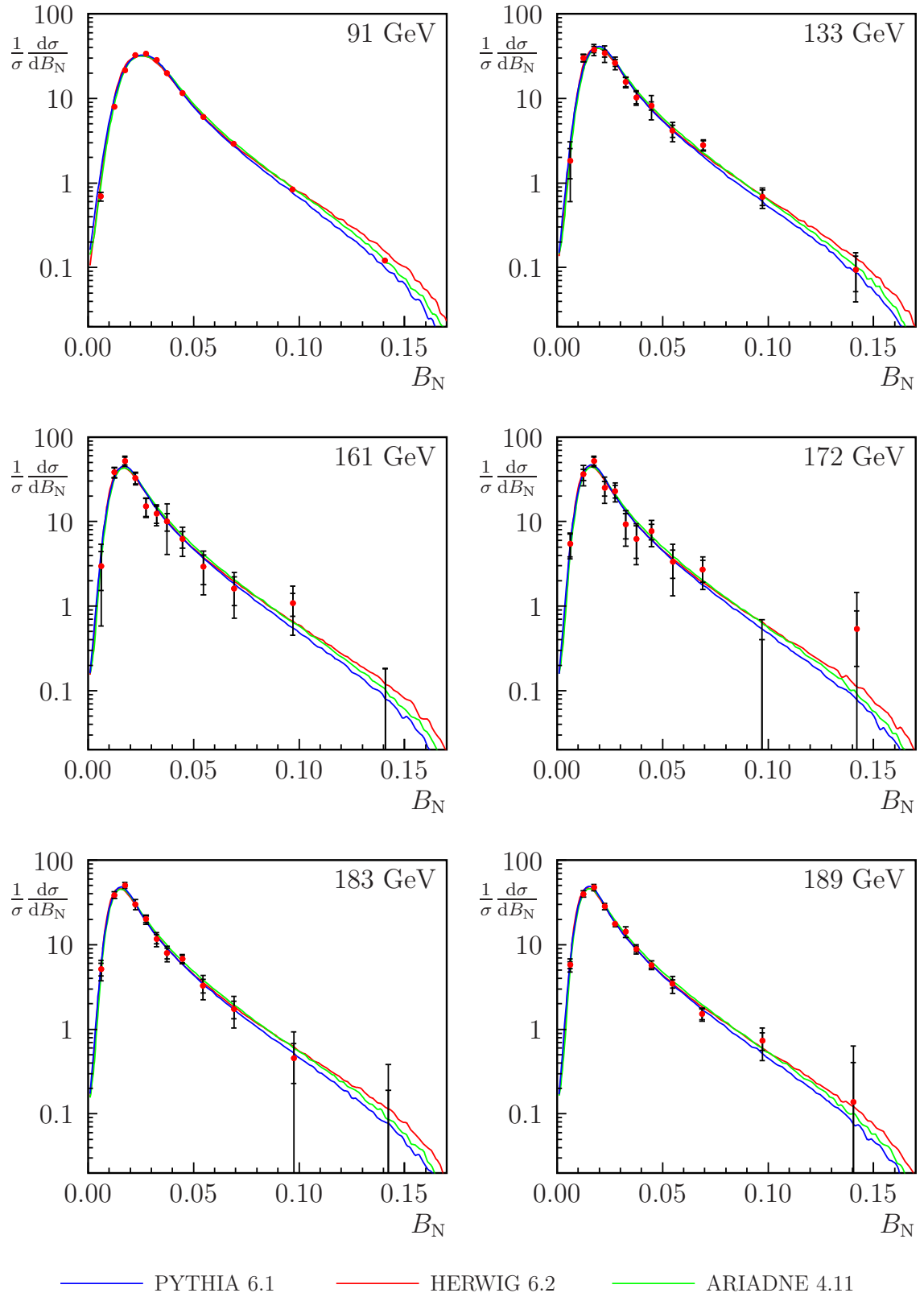Figure B.27: Distributions for the D-parameter, measured by OPAL at centre-of-mass energies $\sqrt{s} = 91$–189 GeV. The inner error bars indicate statistical uncertainties. Each curve is generated using five million non-radiative Monte Carlo events, after hadronisation.

D-parameter (contd.)

D	$R'(D)$ at 192 GeV			$R'(D)$ at 196 GeV		
$0.001 - 0.005$	55.5	± 5.7	± 9.2	62.1	± 3.6	± 2.5
$0.005 - 0.010$	25.4	± 3.4	± 3.8	29.5	± 2.1	± 4.9
$0.010 - 0.015$	15.1	± 2.5	± 4.0	17.3	± 1.7	± 1.8
$0.015 - 0.020$	9.1	± 2.3	± 3.7	11.6	± 1.4	± 1.8
$0.020 - 0.030$	8.3	± 1.3	± 1.2	7.59	± 0.83	± 0.33
$0.030 - 0.045$	5.00	± 0.86	± 0.77	4.98	± 0.54	± 0.61
$0.045 - 0.070$	2.90	± 0.52	± 0.51	3.11	± 0.33	± 0.42
$0.070 - 0.100$	1.48	± 0.36	± 0.42	1.99	± 0.24	± 0.34
$0.100 - 0.150$	0.67	± 0.25	± 0.15	1.18	± 0.16	± 0.19
$0.150 - 0.250$	0.49	± 0.13	± 0.17	0.42	± 0.09	± 0.15
$0.250 - 0.500$	0.34	± 0.10	± 0.25	0.123	± 0.061	± 0.088
$0.500 - 1.000$	0.09	± 0.05	± 0.12	-0.012	± 0.019	± 0.028

D	$R'(D)$ at 200 GeV			$R'(D)$ at 202 GeV		
$0.001 - 0.005$	65.0	± 3.8	± 3.4	63.5	± 5.4	± 7.6
$0.005 - 0.010$	26.2	± 2.2	± 3.7	23.8	± 3.2	± 2.3
$0.010 - 0.015$	15.5	± 1.7	± 2.7	16.7	± 2.4	± 1.5
$0.015 - 0.020$	14.4	± 1.4	± 1.8	8.3	± 2.1	± 2.7
$0.020 - 0.030$	7.69	± 0.85	± 0.66	7.1	± 1.2	± 1.0
$0.030 - 0.045$	5.28	± 0.55	± 0.81	6.3	± 0.8	± 1.4
$0.045 - 0.070$	3.18	± 0.34	± 0.46	3.26	± 0.50	± 0.49
$0.070 - 0.100$	1.71	± 0.26	± 0.27	2.19	± 0.36	± 0.64
$0.100 - 0.150$	0.74	± 0.15	± 0.13	1.12	± 0.23	± 0.30
$0.150 - 0.250$	0.72	± 0.09	± 0.17	0.60	± 0.14	± 0.22
$0.250 - 0.500$	0.144	± 0.064	± 0.078	0.059	± 0.088	± 0.096
$0.500 - 1.000$	-0.029	± 0.038	± 0.064	0.02	± 0.02	± 0.24

D	$R'(D)$ at 205 GeV			$R'(D)$ at 207 GeV		
$0.001 - 0.005$	59.3	± 3.9	± 4.2	64.3	± 3.2	± 2.7
$0.005 - 0.010$	27.2	± 2.3	± 3.4	27.1	± 1.8	± 1.6
$0.010 - 0.015$	19.0	± 1.7	± 1.6	14.4	± 1.4	± 1.1
$0.015 - 0.020$	9.9	± 1.5	± 2.5	12.9	± 1.2	± 0.8
$0.020 - 0.030$	8.4	± 0.9	± 1.3	8.30	± 0.67	± 0.70
$0.030 - 0.045$	5.40	± 0.55	± 0.64	4.87	± 0.44	± 0.35
$0.045 - 0.070$	3.14	± 0.35	± 0.56	2.98	± 0.26	± 0.29
$0.070 - 0.100$	1.38	± 0.25	± 0.48	1.65	± 0.20	± 0.17
$0.100 - 0.150$	0.77	± 0.16	± 0.13	0.78	± 0.13	± 0.13
$0.150 - 0.250$	0.31	± 0.10	± 0.14	0.40	± 0.08	± 0.10
$0.250 - 0.500$	0.21	± 0.06	± 0.24	0.10	± 0.05	± 0.12
$0.500 - 1.000$	0.035	± 0.040	± 0.035	0.045	± 0.044	± 0.053

Table B.28: Distributions for the D-parameter, measured by OPAL at centre-of-mass energies $\sqrt{s} = 192$–207 GeV. The first uncertainty is statistical, while the second is systematic.
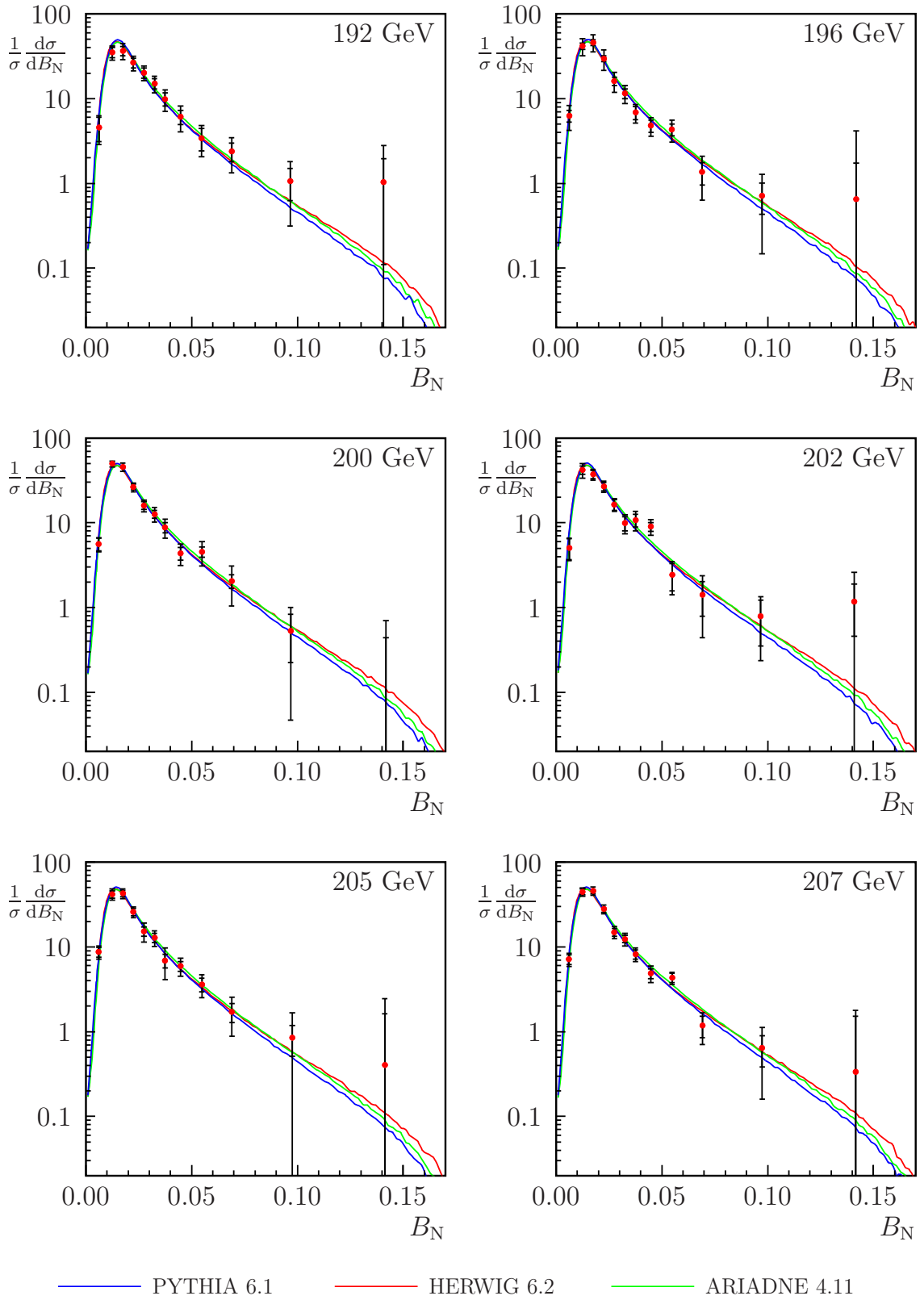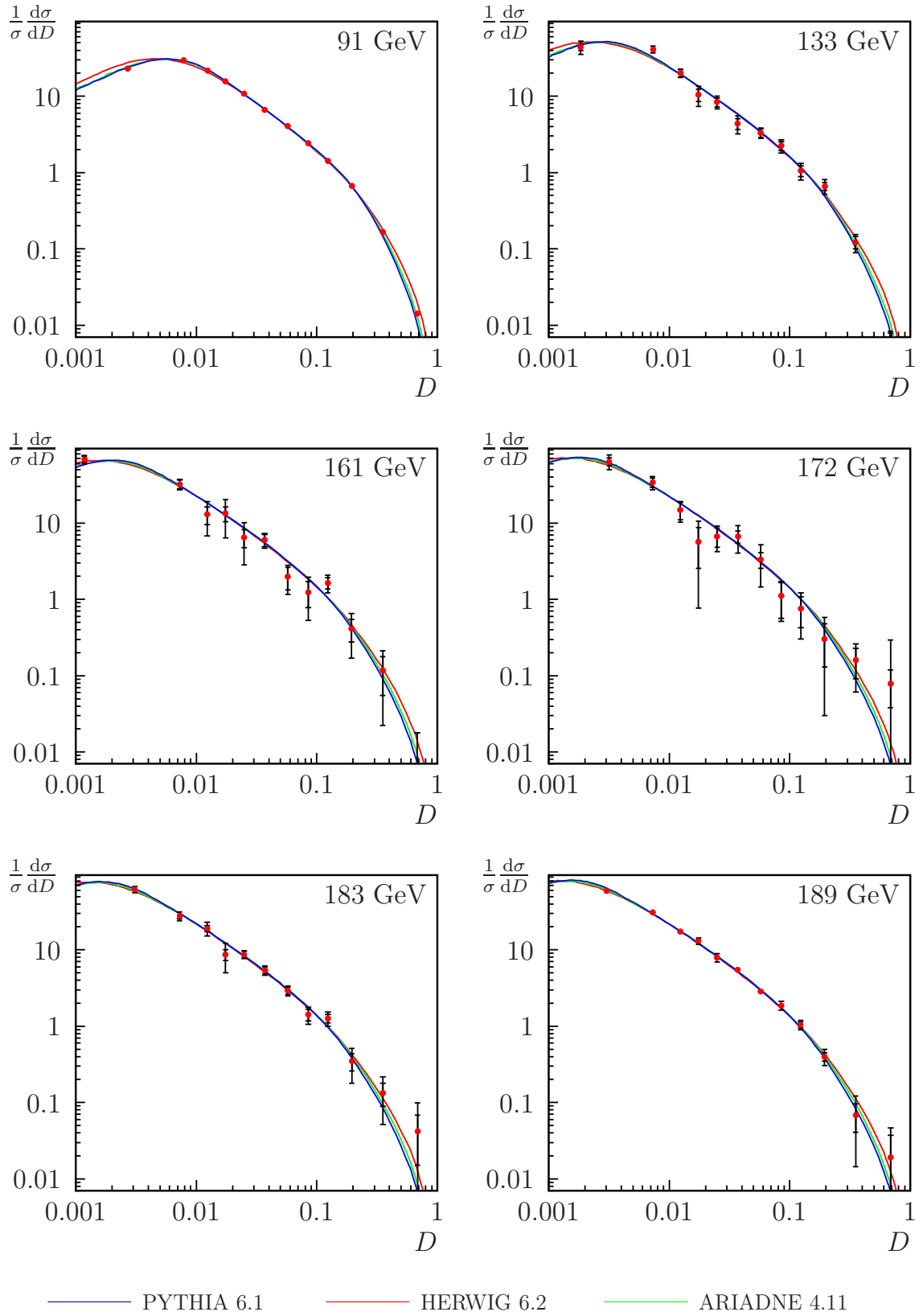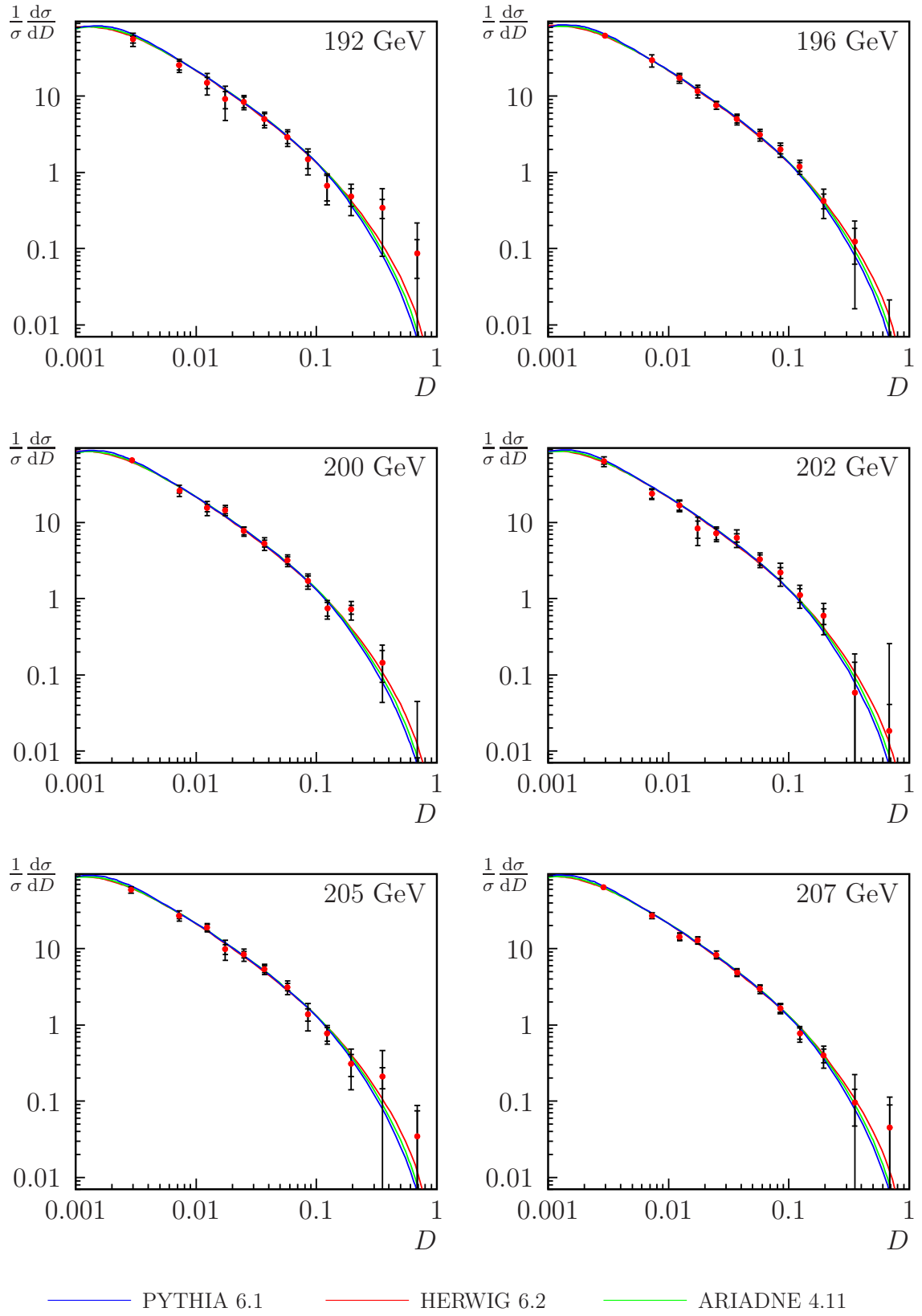
Figure B.28: Distributions for the D-parameter, measured by OPAL at centre-of-mass energies $\sqrt{s} = 192$–207 GeV. The inner error bars indicate statistical uncertainties. Each curve is generated using five million non-radiative Monte Carlo events, after hadronisation.

Appendix C

Fits to the OPAL event shape measurements

We present here the measurements of $\alpha_S(Q)$ derived from OPAL event shape measurements at each energy scale, as discussed in Chapter 3.

In each of Tables C.1–C.12, we list the α_S values obtained from the thrust (T), the heavy jet mass (M_H), the C-parameter, the total jet broadening (B_T), the wide jet broadening (B_W) and the Durham y_{23} parameter. A weighted mean of the six α_S values at each energy is also given; the weights, which are listed under each observable, are determined as outlined in Section 3.6.1.

For each observable, and for the weighted mean, we give a full breakdown of the uncertainties in α_S. The experimental systematic uncertainty is given by the quadratic sum of the contributions labelled with asterisks (*); these sources are described in Section 3.4.4. The hadronisation uncertainty is the larger of the two absolute deviations in our fitted α_S when HERWIG and ARIADNE are used in place of PYTHIA, to apply hadronisation corrections to the predicted distribution; this deviation is also marked with an asterisk. We take our theory uncertainty as the mean of the upper and lower absolute deviations given by the "uncertainty band method," which is outlined in Section 1.8 and described fully in Ref. [12].

Figures C.1–C.12 compare our measured distributions with the fitted hadron-level predictions. Each data point shows the measured bin contents divided by the integral of the predicted distribution across the bin; the inner error bars indicate statistical uncertainties, and the outer bars show the combined statistical and experimental contributions. The blue dashed curves represent fractional variations in

the predicted distributions, corresponding to our perturbative theory uncertainties in α_S. The slightly wider yellow bands indicate the combined theory and hadronisation uncertainties. The ranges used for fitting each distribution are shown by horizontal arrows. Note that the range of the vertical scale in the 91 GeV plots (Figure C.1) is different from that used at higher energies.

C.1   OPAL measurements of α_S at $\sqrt{s} = 91$ GeV

	T	M_H	C
$\alpha_S(91\text{ GeV})$	0.1231	0.1192	0.1178
Statistical error	± 0.0002	± 0.0002	± 0.0002
No MT algorithm	$+0.0002^*$	$+0.0003^*$	$+0.0003^*$
HERWIG det. corr.	-0.0010^*	-0.0001^*	-0.0007^*
$\cos(\theta_T) < 0.7$	-0.0002^*	-0.0002^*	0.0000^*
Experimental syst.	± 0.0011	± 0.0004	± 0.0007
HERWIG hadr. corr.	-0.0018	$+0.0013$	-0.0030^*
ARIADNE hadr. corr.	$+0.0031^*$	$+0.0021^*$	$+0.0029$
Hadronisation error	± 0.0031	± 0.0021	± 0.0030
Upper uncertainty band	$+0.0056$	$+0.0044$	$+0.0057$
Lower uncertainty band	-0.0055	-0.0044	-0.0054
Theory error	± 0.0055	± 0.0044	± 0.0056
Weight	0.12	0.20	0.10

	B_T	B_W	y_{23}	Weighted mean
$\alpha_S(91\text{ GeV})$	0.1224	0.1146	0.1197	0.1193
Statistical error	± 0.0002	± 0.0001	± 0.0001	± 0.0002
No MT algorithm	$+0.0002^*$	$+0.0001^*$	$+0.0001^*$	$+0.0002^*$
HERWIG det. corr.	-0.0007^*	-0.0011^*	-0.0010^*	-0.0008^*
$\cos(\theta_T) < 0.7$	$+0.0001^*$	0.0000^*	0.0000^*	0.0000^*
Experimental syst.	± 0.0007	± 0.0011	± 0.0010	± 0.0008
HERWIG hadr. corr.	-0.0022	-0.0014^*	-0.0024^*	-0.0015^*
ARIADNE hadr. corr.	$+0.0024^*$	$+0.0006$	-0.0008	$+0.0012$
Hadronisation error	± 0.0024	± 0.0014	± 0.0024	± 0.0015
Upper uncertainty band	$+0.0068$	$+0.0054$	$+0.0028$	$+0.0046$
Lower uncertainty band	-0.0062	-0.0054	-0.0030	-0.0045
Theory error	± 0.0065	± 0.0054	± 0.0029	± 0.0045
Weight	0.15	0.12	0.32	$-$

Table C.1: OPAL measurements of α_S at $\sqrt{s} = 91$ GeV

Figure C.1: Ratios of measured event shape distributions to hadron-level predictions, at $\sqrt{s} = 91$ GeV. An explanation is given in the introduction to this appendix, on page 283.

C.2   OPAL measurements of α_S at $\sqrt{s} = 133$ GeV

	T	M_H	C
$\alpha_\mathrm{S}(133\ \mathrm{GeV})$	0.1158	0.1088	0.1056
Statistical error	±0.0041	±0.0038	±0.0043
No MT algorithm	+0.0001*	−0.0001*	−0.0013*
HERWIG det. corr.	+0.0003*	−0.0004*	−0.0005*
$\cos(\theta_\mathrm{T}) < 0.7$	+0.0053*	+0.0024*	+0.0048*
Alternative $\sqrt{s'}$	+0.0010*	+0.0007*	+0.0016*
Experimental syst.	±0.0054	±0.0025	±0.0053
HERWIG hadr. corr.	−0.0005	+0.0020*	−0.0014
ARIADNE hadr. corr.	+0.0024*	+0.0018	+0.0025*
Hadronisation error	±0.0024	±0.0020	±0.0025
Upper uncertainty band	+0.0048	+0.0037	+0.0049
Lower uncertainty band	−0.0047	−0.0038	−0.0047
Theory error	±0.0047	±0.0037	±0.0048
Weight	0.12	0.24	0.08

	B_T	B_W	y_{23}	Weighted mean
$\alpha_\mathrm{S}(133\ \mathrm{GeV})$	0.1102	0.1051	0.1109	0.1093
Statistical error	±0.0039	±0.0032	±0.0031	±0.0032
No MT algorithm	+0.0005*	+0.0007*	+0.0004*	+0.0001*
HERWIG det. corr.	−0.0011*	−0.0003*	−0.0004*	−0.0004*
$\cos(\theta_\mathrm{T}) < 0.7$	+0.0060*	+0.0047*	+0.0046*	+0.0043*
Alternative $\sqrt{s'}$	+0.0012*	+0.0002*	+0.0006*	+0.0007*
Experimental syst.	±0.0063	±0.0047	±0.0047	±0.0044
HERWIG hadr. corr.	−0.0015	−0.0004	−0.0012*	−0.0002
ARIADNE hadr. corr.	+0.0020*	+0.0008*	−0.0005	+0.0012*
Hadronisation error	±0.0020	±0.0008	±0.0012	±0.0012
Upper uncertainty band	+0.0058	+0.0046	+0.0022	+0.0039
Lower uncertainty band	−0.0054	−0.0047	−0.0025	−0.0040
Theory error	±0.0056	±0.0047	±0.0024	±0.0039
Weight	0.17	0.12	0.26	−

Table C.2: OPAL measurements of α_S at $\sqrt{s} = 133$ GeV

Figure C.2: Ratios of measured event shape distributions to hadron-level predictions, at $\sqrt{s} = 133$ GeV. An explanation is given in the introduction to this appendix, on page 283.

C.3 OPAL measurements of α_S at $\sqrt{s} = 161$ GeV

	T	M_H	C
$\alpha_S(161\ \mathrm{GeV})$	0.1103	0.1064	0.1042
Statistical error	±0.0069	±0.0063	±0.0068
No MT algorithm	−0.0023*	−0.0001*	+0.0016*
HERWIG det. corr.	−0.0002*	−0.0001*	−0.0004*
$\cos(\theta_T) < 0.7$	−0.0004*	−0.0014*	+0.0002*
Alternative $\sqrt{s'}$	+0.0023*	+0.0020*	+0.0034*
$L_{qqqq} < 0.10$	−0.0011	−0.0005	+0.0012
$L_{qqqq} < 0.40$	−0.0025*	−0.0033*	−0.0041*
$L_{qq\ell\nu} < 0.25$	+0.0009*	+0.0008*	+0.0009*
$L_{qq\ell\nu} < 0.75$	+0.0002	+0.0001	+0.0001
Background +5%	−0.0001*	−0.0001*	−0.0001*
Background −5%	+0.0001	+0.0001	0.0000
Experimental syst.	±0.0042	±0.0042	±0.0056
HERWIG hadr. corr.	−0.0002	+0.0021*	−0.0009
ARIADNE hadr. corr.	+0.0022*	+0.0015	+0.0022*
Hadronisation error	±0.0022	±0.0021	±0.0022
Upper uncertainty band	+0.0044	+0.0034	+0.0045
Lower uncertainty band	−0.0043	−0.0035	−0.0044
Theory error	±0.0044	±0.0035	±0.0044
Weight	0.12	0.13	0.06

	B_T	B_W	y_{23}	Weighted mean
$\alpha_S(161\ \mathrm{GeV})$	0.1051	0.1010	0.1042	0.1046
Statistical error	±0.0062	±0.0053	±0.0051	±0.0051
No MT algorithm	+0.0020*	+0.0009*	+0.0008*	+0.0005*
HERWIG det. corr.	−0.0001*	+0.0003*	0.0000*	0.0000*
$\cos(\theta_T) < 0.7$	−0.0028*	−0.0002*	−0.0025*	−0.0017*
Alternative $\sqrt{s'}$	+0.0004*	+0.0020*	−0.0001*	+0.0014*
$L_{qqqq} < 0.10$	+0.0001	−0.0002	+0.0002	−0.0001
$L_{qqqq} < 0.40$	−0.0028*	−0.0026*	−0.0019*	−0.0024*
$L_{qq\ell\nu} < 0.25$	+0.0008*	+0.0006*	+0.0005*	+0.0007*
$L_{qq\ell\nu} < 0.75$	+0.0001	+0.0001	+0.0001	+0.0001
Background +5%	−0.0001*	−0.0001	−0.0001*	−0.0001*
Background −5%	+0.0001*	+0.0001*	0.0000	+0.0001
Experimental syst.	±0.0045	±0.0035	±0.0033	±0.0033
HERWIG hadr. corr.	−0.0013	−0.0002	−0.0009*	−0.0002
ARIADNE hadr. corr.	+0.0018*	+0.0007*	−0.0005	+0.0008*
Hadronisation error	±0.0018	±0.0007	±0.0009	±0.0008
Upper uncertainty band	+0.0054	+0.0042	+0.0021	+0.0034
Lower uncertainty band	−0.0051	−0.0044	−0.0024	−0.0035
Theory error	±0.0052	±0.0043	±0.0022	±0.0034
Weight	0.20	0.09	0.40	−

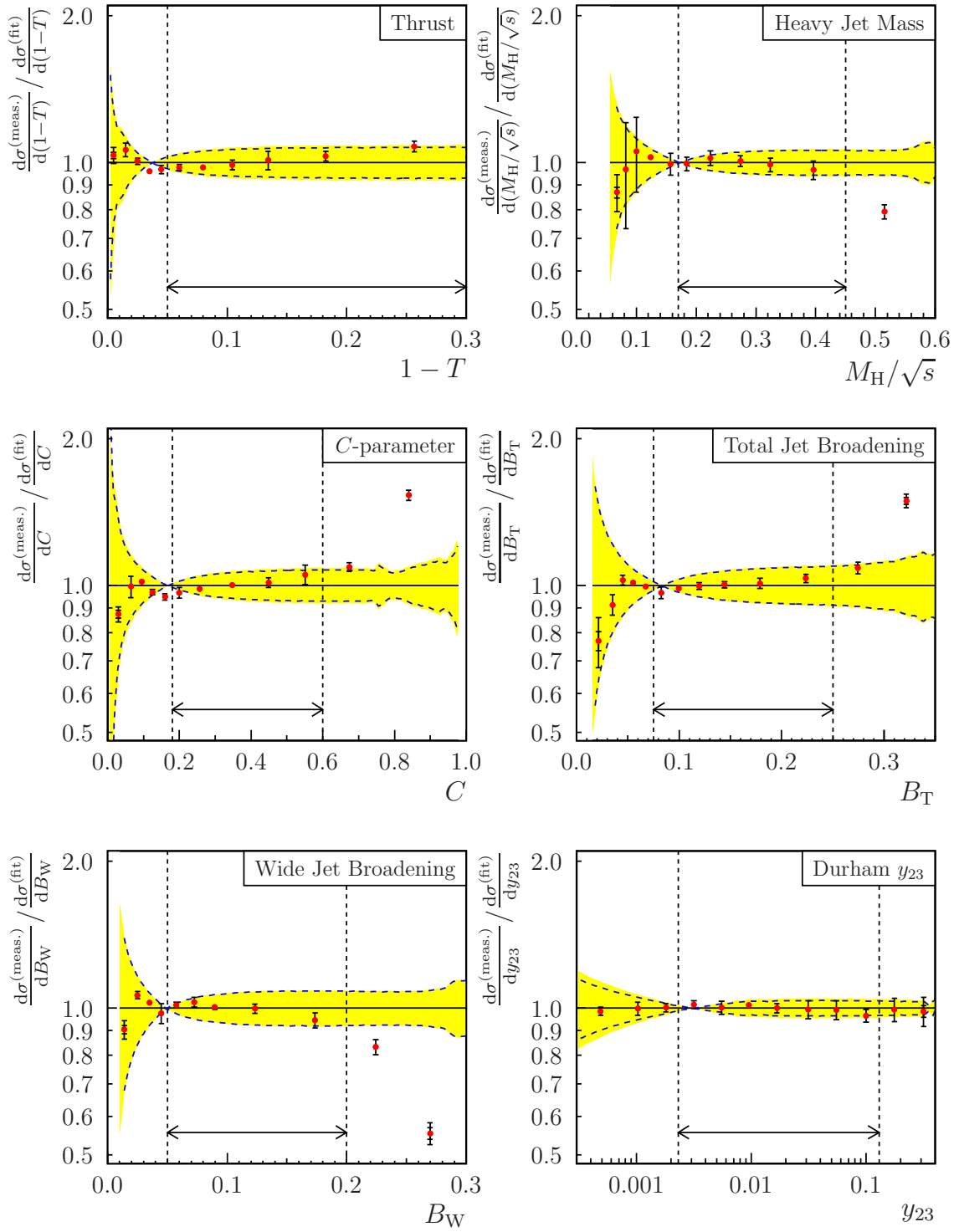Table C.3: OPAL measurements of α_S at $\sqrt{s} = 161$ GeV
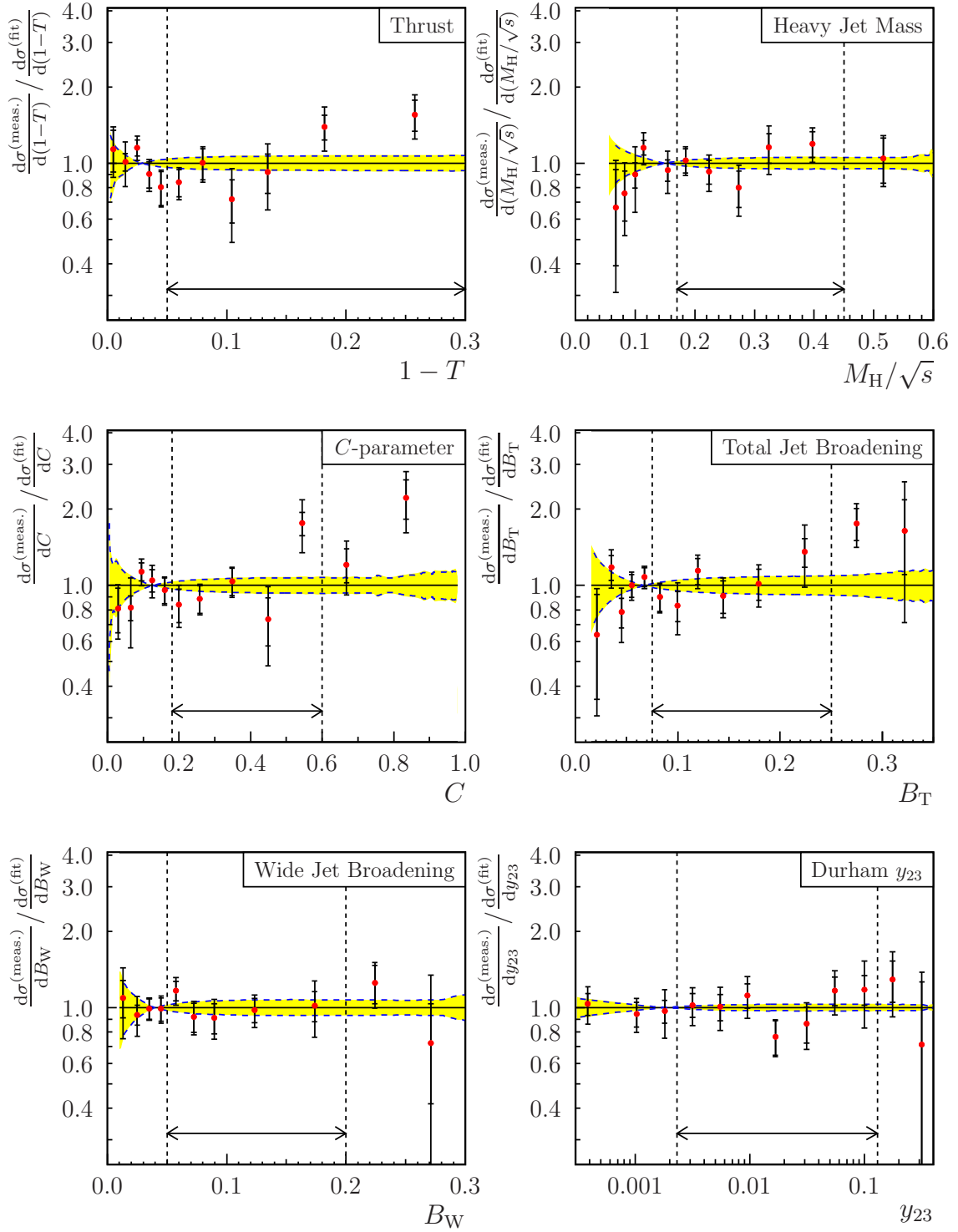
Figure C.3: Ratios of measured event shape distributions to hadron-level predictions, at $\sqrt{s} = 161$ GeV. An explanation is given in the introduction to this appendix, on page 283.

C.4   OPAL measurements of α_S at $\sqrt{s} = 172$ GeV

	T	M_H	C
$\alpha_\mathrm{S}(172\ \mathrm{GeV})$	0.1095	0.1043	0.1039
Statistical error	±0.0077	±0.0069	±0.0075
No MT algorithm	−0.0039*	−0.0071*	−0.0041*
HERWIG det. corr.	−0.0047*	−0.0022*	−0.0031*
$\cos(\theta_\mathrm{T}) < 0.7$	−0.0039*	−0.0019*	−0.0019*
Alternative $\sqrt{s'}$	+0.0019*	+0.0004*	+0.0023*
$L_{\mathrm{qqqq}} < 0.10$	−0.0001	−0.0005	−0.0011
$L_{\mathrm{qqqq}} < 0.40$	−0.0013*	−0.0006*	−0.0023*
$L_{\mathrm{qq}\ell\nu} < 0.25$	−0.0002*	−0.0001	−0.0001
$L_{\mathrm{qq}\ell\nu} < 0.75$	0.0000	+0.0012*	+0.0010*
Background +5%	−0.0003*	−0.0002*	−0.0001*
Background −5%	+0.0003	+0.0002	+0.0001
Experimental syst.	±0.0076	±0.0078	±0.0064
HERWIG hadr. corr.	−0.0002	+0.0022*	−0.0007
ARIADNE hadr. corr.	+0.0023*	+0.0017	+0.0022*
Hadronisation error	±0.0023	±0.0022	±0.0022
Upper uncertainty band	+0.0043	+0.0033	+0.0044
Lower uncertainty band	−0.0042	−0.0034	−0.0043
Theory error	±0.0043	±0.0034	±0.0043
Weight	0.06	0.07	0.11

	B_T	B_W	y_{23}	Weighted mean
$\alpha_\mathrm{S}(172\ \mathrm{GeV})$	0.1016	0.0950	0.1038	0.1012
Statistical error	±0.0070	±0.0060	±0.0056	±0.0055
No MT algorithm	+0.0001*	−0.0010*	−0.0031*	−0.0025*
HERWIG det. corr.	−0.0020*	−0.0022*	−0.0017*	−0.0022*
$\cos(\theta_\mathrm{T}) < 0.7$	+0.0021*	+0.0006*	−0.0024*	−0.0015*
Alternative $\sqrt{s'}$	+0.0019*	+0.0002*	+0.0014*	+0.0009*
$L_{\mathrm{qqqq}} < 0.10$	−0.0014*	−0.0010	−0.0010*	−0.0011*
$L_{\mathrm{qqqq}} < 0.40$	−0.0006	−0.0011*	−0.0002	−0.0009
$L_{\mathrm{qq}\ell\nu} < 0.25$	0.0000	−0.0001	0.0000	−0.0001
$L_{\mathrm{qq}\ell\nu} < 0.75$	−0.0001*	+0.0010*	−0.0006*	+0.0003*
Background +5%	−0.0002*	−0.0002*	−0.0001*	−0.0002*
Background −5%	+0.0002	+0.0002	+0.0001	+0.0002
Experimental syst.	±0.0037	±0.0029	±0.0046	±0.0039
HERWIG hadr. corr.	−0.0012	−0.0002	−0.0007*	−0.0003
ARIADNE hadr. corr.	+0.0018*	+0.0008*	−0.0003	+0.0008*
Hadronisation error	±0.0018	±0.0008	±0.0007	±0.0008
Upper uncertainty band	+0.0053	+0.0041	+0.0020	+0.0034
Lower uncertainty band	−0.0050	−0.0043	−0.0023	−0.0035
Theory error	±0.0051	±0.0042	±0.0022	±0.0034
Weight	0.31	0.06	0.40	−

Table C.4: OPAL measurements of α_S at $\sqrt{s} = 172$ GeV
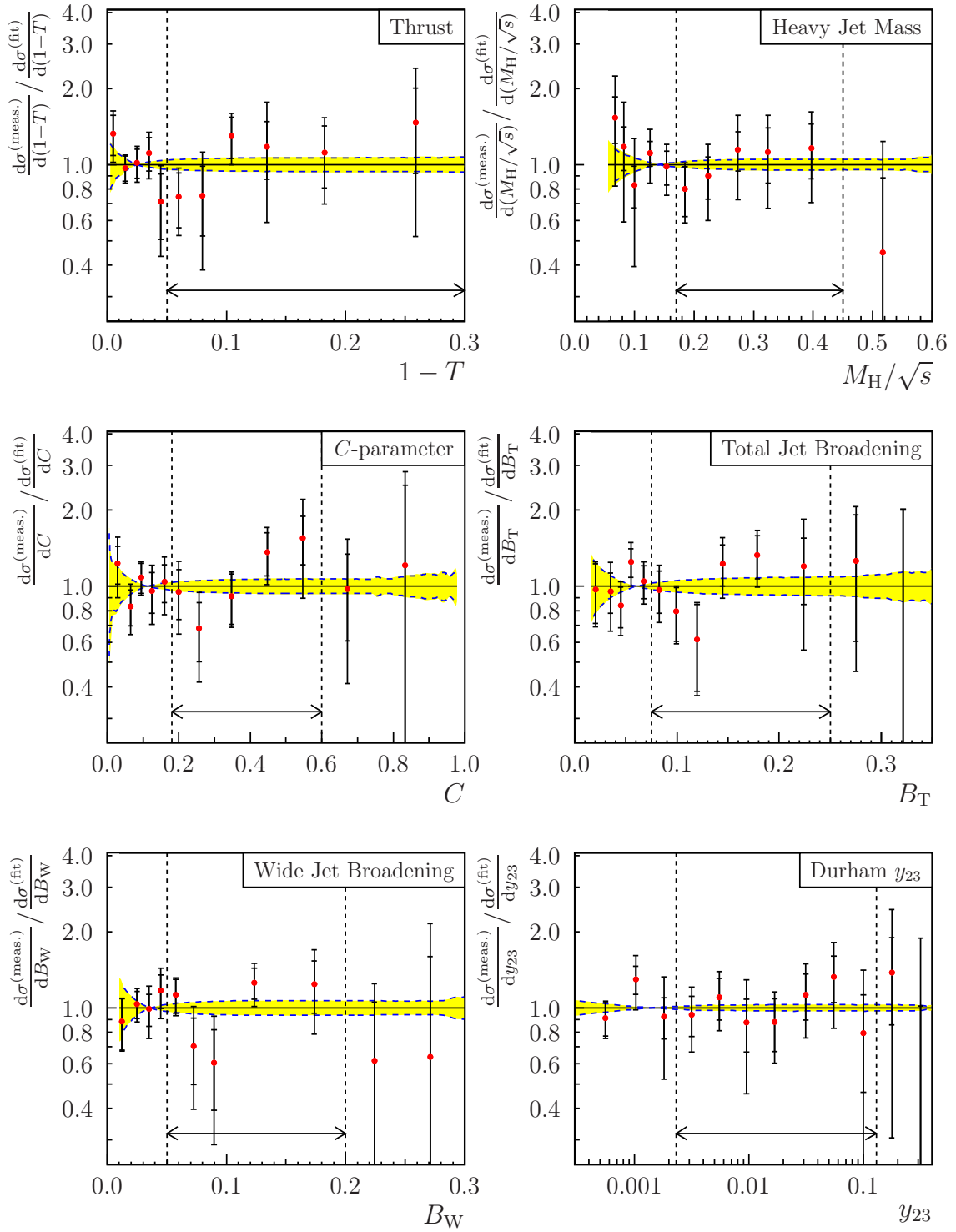
Figure C.4: Ratios of measured event shape distributions to hadron-level predictions, at $\sqrt{s} = 172$ GeV. An explanation is given in the introduction to this appendix, on page 283.

C.5 OPAL measurements of α_S at $\sqrt{s} = 183$ GeV

	T	M_H	C
$\alpha_S(183 \text{ GeV})$	0.1111	0.1076	0.1075
Statistical error	±0.0036	±0.0032	±0.0035
No MT algorithm	$+0.0006^*$	$+0.0015^*$	-0.0005^*
HERWIG det. corr.	-0.0022^*	0.0000^*	-0.0010^*
$\cos(\theta_T) < 0.7$	-0.0010^*	-0.0038^*	-0.0023^*
Alternative $\sqrt{s'}$	-0.0004^*	$+0.0004^*$	-0.0003^*
$L_{qqqq} < 0.10$	-0.0006	-0.0003	$+0.0011^*$
$L_{qqqq} < 0.40$	-0.0008^*	-0.0004^*	$+0.0009$
$L_{qq\ell\nu} < 0.25$	-0.0001	-0.0001^*	$+0.0001^*$
$L_{qq\ell\nu} < 0.75$	$+0.0001^*$	0.0000	-0.0001
Background $+5\%$	-0.0004^*	-0.0002^*	-0.0001^*
Background -5%	$+0.0003$	$+0.0002$	$+0.0001$
Experimental syst.	±0.0027	±0.0041	±0.0028
HERWIG hadr. corr.	-0.0002	$+0.0020^*$	-0.0005
ARIADNE hadr. corr.	$+0.0020^*$	$+0.0014$	$+0.0020^*$
Hadronisation error	±0.0020	±0.0020	±0.0020
Upper uncertainty band	$+0.0042$	$+0.0032$	$+0.0043$
Lower uncertainty band	-0.0041	-0.0034	-0.0042
Theory error	±0.0042	±0.0033	±0.0042
Weight	0.15	0.13	0.09

	B_T	B_W	y_{23}	Weighted mean
$\alpha_S(183 \text{ GeV})$	0.1117	0.1032	0.1084	0.1079
Statistical error	±0.0032	±0.0027	±0.0027	±0.0027
No MT algorithm	-0.0001^*	-0.0013^*	-0.0016^*	-0.0006^*
HERWIG det. corr.	-0.0009^*	-0.0003^*	-0.0012^*	-0.0009^*
$\cos(\theta_T) < 0.7$	-0.0029^*	-0.0026^*	-0.0027^*	-0.0029^*
Alternative $\sqrt{s'}$	$+0.0002^*$	0.0000^*	$+0.0001^*$	0.0000^*
$L_{qqqq} < 0.10$	$+0.0005$	$+0.0002^*$	$+0.0002$	$+0.0001$
$L_{qqqq} < 0.40$	$+0.0011^*$	-0.0001	-0.0005^*	-0.0002^*
$L_{qq\ell\nu} < 0.25$	0.0000	0.0000^*	0.0000^*	0.0000^*
$L_{qq\ell\nu} < 0.75$	0.0000^*	0.0000	0.0000	0.0000
Background $+5\%$	-0.0001^*	-0.0002^*	-0.0001^*	-0.0002^*
Background -5%	$+0.0001$	$+0.0002$	$+0.0001^*$	$+0.0002$
Experimental syst.	±0.0033	±0.0029	±0.0034	±0.0031
HERWIG hadr. corr.	-0.0009	-0.0002	-0.0005^*	-0.0001
ARIADNE hadr. corr.	$+0.0014^*$	$+0.0006^*$	-0.0003	$+0.0009^*$
Hadronisation error	±0.0014	±0.0006	±0.0005	±0.0009
Upper uncertainty band	$+0.0052$	$+0.0041$	$+0.0020$	$+0.0035$
Lower uncertainty band	-0.0049	-0.0042	-0.0022	-0.0035
Theory error	±0.0050	±0.0041	±0.0021	±0.0035
Weight	0.20	0.12	0.31	$-$

Table C.5: OPAL measurements of α_S at $\sqrt{s} = 183$ GeV
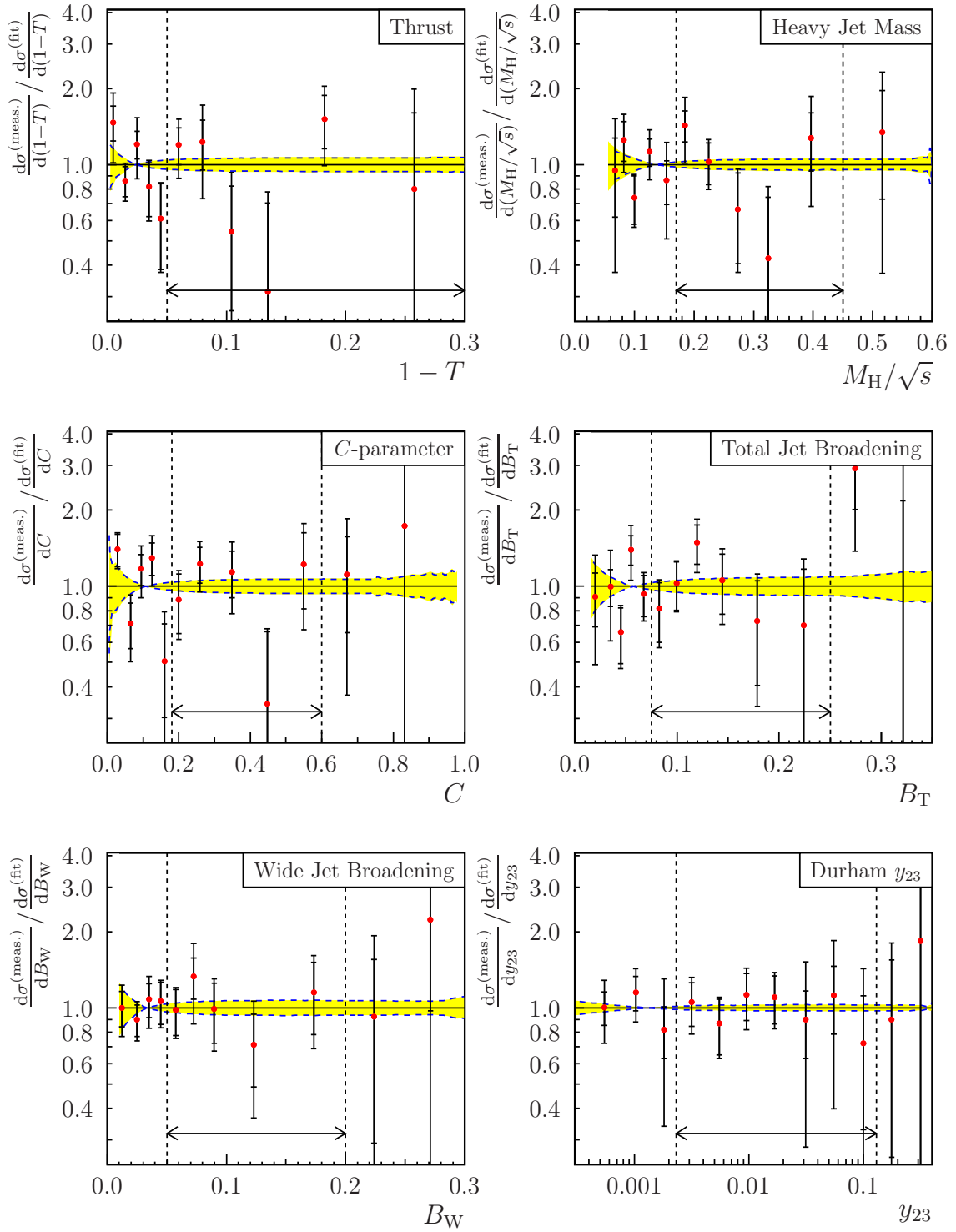
Figure C.5: Ratios of measured event shape distributions to hadron-level predictions, at $\sqrt{s} = 183$ GeV. An explanation is given in the introduction to this appendix, on page 283.

C.6   OPAL measurements of α_{S} at $\sqrt{s} = 189$ GeV

	T	M_{H}	C
$\alpha_{\mathrm{S}}(189\text{ GeV})$	0.1147	0.1069	0.1084
Statistical error	± 0.0021	± 0.0019	± 0.0021
No MT algorithm	-0.0007^*	-0.0002^*	$+0.0007^*$
HERWIG det. corr.	0.0000^*	-0.0009^*	-0.0005^*
$\cos(\theta_{\mathrm{T}}) < 0.7$	-0.0005^*	-0.0015^*	$+0.0001^*$
Alternative $\sqrt{s'}$	$+0.0003^*$	$+0.0004^*$	$+0.0007^*$
$L_{\mathrm{qqqq}} < 0.10$	-0.0012^*	-0.0007	-0.0005^*
$L_{\mathrm{qqqq}} < 0.40$	-0.0005	-0.0008^*	-0.0003
$L_{\mathrm{qq}\ell\nu} < 0.25$	0.0000	$+0.0002^*$	$+0.0002^*$
$L_{\mathrm{qq}\ell\nu} < 0.75$	$+0.0001^*$	-0.0001	$+0.0001$
Background $+5\%$	-0.0003^*	-0.0002^*	0.0000
Background -5%	$+0.0003$	$+0.0002$	0.0000^*
Experimental syst.	± 0.0016	± 0.0020	± 0.0012
HERWIG hadr. corr.	-0.0001	$+0.0022^*$	-0.0005
ARIADNE hadr. corr.	$+0.0019^*$	$+0.0014$	$+0.0019^*$
Hadronisation error	± 0.0019	± 0.0022	± 0.0019
Upper uncertainty band	$+0.0041$	$+0.0032$	$+0.0042$
Lower uncertainty band	-0.0041	-0.0033	-0.0042
Theory error	± 0.0041	± 0.0033	± 0.0042
Weight	0.09	0.11	0.08

	B_{T}	B_{W}	y_{23}	Weighted mean
$\alpha_{\mathrm{S}}(189\text{ GeV})$	0.1128	0.1030	0.1067	0.1076
Statistical error	± 0.0020	± 0.0016	± 0.0016	± 0.0016
No MT algorithm	$+0.0002^*$	$+0.0003^*$	-0.0003^*	-0.0001^*
HERWIG det. corr.	-0.0002^*	$+0.0006^*$	$+0.0001^*$	-0.0002^*
$\cos(\theta_{\mathrm{T}}) < 0.7$	$+0.0006^*$	0.0000^*	$+0.0001^*$	-0.0001^*
Alternative $\sqrt{s'}$	0.0000^*	$+0.0002^*$	$+0.0006^*$	$+0.0004^*$
$L_{\mathrm{qqqq}} < 0.10$	0.0000	-0.0002	-0.0001	-0.0004
$L_{\mathrm{qqqq}} < 0.40$	-0.0006^*	-0.0004^*	-0.0003^*	-0.0004^*
$L_{\mathrm{qq}\ell\nu} < 0.25$	0.0000	0.0000	0.0000	0.0000
$L_{\mathrm{qq}\ell\nu} < 0.75$	-0.0002^*	-0.0002^*	-0.0001^*	-0.0001^*
Background $+5\%$	-0.0001^*	-0.0002^*	-0.0001^*	-0.0001^*
Background -5%	$+0.0001^*$	$+0.0001$	$+0.0001$	$+0.0001$
Experimental syst.	± 0.0009	± 0.0008	± 0.0007	± 0.0007
HERWIG hadr. corr.	-0.0009	-0.0001	-0.0004^*	-0.0001
ARIADNE hadr. corr.	$+0.0014^*$	$+0.0006^*$	-0.0003	$+0.0007^*$
Hadronisation error	± 0.0014	± 0.0006	± 0.0004	± 0.0007
Upper uncertainty band	$+0.0051$	$+0.0040$	$+0.0020$	$+0.0031$
Lower uncertainty band	-0.0048	-0.0042	-0.0022	-0.0032
Theory error	± 0.0049	± 0.0041	± 0.0021	± 0.0031
Weight	0.14	0.11	0.47	$-$

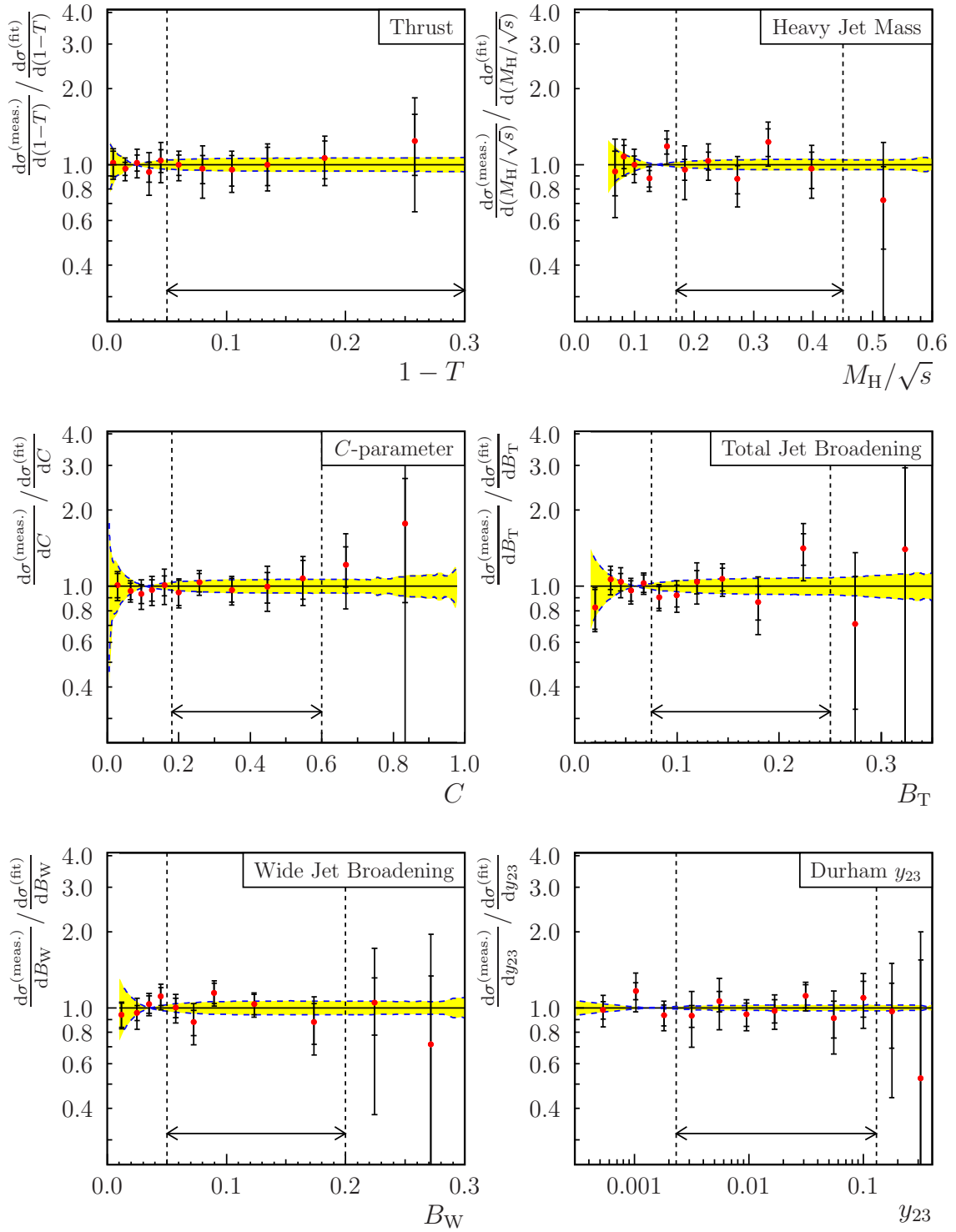Table C.6: OPAL measurements of α_{S} at $\sqrt{s} = 189$ GeV

Figure C.6: Ratios of measured event shape distributions to hadron-level predictions, at $\sqrt{s} = 189$ GeV. An explanation is given in the introduction to this appendix, on page 283.

C.7 OPAL measurements of α_S at $\sqrt{s} = 192$ GeV

	T	M_{H}	C
$\alpha_S(192$ GeV)	0.1125	0.1077	0.1040
Statistical error	±0.0057	±0.0049	±0.0056
No MT algorithm	+0.0020*	+0.0018*	+0.0025*
HERWIG det. corr.	−0.0026*	−0.0018*	−0.0016*
$\cos(\theta_{\mathrm{T}}) < 0.7$	−0.0025*	−0.0010*	−0.0029*
Alternative $\sqrt{s'}$	+0.0004*	−0.0001*	+0.0014*
$L_{\mathrm{qqqq}} < 0.10$	+0.0012	+0.0005	+0.0026
$L_{\mathrm{qqqq}} < 0.40$	−0.0080*	−0.0044*	−0.0039*
$L_{\mathrm{qq}\ell\nu} < 0.25$	+0.0004*	+0.0003*	+0.0007*
$L_{\mathrm{qq}\ell\nu} < 0.75$	−0.0001	+0.0001	0.0000
Background +5%	−0.0002*	−0.0002*	0.0000
Background −5%	+0.0002	+0.0002	0.0000*
Experimental syst.	±0.0091	±0.0052	±0.0059
HERWIG hadr. corr.	−0.0001	+0.0021*	−0.0005
ARIADNE hadr. corr.	+0.0020*	+0.0014	+0.0020*
Hadronisation error	±0.0020	±0.0021	±0.0020
Upper uncertainty band	+0.0041	+0.0032	+0.0042
Lower uncertainty band	−0.0041	−0.0033	−0.0041
Theory error	±0.0041	±0.0032	±0.0042
Weight	0.06	0.21	0.06

	B_{T}	B_{W}	y_{23}	Weighted mean
$\alpha_S(192$ GeV)	0.1063	0.1003	0.1064	0.1051
Statistical error	±0.0053	±0.0042	±0.0042	±0.0037
No MT algorithm	+0.0002*	+0.0021*	+0.0015*	+0.0019*
HERWIG det. corr.	−0.0033*	−0.0013*	−0.0010*	−0.0016*
$\cos(\theta_{\mathrm{T}}) < 0.7$	−0.0041*	−0.0023*	−0.0046*	−0.0028*
Alternative $\sqrt{s'}$	+0.0005*	−0.0005*	−0.0009*	−0.0001*
$L_{\mathrm{qqqq}} < 0.10$	+0.0022	+0.0008	+0.0013	+0.0013
$L_{\mathrm{qqqq}} < 0.40$	−0.0085*	−0.0032*	−0.0033*	−0.0043*
$L_{\mathrm{qq}\ell\nu} < 0.25$	+0.0005*	+0.0003*	+0.0002*	+0.0004*
$L_{\mathrm{qq}\ell\nu} < 0.75$	+0.0001	+0.0001	0.0000	0.0000
Background +5%	−0.0001*	−0.0002*	−0.0001*	−0.0001*
Background −5%	0.0000	+0.0001	+0.0001	+0.0001
Experimental syst.	±0.0100	±0.0047	±0.0060	±0.0057
HERWIG hadr. corr.	−0.0009	−0.0002	−0.0004*	+0.0002
ARIADNE hadr. corr.	+0.0015*	+0.0006*	−0.0003	+0.0009*
Hadronisation error	±0.0015	±0.0006	±0.0004	±0.0009
Upper uncertainty band	+0.0051	+0.0040	+0.0020	+0.0034
Lower uncertainty band	−0.0048	−0.0041	−0.0022	−0.0035
Theory error	±0.0049	±0.0040	±0.0021	±0.0035
Weight	0.26	0.15	0.25	−

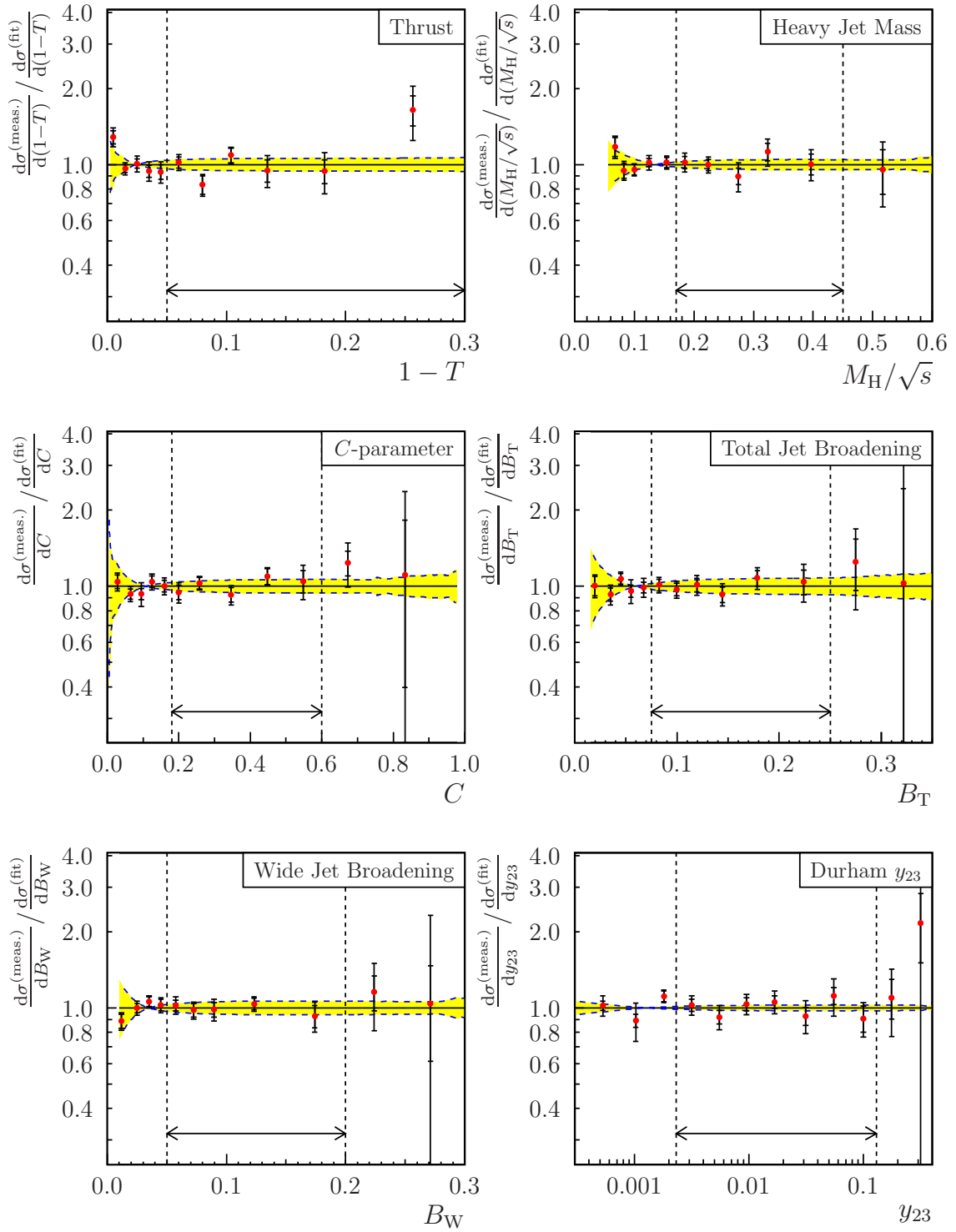Table C.7: OPAL measurements of α_S at $\sqrt{s} = 192$ GeV

Figure C.7: Ratios of measured event shape distributions to hadron-level predictions, at $\sqrt{s} = 192$ GeV. An explanation is given in the introduction to this appendix, on page 283.

C.8   OPAL measurements of α_S at $\sqrt{s} = 196$ GeV

	T	M_H	C
$\alpha_S(196$ GeV$)$	0.1140	0.1041	0.1076
Statistical error	±0.0036	±0.0032	±0.0035
No MT algorithm	-0.0008^*	$+0.0012^*$	-0.0007^*
HERWIG det. corr.	-0.0003^*	-0.0012^*	-0.0017^*
$\cos(\theta_T) < 0.7$	$+0.0028^*$	-0.0013^*	-0.0019^*
Alternative $\sqrt{s'}$	$+0.0005^*$	$+0.0012^*$	$+0.0001^*$
$L_{qqqq} < 0.10$	-0.0010	-0.0002	-0.0006
$L_{qqqq} < 0.40$	-0.0028^*	-0.0020^*	$+0.0018^*$
$L_{qq\ell\nu} < 0.25$	-0.0001^*	0.0000	$+0.0002^*$
$L_{qq\ell\nu} < 0.75$	-0.0001	$+0.0001^*$	-0.0001
Background $+5\%$	-0.0003^*	-0.0003^*	0.0000
Background -5%	$+0.0003$	$+0.0002$	0.0000^*
Experimental syst.	±0.0041	±0.0032	±0.0032
HERWIG hadr. corr.	0.0000	$+0.0021^*$	-0.0004
ARIADNE hadr. corr.	$+0.0019^*$	$+0.0013$	$+0.0018^*$
Hadronisation error	±0.0019	±0.0021	±0.0018
Upper uncertainty band	$+0.0041$	$+0.0031$	$+0.0042$
Lower uncertainty band	-0.0040	-0.0033	-0.0041
Theory error	±0.0041	±0.0032	±0.0042
Weight	0.09	0.15	0.10

	B_T	B_W	y_{23}	Weighted mean
$\alpha_S(196$ GeV$)$	0.1118	0.1023	0.1045	0.1059
Statistical error	±0.0034	±0.0027	±0.0027	±0.0029
No MT algorithm	-0.0020^*	$+0.0004^*$	$+0.0007^*$	$+0.0003^*$
HERWIG det. corr.	-0.0016^*	-0.0004^*	$+0.0002^*$	-0.0006^*
$\cos(\theta_T) < 0.7$	-0.0005^*	-0.0005^*	-0.0031^*	-0.0015^*
Alternative $\sqrt{s'}$	-0.0010^*	$+0.0008^*$	$+0.0015^*$	$+0.0007^*$
$L_{qqqq} < 0.10$	-0.0004	-0.0006	0.0000	-0.0004
$L_{qqqq} < 0.40$	$+0.0007^*$	-0.0014^*	-0.0008^*	-0.0011^*
$L_{qq\ell\nu} < 0.25$	0.0000	0.0000^*	0.0000	0.0000
$L_{qq\ell\nu} < 0.75$	-0.0001^*	0.0000	0.0000^*	0.0000^*
Background $+5\%$	0.0000	-0.0002^*	-0.0001	-0.0001^*
Background -5%	0.0000^*	$+0.0002$	$+0.0001^*$	$+0.0001$
Experimental syst.	±0.0029	±0.0018	±0.0036	±0.0021
HERWIG hadr. corr.	-0.0008	-0.0001	-0.0004^*	0.0000
ARIADNE hadr. corr.	$+0.0013^*$	$+0.0006^*$	-0.0003	$+0.0008^*$
Hadronisation error	±0.0013	±0.0006	±0.0004	±0.0008
Upper uncertainty band	$+0.0050$	$+0.0039$	$+0.0020$	$+0.0034$
Lower uncertainty band	-0.0047	-0.0041	-0.0022	-0.0034
Theory error	±0.0049	±0.0040	±0.0021	±0.0034
Weight	0.24	0.10	0.31	$-$

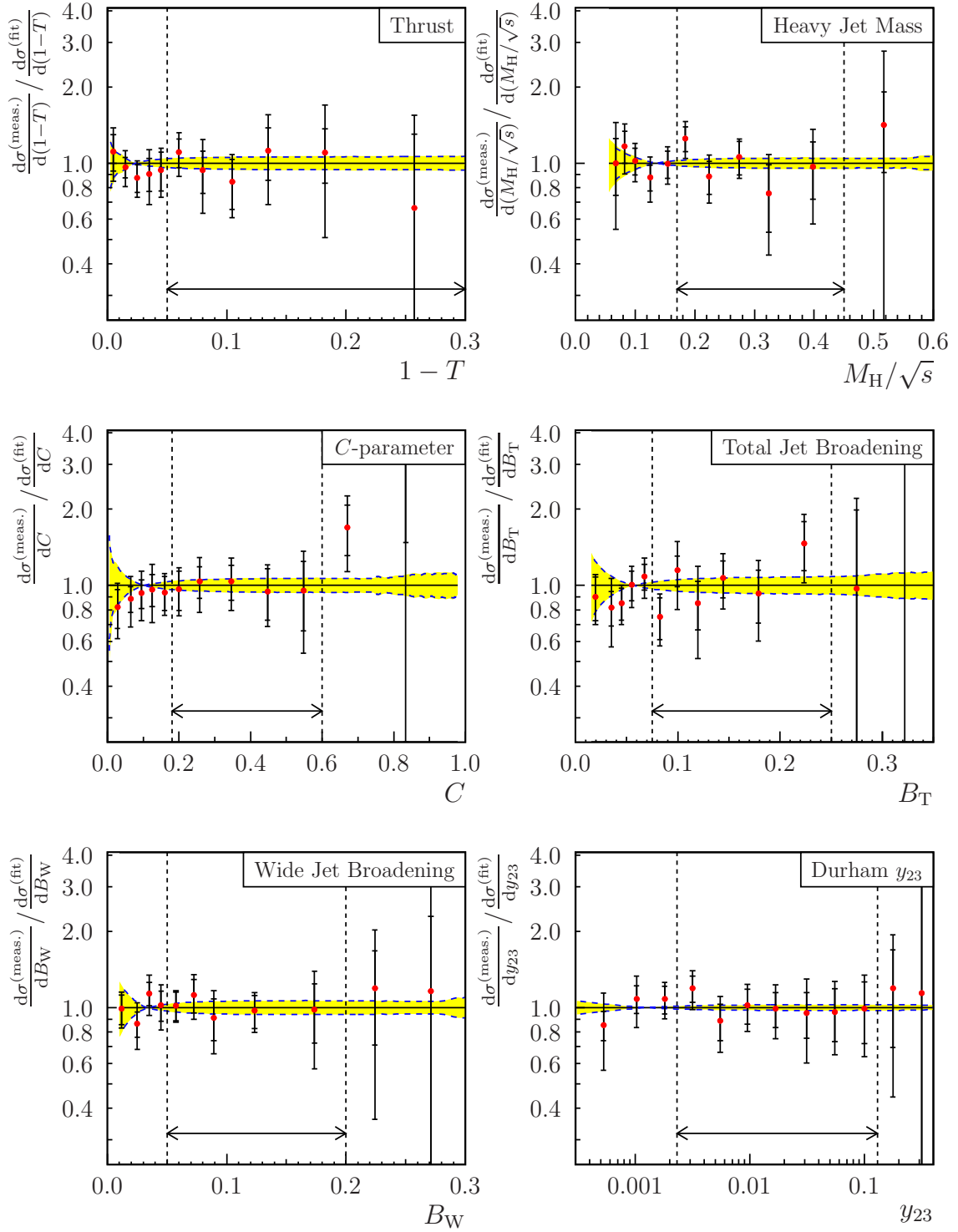Table C.8: OPAL measurements of α_S at $\sqrt{s} = 196$ GeV
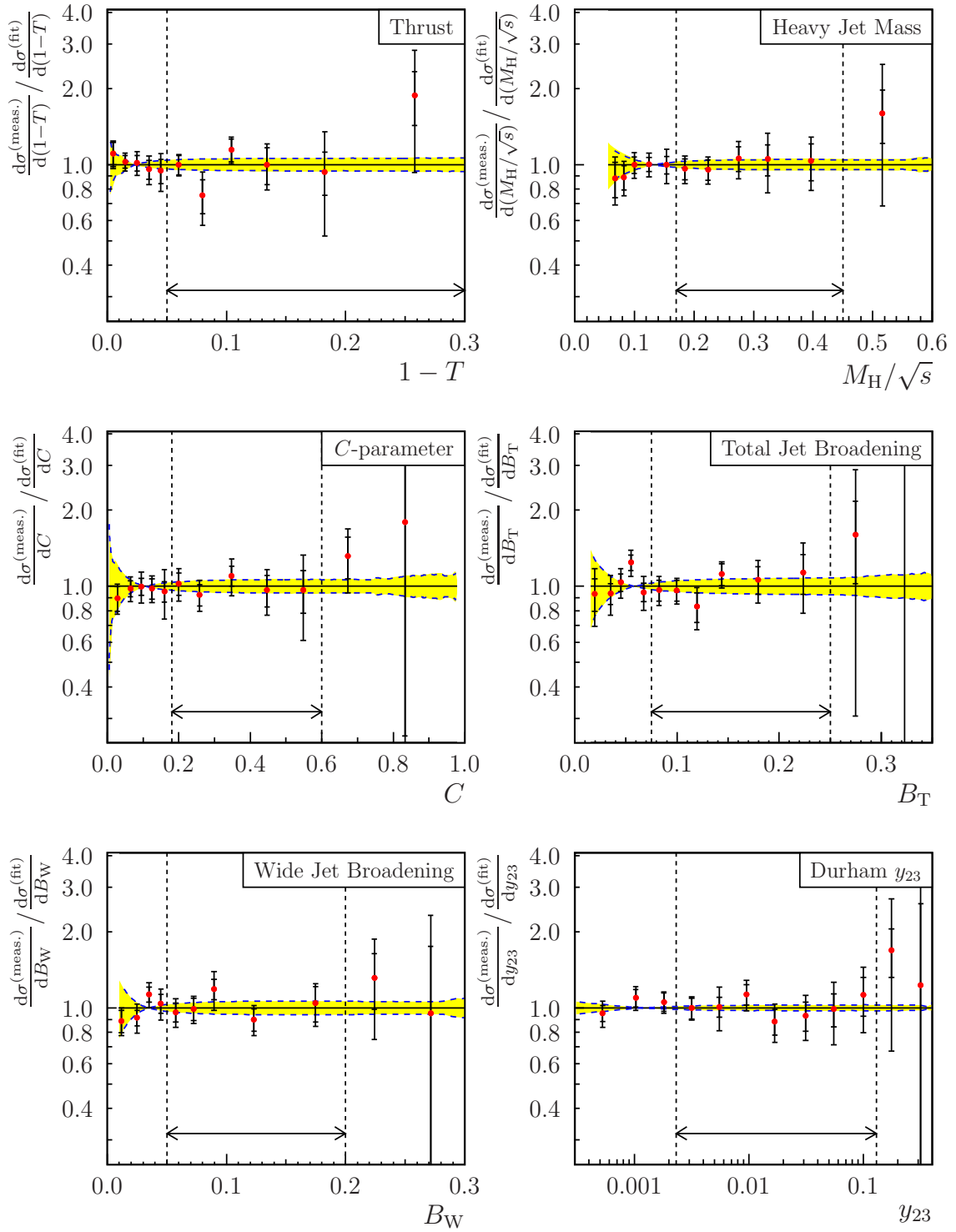
Figure C.8: Ratios of measured event shape distributions to hadron-level predictions, at $\sqrt{s} = 196$ GeV. An explanation is given in the introduction to this appendix, on page 283.

C.9 OPAL measurements of α_S at $\sqrt{s} = 200$ GeV

	T	M_H	C
$\alpha_S(200\text{ GeV})$	0.1128	0.1052	0.1073
Statistical error	±0.0038	±0.0033	±0.0036
No MT algorithm	−0.0002*	+0.0014*	+0.0007*
HERWIG det. corr.	−0.0031*	−0.0006*	−0.0014*
$\cos(\theta_T) < 0.7$	+0.0023*	+0.0023*	+0.0034*
Alternative $\sqrt{s'}$	−0.0009*	+0.0002*	+0.0007*
$L_{qqqq} < 0.10$	−0.0005	−0.0009*	+0.0007
$L_{qqqq} < 0.40$	+0.0043*	−0.0006	+0.0009*
$L_{qq\ell\nu} < 0.25$	+0.0004*	+0.0001*	−0.0003*
$L_{qq\ell\nu} < 0.75$	+0.0002	0.0000	−0.0001
Background +5%	−0.0003*	−0.0003*	0.0000*
Background −5%	+0.0003	+0.0002	0.0000*
Experimental syst.	±0.0059	±0.0029	±0.0039
HERWIG hadr. corr.	0.0000	+0.0021*	−0.0004
ARIADNE hadr. corr.	+0.0018*	+0.0013	+0.0018*
Hadronisation error	±0.0018	±0.0021	±0.0018
Upper uncertainty band	+0.0040	+0.0031	+0.0042
Lower uncertainty band	−0.0040	−0.0033	−0.0041
Theory error	±0.0040	±0.0032	±0.0041
Weight	0.06	0.17	0.08

	B_T	B_W	y_{23}	Weighted mean
$\alpha_S(200\text{ GeV})$	0.1143	0.1037	0.1089	0.1076
Statistical error	±0.0034	±0.0028	±0.0028	±0.0028
No MT algorithm	−0.0027*	−0.0011*	−0.0014*	−0.0007*
HERWIG det. corr.	−0.0009*	+0.0002*	−0.0008*	−0.0009*
$\cos(\theta_T) < 0.7$	+0.0029*	+0.0012*	+0.0020*	+0.0019*
Alternative $\sqrt{s'}$	−0.0009*	−0.0002*	+0.0005*	+0.0002*
$L_{qqqq} < 0.10$	+0.0004	+0.0005	+0.0005	+0.0003
$L_{qqqq} < 0.40$	+0.0019*	−0.0010*	−0.0009*	−0.0006*
$L_{qq\ell\nu} < 0.25$	0.0000	−0.0003*	−0.0003*	−0.0002*
$L_{qq\ell\nu} < 0.75$	0.0000*	0.0000	0.0000	0.0000
Background +5%	0.0000*	−0.0002*	−0.0001*	−0.0001*
Background −5%	0.0000	+0.0001	0.0000	+0.0001
Experimental syst.	±0.0045	±0.0020	±0.0028	±0.0023
HERWIG hadr. corr.	−0.0008	−0.0001	−0.0003*	+0.0001
ARIADNE hadr. corr.	+0.0012*	+0.0006*	−0.0003	+0.0006*
Hadronisation error	±0.0012	±0.0006	±0.0003	±0.0006
Upper uncertainty band	+0.0050	+0.0039	+0.0020	+0.0032
Lower uncertainty band	−0.0047	−0.0041	−0.0021	−0.0033
Theory error	±0.0048	±0.0040	±0.0021	±0.0032
Weight	0.25	0.07	0.37	−

Table C.9: OPAL measurements of α_S at $\sqrt{s} = 200$ GeV
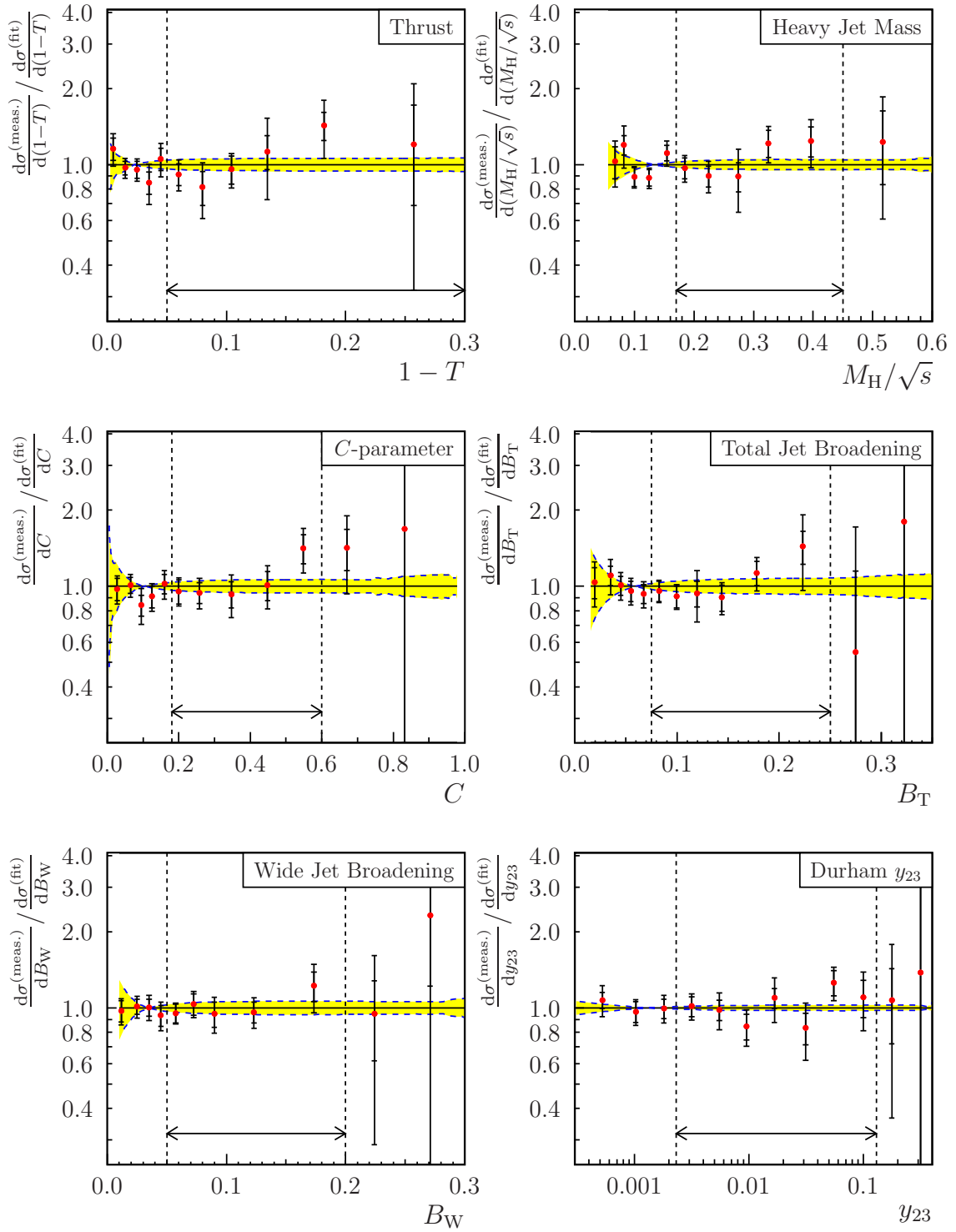
Figure C.9: Ratios of measured event shape distributions to hadron-level predictions, at $\sqrt{s} = 200$ GeV. An explanation is given in the introduction to this appendix, on page 283.

C.10 OPAL measurements of α_S at $\sqrt{s} = 202$ GeV

	T	M_H	C
$\alpha_S(202$ GeV$)$	0.1183	0.1060	0.1120
Statistical error	±0.0052	±0.0048	±0.0052
No MT algorithm	−0.0029*	+0.0015*	−0.0038*
HERWIG det. corr.	−0.0033*	−0.0029*	−0.0046*
$\cos(\theta_T) < 0.7$	−0.0019*	−0.0003*	+0.0001*
Alternative $\sqrt{s'}$	−0.0020*	−0.0010*	−0.0003*
$L_{qqqq} < 0.10$	+0.0012*	0.0000	−0.0025
$L_{qqqq} < 0.40$	−0.0009	+0.0005*	+0.0042*
$L_{qq\ell\nu} < 0.25$	−0.0002*	−0.0001	0.0000
$L_{qq\ell\nu} < 0.75$	+0.0002	−0.0002*	−0.0002*
Background +5%	−0.0003*	−0.0003*	0.0000*
Background −5%	+0.0003	+0.0002	0.0000
Experimental syst.	±0.0053	±0.0035	±0.0073
HERWIG hadr. corr.	0.0000	+0.0021*	−0.0003
ARIADNE hadr. corr.	+0.0017*	+0.0013	+0.0016*
Hadronisation error	±0.0017	±0.0021	±0.0016
Upper uncertainty band	+0.0040	+0.0031	+0.0041
Lower uncertainty band	−0.0040	−0.0033	−0.0041
Theory error	±0.0040	±0.0032	±0.0041
Weight	0.05	0.08	0.10

	B_T	B_W	y_{23}	Weighted mean
$\alpha_S(202$ GeV$)$	0.1123	0.1033	0.1058	0.1067
Statistical error	±0.0049	±0.0040	±0.0040	±0.0037
No MT algorithm	+0.0013*	+0.0012*	−0.0010*	−0.0003*
HERWIG det. corr.	−0.0008*	−0.0010*	−0.0015*	−0.0021*
$\cos(\theta_T) < 0.7$	+0.0020*	+0.0010*	0.0000*	0.0000*
Alternative $\sqrt{s'}$	−0.0014*	+0.0004*	−0.0007*	−0.0007*
$L_{qqqq} < 0.10$	+0.0007*	−0.0010*	−0.0007*	−0.0004
$L_{qqqq} < 0.40$	+0.0004	−0.0004	+0.0006	+0.0005*
$L_{qq\ell\nu} < 0.25$	−0.0001*	−0.0001*	−0.0001	−0.0001
$L_{qq\ell\nu} < 0.75$	−0.0001	−0.0001	−0.0004*	−0.0003*
Background +5%	−0.0001*	−0.0002*	−0.0001*	−0.0001*
Background −5%	+0.0001	+0.0002	+0.0001	+0.0001
Experimental syst.	±0.0030	±0.0021	±0.0021	±0.0024
HERWIG hadr. corr.	−0.0008	−0.0001	−0.0003*	−0.0001
ARIADNE hadr. corr.	+0.0013*	+0.0006*	−0.0003	+0.0004*
Hadronisation error	±0.0013	±0.0006	±0.0003	±0.0004
Upper uncertainty band	+0.0049	+0.0039	+0.0019	+0.0028
Lower uncertainty band	−0.0047	−0.0041	−0.0021	−0.0030
Theory error	±0.0048	±0.0040	±0.0020	±0.0029
Weight	0.19	0.02	0.57	−

Table C.10: OPAL measurements of α_S at $\sqrt{s} = 202$ GeV
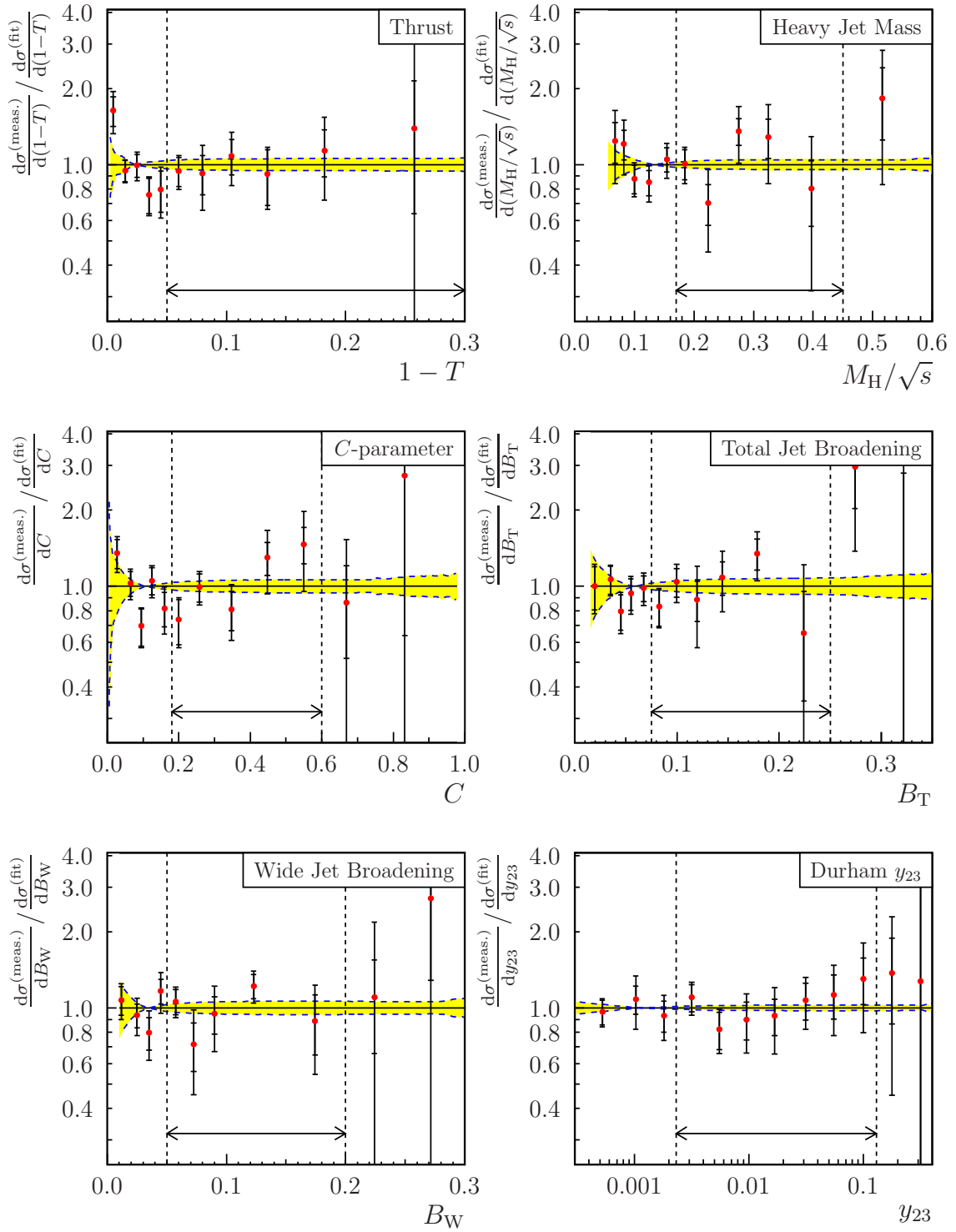
Figure C.10: Ratios of measured event shape distributions to hadron-level predictions, at $\sqrt{s} = 202$ GeV. An explanation is given in the introduction to this appendix, on page 283.

C.11   OPAL measurements of α_S at $\sqrt{s} = 205$ GeV

	T	M_H	C
$\alpha_S(205$ GeV$)$	0.1129	0.1114	0.1075
Statistical error	±0.0037	±0.0032	±0.0036
No MT algorithm	−0.0004*	−0.0018*	+0.0001*
HERWIG det. corr.	−0.0015*	−0.0008*	−0.0027*
$\cos(\theta_T) < 0.7$	−0.0009*	−0.0030*	−0.0015*
Alternative $\sqrt{s'}$	+0.0001*	0.0000*	+0.0018*
$L_{qqqq} < 0.10$	−0.0008	−0.0004	+0.0017
$L_{qqqq} < 0.40$	−0.0029*	−0.0004*	−0.0058*
$L_{qq\ell\nu} < 0.25$	−0.0002*	+0.0002*	−0.0001
$L_{qq\ell\nu} < 0.75$	0.0000	0.0000	−0.0002*
Background +5%	−0.0003*	−0.0002*	0.0000
Background −5%	+0.0003	+0.0002	0.0000*
Experimental syst.	±0.0034	±0.0036	±0.0068
HERWIG hadr. corr.	0.0000	+0.0019*	−0.0003
ARIADNE hadr. corr.	+0.0019*	+0.0012	+0.0018*
Hadronisation error	±0.0019	±0.0019	±0.0018
Upper uncertainty band	+0.0040	+0.0031	+0.0041
Lower uncertainty band	−0.0040	−0.0032	−0.0040
Theory error	±0.0040	±0.0032	±0.0041
Weight	0.11	0.16	0.07

	B_T	B_W	y_{23}	Weighted mean
$\alpha_S(205$ GeV$)$	0.1121	0.1062	0.1119	0.1106
Statistical error	±0.0034	±0.0028	±0.0028	±0.0024
No MT algorithm	+0.0003*	+0.0010*	−0.0006*	−0.0004*
HERWIG det. corr.	−0.0016*	+0.0003*	−0.0003*	−0.0006*
$\cos(\theta_T) < 0.7$	+0.0010*	−0.0024*	−0.0014*	−0.0018*
Alternative $\sqrt{s'}$	+0.0022*	−0.0002*	+0.0006*	+0.0004*
$L_{qqqq} < 0.10$	+0.0004	+0.0005	+0.0003	+0.0002
$L_{qqqq} < 0.40$	−0.0052*	−0.0017*	−0.0022*	−0.0023*
$L_{qq\ell\nu} < 0.25$	0.0000	0.0000	0.0000*	0.0000
$L_{qq\ell\nu} < 0.75$	−0.0002*	0.0000*	0.0000*	0.0000*
Background +5%	−0.0001	−0.0002*	−0.0001*	−0.0001*
Background −5%	+0.0001*	+0.0001	+0.0001	+0.0001
Experimental syst.	±0.0059	±0.0031	±0.0027	±0.0030
HERWIG hadr. corr.	−0.0008	−0.0001	−0.0003*	+0.0001
ARIADNE hadr. corr.	+0.0013*	+0.0006*	−0.0003	+0.0006*
Hadronisation error	±0.0013	±0.0006	±0.0003	±0.0006
Upper uncertainty band	+0.0049	+0.0039	+0.0019	+0.0030
Lower uncertainty band	−0.0047	−0.0040	−0.0021	−0.0032
Theory error	±0.0048	±0.0040	±0.0020	±0.0031
Weight	0.20	0.05	0.42	−

Table C.11: OPAL measurements of α_S at $\sqrt{s} = 205$ GeV
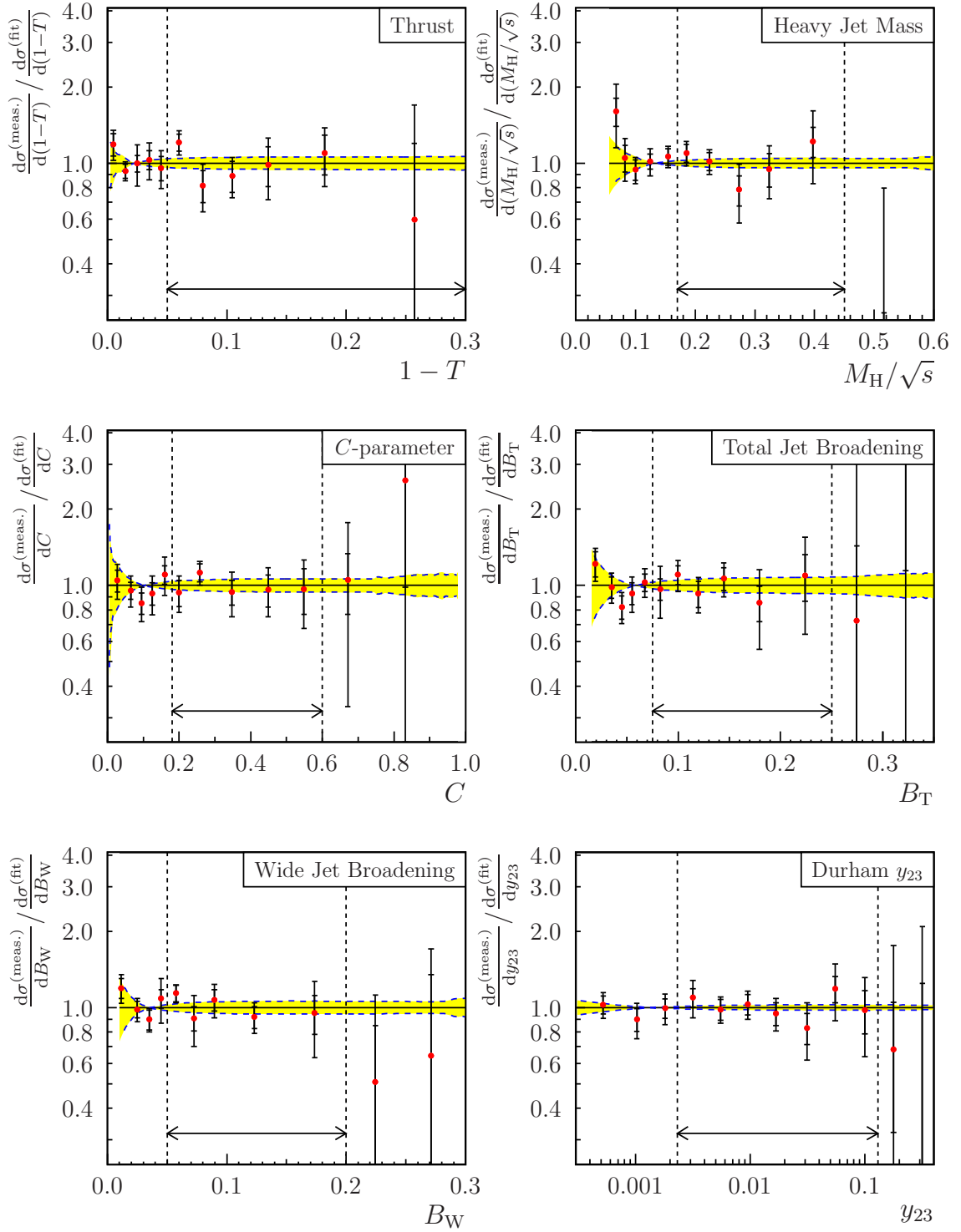
Figure C.11: Ratios of measured event shape distributions to hadron-level predictions, at $\sqrt{s} = 205$ GeV. An explanation is given in the introduction to this appendix, on page 283.

C.12   OPAL measurements of α_S at $\sqrt{s} = 207$ GeV

	T	M_{H}	C
$\alpha_{\mathrm{S}}(207 \text{ GeV})$	0.1077	0.1034	0.1067
Statistical error	±0.0030	±0.0026	±0.0028
No MT algorithm	+0.0001*	−0.0005*	−0.0008*
HERWIG det. corr.	+0.0005*	−0.0007*	−0.0001*
$\cos(\theta_{\mathrm{T}}) < 0.7$	−0.0002*	+0.0006*	−0.0003*
Alternative $\sqrt{s'}$	−0.0002*	−0.0012*	−0.0010*
$L_{\mathrm{qqqq}} < 0.10$	+0.0002	+0.0002	−0.0009
$L_{\mathrm{qqqq}} < 0.40$	+0.0018*	−0.0004*	+0.0016*
$L_{\mathrm{qq}\ell\nu} < 0.25$	−0.0003*	−0.0003*	0.0000*
$L_{\mathrm{qq}\ell\nu} < 0.75$	−0.0002	−0.0002	0.0000
Background +5%	−0.0004*	−0.0003*	0.0000*
Background −5%	+0.0004	+0.0002	0.0000*
Experimental syst.	±0.0020	±0.0017	±0.0021
HERWIG hadr. corr.	0.0000	+0.0022*	−0.0003
ARIADNE hadr. corr.	+0.0019*	+0.0014	+0.0018*
Hadronisation error	±0.0019	±0.0022	±0.0018
Upper uncertainty band	+0.0040	+0.0031	+0.0041
Lower uncertainty band	−0.0040	−0.0032	−0.0041
Theory error	±0.0040	±0.0032	±0.0041
Weight	0.13	0.17	0.09

	B_{T}	B_{W}	y_{23}	Weighted mean
$\alpha_{\mathrm{S}}(207 \text{ GeV})$	0.1126	0.1018	0.1064	0.1059
Statistical error	±0.0026	±0.0022	±0.0022	±0.0021
No MT algorithm	−0.0017*	−0.0006*	−0.0017*	−0.0009*
HERWIG det. corr.	−0.0004*	−0.0003*	−0.0009*	−0.0005*
$\cos(\theta_{\mathrm{T}}) < 0.7$	+0.0003*	+0.0017*	+0.0010*	+0.0008*
Alternative $\sqrt{s'}$	−0.0011*	−0.0009*	−0.0006*	−0.0008*
$L_{\mathrm{qqqq}} < 0.10$	−0.0008	+0.0007*	+0.0005	+0.0002
$L_{\mathrm{qqqq}} < 0.40$	+0.0021*	0.0000	+0.0008*	+0.0007*
$L_{\mathrm{qq}\ell\nu} < 0.25$	−0.0003*	−0.0003*	−0.0001	−0.0002*
$L_{\mathrm{qq}\ell\nu} < 0.75$	0.0000	0.0000	−0.0002*	−0.0001
Background +5%	−0.0001*	−0.0002*	−0.0001*	−0.0002*
Background −5%	+0.0001	+0.0002	+0.0001	+0.0001
Experimental syst.	±0.0030	±0.0022	±0.0024	±0.0018
HERWIG hadr. corr.	−0.0007	−0.0001	−0.0002	+0.0002
ARIADNE hadr. corr.	+0.0012*	+0.0006*	−0.0002*	+0.0008*
Hadronisation error	±0.0012	±0.0006	±0.0002	±0.0008
Upper uncertainty band	+0.0049	+0.0039	+0.0019	+0.0034
Lower uncertainty band	−0.0047	−0.0040	−0.0021	−0.0034
Theory error	±0.0048	±0.0039	±0.0020	±0.0034
Weight	0.17	0.09	0.36	−

Table C.12: OPAL measurements of α_S at $\sqrt{s} = 207$ GeV
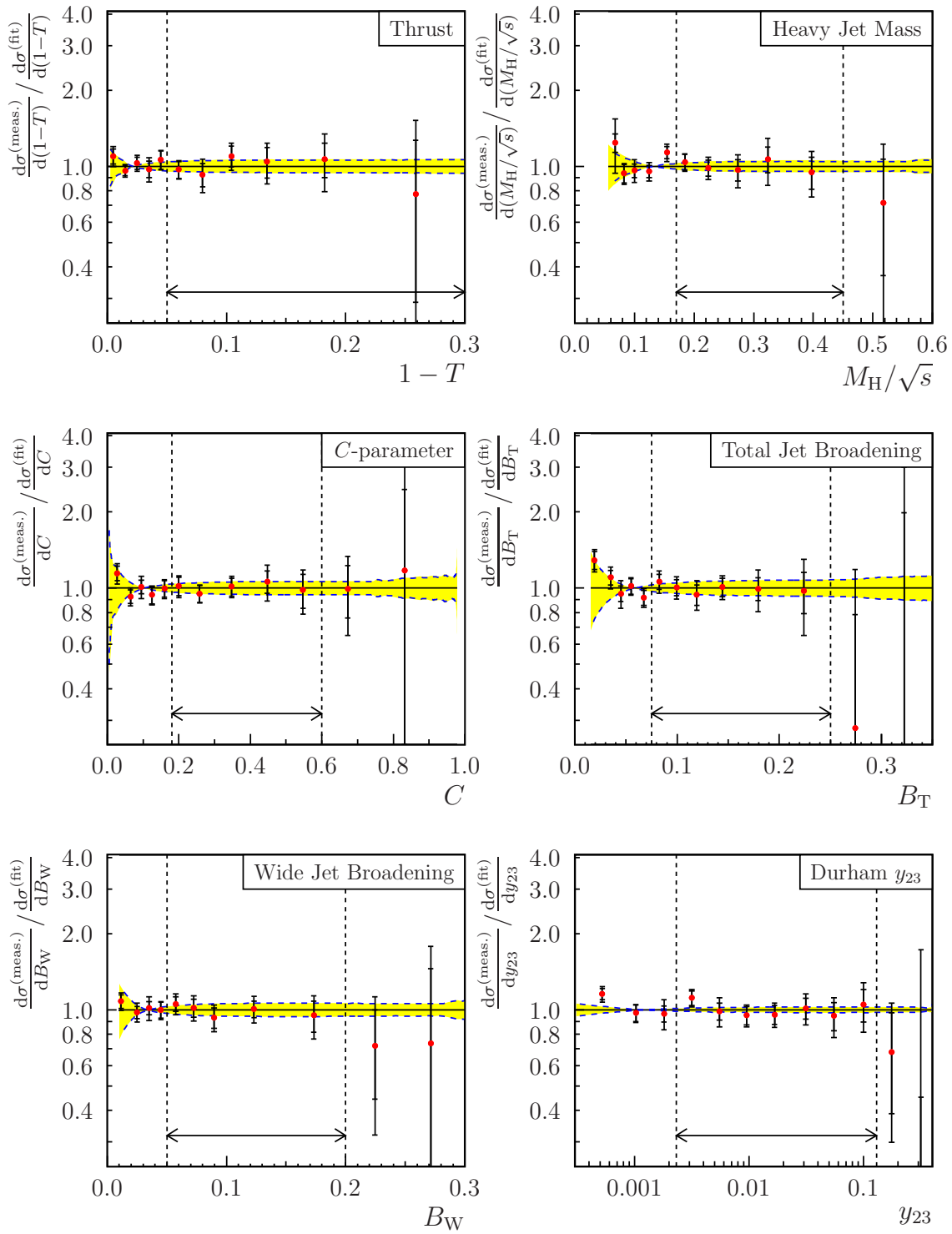
Figure C.12: Ratios of measured event shape distributions to hadron-level predictions, at $\sqrt{s} = 207$ GeV. An explanation is given in the introduction to this appendix, on page 283.

Appendix D

Inputs to the combined LEP α_S measurement

This appendix contains the α_S measurements from the four LEP Collaborations, which contribute to the combination discussed in Chapter 4.

The statistical uncertainties $\sigma_{\text{stat.}}$, and experimental systematic uncertainties $\sigma_{\text{exp.}}$, listed in these tables are the values quoted by the Collaborations. The experimental uncertainties will be averaged between Collaborations in the construction of the covariance matrix. The hadronisation and theory uncertainties given in the tables are the values calculated independently for the LEP combination, as described in Section 4.4.1. The total systematic uncertainties $\sigma_{\text{syst.}}$, and total uncertainties $\sigma_{\text{total.}}$, which do not enter directly into the combination algorithm, have been evaluated after symmetrisation of the theory uncertainties.

Where an asterisk ($*$) appears next to a measurement, the values have not been derived from a single fit to an event shape distribution. Instead, a number of published or preliminary results from neighbouring energy scales have been combined, in order to standardise the energy scales of the input measurements. These 'pre-combinations' were carried out using weights based only on statistical uncertainties, and assuming full correlation between all systematic uncertainties.

The OPAL measurements given in Section D.4 are not the latest results presented in Chapter 3. The LEP α_S combination uses the most recent preliminary results approved by the Collaborations, which in the case of OPAL were presented in Refs. [124, 127].

D.1   Fits to ALEPH data

Thrust, T

Q (GeV)	$\alpha_S(Q) \pm \sigma_{\text{stat.}} \pm \sigma_{\text{exp.}} \pm \sigma_{\text{hadr.}} \quad\quad \pm \sigma_{\text{theo.}}$	$\sigma_{\text{syst.}}$	σ_{total}
91.2	$0.1264 \pm 0.0001 \pm 0.0008 \pm 0.0015 +0.0056/-0.0054$	0.0058	0.0058
133.0	$0.1208 \pm 0.0039 \pm 0.0011 \pm 0.0006 +0.0048/-0.0047$	0.0049	0.0063
161.0	$0.1222 \pm 0.0063 \pm 0.0011 \pm 0.0005 +0.0044/-0.0043$	0.0045	0.0078
172.0	$0.1113 \pm 0.0074 \pm 0.0011 \pm 0.0005 +0.0043/-0.0043$	0.0044	0.0086
183.0	$0.1130 \pm 0.0037 \pm 0.0012 \pm 0.0005 +0.0042/-0.0042$	0.0044	0.0057
189.0	$0.1164 \pm 0.0020 \pm 0.0011 \pm 0.0004 +0.0041/-0.0041$	0.0043	0.0047
200.0	$0.1114 \pm 0.0021 \pm 0.0011 \pm 0.0004 +0.0040/-0.0040$	0.0042	0.0047
206.0	$0.1088 \pm 0.0021 \pm 0.0011 \pm 0.0004 +0.0040/-0.0040$	0.0042	0.0047

Heavy jet mass, M_{H}

Q (GeV)	$\alpha_S(Q) \pm \sigma_{\text{stat.}} \pm \sigma_{\text{exp.}} \pm \sigma_{\text{hadr.}} \quad\quad \pm \sigma_{\text{theo.}}$	$\sigma_{\text{syst.}}$	σ_{total}
91.2	$0.1187 \pm 0.0002 \pm 0.0009 \pm 0.0015 +0.0044/-0.0044$	0.0047	0.0047
133.0	$0.1154 \pm 0.0049 \pm 0.0011 \pm 0.0010 +0.0037/-0.0038$	0.0040	0.0063
161.0	$0.1185 \pm 0.0080 \pm 0.0011 \pm 0.0009 +0.0034/-0.0035$	0.0037	0.0088
172.0	$0.1071 \pm 0.0081 \pm 0.0011 \pm 0.0008 +0.0033/-0.0034$	0.0036	0.0089
183.0	$0.1087 \pm 0.0039 \pm 0.0011 \pm 0.0007 +0.0032/-0.0034$	0.0036	0.0053
189.0	$0.1097 \pm 0.0027 \pm 0.0012 \pm 0.0007 +0.0032/-0.0033$	0.0035	0.0045
200.0	$0.1038 \pm 0.0031 \pm 0.0018 \pm 0.0007 +0.0031/-0.0033$	0.0037	0.0048
206.0	$0.1059 \pm 0.0029 \pm 0.0011 \pm 0.0007 +0.0031/-0.0032$	0.0034	0.0045

Total jet broadening, B_{T}

Q (GeV)	$\alpha_S(Q) \pm \sigma_{\text{stat.}} \pm \sigma_{\text{exp.}} \pm \sigma_{\text{hadr.}} \quad\quad \pm \sigma_{\text{theo.}}$	$\sigma_{\text{syst.}}$	σ_{total}
91.2	$0.1260 \pm 0.0001 \pm 0.0007 \pm 0.0016 +0.0068/-0.0062$	0.0067	0.0067
133.0	$0.1183 \pm 0.0029 \pm 0.0015 \pm 0.0008 +0.0058/-0.0054$	0.0059	0.0065
161.0	$0.1081 \pm 0.0046 \pm 0.0016 \pm 0.0007 +0.0054/-0.0051$	0.0055	0.0072
172.0	$0.1144 \pm 0.0067 \pm 0.0016 \pm 0.0006 +0.0053/-0.0050$	0.0054	0.0086
183.0	$0.1141 \pm 0.0031 \pm 0.0016 \pm 0.0005 +0.0052/-0.0048$	0.0053	0.0061
189.0	$0.1148 \pm 0.0020 \pm 0.0017 \pm 0.0005 +0.0051/-0.0048$	0.0052	0.0056
200.0	$0.1141 \pm 0.0021 \pm 0.0016 \pm 0.0005 +0.0049/-0.0047$	0.0051	0.0055
206.0	$0.1078 \pm 0.0021 \pm 0.0015 \pm 0.0005 +0.0049/-0.0047$	0.0050	0.0055

Wide jet broadening, B_{W}

Q (GeV)	$\alpha_{\mathrm{S}}(Q) \pm \sigma_{\mathrm{stat.}} \pm \sigma_{\mathrm{exp.}} \pm \sigma_{\mathrm{hadr.}} \pm \sigma_{\mathrm{theo.}}$	$\sigma_{\mathrm{syst.}}$	σ_{total}
91.2	$0.1163 \pm 0.0002 \pm 0.0006 \pm 0.0006 +0.0054/-0.0054$	0.0055	0.0055
133.0	$0.1157 \pm 0.0032 \pm 0.0005 \pm 0.0004 +0.0046/-0.0047$	0.0047	0.0057
161.0	$0.1103 \pm 0.0054 \pm 0.0005 \pm 0.0003 +0.0043/-0.0044$	0.0044	0.0069
172.0	$0.1060 \pm 0.0066 \pm 0.0006 \pm 0.0002 +0.0041/-0.0043$	0.0043	0.0079
183.0	$0.1054 \pm 0.0030 \pm 0.0005 \pm 0.0002 +0.0040/-0.0042$	0.0042	0.0051
189.0	$0.1066 \pm 0.0018 \pm 0.0005 \pm 0.0002 +0.0040/-0.0042$	0.0041	0.0045
200.0	$0.1039 \pm 0.0019 \pm 0.0005 \pm 0.0002 +0.0039/-0.0041$	0.0040	0.0045
206.0	$0.1028 \pm 0.0019 \pm 0.0005 \pm 0.0002 +0.0039/-0.0040$	0.0040	0.0044

C-parameter

Q (GeV)	$\alpha_{\mathrm{S}}(Q) \pm \sigma_{\mathrm{stat.}} \pm \sigma_{\mathrm{exp.}} \pm \sigma_{\mathrm{hadr.}} \pm \sigma_{\mathrm{theo.}}$	$\sigma_{\mathrm{syst.}}$	σ_{total}
91.2	$0.1225 \pm 0.0001 \pm 0.0007 \pm 0.0012 +0.0057/-0.0054$	0.0057	0.0057
133.0	$0.1182 \pm 0.0035 \pm 0.0011 \pm 0.0005 +0.0049/-0.0045$	0.0048	0.0060
161.0	$0.1173 \pm 0.0056 \pm 0.0011 \pm 0.0005 +0.0045/-0.0042$	0.0045	0.0072
172.0	$0.1092 \pm 0.0063 \pm 0.0011 \pm 0.0004 +0.0044/-0.0041$	0.0044	0.0077
183.0	$0.1073 \pm 0.0038 \pm 0.0013 \pm 0.0004 +0.0043/-0.0042$	0.0045	0.0059
189.0	$0.1123 \pm 0.0022 \pm 0.0011 \pm 0.0004 +0.0042/-0.0042$	0.0044	0.0049
200.0	$0.1113 \pm 0.0024 \pm 0.0011 \pm 0.0003 +0.0041/-0.0041$	0.0043	0.0049
206.0	$0.1052 \pm 0.0023 \pm 0.0011 \pm 0.0004 +0.0041/-0.0041$	0.0042	0.0048

Durham y_{23} parameter

Q (GeV)	$\alpha_{\mathrm{S}}(Q) \pm \sigma_{\mathrm{stat.}} \pm \sigma_{\mathrm{exp.}} \pm \sigma_{\mathrm{hadr.}} \pm \sigma_{\mathrm{theo.}}$	$\sigma_{\mathrm{syst.}}$	σ_{total}
91.2	$0.1180 \pm 0.0002 \pm 0.0010 \pm 0.0007 +0.0028/-0.0030$	0.0031	0.0031
133.0	$0.1177 \pm 0.0046 \pm 0.0010 \pm 0.0004 +0.0022/-0.0029$	0.0028	0.0054
161.0	$0.1127 \pm 0.0072 \pm 0.0010 \pm 0.0002 +0.0021/-0.0028$	0.0026	0.0077
172.0	$0.1080 \pm 0.0083 \pm 0.0011 \pm 0.0002 +0.0020/-0.0027$	0.0026	0.0087
183.0	$0.1060 \pm 0.0037 \pm 0.0011 \pm 0.0002 +0.0020/-0.0026$	0.0026	0.0045
189.0	$0.1075 \pm 0.0023 \pm 0.0010 \pm 0.0002 +0.0020/-0.0026$	0.0025	0.0034
200.0	$0.1088 \pm 0.0022 \pm 0.0010 \pm 0.0002 +0.0019/-0.0026$	0.0025	0.0033
206.0	$0.1024 \pm 0.0023 \pm 0.0010 \pm 0.0002 +0.0019/-0.0026$	0.0025	0.0034

D.2   Fits to DELPHI data

Thrust, T

Q (GeV)	$\alpha_S(Q) \pm \sigma_{\text{stat.}} \pm \sigma_{\text{exp.}} \pm \sigma_{\text{hadr.}} \qquad \pm \sigma_{\text{theo.}}$	$\sigma_{\text{syst.}}$	σ_{total}
91.2	$0.1256 \pm 0.0001 \pm 0.0012 \pm 0.0020 +0.0056/-0.0054$	0.0060	0.0060
133.0	$0.1155 \pm 0.0044 \pm 0.0012 \pm 0.0014 +0.0048/-0.0047$	0.0051	0.0067
161.0	$0.1142 \pm 0.0068 \pm 0.0010 \pm 0.0008 +0.0044/-0.0043$	0.0046	0.0082
172.0	$0.1058 \pm 0.0085 \pm 0.0009 \pm 0.0011 +0.0043/-0.0043$	0.0045	0.0096
183.0	$0.1071 \pm 0.0043 \pm 0.0022 \pm 0.0009 +0.0042/-0.0042$	0.0048	0.0065
∗ 189.0	$0.1109 \pm 0.0024 \pm 0.0024 \pm 0.0000 +0.0041/-0.0041$	0.0048	0.0053
∗ 200.0	$0.1091 \pm 0.0027 \pm 0.0027 \pm 0.0000 +0.0040/-0.0040$	0.0049	0.0055
∗ 206.0	$0.1085 \pm 0.0027 \pm 0.0030 \pm 0.0002 +0.0040/-0.0040$	0.0050	0.0057

Heavy jet mass, M_{H}

Q (GeV)	$\alpha_S(Q) \pm \sigma_{\text{stat.}} \pm \sigma_{\text{exp.}} \pm \sigma_{\text{hadr.}} \qquad \pm \sigma_{\text{theo.}}$	$\sigma_{\text{syst.}}$	σ_{total}
91.2	$0.1230 \pm 0.0002 \pm 0.0019 \pm 0.0009 +0.0044/-0.0044$	0.0049	0.0049
133.0	$0.1117 \pm 0.0042 \pm 0.0011 \pm 0.0012 +0.0037/-0.0038$	0.0041	0.0059
161.0	$0.1122 \pm 0.0068 \pm 0.0009 \pm 0.0010 +0.0034/-0.0035$	0.0037	0.0077
172.0	$0.1114 \pm 0.0080 \pm 0.0009 \pm 0.0008 +0.0033/-0.0034$	0.0036	0.0088
183.0	$0.1094 \pm 0.0037 \pm 0.0024 \pm 0.0013 +0.0032/-0.0034$	0.0043	0.0057
∗ 189.0	$0.1080 \pm 0.0025 \pm 0.0024 \pm 0.0013 +0.0032/-0.0033$	0.0042	0.0049
∗ 200.0	$0.1060 \pm 0.0023 \pm 0.0025 \pm 0.0012 +0.0031/-0.0033$	0.0043	0.0049
∗ 206.0	$0.1052 \pm 0.0025 \pm 0.0026 \pm 0.0011 +0.0031/-0.0032$	0.0043	0.0049

Total jet broadening, B_{T}

Q (GeV)	$\alpha_S(Q) \pm \sigma_{\text{stat.}} \pm \sigma_{\text{exp.}} \pm \sigma_{\text{hadr.}} \qquad \pm \sigma_{\text{theo.}}$	$\sigma_{\text{syst.}}$	σ_{total}
91.2	$0.1219 \pm 0.0001 \pm 0.0019 \pm 0.0014 +0.0068/-0.0062$	0.0069	0.0069
183.0	$0.1119 \pm 0.0039 \pm 0.0012 \pm 0.0016 +0.0052/-0.0048$	0.0054	0.0067
∗ 189.0	$0.1125 \pm 0.0019 \pm 0.0012 \pm 0.0010 +0.0051/-0.0048$	0.0052	0.0055
∗ 200.0	$0.1120 \pm 0.0020 \pm 0.0012 \pm 0.0010 +0.0049/-0.0047$	0.0051	0.0055
∗ 206.0	$0.1121 \pm 0.0024 \pm 0.0012 \pm 0.0010 +0.0049/-0.0047$	0.0050	0.0056

Wide jet broadening, B_{W}

Q (GeV)	$\alpha_S(Q) \pm \sigma_{\mathrm{stat.}} \pm \sigma_{\mathrm{exp.}} \pm \sigma_{\mathrm{hadr.}} \pm \sigma_{\mathrm{theo.}}$	$\sigma_{\mathrm{syst.}}$	σ_{total}
91.2	$0.1156 \pm 0.0002 \pm 0.0021 \pm 0.0014 +0.0054/-0.0054$	0.0060	0.0060
183.0	$0.1049 \pm 0.0037 \pm 0.0026 \pm 0.0006 +0.0040/-0.0042$	0.0049	0.0061
* 189.0	$0.1035 \pm 0.0022 \pm 0.0028 \pm 0.0005 +0.0040/-0.0042$	0.0050	0.0054
* 200.0	$0.1037 \pm 0.0023 \pm 0.0030 \pm 0.0006 +0.0039/-0.0041$	0.0050	0.0056
* 206.0	$0.1025 \pm 0.0023 \pm 0.0033 \pm 0.0003 +0.0039/-0.0040$	0.0052	0.0057

C-parameter

Q (GeV)	$\alpha_S(Q) \pm \sigma_{\mathrm{stat.}} \pm \sigma_{\mathrm{exp.}} \pm \sigma_{\mathrm{hadr.}} \pm \sigma_{\mathrm{theo.}}$	$\sigma_{\mathrm{syst.}}$	σ_{total}
91.2	$0.1211 \pm 0.0001 \pm 0.0022 \pm 0.0014 +0.0057/-0.0054$	0.0061	0.0061
183.0	$0.1111 \pm 0.0036 \pm 0.0023 \pm 0.0011 +0.0043/-0.0042$	0.0049	0.0061
* 189.0	$0.1099 \pm 0.0021 \pm 0.0023 \pm 0.0011 +0.0042/-0.0042$	0.0049	0.0054
* 200.0	$0.1081 \pm 0.0023 \pm 0.0024 \pm 0.0010 +0.0041/-0.0041$	0.0049	0.0054
* 206.0	$0.1071 \pm 0.0021 \pm 0.0026 \pm 0.0010 +0.0041/-0.0041$	0.0049	0.0054

D.3   Fits to L3 data

Thrust, T

Q (GeV)	$\alpha_{\mathrm{S}}(Q) \pm \sigma_{\mathrm{stat.}} \pm \sigma_{\mathrm{exp.}} \pm \sigma_{\mathrm{hadr.}} \pm \sigma_{\mathrm{theo.}}$	$\sigma_{\mathrm{syst.}}$	σ_{total}
41.4	$0.1500 \pm 0.0054 \pm 0.0030 \pm 0.0068 +0.0082/-0.0077$	0.0109	0.0121
55.3	$0.1310 \pm 0.0052 \pm 0.0047 \pm 0.0094 +0.0071/-0.0067$	0.0126	0.0136
65.4	$0.1458 \pm 0.0036 \pm 0.0050 \pm 0.0070 +0.0065/-0.0063$	0.0107	0.0113
75.7	$0.1290 \pm 0.0029 \pm 0.0064 \pm 0.0069 +0.0061/-0.0059$	0.0112	0.0116
82.3	$0.1224 \pm 0.0036 \pm 0.0051 \pm 0.0064 +0.0059/-0.0057$	0.0100	0.0107
85.1	$0.1184 \pm 0.0051 \pm 0.0044 \pm 0.0062 +0.0058/-0.0056$	0.0095	0.0108
91.2	$0.1233 \pm 0.0009 \pm 0.0023 \pm 0.0040 +0.0056/-0.0054$	0.0072	0.0073
133.0	$0.1153 \pm 0.0029 \pm 0.0026 \pm 0.0030 +0.0048/-0.0047$	0.0062	0.0068
161.0	$0.1018 \pm 0.0051 \pm 0.0022 \pm 0.0028 +0.0044/-0.0043$	0.0056	0.0076
172.0	$0.1109 \pm 0.0055 \pm 0.0026 \pm 0.0025 +0.0043/-0.0043$	0.0056	0.0078
183.0	$0.1132 \pm 0.0023 \pm 0.0012 \pm 0.0024 +0.0042/-0.0042$	0.0050	0.0055
* 189.0	$0.1169 \pm 0.0013 \pm 0.0012 \pm 0.0022 +0.0041/-0.0041$	0.0048	0.0050
* 200.0	$0.1172 \pm 0.0014 \pm 0.0022 \pm 0.0021 +0.0040/-0.0040$	0.0050	0.0052
206.0	$0.1173 \pm 0.0014 \pm 0.0016 \pm 0.0021 +0.0040/-0.0040$	0.0048	0.0050

Heavy jet mass, M_{H}

Q (GeV)	$\alpha_{\mathrm{S}}(Q) \pm \sigma_{\mathrm{stat.}} \pm \sigma_{\mathrm{exp.}} \pm \sigma_{\mathrm{hadr.}} \pm \sigma_{\mathrm{theo.}}$	$\sigma_{\mathrm{syst.}}$	σ_{total}
41.4	$0.1440 \pm 0.0039 \pm 0.0021 \pm 0.0059 +0.0063/-0.0061$	0.0089	0.0097
55.3	$0.1280 \pm 0.0046 \pm 0.0047 \pm 0.0025 +0.0054/-0.0054$	0.0076	0.0089
65.4	$0.1397 \pm 0.0028 \pm 0.0030 \pm 0.0023 +0.0051/-0.0050$	0.0063	0.0069
75.7	$0.1226 \pm 0.0021 \pm 0.0045 \pm 0.0042 +0.0047/-0.0047$	0.0078	0.0081
82.3	$0.1189 \pm 0.0021 \pm 0.0024 \pm 0.0055 +0.0046/-0.0046$	0.0075	0.0078
85.1	$0.1114 \pm 0.0032 \pm 0.0053 \pm 0.0039 +0.0045/-0.0045$	0.0080	0.0086
91.2	$0.1228 \pm 0.0007 \pm 0.0011 \pm 0.0034 +0.0044/-0.0044$	0.0057	0.0057
133.0	$0.1123 \pm 0.0025 \pm 0.0021 \pm 0.0014 +0.0037/-0.0038$	0.0045	0.0052
161.0	$0.1012 \pm 0.0052 \pm 0.0022 \pm 0.0012 +0.0034/-0.0035$	0.0042	0.0067
172.0	$0.1099 \pm 0.0050 \pm 0.0016 \pm 0.0011 +0.0033/-0.0033$	0.0038	0.0063
183.0	$0.1075 \pm 0.0022 \pm 0.0011 \pm 0.0012 +0.0031/-0.0034$	0.0036	0.0042
* 189.0	$0.1107 \pm 0.0012 \pm 0.0011 \pm 0.0010 +0.0031/-0.0033$	0.0035	0.0037
* 200.0	$0.1105 \pm 0.0013 \pm 0.0022 \pm 0.0010 +0.0030/-0.0033$	0.0040	0.0042
206.0	$0.1119 \pm 0.0013 \pm 0.0014 \pm 0.0008 +0.0030/-0.0032$	0.0035	0.0037

Total jet broadening, B_{T}

Q (GeV)	$\alpha_{\mathrm{S}}(Q) \pm \sigma_{\mathrm{stat.}} \pm \sigma_{\mathrm{exp.}} \pm \sigma_{\mathrm{hadr.}} \pm \sigma_{\mathrm{theo.}}$	$\sigma_{\mathrm{syst.}}$	σ_{total}
41.4	$0.1401 \pm 0.0057 \pm 0.0027 \pm 0.0041 +0.0096/-0.0083$	0.0102	0.0117
55.3	$0.1321 \pm 0.0045 \pm 0.0053 \pm 0.0043 +0.0084/-0.0075$	0.0104	0.0114
65.4	$0.1354 \pm 0.0029 \pm 0.0060 \pm 0.0050 +0.0078/-0.0070$	0.0108	0.0111
75.7	$0.1296 \pm 0.0020 \pm 0.0071 \pm 0.0049 +0.0073/-0.0067$	0.0111	0.0113
82.3	$0.1270 \pm 0.0022 \pm 0.0076 \pm 0.0045 +0.0070/-0.0065$	0.0111	0.0113
85.1	$0.1259 \pm 0.0027 \pm 0.0063 \pm 0.0051 +0.0070/-0.0064$	0.0105	0.0108
91.2	$0.1222 \pm 0.0007 \pm 0.0019 \pm 0.0030 +0.0068/-0.0062$	0.0074	0.0074
133.0	$0.1172 \pm 0.0023 \pm 0.0013 \pm 0.0024 +0.0058/-0.0054$	0.0062	0.0067
161.0	$0.1123 \pm 0.0041 \pm 0.0015 \pm 0.0023 +0.0054/-0.0051$	0.0059	0.0072
172.0	$0.1092 \pm 0.0044 \pm 0.0044 \pm 0.0023 +0.0053/-0.0050$	0.0071	0.0084
183.0	$0.1134 \pm 0.0018 \pm 0.0013 \pm 0.0022 +0.0052/-0.0048$	0.0056	0.0059
* 189.0	$0.1140 \pm 0.0011 \pm 0.0014 \pm 0.0021 +0.0051/-0.0048$	0.0055	0.0057
* 200.0	$0.1157 \pm 0.0011 \pm 0.0017 \pm 0.0023 +0.0049/-0.0047$	0.0056	0.0057
206.0	$0.1163 \pm 0.0012 \pm 0.0017 \pm 0.0022 +0.0049/-0.0047$	0.0055	0.0057

Wide jet broadening, B_{W}

Q (GeV)	$\alpha_{\mathrm{S}}(Q) \pm \sigma_{\mathrm{stat.}} \pm \sigma_{\mathrm{exp.}} \pm \sigma_{\mathrm{hadr.}} \pm \sigma_{\mathrm{theo.}}$	$\sigma_{\mathrm{syst.}}$	σ_{total}
41.4	$0.1380 \pm 0.0056 \pm 0.0037 \pm 0.0018 +0.0077/-0.0074$	0.0086	0.0103
55.3	$0.1191 \pm 0.0046 \pm 0.0056 \pm 0.0036 +0.0067/-0.0066$	0.0094	0.0105
65.4	$0.1190 \pm 0.0032 \pm 0.0053 \pm 0.0035 +0.0063/-0.0062$	0.0089	0.0095
75.7	$0.1068 \pm 0.0024 \pm 0.0060 \pm 0.0033 +0.0059/-0.0058$	0.0090	0.0093
82.3	$0.1083 \pm 0.0030 \pm 0.0060 \pm 0.0028 +0.0057/-0.0056$	0.0087	0.0092
85.1	$0.1092 \pm 0.0036 \pm 0.0071 \pm 0.0033 +0.0056/-0.0055$	0.0096	0.0103
91.2	$0.1196 \pm 0.0013 \pm 0.0018 \pm 0.0020 +0.0054/-0.0054$	0.0060	0.0062
133.0	$0.1081 \pm 0.0021 \pm 0.0022 \pm 0.0021 +0.0046/-0.0047$	0.0056	0.0059
161.0	$0.1058 \pm 0.0041 \pm 0.0044 \pm 0.0013 +0.0043/-0.0044$	0.0063	0.0075
172.0	$0.1045 \pm 0.0041 \pm 0.0022 \pm 0.0013 +0.0041/-0.0043$	0.0049	0.0064
183.0	$0.1063 \pm 0.0015 \pm 0.0006 \pm 0.0009 +0.0040/-0.0042$	0.0043	0.0045
* 189.0	$0.1062 \pm 0.0010 \pm 0.0012 \pm 0.0011 +0.0040/-0.0042$	0.0044	0.0045
* 200.0	$0.1079 \pm 0.0013 \pm 0.0014 \pm 0.0012 +0.0039/-0.0041$	0.0044	0.0046
206.0	$0.1077 \pm 0.0014 \pm 0.0013 \pm 0.0010 +0.0039/-0.0040$	0.0043	0.0045

C-parameter

Q (GeV)	$\alpha_{\mathrm{S}}(Q) \pm \sigma_{\mathrm{stat.}} \pm \sigma_{\mathrm{exp.}} \pm \sigma_{\mathrm{hadr.}} \pm \sigma_{\mathrm{theo.}}$	$\sigma_{\mathrm{syst.}}$	σ_{total}
41.4	$0.1371 \pm 0.0061 \pm 0.0034 \pm 0.0047 +0.0082/-0.0074$	0.0098	0.0115
55.3	$0.1197 \pm 0.0046 \pm 0.0073 \pm 0.0091 +0.0072/-0.0065$	0.0135	0.0143
65.4	$0.1258 \pm 0.0035 \pm 0.0018 \pm 0.0079 +0.0066/-0.0061$	0.0103	0.0108
75.7	$0.1143 \pm 0.0027 \pm 0.0067 \pm 0.0072 +0.0062/-0.0057$	0.0115	0.0118
82.3	$0.1153 \pm 0.0029 \pm 0.0052 \pm 0.0073 +0.0060/-0.0056$	0.0106	0.0110
85.1	$0.1115 \pm 0.0038 \pm 0.0024 \pm 0.0073 +0.0059/-0.0055$	0.0095	0.0103
91.2	$0.1170 \pm 0.0002 \pm 0.0016 \pm 0.0053 +0.0057/-0.0054$	0.0079	0.0079
133.0	$0.1120 \pm 0.0028 \pm 0.0019 \pm 0.0054 +0.0049/-0.0047$	0.0075	0.0080
161.0	$0.1043 \pm 0.0055 \pm 0.0025 \pm 0.0038 +0.0045/-0.0044$	0.0064	0.0084
172.0	$0.1121 \pm 0.0064 \pm 0.0024 \pm 0.0031 +0.0044/-0.0043$	0.0058	0.0086
183.0	$0.1081 \pm 0.0028 \pm 0.0010 \pm 0.0029 +0.0043/-0.0042$	0.0053	0.0060
* 189.0	$0.1120 \pm 0.0017 \pm 0.0015 \pm 0.0026 +0.0042/-0.0042$	0.0052	0.0055
* 200.0	$0.1138 \pm 0.0018 \pm 0.0019 \pm 0.0024 +0.0041/-0.0041$	0.0051	0.0054
206.0	$0.1130 \pm 0.0019 \pm 0.0021 \pm 0.0022 +0.0041/-0.0041$	0.0051	0.0054

D.4   Fits to OPAL data

Thrust, T

Q (GeV)	$\alpha_S(Q) \pm \sigma_{stat.} \pm \sigma_{exp.} \pm \sigma_{hadr.} \quad \pm \sigma_{theo.}$	$\sigma_{syst.}$	σ_{total}
91.2	$0.1207 \pm 0.0005 \pm 0.0024 \pm 0.0021 +0.0056/-0.0054$	0.0064	0.0064
133.0	$0.1203 \pm 0.0074 \pm 0.0027 \pm 0.0009 +0.0048/-0.0047$	0.0055	0.0092
161.0	$0.1063 \pm 0.0068 \pm 0.0066 \pm 0.0009 +0.0044/-0.0043$	0.0080	0.0105
172.0	$0.1000 \pm 0.0094 \pm 0.0128 \pm 0.0008 +0.0043/-0.0043$	0.0135	0.0165
183.0	$0.1071 \pm 0.0032 \pm 0.0034 \pm 0.0007 +0.0042/-0.0042$	0.0054	0.0063
$*$ 189.0	$0.1119 \pm 0.0015 \pm 0.0017 \pm 0.0006 +0.0041/-0.0041$	0.0045	0.0047
$*$ 200.0	$0.1073 \pm 0.0024 \pm 0.0033 \pm 0.0007 +0.0040/-0.0040$	0.0053	0.0058
$*$ 206.0	$0.1083 \pm 0.0022 \pm 0.0032 \pm 0.0006 +0.0040/-0.0040$	0.0051	0.0056

Heavy jet mass, M_H

Q (GeV)	$\alpha_S(Q) \pm \sigma_{stat.} \pm \sigma_{exp.} \pm \sigma_{hadr.} \quad \pm \sigma_{theo.}$	$\sigma_{syst.}$	σ_{total}
91.2	$0.1192 \pm 0.0005 \pm 0.0017 \pm 0.0012 +0.0044/-0.0044$	0.0049	0.0049
133.0	$0.1121 \pm 0.0071 \pm 0.0069 \pm 0.0005 +0.0037/-0.0038$	0.0079	0.0106
161.0	$0.1045 \pm 0.0068 \pm 0.0073 \pm 0.0003 +0.0034/-0.0035$	0.0081	0.0106
172.0	$0.0912 \pm 0.0083 \pm 0.0083 \pm 0.0004 +0.0033/-0.0034$	0.0090	0.0122
183.0	$0.1075 \pm 0.0036 \pm 0.0028 \pm 0.0003 +0.0032/-0.0034$	0.0043	0.0056
$*$ 189.0	$0.1051 \pm 0.0016 \pm 0.0026 \pm 0.0003 +0.0032/-0.0033$	0.0042	0.0045
$*$ 200.0	$0.1017 \pm 0.0022 \pm 0.0065 \pm 0.0003 +0.0031/-0.0033$	0.0072	0.0076
$*$ 206.0	$0.1047 \pm 0.0021 \pm 0.0030 \pm 0.0004 +0.0031/-0.0032$	0.0044	0.0048

Total jet broadening, B_T

Q (GeV)	$\alpha_S(Q) \pm \sigma_{stat.} \pm \sigma_{exp.} \pm \sigma_{hadr.} \quad \pm \sigma_{theo.}$	$\sigma_{syst.}$	σ_{total}
91.2	$0.1219 \pm 0.0005 \pm 0.0034 \pm 0.0042 +0.0068/-0.0062$	0.0085	0.0085
133.0	$0.1132 \pm 0.0059 \pm 0.0086 \pm 0.0013 +0.0058/-0.0054$	0.0103	0.0119
161.0	$0.1038 \pm 0.0053 \pm 0.0089 \pm 0.0013 +0.0054/-0.0051$	0.0104	0.0117
172.0	$0.0932 \pm 0.0076 \pm 0.0087 \pm 0.0013 +0.0053/-0.0050$	0.0102	0.0127
183.0	$0.1075 \pm 0.0029 \pm 0.0043 \pm 0.0008 +0.0052/-0.0048$	0.0066	0.0073
$*$ 189.0	$0.1091 \pm 0.0013 \pm 0.0039 \pm 0.0008 +0.0051/-0.0048$	0.0063	0.0065
$*$ 200.0	$0.1063 \pm 0.0020 \pm 0.0029 \pm 0.0008 +0.0049/-0.0047$	0.0057	0.0060
$*$ 206.0	$0.1109 \pm 0.0021 \pm 0.0028 \pm 0.0007 +0.0049/-0.0047$	0.0056	0.0060

Wide jet broadening, B_{W}

Q (GeV)	$\alpha_{\mathrm{S}}(Q) \pm \sigma_{\mathrm{stat.}} \pm \sigma_{\mathrm{exp.}} \pm \sigma_{\mathrm{hadr.}} \quad\quad \pm \sigma_{\mathrm{theo.}}$	$\sigma_{\mathrm{syst.}}$	σ_{total}
91.2	$0.1133 \pm 0.0004 \pm 0.0027 \pm 0.0009 +0.0054/-0.0054$	0.0061	0.0061
133.0	$0.1049 \pm 0.0043 \pm 0.0066 \pm 0.0006 +0.0046/-0.0047$	0.0081	0.0092
161.0	$0.0928 \pm 0.0045 \pm 0.0091 \pm 0.0005 +0.0043/-0.0044$	0.0101	0.0110
172.0	$0.0924 \pm 0.0061 \pm 0.0062 \pm 0.0005 +0.0041/-0.0043$	0.0075	0.0097
183.0	$0.1030 \pm 0.0025 \pm 0.0021 \pm 0.0004 +0.0040/-0.0042$	0.0046	0.0053
$*$ 189.0	$0.1035 \pm 0.0012 \pm 0.0017 \pm 0.0003 +0.0040/-0.0042$	0.0044	0.0046
$*$ 200.0	$0.1001 \pm 0.0017 \pm 0.0021 \pm 0.0004 +0.0039/-0.0041$	0.0045	0.0048
$*$ 206.0	$0.1042 \pm 0.0017 \pm 0.0013 \pm 0.0003 +0.0039/-0.0040$	0.0042	0.0045

C-parameter

Q (GeV)	$\alpha_{\mathrm{S}}(Q) \pm \sigma_{\mathrm{stat.}} \pm \sigma_{\mathrm{exp.}} \pm \sigma_{\mathrm{hadr.}} \quad\quad \pm \sigma_{\mathrm{theo.}}$	$\sigma_{\mathrm{syst.}}$	σ_{total}
172.0	$0.0906 \pm 0.0095 \pm 0.0095 \pm 0.0011 +0.0044/-0.0043$	0.0105	0.0142
183.0	$0.1074 \pm 0.0039 \pm 0.0036 \pm 0.0007 +0.0043/-0.0042$	0.0056	0.0068
$*$ 189.0	$0.1065 \pm 0.0017 \pm 0.0023 \pm 0.0006 +0.0042/-0.0042$	0.0048	0.0051
$*$ 200.0	$0.1026 \pm 0.0022 \pm 0.0043 \pm 0.0007 +0.0041/-0.0041$	0.0060	0.0064
$*$ 206.0	$0.1063 \pm 0.0024 \pm 0.0026 \pm 0.0007 +0.0041/-0.0041$	0.0049	0.0054

Durham y_{23} parameter

Q (GeV)	$\alpha_{\mathrm{S}}(Q) \pm \sigma_{\mathrm{stat.}} \pm \sigma_{\mathrm{exp.}} \pm \sigma_{\mathrm{hadr.}} \quad\quad \pm \sigma_{\mathrm{theo.}}$	$\sigma_{\mathrm{syst.}}$	σ_{total}
91.2	$0.1162 \pm 0.0005 \pm 0.0042 \pm 0.0005 +0.0028/-0.0030$	0.0051	0.0051
133.0	$0.1054 \pm 0.0045 \pm 0.0098 \pm 0.0006 +0.0022/-0.0026$	0.0101	0.0111
161.0	$0.1041 \pm 0.0054 \pm 0.0066 \pm 0.0006 +0.0021/-0.0024$	0.0070	0.0088
172.0	$0.0957 \pm 0.0073 \pm 0.0151 \pm 0.0007 +0.0020/-0.0023$	0.0153	0.0169
183.0	$0.1047 \pm 0.0032 \pm 0.0022 \pm 0.0004 +0.0020/-0.0022$	0.0031	0.0045
$*$ 189.0	$0.1063 \pm 0.0016 \pm 0.0035 \pm 0.0005 +0.0020/-0.0022$	0.0041	0.0044
$*$ 200.0	$0.1041 \pm 0.0019 \pm 0.0033 \pm 0.0004 +0.0019/-0.0022$	0.0039	0.0043
$*$ 206.0	$0.1086 \pm 0.0019 \pm 0.0015 \pm 0.0004 +0.0019/-0.0021$	0.0025	0.0032

Bibliography

[1] O. W. Greenberg, *Spin and unitary spin independence in a paraquark model of baryons and mesons*, Phys. Rev. Lett. **13** (1964) 598.

[2] H. Fritzsch and M. Gell-Mann, *Current algebra: Quarks and what else?*, Proceedings of the 16th International Conference on High Energy Physics, Chicago, IL, USA, 6–13 Sept 1972, Vol. 2, 135.
E-print number: `hep-ph/0208010`.

[3] D. J. Gross and F. Wilczek, *Ultraviolet behaviour of non-Abelian gauge theories*, Phys. Rev. Lett. **30** (1973) 1343.

[4] R. K. Ellis, W. J. Stirling, and B. R. Webber, *QCD and Collider Physics*. Cambridge, UK: CUP (1998).

[5] G. von Dardel et al., *Mean life of the neutral pion*, Phys. Lett. **4** (1963) 51.

[6] ALEPH, DELPHI, L3 and OPAL Collaborations, *A combination of preliminary electroweak measurements and constraints on the standard model*. Report number: ALEPH-2003-017-PHYSICS-2003-005 / DELPHI-2003-072-PHYS-937 / L3-NOTE-2825 / OPAL-PR-392, E-print number: `hep-ex/0312023`.

[7] D. P. Barber et al., *Discovery of three jet events and a test of quantum chromodynamics at PETRA energies*, Phys. Rev. Lett. **43** (1979) 830.

[8] OPAL Collaboration (P. D. Acton et al.), *A Determination of $\alpha_S\left(M_{Z^0}\right)$ at LEP using resummed QCD calculations*, Z. Phys. **C59** (1993) 1.

[9] OPAL Collaboration (G. Alexander et al.), *QCD studies with e^+e^- annihilation data at 130 GeV and 136 GeV*, Z. Phys. **C72** (1996) 191.

[10] OPAL Collaboration (K. Ackerstaff et al.), *QCD studies with e^+e^- annihilation data at 161 GeV*, Z. Phys. **C75** (1997) 193.

[11] OPAL Collaboration (G. Abbiendi et al.), *QCD studies with e^+e^- annihilation data at 172–189 GeV*, Eur. Phys. J. **C16** (2000) 185. E-print number: `hep-ex/0002012`.

[12] R. W. L. Jones, M. Ford, G. P. Salam, H. Stenzel, and D. Wicke, *Theoretical uncertainties on α_S from event-shape variables in e^+e^- annihilations*, JHEP **12** (2003) 007. E-print number: `hep-ph/0312016`.

[13] Particle Data Group (K. Hagiwara et al.), *Review of particle physics*, Phys. Rev. **D66** (2002) 010001.

[14] B. R. Martin and G. Shaw, *Particle Physics.* Chichester, UK: Wiley (1997).

[15] I. J. R. Aitchison and A. J. G. Hey, *Gauge Theories in Particle Physics.* Bristol, UK: IOP (1989).

[16] C.-N. Yang and R. L. Mills, *Conservation of isotopic spin and isotopic gauge invariance*, Phys. Rev. **96** (1954) 191.

[17] R. K. Ellis, D. A. Ross, and A. E. Terrano, *The perturbative calculation of jet structure in e^+e^- annihilation*, Nucl. Phys. **B178** (1981) 421.

[18] S. Brandt, C. Peyrou, R. Sosnowski, and A. Wroblewski, *The principal axis of jets—an attempt to analyze high-energy collisions as two-body processes*, Phys. Lett. **12** (1964) 57.

[19] E. Farhi, *A QCD test for jets*, Phys. Rev. Lett. **39** (1977) 1587.

[20] G. Parisi, *Superinclusive cross sections*, Phys. Lett. **B74** (1978) 65.

[21] T. Sjöstrand, L. Lönnblad, and S. Mrenna, *PYTHIA 6.2: Physics and manual* (2001). E-print number: `hep-ph/0108264`.

[22] J. F. Donoghue, F. E. Low, and S.-Y. Pi, *Tensor analysis of hadronic jets in quantum chromodynamics*, Phys. Rev. **D20** (1979) 2759.

[23] G. C. Fox and S. Wolfram, *Event shapes in e^+e^- annihilation*, Nucl. Phys. **B149** (1979) 413.

[24] S. Catani, G. Turnock, and B. R. Webber, *Jet broadening measures in e^+e^- annihilation*, Phys. Lett. **B295** (1992) 269.

[25] S. Catani, Y. L. Dokshitzer, M. Olsson, G. Turnock, and B. R. Webber, *New clustering algorithm for multijet cross sections in e^+e^- annihilation*, Phys. Lett. **B269** (1991) 432.

[26] OPAL Collaboration (P. D. Acton et al.), *A global determination of $\alpha_S(M_{Z^0})$ at LEP*, Z. Phys. **C55** (1992) 1.

[27] JADE Collaboration (S. Bethke et al.), *Experimental investigation of the energy dependence of the strong coupling strength*, Phys. Lett. **B213** (1988) 235.

[28] S. G. Gorishnii, A. L. Kataev, and S. A. Larin, *The $\mathcal{O}(\alpha_S^3)$ corrections to $\sigma_{tot}(e^+e^- \to hadrons)$ and $\Gamma(\tau^- \to \nu_\tau + hadrons)$ in QCD*, Phys. Lett. **B259** (1991) 144.

[29] L. R. Surguladze and M. A. Samuel, *Total hadronic cross-section in e^+e^- annihilation at the four-loop level of perturbative QCD*, Presented at Beyond the Standard Model II Conf., Norman, OK, USA, 1–3 Nov 1990. Phys. Rev. Lett. **66** (1991) 560.

[30] S. Catani and M. H. Seymour, *The dipole formalism for the calculation of QCD jet cross sections at next-to-leading order*, Phys. Lett. **B378** (1996) 287. E-print number: `hep-ph/9602277`.

[31] G. Altarelli and G. Parisi, *Asymptotic freedom in parton language*, Nucl. Phys. **B126** (1977) 298.

[32] S. Catani, L. Trentadue, G. Turnock, and B. R. Webber, *Resummation of large logarithms in e^+e^- event shape distributions*, Nucl. Phys. **B407** (1993) 3.

[33] Yu. L. Dokshitzer et al., *On the QCD analysis of jet broadening*, JHEP **01** (1998) 011. E-print number: `hep-ph/9801324`.

[34] S. Catani and B. R. Webber, *Resummed C-parameter distribution in e^+e^- annihilation*, Phys. Lett. **B427** (1998) 377. E-print number: `hep-ph/9801350`.

[35] G. Dissertori and M. Schmelling, *An Improved theoretical prediction for the two-jet rate in e^+e^- annihilation*, Phys. Lett. **B361** (1995) 167.

[36] A. Banfi, G. P. Salam, and G. Zanderighi, *Semi-numerical resummation of event shapes*, JHEP **01** (2002) 018. E-print number: `hep-ph/0112156`.

[37] P. Nason and C. Oleari, *Next-to-leading-order corrections to the production of heavy-flavour jets in e^+e^- collisions*, Nucl. Phys. **B521** (1998) 237. E-print number: `hep-ph/9709360`.

[38] F. Krauss and G. Rodrigo, *Resummed jet rates for e^+e^- annihilation into massive quarks*, Phys. Lett. **B576** (2003) 135. E-print number: `hep-ph/0303038`.

[39] S. J. Burby and E. W. N. Glover, *Resumming the light hemisphere mass and narrow jet broadening distributions in e^+e^- annihilation*, JHEP **04** (2001) 029. E-print number: `hep-ph/0101226`.

[40] A. Banfi, Y. L. Dokshitzer, G. Marchesini, and G. Zanderighi, *QCD analysis of D-parameter in near-to-planar three-jet events*, JHEP **05** (2001) 040. E-print number: `hep-ph/0104162`.

[41] L. J. Dixon and A. Signer, *Complete $\mathcal{O}(\alpha_S^3)$ results for $e^+e^- \to (\gamma, Z) \to$ four jets*, Phys. Rev. **D56** (1997) 4031. E-print number: `hep-ph/9706285`.

[42] Z. Nagy and Z. Trócsányi, *Next-to-leading order calculation of four-jet observables in electron positron annihilation*, Phys. Rev. **D59** (1999) 014020. E-print number: `hep-ph/9806317`.

[43] S. Weinzierl and D. A. Kosower, *QCD corrections to four-jet production and three-jet structure in e^+e^- annihilation*, Phys. Rev. **D60** (1999) 054028. E-print number: `hep-ph/9901277`.

[44] J. M. Campbell, M. A. Cullen, and E. W. N. Glover, *Four jet event shapes in electron positron annihilation*, Eur. Phys. J. **C9** (1999) 245. E-print number: `hep-ph/9809429`.

[45] M. Dasgupta and G. P. Salam, *Resummed event-shape variables in DIS*, JHEP **08** (2002) 032. E-print number: `hep-ph/0208073`.

[46] S. Jadach, B. F. L. Ward, and Z. Was, *The precision Monte Carlo event generator KK for two-fermion final states in e^+e^- collisions*, Comput. Phys. Commun. **130** (2000) 260. E-print number: `hep-ph/9912214`.

[47] T. Sjöstrand et al., *High-energy-physics event generation with PYTHIA 6.1*, Comput. Phys. Commun. **135** (2001) 238. E-print number: `hep-ph/0010017`.

[48] G. Corcella et al., *HERWIG 6: An event generator for hadron emission reactions with interfering gluons (including supersymmetric processes)*, JHEP **01** (2001) 010. E-print number: `hep-ph/0011363`.

[49] L. Lönnblad, *ARIADNE version 4: A Program for simulation of QCD cascades implementing the color dipole model*, Comput. Phys. Commun. **71** (1992) 15.

[50] G. Gustafson, *Dual description of a confined color field*, Phys. Lett. **B175** (1986) 453.

[51] G. Gustafson and U. Pettersson, *Dipole formulation of QCD cascades*, Nucl. Phys. **B306** (1988) 746.

[52] B. Andersson, G. Gustafson, and B. Söderberg, *A general model for jet fragmentation*, Z. Phys. **C20** (1983) 317.

[53] B. R. Webber, *A QCD model for jet fragmentation including soft gluon interference*, Nucl. Phys. **B238** (1984) 492.

[54] D. Amati and G. Veneziano, *Preconfinement as a property of perturbative QCD*, Phys. Lett. **B83** (1979) 87.

[55] S. Bethke, α_S *2002*, Proceedings of the 9th High Energy Physics International Conference on Quantum ChromoDynamics ('QCD 02'), Montpellier, France, 2–9 July 2002, Nucl. Phys. Proc. Suppl. **121** (2003) 74. E-print number: `hep-ex/0211012`.

[56] OPAL Collaboration (K. Ackerstaff et al.), *Measurement of the strong coupling constant α_S and the vector and axial-vector spectral functions in hadronic τ decays*, Eur. Phys. J. **C7** (1999) 571. E-print number: `hep-ex/9808019`.

[57] JADE and OPAL Collaborations (P. Pfeifenschneider et al.), *QCD analyses and determinations of α_S in e^+e^- annihilation at energies between 35 GeV and 189 GeV*, Eur. Phys. J. **C17** (2000) 19.
E-print number: `hep-ex/0001055`.

[58] S. Albino, M. Klasen, and S. Söldner-Rembold, *Strong coupling constant from the photon structure function*, Phys. Rev. Lett. **89** (2002) 122004.
E-print number: `hep-ph/0205069`.

[59] B. A. Kniehl, G. Kramer, and B. Potter, *Strong coupling constant from scaling violations in fragmentation functions*,
Phys. Rev. Lett. **85** (2000) 5288. E-print number: `hep-ph/0003297`.

[60] Y. L. Dokshitzer and B. R. Webber, *Calculation of power corrections to hadronic event shapes*, Phys. Lett. **B352** (1995) 451.
E-print number: `hep-ph/9504219`.

[61] A. V. Manohar and M. B. Wise, *Power suppressed corrections to hadronic event shapes*, Phys. Lett. **B344** (1995) 407.
E-print number: `hep-ph/9406392`.

[62] R. Akhoury and V. I. Zakharov, *On the universality of the leading $1/Q$ power corrections in QCD*, Phys. Lett. **B357** (1995) 646.
E-print number: `hep-ph/9504248`.

[63] E. Gardi and G. Grunberg, *Power corrections in the single dressed gluon approximation: The average thrust as a case study*, JHEP **11** (1999) 016.
E-print number: `hep-ph/9908458`.

[64] E. Gardi, *Suppressed power corrections for moments of event-shape variables in e^+e^- annihilation*, JHEP **04** (2000) 030.
E-print number: `hep-ph/0003179`.

[65] G. P. Korchemsky and G. Sterman, *Nonperturbative corrections in resummed cross-sections*, Nucl. Phys. **B437** (1995) 415.
E-print number: `hep-ph/9411211`.

[66] DELPHI Collaboration (P. Abreu et al.), *Energy dependence of event shapes and of α_S at LEP2*, Phys. Lett. **B456** (1999) 322.

[67] A. D. Martin, R. G. Roberts, W. J. Stirling, and R. S. Thorne, *MRST2001: Partons and α_S from precise deep inelastic scattering and Tevatron jet data*, Eur. Phys. J. **C23** (2002) 73. E-print number: `hep-ph/0110215`.

[68] OPAL Collaboration (G. Abbiendi et al.), *A simultaneous measurement of the QCD colour factors and the strong coupling*, Eur. Phys. J. **C20** (2001) 601. E-print number: `hep-ex/0101044`.

[69] OPAL Collaboration (R. Akers et al.), *A Study of QCD structure constants and a measurement of $\alpha_S(M_{Z^0})$ at LEP using event shape observables*, Z. Phys. **C68** (1995) 519.

[70] OPAL Collaboration (R. Akers et al.), *A test of the flavor independence of the strong interaction for five flavors*, Z. Phys. **C60** (1993) 397.

[71] OPAL Collaboration (G. Abbiendi et al.), *Test of the flavour independence of α_S using next-to-leading order calculations for heavy quarks*, Eur. Phys. J. **C11** (1999) 643. E-print number: `hep-ex/9904013`.

[72] OPAL Collaboration (G. Abbiendi et al.), *Charged multiplicities in Z decays into u, d, and s quarks*, Eur. Phys. J. **C19** (2001) 257. E-print number: `hep-ex/0011022`.

[73] OPAL Collaboration (G. Abbiendi et al.), *Charged particle multiplicities in heavy and light quark initiated events above the Z^0 peak*, Phys. Lett. **B550** (2002) 33. E-print number: `hep-ex/0211007`.

[74] ALEPH Collaboration (D. Decamp et al.), *ALEPH: a detector for electron-positron annihilations at LEP*, Nucl. Instrum. Meth. **A294** (1990) 121.

[75] DELPHI Collaboration (P. A. Aarnio et al.), *The DELPHI detector at LEP*, Nucl. Instrum. Meth. **A303** (1991) 233.

[76] L3 Collaboration (B. Adeva et al.), *The construction of the L3 experiment*, Nucl. Instrum. Meth. **A289** (1990) 35.

[77] OPAL Collaboration (K. Ahmet et al.), *The OPAL detector at LEP*, Nucl. Instrum. Meth. **A305** (1991) 275.

[78] F. J. Hasert et al., *Observation of neutrino-like interactions without muon or electron in the Gargamelle neutrino experiment*, Phys. Lett. **B46** (1973) 138.

[79] UA1 Collaboration (G. Arnison et al.), *Experimental observation of lepton pairs of invariant mass around 95 GeV/c^2 at the CERN SPS collider*, Phys. Lett. **B126** (1983) 398.

[80] UA2 Collaboration (P. Bagnaia et al.), *Evidence for $Z^0 \rightarrow e^+ e^-$ at the CERN $\bar{p}p$ collider*, Phys. Lett. **B129** (1983) 130.

[81] UA1 Collaboration (G. Arnison et al.), *Experimental observation of isolated large transverse energy electrons with associated missing energy at $\sqrt{s} = 540$ GeV*, Phys. Lett. **B122** (1983) 103.

[82] UA2 Collaboration (M. Banner et al.), *Observation of single isolated electrons of high transverse momentum in events with missing transverse energy at the CERN $\bar{p}p$ collider*, Phys. Lett. **B122** (1983) 476.

[83] J. R. J. Bennett et al., *Design concept for a 100 GeV $e^+ e^-$ storage ring (LEP)*, CERN report number CERN-77-14 (1977).

[84] *LEP Design Report: Vol. 1. The LEP Injector Chain*, CERN report number CERN-LEP/TH/83-29 (1983).

[85] *LEP Design Report: Vol. 2. The LEP Main Ring*, CERN report number CERN-LEP/84-01 (1984).

[86] E. Picasso and G. Plass, *The machine design: LEP*, Europhys. News **20** (1989) 80.

[87] *LEP Design Report: Vol. 3. LEP2*, CERN report number CERN-AC-96-01-LEP-2 (1996).

[88] P. P. Allport et al., *The OPAL silicon microvertex detector*, Nucl. Instrum. Meth. **A324** (1993) 34.

[89] P. P. Allport et al., *The OPAL silicon strip microvertex detector with two coordinate readout*, Nucl. Instrum. Meth. **A346** (1994) 476.

[90] S. Anderson et al., *The extended OPAL silicon strip microvertex detector*, Nucl. Instrum. Meth. **A403** (1998) 326.

[91] G. Aguillion et al., *Thin scintillating tiles with high light yield for the OPAL endcaps*, Nucl. Instrum. Meth. **A417** (1998) 266.

[92] B. E. Anderson et al., *The OPAL silicon-tungsten calorimeter front end electronics*, IEEE Trans. Nucl. Sci. **41** (1994) 845.

[93] M. Arignon et al., *The pretrigger system of the OPAL experiment at LEP*, Nucl. Instrum. Meth. **A333** (1993) 330.

[94] J. R. Carter et al., *The OPAL vertex drift chamber*, Nucl. Instrum. Meth. **A286** (1990) 99.

[95] H. M. Fischer et al., *The OPAL jet chamber*, Nucl. Instrum. Meth. **A283** (1989) 492.

[96] H. Mes et al., *Design and tests of the z coordinate drift chamber system for the OPAL central detector at LEP*, Nucl. Instrum. Meth. **A265** (1988) 445.

[97] P. W. Jeffreys et al., *Development studies for the OPAL endcap electromagnetic calorimeter using vacuum photo triode instrumented lead glass*, Nucl. Instrum. Meth. **A290** (1990) 76.

[98] C. Beard et al., *Thin, high gain wire chambers for electromagnetic presampling in OPAL*, Nucl. Instr. Meth. **A286** (1990) 117.

[99] G. Artusi et al., *Limited streamer tubes for the OPAL hadron calorimeter*, Nucl. Instr. Meth. **A279** (1989) 523.

[100] R. J. Akers et al., *The OPAL muon barrel detector*, Nucl. Instrum. Meth. **A357** (1995) 253.

[101] G. T. J. Arnison et al., *Production and testing of limited streamer tubes for the endcap muon subdetector of OPAL*, Nucl. Instrum. Meth. **A294** (1990) 431.

[102] OPAL Collaboration (G. Abbiendi et al.), *Precision luminosity for Z^0 lineshape measurements with a silicon-tungsten calorimeter*, Eur. Phys. J. **C14** (2000) 373. E-print number: `hep-ex/9910066`.

[103] M. Arignon et al., *The Trigger system of the OPAL experiment at LEP*, Nucl. Instrum. Meth. **A313** (1992) 103.

[104] A. A. Carter et al., *A fast track trigger processor for the OPAL detector at LEP*, Nucl. Instrum. Meth. **A250** (1986) 503.

[105] J. T. M. Baines et al., *The data acquisition system of the OPAL detector at LEP*, Nucl. Instrum. Meth. **A325** (1993) 271.

[106] D. G. Charlton, F. Meijers, T. J. Smith, and P. S. Wells, *The online event filter of the OPAL experiment at LEP*, Nucl. Instrum. Meth. **A325** (1993) 129.

[107] Z. Kunszt and P. Nason, *QCD*, in "Z Physics at LEP 1", CERN report number CERN-89-08, vol. 1, p. 373 (1989).

[108] T. Omori, *A Matching Algorithm: MT package*, OPAL Technical Note 381 (1996).
[http://opal.web.cern.ch/opal/doc/technote/html/tn381.html].

[109] ALEPH, DELPHI, L3 and OPAL Collaborations (R. Barate et al.), *Search for the standard model Higgs boson at LEP*, Phys. Lett. **B565** (2003) 61. E-print number: hep-ex/0306033.

[110] J. Allison et al., *The detector simulation program for the OPAL experiment at LEP*, Nucl. Instrum. Meth. **A317** (1992) 47.

[111] OPAL Collaboration (G. Alexander et al.), *A comparison of b and uds quark jets to gluon jets*, Z. Phys. **C69** (1996) 543.

[112] OPAL Collaboration (G. Abbiendi et al.), *Tests of models of color reconnection and a search for glueballs using gluon jets with a rapidity gap*, Submitted to Eur. Phys. J. (2003). E-print number: hep-ex/0306021.

[113] M. Skrzypek, S. Jadach, W. Placzek, and Z. Was, *Monte Carlo program KORALW 1.02 for W pair production at LEP2/NLC energies with Yennie-Frautschi-Suura exponentiation*, Comput. Phys. Commun. **94** (1996) 216.

[114] S. Jadach, W. Placzek, M. Skrzypek, B. F. L. Ward, and Z. Was, *Monte Carlo program KORALW 1.42 for all four-fermion final states in e^+e^- collisions*, Comput. Phys. Commun. **119** (1999) 272. E-print number: hep-ph/9906277.

[115] J. Fujimoto et al., *grc4f v1.1: a four-fermion event generator for e^+e^- collisions*, Comput. Phys. Commun. **100** (1997) 128.
E-print number: `hep-ph/9605312`.

[116] D. Ward, *Separation of non-radiative $Z^0/\gamma \to q\bar{q}$ events at LEP2*, OPAL Technical Note 394 (1996).
[`http://opal.web.cern.ch/opal/doc/technote/html/tn394.html`].

[117] C. Ainsley, *Studies of $Z/\gamma \to q\bar{q}$ events with the OPAL detector at LEP II*, PhD thesis, University of Cambridge (2003).

[118] OPAL Collaboration (G. Abbiendi et al.), *W^+W^- production cross section and W branching fractions in e^+e^- collisions at 189 GeV*, Phys. Lett. **B493** (2000) 249. E-print number: `hep-ex/0009019`.

[119] OPAL Collaboration (G. Abbiendi et al.), *Charged particle momentum spectra in e^+e^- annihilation at $\sqrt{s}$ = 192–209 GeV*, Eur. Phys. J. **C27** (2003) 467. E-print number: `hep-ex/0209048`.

[120] M. Thomson, *The OPAL $qq\ell\nu$ event selection*, OPAL Technical Note 635 (2000).
[`http://opal.web.cern.ch/opal/doc/technote/html/tn635.html`].

[121] G. Cowan, *Statistical Data Analysis*. Oxford, UK: Clarendon (1998).

[122] ALEPH Collaboration (D. Buskulic et al.), *Studies of QCD in $e^+e^- \to hadrons$ at E_{cm} = 130 GeV and 136 GeV*, Z. Phys. **C73** (1997) 409.

[123] G. D. Lafferty and T. R. Wyatt, *Where to stick your data points: the treatment of measurements within wide bins*, Nucl. Instrum. Meth. **A355** (1995) 541.

[124] OPAL Collaboration, *Updated measurements of α_S using event shape observables*, OPAL Physics Note 512 (2002).
[`http://opal.web.cern.ch/opal/doc/physnote/html/pn512.html`].

[125] R. Barlow, *Application of the Bootstrap resampling technique to particle physics experiments*, Manchester University HEP preprint number MAN/HEP/99/4 (1999).
[`http://www.hep.man.ac.uk/preprints/manhep99-4.ps`].

[126] OPAL Collaboration, *A measurement of the W boson mass by direct reconstruction*, OPAL Physics Note 279 (1997). [`http://opal.web.cern.ch/opal/doc/physnote/html/pn279.html`].

[127] M. T. Ford for the OPAL Collaboration, *Measurements of α_S from QCD event shapes at OPAL and LEP*, Proceedings of the 9th High Energy Physics International Conference on Quantum ChromoDynamics ('QCD 02'), Montpellier, France, 2–9 July 2002, Nucl. Phys. Proc. Suppl. **121** (2003) 65.

[128] M. Donkers, S. Kluth, and C. Pahl, Private communications (2003). [`http://opalinfo.cern.ch/opal/group/qcd/lep2/lep2tables.html`].

[129] ALEPH Collaboration (R. Barate et al.), *Studies of quantum chromodynamics with the ALEPH detector*, Phys. Rept. **294** (1998) 1.

[130] ALEPH Collaboration (A. Heister et al.), *Studies of QCD at e^+e^- centre-of-mass energies between 91 GeV and 209 GeV*, Submitted to Eur. Phys. J. (2003). Report number: CERN-EP-2003-084.

[131] DELPHI Collaboration (P. Abreu et al.), *Consistent measurements of α_S from precise oriented event shape distributions*, Eur. Phys. J. **C14** (2000) 557. E-print number: `hep-ex/0002026`.

[132] J. Drees et al. for the DELPHI Collaboration, *QCD results from the measurements of event shape distributions between 41 GeV and 189 GeV*, Proceedings of the International Europhysics Conference on High-Energy Physics ('EPS-HEP 99'), Tampere, Finland, 15–21 July 1999 (Bristol, UK: IOP). Report number: CERN-OPEN-99-387 / DELPHI-99-114-CONF-301.

[133] J. Drees et al. for the DELPHI Collaboration, *The running of the strong coupling and a study of power corrections to hadronic event shapes with the DELPHI detector at LEP*, Proceedings of the 30th International Conference on High Energy Physics, Osaka, Japan, 27 July–2 Aug 2000 (Singapore: World Sci.). Report number: DELPHI-2000-116-CONF-415.

[134] L3 Collaboration (O. Adriani et al.), *Determination of α_S from hadronic event shapes measured on the Z^0 resonance*, Phys. Lett. **B284** (1992) 471.

[135] L3 Collaboration (M. Acciarri et al.), *QCD studies in e^+e^- annihilation from 30 GeV to 189 GeV*, Phys. Lett. **B489** (2000) 65.
E-print number: `hep-ex/0005045`.

[136] L3 Collaboration (P. Achard et al.), *Determination of α_S from hadronic event shapes in e^+e^- annihilation at $192 \leq \sqrt{s} \leq 208$ GeV*, Phys. Lett. **B536** (2002) 217. E-print number: `hep-ex/0206052`.

[137] OPAL Collaboration, *Measurement of α_S in radiative hadronic events*, OPAL Physics Note 519 (2003).
[`http://opal.web.cern.ch/opal/doc/physnote/html/pn519.html`].

[138] L3 Collaboration (M. Acciarri et al.), *Study of hadronic events and measurements of α_S between 30 GeV and 91 GeV*,
Phys. Lett. **B411** (1997) 339.

[139] H. Stenzel, Private communication (July 2002).

[140] H. Stenzel and G. P. Salam, Private communication (August 2002).

[141] The LEP QCD Working Group, *Preliminary combination of α_S values derived from event shape variables at LEP*.
Report number: ALEPH 01-038 Physic 01-012 /
DELPHI 2001-043 PHYS 893 / L3 note 2661 / OPAL Technical Note 689.
[`http://delphiwww.cern.ch/~pubxx/www/delsec/delnote/public/`
`2001_043_phys_893.ps.gz`].

[142] D. Wicke, Private communication (2002).

[143] S. I. Alekhin, *Statistical properties of the estimator using covariance matrix* (2000). E-print number: `hep-ex/0005042`.

[144] ALEPH, DELPHI, L3 and OPAL Collaborations, *A combination of preliminary electroweak measurements and constraints on the standard model*, Prepared from contributions of the LEP and SLD experiments to the 2002 summer conferences. E-print number: `hep-ex/0212036`,
ALEPH-2002-042-PHYSIC-2002-018, DELPHI-2002-098-PHYS-927,
CERN-L3-NOTE-2788, OPAL-PR-370.

[145] M. Dasgupta and G. P. Salam, *Event shapes in e^+e^- annihilation and deep inelastic scattering*, Submitted to J. Phys. G (2003).
E-print number: `hep-ph/0312283`.